

Ion Visa *Editor*

The 11th IFToMM
International
Symposium
on Science of
Mechanisms and
Machines

Mechanisms and Machine Science

Volume 18

Series Editor

Marco Ceccarelli, Cassino, Italy

For further volumes:
<http://www.springer.com/series/8779>

Ion Visa
Editor

The 11th IFToMM
International Symposium
on Science of Mechanisms
and Machines

 Springer

Editor
Ion Visa
Product Design, Mechatronics and Environment
Transilvania University of Brasov
Brasov
Romania

ISSN 2211-0984 ISSN 2211-0992 (electronic)
ISBN 978-3-319-01844-7 ISBN 978-3-319-01845-4 (eBook)
DOI 10.1007/978-3-319-01845-4
Springer Cham Heidelberg New York Dordrecht London

Library of Congress Control Number: 2013947817

© Springer International Publishing Switzerland 2014

This work is subject to copyright. All rights are reserved by the Publisher, whether the whole or part of the material is concerned, specifically the rights of translation, reprinting, reuse of illustrations, recitation, broadcasting, reproduction on microfilms or in any other physical way, and transmission or information storage and retrieval, electronic adaptation, computer software, or by similar or dissimilar methodology now known or hereafter developed. Exempted from this legal reservation are brief excerpts in connection with reviews or scholarly analysis or material supplied specifically for the purpose of being entered and executed on a computer system, for exclusive use by the purchaser of the work. Duplication of this publication or parts thereof is permitted only under the provisions of the Copyright Law of the Publisher's location, in its current version, and permission for use must always be obtained from Springer. Permissions for use may be obtained through Rights Link at the Copyright Clearance Center. Violations are liable to prosecution under the respective Copyright Law. The use of general descriptive names, registered names, trademarks, service marks, etc. in this publication does not imply, even in the absence of a specific statement, that such names are exempt from the relevant protective laws and regulations and therefore free for general use.

While the advice and information in this book are believed to be true and accurate at the date of publication, neither the authors nor the editors nor the publisher can accept any legal responsibility for any errors or omissions that may be made. The publisher makes no warranty, express or implied, with respect to the material contained herein.

Printed on acid-free paper

Springer is part of Springer Science+Business Media (www.springer.com)

Foreword

The International Symposium on Science of Machines and Mechanisms, SYROM runs every four years, starting from 1973, therefore the 11th edition in 2013 represents the fortieth anniversary of a scientific and professional meeting which steadily grew in extent and quality. SYROM is the most representative event organized by the Romanian Association for the Science of Machines and Mechanisms, ARoTMM, the Romanian branch of the International Federation for the Promotion of Mechanism and Machine Science, IFToMM.

In the past eight years, ARoTMM Presidency was held by the group in Transilvania University of Brasov; these were important years in defining the place and role of *Mechanisms* in the very fast development dynamics registered in all the knowledge fields; these were years when science, engineering science particularly, started to be more and more linked to industry, growing to meet the economy needs for progress and competitiveness. To face these challenges, new R&D paths must be found along with new education and training solutions. This is why, each year a working seminar was organized in different locations in Romania and organized by the ARoTMM member universities. These meetings represented opportunities for harmonizing the curricula on mechanisms and machines science, adapted to the various focus of the engineering study programs and to their levels (diploma, master's); as a result, a common view on integrating the design software was reached, aiming at preparing the graduates for the requirements of the novel global approach in high-tech product design: interdisciplinary teams, working all over the world and communicating in the common language of creativity and innovation. Quality education is the result of a strong link with research.

Starting already with 2007, the R&D trend set for engineering research was for answering to the needs of the industrial entities, and for stimulating the fast implementation of the research results into up-scalable processes. This was mirrored, at EU and at the Member States levels, complex priorities, focused on the output results—high-tech products, processes, services, etc., leaving behind the traditional approach on segmented input knowledge. This led to re-structuring the research targets which in the mechanisms fields had as consequence a rational approach of the complex high-tech product where all the components (including the mechanisms) should be developed and optimized for satisfying the main function.

This will be extensively continued during 2014–2020, through Horizon 2020, the next R&D program launched by EU. Any research program aims at identifying solutions to the most important problems identified for the community, which in this case is European Union; for EU this is *Energy* in all its aspects: production, consumption, transportation, etc., and the main strategic document that governs the future seven years is *The European Strategic Energy Technology Plan (SET Plan)*. The *SET Plan* is the primary document in defining the R&D priorities in Horizon 2020, having specific energy topics in two out of the three priorities (Industrial Leadership and Societal Challenges). Modifying the energy pattern by a continuous increase in the renewables share represents one key point and opens a large field for the development of novel, efficient renewable energy systems. Therefore mechanisms can well play a key role in the development of the new, green energy world. At the same time, the best way to protect the energy resources (renewable, fossil, or nuclear) is to lower the consumption while keeping (or increasing) the development rate and comfort. This requires complex solutions of energy efficient use, in high-tech products, industrial processes, buildings, automotive and transportation, etc., and here mechanisms are expected to bring significant contributions.

So, as in the past 40 years, SYROM welcomes researchers from all over the world to present the novel results of their work. The conference is timely scheduled for simulative discussions on the future of mechanisms, toward 2020 and beyond, and for developing partnerships able to meet the needs for sustainable development.

Prof. Dr. Eng Ion Visa

Scientific Program Committee

Cătălin Alexandru—Transilvania University of Braşov, Romania
Virgil Atanasiu—“Gh. Asachi” Technical University of Iaşi, Romania
Ioan Ardelean—Technical University of Cluj-Napoca, Romania
Ion Bostan—Technical University of Moldavia, Chişinău, Moldavia
Marco Ceccarelli—University of Cassino, Italy
Burkhard Corves—University of Aachen, Germany
Dorin Diaconescu—Transilvania University of Braşov, Romania
Ioan Doroftei—“Gh. Asachi” Technical University of Iaşi, Romania
Valeriu Dulgheru—Technical University of Moldavia, Chişinău, Moldavia
Grigore Gogu—IFMA Clermond Ferrand, France
Shuo Hung Chang—National Taiwan University, China-Taipei
Zhao Jun—Tianjin University, China-Beijing
Codruţa Jaliu—Transilvania University of Braşov, Romania
Erwin Lovasz—Politehnica University of Timişoara, Romania
Vistrian Mătieş—Technical University of Cluj-Napoca, Romania
Karl-Heinz Modler—Technical University of Dresden, Germany
Mircea Neagoe—Transilvania University of Brasov, Romania
Dumitru Nicolae—University of Craiova, Romania
Nicolae Orlandea—The University of Michigan, Michigan, USA
Victor Petuya—University of the Basque Country, Spain
Doina Pislă—Technical University of Cluj-Napoca, Romania
Alexandru Rus—University of Oradea, Romania
Teresa Zielinska—Technical University of Warsaw, Poland

Contents

Mechanism Design for Robots	1
Marco Ceccarelli	
A New Algorithm for an Efficient Stabilized Index Two STF for the Original ADAMS Computer Program.	9
N. V. Orlandea	
The Transmission of European Mechanical Knowledge into 17th-Century China	25
Baichun Zhang and Miao Tian	
Mechanisms in Building Integrated Renewable Energy Systems: Case Study—Solar Energy Conversion Systems	31
Ion Visa	
Conceptual Design of an Expressive Robotic Head	51
F. Adascalitei, I. Doroftei, D. Lefeber and Bram Vanderborcht	
On the Structural Analysis of the Mechanisms with Elastic Connections	59
Erwin-Chr. Lovasz, Dan Perju, Karl-Heinz Modler, Niels Modler, Corina Mihaela Gruescu, Inocențiu Maniu and Andrei Comșa	
An Innovative Family of Modular Parallel Robots for Brachytherapy	69
N. Plitea, C. Vaida, B. Gherman, A. Szilaghyi, B. Galdau, D. Cocorean, F. Covaciu and D. Pisla	
One 6R Overconstrained Mechanism, Many Applications.	81
Laurentiu Racila	
Research Regarding Modelling of Involute-Bevel Gears	91
Ioan Ardelean, Mircea Bara, Sergiu-Dan Stan and Sorin Besoiu	

Research Regarding the Modeling of the Reciprocal Generation of the Involute-bevel Gears with Crossed Axes	101
Ioan Ardelean, Olimpiu Tătar and Emil Teutan	
A Dynamic Simulation of a Novel Continuous Variable Transmission.	109
Gani Balbayev and Giuseppe Carbone	
Design and Simulation of a Leg Exoskeleton Linkage for a Human Rehabilitation System	117
C. Copilusi, M. Ceccarelli, N. Dumitru and G. Carbone	
Protein Secondary Structure Detection Using Dihedral Angle Parameters Evaluation.	127
Mikel Diez, Víctor Petuya, Imanol Martínez and Alfonso Hernández	
Optimal Design of the Motion Law for a Pseudo-Azimuthal Tracking System	135
Monica Alina Ioniță and Cătălin Alexandru	
Comparative Study of Two 2-DOF Parallel Mechanisms Used for Orientation	145
Tiberiu Itul, Bogdan Gherman and Doina Pîslă	
Kinematic and Dynamic Modeling and Simulation of an Intelligent Adaptive CTLSO Brace	159
D. Mărgineanu, E.-Ch. Lovasz, L. V. Ciupe and L. Ciurdariu	
Virtual Model for Kinematic Analysis of Human Upper Limb	169
Elena Mereuta, Marian Tudoran, Daniel Ganea and Claudiu Mereuta	
Estimating the Muscle Force Using a Kinematic Model of the Human Upper Limb	179
Elena Mereuta, Marian Tudoran, Daniel Ganea and Claudiu Mereuta	
Formulations in Advanced Dynamics of Mechanical Systems	185
I. Negrean, C. Schonstein, K. Kacso and A. Duca	
Gray-Box Modeling and Closed-Loop Temperature Control of a Thermotronic System.	197
C.-R. Rad, O. Hancu and C. Lapusan	

On the Eccentricity Effects in Solar Tracking Triangular Linkage with Eccentric Linear Actuator	209
Radu Saulescu, Olimpiu Munteanu, Mircea Neagoe and Nadia Crețescu	
Influence of Mechanical Press Dimensions on its Kinematic Behavior	217
Iulian Tabără and Constantin Dogariu	
Nonlinear Analysis of Osteoarthritis Process in Virtual Human Knee Joint	223
D. Tarnita, M. Catana and D. N. Tarnita	
Creating Artistic Curves with Planar Mechanisms	233
D. Tarnita, I. Popescu and D. Marghitu	
Optimal Design of the Front Suspension Mechanism Used for a Race Car	243
Vlad Țoțu and Cătălin Alexandru	
Educational Pneumatic Engine for a Small Size Vehicle	255
Tiberiu Vesselenyi, Alexandru Rus, Mircea Bogdan Tătaru and Tudor Mitran	
A Structural Synthesis of a New Leg Mechanism	263
I. Dugaescu, M. Ceccarelli and A. Comanescu	
Regression Model for Optimizing the Thin Films Deposition on Planar Photovoltaic Cells	277
Monica Enescu and Cătălin Alexandru	
About Speed Breaker Synthesis with No Deterioration of the Car Suspension	287
V. Mesaros-Anghel, E. Ianosi, I. Carabas and L. Madaras	
Structural Systematization and Kinematic Analysis of Redundant Kinematic Chains with 7 and 8 Axes for Robots.	297
Ionel Staretu	
A Method for Experimental Identification of Nonlinear Mechanical Systems.	307
Adina Bălan, Mihai Petru Draghici, Radu Donca, Alin Pleșa and Vistrian Mătieș	

Innovative Tracking System for Parabolic Dish Solar Collector	317
Daniela Ciobanu and Codruta Jaliu	
Interactive Animation Production by Means of Advanced Image Processing.	329
V. Ciupe, E.-Ch. Lovasz, M. Reessing, V. Henkel, C. M. Gruescu and E. S. Zabava	
Vibrations Concerning with Safety in Vehicle Rolling Conditions.	339
Mircea Diudea, Victor Hodor, Radu Balan and Mircea Bara	
Control Method Comparison for Pneumatic Artificial Muscle Actuators	351
Mihai Petru Draghici, Calin Rusu, Alin Plesa, Radu Balan and Sorin Besoiu	
Advances in Optomechanical Scanning Technologies for High-End Biomedical Applications	361
V.-F. Duma	
Mechatronic System with Applications in Medical Robotics	371
Nicolae Dumitru and Violeta Cristina Dumitru	
Low-Speed Actuator Used in Solar Tracking Systems.	381
Codruta Jaliu, Mircea Neagoe, Radu Săulescu and Edith-Bianca Dobre	
WiSeIn: Wireless Sensor Network Used for Data Acquisition from Indoor Locations.	391
Marius C. Luculescu, Sorin C. Zamfira and Luciana Cristea	
WiSeManS: Wireless Sensor Network Data Management System for Indoor Climatic Control.	401
Marius C. Luculescu, Sorin C. Zamfira and Luciana Cristea	
Four-Bar Linkages with Linear Actuators Used for Solar Trackers with Large Angular Diurnal Strokes	411
Macedon Dumitru Moldovan, Ion Visa, Radu Saulescu and Mihai Comsit	

Study of the Contact Between Toothed Chains and Guides 425
 Radu Papuc, Radu Velicu and Mihai Lates

Study of the Curved Plate Spring Behavior for Small Displacements 433
 Hariton Poparad

Study of the Motion of Random Axes Using the Coupling with Curved Plate Springs. 443
 Hariton Poparad

Scanners with Risley Prisms: Modelling with Mechanical Design Programs. 453
 A. Schitea, I. Kaposta, M. Tuef, S.-C. Jurca and V.-F. Duma

Applications of the Ackerman Steering and Electronic Differential in Modern Electric Drive Automotive Systems 463
 A. Szilagyi, V. Ciupe and I. Maniu

Geometric Modeling of Power Joints from Bush Chain Drives 471
 A. Todi-Eftimie, R. Velicu, R. Saulescu and C. Jaliu

One-DOF Mechanisms for Dual-Axis Solar Tracking 481
 Ion Visa, Monica Vatasescu, Mircea Neagoe and Bogdan Gabriel Burduhos

Findings on Italian Historical Developments of Machine Technology in 19th Century Towards Industrial Revolution 493
 Yibing Fang and Marco Ceccarelli

Considerations Regarding the Process of Integration the Mechanisms in the Structure of the Mechatronic Systems. 503
 V. Maties, O. Hancu, C.-R. Rad and L. Dache

Dedicated Gripper for Books Handling in a Library 515
 N. Modler, A. Comsa, I. Maniu, E.-Ch. Lovasz and V. Ciupe

Review on Mechanisms Used as Handbrake in Carriages and Locomotives 523
 Ovidiu Antonescu, Ionut Geonea and Paun Antonescu

Using Mathematica Program in Teaching Mechanisms. 531
 Madalina Rus, Silvia Veresiu and Elena Mereuta

Using Computer Aided Design in Teaching Mechanisms	541
Silvia Vereşiu, Mădălina Rus and Elena Mereuță	
Author Index	549

Mechanism Design for Robots

Marco Ceccarelli

Abstract Robots are based on mechanical structures with mechanisms that play an important role on functionality and performance characteristics with a variety of solutions. A short account of mechanisms in robots is presented in this paper with significant examples and main concepts by an illustration approach also with the aim to stressing challenges for future developments.

1 Introduction

Robots are the today machines with the most advanced solutions with such a mechatronic design and operation that it is often believed that their performance do not depend of mechanical aspects. It is indeed true that mechanical components can be less and less and even with reduced influence on the overall design of mechatronic systems. But when the ultimate goal of a machine, even when it is an advanced robot, is related to interaction with humans or performing a human-like tasks, then the role of mechanical aspects are fundamental for the machine success and mechanism functioning is essential (Ceccarelli 2011).

Indeed, a robot design is generally considered by properly looking at the mechanical structure as a first step of the design, as indicated in most of the books and handbooks on Robotics, like for example (Nof 1985; Craig 1986; Siciliano and Khatib 2008; Ceccarelli 2012). A considerable literature is today available worldwide on design of robots with different perspective and approaches both in past and recent publications, like for example (Paul 1982; Popov 1982; Yoram 1987; Kobrinski and Kobrinski 1989; Seling 1992; Ceccarelli 2004; Saha 2011)

M. Ceccarelli (✉)

Laboratory of Robotics and Mechatronics, University of Cassino and South Latium,
South Latium, Italy

e-mail: ceccarelli@unicas.it

just to cite few of the last ones in which a significant role is addressed to mechanics of robots.

Recently, a specific well-focused attention on mechanism design for robots has been addressed through a specific conference on the subject. Namely a conference series Mechanism Design for Robots (MEDER) has been started in 2010 in Mexico City (Acevedo 2010) with a second event in Beijing (Ding 2012) and a third event is scheduled in Copenhagen for 2015. The conference topics include all the aspects of robot design in which the mechanical aspects for mechanism design pay role and influence in performance and operation of robotic solutions.

In this chapter the topic is discussed with an illustration approach to indicate aspects of mechanism design for robots that can be considered with a significant role in robot design and operation.

2 Robot Structure and Mechanism Role

A robot can be defined as a system which is able to perform several manipulative tasks with objects, tools, and even its extremity (end-effector) with the capability of being re-programmed for several types of operations. It is obtained as an integration of mechanical and control counterparts, but it even includes additional equipment and components, concerned with sensorial capabilities and artificial intelligence. The simultaneous operation and design integration of all the above-mentioned systems will provide a robotic system, whose structure is illustrated in Fig. 1a (Ceccarelli 2004). The mechanical capability is concerned with versatile characteristics in manipulative tasks due to the mechanical counterparts, and re-programming capabilities is concerned with flexible characteristics in control abilities due to the electric-electronics-informatics counterparts. Therefore, a robot can be considered as a complex system that is composed of several systems and devices to give:

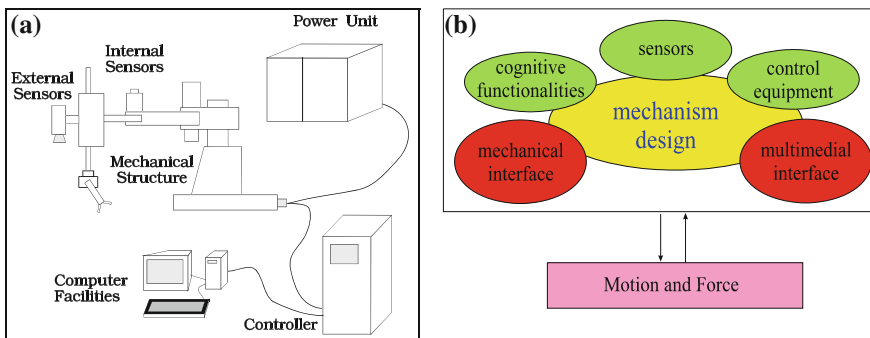


Fig. 1 General structure of robots. **a** Unit components. **b** Functionalities

- mechanical capabilities (motion and force);
- sensorial capabilities (similar to human beings and/or specific others);
- intellectual capabilities (for control, decision, and memory).

Mechanical versatility of a robot can be understood as the capability to perform a variety of tasks because of the kinematic and mechanical design of its mechanical structure performing manipulation tasks. Re-programmability of a robot can be understood as the flexibility to perform a variety of task operations because of the capability of its controller and computer facilities.

In Fig. 1b functionality of a robot system is stressed as function of its structure in which mechanism design pays a fundamental role for the operation goals in motion and force transmission.

A mechanism is well understood as a multi-body mechanical system whose main purposes are related to transmission of motion and force from an input link to an output body within its structure. Mechanisms include a wide class of mechanical systems such as linkages, cam and gearing systems, and even multi-body systems with no-rigid elements. Mechanism Design is the discipline of MMS which is devoted to all the aspects of mechanism development as concerning with theory, analysis, synthesis, practice, and construction of mechanisms, Some times the term mechanism indicate the kinematic structure as well.

As referring to schemes in Fig. 1, emphasis is addressed to the mechanism structure but a robot can be properly designed and operated when all the units are fully integrated and cooperating with each other in fulfilling the robot tasks. Nevertheless, it is evident that the mechanical nature of the interaction with the environment in performing a task makes the mechanism structure of a robot fundamental for its success, much more than the other units. But the other units are necessary for an efficient success both in term of performance characteristics and the above-mentioned versatility and flexibility.

Mechanism structure in a robot is often studied and designed with specific mechanisms within the mechanical structure with primary function to facilitate or to enhance motion transmission from power units to robot links. Thus, mechanisms in robots are in general used with two primary goals, namely to perform the mechanical tasks and to provide powered motion of its structure.

In the following section, few examples are used to illustrated such a role of mechanisms in robot designs.

3 Examples of Mechanisms in Robots

A short illustration survey of examples of mechanism designs in robot designs is presented with the aim to show the structure and role of mechanisms in robot developments.

3.1 Industrial Manipulator Robots

Industrial robots have been designed and are still based on serial open kinematic chains which can be completed with planar mechanisms to increase the static accuracy and to install actuators near to base frame. Examples are shown in Fig. 2.

Other structures for industrial robots have been recently used with architectures of parallel manipulators. In these cases the peculiar performance with high stiffness and high speed are due to the mechanism chains as for the robots in the illustrative examples in Fig. 3.

Mechanisms both as linkages and gearing systems are used even more and more even for balancing purposes, even within their primary purposes of mechanical structure.

As outlined in the examples of Figs. 2 and 3 industrial robots are used for manipulation tasks whose characteristics strongly depend on the mechanism design of the mechanical structure and its operation performance.

3.2 Legged Walking Robots

In mobile robots locomotion is obtained by using mechanism solutions even by mimicking the animals in nature. Nevertheless, for legged walking robots linkages have been the main sources of structure since the early solutions, as in the examples shown in Fig. 4. Today most of the legged robots show an anthropomorphic design or they have a structure which is based on pantograph linkage or even on parallelograms. Examples are illustrated in Fig. 5.

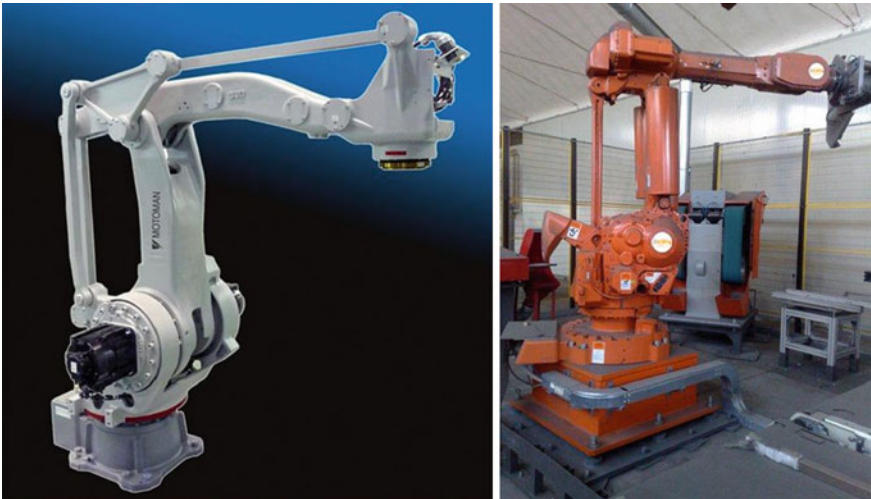


Fig. 2 Examples of mechanisms in the structure of serial manipulator robots

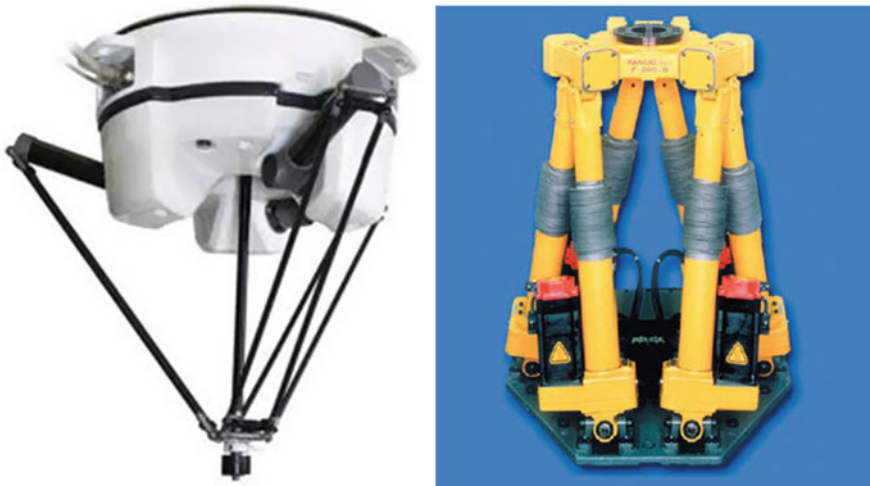


Fig. 3 Examples of parallel architectures in industrial robots

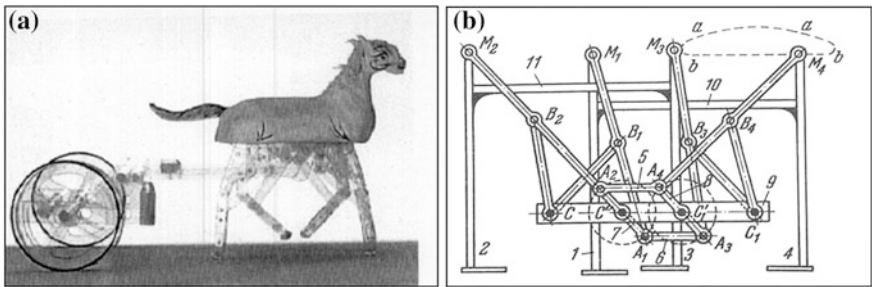


Fig. 4 Linkages in early legged mobile robots. a The Chinese cow machine. b Chebyshev walking machine



Fig. 5 Examples of leg mechanisms in walking robots

The leg mechanisms for walking solutions are examples in which a mechanism design is essential in achieving the action that a robot is devoted to. This is because legged locomotion is a mechanical task and its performance is due to kinematic and dynamic characteristics of the used mechanisms.

3.3 Grasping Devices

Grasping is a mechanism-based task in which both motion and force concur simultaneously to the robotic function. Grippers and fingers in artificial hands are designed as based on mechanisms with proper mobility and force transmission capability both in industrial applications and non-conventional solutions. Examples are shown in Fig. 6.

Grasp is a function whose mechanical nature requires a careful attention to mechanical interaction via mechanical solutions and mechanisms are the core this functioning.

4 Trends for Mechanism Design in Robots

From the above examples it is once again more evident the fundamental role of mechanisms as multi-body mechanical systems performing motion and force transmission both for robot operation and task performance. Although it can be observed that most of the used mechanisms make use of traditional solutions, even if with smart designs and novel designs, nevertheless the functioning as well as the

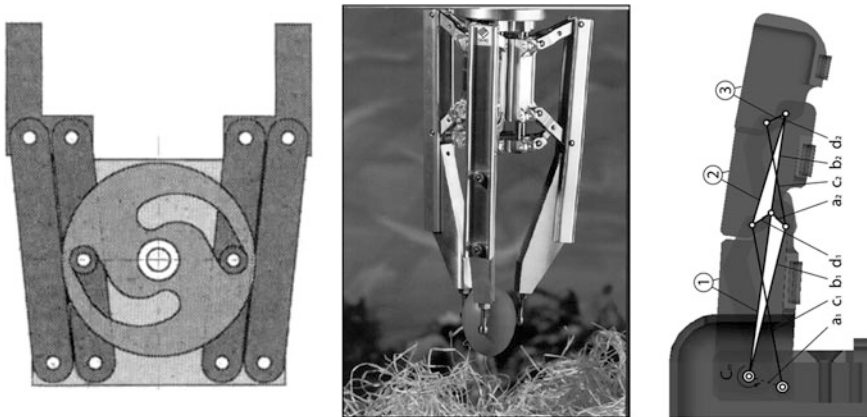


Fig. 6 Examples of mechanism designs in grippers and fingers for artificial hands

size needs to be adjusted to the robot applications. This requires very often a novel attention and approach both to the design and running of those mechanisms.

Thus, problems for a challenging future of mechanism improvements in robots will be attached with novel attention mainly in:

- mechanical efficiency, for better mechanical transmission and reduced actuating power
- light design, for larger payload and size reduction
- static accuracy, for better grasping configurations
- dynamic response, for controlling impulsive actions and better consideration of manipulation dynamics

as concerning traditional subjects but with relationship to the overall robot design. In addition, new problems can be identified for new solutions in:

- topological mechanism structures, for new enhanced designs
- materials, for better mechanical design and environment interaction
- tribology issues, for reduction of wear and longer accurate functioning with limited friction
- energy sustainable solutions, for better attention to energy saving and recycling of wasted components
- contamination free conditions, for considering environment influence of operation and manufacturing of mechanisms.

The short above lists want to indicate that both new issues and reconsideration of existing solution and past experiences, even with more subjects, will be the focus for the challenges in the future mechanism design for robots within increased mechatronic evolutions.

Summarizing these short notes, mechanisms in robots will always have an important role since ultimate goals of a robot include its motion and additional task with mechanical features. Challenges are and will be more demanding in mechanism solutions that will enhance those performance with the help of robot units of different natures in more and more integrated mechatronic solutions both for the design and operation.

5 Conclusions

In this paper a central role of mechanisms in robots is presented as function of the mechanical nature of robot functioning and ultimate tasks. The future is shortly discussed with challenges in making those mechanisms fully integrated in the quick evolution of other units within a mechatronic solution both for design and operation.

References

- Acevedo M (ed) (2010) IFToMM Symposium for mechanism design for robotics. In: CD Proceedings, Mexico City
- Ceccarelli M (2004) Fundamentals of mechanics of robotic manipulation. Kluwer/Springer, Dordrecht (ISBN 1-4020-1810-X)
- Ceccarelli M (2011) Problems and issues for service robots in new applications. *Int J Soc Robot* 3(3):299–312. doi: [10.1007/s12369-011-0097-8](https://doi.org/10.1007/s12369-011-0097-8)
- Ceccarelli M (ed) (2012) Service robots and robotics: design and application. Engineering Science Reference (IGI Global), Hershey. ISBN 978-1-4666-0293-9
- Craig JJ (1986) Introduction to robotics. Addison-Wesley, Boston
- Ding X (ed) (2012) IFToMM symposium for mechanism design for robotics. In: CD Proceedings, Beijing
- Seling JM (1992) Introductory to robotics. Prentice Hall, London
- Siciliano B, Khatib O (eds) (2008) Springer handbook of robotics, Part F: field and service robotics (Alexander Zelinsky), Springer, Berlin. ISBN: 978-3-540-23957-4
- Kobriniski AA, Kobriniski AE (1989) Bras manipulateurs des Robots. MIR, Moscow
- Nof SY (ed) (1985) Handbook of industrial robotics. Wiley, NY
- Paul RP (1982) Robot manipulators. MIT Press, Cambridge
- Popov EP (1982) Modern robot engineering. MIR, Moscow
- Saha SK (2011) Introduction to robotics. Mc Graw Hill, New Delhi
- Yoram K (1987) Robotics for engineers. Mc-Graw Hill, Singapore

A New Algorithm for an Efficient Stabilized Index Two STF for the Original ADAMS Computer Program

N. V. Orlandea

Abstract Numerical integration methods such as Index Two (I2) and Stabilized Index Two (SI2) gave good results. However, one of their drawbacks, especially for SI2 is an increase of the number of equations with a decrease of sparsity, that somehow reduces the simulation productivity. At the same time methods like I2 and Index One (I1) that use only velocity and accelerations constraints, when simulating tough problems, produce a drift in the displacements so that the geometrical constraints are not satisfied anymore. Hence, an ideal solution will be to use a stabilized method that satisfies the geometric constraints, like the Index Three (I3), reduces the noise in the acceleration and Lagrange Multipliers, as the SI2, at the same time, maintaining the number of equation and sparsity of I3. In this way the simulations produce correct results with good productivity. This paper discusses such an algorithm.

Keywords Original ADAMS · MCADA · SI2 · I2 · I1 · I3 · Stabilized index · STF

1 Introduction

In 1973 the first version of Automatic Dynamic Analysis of Mechanical Systems (ADAMS) computer program was announced and used for the first time to simulate the dynamic behavior of mechanical systems like car suspension and glassy carbon lattice that lined nuclear reactors. It was the result of the PhD thesis of this author. The ideas incorporated in this computer program were at the time innovative. Manly they were captured in the formulation because the idea of non eliminating variables gave a mixed system of simple equations composed from

N. V. Orlandea (✉)
University of Michigan, Ann Arbor, MI, US
e-mail: orlanico@umich.edu
URL: <http://www-personal.umich.edu/~orlanico>

“Differential and Algebraic Equations”, in short DAE. Considering the numerical stability of the numerical integration methods, the Gear implicit Backward Difference Formula method or BDF, described in (Gear 1971), was elected. New at the time, the method is a predictor corrector algorithm and the mixed set of equations offered by the formulation became part of its corrector. By not eliminating any variable the system of equations is large, however, in the process of linearization required by the numerical integration method the system’s matrix called the “Dynamic Jacobean” becomes very sparse. This formulation was named the “Sparse Tableaux Formulation” or STF. Special methods designed and developed by Calahan (1972), for sparse matrices were adopted. The effect of this was that the speed of the simulations has been improved substantially and in many occasions it performed better than the traditional methods.

ADAMS computer program originally was designed for mechanisms. Being developed at the University of Michigan, in a very short time was adopted by the Auto Industry and then was extended to Airspace, Ag., Industrial Equipment Industries, Army etc.

The original ADAMS formulation incorporates the idea that it is OK to increase the number of equations as long as the entire system of equation become simpler, than before, and the sparsity of the corrector formula increases. How is the sparsity measured? The sparsity is the inverse of the average number of the nonzero elements per row of the Jacobean matrix. For instance if the average number of the nonzero elements per row of the corrector Jacobean is $n = 3$, then this is a higher sparsity than when $n = 5$. In many cases the speed of solving a system of equations having a sparse matrix decreases with decreasing sparsity. Good results are obtained for a sparsity $n < 10$.

Another important point in ADAMS technology was the modularization that was inspired by the pattern of the nonzero elements of the links, joints and forces. Hence, pattern libraries were assembled for joints such as spherical joints, revolute joints, cylindrical joints and others. Force libraries could be developed based on the fields such as auto industry, aerospace industry, etc. This is important because it permits a one to one mapping of the physical mechanical system into the mathematical form of the Jacobean matrix.

The program worked well with a constant time step. However, when time step changed as it was required by the error control and by the problems at hand, some spikes in the accelerations and Lagrange multipliers were observed. The difficulty was that they were not consistent. In studding these problems it was discover that there were two main factors that influenced these spikes.

The first factor was the users. The real systems in industry have discontinuities. The initial conditions change over discontinuities. The way how theoretically correct one solves these discontinuities is to sense them compute the new initial conditions and then restart the numerical integration. Such an example can be a mechanical impact during the simulation. It is know that the conditions such as velocities changes during of impact and a δ function that expresses an instant infinite force is not very helpful either. Nor are the Laplace transforms in the time

domain simulations. So based on the momentum conservation law the new velocities can be computed.

Adopting the computed velocities as new initial conditions the integration can be restarted. In general the users do not do that. What are they doing? They are “plowing” their way through discontinuities and of course they get errors that can not be interpreted.

A good way to fix this situations is to smooth the functions. Such an example is the crank—rocker linkage from Fig. 1, that has an impact in the point M. In this case the mechanism starts moving under the initial conditions. After 1.3 s the rocker hits a steel stop M. The last frame to the right in Fig. 1 is close to the impact position. The restitution coefficient is 0.75 determined by the steel on steel impact. After reducing the mass of the mechanism in the impact point the impulse is calculated based on the momentum conservation law. By choosing a very small time interval as $t_0 = 0.0125$ s it results the rectangle represented in the Fig. 2. What criteria exists for choosing the time interval? Nowadays it is determined experimental by using high speed photography or electronic measuring systems. For instance in this case the height “ H ” of the rectangle represents the force and the rectangle area represents the computed impulse. By considering a continuous and smooth function as $H \times (1 - \cos(2\pi \times t/t_0))$ that is tangent to the time axis it result the curve from Fig. 2. The curve has the height equal to $2 \times H$ and an area equal with the area of the rectangle. This smoothing has an effect on the variation of the velocities during the impact.

The jump of the velocities has a ramp close to a step, Fig. 3, that is upwards and it extends over the interval $t_0 = 0.0125$ s. Of course this is an approximation,

Fig. 1 The mechanism has an impact in point M

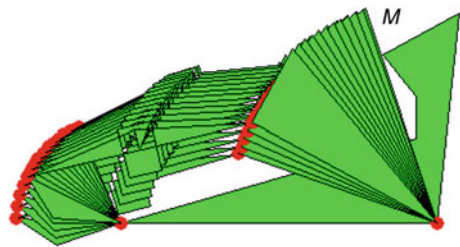


Fig. 2 Force and impulse

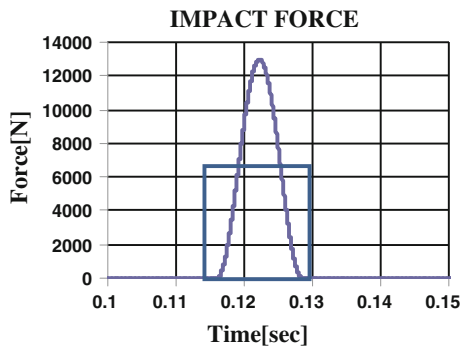
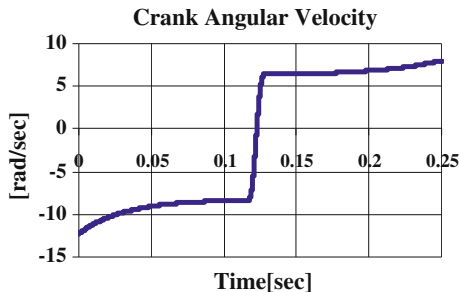


Fig. 3 Impact velocity jump



however, the results are comparable to the classical theory of the impact. A correction of 0.035 in the restitution factor gives identical results.

The second factor is the index problem. Gear introduced the concept of index and is discussed in detail in (Gear 1988) and (Brenan et al. 1989). Basically the index is an way to measure the difference between the DAE and ODE “Ordinary Differential Equations”. The measure is the number of derivatives that must be performed to transform the DAE system into an ODE system.

However, for the mechanism people it is important to know that the index may be expressed as a function of the constraint equation. For instance if one uses the displacement (position) constraints the system has an index, I3. In this case the system is stabilized in a sense that is not going to introduce drifting in the mechanism’s joints. However, without reducing to a lower index the simulations have spikes in accelerations and Lagrange Multipliers when the integration changes the time step.

Using the velocity constraints gives the I2 method. This is more accurate for the computed velocities and accelerations than I3. This method, for very tough problems, introduces a drift in joints, but not as much as when using the acceleration constraints, I1. For normal problems it works well and the results are excellent. For tough problems there are two solutions: the first one is to consider the displacement constraint together with velocity constraints. This is defined as a “Stabilized Index 2” method or in short is the SI2. This method increases the number of equations and also decreases the sparsity. It does loose part of the simulation speed. It works very well for any problem. The second solution is to monitor the drift in joints and to construct an error control on the drift. If the drift is greater than the error value then switch to SI2 for a short time (3–4 time steps) and then switch back to I2. This will allow for the simulation productivity to be better than the SI2.

Using the acceleration constraints will give an “Index 1” method or in short I1. For this situation the problems are growing. First, because the acceleration constraints are more dense the sparsity of the system decrease. Second, the drift in joints is pronounced quadratically. As a solution the acceleration constraints can be combined with the displacement constraints and the velocity constraints to give the SI1. Orlandea and Coddington (1996), has shown that SI1 does not have substantial accuracy advantages over SI2.

There are other ways to reduce the index of the STF formulation. That will be discussed further in this paper.

2 Reducing the STF Index

In this part it will be shown some proprieties of the BDF formula used in the context of ADAMS computer program. Then the original formulation of the ADAMS's numerical engine and how this formulation has to be changed for a new stable index reduction method.

The BDF Gear formula as given in (Calahan 1972) and is:

$$\alpha_0 \underline{x}^{n+1,m+1} = -h\beta_0 \dot{\underline{x}}^{n+1,m} - \sum_{j=1}^k (\alpha_j \underline{x}^{n-j+1}). \quad (1)$$

n represents the number of the successful integration steps, m represents the iteration number at point n , h is the time step, α_0 and β_0 are BDF coefficients and finally \underline{x} and $\dot{\underline{x}}$ are the vectors of the displacements and velocities. The summation refers to the points from n to $n-k$ that is part of the history. Its value remains constant when computing point $n + 1$.

Linearizing (1) for a Newton-Raphson iteration the result is:

$$-\alpha_0 \Delta \underline{x}^m - \beta_0 h \Delta \dot{\underline{x}}^m = \alpha_0 \underline{x}^m + h\beta_0 \dot{\underline{x}}^m + \sum_{j=1}^k (\alpha_j \underline{x}^{n-j+1}). \quad (2)$$

Considering that $\Delta \underline{x}^m = \underline{x}^{m+1} - \underline{x}^m$ and $\Delta \dot{\underline{x}}^m = \dot{\underline{x}}^{m+1} - \dot{\underline{x}}^m$ formula (2) changes to

$$-\alpha_0 \underline{x}^{m+1} - \beta_0 h \dot{\underline{x}}^{m+1} = \sum_{j=1}^k (\alpha_j \underline{x}^{n-j+1}) \quad (3)$$

writing a similar relation for iteration m it is obtained:

$$-\alpha_0 \underline{x}^m - \beta_0 h \dot{\underline{x}}^m = \sum_{j=1}^k (\alpha_j \underline{x}^{n-j+1}) \quad (4)$$

By subtracting Eq. (4) from Eq. (3) the result is,

$$\Delta \dot{\underline{x}}^m = -\frac{\alpha_0 \Delta \underline{x}}{\beta_0 h}. \quad (5)$$

Formula (5) represents the fundamental BDF formula. The method starts with the first order which is known as the backward Euler Numerical Integration Algorithm and it goes up to the sixth order based on the error control decisions.

Higher order means higher accuracy. It also means less numerical stability. The order is given by the highest degree of the interpolation polynomial that the method uses.

An interpolation polynomial can be defined by the number of points that are required for it to satisfy. The same polynomial can also be defined by its higher order derivatives with respect to the integration variables. The last procedure is favored here because it determines a Taylor series as an explicit predictor. The transformation from the form (4) to the form that uses higher order derivatives is done by means of so called Nordsiek vector (Gear 1971). An order equal with p for the numerical integration method will require the highest order derivative to be of the order $p + 1$. This is called the normal form. However, the form (5) remains the same and only the coefficients in (5) changes. Using a Taylor series as a predictor is part of the normal form of the BDF method. The coefficients for the BDF normal form for different orders of the method can be found in (Gear 1971). And the form used in ADAMS is the normal form:

$$\Delta \underline{\dot{x}}^m = - \frac{\Delta \underline{x}^m}{l_0 h} \quad (6)$$

l_0 changes as a function of the order, but for the Backward Euler it is equal with 1.

For a mechanical stand point, the original ADAMS formulation is at the basis of the index reduction method that will be further described here. Based on the principles of the theoretical mechanics, the fundamental true assumption that stands at the root of this formulation is that any constrained mechanical body can be dynamically treated as a free moving body if the constraints forces and the applied forces are determined correctly and are applied on that body.

For determining the forces given by the constraints it is considered the vector

$$\underline{\Phi}_c(\underline{q}) = \underline{0} \quad (7)$$

of the constraints as functions of the generalized coordinates vector $\underline{q}(t)$.

The velocity constraints are:

$$\frac{\partial(\underline{\Phi}_c)}{\partial \underline{q}} \underline{\dot{q}} = \underline{0}, \quad (8)$$

for accelerations the constraints are:

$$\underline{\dot{q}}^t \frac{\partial^2(\underline{\Phi}_c)}{\partial \underline{q}^2} \underline{\dot{q}} + \frac{\partial(\underline{\Phi}_c)}{\partial \underline{q}} \underline{\ddot{q}} = \underline{0} \quad (9)$$

Using (9), the drift in the geometric and velocity constraints is large (quadratic) and it must be used only in conjunction with Eq. (7) or the Baumgarte stabilization method (Baumgarte 1972). Although it looks innocent, the first term of the Eq. (9) require a tensor evaluation that has a large number of operations reducing

substantially the simulation speed. A lot of people are using Eq. (9) because it is linear in generalized accelerations.

The internal reaction forces in a matrix format are:

$$\frac{\partial \underline{\Phi}_c^t}{\partial \underline{q}} \underline{\lambda} = \underline{F}_c \quad (10)$$

t in formula (10) indicates the transpose of the matrix of the partial derivatives of the constraints functions with respect to generalized coordinates. \underline{F}_c is the vector of constraints forces. It is also called the internal force vector or the vector of the reaction forces. One important result is that the number of the Lagrange Multipliers λ must be equal with the number of scalar functions of constraints. When simulating a mechanical system the Lagrange Multipliers are unknowns and they are iterated together with displacements and velocities. Because ADAMS started as a simulation program for mechanisms, by means of modularization, a library of joints was developed. It contains the partial derivatives of the constraints functions, $\partial \underline{\Phi}_c / \partial \underline{q}$ and $\partial \underline{\Phi}_c^t / \partial \underline{q}$, for different types of joints as described in (Orlandea 2008). The geometric constraints and the Lagrange Multipliers λ are algebraic equations and algebraic variables. Gear has shown in (Gear 1988) that the index for this case is three and has to be reduced for consistent, not only sporadic, good results in accelerations and Lagrange Multipliers.

The differential equations of motion has to be determined and combined with the constraint functions and Lagrange Multipliers. For simulation of mechanical systems the stabilized index two DAE system is:

$$\begin{aligned} \underline{F}_d &= \underline{F}_i(\underline{\dot{u}}_i, \underline{u}_i, \underline{q}_i, t) + \sum_j \frac{\partial \underline{\Phi}_j^t}{\partial \underline{q}} \lambda_j + \sum_k \underline{F}_k(\underline{u}_i, \underline{q}_i, t), \\ \underline{F}_r &= \underline{u}_i - \underline{\dot{q}}_i + \sum_j \frac{\partial \underline{\Phi}_j^t}{\partial \underline{q}} \eta_j, \\ \underline{F}_g &= \underline{\Phi}_j, \\ \underline{F}_v &= \frac{\partial \underline{\Phi}_j}{\partial \underline{q}_i} \underline{\dot{q}}_i. \end{aligned} \quad (11)$$

In the Eq. (11), \underline{F}_d represents the differential equations for body i , \underline{F}_r represents the reduced order of the differential equations for body i , \underline{F}_g represents the geometric constraints of the body i , and, \underline{F}_v represents the velocity constraints of the body i . \underline{F}_k represents the external forces that may be applied on body i , and they can be combined with the functions \underline{F}_i . $\underline{\eta}$ is the vector of the supplementary Lagrange Multipliers that are used to square the linearized Jacobean matrix when the geometric and velocity constraints are used for the index reduction.

For the Newton–Raphson iteration the system of the DAE (11) should be put in the residual form:

$$\underline{E}_d = \underline{0}, \underline{E}_r = \underline{0}, \underline{E}_g = \underline{0}, \underline{E}_v = \underline{0}. \quad (12)$$

Linearizing (11) and considering (12) it is obtained the corrector formula for a traditional stabilized index 2 system of DAE

$$\begin{bmatrix} \frac{\partial \underline{F}_d}{\partial \underline{u}} + \frac{\partial \underline{F}_d}{\partial \underline{u}} & \frac{\partial \underline{F}_d}{\partial \underline{q}} & \left(\frac{\partial \Phi}{\partial \underline{q}}\right)^t & \tilde{0} \\ \tilde{I} & \frac{1}{l_0 h} & \tilde{0} & \left(\frac{\partial \Phi}{\partial \underline{q}}\right)^t \\ \tilde{0} & \frac{\partial \Phi}{\partial \underline{q}} & \tilde{0} & \tilde{0} \\ \frac{\partial \Phi}{\partial \underline{q}} & \frac{\partial^2 \Phi}{\partial \underline{q}^2} \underline{\dot{q}} & \tilde{0} & \tilde{0} \end{bmatrix} \begin{bmatrix} \underline{\Delta u} \\ \underline{\Delta q} \\ \underline{\Delta \lambda} \\ \underline{\Delta \eta} \end{bmatrix} = - \begin{bmatrix} \underline{F}_d \\ \underline{F}_r \\ \underline{F}_c \\ \underline{F}_v \end{bmatrix} \quad (13)$$

In the formula (13) the subscript j of the constraints functions Φ was dropped because it is not needed in the matrix form. h represents the time step \tilde{I} and $\tilde{0}$ represents identity and zero sub-matrices. η can have different solutions. However, there is only one solution that satisfy the equation for the residual of \underline{F}_r of the system (11) for arbitrary values of the terms of the matrix $\left(\partial \Phi / \partial \underline{q}\right)^t$. Because the good solution for $\underline{\eta}$ it is a priory known, the iterations can start initially by guessing the correct solution $\underline{\eta} = \underline{0}$ and then forcing, during the iteration, $\underline{\Delta \eta} = \underline{0}$. Hundreds of very good solutions for mechanical systems were obtained by using this method. Normally the iteration should satisfy $\underline{\eta} = \underline{0}$. The practice shows that this takes a long time to be achieved with no difference in the results. Beside this the residuals are simplified and it avoids the evaluation of the $\partial / \partial \underline{q} \left(\partial \Phi / \partial \underline{q}\right)^t$ that is a tensor evaluation that require a large amount of calculations.

By attaching the supplementary Lagrange Multipliers to the system gives the opportunity to solve the geometric constraints together with velocity constraints and reduce the index as described in (Orlandea and Coddington 1996). However, there is another way to reduce the index without increasing the number of equations that is very important to this write up. Beside the advantage of not increasing the number of equations, and not using supplementary Lagrange Multipliers, it is using only the stabilized position constraints. **The DAE also approaches an ODE by changing some algebraic variables into differential variables, (Gear 1988; Brennan et al. 1989). Hence, another way of reducing the index of the Eq. (11), is to introduce a vector $\underline{\dot{\mu}}$ that represent the Lagrange multipliers.**

Therefore, it can be written,

$$\underline{\dot{\lambda}} = \underline{\dot{\mu}} \quad (14)$$

Equivalent index two and index one systems of equations are obtained by substituting Eq. (14) in Eqs. (11) and (13) and for index two dropping $\underline{\eta}$ and the velocity constraints. By doing these things are obtained two systems of equations having index one and index two.

Writing directly the discretized residuals of (11), for index one the result is

$$\begin{aligned}
E_i \left(\frac{\Delta u_i}{h}, u_i, q_i, t \right) + \sum_j \frac{\partial \Phi^t}{\partial q} \frac{\Delta \mu_j}{h} + \sum_k E_k \left(u_i, q_i, t \right) &= \underline{0}, \\
u_i - \frac{\Delta q_j}{h} + \sum_j \frac{\partial \Phi^t}{\partial q} \eta_j & \\
\underline{\Phi} = \underline{0}, & \\
\frac{\partial \underline{\Phi}}{\partial q_i} \dot{q}_i = \underline{0}, &
\end{aligned} \tag{15}$$

and the residuals for the new index two are,

$$\begin{aligned}
\underline{F}_i \left(\frac{\Delta u_i}{h}, u_i, q_i, t \right) + \sum_j \frac{\partial \Phi^t}{\partial q} \frac{\Delta \mu_j}{h} + \sum_k \underline{E}_k \left(u_i, q_i, t \right) &= \underline{0}, \\
u_i - \frac{\Delta q_j}{h} &= \underline{0}, \\
\underline{\Phi} &= \underline{0},
\end{aligned} \tag{16}$$

The associate BDF corrector formula for index one is,

$$\begin{bmatrix} \frac{1}{l_0 h} \frac{\partial F_d}{\partial \underline{u}} + \frac{\partial F_d}{\partial \underline{u}} & \frac{\partial F_d}{\partial q} & \frac{1}{l_0 h} \left(\frac{\partial \Phi}{\partial q} \right)^t & \tilde{0} \\ \tilde{I} & \frac{1}{l_0 h} & \tilde{0} & \left(\frac{\partial \Phi}{\partial q} \right)^t \\ \tilde{0} & \frac{\partial \Phi}{\partial q} & \tilde{0} & \tilde{0} \\ \frac{\partial \Phi}{\partial q} & \frac{\partial^2 \Phi}{\partial q^2} \dot{q} & \tilde{0} & \tilde{0} \end{bmatrix} \begin{bmatrix} \frac{\Delta u}{h} \\ \frac{\Delta q}{h} \\ \frac{\Delta \mu}{h} \\ \underline{0} \end{bmatrix} = - \begin{bmatrix} \underline{F}_d \\ \underline{F}_r \\ \underline{F}_c \\ \underline{F}_v \end{bmatrix}, \tag{17}$$

and the associate BDF corrector for the new index two is,

$$\begin{bmatrix} \frac{1}{l_0 h} \frac{\partial F_d}{\partial \underline{u}} + \frac{\partial F_d}{\partial \underline{u}} & \frac{\partial F_d}{\partial q} & \left(\frac{\partial \Phi}{\partial q} \right)^t \\ \tilde{I} & \frac{1}{l_0 h} & \tilde{0} \\ \tilde{0} & \frac{\partial \Phi}{\partial q} & \tilde{0} \end{bmatrix} \begin{bmatrix} \frac{\Delta u}{h} \\ \frac{\Delta q}{h} \\ \frac{\Delta \mu}{h} \end{bmatrix} = - \begin{bmatrix} \underline{F}_d \\ \underline{F}_r \\ \underline{F}_c \end{bmatrix} \tag{18}$$

The Eq. (16) and the corrector (18), are sufficient for simulations of mechanical systems.

It is recommended that a discussion about error control must be done regarding the solution vector. A user can define an acceptable error based on the units that he is using. For instance if the units are meters and the device that is simulated has tolerances in microns it can be estimated that an error per step of one thousand of a micron can be practically sufficient. It has to be understood that smaller errors do increase the number of operations therefore it takes longer for simulations to complete. Larger errors decrease the precision, however, they are faster. So it is recommended that the errors be chosen based on the need. For instance when

setting up new models the errors can be large. For the final simulations is recommended that the error to be small. It has to be also mentioned here that if a problem has a closed form solution, when using numerical iterative methods, it will take an infinite number of iterations to achieve that accuracy. Therefore this is an approximate world where there will always be an ε . This ε can be made arbitrarily small (not zero) giving excellent practical results but at a cost.

Then, why numerical simulation?

1. The errors are finite numbers different of zero. This attracts a finite number of iterations.
2. A series of nonlinear problems do not have closed form solutions. Also in many cases a closed form solution will be very difficult to obtain.
3. Numerical solution have the potential for generalizations, at least for a group of practical problems.

In general the values for the errors are small and their values has to represent all the variables. Unfortunately not all the variables are similar. For instance there are the position or geometrical variables, velocity variables and variables proportional with the accelerations such as Lagrange Multipliers. It is recommended that the errors for velocities and Lagrange Multipliers be found based on the method and the equivalency to the geometrical errors and the integration method.

It will be very hard to guess the errors for velocities and accelerations and for Lagrange Multipliers. Hence, a vector of errors for velocities, accelerations and Lagrange Multipliers as functions of the acceptable errors for position (displacement) is established based on the BDF formula (6).

$$\underline{\Delta q}^e = -l_0 h \underline{\Delta \dot{q}}$$

where e exponent means equivalent vector, or,

$$\underline{\Delta q}^e = -l_0 h \underline{\Delta u} \quad (19)$$

For Lagrange Multipliers contained in the Eq. (13), the equivalent errors for accelerations are found

$\underline{\Delta u} = -l_0 h \underline{\Delta \dot{u}}$, or substituting this in (19) the result is,

$$\underline{\Delta q}^{e1} = (l_0 h)^2 \underline{\Delta \dot{u}}.$$

A vector of errors can be set up for the corrector (13). Each component of this vector has to be smaller or equal to a user defined boundary, $BND = \frac{0.5 \times \varepsilon}{(NQ+2) \times N}$ where, ε is a user error defined by physical considerations like tolerances and units. NQ is the order of integration. As the order increases the approximations are more accurate and the errors can be smaller. N is the total number of equations or variables. The resulting relation is:

$$\begin{bmatrix} \underline{\Delta q} \\ l_0 h \underline{\Delta u} \\ \frac{1}{m} (l_0 h)^2 \underline{\Delta \lambda} \\ \underline{0} \end{bmatrix} \leq \begin{bmatrix} BND \\ BND \\ BND \\ \underline{0} \end{bmatrix} \quad (20)$$

m in inequality (18) represents the mass of the link.

In a similar way it can be set the error vector for the corrector (18)

$$\begin{bmatrix} \underline{\Delta q} \\ l_0 h \underline{\Delta u} \\ \frac{1}{m} (l_0 h) \underline{\Delta \mu} \end{bmatrix} \leq \begin{bmatrix} BND \\ BND \\ BND \end{bmatrix} \quad (21)$$

As mentioned before, similarly in the error vector, the zero vector in Eq. (18) can be accomplished by starting with the initial conditions zero and then forcing the Newton differences $\underline{\Delta \eta} = \underline{0}$. This works practically very well because $\underline{\eta} = \underline{0}$ is the good and the desired solution. It also speeds up the simulations by increasing the sparsity, simplifying the residuals and canceling a tensor evaluation that could have a substantial number of operations at each iteration.

In Eq. (21) the error control is on μ that is the integral of the Lagrange Multipliers λ . The advantage, of this method, is that the integral smoothes the signal, hence, the error control is satisfied more easily.

Both methods work well for simulation of the mechanical systems except when one or more degrees of freedom are displacements function of time approximated by cubic splines. The reason is that in this case the accelerations are closed or open polygons with discontinuities. In this situations it is advantageous to define the piecewise velocities and approximate the velocities by cubic splines instead the displacements and use an I2 method, at together with monitoring the errors on the residuals. It works well. This result is based on the smoothing concept and the proprieties of the functions and their derivatives.

3 Numerical Example

It is important for this paper to test the formulation (16) and the corrector formula (18) against traditional methods known to give good results. To the best knowledge of this writer these two relations are not implemented in any version of ADAMS computer program. They are now implemented in the three dimensional Mechanism Computer Aided Dynamic Analysis (MECADA) that will be tested by the following model that is a modified Infiniti G37x car, Fig. 4. The modification consists in the front suspension. Instead the double wish bone suspension it is adopted a five link suspension designed with king pin and tie-rods for steering. This suspension is in the study for the optimization of the tire contact patch. The model is prepared for future durability studies based on a field history and acquired data. Being a four wheel drive car, all four wheels are driven on rollers and they

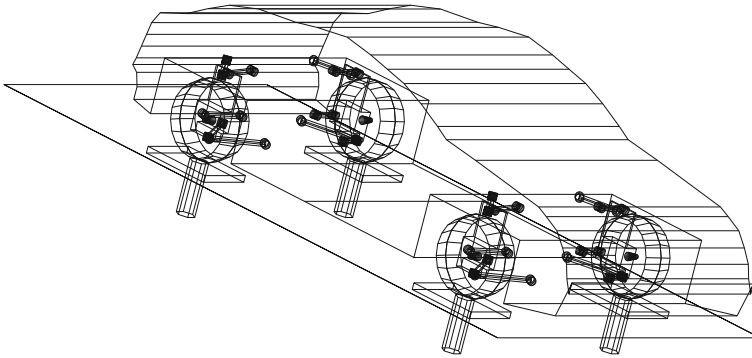


Fig. 4 Infiniti G37x durability computer model

are vertically displaced in a control manner by hydraulic actuators. The car's mass is 2,000 kg. The mass of the king-pin and the tie-rods are considered in the model, however, they are not represented graphically because of the purpose of the model. If the simulation is to be used for handling purposes then the king pin and tie rods have to be included in the model. All the geometric data of the car can be found in G37x Owner Manual, Technical Consumer Information (2009).

There is an unusual situation also connected to durability. In many cities in the US the cities decided to slow the motorists down by creating bumps on the road. They also are cited to say that is cheaper to have bumps than having the "Police" patrolling the streets. This happens more in residential areas. Such a bump is represented in Fig. 5, and it is 1 m wide and at 28.5 km/h takes 0.125 s (8 Hz) to go over it. The bump height is 8 cm. To avoid damaging the tires at the beginning and the end of the bumps they are tangent to the original road. This smoothing will happen anyway because the tires envelop the bump. Otherwise, the tires and the wheel rims will be damaged especially if there is a step bump at high speeds. Depending on the situations, the bumps are arranged from one to four successive bumps at 2 m between them. It is considered that the most damaging situation is given by the four successive bumps. Hence, this was the cycle also adopted for the computer simulation.

After the simulation started the first bump is met by the front wheels after 1 s and rear wheels 1.375 s. The entire car goes over the bump in 1.875 s. The next

Fig. 5 The graph of the street bump as a $f(\text{time})$

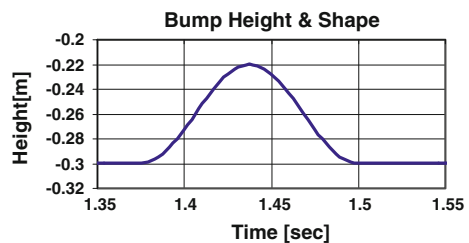


Fig. 6 Chassis vertical accelerations as $f(\text{time})$

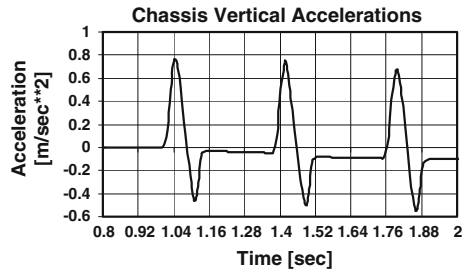
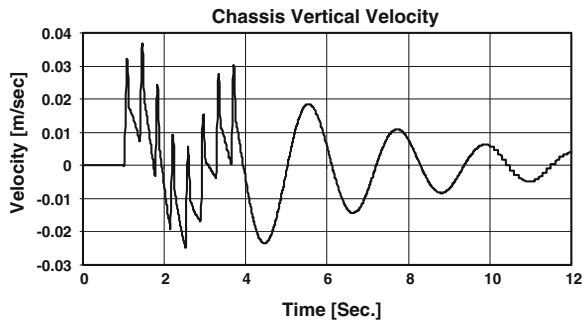


Fig. 7 The chassis velocity $f(\text{time})$



bump is met by the front wheels after 1.875 s and so on for the other two bumps. It takes 3.85 s for the entire car to go over the four bumps.

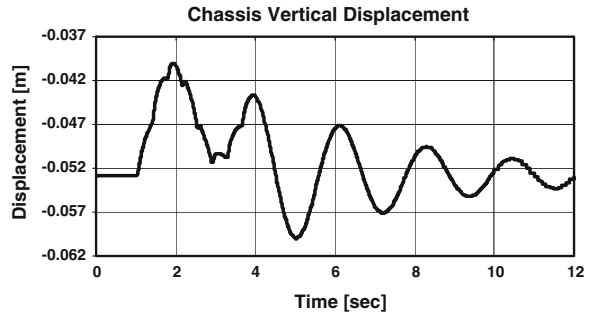
The accelerations of the CG of the chassis are represented in Fig. 6. The interesting thing in the response, is that there are two signals added together. One is a sine wave of the vertical natural frequency of the car and second is the bump’s excitations for the 3.85 s.

The chassis CG vertical velocity follows the same pattern as shown in Fig. 7, where the two signals are added together. Unless one does a Fourier analysis for the vertical displacement it will be very hard to separate visually the superposition of the chassis fundamental signal and the bump contributions to this signal.

There are some disturbances in the total displacement signal as shown in Fig. 8 for the first 3.85 s. Of course the difference between the total signal and the fundamental chassis signal will be the bumps contribution. It is not clear that for this velocity of the car $v = 28.5 \text{ km/h}$ the contribution of the bumps signal is very significant. However, to avoid any confusion regarding the two signals it must be mention here that the fundamental and natural signal of the chassis (the nice sine wave) is also triggered by the bump excitations.

In Figs. 9 and 10 are represented the forces from the spring and dashpot of the four suspensions together with the tire forces. Series 1 and Series 2 refer to the front suspensions and Series 3 and Series 4 refer to the rear suspensions. However, two by two are equal. The front left and right and the rear left and right. Looking at the distribution of forces front to rear it is a small difference between them

Fig. 8 The chassis vertical displacement $f(\text{time})$



favoring the rear suspension and tires. This is not a surprise because the car is a rear wheel drive car except when the road conditions get to be slippery, it changes to all wheel drive automatically. The forces from the suspension are larger than the forces in the tires. That is because there is a mechanical leverage between the suspension struts and tires. Some important observations are that qualitatively the forces in the suspension have the same shape with the chassis accelerations. The forces in the tires at the beginning and at the end of each bump have a *step shape*. That is because the bump shape emulates a cosine law for cams. It smoothes the displacement and velocities, however, the accelerations have a step. Unfortunately the step is approximated by a very steep ramp, because the smoothing. Otherwise the simulation could not proceed continuously.

The suspension certainly is doing its job. The height of the bump is 8 cm and this is reduced for the chassis to 2 cm. For the speed lovers, a speed of 256 km/h reduces the chassis displacement to 1.8 mm. For this case the impact forces between bumps and wheels increases by more than 50-fold. These impact forces can destroy the suspension and alignment.

Fig. 9 The suspension struts forces $f(\text{time})$

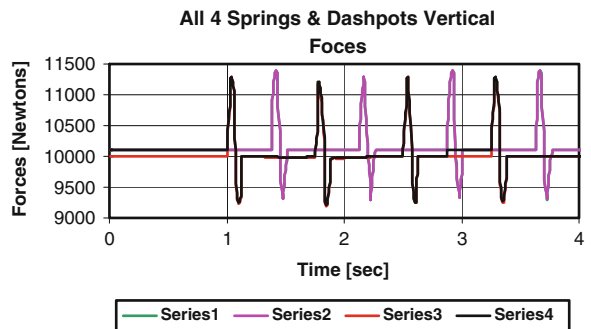
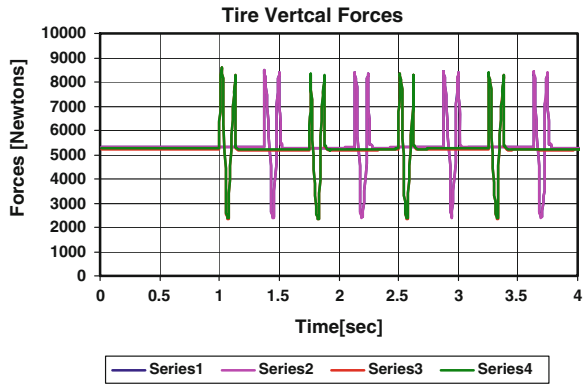


Fig. 10 Tire forces as $f(\text{time})$



4 Conclusions

The idea in this paper is to introduce the Original ADAMS and MCADA to a new method for stabilized index 2 method of numerical integration that possesses some advantages for accuracy and the simulation speeds. **This method reduces the index by using differential variables instead of the algebraic variables decreasing the difference of the DAE from an ODE set of equations.** Specifically this new method uses as differential variables the time derivatives of the Lagrange Multipliers. It can also be used together with the traditional SI2 method, as represented by Eqs. (15), (17), to obtain a SI1 method. The algorithm is represented by Eq. (16) and the corrector (18).

The test model is a medium to large model of an Infiniti G37x car that was set for durability and new suspension concept studies. It has 587 differential equations and variables in contrast to 767 equations and variables for the traditional SI2. The model worked well and together with the smoothing algorithms it gave quantitative and qualitative good results identical with the traditional methods especially SI2. The CPU time on a computer having an I7 processor and Windows 8, 64 bit operating system is 31.7181 s for 12 s real time simulation and 1,440 integration steps. This is an improvement by a factor of 2.44339 over the traditional SI2 for the same running parameters.

This method is highly recommended for simulations of mechanical systems. It gives comparable CPU times with a BDF Index 3 method and accurate results identical with the constraint oriented SI2.

References

Baumgarte J (1972) Stabilizations of constraints and integrals of motion in dynamical systems. *Comp Math Appl Mech Eng* 1:1–16
 Brenan KE, Campbell SL, Petzold LR (1989) Numerical solutions of initial-value problems in differential- algebraic equations, vol 4. Siam, North-Holland
 Calahan DA (1972) Computer aided network design, McGraw-Hill, New York City

- Gear CW (1971) Numerical initial value problems in ordinary differential equations. Printce-Hall, NJ
- Gear CW (1988) Differential-algebraic equation index transformation. *SIAM J Sci Stat Comp* 9:39–47
- Infinity G37x owner manual (2009) Technical consumer information, pp 9–11
- Orlandea NV (2008) From Newtonian dynamics to sparse Tableaux formulation and multi-body dynamics. *Proc Inst Mech Eng Part K J Multi-body Dyn* 222(4):301–314
- Orlandea NV, Coddington R (1996) Reduced index sparse tableau formulation for improved error control of the original ADAMS program. *Mech Des* 1:219–228

The Transmission of European Mechanical Knowledge into 17th-Century China

Baichun Zhang and Miao Tian

Abstract As you know, from the end of the 16th century on, Jesuit missionaries in China aimed at the Christianization of this country. The transmission of western scientific knowledge was one of their long-term strategies.

We have much understanding of the transmission of astronomy, mathematics and technology from Europe to China, so that we know how such kind of European knowledge changed the traditional Chinese knowledge system, and interacted with traditional system. Having made a deeper investigation of transmission of mechanics, we found out another phenomenon which is different from that in the fields of astronomy and mathematics.

European mechanical knowledge was transmitted into China through the following three channels:

- (1) Ballistics related to firearm-making.
- (2) Mechanical theory concerning construction of machines.
- (3) Mechanical explanations of astronomical instruments.

1 Ballistics Related to Western Firearm-Making as Practitioners' Knowledge

During the 16–17th centuries, there were rebellions in China and fights at the boundary. Therefore, advanced weapons were in dire need. Knowledge about weapon-making was significant to Chinese.

B. Zhang (✉) · M. Tian

CAS Institute for the History of Natural Science, Beijing, China

e-mail: zhang-office@ihns.ac.cn

Early in the 16th century, such western weapons as the breech-loading cannon and the musket were brought to China from Europe. By the early 17th century, China obtained western cannons and its manufacturing technology. The German Jesuit Adam Schall von Bell, and the Belgian Jesuit Ferdinand Verbiest helped China's governors constructed several hundred cannons.

Some military books on the construction and use of weapons were written partly by Chinese authors and their Jesuit co-authors. Among them, there are such books as *籌海圖編*, *練兵實紀雜集*, *西法神機*, *兵錄*, *火攻挈要*.

In *Xinzhì lingtái yìxiàng zhì* *新製靈臺儀象志* [*A Record of Newly-Built Astronomical Instruments at the Observatory of Beijing*] published in 1674, Verbiest discussed the relation between time and distances when cannonball moved. He drew trajectories of a crossbow and a cannon.

Western knowledge about trajectories was gradually combined with traditional Chinese knowledge and experience. The above-mentioned books contain several descriptions of the trajectory of projectiles. To certain extent, Western knowledge about the projectile motion was reformulated in Chinese terminology based on practitioners' techniques of shooting. Chinese people's main interest in military knowledge was focused on its practical skills rather than on the theory of ballistics.

2 Mechanics in *Qiqi Tushuo* as Theoretical Knowledge

At the end of the 16th century, European clocks started to be brought into China. As valuable gifts, clocks were presented to Chinese officials and emperors. And then, clock-manufacturing became a new kind of industry in Kanton and in Suzhou.

Inspired by mechanism of European clocks, Wang Zheng to reconstruct ancient devices, and invented a time-keeping device (*輪壺*).

In 1627, Wang Zheng and Johannes Schreck Terrentius accomplished the book entitled “*遠西奇器圖說錄最*”.

The first paper contained the detailed discussion about all the knowledge of weight. It begins with Aristotle's cosmography and the concept of weight, and then was followed with Archimedean theories of center of gravity, floatation and specific gravity.

The second paper mainly introduced such simple devices as balance, steelyard, lever, pulley, wheel and screw, as well as mechanical theories related to them.

Just as the name of the book implied, the most contents of the book came from “the Far West”. The first and second papers of *QQTS* were mainly from the following books:

Steven's *Tomus Quartus Mathematicorum Hypomnematum* (1605–1608) (*De Beghinselen der Weeghconst* 1586).

Guidobaldo's *Guidiubaldi e Marchionibus Montis Mechanicorum liber* (1577).

It was possible that Johannes Schreck selected treatises written by other European authors at the same age of Steven, probably including the following treatises:

Comandino, Federico. *Federici Commandini Urbinitis Liber de Centro Gravitatis Solidorum*, 1565.

Tartaglia, Niccolò. *La Nova Scientia*, 1537.

Tartaglia, Niccolò. *Quesiti et Inventioni Diverse*, 1546.

Benedetti, Giovanni Battista. *Demonstratio Proportionum Motuum Localium*, 1554.

Benedetti, Giovanni Battista. *Diversarum Speculationum Mathematicorum et Physicarum Liber*, 1585.

The third paper of *QQTS* consists of the illustrations and descriptions of 54 machines. This paper is derived from the following five books:

- (1) Jacques Besson. *Théâtre de Instruments Mathématiques et Mecaniques*, 1578, latined. 1582.
- (2) Agostino Ramelli, *Le Diverse e Artificiose Machine del Capitano*, 1588.
- (3) Faustus Verantius (Veranzio), *Machinae Novae Fausti Verantii Siceni, cum Declaratione Latina, Italica, Hispanica, Gallica et Germanica* (written c. 1595). Florence, 1615.
- (4) Heinrich Zeising. *Theatrum Machinarum*. Leipzig: Lanckischen, 1612 and 1708.
- (5) Vittorio Zonca. *Novo Teatro di Machini e Edificii*. Padua: Bertelli, 1607 and 1621.

At the beginning of this book were listed “references”, which all were published in Chinese, and written by the Jesuits and their Chinese co-authors. Wang Zheng listed 18 referenced books in the “references” of Fanli (The Guide to its use), *QQTS*, including:

Huan Rong Jiao Yi (圖容較義, translated by LI Zhizao and Matteo Ricci, 1608).
 Taixi Shuifa (泰西水法, Hydraulic technology of the Far West) (interpreted by Sabbathinus de Ursis, noted down by XU Guangqi, revised by LI Zhizao, 1612).
 Jihe Yuanben (幾何原本, Euclid’s Elements, interpreted by Matteo Ricci and noted down by XI Guangqi, 1607).

Tian Wen Lue (天問略, by Emmanuel Diaz, 1615).

Tongwen Suanzhi (同文算指, A Guide to Arithmetic in Common Language, written and edited by LI Zhizao and Matteo Ricci, 1613).¹

Wang Yuan Jing Shuo (望遠鏡說, Descriptions of Telescopes, by Adam Schall von Bell).

Zhi Fang Wai Ji (職方外紀, Record of the Places outside the Jurisdiction of the Office of Geography, by J. Aleni, 1623).

¹ This book introduced mostly European calculations. Some contents were adopted from *Suan Fa Tong Zong* (1592) by CHENG Dawei, a Chinese mathematician. European mathematical calculations from *Epitome Arithemticae Practicae* (1583) written by Clavius.

Generally, the researchers on this book paid little attention to this list before. In fact, Johannes Schreck and WANG Zheng really quoted and referred to the above-mentioned books and other Chinese books.

Schreck and Wang Zheng reconstructed the Western representation of mechanics, so that a new logical system of knowledge came into being. They dealt with mechanics in the following ways:

Firstly, different contents, such as definitio, theorema, propositio, postulatum and problema in sources, are unified into the same kind of representations, namely the key sentence of a ‘section’ 款.

Secondly, exemple, declaratio, nota or consecrarium are unified into ‘example’, and are listed after key sentences respectively. The structure of first and second papers is ‘key sentence + example’.

Thirdly, all the mathematical proofs are cancelled. The rule of three is emphasized.

Fourthly, Wang Zheng added his commentaries to the introduction to Qiqi Tushuo. The commentaries are derived from some books in Chinese.

Fifthly, drawing methods of different illustrations are unified. Traditional Chinese pictorial representations contributed to copying all the illustrations.

3 Mechanics in *XZLTYXZ* as Practitioners’ Knowledge

Having constructing six instruments, Verbiest accomplished his 新制靈台儀象志 in 1674. This book mainly explained his astronomical instruments and stars tables.

He classified problems about the instruments as several issues, and made full use of western mechanical knowledge to explain how reasonable and excellent is the construction of his new instruments, and why the instruments are superior in quality to Chinese instruments.

Firstly, Verbiest exploited Galilean theory on the strength of materials to prove ‘reasons for firmness of his new instruments’. The relation between the length or material and their strength is exemplified.

Secondly, Verbiest confirmed the importance of finding out [ascertaining the center of gravity when building instruments.

Thirdly, Verbiest narrated how to use single pendulum to count time.

Fourthly, Verbiest gave an example of a falling body with very concrete numerical values and an attached table. This table listed swinging times of pendulum, the time experienced, the height that objects passed in each unit time, as well as the height passed in a period of time in total.

Fifthly, Verbiest made some copies from the technical drawings and mechanical illustrations of Tycho Brahe, Simon Stevin, Agostino Ramelli, Jacques Besson, Vittorio Zonca, Johann Schreck Terrenz and Wang Zheng.

4 Integrating or Ignoring Mechanics

In 1664, Xue Fengzuo, astronomer and mathematician, reconstructed the mechanical knowledge in *Qiqi Tushuo* (A Record of the Best Illustrations and Descriptions of Extraordinary Devices of the Far West, 1628) and Wang Zheng's *Zhuqi Tushuo* (Illustrations and Descriptions of Several New-built Devices, 1628), and accomplished the edition of *Zhongxue* (science of weights) in 1664. Xue had a good understanding of western mechanical knowledge, and then summarized the original texts and illustrations. He thought that science of weights and mathematics will help people know why devices can be constructed.

Mei Wending studied *the Qiqi Tushuo*, and wrote at least two books concerning it. According to a new discovered handwriting version of *Qiqi Tushuo* with Mei Wending's commentaries, we know that Mei Wending understood the European mechanical problems mainly from a perspective of mathematics instead of mechanics. Different from Wang Zheng, Mei Wending tried to make mathematic proofs of mechanical theories.

In 1683, Verbiest accomplished his book draft on the principle of western technology *Qiongli xue* (窮理學 *The Learning of Making a Thorough Inquiry into Principles*), which consists of Aristotelian philosophy, logic, mechanics and astronomy. Verbiest quoted paper one and paper two of *Qiqi Tushuo*, as well as *LTXYZHI*.

Verbiest dedicated *Qiongli Xue* to the emperor Kangxi 康熙 and explained that his intention to write the book was to present the western theory of the calendar and to demonstrate why and how knowledge can be deduced from basic theories. He emphasized that *Qiongli xue* have the same importance as Confucianism. However, his attitude made the emperor be afraid of theory system edited by Verbiest, and finally refused to allow this book to be published.

Mechanical knowledge about trajectories, the strength of materials and falling body was ignored by Chinese. We have not found out any Chinese scholar who followed Verbiest's research on those mechanical problems.

5 Concluding Remarks

Generally, the ambitious goals of the Jesuits to transmit the religious, cultural, scientific, and technological heritage of the West to China for a time had a very limited success.

Firstly, the transmission of mechanics into China did not create a group of Chinese specialist in mechanics. Western knowledge made Chinese astronomy and mathematics flourish, while it was not able to activate the Mohist School.

Thirdly, it is not necessary for Jesuit missionaries to transmit the theoretical mechanics beyond Chinese interest and need for knowledge, especially the

mechanical theories against Aristotelian explanations of mechanical problems. In fact, theoretical mechanics did not cause any controversy in Chinese intelligentsia.

Thirdly, Chinese society needed European competitive clock-constructing and firearm-constructing technology. However, theoretical mechanics was not a necessary part of traditional Chinese knowledge system in the 17th century. Some theoretical mechanics, which was integrated into *Shuli jingyun* (數理精蘊 *Collected Basic Principles of Mathematics*, 1723), was still away from the main stream of Western mechanics. Theoretical mechanics did not really become one important branch of Chinese knowledge system before the mid-19th century.

Mechanisms in Building Integrated Renewable Energy Systems: Case Study—Solar Energy Conversion Systems

Ion Visa

Abstract The short and medium term development strategy in Europe—and not only, focuses on Energy as the key issue, particularly on energy efficiency and renewable energy systems in the built environment. To implement these strategies, novel solutions are expected from R&D giving a better use to the on-site renewable energy potential. Certain candidates to implement the Energy Strategy are the solar energy conversion systems. Increasing the performance of the photovoltaic and solar-thermal convertors by harvesting a larger amount of solar radiation can be done by tracking systems. The paper presents a review of the mostly used tracking systems and comparatively analyses various solutions according to the type of the conversion systems, the input data and restrictions and the output properties. Relevant case studies were presented for tracking mechanisms developed and implemented in the R&D Center Renewable Energy systems and Recycling in the Transilvania University of Brasov.

Keywords Solar energy conversion · Tracking mechanisms · Photovoltaic systems · Solar-thermal systems

1 Introduction

Identified by Nobel Prize winner Richard Smalley in 2003 as the No. 1 problem in a top-ten ranking of humanity major problems, (Smalley 2003), Energy still remains the major development driving force and the most sensitive problem in the world. A combined result of fossil fuels depletion and alarming increase in greenhouse gases made most of the countries to consider mid- and long-term

I. Visa (✉)

Research Center Renewable Energy Systems and Recycling,
Transilvania University of Brasov, R&D Institute, Brasov, Romania
e-mail: visaion@unitbv.ro

energy strategies that aim at reducing the energy consumption while preserving the development trend (energy efficiency—EE) and at increasing the share of non-fossil based energy resources, particularly of renewables (novel renewable energy sources, pushing for the development of novel renewable energy systems—RES, matching renewable energy technologies—RET). This is fully valid for Europe, N-America and Australia and this starts to be valid for China and other Asian countries, (Wyman 2012).

One key issue is the built environment, accounting for 40 % of the total energy used in US and over 44 % in EU. These amounts are almost equally divided between residential and commercial buildings, and the largest share is dedicated to heating and cooling, amounting in Romania over 75 %. Therefore, solutions for the efficient and clean energy production and use in the built environment are identified as priorities for the next years, up to 2020.

The built environment is represented by buildings and their surroundings, associated in communities which are using thermal energy, power, water.

Starting with 2007, the European Union developed a strategy and a set of instruments that support EE and RES/RET extended implementation, and corresponding instruments were developed at the Member States level. The European Strategic Energy Technology Plan (SET-Plan, COM (2007)723 final) was launched in 2008 and establishes the mid-term (2020) and long-term (2050) energy technology policy for Europe, targeting the acceleration in the development of cost-effective low carbon technologies, through measures for planning, implementation, resources and international cooperation. According to the SET Plan, legal decisions were formulated, among which two are of particular importance: (1) 20-20-20 EU Directive (2009/28/CE)—asking for an EU average of 20 % reduction in greenhouse gases emissions, 20 % renewable energies increase and 20 % improvement in energy efficiency by 2020, having specific targets for renewables set for each Member State; (2) Directive 2012/27/EU on Energy Efficiency aiming at providing support for reaching the 20 % increase in EE by 2020 and for more significant reductions by 2050. This directive requires each Member State to set an indicative national energy efficiency target, based on either primary or final energy consumption, primary or final energy savings, or energy intensity. Romania, as Member State, developed the appropriate legal frame: The National Action Plan on Renewable Energy Sources and the corresponding laws (L. 220/2008, modified as OUG 88/2011 and L. 134/2012 for promoting energy production from renewables), being close to reach the 24 % renewable in the electrical energy production, stated by the 20-20-20 directive for our country, and the 2nd Action Plan for EE, (2011–2020) supporting the EE law (to be launched latest in June 2014, according to the EU directive).

The SET Plan Conference in Dublin (May 2013) made a critical analysis of the implementation progress, concluding on the need to further develop strategic tools, legal instruments and concrete actions for developing and implementing “clean, efficient, low carbon technologies”. The EU Commissioners for Energy (Gunther Oettinger) and for Research and Innovation (Maire Goeghegan Quinn) identified innovation as the key for reaching the clean, secure and affordable energy target

and outlined the need to address measures for “faster track from research to market”; this is why the next framework programme Horizon 2020 will particularly focus on academia-industry cooperation in the field of energy technologies and high tech products. Based on the experience gained since the SET Plan was launched, the EU and Members States strategies tend to coagulate in two approaches:

1. Electricity production using large RES facilities (solar PV, concentrated solar-power, off shore wind farms, tides, etc.) that are supported by smart grid connected solutions; on-site production remains an option, either for grid insertion or as stand-alone systems where no grid is available.
2. Thermal energy on-site production based on RES, for buildings up to districts.

As major utilities consumers, the buildings are subject of special legal provisions. Most of the buildings nowadays were developed in the ‘70...’80 (or before) and are using low-performance insulation materials and high electrical energy consumers, being quite far from the EE requirements. But, the new buildings should be developed based on energy efficiency concepts and indicators, and refurbishing the old buildings should accordingly be done. This is also stated in the Romanian legislation, which adopted the EU roadmap, setting for the end of 2018 the target of *nearly zero energy* status for new public buildings (and similarly till the end of 2020 for any other new building), the demand being covered preferably based on renewables and on-site production (especially for meeting the thermal energy demand).

There are not unitary indicators for defining the energy efficiency in buildings yet, (Marszal et al. 2011); the *low energy building* status is usually correlated with the amount of energy consumed for heating, cooling and domestic hot water (most countries setting a threshold yearly value at 60 kWh/m²), while the *passive house* status is defined considering the overall energy consumption in buildings and is strongly depending on the geographical location, ranging thus between 51 kWh/m² in the Czech Republic and 120 kWh/m² in Germany and Switzerland, but setting the maximum threshold value for heating at 15 kWh/m². When meeting these needs fully by using renewable energy, the efficiency status is defined as *zero energy*.

The *zero energy* status can be reached stepwise considering to:

- Step 1. Minimize the energy need through EE measures (especially for heating and cooling, accounting in Romania for up to 75 % from the total building energy demand);
- Step 2. Adopt RET to meet the remaining energy needs, (Li et al. 2013).

These requirements are supporting a revised approach on renewable energy systems, particularly integrated in buildings. Novel renewable energy systems using the existing technologies and even emerging technologies are expected; this also asks for a novel building design, considering the efficiency and sustainability issues from the early stages, along with the further integrated renewables, (Da-wood et al. 2013).

Architectural integration and societal acceptance represent a must but key specific technical features should complete the usual quality indicators. The renewables must function in a restricted space, therefore efficient systems are compulsory, able to exploit as much as possible of the renewable energy sources available on-site. Some of the most common RES, as heat pumps and biomass burners are less sensitive to the climatic data being the source of predictable energy amounts; their drawback is related to the need for available space for implementation and operation and in their sustainability, since heat pumps need to be powered (thus require a renewable power generator) and biomass is a source of CO₂. The systems relying on wind and/or solar energy produce a fully green energy but are highly depending on the renewables' potential, which in turn depends on the implementation location and seasons. The solution is the use of energy mixes and hybrid systems based on renewables. The novel smart design concept has to consider the multi-source (hybrid)—multi-function (utilities) systems. For reaching their maximal potential, these energy mixes need to be carefully designed (considering the actual renewable energy potential) and operated by using building energy management systems.

Plenty of work is now-a-days dedicated to renewables integrated in the built environment, considering the particularities of low wind potential, shading, radiative energy, etc. The solar energy conversion systems for power (photovoltaic—PV—systems) and thermal energy production (solar-thermal—ST—systems for heating, cooling and domestic hot water) are part of almost any energy mix designed for the built environment; these are intensively investigated as technologies that registered a steady increase in efficiency and as systems that can be installed virtually everywhere. The most often mentioned major drawback, the initial investment, tends to be compensated, considering that, for PVs the costs dropped from 2USD/W to 1 USD/W in only 4 years, (Devabhaktuni et al. 2013).

2 Solar Energy Conversion Systems in the Built Environment: The Problem

The technical steps in the design of the solar energy conversion systems are outlined in Fig. 1 and are related to the definition of the input data and the system design for optimising the efficiency targeting high output as electric or thermal energy:

Each of these steps is subject of research but the key issue is related to an integrated approach of the following issues:

- Weather data monitoring and modelling, not only solar radiation but also the associated heat (temperature), wind (direction and velocity) and humidity that can significantly disturb the solar energy conversion process; the use of the data in the implementation location is recommended, especially in early spring and late summer when deviations up to 50 % were registered for the Brasov city

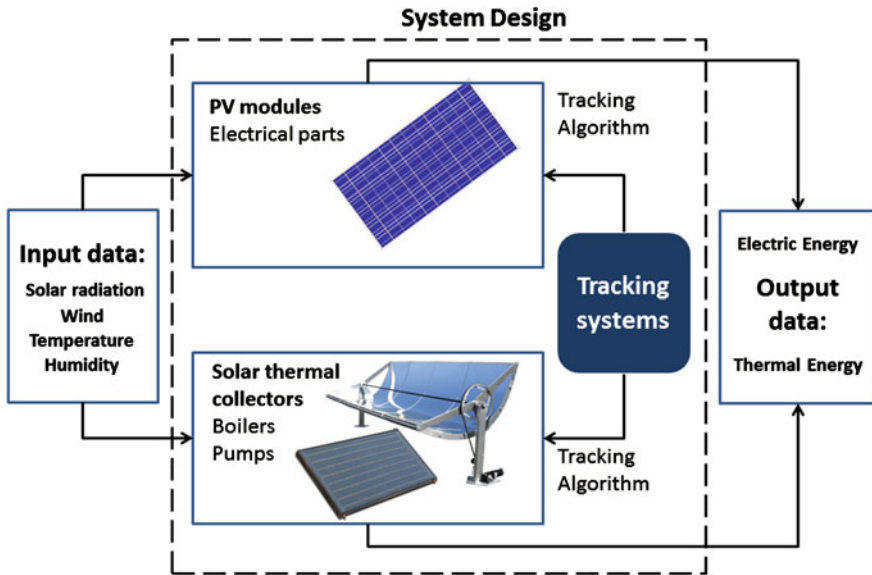


Fig. 1 Design of solar energy conversion systems

between the in-field data and the data generated using simulation software (Meteonorm).

- Solar energy converters (PV modules, ST collectors) able to use a large portion of the solar spectrum, by novel materials (mainly composites with highly controlled properties); the trend is to look after materials based on common, abundant, low cost and low toxicity elements;
- PV and ST systems able to use a large amount of the solar energy, by using tracking systems.
- Energy efficient PV and ST systems, including efficient tracking solutions and algorithm focusing on the optimum between accuracy and energy saving.

In the built environment, where limited mounting space is available, the use of tracking systems for harvesting a large amount of solar radiation from sunrise to sunset represents a path to increase the output, as the amount of energy produced depends on the input solar energy. Comparing to the general pre-requisites for tracking systems with high efficiency and energy saving potential, in the built environment there are additionally pre-requisites defining compact, safe and architecturally acceptable systems. Therefore, the tracking system has to be selected, considering the special functions of the solar energy conversion systems:

- The type: solar-thermal or photovoltaic systems;
- The converters association: individual module/collector, strings, arrays, platforms;

- The mounting spot: on a flat, horizontal surface (on the ground or on a terrace), on inclined surfaces (roofs) or on vertical surfaces (facades);
- The mounting position, ideally South-orientated with tilting possibilities but this is not always possible due to the building position, shading effects, etc.

Adding a tracking mechanism obviously raises the costs, thus, the optimal devices must be as simple as possible (from a constructive point of view) and must reproduce the sun path with high accuracy (usually estimated by the tracking efficiency). These are the prerequisites of many studies developed in the past years, (Schubnell and Ries 1990; Davies 1993; Abu-Khader et al. 2008; Mousazadeh et al. 2009). There are also other side-effects of tracking related to heating (using the infra-red part of the solar radiation) that has a beneficial effect on solar-thermal conversion and an opposite result for PV systems using silicon-based modules (that are still dominating the PV market) (Gómez-Gil et al. 2012).

Thus, developing tracking systems for building integrated solar energy conversion systems is a complex task and represents an open problem where the science of mechanisms is expected to formulate answers in direct collaboration with the system designers.

3 Tracking Systems for Solar Energy Convertors

The tracking system is installed in a location, Q having the position on the Globe defined by the intersection of the meridian and the parallel (geographic coordinates) of the implementation location. This position is described by (Comsit and Visa, 2007; Comsit and Visa, 2005; Visa et al., 2008; Kelly and Gibson, 2011):

- The λ angle defined in the equatorial plane, between plane containing the Prime Meridian (passing Greenwich) and the plane of the meridian containing the Q point, called *longitude* (East or West);
- The φ angle, defined in the plane of the meridian containing the Q point, between the OQ direction (O being the Earth centre) and the intersection line of the meridian plane with the equatorial plane, called *latitude*.

The horizontal plane in the implementation location (Q) is defined by the North–South direction (tangent to the meridian containing the Q point) and the on-site East–West direction (tangent to the parallel containing the Q point).

As we well known, the Earth's motion versus the Sun is defined by:

- The rotation motion around its own polar N–S axis, from West to East (one full rotation per day); this motion defines, for the observer on Earth, the diurnal apparent motion of the Sun on the celestial vault;
- The Earth movement around the Sun, following an elliptic trajectory that is fully covered over one year and which is responsible for the seasons and the altitude of the apparent trajectory of the Sun on the celestial vault; the N–S Earth axis is inclined at 23.5° at the summer solstice down to -23.5° at the winter solstice.

Considering the large distance between Earth and Sun ($1.47... 1.52 \times 10^{11}$ m) the sun rays can be considered to reach the Earth on a direction that is parallel to the imaginary line between the centers of the two celestial bodies.

The direction and the position of the solar ray on the horizontal plane in the implementation location can be defined using two angles:

- The angle between the solar ray direction and its projection on the horizontal plane, called altitude angle; this angle depends on the geographic location, the day in the year and the solar hour (Seme and Štumberger 2011; Badescu 2008);
- The angle of the projection of the solar ray on the horizontal plane and the local N–S direction, called azimuth angle, also depending on location, day in the year and the solar hour, (Seme and Štumberger 2011; Badescu 2008).

In a given location, the maximum amount of solar radiation can be collected when tracking the PV modules (or generally the solar energy convertor), respecting the geometric condition according to which the normal to the modules surface superpose the solar ray, with the previously described position towards the local coordinates. This requires a continuous tracking motion of the module, following the solar ray. By using tracking mechanisms, this motion is stepwise developed, using a rational number of steps for insuring a high tracking accuracy of the solar rays, (Visa et al. 2008; Diaconescu et al. 2008).

Many mechanical tracking systems were developed, and these can be described by the directions of the rotation axes of the PV modules and the magnitude of the rotation angles around these axes, aiming at exposing the PV surface perpendicularly towards the solar rays. Four types of tracking systems are mainly defined, according to this:

1. **Tracking system with the fixed axis parallel with the Earth polar axis,** Fig. 2a, (motion I) and the mobile axis perpendicular on the polar one and parallel with the equatorial plane—having the position defined by the on-site E–W direction (motion II). In this case, the main motion is I has large amplitude and is daily done from East to West (considering the implementation location). Its linear variation for the Brasov location (latitude: $45^{\circ}38'$ N, longitude: $25^{\circ}35'$ E) at summer solstice (day N-172, date: 21st of June) is presented in Fig. 2b. The II motion can be considered constant during a 1 day (or even longer) period, Fig. 2b.
2. **Tracking system with the fixed axis parallel with the E–W direction of the implementation location:** in the same axes orientation as in the previous example, this motion is defined when fixing the E–W axis (Fig. 3a) and requires daily modification for both I and II motions. The rotation angles vary as presented in Fig. 3b. A comparative analysis shows that the amplitude of motion I decreases from 240° (Fig. 2b) to 133° (Fig. 3b), while the constant motion II is increasing up to 112.2° in the second case. As result, the sum of angles characterizing motions I and II is quite close for both situations: 240° (case 1) and 252.2° , respectively.

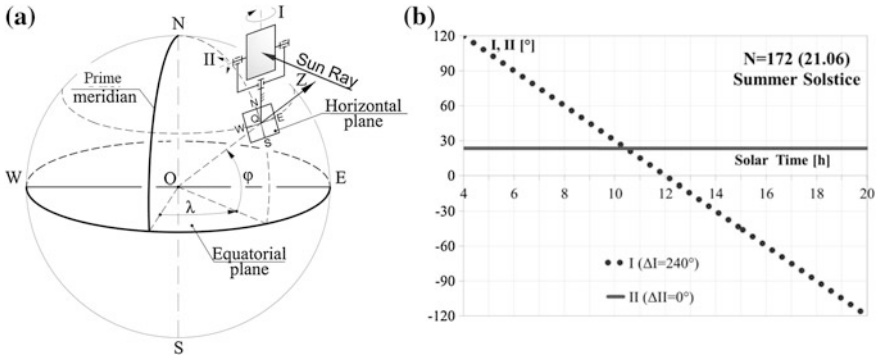


Fig. 2 a Solar tracking system with fixed polar axis, and b variation of the corresponding angles during the Summer Solstice at 45° northern latitude

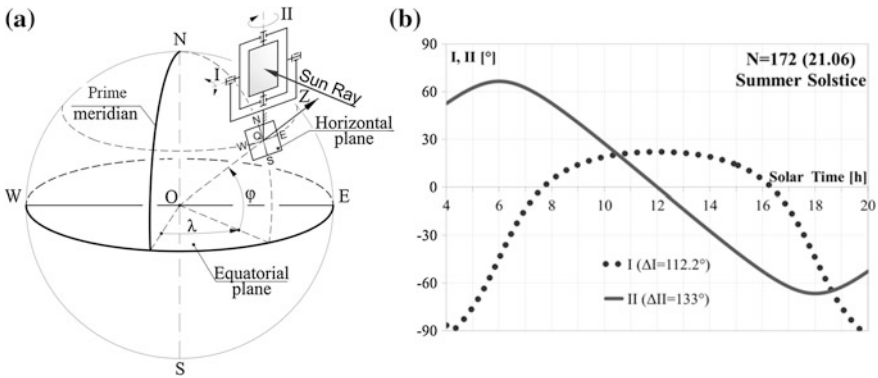


Fig. 3 a Solar tracking system with local E–W horizontal fixed axis and b variation of the corresponding angles during the Summer Solstice at 45° northern latitude

3. **Tracking system with the fixed axis perpendicular on the plane of the implementation location:** the tracking system presented in Fig. 4a has the fixed rotation axis oriented following the normal to the horizontal plane of the implementation location and the second axis is perpendicular on the first one, with the E–W reference direction. Both, motions I and II are daily and their amplitude for the Brasov location is presented in Fig. 4b, corresponding to 250° (I) and 67.8° (II) respectively. It is to notice the very large amplitude of motion I to which the correspondent value of II is added, resulting in very large tracking strokes.
4. **Tracking system with the fixed axis parallel to the N–S axis of the implementation location:** the orientation in Fig. 5a has the fixed rotation axis parallel to the N–S axis of the implementation location (motion I) and the second axis is perpendicular on the first one having as reference position the E-W

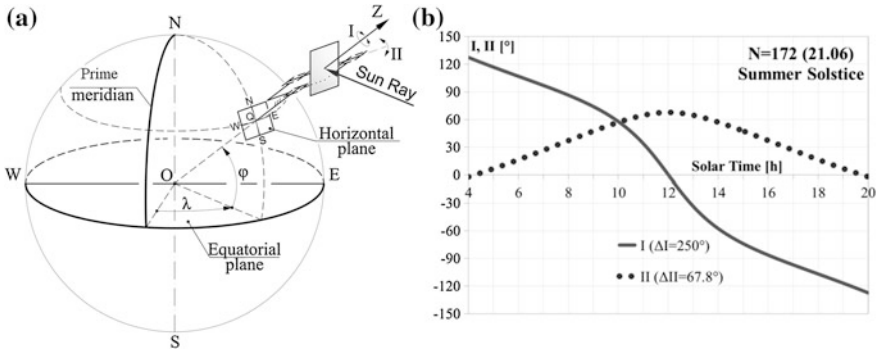


Fig. 4 a Solar tracking system with vertical fixed axis and **b** variation of the corresponding angles during the Summer Solstice at 45° northern latitude

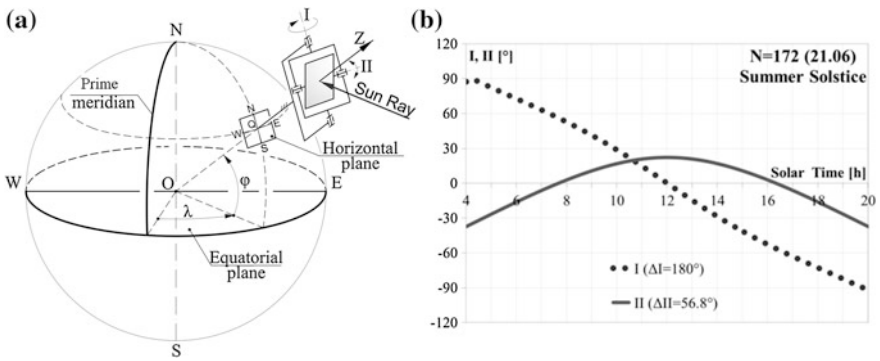


Fig. 5 a Solar tracking system with local N-S horizontal fixed axis and **b** variation of the corresponding angles during the Summer Solstice at 45° northern latitude

direction of the implementation location (motion II). The amplitudes corresponding to these motions (for the Brasov location) have, according to Fig. 5b, variations up to 180° and 56.8° respectively. Comparing to the previous case, these amplitudes (and their sum) are significantly less.

When choosing any of the above tracking solutions there must be considered the implementation location (which directly influences the motions amplitude), the complexity of the constructive solution, the external loads (wind, snow), etc.

There are further presented concrete mechanisms adapted to various applications, for developing the tracking motions according to their amplitudes. These examples were analyzed, developed and proposed for patenting being further implemented in the research center Renewable Energy Systems and Recycling, in the R&D Institute of the Transilvania University of Brasov.

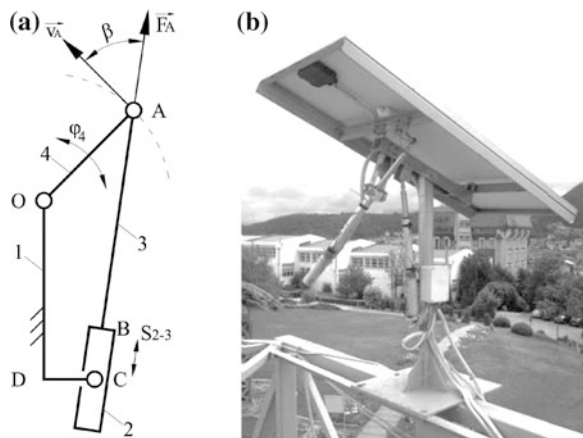
4 Tracking Mechanisms for Solar Energy Conversion Systems Implemented in the Built Environment

Tracking systems can be developed using a broad variety of mechanisms as linkages, gears, cams, chain mechanisms or combinations of these which are selected considering the type and the size of the tracking system, the motions' amplitudes for efficient tracking and the cost. Driving these mechanisms is done using linear actuators with the length (l_{min}/l_{max}) that is directly correlated with the amplitude of the input motion and/or using rotary actuators (e.g. speed-reducer, electrical motor) that can develop large angular strokes, (Visa et al. 2011).

Small rotation angles (usually below 120°) can be obtained using single loop linkages as the one described in Fig. 6. This is a variant of the planar RRTR crank mechanism, (Burduhos et al. 2009, 2010). The actuator develops a translation motion between elements 2–3 and element 4 insures the rotation needed to track the PV module. For an actuator with a given length and stroke, by selecting the geometric parameters ($l_1 = OD$, $e = DC$, $l_4 = OA$) and the position on the joint actuator at the basis, the angular motion of element 4 can be insured with pressure angles below the maximum admissible values (of $60...65^\circ$), Fig. 6a. These mechanisms can be used for both motions of the PV module and one practical application is presented in Fig. 6b as a variant of the tracking mechanism with fixed E-W axis (Fig. 3a). Tracking mechanisms as those presented in Fig. 6a have a simple construction and are low cost being thus feasible in tracking systems implementation.

The Tracking mechanism in Fig. 7 corresponds to a PV platform used for in-field testing of different PV modules (Visa and Comsit 2004). This system is also developed respecting the tracking system presented in Fig. 3a where the motion around the fixed axis is developed by the linkage from Fig. 6a but for the second motion such a mechanism is hardly feasible because of the large forces and large

Fig. 6 Structural scheme (a), and implementation (b) Patent request no. A/00622/2008



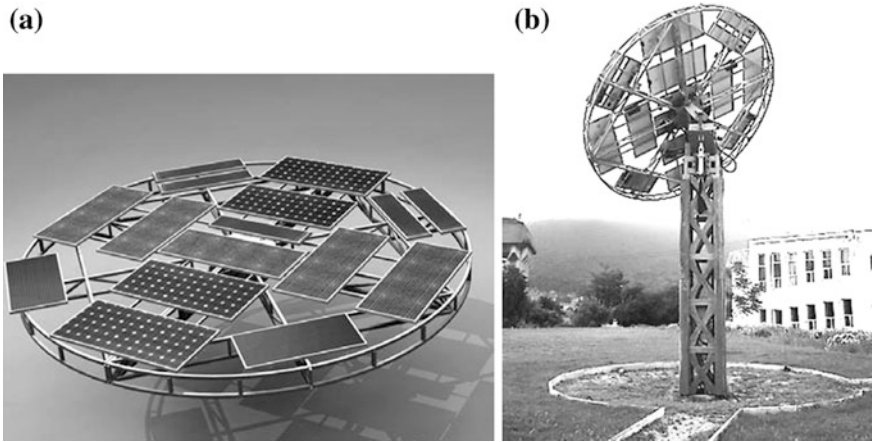


Fig. 7 Solar tracking system with E–W horizontal fixed axis: **a** PV platform and **b** implementation

motion amplitude. In this case a hydraulic motor was used (Comsit and Visa 2009) which will obviously raise the costs; still, since this platform represents a testing rig, the cost was not the main selection design criterion.

Large tracking angles (usually above 120°) can be obtained using multi-loop linkages, gear mechanisms or combinations of these. In Fig. 8a two loops (bi-contour) mechanism is presented, where the first loop is similar to those presented in Fig. 6a (type RRTR) and the second loop is of four-bar planar type (Fig. 8a) or spatial (Fig. 8b), used to amplify the rotation angle of the element 4, (Visa et al. 2008, 2009). The input translation motion between the elements 2–3 is given by the linear actuator for the output rotation of element 6, which tracks the PV module. The required rotation angle can be obtained by choosing the geometrical parameters of the two loops in the linkage mechanism, considering an optimal pressure angle ($\beta \leq \beta_a$). A concrete application is presented in Fig. 8c for a tracking system having the fixed axis parallel with the vertical axis of the implementation location, where the rotation around this axis is done using the mechanism presented in Fig. 8b and the second motion uses a mechanism as presented in Fig. 6a. The constructive solution of this mechanism has a lower cost and easier maintenance comparing to a gear mechanism, being thus preferred. The main disadvantage is the need of two actuators (one for each tracking motion).

Literature mentions various alternatives for the rotation motion around the vertical axis corresponding to the implementation location, by using gear mechanisms and for the rotation around the E–W axis by using linear actuators, by the mechanism presented in Fig. 6a. These solutions have a higher cost and require increased maintenance.

One possible solution based on gear mechanisms for both motions is presented in Fig. 9a, with the implemented model presented in Fig. 9b, (Moldovean et al. 2010).

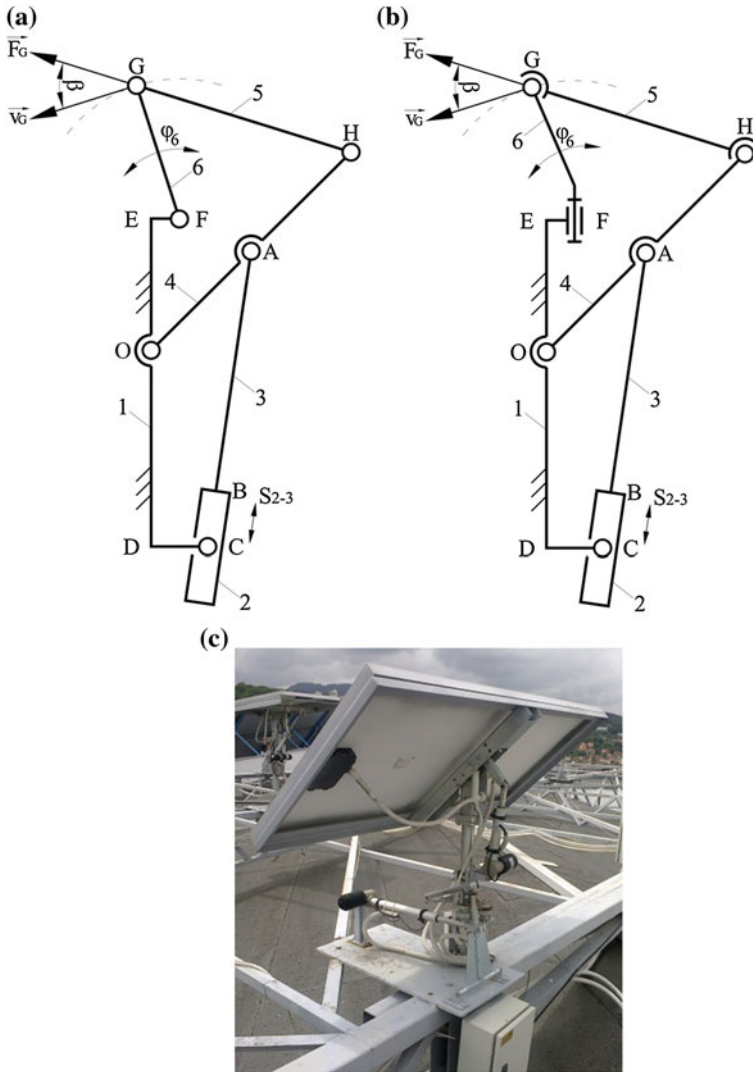


Fig. 8 Solar tracking system with vertical fixed axis: **a** structural scheme for the diurnal planar and **b** spatial mechanism, and **c** implementation, patent request no. A/00622/2008

The required motions are obtained by coupling/decoupling the three couplings C_1 , C_2 , C_3 . So, C_1 is coupled for the motion around the vertical axis while C_2 and C_3 are decoupled and for the E-W motion (in direct or reverse sense) C_1 is decoupled and C_2 or C_3 are coupled. This is a rather complex constructive solution, with a higher cost but it uses a single driving motor.

A tracking mechanism solution for large angular strokes around the vertical axis is the combined mechanism with linkage and gears, presented in Fig. 10.

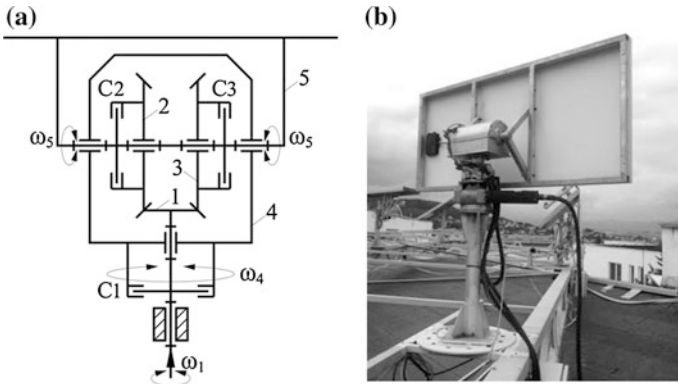


Fig. 9 Solar tracking system with vertical fixed axis: **a** structural scheme, and **b** implementation, patent request no. RO 126150-A2/2010

The linear actuator 2–3 gives the input S_{2-3} motion for the rotation of the driven gear 5. The mechanism contains a planetary differential gear mechanism where the two input motions are obtained through the rotation of the 3' gear along with the 2–3 assembly and through element 4, (Creangă et al. 2011; Neagoe et al. 2012). The mechanism is efficient and has a more simple construction comparing to that presented in Fig. 9, having therefore a lower cost.

An implementation example is presented in Fig. 10b, where the rotation around the vertical axis uses the mechanism in Fig. 10a and the rotation around E-W uses a similar mechanism as those presented in Fig. 6a. The drawback of this tracking system is the need for two actuators.

A linkage mechanism with a single actuator is presented in Fig. 11a; this is a variant of the general spatial 7R mechanism, using in B and C cardanic couplings.

The angular actuator is driving the vertical rotation motion φ_5 , which—based on the linkage mechanism, imposes the PV tracking motion through the second rotation φ_4 , (Vătăşescu et al. 2011; Diaconescu et al. 2011). This represents an

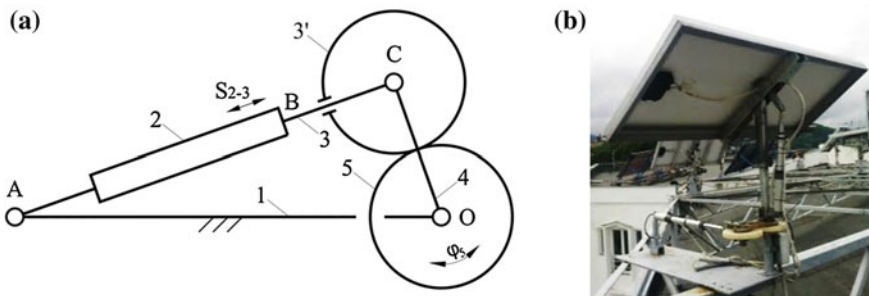


Fig. 10 Solar tracking system with vertical fixed axis: **a** structural scheme for the diurnal mechanism and **b** implementation, patent request no. A/01074/2010

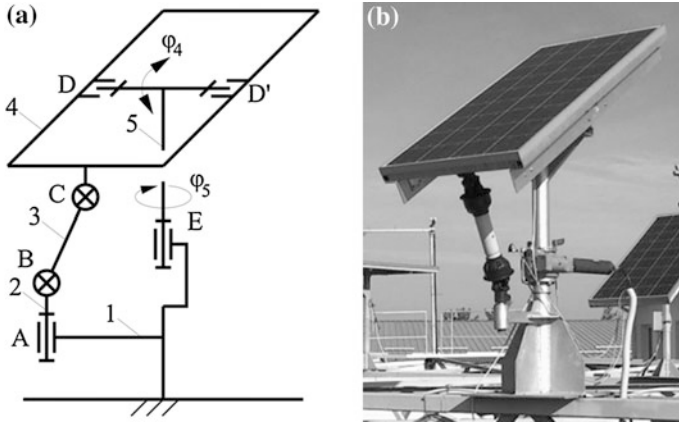


Fig. 11 Solar tracking system with vertical fixed axis: **a** structural scheme and **b** implementation, patent request no. RO126335-A0/2011

efficient and simple constructive solution, insuring a large amount of solar radiation on the PV module. The implemented version of this mechanism is presented in Fig. 11b.

An important group of tracking mechanisms is based on linkages where the angular driving motion around the fixed N–S axis in the implementation location using two linear actuators, parallel mounted in a five-bar loop with mobility 2. The mechanism in Fig. 12 has the five-bar loop formed by the elements 1...5, where point—common for both actuators, describes a planar coupler curve, according to the motions imposed by the two actuators. By amplifying the contour with the elements 6 and 7 the tracking mechanism in Fig. 12a is obtained and is able to describe large angular strokes (above 180°) while maintaining a simple constructive solution with optimal pressure angles (lower than 60°). By using the two

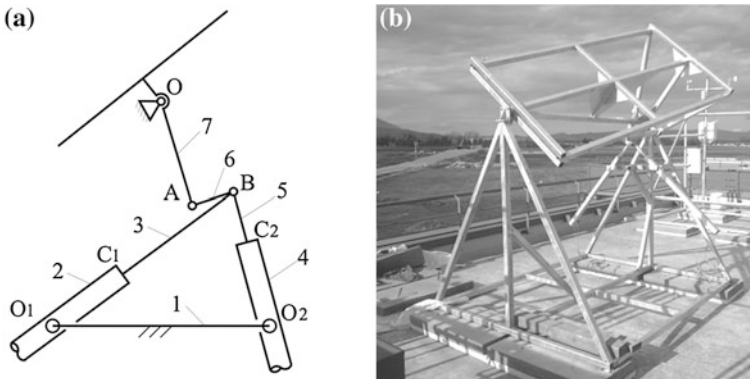
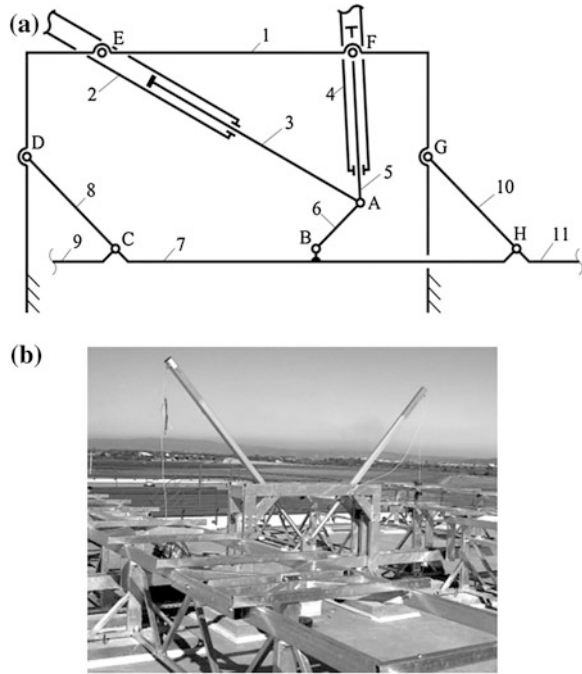


Fig. 12 Solar tracking system with N–S horizontal fixed axis: structural scheme for diurnal mechanism **(a)**, and implementation **(b)**, patent request no. A/00109/2012

Fig. 13 Solar tracking systems with N-S horizontal fixed axis: **a** structural scheme and **b** implementation, patent request no. A/00467/2012



actuators, the tracking accuracy is increased and by correlating their motions, a very low pressure angle results in point A (close to zero). The concrete solution of this mechanism is presented in Fig. 12b.

The tracking mechanism in Fig. 13 similarly contains a five-bar loop with two parallel actuators; the resulting motion drives the PV strings through the elements 8 and 10 from the parallelogram loop described by DCHG, having the coupler driven through element 6, linked in the joint point A (corresponding to the two actuators), (Moldovan et al. 2011; Visa et al. 2012). The dimensional synthesis of the mechanism and the motion laws corresponding to the two actuators allow obtaining the tracking angular strokes, with optimal pressure angles. The constructive solution of this mechanism is presented in Fig. 13b.

The energy output of the solar energy conversion systems can be increased by tracking, by concentrating the solar radiation or by combining these two. Low solar radiation concentrators can be done using mirrors, as for the PV system presented in Fig. 14a. By using double mirrors, the amount of solar radiation reaching the PV surface can be enhanced by 60 %, as Fig. 14b shows, (Hermenean et al. 2010, 2011).

The mirrors' based solution can also be used for solar-thermal flat plate collectors, for correlating the available amount of solar radiation with the users' needs, as presented in Fig. 15; this can be done either by concentrating the solar

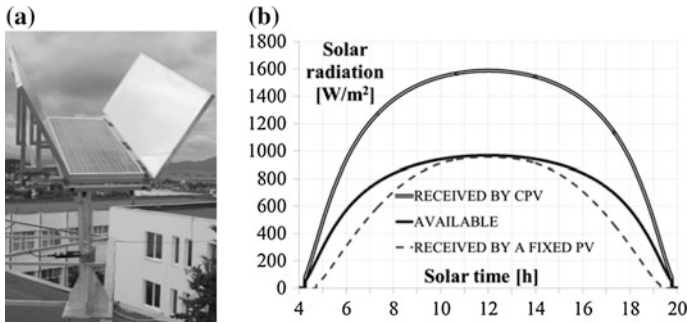


Fig. 14 Solar tracking system with vertical fixed axis and CPV: **a** implementation and **b** simulations, patent request no. RO126149-A0/2011

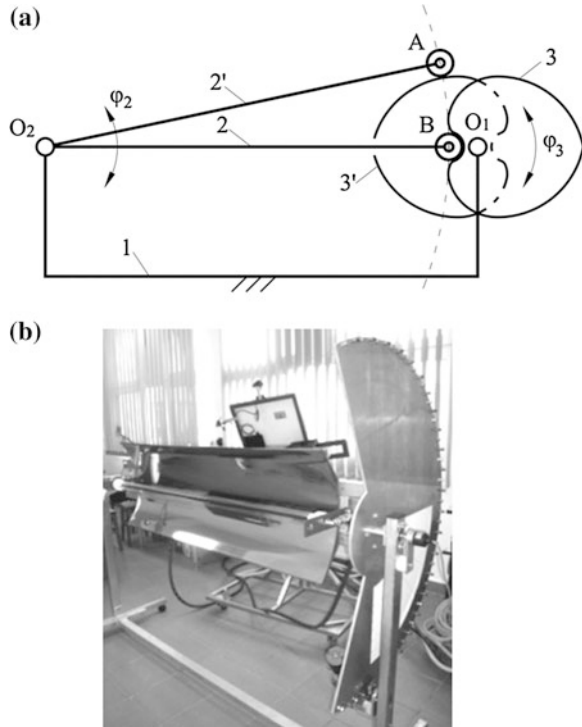
Fig. 15 Solar tracking system with low concentration for solar thermal collectors, patent request no. A/00109/2012



radiation when the demand is high or by shadowing the collector when the thermal needs are low, (Dombi et al. 2010).

Low solar radiation concentration can be applied also to parabolic solar-thermal collectors (dish or trough). This case requires accurate tracking solutions, using dedicated mechanisms. A constructive solution is presented in Fig. 16b; the mechanism has a horizontal rotation axis, N–S oriented and uses a double cam and multiple followers, Fig. 16a. The cam has a cardioid profile and the followers define the pins disposal on the pin wheel. The two cams are in direct contact with the followers, insuring a continuous motion transmission from the cams to the pin wheels, (Ciobanu and Visa 2005; Ciobanu et al. 2008), with a high transmission ratio.

Fig. 16 Solar tracking systems with N-S horizontal fixed axis: **a** structural scheme for the diurnal mechanism and **b** implementation, patent request no. A/00628/2008



5 Conclusions

1. Tracking systems can significantly increase the amount of solar radiation reaching the surface of photovoltaic modules or solar-thermal collectors, thus increasing the energy output and contributing to the *Green Energy* EU target.
2. Even when considering clear sky, solar radiation has a variable profile, depending on the implementation location, day of the year, hour of the day, etc.
3. Therefore, tracking systems must consider the apparent Sun path on the celestial vault and this can be stepwise done using mechanisms with various complexity degrees.
4. The four mostly used types of coupled motions are described, outlining the differences between the reference systems defined considering the fixed and mobile axes and their position towards the implementation plane and/or the polar axis.
5. Various types of mechanisms are presented, according to the motions defined for the general cases, and are analyzed considering their angular stroke, pressure angles, constructive complexity and feasibility.
6. For systems also including solar radiation concentration, accurate tracking mechanisms are discussed.

References

- Abu-Khader M, Badran O, Abdallah S (2008) Evaluating multi-axes sun-tracking system at different modes of operation in Jordan. *Renew Sustain Energy Rev* 12:864–873
- Badescu V (2008) Modeling solar radiation at the earth surface. Springer, Berlin
- Burduhos B, Visa I, Diaconescu D, Saulescu R (2009) Novel orientation step-program of a pseudo-equatorially tracked PV panel. In: 24th EU PVSEC—24th European photovoltaic solar energy conference and exhibition, Hamburg, Germany, pp 3835–3843
- Burduhos B, Visa I, Diaconescu D, Saulescu R (2010) The influence of the orientation axis number on the efficiency of a pseudo-equatorial tracker in Brasov—Romania. In: 25th European photovoltaic solar energy conference and exhibition, Valencia Spain, pp 4491–4496, 2010
- Ciobanu D, Visa I (2005) Modeling and kinematic analysis of cam mechanics as multibody systems. In: Proceedings of the 9th IFTOMM international symposium on theory of machines and mechanisms, Bucharest, Romania pp 21–26
- Ciobanu D, Visa I, Diaconescu D (2008) Optimizing of a new tracking systems for small parabolic trough collectors. In: International Conference EUROSUN, CD based
- Comsit M, Visa I (2005) Design of the tracking systems for solar panels. In: 20th PV conference, Barcelona 2005 (CD based)
- Comsit M, Visa I (2007) Design of the linkages type tracking mechanisms of the solar energy conversion systems by using Multi Body Systems Method. 12th IFTOMM World Congress, Besançon (France), June 8–21, 2007
- Comsit M, Visa I (2009) Integrated prototyping platform for tracked PV Systems. EUPVSEC, 2009
- Creangă N, Visa I, Diaconescu D, Hermenean I, Butuc B (2011) Geared linkage driven by linear actuator used for PV platform azimuth orientation. *Renewable Energy Power Qual J* 9: 456
- Davies PA (1993) Sun-tracking mechanism using equatorial and ecliptic axes. *Sol Energy* 50(6):487–489
- Dawood S, Crosbie T, Dawood N, Lord R (2013) Designing low carbon buildings: a framework to reduce energy consumption and embed the use of renewables. *Sustain Cities Soc* 8:63–71
- Devabhaktuni V, Alam M, Depuru SS, Green RC II, Nims D, Near C (2013) Solar energy: trends and enabling technologies. *Renew Sustain Energy Rev* 19:555–564
- Diaconescu D, Vișa I, Burduhos B, Saulescu R (2008) On the steps' optimization of a pseudo-equatorially tracked PV panel. In: 23rd EU PVSEC—23rd European photovoltaic solar energy conference and exhibition, Valencia Spain, pp 3160–3164
- Diaconescu D, Vișa I, Vătășescu MM, Săulescu R, Burduhos B (2011) The optimization of a bi-axial adjustable mono-actuator PV tracking spatial linkage. *New trends in mechanism science. Analysis and Design*, Springer Science & Media, pp 181–188
- Dombi V, Vișa I, Moldovan M, Burduhos B (2010) Step orientation system for a solar thermal platform. In: Proceedings of 6th international symposium shape, mechanical and industrial design of products. In *Mechanical Engineering Kod* 2010, pp 265–268, Palic, Serbia
- Gómez-Gil FJ, Wang X, Barnett A (2012) Energy production of photovoltaic systems: fixed, tracking, and concentrating. *Renew Sustain Energy Rev* 16:306–313
- Hermenean I, Vișa I, Duță A, Diaconescu D (2010) Modelling and optimization of a concentrating PV-mirror system. *Renewable Energy Power Qual J* 8
- Hermenean I, Vișa I, Diaconescu D, Duță A (2011) Comparative analysis of the energy response for three tracking system types used for CPV convertors. The 13th world Congress in mechanism and machine science, Mexico
- Kelly NA, Gibson TL (2011) Increasing the solar photovoltaic energy capture on sunny and cloudy days. *Sol Energy* 85:111–125
- Li DHW, Yang L, Lam JC (2013) Zero energy buildings and sustainable development implications—a review. *Energy* 54:1–10

- Marszal AJ, Heiselberg P, Bourrelle JS, Musall E, Voss K, Sartori I, Napolitano A (2011) Zero energy building—a review of definitions and calculation methodologies. *Energ Build* 43:971–979
- Moldovan M, Visa I, Burduhos B (2011) Energy modeling of a single axis tracked string PV system from a hybrid RES. In: *Proceedings of 26th EUPVSEC*, pp 3804–3807, Hamburg, Germany
- Moldovean GH, Visa I, Velicu R, Butuc B (2010) Static stress calculation of straight bevel gears applied to a PV tracking system. In: *The first IFToMM Asian conference on mechanism and machine science*, Taipei
- Mousazadeh H, Keyhani A, Javadi A, Mobli H, Abrinia K, Sharifi A (2009) A review of principle and sun-tracking methods for maximizing solar systems output. *Renew Sustain Energy Rev* 13:1800–1818
- Neagoe M, Vătăşescu MM, Săulescu R, Creangă N (2012) On new high performance systems with linear actuators for diurnal orientation of PV platforms. *Appl Mech Mater J* 162:214–223
- Schubnell M, Ries H (1990) Velocity-controlled tracking of the sun. *Sol Energy Mater Sol Cells* 21(2–3):207–212
- Seme S, Štumberger G (2011) A novel prediction algorithm for solar angles using solar radiation and differential evolution for dual-axis sun tracking purposes. *Sol Energy* 85:2757–2770
- Smalley RE (2003) Top ten problems of humanity for next 50 years. In: *Energy & nanotechnology conference*, Rice University, 3 May 2003
- Vătăşescu MM, Visa I, Diaconescu D, Săulescu R (2011) Synthesis of a RRSS Linkage for tracking a two axis photovoltaic system. In: *13th world Congress in mechanism and machine science*, Universidad de Guanajuato (UCEA), México
- Visa I, Comsit M (2004) Tracking systems for solar energy conversion devices. In: *Proceedings of EUROSUN 2004*, vol 2, pp 143–148
- Visa I, Diaconescu D, Popa V, Burduhos B, Saulescu R (2008) The synthesis of a linkage with linear actuator for solar tracking with large angular stroke. In: *Ceccarelli M (ed) EUCOMES 2008—2nd European conference on mechanism science*, C_ Springer Science and Business Media B.V., 2009, pp 457–464
- Visa I, Diaconescu D, Saulescu R, Vatasescu MM, Burduhos B (2011) New linkage with linear actuator for tracking PV systems with large angular stroke. *Chin J Mech Eng* 24(5):744–751
- Visa I, Diaconescu D, Popa V (2008) On the dependence between the step orientation and the received direct solar radiation of a PV panel. Part I: the step azimuthal orientation. In: *Proceedings of ICREPQ'08—international conference on renewable energies and power quality*, Santander, Spain, pp 77–78
- Visa I, Diaconescu D, Popa V, Burduhos B, Saulescu R (2008) The synthesis of a linkage with linear actuator for solar tracking with large angular stroke, Springer. In: *Proceedings of EUCOMES 08*, pp 457–464
- Visa I, Diaconescu D, Popa V, Burduhos B (2009) Synthesis of linkages for tracking systems with increased angular stroke. In: *International symposium on science of mechanisms and machines*, Brasov–Romania, pp 193–206, Springer
- Visa I, Diaconescu D, Moldovan MM (2012) A new solar tracking linkage with 2 actuators in parallel connected. In: *The 2nd IFToMM Asian conference on mechanism and machine science*, Tokyo, Japan
- Wyman O (2012) World energy Trilema; time to get real—the case for sustainable energy policy. World Energy Council

Conceptual Design of an Expressive Robotic Head

F. Adascalitei, I. Doroftei, D. Lefeber and Bram Vanderborght

Abstract In this paper, a new conceptual design of the huggable robot Probo is proposed. The new robotic head, with 21 degrees of mobility, is actuated using only “hobby” servos and consists of five different functional systems such as the eye-system, the ear-system, the trunk system, the mouth system and the neck system, which will be described in detail in terms of mechanical aspects. Then, some kinematic aspects concerning the eye-system will be discussed.

Keywords Conceptual design · Human-robot interaction · Social robot

1 Introduction

Facial expression plays an important role in our daily activities the human being a rich and powerful source, which is full of communicative information about human behavior and emotion. The most expressive way that humans display emotions is through facial expressions, which play a major role in human interaction and nonverbal communication (Ge et al. 2008).

F. Adascalitei · I. Doroftei (✉)
Mechanical Engineering, Mechatronics and Robotics Department,
“Gh. Asachi” Technical University of Iasi, Iasi, Romania
e-mail: idorofte@mail.tuiasi.ro

F. Adascalitei
e-mail: adascalitei_florentina@yahoo.com

D. Lefeber · B. Vanderborght
Vrije Universiteit Brussel (VUB), Brussels, Belgium
e-mail: dirk.lefeber@vub.ac.be

B. Vanderborght
e-mail: bram.vanderborght@vub.ac.be

For the robot, to express a full range of emotions and to establish a meaningful communication with a human being, nonverbal communications such as body language and facial expressions is vital. The ability to mimic human body and facial expressions lays the foundation for establishing a meaningful nonverbal communication between humans and robots (Brethes et al. 2005). Moreover, in any face to face communication, there are three basic elements: words, tone of voice and body language (Mehrabian 1971). The author of this reference stated that body language and nonverbal communication represents 55 % of the communication of feelings and attitudes.

Through facial expressions, robots can display their own emotion just like human beings. The primary components of a robotic head used to express emotion are: mouth (lips), cheeks, eyes, eyebrows, neck and forehead. Most robot faces express emotion in accordance with Ekman and Frieser's Facial Action Coding System (FACS) system (Ekman et al. 1982).

In this paper, a new conceptual design of the huggable robot Probo, developed by Robotics and Multibody Mechanics Research Group, Vrije Universiteit Brussel (VUB), Belgium, is proposed and described. The novel design is a result of the collaboration between this group and Mechanical Engineering, Mechatronics and Robotics Department, "Gheorghe Asachi" Technical University of Iasi, Romania.

2 New Version of Probo

2.1 Motivation

The main goal of the Probo concept was the development of a social robot, to study Human-Robot Interaction (HRI) and Robot-Assisted Therapy (RAT) for children with Autistic Spectrum Disorders (ASD) (Goris et al. 2012). Another aspect was to develop a multi-disciplinary research community; therefore collaboration with pediatricians, sociologists and psychologists was a necessity (Goris et al. 2011).

Since most of the communication passes through non-verbal cues, and since people rely on face-to-face communication, the focus of Probo communicative skills laid initially on rendering facial expressions. To achieve the emotional behavior, the robot was equipped with 20° of mobility (d.o.m).

Based on the preliminary results, it was investigated the possibility to reproduce the robotic platform to be used by other research groups around the world. But, due to the fact that the existing prototype of the robot Probo has a certain degree of complexity and it is equipped with expensive hardware components, the idea of creating a commercial version of it could not be reached. Therefore, the development of a new version, to meet and solve these disadvantages, became a necessity. To achieve this goal, several design criteria were adopted, namely:

modularity; reliability; low cost price; usage of cheap, easy and rapid prototyping techniques; compliance and flexibility.

2.2 Conceptual Design

The new concept (Fig. 1) has 21 d.o.m., providing independent motions of all the actuated parts. It is a modular version, since it contains five subsystems, namely: eye, ear, trunk, mouth and neck system.

In terms of affordability and reproduction, it is a low-cost solution, since it makes usage of cheap, easy and rapid prototyping techniques and uses cheaper actuators and materials. Due to the fact that the robot is equipped with a silicone mouth, flexible foam trunk and elastic elements used in the ears and neck system, a high degree of compliance and flexibility it is provided.

The eye system (noted with 4 in Fig. 2) has 10 d.o.m. and includes the eyeballs (4 d.o.m.), the eyelids (2 d.o.m.) and the eyebrows (4 d.o.m.). Compared with the previous version, this new solution has an additional degree of mobility, providing independent motions for all the actuated parts. The eyes can pan ($\pm 45^\circ$) and tilt ($\pm 60^\circ$) independently, the eyelids can open and close (70°) and the motion of eyebrows (20°) intensify the facial expressions. Compared to the previous design, where eyes were operated through cables and the motors were mounted in the belly

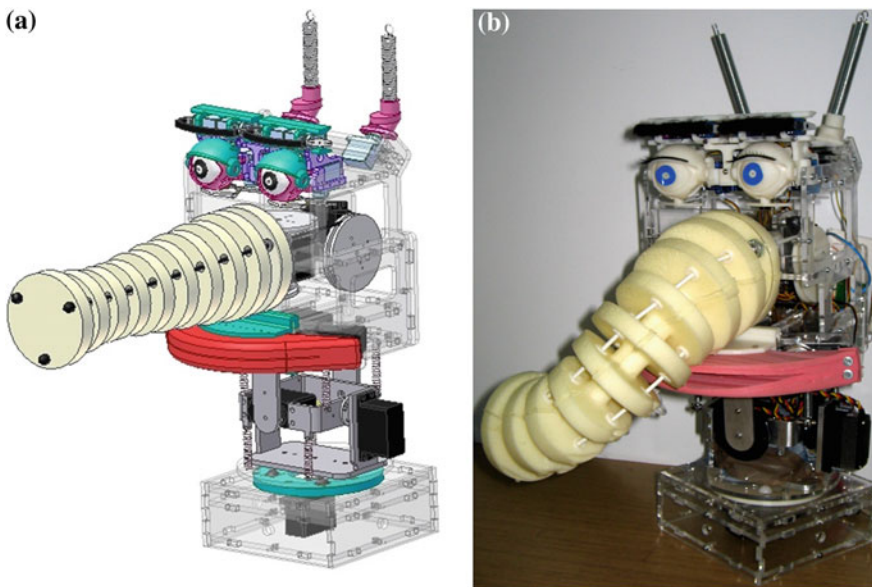


Fig. 1 New design of the robot Probo. **a** CAD solution. **b** Real prototype

of the robot, under the new concept the components are driven directly or through bar mechanisms.

The ears (with 1 d.o.m. each), 5 in Fig. 2, are represented by two helical springs, placed at an angle of 45° from the top of the head, having a range of motion of $\pm 60^\circ$ and ensuring compliance during interaction. The helical springs will be covered with a flexible foam core, which will have the shape of an animal ear. In comparison with Kismet's ears which have 2 d.o.m. each (Breazeal 2002), so they can be lowered and elevated while they can point the ear's opening separately, in our case, to reduce complexity, the two rotations are combined in a single one.

In contrast to other robotic heads, an intriguing anatomical part was added to the robot, namely the trunk (noted with 3 in Fig. 2), to enhance certain facial expressions and to increase interactivity. This part has three combined d.o.m. The main components of this system are represented by the trunk itself, made from an

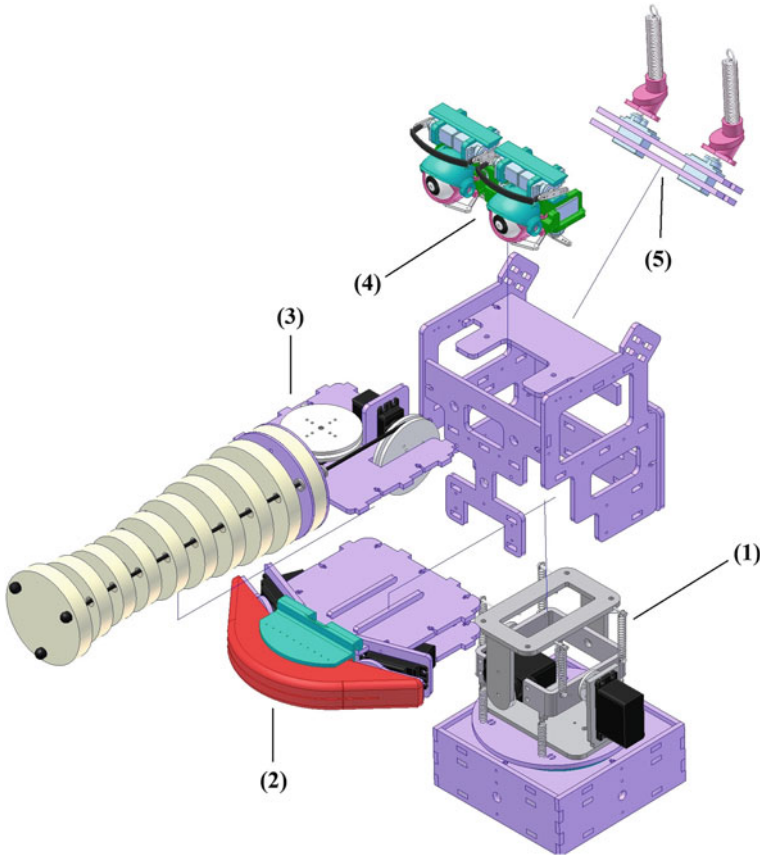


Fig. 2 Exploded view of the new concept

expandable foam core, three flexible cables, separated 120° apart, and the drive mechanism. The cables are wound around three discs attached directly to the servo output shaft providing a spatial movement of the trunk. Depending on the number of actuated cables, on their position in relation to a system of axes attached to this subsystem, and on the stroke of each wire, we obtain a spatial deformation of the trunk, similar to a trunk type flexible manipulator. Due to the fact that the trunk's core and cables are flexible, the trunk system gives a safe and compliant characteristic.

The silicone mouth (3 d.o.m.) has three actuated parts (lower lip and mouth corners) and a fixed part (upper lip), constrained by the acrylic glass structure (2 in Fig. 2). The range of motion of the lower lip is limited by the mechanical construction to a value of 40°, and the mouth corners can realize a rotation of ±25°. Because in the previous prototype the trunk obstructed the visibility of the mouth (disadvantage in creating facial expressions), for the new concept, in order to prevent this drawback, greater dimensions were adopted for this part.

The Fitzpatrick's model (Fitzpatrick 2010) has been chosen as the most suitable solution for the neck system of the new social robot. The mechanical solution (noted with I in Fig. 2) is a serial mechanism, equivalent to a spherical wrist, with three degrees of mobility, providing three motions: head pan, head tilt and head swing. To compensate the gravity, and consequently to reduce the required motor torque for tilting or swinging the head, the neck was equipped with helical tension springs, similar to the robotic head ROMAN (Berns and Braum 2005) which concluded that if the set of spring pairs are well dimensioned, the required torque around the motor shaft is reduced to approximately the torque introduced by the inertia of the head.

The aluminum frame and most of 3D printed parts of the head have been replaced with an acrylic glass frame, respectively parts obtained with laser-cutting technology, reducing the weight and also the cost of the robotic head.

3 Some Kinematic Aspects

The eye-system is one of the most complex components of the robotic head. Because its design is based on a natural anthropomorphic model it gives the impression of being natural. In this paper, we will concentrate on its kinematics.

A RSUR spatial linkage is used to actuate the eyelid (Fig. 3a). Its inverse kinematics leads to:

$$\theta_4 = \text{Atan } 2 \left(\frac{2t}{1+t^2}, \frac{1-t^2}{1+t^2} \right) \quad (1)$$

where $t = \frac{q \pm \sqrt{p^2(\theta_1) + q^2 - r^2(\theta_1)}}{p(\theta_1) + r(\theta_1)}$, with: $p(\theta_1) = 2 \cdot l_3 \cdot (l_1 \cdot c_1 - b)$; $q = 2 \cdot c \cdot l_3$; $r(\theta_1) = l_1^2 - l_2^2 + l_3^2 + a^2 + b^2 + c^2 - 2 \cdot a \cdot l_1 \cdot s_1 - 2 \cdot b \cdot l_1 \cdot c_1$; $s_1 = \sin \theta_1$ and $c_1 = \cos \theta_1$.

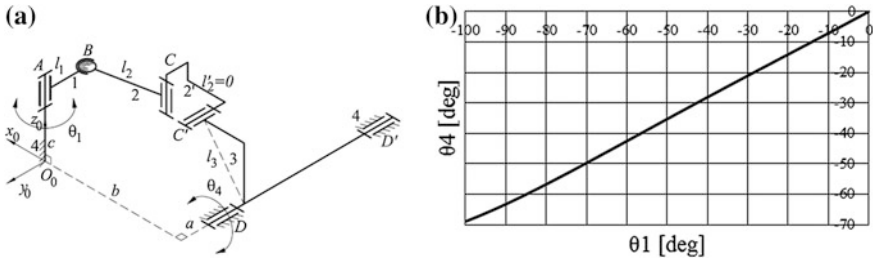


Fig. 3 Eyelid kinematics. **a** Eyelid mechanism. **b** Diagram $\theta_4(\theta_1)$

In order to prove the effectiveness of the spatial four-bar mechanism used to actuate the eyelid, a numerical simulation has been done. As we see in Fig. 3b, the variation of the eyelid orientation angle, θ_4 , according to the servo orientation angle, θ_1 , is approximately linear, proving the effectiveness of the four-bar linkage and simplifying the algorithm control.

The eyeball subsystem has a more complex design because the eyeball itself should have a spatial motion (2 degrees of freedom). Consequently, we are using two servos and two spatial four-bar mechanisms in series to drive the eyeball (Fig. 4).

In Fig. 5, simulation results for eyeball angular positions are shown. As we see in this figure, if we consider one of the servos angles (θ_1 or $\theta_{1'}$) constant, the variation of the eyeball orientation angles, θ_4 (for horizontal movement) and θ_5 (for vertical movement), according to the servos orientation angles, is approximately linear, simplifying the eyeball motion control. In order to get the mathematical relations $\theta_4(\theta_1, \theta_{1'})$ and $\theta_5(\theta_1, \theta_{1'})$ kinematics of the eyeball mechanism should be solved. It will be the subject of another paper.

If we consider that the eyeball spatial motion may be decoupled in horizontal (tilt) and vertical (pan) movements, two equivalent mechanisms with one degree of mobility each may be used to actuate the eyeball (see Figs. 6 and 7). Because two

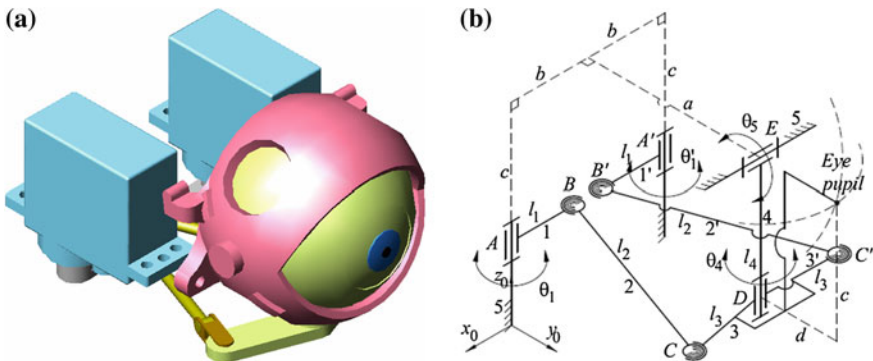


Fig. 4 Eyeball subsystem. **a** CAD solution. **b** Kinematics

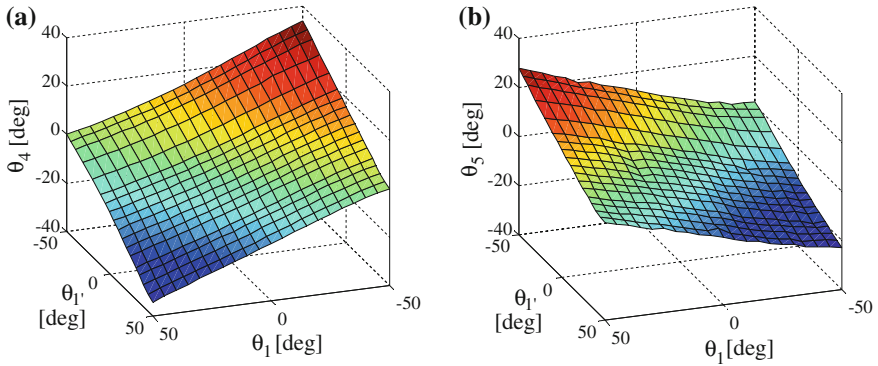


Fig. 5 Simulation results for eyeball mechanism. **a** Diagram $\theta_4(\theta_1, \theta_1')$. **b** Diagram $\theta_5(\theta_1, \theta_1')$

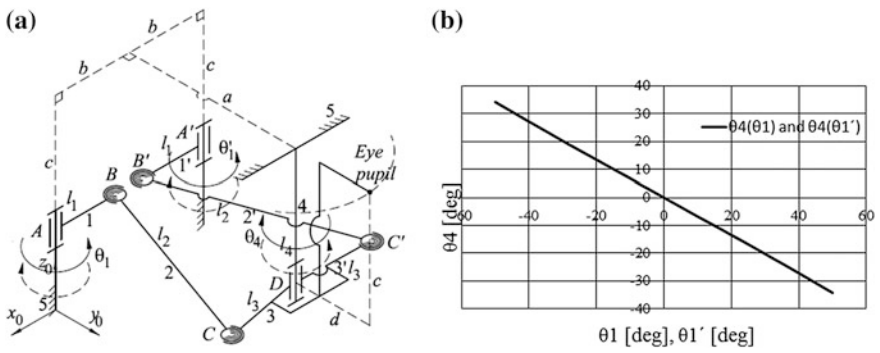


Fig. 6 Eyeball equivalent mechanism for *horizontal* movement. **a** Kinematics. **b** Diagrams $\theta_4(\theta_1)$, $\theta_4(\theta_1')$

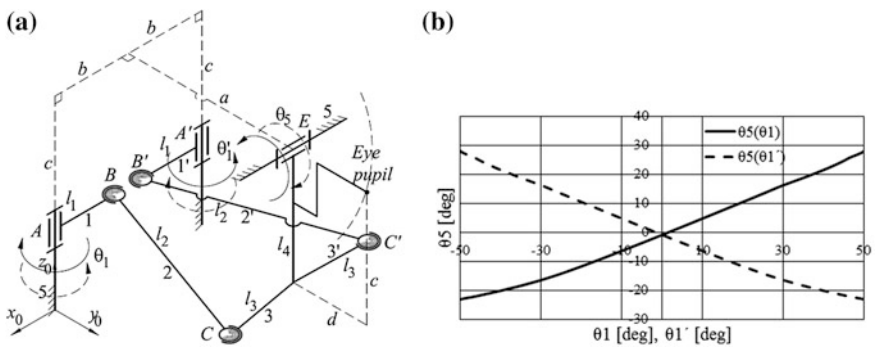


Fig. 7 Eyeball equivalent mechanism for *vertical* movement. **a** Kinematics. **b** Diagrams $\theta_5(\theta_1)$, $\theta_5(\theta_1')$

servos are used to actuate the eyeball, for these particular movements the mechanism is over actuated. In these cases the two servos have to be controlled so that their orientation angles should be $\theta_1(t) = \theta_{1'}(t)$ (for horizontal movement) or $\theta_1(t) = -\theta_{1'}(t)$ (for vertical movement).

4 Conclusion

In this paper, a new conceptual design and some kinematics aspects of the new version of the huggable robot Probo have been presented. Based on the simulations, we demonstrated the effectiveness of the robot eye-system. Some work in the control of the robot and experimental tests for facial expressions recognition, using different human subjects, will be done in the future.

Acknowledgments This paper was realized with the support of POSDRU CUANTUMDOC “DOCTORAL STUDIES FOR EUROPEAN PERFORMANCES IN RESEARCH AND INNOVATION” ID79407 project, funded by the European Social Fund and Romanian Government. We are also grateful to the Robotics & MultiBody Mechanics Research Group (VUB) for their support and collaboration.

References

- Berns K, Braum T (2005) Design concept of a human-like robot head. In: Proceedings of the 2005 IEEE-RAS 5th international conference on humanoid robots, pp 32–37
- Breazeal CL (2002) Designing sociable robots. MIT Press, Massachusetts
- Brethes L, Lerasle F, Danes P (2005) Data fusion for visual tracking dedicated to human-robot interaction. In: Proceedings of the 2005 IEEE international conference on robotics and automation, Barcelona, Spain, pp 2075–2080
- Ekman P, Friesen WV, Ellsworth P (1982) Does the face provide accurate information? In: Ekman P (ed) Emotion in the human face, 2nd edn. Cambridge University Press, Cambridge, UK, pp 56–97
- Fitzpatrick R (2010) Designing and constructing an animatronic head capable of human motion programmed using face-tracking software. A graduate capstone project report submitted to the faculty of the Worcester polytechnic institute
- Ge SS, Wang C, Hang CC (2008) A facial expression imitation system in human robot interaction. In: The 17th international symposium on robot and human interactive communication
- Goris K, Saldien J, Vanderborght B, Lefeber D (2011) Mechanical design of the huggable robot Probo. *Int J Humanoid Rob* 8(3):481–511
- Goris K, Saldien J, Vanderborght B, Lefeber D (2012) Mechanical design of the huggable robot Probo. *Int J Humanoid Rob* 8(3):481–511
- Mehrabian A (1971) Silent messages. Wadsworth, Belmont, CA. ISBN 0-534-00910-7

On the Structural Analysis of the Mechanisms with Elastic Connections

Erwin-Chr. Lovasz, Dan Perju, Karl-Heinz Modler, Niels Modler, Corina Mihaela Gruescu, Inocențiu Maniu and Andrei Comșa

Abstract The paper deals with the structural analysis of the mechanisms with elastic connections. This study is based on the up-to-date development of the technologies in the field of smart compound materials with controlled elastic deformation and the nanotechnologies. The aim of the study is to define the elastic connections in the context of the classical mechanism theory and to develop the relationships in order to compute the mobility of the mechanisms with elastic connections. In order to illustrate the theoretical development, the authors present several numerical examples. All methods are based on preserving of the kinetostatic conditions in a movement cycle. The authors present the classification of elastic connections in correlation with the classical ones.

Keywords Structural analysis · Elastic connection · Degree of freedom · Mobility

1 Introduction

The technical requirements of mechanical and mechatronic products are generally complex and impose well-defined movements to ensure a mechanical constraint. The development of mechanisms theory focused primarily on the use of rigid links in the structure of mechanisms (classical theory). Following the new developments

E.-C. Lovasz (✉) · D. Perju · C. M. Gruescu · I. Maniu · A. Comșa
Mechanical Engineering Faculty, Department of Mechatronics,
Politehnica University of Timișoara, 1 Bv. Mihai Viteazul,
300222 Timișoara, Romania
e-mail: erwin.lovasz@mec.upt.ro

K.-H. Modler · N. Modler
Department for Rigid Body Mechanics, Chair for Nonlinear Rigid Body Mechanics,
Technische Universität Dresden, Fakultät Maschinenwesen, 10 Helmholtzstr 01069
Dresden, Germany

in the field of smart compound materials with controlled elastic deformation and alongside the advance of nanotechnologies, the use of elastic deformable components belonging to elastic connections is more and more frequent (modern theory).

The main structural parameter of a kinematic chain or of a mechanism is the degree of freedom, respectively the degree of freedom (mobility) of the mechanism (DOF). The condition to have a mechanical constrained motion is to impose the mobility equal to the number of the driving links. The mobility of mechanisms was studied by many scientists beginning with Chebyches (1869) and continuing with (Grübler 1883, 1885; Kutzbach 1929; Dobrovolski 1951; Artobolevski 1953; Manolescu 1968; Waldron 1966; Antonescu 1973; Hervé 1978; Gronowicz 1981; Angeles and Gosselin 1988; Huang et al. 2009; Yang et al. 2008; Zhang and Mu 2010 and others. Gogu presented in (2005a, b) an overview on the calculation of the mobility of the mechanisms with rigid bodies as elements.

In order to achieve an unitary theory of mechanisms, the use of both rigid elements and elastic connections requires the development of a proper, up-to-date structural analysis. In this regard, one should reconsider the definition of the kinematic joint, of the link and then, express the formula of mechanism's degree of freedom (mobility) within a new form of structural analysis of these mechanisms (Comşa A).

2 Basics and Definitions

The classical theory of mechanisms considers the links/elements as rigid bodies. In regard with the strength characteristics, the rigid elements are considered theoretically non-deformable by tensile/compression, bending and torsion.

“The link is defined in¹ (Ionescu 2003). As a rigid mechanism element (component) carrying kinematic pairing elements.”

The links are connected through kinematic pairs and the closure of the kinematic pairs is a process of constraining two rigid bodies to form a kinematic pair by force (force closure), geometric shape (form closure) or flexible materials (material closure) (Ionescu 2003) (see footnote 1).

“The kinematic pair is defined as a mechanical model of the connection of two pairing elements having relative motion of a certain type and degree of freedom (Ionescu 2003) (see footnote 1).”

The kinematic pairs are classified regarding the degree of freedom or the constrained motion in five classes. The class of the kinematic pair is given by the number of constrained movements in respect with the attached reference system.

¹ http://www.iftomm.org/index.php?option=com_content&view=article&id=101&Itemid=196.
Last accessed 15 Mar 2013

“The degree of freedom of a kinematic pair is expressed as the number of independent coordinates needed to describe the relative positions of pairing elements (Ionescu 2003) (see footnote 1).”

The connected links through kinematic pairs of different classes build a kinematic chain.

“The kinematic chain is defined as an assemblage of elements/links and joints (Ionescu 2003) (see footnote 1).”

The mechanism can be defined starting from the definition of the kinematic chain or according with its mechanical functions, as follows:

“Kinematic chain with one of its components (links) taken as a frame (Ionescu 2003) (see footnote 1).”

“System of bodies designed to convert motions of, and forces on, one or several bodies into constrained motions of, and forces on, other bodies (Ionescu 2003) (see footnote 1).”

The structural parameter of the kinematic chain and mechanism are defined in (Ionescu 2003) (see footnote 1) as:

“The degree of freedom of a kinematic chain or the degree of freedom (mobility) of a mechanism represents the number of independent coordinates needed to define the configuration of a kinematic chain or mechanism.”

The degree of freedom of a kinematic chain (Fig. 1) in respect with a reference system may be calculated according to (Dobrovolski 1951) as:

$$L = 6n - \sum_{i=1}^5 i \cdot c_i, \tag{1}$$

where c_i is the number of kinematic pairs of class i , $i = 1, 2, \dots, 5$; n —the number of links of the kinematic chain.

The relationship describing the degree of freedom (mobility) of mechanism is:

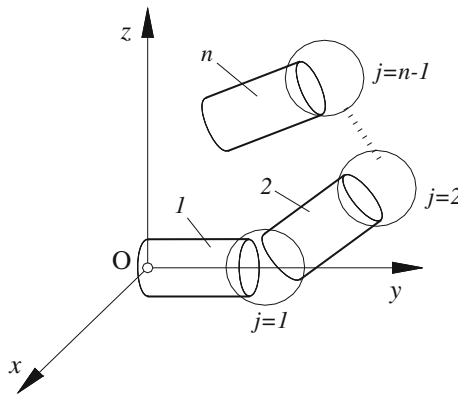


Fig. 1 Kinematic chain

$$M = (6 - f) \cdot (n - 1) - \sum_{i=f+1}^5 (i - f) \cdot c_i, \quad (2)$$

where f represents the number of common restricted motions of the mechanism's elements usually named "the family" (Manolescu 1968; Antonescu 1973; Kovács et al. 1976).

For the planar mechanisms, with $f = 3$, the relationship (2) becomes:

$$M = 3 \cdot (n - 1) - 2 \cdot c_5 - c_4, \quad (3)$$

where c_5 is the number of kinematic pairs of class V and c_4 —the number of kinematic pairs of class IV.

The mechanical constrained motion is ensured according to the above mentioned condition (see Sect. 1) if the relationship:

$$M = n_i \quad (4)$$

is satisfied, where n_i represents the number of driving elements with $\text{DOF} = 1$.

The works (Kovács 1969; Kovács et al. 1976) introduced the structural concept of connection. Connection means all the restrictions occurring in the relative movement between the elements in order to provide a constrained motion of the mechanism. The connections can be of kinematic/geometric type and of dynamic type. The kinematic/geometric connections are connections, which impose restrictions in terms of geometry and the dynamic connections in terms of forces equilibrium.

The definition of the connection (Kovács 1969; Kovács et al. 1976) is:

Open kinematic chain which is interposed between two elements with known or imposed relative movement.

The connections can be classified according to the number of their links and kinematic pairs (Fig. 2) in three types: connection of type A, which contains one kinematic pair, connection of type B, which contains one element and two kinematic pairs and connection of type C, which may have any structure.

3 Elastic Connections in Mechanisms Structure

The up-to-date development of smart compound materials with controlled elastic deformation and their applications in mechanical structures requires the reconsidering of some definitions and at least the mobility relationship.

Generally, an element may contain one or more elastically deformable sections, called further on as elastic connections. Considering the definition of the dynamic connection the elastic connection may be defined as follows:

The elastic connection is a dynamic/kinetostatic connection, which contains one or more elastically deformable sections materially closed with rigid sections of the element having a constrained relative motion.

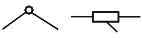

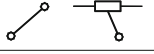


Type of connection	Number of elements	Kinematic pairs		Kinematic schema of connection	Degree of freedom L_k	Notation
		Nr.	Class			
A	$n_k = 0$	1	$c_{5k} = 1$		-2	$K_A(-2)$
			$c_{4k} = 1$		-1	$K_A(-1)$
B	$n_k = 1$	2	$c_{5k} = 2$		-1	$K_B(-1)$
			$c_{5k} = 1$ $c_{4k} = 1$		0	$K_B(0)$
C	$n_k = 2$	3	$c_{5k} = 3$		0	$K_C(0)$
			any		L_k	$K_C(L_k)$

Fig. 2 Classification of connections

The elastic connection allows supplemental degrees of freedom. These degrees of freedom result from the elastic deformation corresponding to the bending and/or compression loading. These deformations generate a quasi-rotation and/or translation motion between the considered elements.

Figure 3 presents a classification of elastic connections of type B, similarly with the kinematic connections. The classification takes into account only the kinematic pairs of class V. The other types of elastic connections are combinations of the kinematic and elastic connections of type B.


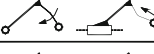

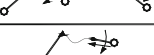
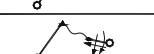
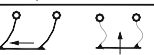
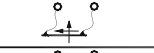


Type of elastic connection	Number of elements	Nr. of rigid sections	Nr. of elastic connection	Number of kinematic pairs	Kinematic schema of elastic connection	Supplemental degrees of freedom f_{elK}	Degree of freedom L	Notation
B	1	0	1	2		1	0	$K_{Bel}(0)$
		1	1			1	0	$K_{Bel}(0)$
		1	1			2	1	$K_{Bel}(1)$
		2	1			1	0	$K_{Bel}(0)$
		2	1			2	1	$K_{Bel}(1)$
		2	1			3	2	$K_{Bel}(2)$
		1	2			1	0	$K_{Bel}(0)$
		1	2			2	1	$K_{Bel}(1)$
		1	2			3	2	$K_{Bel}(2)$

Fig. 3 Classification of elastic connections of type B

In order to up-date the definition of the mechanism, which contains elastic connections one must ensure preservation of the kinetostatic/dynamic conditions in a motion cycle. Therefore, the mechanism definition may be:

System of rigid bodies with/without elastic sections designed to convert motions of, and forces on, one or several bodies into constrained motions of, and forces on, other bodies.

The degree of freedom of a kinematic chain containing elastic connections results from the relationship:

$$L = 6 \cdot n + \sum_{k=1}^m f_{elK_k} - \sum_{i=1}^5 i \cdot c_i, \quad (5)$$

where m is the total number of elastic connections, f_{elK} —the number of the supplemental degrees of freedom of the connection k .

Using the same logics, the degree of freedom (mobility) of the spatial mechanism is:

$$M = 6 \cdot (n - 1) + \sum_{k=1}^m f_{elK_k} - \sum_{i=1}^5 i \cdot c_i, \quad (6)$$

And for a planar mechanism the DOF is:

$$M = 3 \cdot (n - 1) + \sum_{k=1}^m f_{elK_k} - 2 \cdot c_5 - c_4 \quad (7)$$

As the mechanisms with elastic connection contain dynamic/kinetistatic connections, the constrained motion is ensured if the relationship:

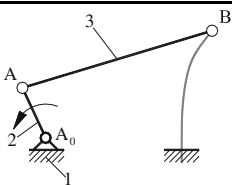
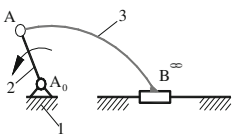
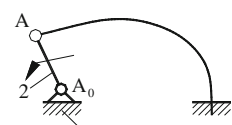
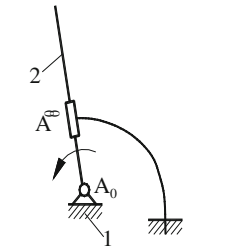
$$n_i \leq M \leq n_i + n_d \quad (8)$$

is satisfied, n_d being the number of links in dynamic equilibrium and n_i represents the number of driving links.

4 Example of Elastic Connections Structural Analysis

Table 1 gives several numerical examples with the computation of the degree of freedom (mobility) of structures containing elastic connections. The examples are derived from the classical linkages.

Table 1 Examples of mechanisms with elastic connections

Nr.	Kinematic schema
<p>1.</p>  <p>Four bar linkage with elastic connection</p>	<p>Number of the links and elastic connections $n = 3$ $m = 1$ with $f_{eIK} = 1$ Number of kinematic pairs Class V Class IV $c_5 = 3$ $c_4 = 0$</p> <p>Degree of freedom (mobility) of the mechanism $M = 3 \cdot (3 - 1) + 1 - 2 \cdot 3 - 0 = 1$</p> <p>Number of driving links $n_i = 1$ $n_d = 1$ Constrain motion condition $1 \leq 1 \leq 1 + 1 = 2$ (fulfilled)</p>
<p>2.</p>  <p>Slider crank with elastic connection</p>	<p>Number of the links and elastic connections $n = 3$ $m = 1$ with $f_{eIK} = 1$ Number of kinematic pairs Class V Class IV $c_5 = 3$ $c_4 = 0$</p> <p>Degree of freedom (mobility) of the mechanism $M = 3 \cdot (3 - 1) + 1 - 2 \cdot 3 - 0 = 1$</p> <p>Number of driving links $n_i = 1$ $n_d = 1$ Constrain motion condition $1 \leq 1 \leq 1 + 1 = 2$ (fulfilled)</p>
<p>3.</p>  <p>Mechanism with elastic connection and 2 joints RR</p>	<p>Number of the links and elastic connections $n = 2$ $m = 1$ with $f_{eIK} = 2$ Number of kinematic pairs Class V Class IV $c_5 = 2$ $c_4 = 0$</p> <p>Degree of freedom (mobility) of the mechanism $M = 3 \cdot (2 - 1) + 2 - 2 \cdot 2 - 0 = 1$</p> <p>Number of driving links $n_i = 1$ $n_d = 1$ Constrain motion condition $1 \leq 1 \leq 1 + 1 = 2$ (fulfilled)</p>
<p>4.</p>  <p>Mechanism with elastic connection and 2 joints RT</p>	<p>Number of the links and elastic connections $n = 2$ $m = 1$ with $f_{eIK} = 2$ Number of kinematic pairs Class V Class IV $c_5 = 2$ $c_4 = 0$</p> <p>Degree of freedom (mobility) of the mechanism $M = 3 \cdot (2 - 1) + 2 - 2 \cdot 2 - 0 = 1$</p> <p>Number of driving links $n_i = 1$ $n_d = 1$ Constrain motion condition $1 \leq 1 \leq 1 + 1 = 2$ (fulfilled)</p>

5 Conclusions

The paper proposes the redefinition of several basic terms in the mechanisms theory in order to include the elastic connections. The paper defines the elastic connection, which contains beside the rigid sections one or more elastic ones and proposes a classification of the elastic connections of type B similarly to the classification of the kinematic connections. In this case, it was necessary to redefine the term of mechanism, implicitly the kinematic chain with elastic connections.

The computation of the degree of freedom of kinematic chains and the degree of freedom (mobility) of the mechanisms with elastic connections imposed the development of new formulae. The paper proposed the relationship for constrained motion for this kind of mechanisms. Several examples illustrate the structural analysis for different structures of mechanisms with elastic connections.

Acknowledgments The authors would like to express their gratitude towards the German Research Foundation (DFG), which supports this research within the scope of the subproject D2 of the Collaborative Research Centre SFB 639 Textile-Reinforced Composite Components in Function-Integrating Multi-Material Design for Complex Lightweight Applications.

References

- Angeles J, Gosselin C (1988) Determination du degré de liberté des chaînes cinématique. *Trans Can Soc Mech Eng* 12(4):219–226
- Antonescu P (1973) Extending of structural formula of Dobrovolski to the complex mechanisms with apparent family. In: *Proceedings of the SYROM'73* 2, pp 1–10
- Artobolevskii II (1953) *Theory of mechanisms and machines*. Moscow
- Chebichev PA (1869) *Théorie des mécanismes connus sous le nom de parallélogrammes*, 2ème partie *Mémoires Présentés à l'Académie Impériale des Sciences de Saint-Petersbourg par divers savants*
- Comşa A (2013) *Contribuții privind automatizarea procesului de manipulare a cărților în biblioteci*, PhD Thesis, Timsoara
- Dobrovolski VV (1951) *Theory of mechanisms*. Moscow
- Gogu G (2005a) Mobility of mechanisms: a critical review. *Mech Mach Theory* 40:1068–1097
- Gogu G (2005b) Chebichev-Grübler-Kutzbach's criterion for mobility calculation of multi-loop mechanisms revisited via theory of linear transformations (Review). *Eur J Mech, A/Solids* 24(3):427–441
- Gronowicz A (1981) Identifizierungsmethode der Zwanglaufbedingungen von kinematischen Ketten. *Mech. Mach Theory* 16(2):127–135.3
- Grübler M (1883) *Allgemeine Eigenschaften der Zwangläufigen ebenen kinematischen Ketten*, Part I, *Zivilingenieur*, 29:167–200
- Grübler M (1885) *Allgemeine Eigenschaften der Zwangläufigen ebenen kinematischen Ketten*, Part II, In: *Verein zur Beförderung des Gewerbefleißes. Verhandlungen*, 64:179–223
- Hervé JM (1978) Analyse structurelle des mécanismes par groupe des déplacements. *Mech Mach Theory* 13(4):437–450
- Huang Z, Liu JF, Zeng DX (2009) A general methodology for mobility analysis of mechanism based constraint screw theory. *Sci China Serie E: Technol Sci* 52(5):1337–1347

- Ionescu TG (2003) Terminology for mechanisms and machine science. *Mech Mach Theory* 38:597–1111
- Kovács FV (1969) Contributii la elaborarea unei metode unitare de sinteza a mecanismelor (Contribution to the elaboration of a unitary method for mechanisms synthesis), Ph. D. Thesis, Polytechnic Institute “Traian Vuia” Timișoara
- Kovács FV, Perju D, Savii G (1976) Metode noi in sinteza mecanismelor (New methods in mechanisms' synthesis). Editura Facla, Timișoara
- Kutzbach K (1929) Mechanische Leitungsverzweigung, ihre Gesetze und Anwendungen, *Maschinenbau. Betrieb.*, 8:710–716
- Manolescu I (1968) For a united point of view in the study of the structural analysis of kinematic chains and mechanisms. *J Mech* 3(3):149–169
- Waldron KJ (1966) The constrain analysis of mechanisms. *J Mech* 1(2):101–114
- Yang D-C, Xiong J, Yang X-D (2008) A simple method to calculate mobility with Jacobian. *Mech Mach Theory* 43:1175–1185
- Zhang YT, Mu DJ (2010) A new concept and new theory of mobility calculation for multi-loop mechanisms. *Sci China Technol Sci* 53(6):1598–1604

An Innovative Family of Modular Parallel Robots for Brachytherapy

N. Plitea, C. Vaida, B. Gherman, A. Szilaghyi, B. Galdau,
D. Cocorean, F. Covaciu and D. Pislă

Abstract Brachytherapy (BT) is an advanced form of radiation therapy enabling the concentration of high doses in specific target points, enabling the direct treatment of tumors without damaging the proximal healthy tissues. BT usage is limited by the insufficient accuracy of radioactive seeds placement in the body. For this purpose, the paper presents an innovative family of modular parallel robots designed specifically to overcome the limitations of current BT procedures. The robotic structures employ two distinct modules in conjunction, which result in a reduced number of moving parts and removal of unwanted motions.

N. Plitea (✉) · C. Vaida · B. Gherman · A. Szilaghyi · B. Galdau
D. Cocorean · F. Covaciu · D. Pislă
Technical University of Cluj-Napoca, Cluj-Napoca, Romania
e-mail: Nicolae.Plitea@mep.utcluj.ro

C. Vaida
e-mail: Calin.Vaida@mep.utcluj.ro

B. Gherman
e-mail: Bogdan.Gherman@mep.utcluj.ro

A. Szilaghyi
e-mail: Andras.Szilaghyi@mep.utcluj.ro

B. Galdau
e-mail: Bogdan.Galdau@mep.utcluj.ro

D. Cocorean
e-mail: Dragos.Cocorean@mep.utcluj.ro

F. Covaciu
e-mail: Florin.Covaciu@mep.utcluj.ro

D. Pislă
e-mail: Doina.Pislă@mep.utcluj.ro

1 Introduction

Several specific medical applications require different devices able to insert substances or medical instruments inside the human body. Considering the nature of these tasks it is desirable to perform these actions with visual feedback, whereas the imagistic investigations range from simple radiologic exams to echography, computed tomography (CT) and magnetic resonance imaging (MRI).

The third millennium encounters a very provocative challenge: there are more and more cancer patients mainly because the increase of the average life span of the population and the curative treatments discovered for other diseases. This makes cancer one of the main causes of death nowadays, due to a complex set of uncontrollable natural and artificial factors. There are many cases where the treatment options for cancer are scarce (Tornes and Eriksen 2009; Delvin 2007; Podder and Fichtinger 2010, Kacso), but at the same time are many therapeutic approaches in the fight against cancer like: surgery, irradiation, chemotherapy or a combination of them, followed by rehabilitation in strong dependence with the specific patient needs: inversion therapy (Rea et al. 2013), robotized massage beds and so on. In radiation therapy high-energy rays are used to damage cancerous cells. It can be used as single therapy or in combination with cancer treatments (Delvin 2007). The traditional radiation therapy affects the entire body damaging also healthy tissue, but the researchers developed alternative therapies, aiming to concentrate the radiation in the tumor area with higher dosage, to increase the treatment positive effects while minimizing the adverse ones. One of the advanced techniques is the brachytherapy (BT). This involves the placement of the miniaturized radioactive sources very precisely in the tumor area, delivering high dosage of radiation in the cancerous cells. Its positive results are demonstrated, and its side effects are reduced to a minimum, but it requires very high positioning precision and a clear linear path to the tumor (Delvin 2007). BT is used for the treatment of tumors located in areas proximal to the skin, such as cervical (Viani et al. 2009), lung (Revez et al. 2012), breast but many studies showed its positive results in other body sites (Oudard et al. 2009). The widest spread BT application is the treatment of prostate cancer (Spârchez et al. 2010).

As a clear limitation in the use of BT stand its accuracy requirements for the radioactive seeds placement inside the tumors (Strassman et al. 2011). For that, many research institutes focused on the development of robotic devices aiming to increase the placement precision of the BT devices, but most of them are dedicated only for prostate therapy. Yu et al. present in (2007) a modular robot for ultrasound guided robotic prostate BT, consisting of a ultrasound probe drives and a 3-DOF gantry robot. G. S. Fischer et al. (2006) presents a 4-DOF hybrid robot for real-time control transperineal prostate needle orientation under MRI guidance and perform the insertion motion manually. Shan Jiang et al. (2010) developed a prototype and 3D model of a 5-DOF hybrid robot for prostate needle insertion surgery under continuous MRI guidance. In (Jiang et al. 2008) another robotic system, entitled MrBot is designed for the treatment of prostate cancer with real-time MRI visual

feed-back. As one can see from the above presented papers, most of the robotic systems developed for BT are intended for prostate cancer treatment. The present paper proposes a family of brachytherapy robotic systems for general BT, including cancer treatment for internal organs like: liver, lungs, paravertebral areas, etc.

The paper is organized as follows: [Sect. 2](#) presents a new family of innovative structures of parallel robots for BT, developed based on the medical specifications. [Section 3](#) shows the medical protocol of the robotized brachytherapy procedure. Some conclusions and future work are presented in the last section.

2 Structural Synthesis of a Family of Modular Parallel Robots for Brachytherapy

A modular robot is a robot built from components with standard electro-mechanical interfaces, making it possible to assemble in a variety of ways to suit a variety of purposes, such as the Geneva mechanisms in (Figliolini and Rea 2012). Modularity has many advantages: scalability, reusability, reconfigurability, ease of change and simpler maintenance. The new family of parallel robots is achieved through combinations of different parallel modules, enabling the development of an optimized structural model from the initial design phases. As the modules can be assembled in different configurations on the fixed frame, robotic structures with different configurations in terms of geometry, degrees of freedom and motion range capabilities of the end-effector can be obtained. This allows specific structural optimizations in terms of the BT application together with flexibility, variety in use, rapid changeover and ease of maintenance. Modules can have functional and logical separation. Functional separation of modules refers to a physical modularity that could be mechanical and/or electrical, while logical separation refers to the division of control between the modules.

Introducing the notations: M —the degree of freedom of the parallel robot; F —the mechanism family (the number of simple motions restricted for all the elements of the parallel mechanism out of the six possible ones); N —the number of mobile elements of the parallel mechanism; C_i —the number of class “ i ” joints, with, $i = 5, 4, 3, 2, 1$, where the joint class represents the number of restricted DOF, k —the number of kinematic guidance chains of the mobile platform; n —the number of elements for a single kinematic guidance chain for symmetric structures; c_i —the number of class “ i ” joints for a single kinematic chain. For a parallel mechanism of family F , the structural synthesis equations are (Plitea et al. 2006):

$$M = (6 - F) \cdot N - \sum_{i=1..5} (i - F) \cdot C_i, N = \frac{1}{6 - F} \cdot \left(M + \sum_{i=1..5} [(i - F) \cdot C_i] \right) \quad (1)$$

where $(5 - F)$, $(4 - F)$, $(3 - F)$, $(2 - F)$, $(1 - F)$ cannot take negative values.

For the symmetric parallel structures, the following equations are introduced:

$$N = k \cdot n + 1, \quad C_i = k \cdot c_i \quad (i = 1, 2, \dots, 5). \quad (2)$$

Using (2), it results from (1) the equation for the determination of the number of mobile elements of a single kinematic guidance chain for symmetric structures:

$$n = \frac{1}{k \cdot (6 - F)} \cdot \left\{ M - (6 - F) + k \cdot \sum_{i=1..5} (i - F) \cdot c_i \right\}. \quad (3)$$

For the particular case of parallel mechanisms of family $F = 1$ the Eqs. (1) and (3) become:

$$M = 5 \cdot N - \sum_{i=2..5} (i - 1) \cdot C_i; \quad N = \frac{1}{5} \cdot \left(M + \sum_{i=2..5} [(i - 1) \cdot C_i] \right); \quad (4)$$

$$n = \frac{1}{5k} \cdot [M - 5 + k(4c_5 + 3c_4 + 2c_3 + c_2)]. \quad (5)$$

In the following subchapters a family of modular parallel robots for brachytherapy specific tasks is presented (Plitea et al. 2013a, b, c, d). The two innovative solutions, are mechanisms of family $F = 1$, with 5-DOF, namely three translations in space and two orientations, eliminating the rotation around the longitudinal axis of the needle which is not needed. The robotic structures use different modules with 3-DOF with two or three active joints, mounted on a fixed frame which is positioned over the CT-table, to enable fast needle placement control after its insertion. In order to reduce to a minimum the number of moving elements, each structure uses two kinematic chains for guiding the end-effector (and thus the brachytherapy needle).

2.1 Parallel Robot for Brachytherapy with Two Kinematic Chains of the Platform of Type 2-CRRU and CYL-U

The first parallel structure, has a modular architecture, consisting of a parallel module with $M = 3$ DOF and family $F = 1$, of type 2-CRR (Cylindrical-Revolute-Revolute) with three active joints and a second parallel module with $M = 3$ DOF, of type CYL (Cylindrical) with two active joints, working in cylindrical coordinates.

The two modules form with two Cardan joints, the two kinematic chains for the platform guidance, namely 2-CRRU and CYL-U. Two constructive variants are presented, one using linear actuators for the active joints 1, 3, 4 and 5 (Fig. 1) and

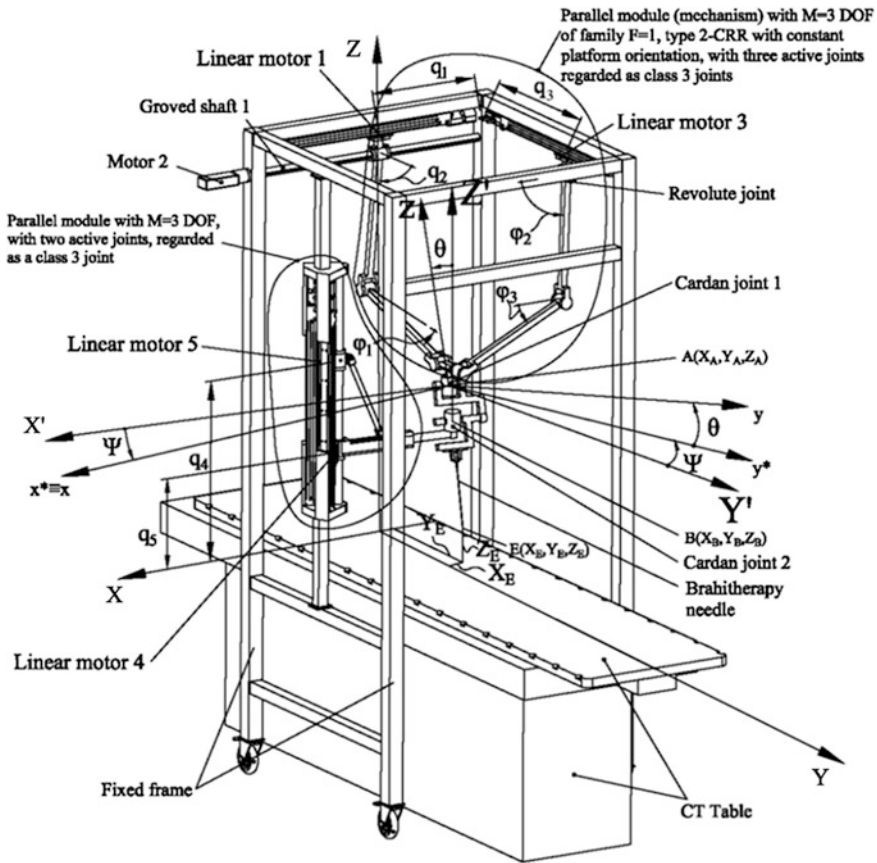


Fig. 1 Parallel robot with $M = 5$ DOF and family $F = 1$ with modular construction having two kinematic chains for the platform guidance of type 2-CRRU and CYL-U using linear actuators

the second using rotary motors with screw-ball for the same active joints (Fig. 2). The 2-CRR module is positioned on two lateral proximal sides of the fixed frame, on one side having two active joints actuated by motors 1 and 2, the first being a translational one, materialized by linear actuator (Fig. 1) and a ball-screw (Fig. 2) and the second one a revolute joint, materialized by a grooved shaft. This part can be seen as a cylindrical joint. On the proximal frame side the module consists in an active translational joint represented by the linear motor 3 (Fig. 1) and a ball-screw (Fig. 2) and a passive revolute joint materialized by the cylindrical shaft. The module integrates also 4 revolute passive joints which connect the mobile platform of the module 2CRR to the first Cardan joint.

For the structural synthesis the module 2-CRR, is decomposed in two class 4 joints, four rotational joints of class 5 and 5 mobile elements. Thus, it yields:

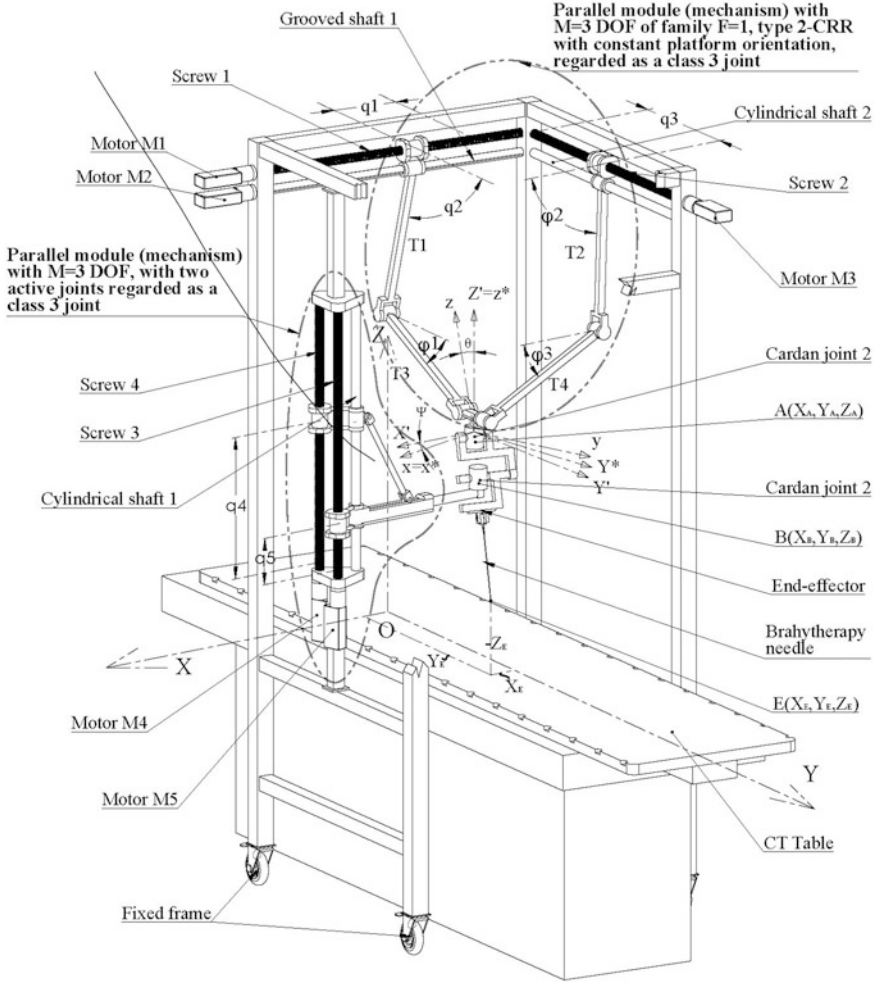


Fig. 2 Parallel robot with $M = 5$ DOF and family $F = 1$ with modular construction having two kinematic chains for the platform guidance of type 2CRRU and CYL-U using rotary motors

$$\begin{aligned}
 N &= 5, \quad C_5 = 4, \quad C_4 = 2, \\
 M &= 5 \cdot N - 4 \cdot C_5 - 3 \cdot C_4 = 3.
 \end{aligned}
 \tag{6}$$

The CYL module consists in two active translational joints positioned in a plane parallel with the OYZ plane and a cylindrical shaft in front of the two ball-screws which acts as a passive revolute joint. The cylindrical module is connected to the second Cardan joint. For the structural synthesis of the mechanism the two modules 2-CRR and CYL, are regarded as 3-DOF joints of class 3, each with one

mobile element. The two modules are connected with two Cardan joints of class 4, the final moving element being the end-effector. Thus:

$$\begin{aligned}
 N &= 3, C_4 = 2, C_3 = 2, \\
 M &= 5 \cdot N - 3 \cdot C_4 - 2 \cdot C_3 = 5.
 \end{aligned}
 \tag{7}$$

2.2 Parallel Robot for Brachytherapy with Two Parallel Modules, One for Positioning and One for Orientation

The second parallel robotic structure for brachytherapy consists in a positioning module with 3-DOF type 2CRR on whose mobile platform there is positioned a parallel orientation module with 2-DOF.

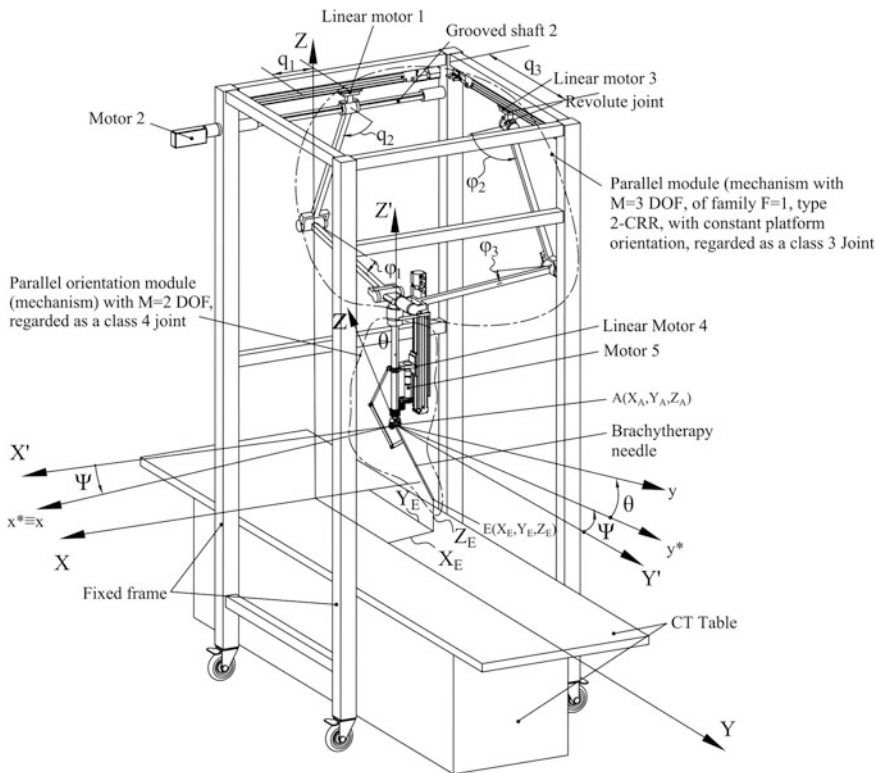


Fig. 3 Parallel robot with $M = 5$ DOF and family $F = 1$ with modular construction having a module for positioning and one for orientation using linear actuators

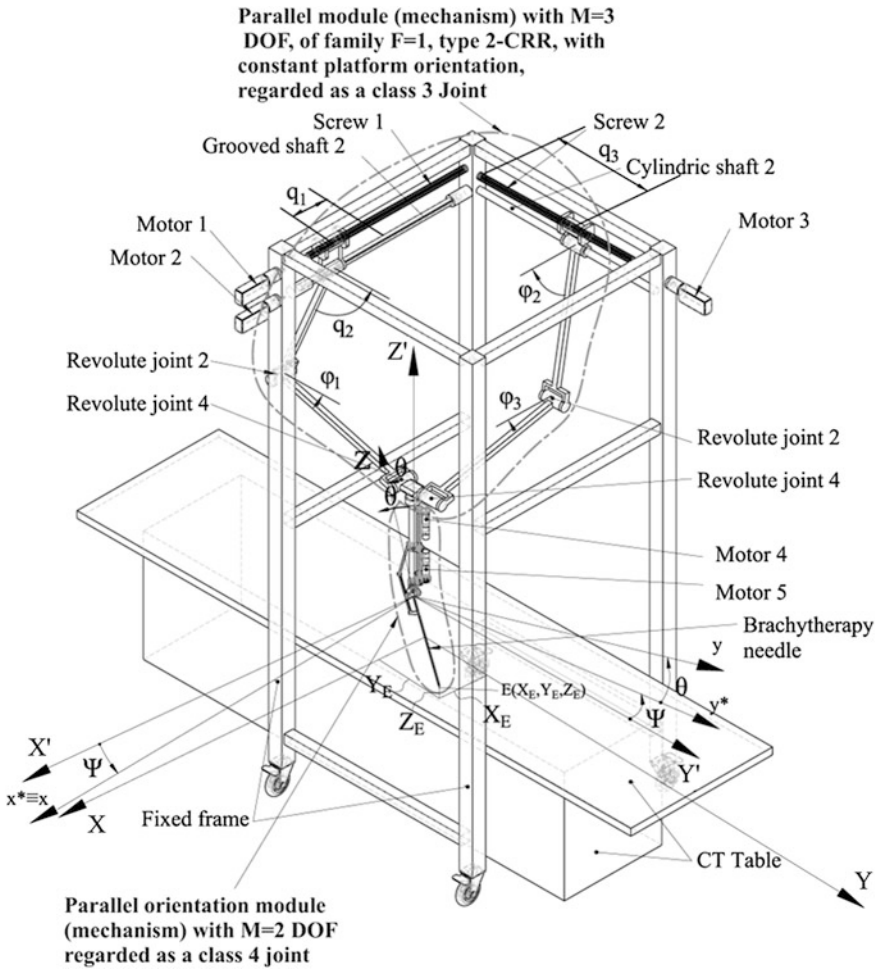


Fig. 4 Parallel robot with $M = 5$ DOF and family $F = 1$ with modular construction having a module for positioning and one for orientation using rotational motors

Two constructive variants are presented, one using linear actuators for the active joints 1, 3 and 4 (Fig. 3) and the second using a rotary motor with screw-ball for the same active joints (Fig. 4).

Through the motion of the two parallel modules the needle can be positioned and oriented based on the application requirements. From the structural point of view, the first module is regarded as a class 3 joint with one mobile element, namely the mobile platform. On the mobile platform of the first module is positioned the orientation one, so the robot has only one additional mobile element, the brachytherapy needle, and one class 4 joint.

Thus it yields:

$$\begin{aligned} N &= 2, C_4 = 1, C_3 = 1, \\ M &= 5 \cdot N - 3 \cdot C_4 - 2 \cdot C_3 = 5. \end{aligned} \quad (8)$$

3 Protocol for the Robotized Brachytherapy Procedure

Definition of the medical application. The robotic structure should introduce, based on radiologic data, rigid needles of diameter varying from 0.6 up to 2 mm and a length from 50 up to 250 mm inside the patient body following a linear trajectory. Due to the long distances, the variable tissue density it is compulsory to ensure constant precision for the entire displacement and to avoid any deviations from the predefined trajectory.

The areas of interest for needle placement in brachytherapy where the use of a robotic device is justified cover the human thoracic and abdominal area where the target point can be situated in close vicinity to different structures (blood vessels, ganglions, other organs) whereas an error can cause a cataclysmic event leading up the death of the patient. Generally, brachytherapy requires the placement of multiple needles in a circular or rectangular matrix, making motion repeatability a very important feature for the robotic system. Figure 5a illustrates an example of a CT machine equipped with supplementary laser sensors (the lasers were enhanced in the figure to provide better contrast) for position calibration. This type of CT scanners is designed especially for fast real-time image feedback but they cannot be used in diagnostics (Platten et al. 2005). Figure 5b shows a CT image with a needle inserted inside the human body.¹

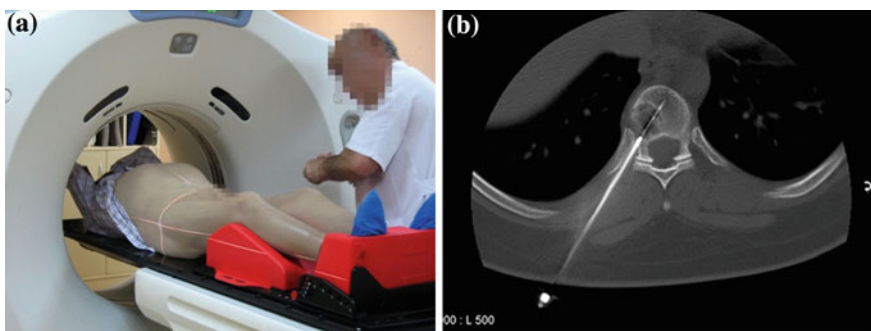


Fig. 5 Brachytherapy procedure: **a** Placement of external markers on the patient body for calibration, **b** Validating the correct needle insertion by CT scan control (See Footnote 1)

¹ Courtesy of RadiologyInfo.org

Procedure defining for needle insertion in brachytherapy. The procedure description is presented as a sequence of logical and safety proof steps, defined together with a team of oncologists from the “Ion Chiricuta” Oncology Institute in Cluj-Napoca, Romania.

1. Definition of the target points and the desired linear trajectories;
2. Positioning the external needle template;
3. Image acquisition with external markers to define the patient geometrical parameters;
4. Definition of the implant plan (number of needles and their positions);
5. Robot assisted needle implant with real-time echography monitoring;
6. Post-implant image acquisition for needle positions validation;
7. Calculation of the implant accuracy and the radiation dosages based on the real needle positions;
8. The seeds placement for the local tumor irradiation.

4 Conclusions

The paper presents a new family of modular parallel robots entitled PARA-BRACHYROB which proves to be suitable for brachytherapy applications and generally for needle placement techniques in medical applications. The modular construction of the PARA-BRACHYROB family of parallel robots enables their geometrical and structural optimization with respect to the BT requirements, as the modules can be positioned on the fixed frame to suit different CT scan devices and intervention rooms. The PARA-BRACHYROB family of parallel robots integrates any combination of two parallel mechanisms with 3-DOF connected to the end-effector through two Cardan joints where the first rotation axis is always parallel with the OZ vertical axis. The structural synthesis enabled a modular design approach with a minimum number of guiding chains. Based on this study the structures will be further kinematically analyzed and the best structure will lead to the experimental model for brachytherapy.

Acknowledgments The research work reported here was financed by the UEFISCDI project code PN-II-PT-PCCA-2011-3.2-0414, no. 173/2012 entitled “Robotic assisted brachytherapy, an innovative approach of inoperable cancers - CHANCE” and the project Scopes International Grant IZ74Z0-137361/1 entitled Creative Alliance in Research and Education focused on Medical and Service Robotics (CARE-Robotics).

References

- Delvin PM (2007) Brachytherapy: applications and techniques, 1st edn. Lippincott Williams & Winkins, Bultimera, ISBN-10: 0781762774
- Figliolini G, Rea P (2012) Effects of the design parameters on the synthesis of geneva mechanisms. Proc IMechE Part C: J. Mech Eng Sci. doi: [10.1177/0954406212466194](https://doi.org/10.1177/0954406212466194)

- Fischer GS, Iordachita J, Fichtinger G (2006) Design of a robot for transperineal prostate needle placement in MRI scanner. In: *Mechatronics conference on digital object identifier*, pp 592–597
- Jiang S, Hata N et al (2008) Needle insertion simulation for image-guided brachytherapy of prostate cancer. *Bioinf Biomed Eng* 1682–1685
- Jiang S, Guo J, Liu S, Liu J, Yang J (2010) Kinematic analysis of a 5-DOF hybrid-driven MR compatible robot for minimally invasive interventions in the prostate. *Robotica*
- Kacso G (2005) Brachytherapy as minimal invasive alternative with curative intent in early prostate cancer. Phd thesis, UMF “Iuliu Hatieganu” Cluj
- Oudard S, Banu E, Medioni J, Scotte F, Banu A, Levy E, Wasserman J, Kacso G, Andrieu JM (2009) What is the real impact of bone pain on survival in patients with metastatic hormone-refractory prostate cancer treated with docetaxel? *BJU Int* 103(12):1641–1646
- Platten D et al (2005) GE light speed RT CT scanner technical evaluation. Report 05070, National Health Service (NHS), 2005
- Plitea N et al (2006) Innovative development of parallel robots and microrobots. *Acta Tech Napoc Ser Appl Match Mech* 46(1): 15–26
- Plitea N. et al (2013a) Parallel robot for brachytherapy with two kinematic guiding chains of the platform (the needle) type 2CRRU and CRU. Patent pending, A/10004/2013
- Plitea N et al (2013b) Parallel robot for brachytherapy with two kinematic guiding chains of the platform (the needle) Type 2CRRU and CYL-U. Patent pending, A/10005/2013
- Plitea N et al (2013c) Parallel robot for brachytherapy with two kinematic guiding chains of the platform (the needle) Type CYL-U. Patent pending, A/10006/2013
- Plitea N et al (2013d) Parallel robot for brachytherapy with two parallel modules, one for positioning and one for orientation. Patent pending, A/10007/2013
- Podder TK, Fichtinger G (2010) Robotic brachytherapy—overview of robotic brachytherapy approaches and synergistic applications. *AAPM Annual Meeting*, 19 July 2010
- Rea P, Ottaviano E, Conte M, D’Aguanno A, De Carolis D (2013) The design of a novel tilt seat for inversion therapy. *Int J Imaging Robot* 11(3):1–10
- Revez L, Rueda JR, Cardona AF (2012) Palliative endobronchial brachytherapy for non-small cell lung cancer. *Cochrane Database Syst Rev* Dec 12; 12: CD004284. doi: [10.1002/14651858.CD004284.pub3](https://doi.org/10.1002/14651858.CD004284.pub3)
- Spârchez Z, Radu P, Zaharia T, Kacso G, Grigorescu I, Badea R (2010) Contrast enhanced ultrasound guidance: a new tool to improve accuracy in percutaneous biopsies. *Med Ultrason* 12(2):133–138
- Strassman G et al (2011) Advantage of robotic needle placement on a prostate model in HDR brachytherapy. *Strahlenther Onkol* 187(6):367–372
- Tornes A, Eriksen M (2009) A new brachytherapy seed design for improved ultrasound visualisation. *Ultrasonics* 2:1278–1283
- Viani GA, Manta GB, Stefano EJ, de Fendi LI (2009) Brachytherapy for cervix cancer: low-dose rate or high-dose rate brachytherapy—a meta-analysis of clinical trials. *J Exp Clin Cancer Res* 28(1):47
- Yu Y et al (2007) Robot-assisted prostate brachytherapy. Department of Radiation Oncology Faculty Papers. Paper 5. <http://jdc.jefferson.edu/radoncfp/5>

One 6R Overconstrained Mechanism, Many Applications

Laurentiu Racila

Abstract The aim of the paper is to present many possible applications based on a very special 6R overconstrained mechanism. This mechanism is based on 6R Wohlhart overconstrained mechanism, but not in its original disposition, that is with one fixed element. A new spatial disposition is used, with three non-adjacent joints that are constrained to remain in a fixed plane. This disposition allows the conception of many possible devices. The input–output equations, special characteristics, the advantages and disadvantages of each device are presented.

Keywords Over constrained mechanism · Kinematics · Industrial application

1 Introduction

Overconstrained mechanisms are a particular class of mechanisms. According to the usual mobility relations, these mechanisms have no mobility, but some special geometrical properties between their elements allow these mechanisms to become mobile.

The Sarrus mechanism is considered today as the first spatial overconstrained mechanism (Sarrus 1853), a closed-loop one, with six revolute joints (6R mechanism), able to transform a rotational movement into a translational one.

Overconstrained mechanisms have always been studied by researchers, but in the most cases, only from theoretical point of view (Baker 1980; Dietmaier 1995; Waldron 1979; Wohlhart 1987). There exists few industrial applications based on overconstrained mechanisms, like “Turbula” mechanism (Schatz 1975), or deployable structures of Chen et al. (2005) and Gan and Pellegrino (Gan and

L. Racila (✉)

Department of Applied Mechanics—Faculty of Mechanics, University of Craiova,
Craiova, Romania

e-mail: racila_laurentiu@yahoo.com

Pellegrino 2003). The “Turbula” mechanism is a Bricard 6R orthogonal mechanism with two adjacent revolute joints in a special disposition, and is used to mix liquids and powders. Deployable structures based on overconstrained mechanisms were also developed. In this case many mechanisms are used, with a concept similar to pantographs, to obtain industrial applications like deployable antennas.

Another possible device is presented by Racila and Dahan (Racila and Dahan 2010). This device is based on Wohlhart 6R symmetric mechanism (Wohlhart 1987) with identical links, but in a special spatial disposition, with three non successive joints constrained to remain in a fixed horizontal plane. Due to the mechanism’s symmetry, these three joints are the vertexes of an equilateral triangle (Fig. 4, blue line). The movement of these three joints is along the heights of the triangle (Fig. 4, O_1O line), to the centre of the circumscribed circle. The other three joints are also disposed in the vertexes of a triangle (Fig. 4, red line), and describe a plane, parallel with the fixed one. Some important properties derive from this new spatial disposition. These properties are useful to imagine many devices based on this mechanism.

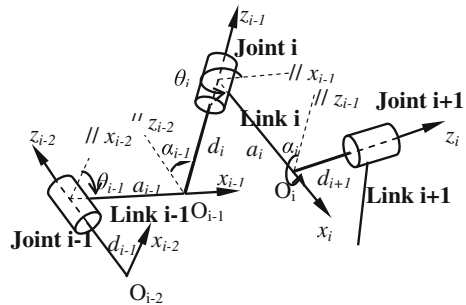
2 Closure Equations of Wohlhart 6R Symmetric Mechanism

To obtain closure equations of a closed-loop 6R mechanism, the classical Denavit-Hartenberg parameterization for a mechanism with revolute joints (Fig. 1), is being used (Denavit and Hartenberg 1955). The twist angle between two successive joints (i) and ($i + 1$) is noted α_i , the link lengths are noted a_i and the offset distance between two elements ($i-1$) and (i) is noted d_i . The fourth parameter is the angle between two successive elements ($i - 1$) and (i), noted θ_i .

The closure condition for a 6R single loop mechanism expresses that the product of the six transfer matrices ${}^{i-1}Q_i$ is equal to the unity matrix, and can also be written:

$${}^3Q_4 \cdot {}^4Q_5 \cdot {}^5Q_6 = {}^3Q_2 \cdot {}^2Q_1 \cdot {}^1Q_6 \tag{1}$$

Fig. 1 Denavit–Hartenberg parameters



Developing this equation, a twelve equations system and four identities are obtained. Some particular geometrical properties characterise 6R Wohlhart mechanism (Fig. 2):

$$\begin{cases} d_1 = d_2 = d_3 = d_4 = d_5 = d_6 = 0 \\ \alpha_1 = \alpha_3 = \alpha_5 = \alpha \\ \alpha_2 = \alpha_4 = \alpha_6 = 2\pi - \alpha \\ a_1 = a_2 = a_3 = a_4 = a_5 = a_6 = a \end{cases} \quad (2)$$

The equations system can be reduced to a single equation (Racila and Dahan 2010), between the input angle θ ($\theta = \theta_1 = \theta_3 = \theta_5$) and the output angle φ ($\varphi = \theta_2 = \theta_4 = \theta_6$):

$$\begin{aligned} &\cos \theta \cdot \cos \varphi \cdot (1 + \cos^2 \alpha) \\ &+ (\cos \theta + \cos \varphi) \cdot \sin^2 \alpha \\ &- 2 \cdot \sin \theta \cdot \sin \varphi \cdot \cos \alpha + \cos^2 \alpha = 0 \end{aligned} \quad (3)$$

The Fig. 3 shows the output angle φ according to the input angle θ , when the twist angle α varies from $\pi/2$ to $2\pi/3$. The links length is $a = 120$ mm.

In fact, depending on the twist angle α , the input angle has a limited variation domain, due to geometrical constrains. For example, when the twist angle $\alpha = \pi/2$, the input angle varies between $-\pi/3$ and $\pi/3$.

For a twist angle $\alpha = \pi/2$, the input–output equation of 6R symmetric Bricard rectangular mechanism is obtained (Racila and Dahan 2010):

$$\cos \theta \cdot \cos \varphi + \cos \theta + \cos \varphi = 0 \quad (4)$$

The input–output equation is symmetrical in θ and φ , so the output angle can also serve as input angle.

Fig. 2 Wohlhart symmetric mechanism

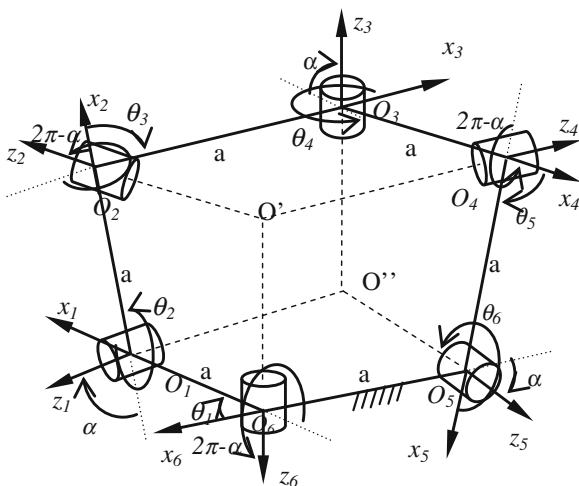
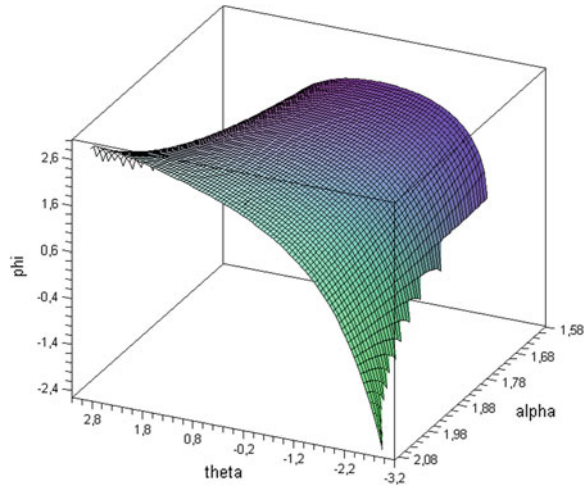


Fig. 3 Output angle φ according to input angle θ and twist angle α



3 Special Spatial Disposition

For the 6R Wohlhart symmetric mechanism we constrain three revolute joints O_1 , O_3 and O_5 to remain in a fixed (reference) plane and make a movement on three line segments, along the heights of the triangle $O_1O_3O_5$, to the centre of the triangle circumscribed circle. The other three joints O_2 , O_4 and O_6 will always remain in a parallel plane with the first one (Fig. 4).

In the initial position all the six joints are in the horizontal plane and the input angle θ has zero degrees. When the odd joints O_1 , O_3 and O_5 make movements to the centre O of the triangle circumscribed circle, the even joints O_2 , O_4 and O_6 will describe a parallel plane with the reference one. The distance between the two planes is noted h . This distance is dependant to the input angle θ (Fig. 5).

Fig. 4 New spatial disposition

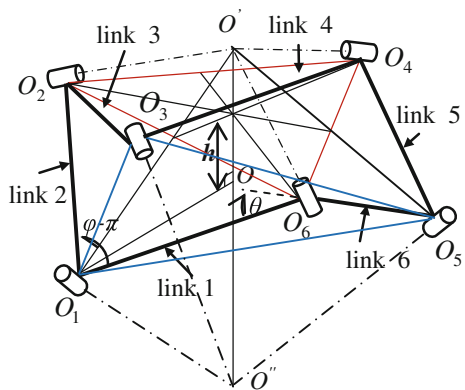
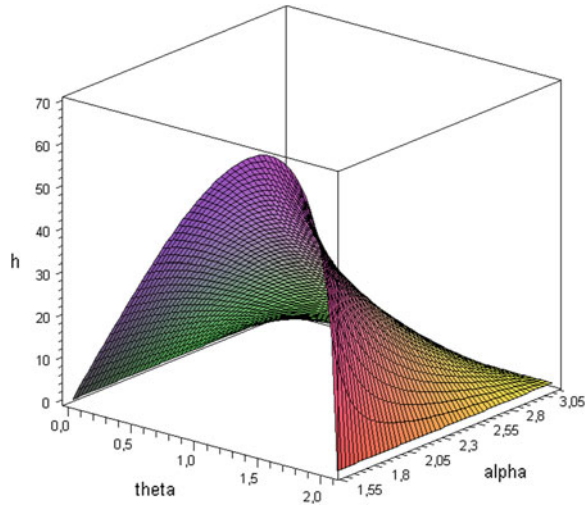


Fig. 5 Distance h according to input angle θ and twist angle α



We can observe the importance of twist angle α for the distance between the planes: when α increases h decreases. Finally, when the twist angle $\alpha = \pi$, the two planes are superposed, because the mechanism has become a plane one with all joints axes parallel.

4 New Devices

Many important properties can be revealed from this new special disposition. Starting with these properties, many possible devices can be imagined with practical industrial applications.

4.1 6R Translational Device

The first important properties are the parallelism between the fixed reference plane $O_1O_3O_5$ and the mobile plane $O_2O_4O_6$, when the odd joints make a movement to the point O , the centre of circumscribed circle of $O_1O_3O_5$ triangle.

This properties can be used to realise a parallel translational device.

The distance between the two planes is noted h and the input movement of the actuated joint O_1 is noted b .

The dependence of h according to b and twist angle α is presented in Fig. 6.

The twist angle α varies between $\pi/2$ and $5\pi/6$. When the twist angle increases the distance between planes decreases, and the slope is smaller. So, for a better accuracy the twist angle must be increased.

Fig. 6 Distance h according to input distance b and twist angle α

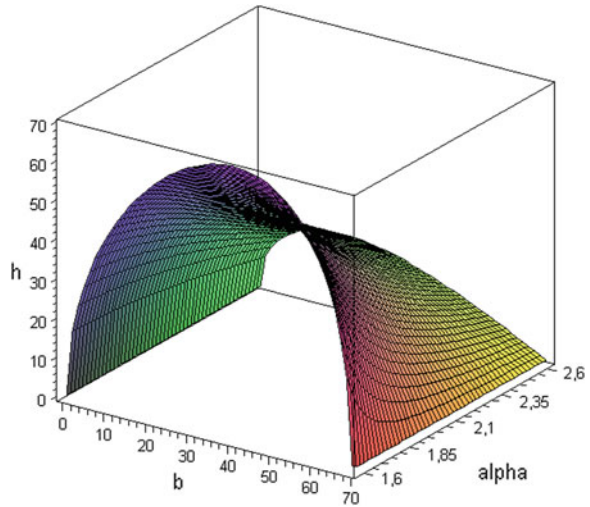


Figure 7 shows a prototype of this device, realised in the Department of Applied Mechanics, FEMTO-ST Institute.

4.2 Centring Device

Another important property of this mechanism is the position of even joints in the mobile plane during the movement. The even joints O_2 , O_4 and O_6 have a radial displacement along the radius of circumscribed circle of triangle $O_2O_4O_6$.

This property allows the mechanism to work like a centring device.

Figure 8 shows the variation of the radius of the circumscribed circle of even joints, according to displacement b of actuated joint O_1 and twist angle α .

The variation of the radius depends on the links length. Figure 8 shows this variation for a links length $a = 120$ mm.

In the initial position all six links and joints are in the same plane. When b increases, the radius also increases, until the final position, and then again, all six links and joints are in the same plane, the reference one.

Figure 8 shows the variation of the radius of circumscribed circle of even joints, according to displacement b of actuated joint O_1 and twist angle α .

4.3 Focusing Table

A very interesting property of this mechanism is about the intersection point of even joints axes O' and the intersection point of odd joints axes O'' . These two points determine a line $O'O''$ always orthogonal to the two planes involved in the movement of the mechanism, the reference plane and the mobile one (Fig. 4).

Fig. 7 Prototype of 6R translational device



In the initial position, when all six links and joints are in the reference plane, the O' point is to infinity (the odd joints axes are parallel) and the O'' point is in the same plane with the links (for a twist angle $\alpha = \pi/2$). When the input parameter increases (b or θ for example), the O' point will go down from infinity to the reference plane, while the O'' point will be going under the reference plane, arriving finally to infinity when again all six links and joints will be in the same reference plane. In this final position the O' point is situated in the reference plane (for a twist angle $\alpha = \pi/2$).

For a different twist angle the intersection points O' and O'' are not in limit positions in the reference plane.

Fig. 8 Variation of radius of circumscribed circle of even joints

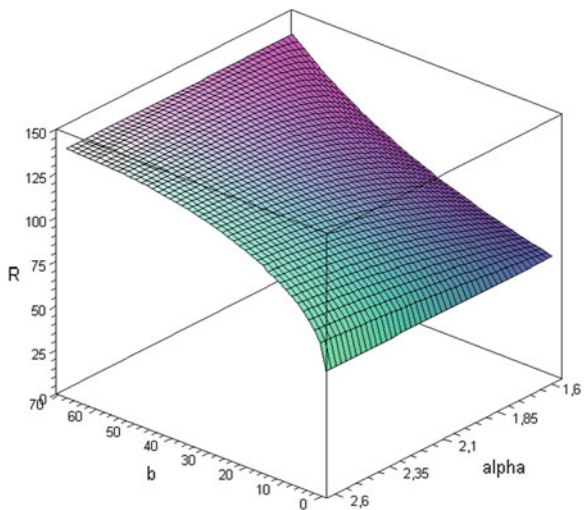


Fig. 9 Variation of distance OO'' according to input angle θ

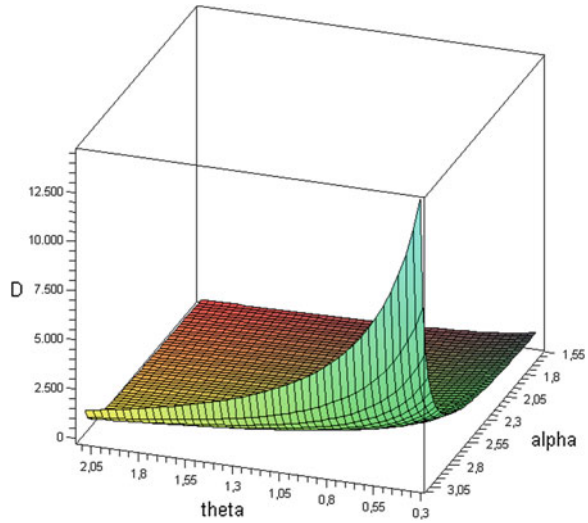


Figure 9 shows the variation of the distance OO'', noted D , according to the input angle θ , for a variation of twist angle between $\pi/2$ and $5.9 \pi/6$ (for $\alpha = \pi$ we obtain a plane chain, so all joints axes are parallel).

Figure 10 shows the other distance OO', noted d , this time, according to the input distance b of actuated joint O_1 .

This property can be used to realise a focusing device (like a telemeter), for example, but it can also be used another way. We can consider this distance, OO'' for example, as input. The output can be the distance h between the reference plane and the mobile plane.

Fig. 10 Variation of distance OO' according to input distance b

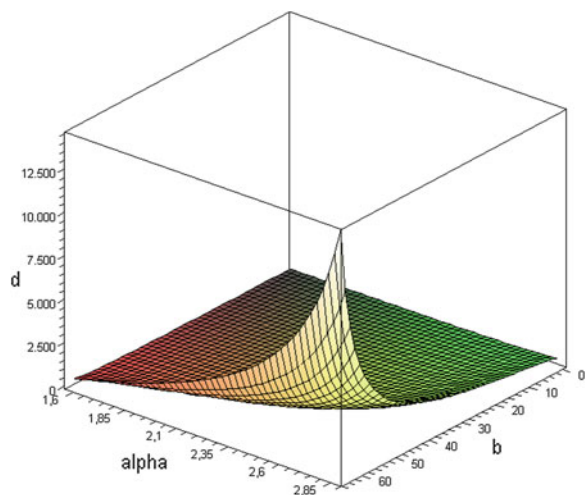


Fig. 11 Variation of distance h according to distance OO''

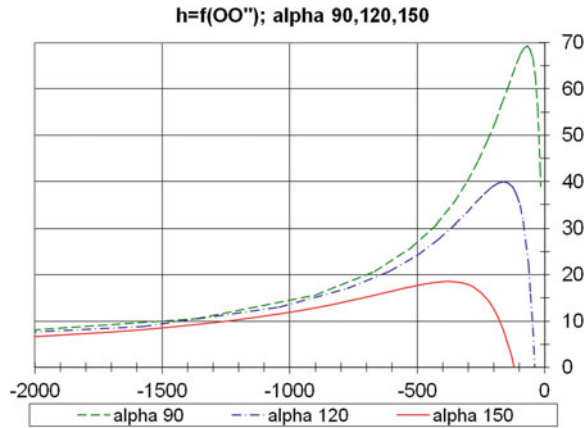


Figure 11 shows the variation of the distance between these two planes according to the input distance $OO'' = D$, for three twist angles: $\alpha = \pi/2$, $\alpha = 2\pi/3$ and $\alpha = 5\pi/6$.

This property can be used to realise a focusing table for optical microscope, for example, or as plate in rectifying machines, due to the accuracy of the device in this particular position.

This accuracy can vary from 1:100 to 1:1,000 (depending of the links length and $O''O$ variation domain).

All the results presented in this paper have been confirmed the analytical way (Racila and Dahan 2010), geometrical (Racila and Dahan 2008) and also by experimental calculus (Racila and Dahan 2011).

5 Conclusions

The paper presents many capabilities of a 6R overconstrained closed-loop mechanism, not in its classical position, that is, with one fixed element. A special spatial position is used to obtain a new device, with no fixed elements, but with three joints imposed to make a particular movement in a fixed plane.

This device can be used to develop many applications, for the industrial or even entertainment area. Some of such devices are presented above, others can be imagined, depending on the domain in which they are intended to be used.

References

Baker JE (1980) An Analysis of the Bricard linkages. *Mech Mach Theory* 15:267–286
 Chen Y, You Z, Tarnai T (2005) Threefold-symmetric Bricard linkages for deployable structures. *Int J Solids Struct* 42:2287–2301

- Denavit J, Hartenberg RS (1955) A kinematic notation for lower-pair mechanism based on matrices. *J Appl Mech* 22:215–221
- Dietmaier P (1995) A new 6R space mechanism. In: Proceedings of the 9th IFToMM World Congress, Milano, pp 52–56
- Gan WW, Pellegrino S (2003) Closed-loop deployable structures. In: Proceedings of 44th AIAA/ASME/ASCE/AHS/ASC structures, structural dynamics, and materials conference, Norfolk
- Racila L, Dahan M (2008) 6R Translator: a geometrical approach. In: Proceedings of the 17th CISM-IFToMM symposium on robot design, dynamics, and control—RoManSy, Tokyo, 2008, pp 511–517
- Racila L, Dahan M (2010) Spatial properties of Wohlhart symmetric mechanism. *Meccanica* 45(2):153–165
- Racila L, Dahan M (2011) 6R *Parallel Translational Device*. In: Proceedings of the 13th IFToMM World Congress, Guanajuato
- Sarrus PF (1853) Note sur la transformation des mouvements rectilignes alternatifs, en mouvements circulaires; et réciproquement. *Comptes Rendus des Séances de l'Académie des Sciences* 36 pp 1036–1038
- Schatz P (1975) *Rhythmusforschung und Technik*. Verlag Freies Geistesleben, Stuttgart
- Waldron KJ (1979) Overconstrained linkages. *Environ Plann B*:393–402
- Wohlhart K (1987) A New 6R space mechanism. In: Proceedings of the 7th IFToMM World Congress, Sevilla, pp 193–198

Research Regarding Modelling of Involute-Bevel Gears

Ioan Ardelean, Mircea Bara, Sergiu-Dan Stan and Sorin Besoiu

Abstract Involute-bevel gears, as well as gears containing them, have a difficult “task” in motion transmission than gears with parallel axes. A difficulty is related to the fact that axes, although coplanar, are concurrent, thus, between driver gear axis and driven gear axis there is an angle “ $< 180^\circ$ ”. Difficulty is even bigger, when the gear is considered bevel only gear only due to the fact that axes are concurrent, and only one gear is bevel gear, the other one being spur gear with straight teeth. Such gears can be used in many applications, although, more frequently in machine building resulting constructive and optimal exploitation solutions. It can be noticed, that analysis and synthesis of different types of gears formed from involute-bevel gears it’s made based on a particular example, with its peculiarities, which usually leads to a planar involute gear, (Alexandru et al. 1999; Bocian 1976; Herciu 2011; Szekely et al. 1981). In this paper, it’s elaborated a general theory of involute-bevel gears (starting from a gear with crossed axes), based on a new concept that reflects perfect reality. It presents the principle of geometric calculus of involute-bevel gears function of the manufacturing mode. Also, there are presented the methods of determination of the main characteristics of the gears that can be developed using these gears.

Keywords Involute-bevel gears · Numerical modeling method · Reference element

I. Ardelean (✉) · M. Bara · S.-D. Stan · S. Besoiu
Department of Mechatronics and Dynamics of Machines,
Technical University of Cluj-Napoca, Cluj Napoca, Romania
e-mail: ioan_ardelean@yahoo.com

1 Introduction

In this paper, are presented a new numerical modeling method, with great results, of a category of gears formed by a spur gear and one involute-bevel gear, (Bocian 1976; Litvin et al. 2002) or with two involute-bevel gears. The mathematical model is generally acceptable for cases when gear axes are crossed, concurrent or parallel. This model take into account the type of tool used to manufacture the spur and involute-bevel gears. The terms used for denoting gears are the following:

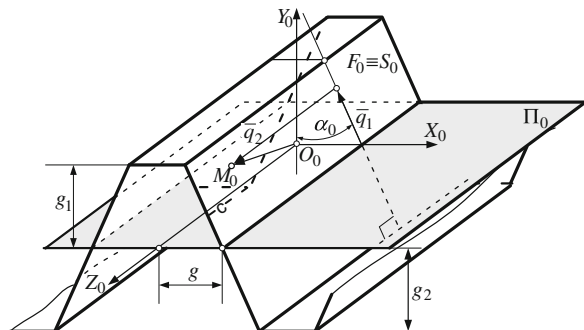
- g_1, g_2 —Constant parameters in modeling; g_1 —height of the head of modeling rack; g_2 —height of the foot of modeling rack;
- S_0 —Surface of the F_0 flank;
- \sum_0 —Reference system linked to the flank F_0 , having axes of coordinates $O_0X_0Y_0Z_0$; $T_{g_1g_2}$ —Transfer matrix from the system g_2 in g_1 ;
- $\overline{O_0M_0}$ —Vector radius, with projections O_0M_x, O_0M_y, O_0M_z , of a current point on the surface S_0 , reported to the reference system \sum_0 ;
- $\overline{O_0N_0}$ —Perpendicular vector with projections $n_{x_0}, n_{y_0}, n_{z_0}$, attached to a vector radius $\overline{O_0M_0}$.

2 Reference Element in Modelling

Next, it's adopted as reference element in modeling process, a rack, having standard geometric parameters, no matter what the manufacturing method and type of tool used for gear realization which forms the involute-bevel gears.

The surface S_0 of reference rack, Fig. 1 it's expressed in the system \sum_0 , function of the independent parameters g_1 and g_2 , with position vector O_0M_0 of type:

Fig. 1 Rack's reference element



$$O_0M_0 = \begin{bmatrix} A_0[(3 - 2B_0)g - q_1 \sin \alpha_0] \\ q_1 \cos \alpha_0 \\ q_2 \\ 1 \end{bmatrix} = \begin{bmatrix} X_0 \\ Y_0 \\ Z_0 \\ 1 \end{bmatrix} = O_0M_0(q_1, q_2), \quad (1)$$

where: $-A_0$ and B_0 are generalized coefficients; A_0 takes the value ± 1 , as relation (1) refers to right side or left side of the rack; B_0 takes the value 1 or 2, as the reference plan $X_0O_0Z_0$ overlaps with the symmetry plan of the tooth or the tooth gap;

- g_0 represents the width tooth rack measured in the median plan (\prod_0);
- α_0 —pressure angle/standardized gearing.

Perpendicular vector, $\overline{O_0N_0}$ attached to the vector (1) it's expressed by relation:

$$O_0N_0 = \begin{bmatrix} A_0 \\ tg \alpha_0 \\ 0 \\ 0 \end{bmatrix} = \begin{bmatrix} n_{X_0} \\ n_{Y_0} \\ n_{Z_0} \\ 0 \end{bmatrix}. \quad (2)$$

To manufacturing the involute-bevel gears having the half-angle at vertex δ (Fig. 2) and inclined teeth with angle β are taken into account the following.

- Standardized rack, Fig. 1 is fixed in relation to the half-finished part such a way that the median plan (\prod_0) to be parallel with the generatrix OM of division cone, Fig. 2, (Csibi et al. 2007, 2008; Herciu et al. 2008).
- In case of inclined teeth, the rack is rotated in relation with the half-finished part thus axis O_0Z_0 , Fig. 1 to close the angle β with generatrix OM , Fig. 2.
- Origin O_0 of the system \sum_0 it's considered placed in the median plan of the gear. As a consequence, the parameters q_1 and q_2 , of the surface S_0 will be limited by the teeth height and the gear width that is manufactured.

Fig. 2 Rack's reference positioning

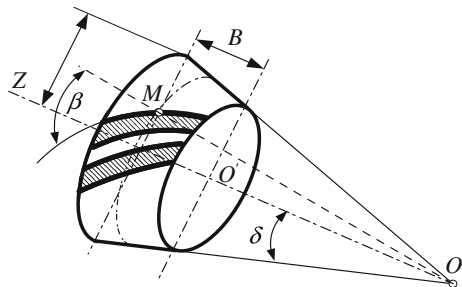
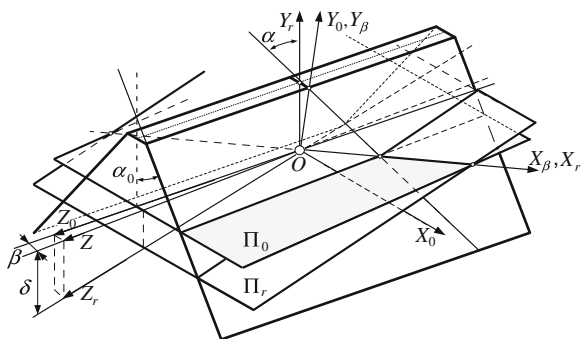


Fig. 3 Generalized reference element



For generalization of the calculus method it's introduced a new reference system \sum_r linked to the rack thus axis O_{Z_r} , Fig. 3 to remain parallel with axis O_Z , Fig. 2 of the involute-bevel gear, during all the time of it's development.

For shifting from the system \sum_0 in \sum_r , based on the scheme from Fig. 3, it's used the transfer matrix T_{r0} as it follows:

$$T_{r0} = \begin{bmatrix} \cos\beta & 0 & -\sin\beta & 0 \\ \sin\beta\sin\delta & \cos\delta & \cos\beta\sin\delta & 0 \\ \sin\beta\cos\delta & -\sin\delta & \cos\beta\cos\delta & 0 \\ 0 & 0 & 0 & 1 \end{bmatrix} \quad (3)$$

During the generation teeth phase, the rack is expressed by the vectors: OX_r and ON_r that can be expressed by relations:

$$OX_r = \begin{bmatrix} q_1A_x + q_2B_x + C_x \\ q_1A_y + q_2B_y + C_y \\ q_1A_z + q_2B_z + C_z \\ 1 \end{bmatrix} = \begin{bmatrix} X_r \\ Y_r \\ Z_r \\ 1 \end{bmatrix} = OX_r(q_1, q_2), \quad (4)$$

$$ON_r = \begin{bmatrix} A_0 \cos\beta \\ A_0 \sin\beta \sin\delta + tg\alpha_0 \cos\delta \\ A_0 \sin\beta \cos\delta - tg\alpha_0 \sin\delta \\ 0 \end{bmatrix} = \begin{bmatrix} n_{X_r} \\ n_{Y_r} \\ n_{Z_r} \\ 0 \end{bmatrix} = const., \quad (5)$$

where were used the notations:

$$\begin{aligned} A_X &= -A_0 \sin\alpha_0 \cos\beta; & A_Y &= (\cos\alpha_0 \cos\delta + A_0 \sin\alpha_0 \sin\beta \cos\delta); \\ A_Z &= -(\cos\alpha_0 \sin\delta + A_0 \sin\alpha_0 \sin\beta \cos\delta); & B_X &= -\sin\beta; \\ B_Y &= \cos\beta \sin\delta; & B_Z &= \cos\beta \cos\delta; & C &= (2 - K)A_0g; & C_X &= C \cos\beta; \\ C_Y &= C \sin\beta \sin\delta; & C_Z &= C \sin\beta \cos\delta; \end{aligned} \quad (6)$$

The vector (5) and notations (6) are constant for any applications, thus favoring the definition of rack given by Eq. (4).

Also, they contain all the feature parameters for involute-bevel gears with straight-teeth ($\beta = 0$) or for spur gears ($\delta = 0$).

From vector (5) projections on the system axes \sum_r results the front profile angle of the rack;

$$tg\alpha = tg\beta sin\delta \pm tg\alpha_0 \frac{cos\delta}{cos\beta} \tag{7}$$

Remark From this equation it results that the right side, respectively the left side of the teeth has different shapes, which corresponds to two basis circles different of the manufactured gear. Knowing the profile angle α of the rack, according to the Eq. (7), it can be computed the basis circle radii with known formula.

3 Modelling the Teeth of Involute-bevel Gears

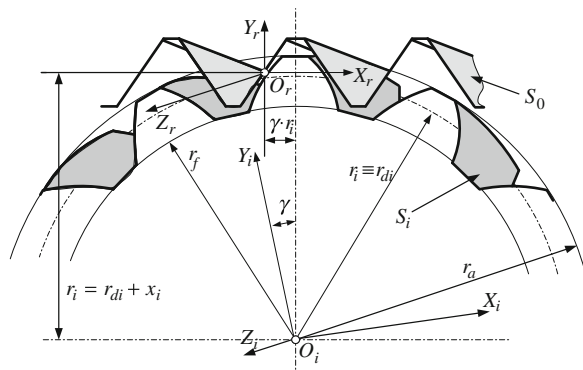
In the process of generation, the half-finished gear executes a rotation motion, and the rack S_0 with side F_0 a translation motion in direction of axis $O_r X_r$, Fig. 4.

The relative instantaneous position between the systems \sum_r and \sum_i (linked to the rack, respectively the gear) is defined by the parameter γ by the transfer matrix:

$$T_{ir} = \begin{bmatrix} cos\gamma & sin\gamma & 0 & (r_{di} + x_i)sin\gamma - \gamma r_{di}cos\gamma \\ -sin\gamma & cos\gamma & 0 & (r_{di} + x_i)cos\gamma + \gamma r_{di}sin\gamma \\ 0 & 0 & 1 & 0 \\ 0 & 0 & 0 & 1 \end{bmatrix}, \tag{8}$$

In which the x_i is the addendum modification coefficient of the gear of order i with unitary module; r_{di} is the division circle given by the known formula;

Fig. 4 Gear's generation scheme



$r_{di} = mz_i/2\cos\beta$; z_i – number of teeth of the gears; β – the inclined angle of teeth; m –module, considered as unitary value.

The side S_i of the teeth gear is expressed by the help of matrix product $[T_{ir}] \cdot [x_r]$, obtained for S_i the position vector:

$$O_i X_i = \begin{bmatrix} (X_r - \gamma r_{di})\cos\gamma + (Y_r + r_{di+i})\sin\gamma \\ (\gamma R r_{di} - X_r)\sin\gamma + (Y_r + r_{di+i})\cos\gamma \\ Z_r \\ 1 \end{bmatrix} = \begin{bmatrix} X_i \\ Y_i \\ Z_i \\ 1 \end{bmatrix} = X_i(q_1, q_2, \gamma) \quad (9)$$

To reduce the number of parameters to tow, the vector (9) is attached the condition of the general gearing: $N_r \cdot V_r = 0$, in which the V_r is the relative velocity vector in the contact points between the surfaces S_0 and S_i .

In the present case, the gearing condition can be developed using matrix method obtaining:

$$N_r V_r = N_r \left(T_{ri} \frac{dT_{ir}}{d\gamma} X_r \right) = (Y_r + x_i)n_{xr} + (X_r - \gamma r_{di})n_{yr} = 0 \quad (10)$$

where it was denoted with T_{ri}^{-1} the inverse matrix (8).

Solution of the Eq. (10) that defines the parameter γ for expression (9), is:

$$\gamma = \frac{1}{r_{di}} [X_r + (Y_r + x)] \frac{n_{Xr}}{n_{Yr}} \quad (11)$$

Taking into account that the chosen perpendicular vector is invariant toward-translation, it results that the perpendicular in the point of contact, on the side S_i is determined with Eqs. (5), (8) and (11), thus:

$$N_i = T_{ir} N_r = \begin{bmatrix} n_{xr}\cos\gamma + n_{yr}\sin\gamma \\ n_{yr}\cos\gamma + n_{xr}\sin\gamma \\ n_{Zr} \\ 0 \end{bmatrix} = \begin{bmatrix} n_{Xi} \\ n_{Yi} \\ n_{Zi} \\ 0 \end{bmatrix} \quad (12)$$

Equations (9) and (12) together with (11), define in a unique way the teeth of gear.

Remarks

- Modeling the generation is particularized by the index i to all the gears that belong to the definition of the involute-bevel gears, including the generated gear in the case of the realization with the Fellow or Skiwing procedure.
- Dimensions of the half-finished gear are limited to the width B of the gear and by the external bevel that is computed with known equations, (Alexandru et al. 1999).
- The reference plan $X_i O_i Y_i$ overlaps with the median plan of the gears.

4 Modeling the Generation from the Point of View of its Limits

It presents great interest two aspects regarding the modeling of generation from the point of view of its limits such as: undercutting and sharpening of the teeth of generated gears, (Litvin and Fuentes 2004; Litvin et al. 2002).

It's admitted that based on the constructive consideration and known calculus algorithms, (Csibi et al. 2007), it was determined the maximal external radius r_m and width B of the gears, Fig. 2.

Also, it's known the height of the teeth defined by the corresponding limitation of the profile parameter q_1 (see Fig. 1) at value $q_{10} \cdot q_1, q_2$.

In the general case, undercutting is shown mathematically by appearance of the turning point on the generated profile. This phenomenon appears to a given scheme of generation, as the minimal realizable radius on the side gears.

In the case of the involute-bevel gears undercutting appears for the first time at $Z_r = B/2$ for solution to the limit q_{1L} of equation $dr_i/dq_1 = 0$. Developing these two equations with the Eqs. (9) and (11) leads to the check relation:

$$q_{10} \geq \frac{B_Y(\frac{B}{2} + C_Z) - B_Z C_Y + (r_{di} + x_i) \cos^2 \alpha_0}{A_Y - B_Y A_Z}; \tag{13}$$

where $B_Z, B_Y, A_Y, A_Z, C_Y, C_Z$ are from (6).

In which the notations are in accordance with (6), q_{10} being the minimum value of q_1 , corresponding to the point from the basis of tooth.

Undercutting of the gears is a similar phenomenon but the analytical equations contain transcendent expressions. That's why, for verification of the undercutting is recommended a numerical method.

Based on the Eqs. (5) and (2), (7) it's obtained:

$$Q(q_2) = 2Z_2(q_1, q_2) + B = 0 \tag{14}$$

Solution q_2 from Eq. (14) it's introduced in the expression:

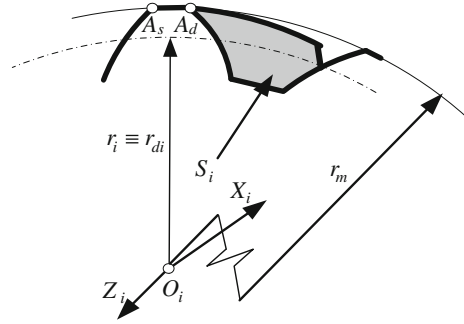
$$R_2^2 = X_2^2 + Y_2^2 = R_2^2(q_1), \tag{15}$$

Which, the same, it's minimized in relation with q_1 . The minimal solution q_1 , has to verify the inequality $q_1 \leq q_0$. Solving the Eq. (14) and minimization of the Eq. (15) leads to two overlapped iterative processes, thus for PC it represents easy to solve.

Regarding the sharpening of the teeth, the problem is how to determine the extreme points for left or right profile, situated at the maximum radius r_m , and then evaluation of the distance $A_s A_d$ (Fig 5). The problem gives certain difficulties even for the involute circular gear.

In this case the checking method resumes to the solving of the system of equations:

Fig. 5 Limitation of tooth's sharpening



$$F_1(q_2) = 2Z_i - B = 0, F_2(q_1) = r_m - \sqrt{X_i^2 + Y_i^2} = 0, \tag{16}$$

Which, by the constant A_0 from Eq. (1), it get the q_{2x} once with the right side, obtained by the point A_d (of coordinates X_d, q_{2d}) given by the Eq. (9) or (19), then for the left side of the rack, obtaining of the point A_s (of coordinates X_s, Y_s).

Following these calculus it's applied the equation to check the results: $\delta_\vartheta \leq X_d - X_s$ where δ_ϑ is the minimal teeth width, adopted usually at the value δ_ϑ, m being the module.

5 Conclusions

For solving some complex problems regarding the generation of the gears with crossed axes, are known more techniques. There are taken into account the undercutting and sharpening of the gear's teeth, as well as correct positioning of the contact area between teeth sides.

In the paper, is presented the structure of some modeling techniques of these problems. There are studied as well some features of this modeling. The features are given by the position of the axes of the two gears and directly, the position of the teeth sides. The resulted model is in this way spatial.

References

Alexandru P, Visa I, Alexandru C, Talaba D (1999) Proiectarea functionala a mecanismelor. EdituraLibris, Brasov
 Bocian I (1976) Studiul geometric al angrenajelor globoidale in vederea maririicapacitatii portante a acestora. Teza de doctorat Institutul Politehnic, Cluj-Napoca
 Csibi VI, Herciu D, Sudrijan M (2007) Tool for precise grinding of crown gears. 12th IFTOMM World Congress, Besancon, pp 18–21
 Csibi VI, Herciu D, Sudrijan M (2008) Scula pentru rectificarea precisa a rotilor dintate frontale. Brevet de Inventie OSIM RO 121729 B1. Int, C1. B24 B1/00 (2006001). BOPI nr. 3/2008

- Herciu D, Csibi VI, Pop RO, Sudrijan M (2008) Tool for grinding of face gears. *Hungarian Technical Review*, pp 91–95, Cluj-Napoca, ISSN 1454-0746
- Herciu D (2011) Contributii la cresterea performantelor angrenajului pinion cilindric-roata frontal, Teza de doctorat. Universitatea Tehnica din Cluj-Napoca, Cluj-Napoca
- Litvin FL, Fuentes A (2004) *Gear geometry and applied theory*, 2nd edn. Cambridge University Press, Cambridge, pp 543–582
- Litvin FL, Fuentes A, Fan Q, Handschuh RF (2002) Computerized design, simulation of meshing and contact, and stress analysis of face-milled formate generated spiral bevel gears. *Mech Mach Theory* 37(5):441–458
- Szekely E, Bocian I, Chiorean V (1981) Aspecte noi in teoria angrenajelor conico-evolvenice. *Studii si cercetari de mecanica aplicata*, Tom 40:721–733

Research Regarding the Modeling of the Reciprocal Generation of the Involute-bevel Gears with Crossed Axes

Ioan Ardelean, Olimpiu Tătar and Emil Teutan

Abstract For this type of gearing the gear's teeth are in point contacts. Intensive research regarding these types of gearing have been started since 1968, (Alexandru et al. 1999; Herciu 2011; Litvin and Fuentes 2004; Szekely et al. 1981). With all the intensive research made in this field the raised problems weren't solved entirely. A way to solve in a better and operative method of problems with gears with crossed axes is modeling of its generation, (Bocian 1976; Csibi et al. 2007, 2008). In the paper, are presented the basic elements regarding the modeling of generation process of the crossed axes gears. It's presented the structure of the algorithm regarding the mathematic modeling. For defining the surfaces of the tooth's sides are used continuous and differentiable mathematical functions.

Keywords Gear axes · Gearing modeling · Contact area

1 Introduction

It is assumed that one of the gear wheels, for example the gear 1, it was made with a certain method and the tooth flank is defined mathematically, function of the independent parameters q_1 and q_2 , by the vector radius $X_1 = X_1(q_1, q_2)$ and perpendicular $N_1 = N_1(q_1, q_2)$ (Herciu 2011; Szekely et al. 1981). Also, it's known the relative position of the gear axes and the transmission ratio. It's asked to determine the side of the gear S_2 .

Thus, it's considered the generation scheme from the Fig. 1, in which it was presented:

I. Ardelean (✉) · O. Tătar · E. Teutan
Department of Mechatronics and Dynamics of Machines,
Technical University of Cluj-Napoca, Cluj Napoca, Romania
e-mail: ioan_ardelean@yahoo.com

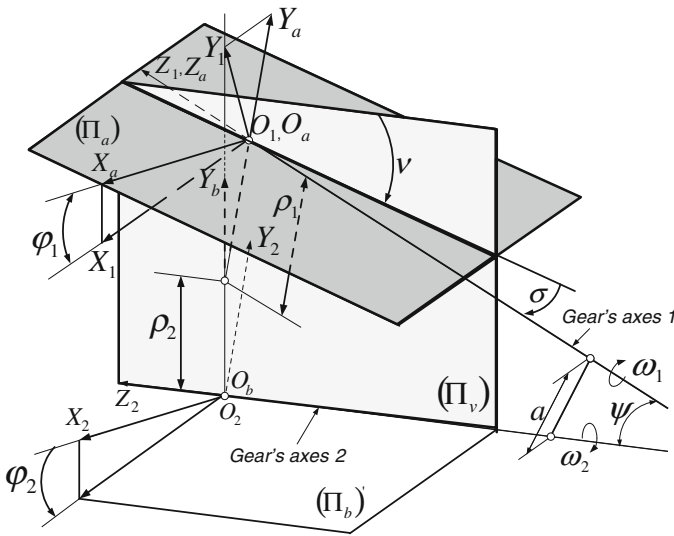


Fig. 1 Crossed axes gear's generation scheme

- fixed systems \sum_a and \sum_b having the axes O_aZ_a and O_bZ_b overlapped with axes of gears 1 and 2;
- the systems \sum_1 și \sum_2 in which are defined the side S_1 of gear 1, respectively in which it will define the side S_2 of gear 2.

For determination of the relative position of the crossed gear it's adopted two reference circles, linked with the two gears, with radius ρ_1 , respectively ρ_2 , chosen after certain considerations. Also, are introduced the constructive angles:

- convergence, ν , formed by the plan (Π_b) and projection on the axis 1 on plan (Π_a) and deviation angle σ determined by the plan (Π_a) and axis O_1Z_1 of gear 1.

In the process of gearing the systems, the systems \sum_1 and \sum_2 rotates after the parameters φ_1 , respectively φ_2 , where exists the relation of interdependence $i_{12} = \varphi_1/\varphi_2 = \omega_1/\omega_2$.

Between the systems \sum_1 and \sum_2 , it's established the square matrix of transfer.

$$T_{21} = \begin{bmatrix} a_\varphi \cos\varphi_1 - \cos v \sin\varphi_1 \sin\varphi_2 & a_\varphi \sin\varphi_1 + \cos v \cos\varphi_1 \sin\varphi_2 \\ -b_\varphi \cos\varphi_1 - \cos v \sin\varphi_1 \cos\varphi_2 & -b_\varphi \sin\varphi_1 + \cos v \cos\varphi_1 \cos\varphi_2 \\ \sin\sigma \cos v \cos\varphi_1 + \sin v \sin\varphi_1 & \sin\sigma \cos v \sin\varphi_1 - \sin v \cos\varphi_1 \\ 0 & 0 \\ -\sin\sigma \cos\varphi_2 + \cos\sigma \sin v \sin\varphi_2 & (\rho_1 \cos v + \rho_2) \sin\varphi_2 \\ \sin\sigma \sin\varphi_2 + \cos\sigma \sin v \cos\varphi_2 & (\rho_1 \cos v + \rho_2) \cos\varphi_2 \\ \cos\sigma \cos v & -\rho_1 \sin v \\ 0 & 1 \end{bmatrix} \quad (1)$$

Where it was used the notations:

$$\begin{aligned} a_\varphi &= \cos\sigma \cos\varphi_2 + \sin\sigma \sin v \sin\varphi_2, \\ b_\varphi &= \cos\sigma \sin\varphi_2 - \sin\sigma \sin v \cos\varphi_2. \end{aligned} \quad (2)$$

Engagement of surfaces S_1 and S_2 is mono-parametric because the relative motion is defined by a single parameter, either φ_1 or by φ_2 , the relationship between these parameters is given by the law of motion.

It results that the contact between S_1 and S_2 will be a curve (even a line), the geometric locus of the points that satisfy the general equation of the gears being expressed by $\bar{V}_{12}\bar{N}_1 = 0$, in which \bar{V}_{12} is the relative velocity, it's value if given by the expression:

$$V_{12} = \left(T_{12} \frac{dT_{21}}{d\varphi_2} \right) X_1 = V_{12}(\varphi_2), \quad (3)$$

where T_{12} is the inverse of the square matrix (1).

From Eq. (3), it's obtained:

$$V_{12} = \begin{bmatrix} \{-Z_1 \sin\vartheta \sin\varphi_1 + [Z_1 \sin v + (\rho_1 \cos\vartheta + \rho_2) \cos\sigma] \cos\varphi_1 \\ + Y_1 (\cos\sigma \cos\vartheta + i_{12})\} \\ \{Z_1 \sin\vartheta + (\rho_1 \cos\vartheta + \rho_2) \cos\sigma \sin\varphi_1 + Z_1 \sin\sigma \cos\varphi_1 \\ - x_1 (\cos\sigma \cos\vartheta + i_{12})\} \\ \{(x_1 \sin\sigma \cos\vartheta - y_1 \sin\vartheta) \sin\varphi_1 - (y_1 \sin\vartheta + x_1 \sin\sigma) \\ \cos\varphi_1 - (\rho_1 \cos\vartheta + \rho_2) \sin\sigma\} \end{bmatrix} = \begin{Bmatrix} V_X \\ V_Y \\ V_Z \\ 0 \end{Bmatrix} \quad (4)$$

Knowing the vector \bar{N}_1 , the Eq. (4) becomes:

$$\varphi_1 = 2 \arctg \left[\frac{-C_1 \pm \sqrt{C_1^2 + C_2^2 - C_3^2}}{C_3 - C_2} \right] \quad (5)$$

where it was denoted

$$\begin{aligned}
 C_1 &= (n_{y1}Z_1 - n_{z1}Y_1)\sin\vartheta + (n_{x1}Z_1 - n_{z1}x_1)\sin\sigma\cos\vartheta + n_{y1}(\rho_1\cos\vartheta + \rho_2)\cos\sigma \\
 C_1 &= (n_{y1}Z_1 - n_{z1}X_1)\sin\vartheta + (n_{y1}Z_1 - n_{z1}Y_1)\sin\sigma\cos\vartheta + n_{x1}(\rho_1\cos\vartheta + \rho_2)\cos\sigma \\
 C_3 &= (n_{x1}Y_1 - n_{y1}X_1)(\cos\sigma\cos\vartheta + i_{12}) + n_{z1}(\rho_1\cos\vartheta + \rho_2)\sin\sigma.
 \end{aligned} \tag{6}$$

Introducing solution (17) in (13) and multiplying the last one with vector \bar{X}_1 , it's obtained the vector radius of the contact point as:

$$X_2 = T_{21}X_1 = \begin{bmatrix} (X_1\cos\varphi_1 + Y_1\sin\varphi_1)a_\varphi - (X_1\sin\varphi_1 - Y_1\cos\varphi_1)\sin\vartheta\sin\varphi_2 \\ -(X_1\cos\varphi_1 + Y_1\sin\varphi_1)b_\varphi - (X_1\sin\varphi_1 - Y_1\cos\varphi_1)\cos\vartheta\sin\varphi_2 \\ \quad + (X_1\cos\varphi_1 + Y_1\sin\varphi_1)\sin\sigma\cos\vartheta + (X_1\sin\varphi_1 \\ \quad - Y_1\cos\varphi_1)\sin\vartheta \\ Z_1(\cos\sigma\sin\varphi_2 - \sin\sigma\cos\varphi_2) + (\rho_1\cos\vartheta + \rho_2)\sin\varphi_2 \\ Z_1(\cos\sigma\sin\vartheta\cos\varphi_2 + \sin\varphi_2) + (\rho_1\cos\vartheta + \rho_2)\cos\varphi_2 \\ \quad Z_1\cos\sigma\cos\vartheta - \rho_1\sin\vartheta \end{bmatrix} = X_2(q_1, q_2) \tag{7}$$

The vector (7), together with Eq. (5), defines the surface of the side S_2 , as a geometric locus of the points in the axes systems \sum_2 that satisfy the gear equation.

Remarks

- If the surface S_1 , expressed by the vectors \bar{X}_1 and \bar{N}_1 , is the involute surface described by the edge of tool of type wheel, then the side S_2 obtained represents the teeth of the hyperbolic gear.
- the angle between gear axes is defined by the equation:

$$\cos\psi = \cos\sigma\cos\vartheta, \tag{8}$$

and axial distance A results from the formula

$$A = \sqrt{t^2 + 2t(\rho_2\sin\vartheta - \gamma\cos\vartheta)\cos\sigma + (\gamma + \rho_1\sin\vartheta)^2 + (\rho_1\cos\vartheta + \rho_2)^2} \tag{9}$$

for

$$\begin{aligned}
 t &= -\frac{\rho_1\cos\sigma\cos\vartheta + \rho_2}{1 - \cos^2\vartheta\cos^2\sigma}\sin\vartheta; \\
 \gamma &= t\cos\vartheta\cos\sigma - \rho_1\sin\vartheta
 \end{aligned} \tag{10}$$

Generation scheme from the Fig. 1, (Szekely et al. 1981) is used also for the general study of gear theory.

2 Aspects Regarding the Gearing Modeling

In modeling of gears it's aimed three main aspects:

- Verification of the gear process of the side gears;
- Evaluation of the contact area;
- Calculus of gear contact ratio;

It's assumed known the surfaces S_1 and S_2 of the sides teeth of gears 1 and 2 reported to the systems \sum_1 and \sum_2 (linked to the two gears), defined by the vector radii and normal, under the form:

$$\begin{aligned} X_1 &= X_1(q_1, q_2); & N_1 &= N_1(q_1, q_2), \\ X_2 &= X_2(Q_1, Q_2); & N_2 &= N_2(Q_1, Q_2), \end{aligned} \tag{11}$$

It can be seen that relative position of the systems \sum_1 and \sum_2 is difference according to the scheme from Fig. 1.

The gearing study according to the classic concepts is based on the position analysis relative to the surfaces S_1 and S_2 corresponding to the different rotation angles, that represents the drawback of complex calculus.

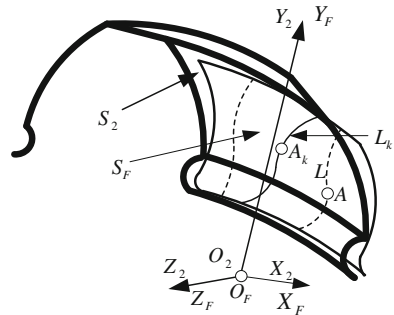
The calculus are simplified by introducing a fictive surface, S_F , which in the system \sum_2 represents the enveloping mono-parameter of the surface S_2 , in fact, this approach generalize the idea exposed in the paper (Herciu et al. 2008; Litvin et al. 2002).

The surface S_{F2} (Fig. 2) is expressed with the help of algorithm from the Eqs. (1), (7), particularized by replacing in algorithm the index 2 with F . It results that the surface S_F is defined in the system \sum_2 , by the vector radius $X_F = X_F(q_1, q_2)$ by identical expression with (7).

Thus, the contact analysis, respectively the gearing process, it resumes to evaluation of the relative position of the surfaces S_2 and S_F . In this aim, first it defines between S_2 and S_F a distant function, Φ .

$$\Phi(q_1, q_2, Q_1, Q_2) = \frac{X_F - X_2}{n_{x2}} \tag{12}$$

Fig. 2 Scheme of the gearing modeling



In which the parameters p, q, P, Q , represents the solution of the nonlinear equation system:

$$\begin{aligned}
 F_1(q_1, q_2, Q_1, Q_2) &= Y_2 - Y_F + (X_F - X_2) \frac{n_{y2}}{n_{x2}} = 0; \\
 F_2(q_1, q_2, Q_1, Q_2) &= Z_2 - ZY_F + (X_F - X_2) \frac{n_{z2}}{n_{x2}} = 0; \\
 F_3(q_1, q_2, Q_1, Q_2) &= n_{x2}n_{yF} - n_{y2}n_{x1} = 0; \\
 F_4(q_1, q_2, Q_1, Q_2) &= n_{x2}n_{zF} - n_{z2}n_{x1} = 0.
 \end{aligned} \tag{13}$$

Equation (12) together with the system (13) express the minimal distance between the sides S_2 and S_F , oriented after the normal vector N_2 .

In relation with the value of the function (12) and the system behavior (12) are found 5 distinct situations:

- (a) If the system (12) does not admit solutions, then the surfaces S_2 and S_F are secant. As a consequence, the gears between the side S_1 and S_2 are compromised.

Eventual repair of the situation can be made by correcting the angles σ and ν from the scheme represented in Fig. 2.

- (b) if the system (13) is verified and $\Phi \neq 0$, the surfaces S_2 and S_F are intersecting. The gearing between the sides S_1 and S_2 will take place only in a single point with condition of correcting the distance between the axes, respectively by co-rrection of the radius ρ_1 and ($\Phi < 0$), Fig. 1. This case, corresponds to the blocking ($\Phi < 0$) of the gears or existence ($\Phi > 0$).
- (c) if the system (13) is verified and $\Phi = 0$, then the contact is in a single point that corresponds to the previous case, corrected.
- (d) If the system (13) is over-determined, in the sense that is verified for more values of one parameters (for example P), then the contact between S_2 and S_F is linear (Fig. 2). It results that between the sides of the surfaces S_1 — surface of the side of gear 1 from the real gearing; S_2 —surface of the side of the gear 2; and gearing is point type, or in the used terminology, gearing is dual parametric. In this situation, the contact line L_K is function of the P parameter and through any point $M_k \in L_K$; $\Phi = 0$. It's assumed that along the curve L_K , the P parameter takes extreme values P_S and P_1 which, based on the Eq. (5) together with the system (13), define the two extreme values φ_S and φ_1 corresponding to φ_1 .

The point gearing is done in the limits φ_S and φ_1 .

From here it results that the contact area is given by the formula:

$$\varepsilon_{ra} = \frac{\varphi_S - \varphi_1}{2\pi} Z_1, \tag{14}$$

In which Z_1 represents the number of teeth of gear 1.

- (a). The surfaces S_2 and S_F are overlapped in the case in which the system (13) is insensible to variation of two parameters (double over determined). It results

that gearing between the S_1 and S_2 is mono parametric, between S_1, S_2 exists an instantaneous contact line. Similarly with the previous example it can be established numerically the limit values φ_s and φ_1 of solution (15), then for determination of the contact area degree it's used the Eq. (14).

Contact area is placed in the neighborhood of the contact line L_K , or around the contact point in cases (b) and (c).

It's admitted that due to the external forces, the sides S_1 and S_2 , respectively S_2 and S_F , are approaching with quantity ϵ_K . In this hypothesis the geometric locus of the points in which the distance between S_2 and S_F is ϵ_K represents the contour of L of the contact area, Fig. 2.

It results that the contact of equal distance L traced on the surface S_2 is built as a geometric locus of the points M of vector radii $X_2 = X_2(P, Q)$ which satisfy the system of equations:

$$\begin{aligned} f_1(q_1, q_2, Q_1, Q_2) &= X_2 - X_F + \epsilon_K n_{x2} = 0 \\ f_2(q_1, q_2, Q_1, Q_2) &= Y_2 - Y_F + \epsilon_K n_{y2} = 0 \\ f_3(q_1, q_2, Q_1, Q_2) &= W_2 - Z_F + \epsilon_K n_{w2} = 0 \end{aligned} \tag{15}$$

3 Conclusions

Solution of the system (15) defines three parameters q_1, q_2, Q_1, Q_2 and one remains variable along the curve of equal distance L .

Adopting a sequence of discrete values for ϵ_k through the system (15) it's obtained a variation of the contour L that represents the image of the evolution of the contact area, function of the elastic-plastic deformation of the teeth sides or function of the usage of them.

The article presents in details the structure of the modeling algorithm specific to a 3D mobile mechanical structure. It was described in details, mainly the modeling of the tooth sides which are the gear's teeth sides from the structure of the spatial gearing. The researches in this this field will continue to obtain a variant of interactive modeling techniques.

References

Alexandru P, Visa I, Alexandru C, Talaba D (1999) Proiectarea functionala a mecanismelor. EdituraLibris, Brasov
 Bocian I (1976) Studiul geometric al angrenajelor globoidale in vederea maririicapacitatii portante a acestora. Teza de doctorat Institutul Politehnic, Cluj-Napoca
 Csibi VI, Herciu D, Sudrijan M (2007) Tool for precise grinding of crown gears. 12th IFTOMM World Congress, Besancon, 18-21 June, 2007

- Csibi VI, Herciu D, Sudrijan M (2008) Scula pentru rectificarea precisa a rotilor dintate frontale. Brevet de Inventie OSIM RO 121729 B1. Int, C1. B24 B1/00 (2006001). BOPI nr. 3/2008
- Herciu D, Csibi VI, Pop RO, Sudrijan M (2008) Tool for grinding of face gears, Hungarian Technical Review, Cluj-Napoca, ISSN 1454-0746, pp 91–95
- Herciu D (2011) Contributii la cresterea performantelor angrenajului pinion cilindric-roata frontal. Universitatea Tehnica din Cluj-Napoca, Teza de doctorat
- Litvin FL, Fuentes A (2004) Gear geometry and applied theory, 2nd edn. Cambridge University Press, Cambridge, pp 543–582
- Litvin FL, Fuentes A, Fan Q, Handschuh RF (2002) Computerized design, simulation of meshing and contact, and stress analysis of face-milled formate generated spiral bevel gears. Mech Mach Theory 37(5):441–458
- Szekely E, Bocian I, Chiorean V (1981) Aspecte noi in teoria angrenajelor conico-evolvenice. Studii si cercetari de mecanica aplicata, Tom 40:721–733

A Dynamic Simulation of a Novel Continuous Variable Transmission

Gani Balbayev and Giuseppe Carbone

Abstract This paper briefly describes the design of a novel continuous variable transmission that can be used to adjust the transmission ratio according to the externally applied load. A detailed 3D CAD model has been proposed in order to investigate the engineering feasibility of the proposed design solution. Main design variables and constraints have been selected by referring to a practical application as a speed reducer on a small wind mill. A proper dynamic model has been developed within MSC ADAMS software. Simulation tests have been carried out and preliminary discussed to validate the proposed design solution.

Keywords Transmission • Design • Simulation • Gears • Planetary gears

1 Introduction

Power transmission and speed reduction are key issues in many different application fields. Continuous variable transmissions have significant practical interest when there is a need to adjust the transmission ratio according to the externally applied load.

Several design solutions have been proposed in the literature. For example, a face-gear train is presented in (Litvin et al. 2004). Three stage micro planetary gear and the technical characteristics are described in (Gold 2002). Cam-based infinitely variable transmission are proposed for example in Lahr and Hong (2006). Planetary

G. Balbayev (✉)

Almaty University of Power Engineering and Telecommunication, Almaty, Kazakhstan
e-mail: gani_b@mail.ru

G. Carbone

LARM: Laboratory of Robotics and Mechatronics, University of Cassino and South Latium, Latium, Italy

gears can be designed as a continuously variable transmission as proposed for example in Harries (1991), Ivanov (2012), Carbone et al. (2007) and Lan et al. (2009). This mechanism can change the gear ratio depending on the load by having two degrees of freedom and eventually by using a brake (Harries 1991). A mechanism with a planetary gear set and a torque converter is designed as a continuously variable transmission in Crockett (1990). This mechanism has two degrees of freedom and uses an external torque to start the movement (Crockett 1990).

This paper describes the design of a novel continuous variable transmission. It is composed of planetary gears to achieve a two degrees of freedom transmission. The main purpose of this novel variable continuous transmission is its capability to adapt its operation to variable loading by preserving efficiency and input–output load ratio. The proposed design solution provides a motion of the output link with a speed that is inversely proportional to the loading of the shaft. These features are suitable for using the proposed design in practical applications such as a differential planetary gear box in the transmissions of vehicles, metal cutting tools, wind mills and other transmission applications needing smooth control of the transmission ratio. A proper dynamic model has been developed within MSC ADAMS software to provide information on the feasibility of the proposed design solution. Simulation tests have been carried out and preliminarily discussed for validating the proposed design.

2 A CAD Simulation

The herein proposed differential planetary gear set consists of a mechanical planetary gear set without additional devices such as torque converters or electronic parts. General design characteristics have been selected for the practical applications of the transmission, for example, to wind mills. A wind turbine installation can be identified, for example, by referring to a small wind turbine of 3–4 kW power.

The new planetary gear box is conceived with two degrees of freedom with a mechanism consisting of an input carrier H_1 , an output carrier H_2 , central (sun) gears 1 and 4, which are fixed on a shaft, satellites 2 and 5, central internal gears 3 and 6, which are fixed together, Fig. 1. Main characteristics of the proposed design can be recognized in two input mobile links, two degrees of freedom, stepless operations, smoothly and automatically changing reduction ratio depending on the load of the output link.

A CAD design of a gearbox with planetary gear set has been worked out in SolidWorks software. Figure 2 shows an exploded CAD design of planetary gear box with the following main components: (1) output carrier; (2) bearing; (3) output satellite; (4) spindle of output satellite; (5) bearing; (6) bearing of internal gears; (7) gearshuft; (8) sun gear; (9) epicyclic gears; (10) input satellite; (11) spindle of input satellite; (12) input carrier. The mechanical design of the mechanism with housing and cover is shown in Fig. 3.

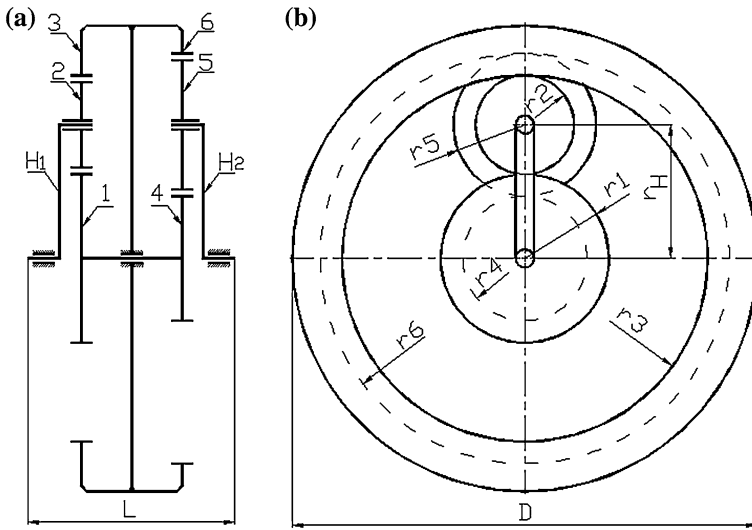


Fig. 1 A kinematic scheme for the new planetary gear box: **a** H_1 -input carrier, 1-input sun gear, 2-input satellite, 3-input epicyclic gear, 4-output sun gear, 5-output satellite, 6- output epicyclic gear, H_2 -output carrier; **b** r_H -radius of carrier, r_1 -radius of sun gear, r_2 -radius of input satellite, r_3 -radius of input internal gear, r_4 -radius of output sun gear, r_5 -radius of output satellite, r_6 -radius of output internal gear

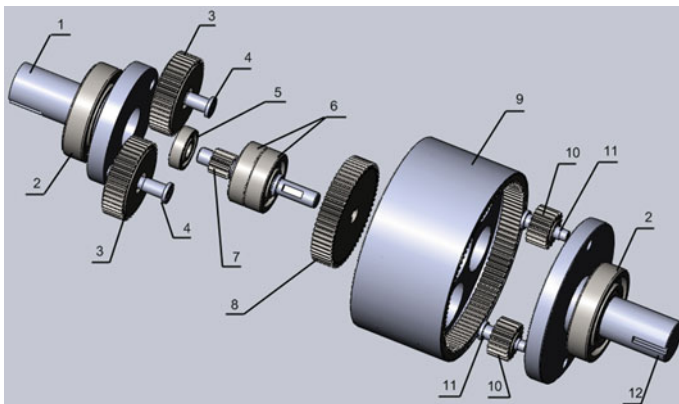


Fig. 2 CAD exploded assembly of the new gear box design

All the geometrical parameters have been defined within the CAD model in Figs. 1, 2 and 3 so that the main dimensions can be as equal to a maximum diameter D (in Fig. 1b) of 180 mm, a maximum longitudinal size L (in Fig. 1a) of 95 mm. The input and output shafts have a diameters of 16 and 13 mm, respectively. The overall weight is 3 kg.

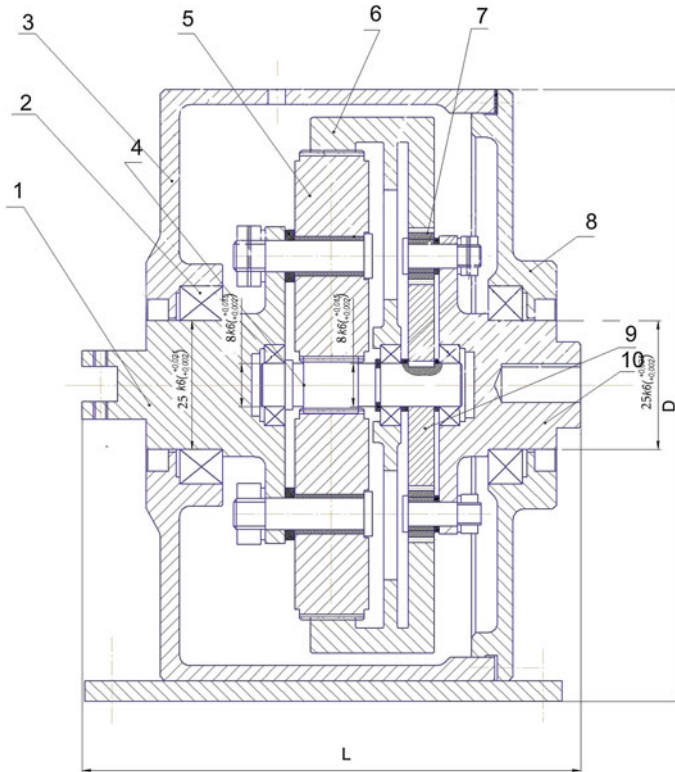


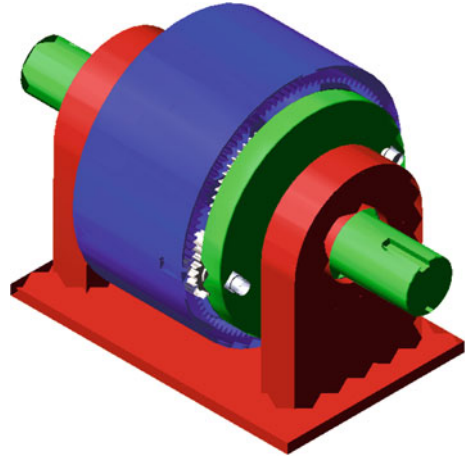
Fig. 3 Mechanical design of a new planetary gear box in Fig. 2: 1-output carrier; 2-bearing; 3-housing; 4-gear shaft; 5-output satellite; 6-epicyclic gears; 7-input satellite; 8-cover; 9-sun gear; 10-input carrier

3 Dynamic Simulation

A dynamic simulation of the planetary gear box has been carried out by using MSC ADAMS software. The MSC ADAMS model of the proposed planetary gear box is presented in Fig. 4. Input values such as angular velocity, stiffness, dumping coefficients, and friction forces have been defined accordingly as listed in Table 1. Input angular velocity has been set as a constant value of 100 rpm. All gears are spur gears with module 1 mm. Friction coefficient of gears has been set as equal to 0.2 by referring to the contact of steep surfaces. Table 1 summarizes main other parameters that have been assumed by referring to feasible values for a real case of study.

All the geometrical dimensions have been set as by referring to the models in Figs. 1, 2 and 3. After setting the above-mentioned parameters significant attention has been addressed in properly modeling all the constraints and joints in order to achieve a reliable operation of the proposed model.

Fig. 4 ADAMS model of gear box design in Figs. 2 and 3



Several cases of study have been considered in order to investigate the dynamic behavior of the proposed transmission. In particular, preliminary tests have been carried out by considering a constant input speed. Then, it has been verified that the input and output speeds and torques are in accordance with the expected smooth variable transmission ratio. Examples of the results that have been obtained are reported in the plots of Figs. 5, 6, 7, 8 and 9. In particular Fig. 5a, b show the contact forces between the gears of output and input links.

Figure 6 shows the computed results of the input and output angular velocities. Input velocity is constant and given as 100 rpm. Computed output angular velocity which is shown in the plot of Fig. 6b is approximately 50 rpm. The plot in Fig. 7 shows the results of the computed torques. Input torque is constant and output torque is approximately constant. Angular velocities of the input and output epicyclic internal gears are presented in Fig. 8a. The epicyclic internal gears rotate with the same speed as shown in the plot in Fig. 8a. Figure 8b shows the plots of the computed torques of the epicyclic internal gears.

Computed results of contact forces between gears of the output link and the input link are presented in Fig. 9a, b. In Fig. 9a, b contact forces are plotted as during the simulated motion for a full rotation of the output shaft. Figure 9a shows the plots of the computed contact forces between output satellite and sun gear, which are shown as number 1 and 2 in Fig. 5a. Comparing these curves in Fig. 9a, the highest contact force of 0.04 N is related to the contact No. 2 in Fig. 5a between output satellite and epicyclic internal gear. Computed results of contact forces of the input link are presented in Fig. 9b. Figure 9b shows the plot of the contact forces between input satellite and epicyclic internal gear, which are shown as numbers 3 and 4 in Fig. 5b. The highest contact force of 0.6 N is related to the contact No. 4 Fig. 5b between input satellite and epicyclic internal gear. The values of contact forces increase by increasing the values of the external loads on the output shaft.

Table 1 Input parameters for simulation of model in Fig. 4

Parameter	Value	Units
Input angular velocity	100	rpm
Input torque	Plots in Fig. 9	Nm
Output angular velocity	Plots in Fig. 8	Nm
Output torque	Plots in Fig. 9	Nm
Damping	40	N*sec/mm
Young's modulus	2.07 E + 005	N/mm**2
Density	7.801 E-006	kg/mm**3
Penetration depth	0.1	mm
Force exponent	1.8	

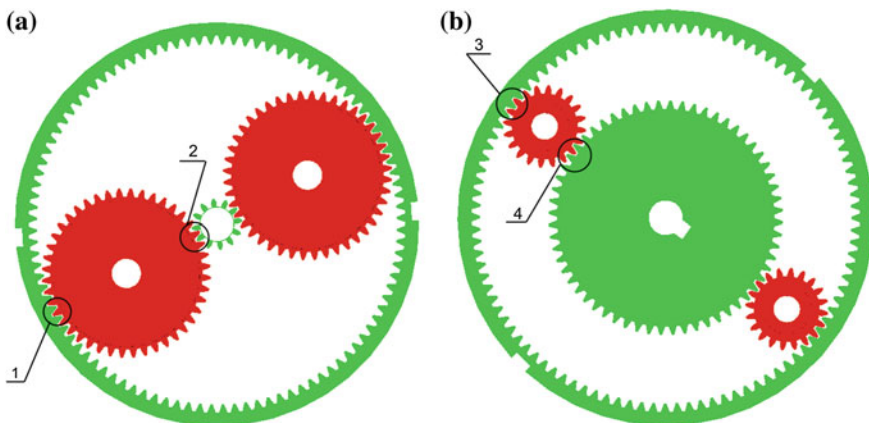


Fig. 5 Contact forces between gears: **a** 1, 2 contact forces in output link; **b** 3, 4 contact forces in input link

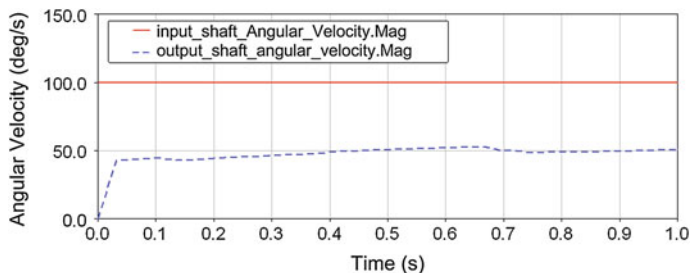


Fig. 6 Computed plot of the input and output angular velocities

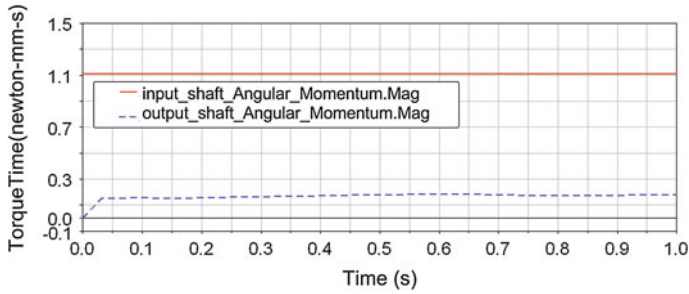


Fig. 7 Computed plot of the input and output torques

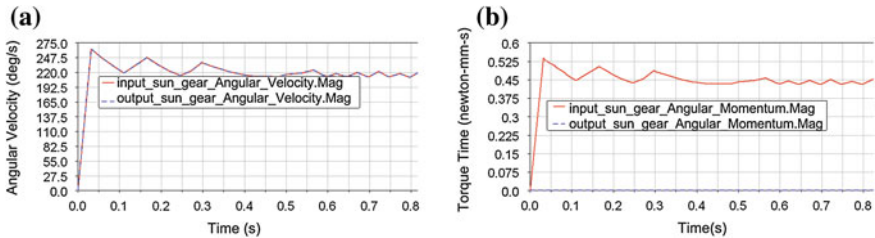


Fig. 8 Computed plots of the parameters of the sun gears: **a** angular velocity of the sun gears; **b** torque of the sun gears

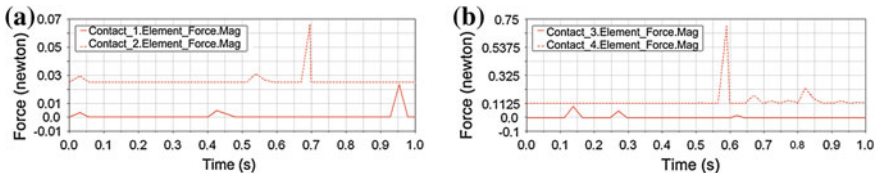


Fig. 9 Plots of contact forces of gears in the output and input links: **a** contact forces numbers 1 and 2 in Fig. 5a; **b** contact forces numbers 3 and 4 in Fig. 5b

4 Conclusion

In this paper, a new planetary gear box with two degrees of freedom is proposed. A 3D CAD model of the proposed design has been proposed. A proper dynamic model and simulations have been carried out in MSC ADAMS environment. Simulation results show that the proposed planetary gear box has suitably constant output values both in terms of speed and torque. The simulation results also show that the proposed gear box smoothly changes the reduction ratio at constant input speed. Contact forces between gears are small enough to use the proposed system under the expected loading conditions.

References

- Carbone G, Mangialardi L, Bonsen B, Tursi C, Veenhuizen PA (2007) CVT dynamics: theory and experiments. *Mech Mach Theory* 42:409–428
- Crockett JS (1990) Shiftless, continuously-aligning transmission. Patent of USA 4,932,928, Cl.F16H 47/08, U.S. Cl. 475/51; 475/47
- Gold PW (2002) Micro gears. *Gearing Transm* 1:44–61
- Harries J (1991) Power transmission system comprising two sets of epicyclical gears. Patent of Great Britain GB2238090 (A)
- Ivanov K (2012) Design of toothed continuously variable transmission in the form of gear variator. *Balkan J Mech Transm (BJMT)* 2(1):11–20
- Lan L, Geng L, Zhaoxia H, Li H (2009) Simulation flow management for planetary gear transmission. In: IEEE 16th international conference on industrial engineering and engineering management, pp 1865-1868. Available via <http://ieeexplore.ieee.org/xpls/>
- Lahr DF, Hong DW (2006) The operation and kinematic analysis of a novel cam-based infinitely variable transmission. In: ASME 2006 international design engineering technical conferences and computers and information in engineering conference, Philadelphia, pp 1–6
- Litvin F, Fuentes A, Vecchiato D, Gonzalez-Perez I (2004) New design and improvement of planetary gear trains. University of Illinois at Chicago, NASA/CR-2004-213101, Chicago

Design and Simulation of a Leg Exoskeleton Linkage for a Human Rehabilitation System

C. Copilusi, M. Ceccarelli, N. Dumitru and G. Carbone

Abstract This paper addresses the design and simulation of a leg exoskeleton for a human rehabilitation system. The proposed novel leg exoskeleton is based on a linkage mechanism that has been designed in order to fulfil main human locomotion tasks with low-cost easy-operation features. A proper kinematic model of the proposed linkage mechanism has been settled up and it has been implemented into Maple environment for numerical simulations of the kinematic behavior. A proper 3D CAD model has been developed and the full leg exoskeleton has been modeled and simulated into MSC.ADAMS environment. Results of simulations demonstrate the engineering feasibility of the proposed design.

Keywords Human locomotion · Exoskeletons · Kinematics · Design simulation

1 Introduction

Nowadays there are a lot of persons with locomotion disabilities due to several diseases and accidents such as stroke and bone fractures. For these persons different research centres develop exoskeletons which can improve or increase the human locomotion ability and its rehabilitation. An assessment system of the gait phase using biomechanical equipment can help to monitor the rehabilitation program and to restore skills of each joint for each phase of gait.

Significant existing systems are presented in Pratt et al. (2004); Kawamoto et al. 2003, Kazerooni and Steger (2006), Kong and Jeon (2006), Tavolieri et al. (2007);

C. Copilusi (✉) · N. Dumitru

Applied Mechanics Department, Faculty of Mechanics, University of Craiova,
Craiova, Romania
e-mail: cristache03@yahoo.co.uk

M. Ceccarelli · G. Carbone

University of Cassino and South Latium, Cassino, Italy

Walsh et al. (2006), Yagn (1890), McMahon and Cheng (1990) Zoss and Kazerooni (2006) with different designs. But a major common drawback can be considered the cost and user-oriented implementation for persons with locomotion problems. Kinematic analysis methods can be developed to model the human natural walking, like in Ceccarelli et al. (2010), Copilusi (2009), Dumitru et al. (2008), Grande and Ottaviano (2008). They can be also used as starting points for dynamic analyses and for designing locomotion exoskeletons or robot biped legs.

In this paper a novel exoskeleton is proposed as based on a linkage mechanism which fulfils main locomotion tasks. The new exoskeleton has been designed with a low-cost concept, easy-operation features and reduced number of DOFs. The design has been characterized with results from simulations of basic functionality.

2 Human Walking Characteristics

Human walking motions are difficult to study from a theoretical viewpoint. Today there are different equipments and software which help to understand and to study these motions through walking tests for biomechanics characterization. In particular, Figs. 1, 2, 3 and 4 report results that have been obtained at Craiova University by using CONTEMPLAS system (CONTEMPLAS 2010).

Human joints (hip, knee and ankle) were analyzed for a male of 1.68 m height, 65 kg, age 28 by using a marker on each human joint. With the aid of CONTEMPLAS equipment trajectories and angular variations of each joint were recorded and analyzed even by comparison with data from special literature (Williams 1996).

3 Leg Exoskeleton Mechanism

The proposed leg mechanism is composed by a Chebyshev linkage and a pantograph as shown in Fig. 5. The Chebyshev mechanism generates an approximately ovoid trajectory. The links lengths can be sized so that the leg shape end point

Fig. 1 Hip joint angle (degrees) versus Gait (%)

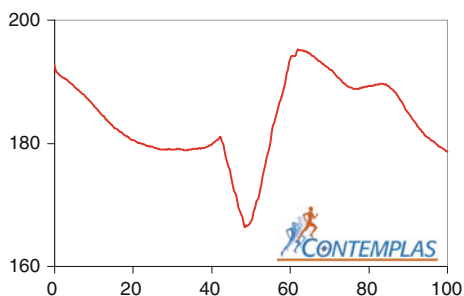


Fig. 2 Knee joint angle (degrees) versus Gait (%)

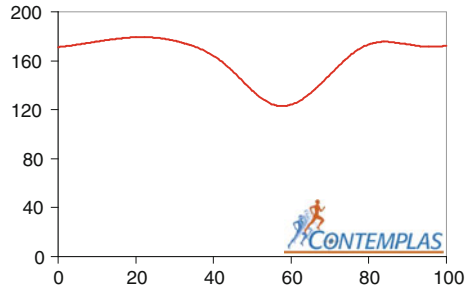


Fig. 3 Ankle joint angle (degrees) versus Gait (%)

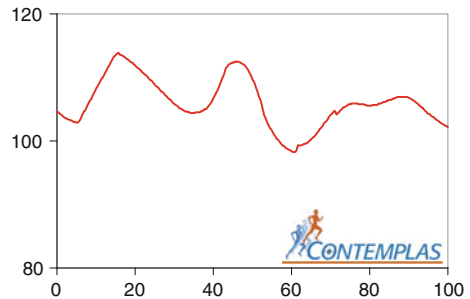
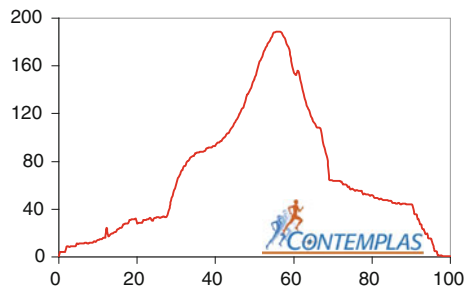
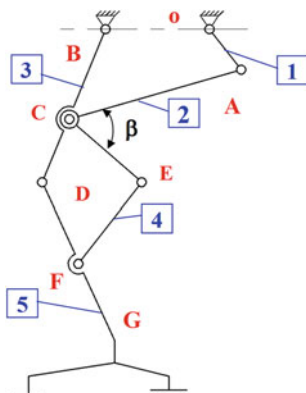


Fig. 4 Foot trajectories (mm) versus Gait (%)



trajectory is similar to the shape of a man’s point, in accordance with Fig. 4. Moreover, the straight part of the trajectory can be very accurate. In Fig. 5 reference points are A, B, C, D, E, F and G and the mechanism is with one DOF. Several walking robots have a design containing a pantograph as fundamental mechanism and even Chebyshev linkage has been used for actuating purposes (Ceccarelli et al. 2010; Conghui Liang et al. 2008; Grande and Ottaviano 2008; Tavolieri et al. 2007; Walsh et al. 2006). This leg mechanism can be used for mobility of knee and hip joints. The ankle joint can be neglected because its angular amplitude during walking is small.

Fig. 5 A structural scheme of the proposed leg exoskeleton



4 A Kinematic Analysis

An analysis of the leg exoskeleton kinematics was carried out in order to evaluate and simulate performances and operations. The point D position, with respect to the reference OXY, Fig. 6, can be evaluated as a function of input crank angle φ_1 and kinematic parameters of the Chebyshev linkage OABC. Point B position, according with reference system is given by:

$$x_C = x_B + l_{BC} \cos \varphi_3, \quad y_C = y_B + l_{BC} \sin \varphi_3 \tag{1}$$

Position of point G with respect to the fixed frame can be given as:

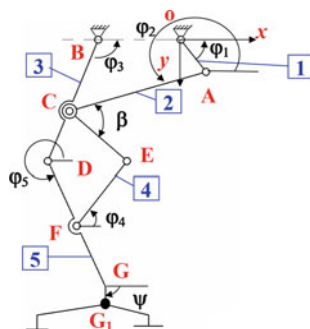
$$x_G = x_D + l_{DG} \cos \varphi_5 \quad y_G = y_D + l_{DG} \sin \varphi_5 \tag{2}$$

And the G_1 point, according with reference system can be written as:

$$x_{G_1} = x_G + l_{GG_1} \cos \Psi \quad y_{G_1} = y_G + l_{GG_1} \sin \Psi \tag{3}$$

The B, G and G_1 velocity can be evaluated by using time derivatives from Eqs (1) to (3) and angles φ_i ($i = 1-5$) can be solved from closure loops equations as function of $\varphi_1 = \omega \cdot t$.

Fig. 6 Kinematic model of the proposed leg mechanism



$$\varphi_2 = 2\tan^{-1}\left(\frac{A_1 \pm \sqrt{A_1^2 + A_2^2 - A_3^2}}{A_2 - A_3}\right) \quad \varphi_3 = 2\tan^{-1}\left(\frac{B_1 \pm \sqrt{B_1^2 + B_2^2 - B_3^2}}{B_2 - B_3}\right) \quad (4)$$

$$\varphi_4 = 2\tan^{-1}\left(\frac{D_1 \pm \sqrt{D_1^2 + D_2^2 - D_3^2}}{D_2 - D_3}\right) \quad \varphi_5 = 2\tan^{-1}\left(\frac{C_1 \pm \sqrt{C_1^2 + C_2^2 - C_3^2}}{C_2 - C_3}\right) \quad (5)$$

With:

$$\begin{aligned} A_1 &= -2l_{AC}(y_A - y_B) & A_2 &= -2l_{AC}(x_A - x_B) \\ A_3 &= -(y_A - y_B)^2 - (x_A - x_B)^2 - l_{AC}^2 + l_{BC}^2 \\ B_1 &= 2l_{BC}(y_A - y_B) & B_2 &= 2l_{BC}(x_A - x_B) \\ B_3 &= -(y_A - y_B)^2 - (x_A - x_B)^2 + l_{AC}^2 - l_{BC}^2 \end{aligned} \quad (6)$$

G_1 point acceleration can be computed by using the expressions:

$$\begin{aligned} \ddot{x}_{G1} &= -l_{AC}(\cos \varphi_2 \cdot \dot{\varphi}_2^2 + \sin \varphi_2 \cdot \ddot{\varphi}_2) - l_{CD}(\cos \varphi_3 \cdot \dot{\varphi}_3^2 + \sin \varphi_3 \cdot \ddot{\varphi}_3) \\ &\quad - l_{DG}(\cos \varphi_5 \cdot \dot{\varphi}_5^2 + \sin \varphi_5 \cdot \ddot{\varphi}_5); \quad \ddot{y}_{G1} = l_{DG}(2 \cos(\ddot{\varphi}_5 + \dot{\varphi}_5^2) - \sin \varphi_5 \cdot \dot{\varphi}_5^2) \end{aligned} \quad (7)$$

A kinematic analysis can be worked out the above equations. An algorithm was created in MAPLE, with the input data as: $l_{OA} = 65$ mm; $l_{AC} = 250$ mm; $l_{BC} = 195$ mm; $l_{CD} = 205$ mm; $l_{EF} = 165$ mm; $l_{DF} = l_{DF} = 185$ mm; and $\beta = \psi = 90^\circ$. Some of these parameters were identified from evaluating a human subject locomotion system on experimental walking research (Copilusi 2009).

Numerical results have been obtained without considering the leg's interaction with the ground as in Figs. 7 and 8 with linear and angular displacements, velocities and accelerations of the kinematic joints and elements.

The computed hip and knee joints angular displacements from Fig. 7 respects the limits obtained from experimental research of human walking. For hip joint this limit is between 160 and 190° and for knee this is between 130 and 165° . Similarly it can be observed in case of foot trajectory where the theoretical results are appropriate with the ones from the experimental research (200 mm distance for a single gait—Fig. 8).

Fig. 7 Computed angular displacement of hip and knee for a single gait case

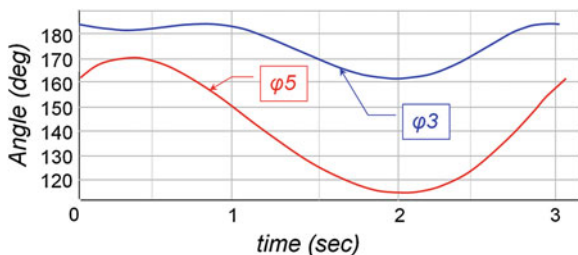
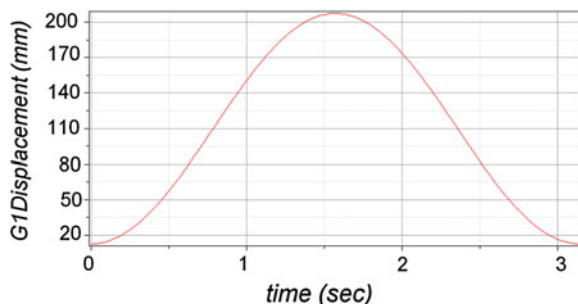


Fig. 8 Computed G1 point displacement of foot for a single gait case



5 CAD Design and Dynamic Simulation

A mechanical design of a low-cost exoskeleton is presented in Fig. 9. The structure was designed to permit adjustments of mechanism links in accordance with different human body constitution. A dynamic analysis has been worked out by using a proper model for operation tests in ADAMS environment (Adams 2010). Contact, stiffness, dumping coefficients, and friction force have been defined accordingly as listed in Table 1 with links made of aluminum alloy.

Computed walking sequences are represented in Fig. 10 and main kinematic results are shown in Figs. 11 and 12. From Figs. 12 and 13 it can be observed that appropriate values are obtained as compared with those from experimental tests and numerical kinematic analysis. In Figs. 13 and 14 contact forces are plotted as during the simulated motion for a single gait. The highest value of 67.5 N is related to the left knee joint as due to the servomotor position.

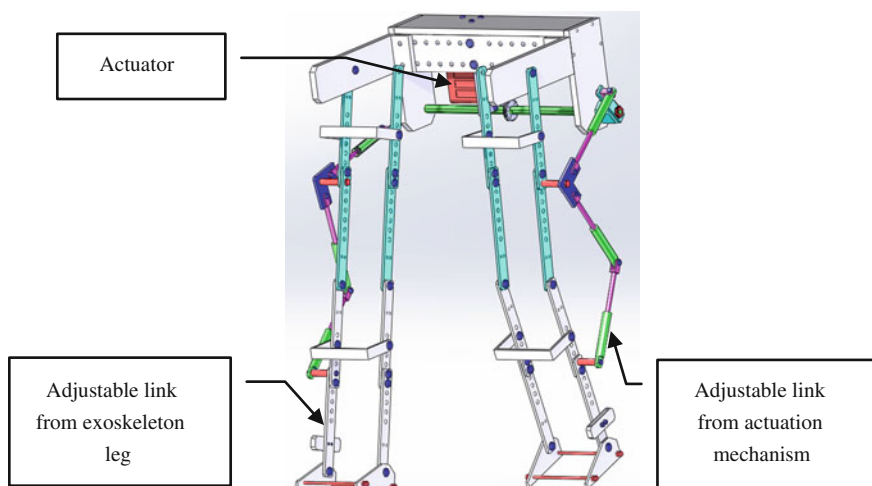


Fig. 9 A mechanical design of the proposed low-cost exoskeleton

Table 1 Input parameters for dynamic simulation

Parameter	Type/value	Units	Parameter	Type/value	Units
Elasticity modulus	7.17054E+004	N/mm ²	Contact μ s	0.7	–
Density	2.74E–006	kg/mm ³	Contact μ d	0.5	–
Penetration depth	0.1	mm	Force exponent	1.8	–
Friction force	Coulomb	N	Damping	40	N·sec/mm

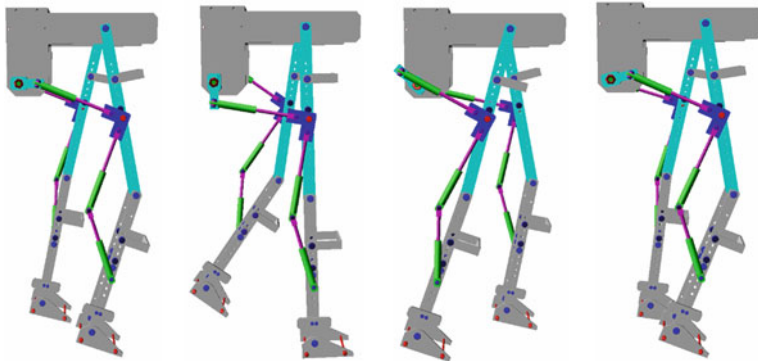


Fig. 10 A walking sequence in ADAMS simulation for the low-cost exoskeleton

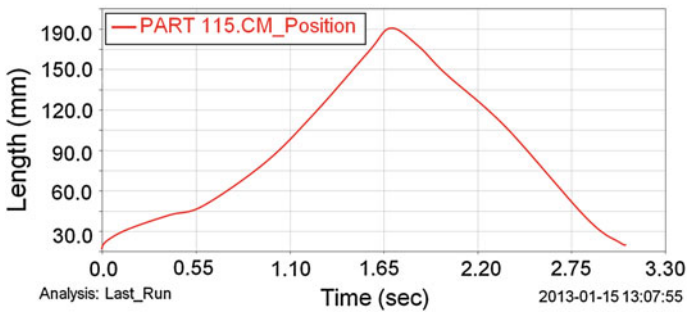


Fig. 11 Computed plot of the foot displacement in exoskeleton model of Fig. 10

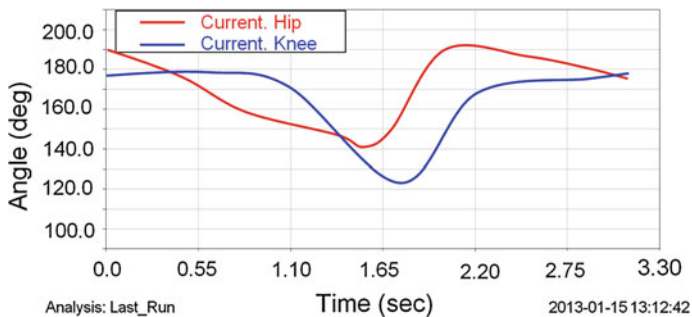


Fig. 12 Computed plot of the hip and knee joint variation in exoskeleton model of Fig. 10

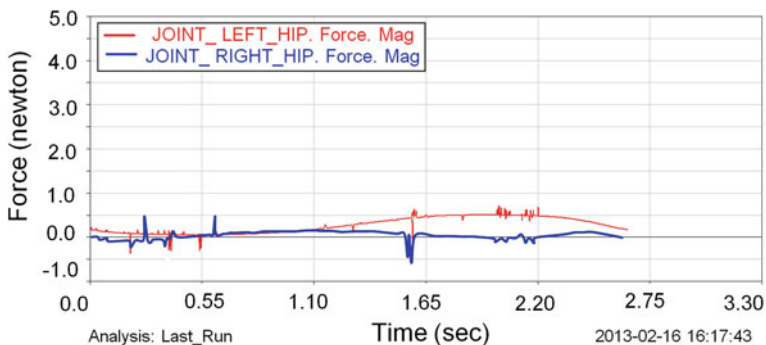


Fig. 13 Computed plot of the left and right hip joint force contact in model of Fig. 10

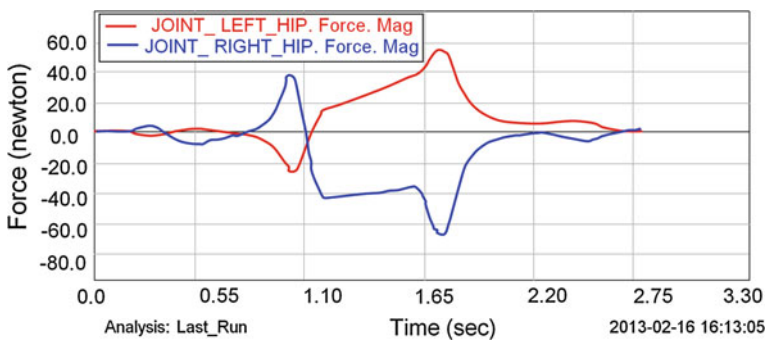


Fig. 14 Computed plot of the left and right knee joints force contact in model of Fig. 10

6 Conclusions

A new prototype of a low-cost exoskeleton for human locomotion rehabilitation is proposed with easy-operation features. Simulation results have outlined suitable performance for suitable user-oriented operation in walking rehabilitation application, although its design may require additional components in future developments. The proposed design is fairly simple wearable and light with adjustable structure and its operation is run with only one actuator that can be regulated to fully help or partially assist human walking, even with monitoring purposes.

References

- Adams MSC (2010) Guide mechanical dynamics rev. 10.0
- Ceccarelli M, Carbone G, Ottaviano E (2010) Mechanism solutions for legged robots overcoming obstacles. *New trends in mechanism science*, vol 5. Springer, Dordrecht, pp 545–553
- CONTEMPLAS (2010) Motion analysis equipment user manual
- Copilusi C (2009) Research regarding some mechanical systems applicable in medicine. Ph.D. thesis. University of Craiova
- Dumitru N, Nanu G, Vintilă D (2008) Mechanisms and mechanical transmissions. Classical and modern modelling techniques. Editura Didactică și Pedagogică. Bucuresti
- Grande S, Ottaviano E (2008) A biped walking mechanism for a Rickshaw Robot. In: CD proceedings of IFToMM-FelbIM international symposium on mechatronics and multibody systems MUSME08. San Juan. paper no.20
- Kawamoto H, Lee S, Kanbe S, Sankai Y (2003) Power assist method for HAL-3 using EMG-based feedback controller. In: Proceedings of the IEEE international conference on systems, man, and cybernetics. pp 1648–1653
- Kazerooni H, Steger R (2006) The Berkeley lower extremity exoskeleton. *Transactions of the ASME. J Dyn Syst Meas Control* 128:14–25
- Kong K, Jeon D (2006) Design and control of an exoskeleton for the elderly and patients. *IEEE Trans Neural Syst Rehab Eng* 15:367–378
- Liang C, Ceccarelli M, Takeda Y (2008) Operation analysis of a One-DOF pantograph leg mechanisms. In: Proceedings of the RAAD. 17th Int. Workshop on Robotics in Alpe-Adria-Danube Region, Ancona
- McMahon TA, Cheng GC (1990) The mechanics of running: how does stiffness couple with speed? *J Biomech* 23(suppl. 1):65–78
- Pratt JE, Krupp BT, Morse CJ, Collins SH (2004) The RoboKnee: an exoskeleton for enhancing strength and endurance during walking. In: Proceedings of IEEE international conference on robotics and automation. New Orleans, USA. pp 2430–2435
- Tavolieri C, Ottaviano E, Ceccarelli M (2007) Design and problems of a new leg-wheel walking robot. In: 10th international conference on climbing and walking robots CLAWAR, Singapore
- Walsh J, Paluska D, Pasch K et al (2006) Development of a lightweight, under actuated exoskeleton for load-carrying augmentation. In: Proceedings of IEEE international conference on robotics and automation. Orlando, USA. pp 3485–3491
- Williams M (1996) Biomechanics of human motion. W.B. Saunders Co, Philadelphia
- Yagn N (1890) Apparatus for facilitating walking, running, and jumping. U.S. Patent 420179
- Zoss A, Kazerooni H (2006) Design of an electrically actuated lower extremity exoskeleton. *Adv Robot* 20(9):967–988

Protein Secondary Structure Detection Using Dihedral Angle Parameters Evaluation

Mikel Diez, Víctor Petuya, Imanol Martínez and Alfonso Hernández

Abstract The detection of proteins secondary structures constitutes an essential task in the protein motion simulation. Secondary structures constitute rigid parts of the protein structure, hence, their detection is crucial so as to properly define the movement of the protein. During the simulation process, these rigid structures can be identified and, accordingly, their associated degrees of freedom are neglected. As a consequence, the computational cost is reduced. Current methods existing in the literature are based on the analysis of geometrical parameters distribution, such as $C\alpha$ atoms distribution, and hydrogen bonds detection. These methods require specific procedures, independent of the simulation process, to determine these geometrical parameters, thereby increasing the computational cost. In this paper, a novel method for protein secondary structure detection is presented. This new method relies only on the evaluation of dihedral angles so as to detect the existence of secondary structures. The use of dihedral angles, which have been already evaluated during the simulation process, does not increase the computational cost of the simulation process.

Keywords Proteins · Secondary structure · Rigidity analysis · Protein simulation

1 Introduction

Protein structure analysis allows to differentiate rigid zones from flexible ones of the structure of proteins. These studies provide a better characterization of the protein structure and a better understanding of each protein's kinematic capabilities. Another advantage of this analysis is that they can feed the simulation

M. Diez (✉) · V. Petuya · I. Martínez · A. Hernández
University of the Basque Country, Bilbao, Spain
e-mail: mikel.diez@ehu.es

procedures with information regarding rigid zones of the protein structure, thus allowing to eliminate the degrees of freedom located in those zones in order to reduce the computational cost of the simulation.

Secondary structure detection is a troublesome problem. Results provided by different methods tend to diverge on their results by more than 25 % (Frishman and Argos 1995; Colloc'h et al. 1993). There are several methods for protein rigidity analysis which can be divided in two categories: general rigidity analysis and exclusive secondary structure detection. Methods from the first family do not only detect secondary structures, but whole rigid zones of the protein. For example, in (Nichols et al. 1995) several structures of the same protein, in different steps of its motion, are compared in order to determine the rigid and flexible zones. Other example of this kind of methods is the *pebble game* (Jacobs et al. 2001). This method uses distance constraints to determine over and under restricted zones of the protein structure.

Methods focused on the exclusive detection of secondary structures, usually rely exclusively on geometrical parameters of the protein structure. For example, in (Richards and Kundrot 1987) $C\alpha$ atoms relative positions are calculated and compared with a database of $C\alpha$ atoms arrangements in secondary structures. In (Labesse et al. 1997), apart from the $C\alpha$ atoms distances, rotation angles between two consecutive $C\alpha$ atoms are included as comparative data. Hydrogen bond pattern recognition is also used for secondary structure detection in (Kabsch and Sander 1983) and in (Frishman and Argos 1995), where on this last work is prosed to complete the hydrogen bond analysis with dihedral angle information.

One of the drawbacks of these methods found in the bibliography, is the need of additional geometrical calculus or procedures in order to implement them into a simulation process. In this paper a new method for secondary structure detection is proposed relying only on dihedral angle values. The objective is to develop a procedure, able to be implemented in a protein simulation program (Diez et al. 2011), in order to extract the degrees of freedom located in the secondary structures and, thus, reduce the computational cost and improve the accuracy of the procedure.

2 Protein Secondary Structures

Although, in principle, a polypeptide chain could adopt any form, proteins tend to repeat certain structures inside their functional form. These structures, found in every protein, are called secondary structures and they practically do not have relative motion between their atoms.

Secondary structures can be divided in two groups, α -helices and β -sheets (see Fig. 1). Also, α -helices can be divided into α , π or 3_{10} helices depending on their form. Secondary structures are considered rigid entities inside the protein structures. This is due to the hydrogen bonds that tie the atoms inside them. In the Fig. 1 Hydrogen bonds are represented by dotted blue lines.

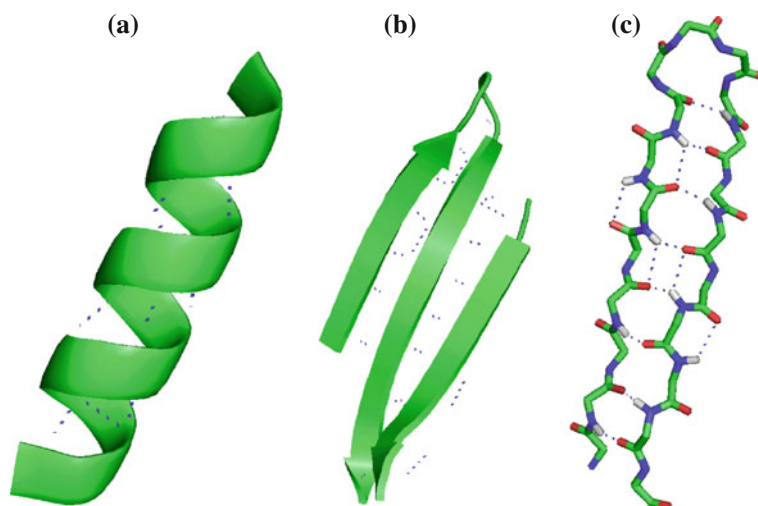


Fig. 1 **a** α -helix and **b** β -sheet. Hydrogen bonds that tie atoms inside the structures are represented with *blue dotted lines*. **c** *Ball and rods* representation of a protein section for a better appreciation of the atoms tied by the hydrogen bonds

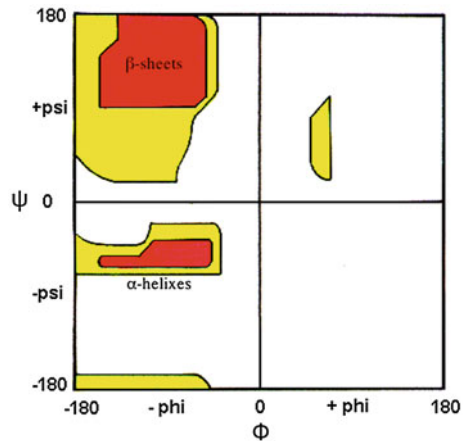
When the protein chain adopt these secondary structures form, dihedral angle values must have certain values. These structural theoretical values for each secondary structure can be found in the bibliography (Petsko and Ringe 2004). In Table 1 each secondary structure dihedral angle values are presented as well as the frequency at which the structure is found in proteins.

The values presented in Table 1 are the theoretical ones, nevertheless the dispersion on those values in biology may reach 30° . Ramachandran plots are one of the best ways to reflect this circumstance. On Fig. 2 zones corresponding to β -sheets and α -helices are represented in red. As it can be noticed, those zones cover a wide range of dihedral angle values. Relating to the dispersion on the dihedral angles values found in proteins' secondary structures, on (Frishman and Argos 1995), a very interesting work is presented regarding the probability of a amino acid to belong to a secondary structure as a function of its dihedral angle values.

Table 1 Dihedral angle values for different secondary structures

Secondary structure	Presence in protein structure	ϕ°	ψ°
α -helix	Very frequent	-57	-47
3.10 helix	Infrequent	-74	-4
Π -helix	Rarely	-57	-69
β -sheet	Very frequent	-139	-135

Fig. 2 Ramachandran plot zones corresponding to most frequent secondary structures



3 Procedure for Secondary Structure Detection by Dihedral Angle Parameters Evaluation

As stated before the objective of the procedure presented in this paper is to make use of the dihedral angle values, usually already available in any simulation program, in order to detect proteins' secondary structures. In order to do so, before starting the assessment of each amino acid, a previous classification must be done. With these objectives, amino acids within protein structure are classified as follows:

- **Candidate:** an amino acid is considered as a candidate when its dihedral angles lay on a zone of the Ramachandran plot belonging to a secondary structure.
- **Stable:** an amino acid is considered stable when the procedure has checked that it belongs to a secondary structure.
- **Unstable:** an amino acid is considered unstable when it cannot be classified as candidate or stable.

In order to define an amino acid as a candidate a tolerance has been introduced to the theoretical values of the dihedral angles presented in Table 1. This tolerance has been fine tuned in order to obtain the best possible results, obtaining a final tolerance value of 30° for each type of secondary structure. Although the tolerance may seem high, looking at Fig. 2 we can see how the β -sheet ψ angle zone almost covers a 90° area.

Once every amino acid has been classified as candidate, stable or unstable it is possible to start searching for secondary structures. First, the first candidate amino acid of the protein chain is located and selected. After that, it is checked if the two following amino acids are candidates of the same type of secondary structure. If that's the case, the three amino acids are classified as stable amino acids. The process continues by checking for amino acids of the same type of secondary

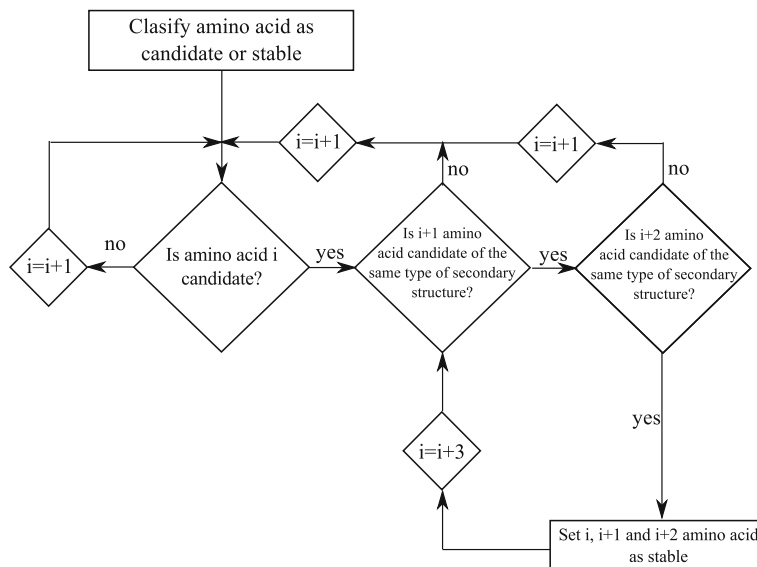


Fig. 3 Secondary structure detection process diagram

structures, until an unstable amino acid or an amino acid of another type of secondary structure is found. This process repeats until every amino acid of the protein has been checked. In Fig. 3 a diagram of the secondary structure detection process is shown.

As stated, one of the conditions for an amino acid to be set as a stable amino acid is to be part of a chain of three consecutive amino acids of the same type of secondary structure. The use of a high tolerance value delivered bad results, specifically on coil parts of the protein structure. This condition reduces the detection of secondary structures on coils of the protein structure, allowing to maintain the tolerance value.

4 Case Study

In order to test the results seven proteins have been selected. The selection of the proteins under study has been done in order to test the algorithm against different protein sizes and different secondary structure distribution. To check the results obtained with the procedure, they have been compared with each proteins' structural data, available on the Protein Data Bank (PDB) and experimentally obtained. Results are shown on Table 2.

The produce presents a very high accuracy, always placing correctly more than 80 % of each protein amino acids in their correspondent secondary structure.

Table 2 Results of the procedure for the detection of secondary structures in the selected proteins

Protein	Percentage of amino acids correctly located
1zac	96.6
1k9p	96.62
3cln	97.2
1k20	93.48
2peq	100
4fkx	82.35
3sza	86.6

Comparing precision related to each secondary structure type, the procedure is more accurate on the detection of α -helices, detecting 95 % of them, being most of the inaccuracies associated to the detection of β -sheets. Nevertheless the percentage of detected β -sheets is always over 70 %. For example, on 4fkx and 3sza proteins, shown in Fig. 4, which present the higher number of beta sheets, respectively 75 % (3 of 4) and 87 % (13–15) β -sheets have been correctly placed. The main difficulty in β -sheets detection is that they are not formed by consecutive amino acids of the protein chain, but by amino acids belonging to different sections of it (see Fig. 1). As the procedure only checks for dihedral angle parameters, it lacks the ability to detect the proximity of any other section of the protein chain. Thus, as said, the procedure, is less accurate on the detection of β -sheets, either by not detecting or incorrectly detecting amino acids placed in them. Another problem arises with the detection of 3_{10} -helices. This secondary structures usually appear on the edges of an α -helix and they usually contain only two amino acids. This makes the process to fail on the detection of this type of structure as there are no three consecutive amino acids. Several attempts has been done modifying both the tolerance and the number of consecutive amino acids with no improvements on the results. Actually we are working in order to solve these inaccuracies by including new procedures for the detection of near $C\alpha$ atoms and two amino acid long secondary structures.

Regarding the computational cost of the procedure, the whole process, classification of amino acids and assignment of each amino acid to its secondary structure, only takes 8 ms on the bigger studied protein, 3sza. Thus, its implementation on a simulation procedure will not increase the overall computational cost. On behalf of the reduction of the simulation process computational cost, as stated before, the procedure provides information that allow to extract the degrees of freedom from the simulation process. In previous works (Diez et al. 2011), 1zac, 1k20, 1k9p and 3cln proteins molecular mechanism movements were studied. The introduction of this information will allow to reduce the number of degrees of freedom of the simulation by 60 % for 1k20 protein, 67 % for 1zac protein, 61 % for 1k9p protein and 58 % for 3cln protein.

Recently, the procedure has been implemented in the simulation process and simulations have already been done on two of the proteins, 1k20 and 1zac. On this

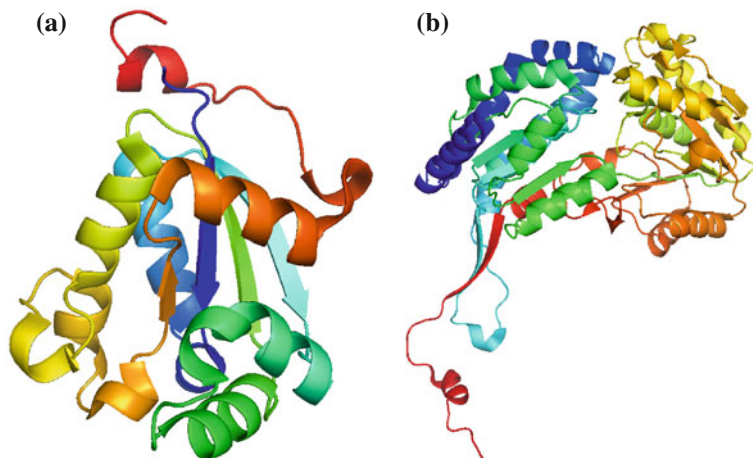


Fig. 4 a 4fkx protein. b 3sza protein

proteins, the step time, the time required for the procedure to obtain a new valid position of the protein movement, has been reduced from 43 to 31 min on 1k20 protein and from 121 to 92 s on 1zac protein. As can be noted, each step time has been considerably reduced.

5 Conclusions

In this paper a new procedure for the detection of secondary structures on proteins structures has been presented. The procedure makes use of dihedral angles parameters, already calculated during the simulation of the protein molecular mechanism, to determine if an amino acid is part of a secondary structure type. This avoids the introduction of new calculus procedures in a simulation program that would increase the computational cost. Results show how the procedure has a high accuracy, specially on the detection of α -helices.

Regarding the computational cost of the procedure, it has fulfilled its objective presenting a very reduced overall cost, even for big proteins like 3sza. The procedure has also proven able to reduce the computational cost of a step of a simulation procedure, reducing the step time by 25 % in the two studied proteins.

Future work will be focused on the improvements of the results, specifically on the detection of β -sheets and 3_{10} -helices. As the computational cost of the process is very small the introduction of additional geometrical parameters like $C\alpha$ distances, may prove useful to increase the precision of the method without a penalization on the simulation procedure computational cost.

Acknowledgments The authors wish to acknowledge the financial support received from the Spanish Government through the Ministerio de Economía y Competitividad (Project DPI2011-22955), the European Union (Project FP7-CIP-ICT-PSP-2009-3) and the Regional Government of the Basque Country through the Departamento de Educación, Universidades e Investigación (Project IT445-10) and UPV/EHU underprogram UFI 11/29.

References

- Colloc'h N, Etchebest C, Thoreau E, Henrissat B, Mornon JP (1993) Comparison of three algorithms for the assignment of secondary structure in proteins: the advantages of a consensus assignment. *Protein Eng Des Sel* 6(4):377–382
- Diez M, Petuya V, Martínez-Cruz LA, Hernandez A (2011) A biokinematic approach for the computational simulation of proteins molecular mechanism. *Mech Mach Theory* 46(12):1854–1868
- Frishman DD, Argos PP (1995) Knowledge-based protein secondary structure assignment. *Proteins: Struct Funct Bioinf* 23(4):566–579
- Jacobs DJ, Rader AJ, Kuhn LA, Thorpe MF (2001) Protein flexibility predictions using graph theory. *Proteins Struct Funct Genet* 44(2):150–165
- Kabsch WW, Sander CC (1983) Dictionary of protein secondary structure: pattern recognition of hydrogen-bonded and geometrical features. *Biopolymers* 22(12):2577–2637
- Labesse G, Colloc'h N, Pothier J, Mornon JP (1997) P-SEA: a new efficient assignment of secondary structure from C alpha trace of proteins. *Comput Appl Biosci* 13(3):291–295
- Nichols WL, Rose GD, Ten Eyck LF, Zimm BH (1995) Rigid domains in proteins: an algorithmic approach to their identification. *Proteins Struct Funct Genet* 23(1):38–48
- Petsko GA, Ringe D (2004) *Protein structure and function*. Blackwell Publishing, Hoboken
- Richards FM, Kundrot CE (1987) Identification of structural motifs from protein coordinate data: secondary structure and first-level super secondary structure. *Proteins: Struct Funct Bioinf* 3(2):71–84

Optimal Design of the Motion Law for a Pseudo-Azimuthal Tracking System

Monica Alina Ioniță and Cătălin Alexandru

Abstract The paper approaches the optimization of the motion law for a pseudo-azimuthal tracking system, which is used to increase the energetic efficiency of a photovoltaic platform. The optimization goal is to maximize the energetic efficiency, by maximizing the solar energy absorption (i.e. the incident radiation) and minimizing the energy consumption for performing the tracking. The step-by-step tracking law, which is configured through a parametric optimization in the MBS (Multi-Body Systems) software environment ADAMS of MSC Software, brings a significant energetic gain relative to the fixed system (without tracking).

Keywords Photovoltaic platform · Tracking system · Motion law · Optimization

1 Introduction

The solution for making the conversion of the solar radiation into electricity is well known: the photovoltaic (PV) effect. The efficiency of the PV systems depends on the degree of use of the solar radiation, which can be maximized by using systems for tracking the PV modules. The solar trackers are actually mechatronic systems, which ensure the optimal positioning of the module relative to the Sun, bringing an increase of the energetic efficiency from 20 to 50 % (Alexandru and Pozna 2010; Calabrò 2009; Kumar Chinnaiyan et al. 2013; Seme and Stumberger 2011; Singh 2013; Vișa, I. et al. 2009).

In one year, the Earth defines an elliptical rotation movement around the Sun, and on the other hand, during one day, a complete rotation around its own axis.

M. A. Ioniță · C. Alexandru (✉)

Transilvania University of Brașov, 29 Eroilor Bvd 500036 Brașov, Romania
e-mail: calex@unitbv.ro

Viewing the two movements, there are two fundamental types of tracking systems: mono-axis (for the daily motion), and dual-axis (for the daily and seasonal/elevation motions) trackers. The dual-axis mechanisms combine the two motions, so that they ensure a precise orientation of the PV module without the need of further positioning adjustments. Regarding how the rotational axes are located, there can be distinguished two types of dual-axis systems: equatorial systems—where the daily motion axis is parallel to the polar axis, and azimuthal systems—which perform the daily motion around the vertical axis.

This paper approaches a pseudo-azimuthal tracking mechanism, which is derived from the azimuthal system, having the main/daily rotational axis positioned on the horizontal (North–South). The main advantage is the structure stability, being the best option for orientating the platforms of photovoltaic modules strings. The paper targets the growth of the energetic efficiency through the optimal design of the motion/tracking law (by maximizing the solar energy absorption, and minimizing the energy consumption for performing the tracking).

2 Modeling the Solar Radiation

The energetic efficiency of the PV systems can be increased by adding a tracking mechanism, which maximizes the received solar radiation by ensuring an optimal PV system—Sun position. The main input parameter for the tracking systems design is the solar radiation. For this paper, the direct component of the solar radiation has been considered (assuming that the sky is clear), while the diffuse component (useful in cloudy conditions) will be approached in a future research.

The direct solar radiation (G_D) depends on certain parameters and climatic conditions (location, month, atmosphere clarity and others), and it can be determined through various mathematical models. For this paper, a prediction model based on the Meliř's empirical model (Meliř 1997) has been approached, as follows:

$$G_D = G_0 \cdot (1 + 0.0334 \cdot \cos x) \exp\left(-\frac{t_f}{0.9 + 9.4 \cdot \sin \alpha}\right), \quad (1)$$

$$x = 0.9856^\circ \times n - 2.72^\circ, \omega = 15^\circ \times (12 - T), \quad (2)$$

$$\alpha = \sin^{-1}(\sin \delta \cdot \sin \varphi + \cos \delta \cdot \cos \varphi \cdot \cos \omega), \quad (3)$$

where G_0 is the medium solar constant ($1,367 \text{ W/m}^2$), n —day number in the year (e.g. $n = 1$ for January, 1st), t_f —turbidity factor, α —altitudinal solar angle, φ —location latitude, ω —hour angle, δ —solar declination, T —solar time.

The incident radiation (G_I), which is normal to the PV module surface, depends on the direct solar radiation (G_D) and the incidence angle (i),

$$G_I = G_D \times \cos i \quad (4)$$

The incidence angle, which is defined as the angle between the sunray and the normal axis on the PV module, can be expressed in the following way:

$$i = \cos^{-1}(\cos\rho \cdot \cos\rho^* \cdot \cos(\varepsilon - \varepsilon^*) + \sin\rho \cdot \sin\rho^*), \quad (5)$$

$$\varepsilon = \cos^{-1} \frac{(\cos\delta \cdot \cos\omega \cdot \cos\varphi + \sin\delta \cdot \sin\varphi)}{\cos\rho}, \quad (6)$$

$$\rho = \sin^{-1}(\cos\delta \cdot \cos\omega \cdot \sin\varphi - \sin\delta \cdot \cos\varphi), \quad (7)$$

in which ε and ρ are the diurnal and seasonal angles of the sunray, while ε^* and ρ^* are the daily and elevation angles of the PV module.

The quantity of electric energy produced by the PV system (E) depends on the incident solar radiation (G_I), the active surface (S) and the conversion yield (η) of the modules, as follows:

$$E = S \cdot \eta \cdot \int_{t_0}^t G_I dt \quad (8)$$

In every month, there is a day whose irradiation is almost equal to the monthly average. Following this statement, there have been determined the 12 representative days of the year (Table 1). These have been compared with the results obtained by the declination method (Duffie and Beckman 1991), obtaining an excellent correlation.

Depending on the value of the elevation angle, there have been developed two tracking programs: seasonal (one value per month), and annual (keeping the elevation angle at a fixed value throughout the year). To evaluate the tracking efficiency, various values have been considered for the daily (ε^*) and elevation (ρ^*) angles, as follows: ε^* varies in the fields $[+15^\circ, -15^\circ]$, $[+30^\circ, -30^\circ]$, $[+45^\circ, -45^\circ]$, $[+60^\circ, -60^\circ]$, $[+75^\circ, -75^\circ]$, $[+90^\circ, -90^\circ]$, the null value corresponding to the solar noon position; ρ^* has constant values within the field $[0^\circ, 90^\circ]$.

Considering the possible combinations of fields/values for these angles, the direct and incident solar radiation curves were obtained for the 12 representative days. Then, for each case, the tracking efficiency was established as the percentage ratio between the produced and available energy (Fig. 1), and the optimal values of the daily and elevation angles were found at the point where the efficiency is highest. The pseudo-azimuthal system has an optimum tracking efficiency in the case of a daily motion domain of 120° – 180° . As the difference between the tracking efficiency of the minimum (120°) and maximum (180°) fields is very small, the angular domain $\varepsilon^* \in [+60^\circ, -60^\circ]$ was selected for the daily motion. In addition, the optimal values of the elevation angle are presented in Table 2.

Table 1 The representative days of the year

Month	1	2	3	4	5	6	7	8	9	10	11	12
Day	16	45	75	105	135	160	198	229	259	289	319	344

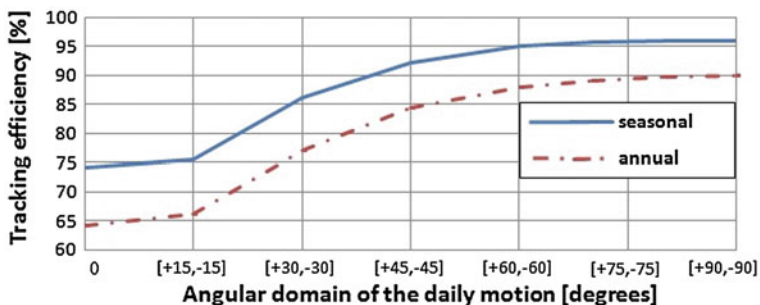


Fig. 1 The tracking efficiency of the pseudo-azimuthal system

Table 2 The optimal values of the elevation angle

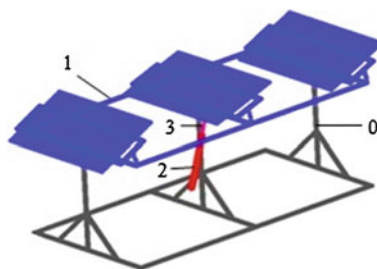
Seasonal	Month	1	2	3	4	5	6	7	8	9	10	11	12
	ρ^*	70°	62°	49°	32°	17°	10°	13°	26°	44°	58°	68°	70°
Annual		40°											

3 Optimizing the Motion (Tracking) Law

The purpose of this paper is to develop an algorithm for increasing the energetic efficiency of the PV tracking systems, by maximizing the quantity of incident solar radiation and minimizing the energy consumption for performing the tracking. The study is developed for a pseudo-azimuthal tracking system, in the mono-axial variant (for performing the daily motion).

The solid model of the tracking mechanism was developed by using the CAD environment CATIA. Then, the solid model was transferred to the MBS software environment ADAMS, through the STEP file format. After importing the geometry, the multi-body system model of the tracking mechanism was developed in ADAMS/View (Fig. 2). The mechanism tracks a PV platform (1) that contains 3 modules (disposed 1 per string), the active surface being of 5.1 m². The whole mobile structure has a mass of 100 kg. The driving element is a linear actuator,

Fig. 2 The MBS model of the tracking mechanism



whose cylinder (2) is connected to the fixed pillar (0), while the piston (3) moves the platform.

The proposed tracking system is a mechatronic one, which integrates the MBS mechanical device (shown in Fig. 2) and the control system. The optimal design of the control system was approached in (Ioniță and Alexandru 2012), by using the Design for Control (DFC) software solution EASY5. There is a two-loop control system with low-pass filters (LPF controllers). The external loop controls the daily angle of the PV platform, while in the internal loop the linear velocity in actuator is controlled. The input in the MBS model is the motor force developed by the linear actuator.

The mathematical model for computing the electric energy produced by the PV system (Eq. 1–8) was implemented in the MBS model of the tracking mechanism, using the function builder in ADAMS/View. In this way, there is possible to evaluate the energy gain obtained by tracking and the energy consumption for performing the tracking, in the same model (all within the MBS environment).

The daily orientation of the PV system can be realized with continuous motion or in steps. The continuous tracking has the advantage of obtaining the best incidence, but it raises a series of problems, such as the high operating time and the need to ensure large transmission ratios. Thus, the step-by-step tracking is preferable, even if it is less efficient. As mentioned, the application is for the mono-axial variant of a pseudo-azimuthal mechanism, so that the optimization study will be focused on the step-by-step tracking law for the daily motion.

In the general case, there are the following parameters (design variables) that define the step-by-step tracking law: the angular motion field, the number of motion steps, the size of these steps, and the actuating times (when the motion steps are performed). By the optimal correlation of these data, there can be obtained a step-by-step tracking law close as efficiency to the continuous (ideal) tracking case. Obviously, there are some correlations between the design variables, e.g. the sum of the steps sizes is equal with the amplitude of the angular motion field.

Because the direct and incident radiation curves are symmetrical relative to the solar noon position, the motion law will be also symmetrical (with positive values of the daily angle in the morning, and negative values in the afternoon). Due to this consideration, a noticeable facilitation is introduced in the tracking law design, considering just half of law (from sunrise to noon). Then, this law is transposed for the tracking from noon to sunset, by inverting the daily angle sign.

The imposed tracking law (which gives the daily angle variation) is modeled as a sum of STEP functions. STEP is a run-time function, with the following format: STEP (x , x_0 , f_0 , x_1 , f_1), where x is the independent variable (time), x_0 —value of independent variable at which the function begins, f_0 —initial value of the step, x_1 —value of independent variable at which the function ends, f_1 —final value of the step (relative to the initial value). For simplification, there was considered the same duration for all motion steps (no matter what is the step size). Thus, the following half-law (from sunrise to noon) for the daily motion was obtained (Fig. 3):

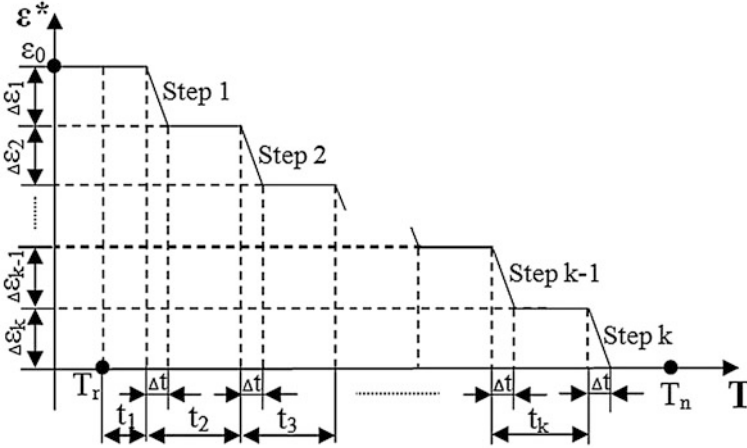


Fig. 3 The configuration of the step-by-step tracking (half-law)

$$\begin{aligned} & \text{STEP}(\text{time}, (T_r + t_1), \varepsilon_0, (T_r + t_1 + \Delta t), -\Delta\varepsilon_1) + \text{STEP}(\text{time}, (T_r + t_1 + t_2), 0, \\ & (T_r + t_1 + t_2 + \Delta t), -\Delta\varepsilon_2) + \dots + \text{STEP}(\text{time}, (T_r + t_1 + t_2 + \dots + t_k), 0, \\ & (T_r + t_1 + t_2 + \dots + t_k + \Delta t), -\Delta\varepsilon_k), \end{aligned} \tag{9}$$

where: T_r —sunrise time; T_n —solar noon; t_1 —time at which the first motion step begins, relative to T_r ; t_2 —time at which the second motion step begins; t_k —time at which the final motion step begins; Δt —motion step duration; ε_0 —initial daily angle; $\Delta\varepsilon_1$ —first step size; $\Delta\varepsilon_2$ —second step size; $\Delta\varepsilon_k$ —final step size.

In the study performed in this paper, there were considered as design variables only the actuating times of the motion steps, which are defined by the following parameters: t_1, t_2, \dots, t_k . The other parameters have been established as follows: the initial value of the daily angle was selected in accordance with Sect. 2 ($\varepsilon_0 = 60^\circ$); the number of motion steps from sunrise to noon (k) was manually changed, by successively considering the following values $k = 1, 2, 3, 4, 5, 6$ (in other words, there have been developed six optimization studies, one for each number of steps); the step size is the same for all motion steps ($\Delta\varepsilon_1 = \Delta\varepsilon_2 = \dots = \Delta\varepsilon_k$), in relation with the number of steps (i.e. $\Delta\varepsilon = \varepsilon_0/k$); the step duration is $\Delta t = 60$ s.

As was mentioned, the optimization goal is to maximize the energetic efficiency of the PV system, which is expressed by the following design objective (DO):

$$\text{DO} = E_T - (E_F + E_C), \tag{10}$$

where E_T is the energy produced by the PV system with tracking, E_F —the energy produced by the fixed equivalent system, and E_C —the energy consumption for performing the tracking. Practically, after the determination of the actuating times for the half-law (from sunrise to noon), the tracking law is transposed for the

whole day (from sunrise to sunset). For the energy consumption, the return of the solar tracker in the initial position, after the sunset, is also considered.

In addition, there has been modeled a design constraint (a boundary that eliminates unacceptable designs), which refers to the fact that the final motion step for the half-law must be completed before the solar noon (T_n). The design constraint (DC) creates an inequality, the optimization keeping the value less than zero,

$$DC = (T_r + t_1 + t_2 + \dots + t_k + \Delta t) - T_n < 0 \tag{11}$$

The numeric simulations were performed considering the Braov geographic area, with the following input data: $\varphi = 45.5^\circ$, $\delta = 22.93^\circ$, $n = 160$, $t_r = 3$, $\rho^* = 10^\circ$, $S = 5.1 \text{ m}^2$, $\eta = 15 \%$, $T_r = 4.29$, and $T_n = 12$. The algorithm used in optimization is OptDes-SQP, which is provided with ADAMS/View. As result of the optimization process, there were obtained the optimal actuating times for the considered tracking cases (the half-laws, from sunrise to noon, with $k = 1, \dots, 6$ motion steps), which are shown in Table 3. Then, these laws were transposed for the day-light tracking (the whole-laws, from sunrise to sunset). For exemplification, Fig. 4 shows the obtained motion law for the 12-steps (6×2) tracking.

Then, the motion law was applied as input for the control system, the co-simulation being performed with ADAMS and EASY5. As a result of the dynamic analysis, there was obtained the energy consumed during tracking. As instant, the energy consumption for the 12-steps (6×2) law is shown in Fig. 5. At the same time, the energy produced by the PV system was obtained from Eq. (1–8).

With these values, the energetic balance of the pseudo-azimuthal tracking system can be performed. As instant, Table 4 shows the data for the 12-steps tracking law. The energy gain is expressed relative to the fixed equivalent system. The energy consumption for the step-by-step tracking is slightly larger than for the continuous motion, and this is because of the over-shootings that appear when the actuator is turned-on. There can be observed that the step-by-step tracking strategy is close to the ideal case (continuous tracking), and this demonstrates the viability of the implemented optimization algorithm. Similar computations have been performed for all representative days of the year, validating the previous conclusion.

Table 3 The optimal values of the design variables

	t_1	t_2	t_3	t_4	t_5	t_6
1 step	5.62					
2 steps	4.42	2.27				
3 steps	3.96	1.65	1.94			
4 steps	3.61	1.09	1.90	1.00		
5 steps	3.51	1.10	1.00	1.00	0.94	
6 steps	3.50	0.89	0.82	0.76	0.72	0.68

Fig. 4 The 12-steps motion law

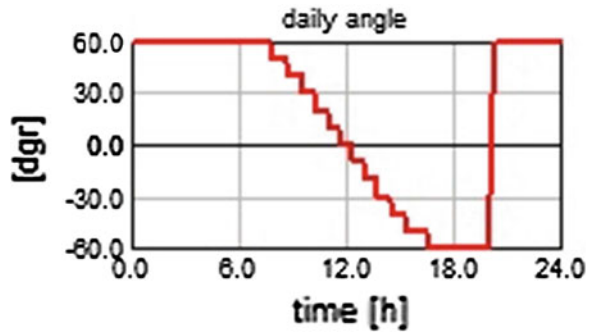


Fig. 5 The energy consumption for tracking

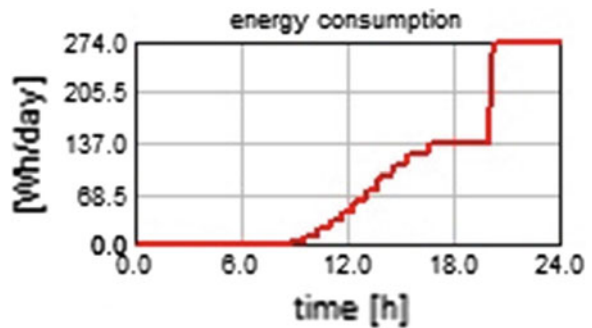


Table 4 The energy balance of the PV system for the 12-steps tracking case

Tracking case	$E_{T/F}$ (Wh/day)	E_C (Wh/day)	Gain (%)
Step-by-step	8670.72	274.31	45.66
Continuous	9052.19	248.52	52.72
Fixed	5764.39	–	–

4 Final Remarks

The proposed optimization strategy leads to an efficient solar tracker, without developing expensive hardware prototypes. Thus, the behavioral performance predictions are obtained much earlier in the design cycle, thereby allowing more effective and cost efficient design changes and reducing overall risk substantially.

The optimization will be extended with more design variables, for taking into account the angular motion field, the number of motion steps, the steps size, and the duration of the motion steps. At the same time, the pseudo-azimuthal tracking system will be approached in the dual-axis variant, by considering the elevation motion as well. The tracking system has been manufactured, and it will be tested in the RD&I Institute from the Transilvania University of Braşov, creating a real perspective for the research in the field.

Acknowledgments This paper is supported by the Sectoral Operational Programme Human Resources Development (SOP HRD), ID76945 financed from the European Social Fund and by the Romanian Government.

References

- Alexandru C, Pozna C (2010) Simulation of a dual-axis solar tracker for improving the performance of a photovoltaic panel. Proceedings of the Institution of Mechanical Engineers. Part A J Power Energy 224(6):797–811
- Calabrò E (2009) Determining optimum tilt angles of photovoltaic panels at typical north-tropical latitudes. J Renew Sustain Energy 1(3):033104 (1–6)
- Kumar Chinnaiyan V, Jerome J, Karpagam J (2013) An experimental investigation on a multilevel inverter for solar energy applications. Electr Power Energy Syst 47:157–167
- Seme S, Stumberger G (2011) A novel prediction algorithm for solar angles using solar radiation and differential evolution for dual-axis sun tracking purposes. Sol Energy 85(11):2757–2770
- Singh GK (2013) Solar power generation by PV (photovoltaic) technology: A review. Energy 53:1–13
- Vişa I et al (2009) Synthesis of linkages for tracking systems with increased angular stroke. In: Proceedings of the 10th SYROM symposium, pp 193–206
- Meliß M (1997) Regenerative Energiequellen—Praktikum. Springer, Berlin
- Duffie JA, Beckman WA (1991) Solar engineering of thermal processes. Wiley, New York
- Ionîţă M, Alexandru C (2012) Dynamic optimization of the tracking system for a pseudo-azimuthal photovoltaic platform. J Renew Sustain Energy 4(5):053117(1–15)

Comparative Study of Two 2-DOF Parallel Mechanisms Used for Orientation

Tiberiu Itul, Bogdan Gherman and Doina Pîslă

Abstract The paper presents two parallel orientation mechanisms, each with two degrees of freedom (DOF). The kinematics, the workspace and the singularities of these mechanisms are presented. The static generalized forces in the legs, the torques taken by the main universal joints and the performance indices concerning the control and the stiffness of the mechanisms (global conditioning index and global stiffness index) are also assessed.

1 Introduction

The design of the orientation mechanisms was boosted by necessity to their application as support for radio antennas, satellite TV antennas, telescopes, cameras, solar panels, etc. Other applications that these mechanisms would serve well are in the field of medical robotics, for example the orientation of an end-effector in needle placement interventions, like brachytherapy. A lot of mechanisms for this task have serial architecture. Lately, the mechanisms with parallel architecture started to impose, taking into account their characteristics: high stiffness and kinematic accuracy, advantageous ratio between payload and its own weight, possibility of installing of the actuators on the base. The drawbacks of parallel mechanisms are their more limited workspace and in many case the presence of the over mobility singularities.

T. Itul (✉) · B. Gherman · D. Pîslă
Technical University of Cluj-Napoca, Cluj-Napoca, Romania
e-mail: Tiberiu.Itul@mep.utcluj.ro

B. Gherman
e-mail: Bogdan.Gherman@mep.utcluj.ro

D. Pîslă
e-mail: Doina.Pisla@mep.utcluj.ro

The basic structural scheme of the mechanisms studied in the paper is found in (Parenti-Castelli 2004). Many researchers have studied the workspace of parallel mechanisms, the main concern being its growth. In this paper, the evaluation and representation of the workspace are achieved by using the binary matrices method (Ceccarelli 2004).

The assessment of generalized static actuating forces and stiffness of a 2-DOF parallel manipulator is studied without taking into account the elasticity and actuators compliance. The values of generalized forces are necessary for sizing telescopic legs and command linear actuators.

Stiffness is defined as the ability to retrieve loads without excessive deformations (Júnior et al. 2011). Stiffness is a very important performance indicator of a parallel kinematic structure. There are three main methods to derive the stiffness model of parallel manipulators: the method based on the calculation of the Jacobian matrix, the finite element analysis (FEA) and the matrix structural analysis (MSA) (Gonçalves 2008). The stiffness analysis of a parallel mechanism has been studied by many researches (Gosselin and Zhang 2002; Chakarov 1998; Simaan and Shoham 2003; Liu et al. 2000; Gosselin and Angeles 1991; Carbone 2007; Hesselbach et al. 2004). The study of (Arai 1992) did not include elastic deformations. Gosselin (1990) studied the stiffness considering only the stiffness of each actuator. Complex studies about stiffness can be found in papers (Ceccarelli 2004; Carbone 2004; Merlet 2006).

The paper is organized as follows: Sect. 2 deals with kinematics of the parallel orientation mechanisms; Sect. 3 presents their workspace and singularities. The evaluation of the static generalized forces is exposed in the Sect. 4. In Sect. 5 is studied the stiffness of the parallel mechanisms. The conclusions are described in Sect. 6.

2 Kinematics

The kinematic schemes of the two symmetrical parallel mechanisms, named 2S-2S-U_V and 2S-2S-U_H, are shown in Figs. 1 and 2 (Itul et al. 2010 Itul and Pisla 2010). These both mechanisms consist in a fixed base OB₁B₂ and a mobile platform OA₁A₂ connected through a main universal joint in O and two telescopic legs B₁A₁, B₂A₂ ended with spherical joints.

The mechanisms differ by the vertical (Fig. 1) or horizontal (Fig. 2) of the fixed axis of the universal passive joint. For the 2S-2S-U_V parallel mechanism, the rotation matrix, corresponding to the φ (azimuth) and θ (elevation) operational angles, has the following form:

$$[R_{x(\varphi),y(\theta)}] = \begin{bmatrix} \cos(\theta) & 0 & \sin(\theta) \\ \sin(\varphi)\sin(\theta) & \cos(\varphi) & -\sin(\varphi)\cos(\theta) \\ -\cos(\varphi)\sin(\theta) & \sin(\varphi) & \cos(\varphi)\cos(\theta) \end{bmatrix} \quad (1)$$

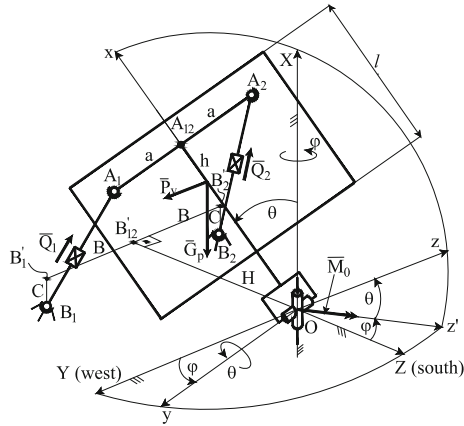


Fig. 1 The kinematic scheme of the 2S-2S-U_V parallel mechanism

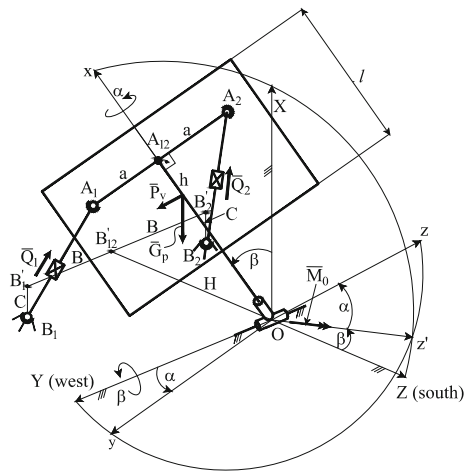


Fig. 2 The kinematic scheme of the 2S-2S-U_H parallel mechanism

The rotation matrix of the 2S-2S-U_H mechanism, corresponding to β and α angles, is:

$$[R_{y(\beta),x(\alpha)}] = \begin{bmatrix} \cos(\beta) & \sin(\alpha)\sin(\beta) & \cos(\alpha)\sin(\beta) \\ 0 & \cos(\alpha) & -\sin(\alpha) \\ -\sin(\beta) & \sin(\alpha)\cos(\beta) & \cos(\alpha)\cos(\beta) \end{bmatrix} \quad (2)$$

The following conditions should be accomplished, in order for the Oz axis to be directed towards the same point in space in both cases:

$$\begin{bmatrix} \cos(\alpha)\sin(\beta) \\ -\sin(\alpha) \\ \cos(\alpha)\cos(\beta) \end{bmatrix} = \begin{bmatrix} \sin(\theta) \\ -\sin(\varphi)\cos(\theta) \\ \cos(\varphi)\cos(\theta) \end{bmatrix} \quad (3)$$

As $-90^\circ \leq \varphi \leq 90^\circ$ and $0 \leq \theta \leq 90^\circ$, it yields:

$$\begin{cases} \beta = \operatorname{atan}(\cos(\varphi)\tan(\theta)) \\ \alpha = \operatorname{atan}(\sin(\varphi)\cos(\theta)) \end{cases}; \begin{cases} \varphi = \operatorname{atan}\left(\frac{\tan(\alpha)}{\cos(\beta)}\right) \\ \theta = \operatorname{asin}(\cos(\alpha)\sin(\beta)) \end{cases} \quad (4)$$

The relationships between the position vectors of guided points A_i ($i = 1, 2$) in two systems of reference are:

$$\bar{P}_i = [R] \cdot \bar{p}_i; i = 1, 2 \quad (5)$$

where $[R]$ is the rotation matrix according to (1) or (2)

$$\bar{P}_i = \begin{bmatrix} X_i \\ Y_i \\ Z_i \end{bmatrix}; \bar{p}_i = \begin{bmatrix} x_i \\ y_i \\ z_i \end{bmatrix}; i = 1, 2; x_1 = x_2 = h; y_1 = -y_2 = a; z_1 = z_2 = 0 \quad (6)$$

The position of the fixed points B_i ($i = 1, 2$) is known:

$$\bar{P}_{B_i} = \begin{bmatrix} X_{B_i} \\ Y_{B_i} \\ Z_{B_i} \end{bmatrix}; i = 1, 2; X_{B_1} = X_{B_2} = -C; Y_{B_1} = -Y_{B_2} = B; Z_{B_1} = Z_{B_2} = -H \quad (7)$$

Using the above relationships, in both cases, the generalized coordinates q_1 and q_2 of the mechanisms, represented by the lengths of the legs B_iA_i ($i = 1, 2$), can be calculated:

$$q_i = \sqrt{(\bar{P}_i - \bar{P}_{B_i})^2} = \sqrt{(X_i - X_{B_i})^2 + (Y_i - Y_{B_i})^2 + (Z_i - Z_{B_i})^2}; i = 1, 2 \quad (8)$$

The kinematic model is obtained by deriving the square of Eq. (8) with respect to the time:

$$\dot{\bar{X}} = [J] \dot{\bar{q}} \quad (9)$$

where $[J]$ is the Jacobi matrix, $\dot{\bar{X}}$ is vector of the mobile platform angular velocities and $\dot{\bar{q}}$ is vector of active joint velocities.

For 2S-2S-U_V:

$$[J] = \begin{bmatrix} \frac{(\bar{P}_1 - \bar{P}_{B1})}{q_1} \cdot \frac{\partial \bar{P}_1}{\partial \varphi} & \frac{(\bar{P}_1 - \bar{P}_{B1})}{q_1} \cdot \frac{\partial \bar{P}_1}{\partial \theta} \\ \frac{(\bar{P}_2 - \bar{P}_{B1})}{q_2} \cdot \frac{\partial \bar{P}_2}{\partial \varphi} & \frac{(\bar{P}_2 - \bar{P}_{B2})}{q_2} \cdot \frac{\partial \bar{P}_2}{\partial \theta} \end{bmatrix}^{-1}; \dot{X} = \begin{bmatrix} \dot{\varphi} \\ \dot{\theta} \end{bmatrix}; \dot{q} = \begin{bmatrix} \dot{q}_1 \\ \dot{q}_2 \end{bmatrix} \quad (10)$$

For 2S-2S-U_H:

$$[J] = \begin{bmatrix} \frac{(\bar{P}_1 - \bar{P}_{B1})}{q_1} \cdot \frac{\partial \bar{P}_1}{\partial \alpha} & \frac{(\bar{P}_1 - \bar{P}_{B1})}{q_1} \cdot \frac{\partial \bar{P}_1}{\partial \beta} \\ \frac{(\bar{P}_2 - \bar{P}_{B1})}{q_2} \cdot \frac{\partial \bar{P}_2}{\partial \alpha} & \frac{(\bar{P}_2 - \bar{P}_{B2})}{q_2} \cdot \frac{\partial \bar{P}_2}{\partial \beta} \end{bmatrix}^{-1}; \dot{X} = \begin{bmatrix} \dot{\alpha} \\ \dot{\beta} \end{bmatrix}; \dot{q} = \begin{bmatrix} \dot{q}_1 \\ \dot{q}_2 \end{bmatrix} \quad (11)$$

3 Workspace and Singularities

We consider that in the ideal case, the shape of workspace is a rectangle located in the plane defined by φ and θ coordinates with the sides π and $\pi/2$. In real case, the workspace area and its shape are affected by the constraints due to: allowed spherical joints angles; actuated joints stroke; transmission angles; presence of singularities.

The upper spherical joints restraints could be avoided by replacing them with universal joints.

The following conditions for the actuated joints are imposed:

$$q_{\min} \leq q_i \leq q_{\max}; i = 1, 2 \quad (12)$$

and for transmission angles:

$$\psi_i = a \sin \frac{|(\bar{P}_i - \bar{P}_{Bi}) \cdot (\bar{P}_1 \times \bar{P}_2)|}{|\bar{P}_i - \bar{P}_{Bi}| \cdot |\bar{P}_1 \times \bar{P}_2|}; i = 1, 2 \quad (13)$$

the following condition is imposed:

$$\psi_i \geq 20^\circ \quad (14)$$

The curves of singularity result from the following condition:

$$\text{Det}[J]^{-1} = 0 \quad (15)$$

In this case the reachable workspace can be determined imposing the condition:

$$\text{Det}[J]^{-1} < 0 \quad (16)$$

In order to determine the workspace of the robot, the chosen values for the geometric parameters are: $a = 0.25$ m; $h = 0.3$ m; $H = 0.8$ m; $B = 0.05$ m; $C = 0.9$ m; $q_{\min} = 1.0$ m; $q_{\max} = 1.6$ m, the constraints (12, 13) and (14) yields to the workspace shown in Figs. 3 and 4. Area of reachable workspace (white

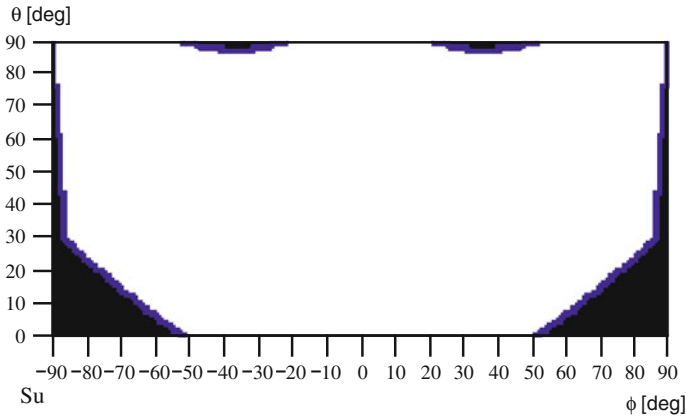


Fig. 3 The reachable workspace of the 2S-2S-U_V parallel mechanism

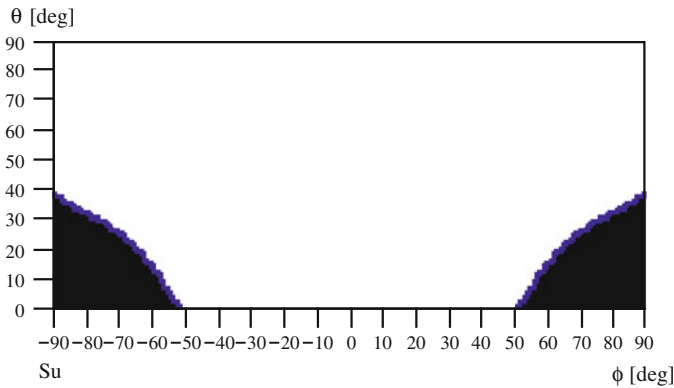


Fig. 4 The reachable workspace of the 2S-2S-U_H parallel mechanism

zone) is $A = 4.50 \text{ rad}^2$ for the first mechanism and 4.20 rad^2 for the second; (ideal area is $= 4.93 \text{ rad}^2$).

Checking the condition (16) for 2S-2S-U_H it results that in ideal workspace we do not have singularities.

4 Static Generalized Forces

For the evaluation of the generalized forces Q1 and Q2, the virtual power principle is applied.

For 2S-2S-U_V, the virtual power principle has the following form:

$$\begin{bmatrix} Q_1 \\ Q_2 \end{bmatrix} = -[J]^T \begin{bmatrix} M_\phi \\ M_\theta \end{bmatrix} \tag{17}$$

where, $M_\phi = 0$ and $M_\theta = (P_v + G_p \sin \theta) \cdot \frac{l}{2}$

And for 2S-2S-U_H:

$$\begin{bmatrix} Q_1 \\ Q_2 \end{bmatrix} = -[J]^T \begin{bmatrix} M_\alpha \\ M_\beta \end{bmatrix} \tag{18}$$

where, $M_\alpha = 0$ and $M_\beta = (P_v \cos \alpha + G_p \sin \beta) \cdot \frac{l}{2}$

It has been considered that the distance from point O to the application point of the panel weight (G_p) and the resultant force of the wind pressure (P_v) is $l/2$. For $P_v = 100 \text{ daN}$, $G_p = 19,6 \text{ daN}$, $l = 1 \text{ m}$, the izogeneralized forces curves of Q_1 (Figs. 5, 6) and Q_2 in ideal workspace are obtained.

In both cases the maximum value of the generalized forces $Q_{\max} = 151,73 \text{ daN}$ is recorded when the panel is vertical and facing south.

A measure of the mechanism performance is the torque that loads the universal joint, having the following expression, for both structures:

$$M_0 = [\overline{OA_1} \times Q_1 \overline{\ell_1} + \overline{OA_2} \times Q_2 \overline{\ell_2} + \overline{OC} \times (\overline{P_v} + \overline{G_p})] \cdot \overline{k_{z'}} \tag{19}$$

where $\overline{\ell_1}$, $\overline{\ell_2}$ are the unit vectors; C is the panel center; $\overline{k_{z'}}$ is the unit vector of the Oz' axis perpendicular on the main universal joint axes. The contour plot of M_0 is shown in Figs. 7 and 8.

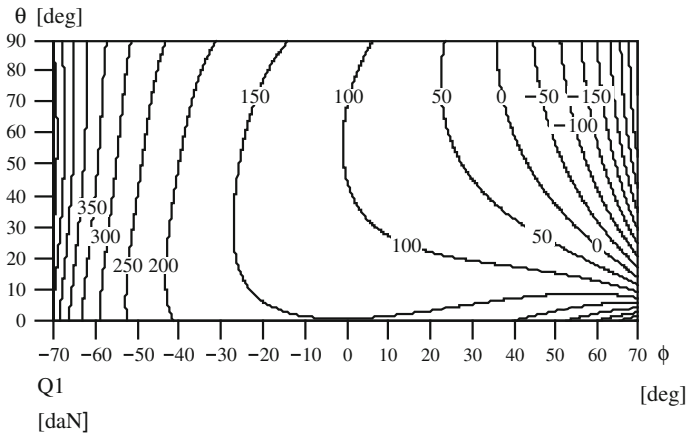


Fig. 5 The izogeneralized forces curves of Q_1 for 2S-2S-U_v mechanism

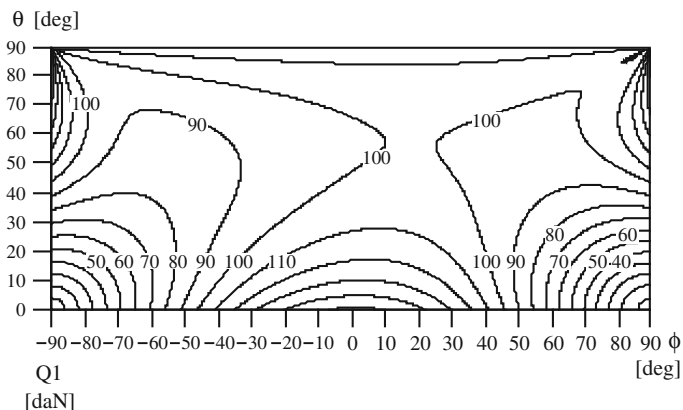


Fig. 6 The izogeneralized forces curves of Q_1 for 2S-2S- U_H mechanism

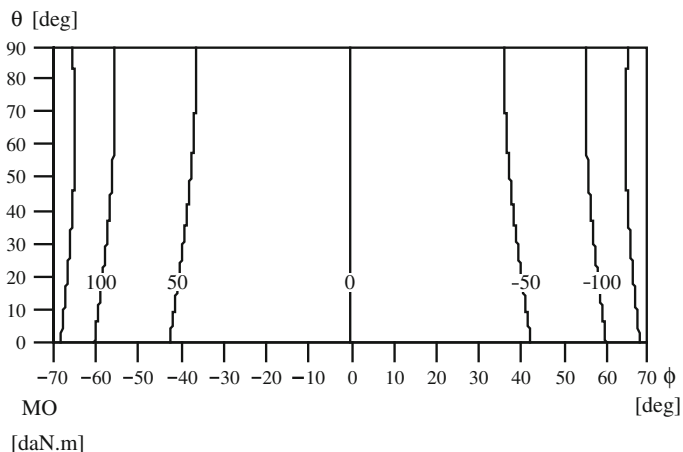


Fig. 7 Moment in the main universal joint of the 2S-2S- U_V mechanism

5 Condition Number and Stiffness Assessment

The stiffness of the mechanism has a direct influence on the accuracy of positioning and orientation. The studied case does not take into account the elasticity and actuators compliance of the active joints.

Control precision of the parallel device depends on the condition Jacobi matrix number, defined by:

$$C = norm[J] \cdot norm[J]^{-1} \tag{20}$$

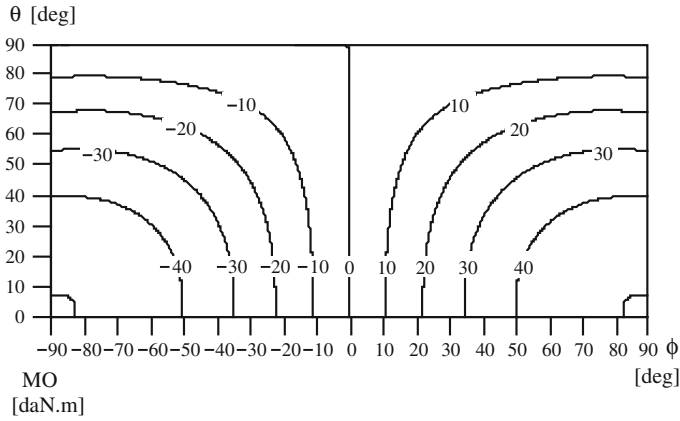


Fig. 8 Moment in the main universal joint of the 2S-2S-U_H mechanism

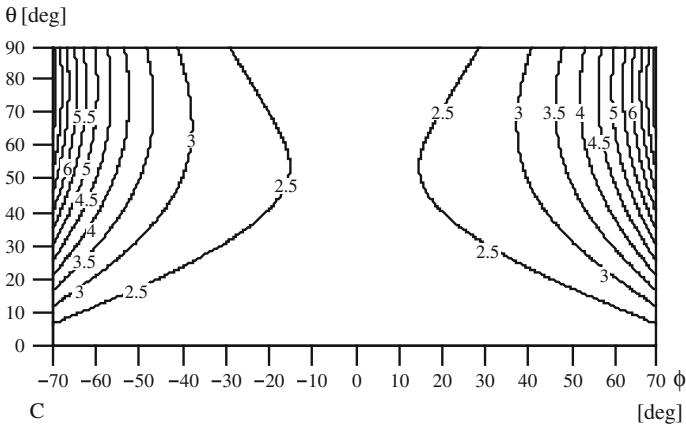


Fig. 9 Condition number of the 2S-2S-U_V parallel mechanism

where the Euclidean norm is used.

Figures 9 and 10 illustrate the maps of the condition number level curves. It is known that the performance is better when the condition number is lower.

Starting from the condition number, (Gosselin and Angeles 1991) defined a performance index called the Global Conditioning Index, given in Figs. 11 and 12:

$$\eta_c = \frac{1}{C} \tag{21}$$

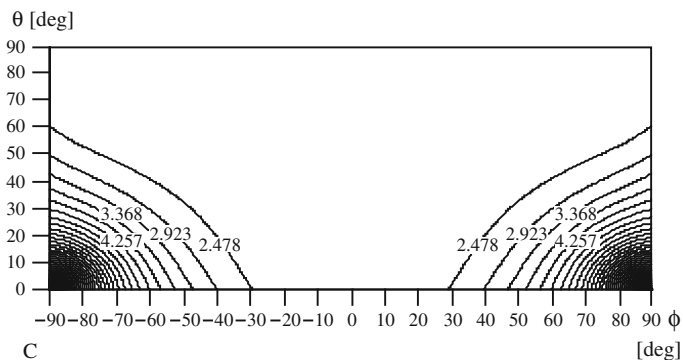


Fig. 10 Condition number of the 2S-2S-U_H parallel mechanism

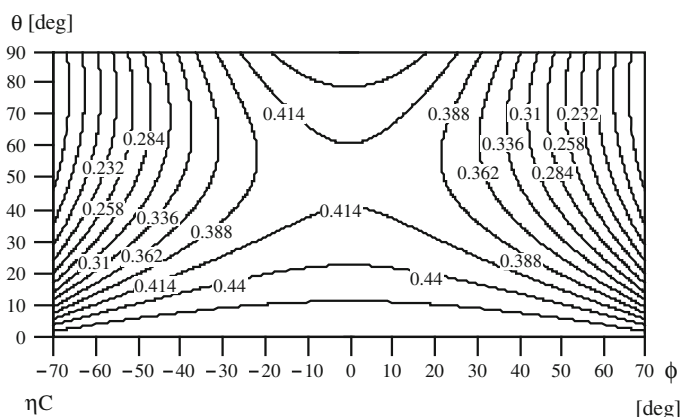


Fig. 11 Global Conditioning Index of the 2S-2S-U_V parallel mechanism

Knowing the stiffness matrix:

$$[K] = k[J]^T \cdot [J]; \quad k = 1 \tag{22}$$

the stiffness index can be computed:

$$KI = \text{norm}[K]^{-1} \cdot \text{norm}[K] \tag{23}$$

and the Global Stiffness Index (Hesselbach et al. 2004):

$$\eta = \frac{1}{KI} \tag{24}$$

whose maps are given in Figs. 13 and 14, respectively 15 and 16.

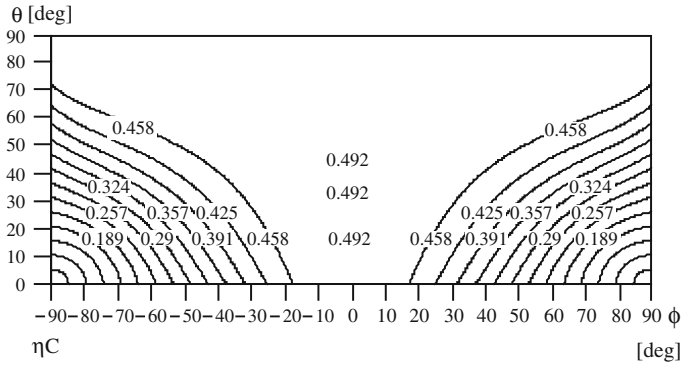


Fig. 12 Global Conditioning Index of the 2S-2S- U_H parallel mechanism

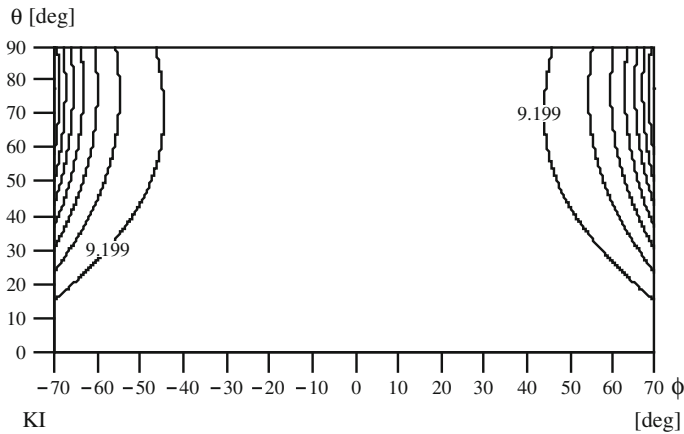


Fig. 13 Stiffness Index of the 2S-2S- U_V parallel mechanism

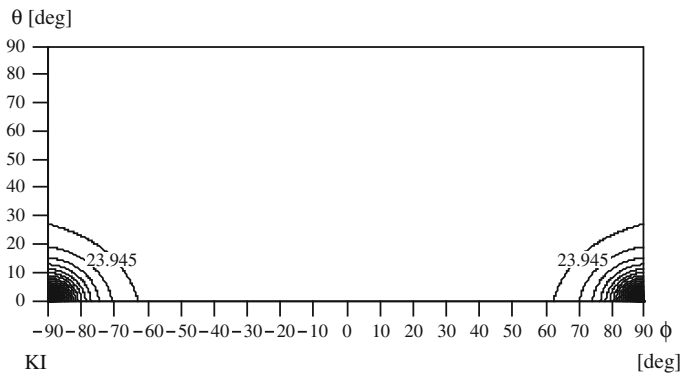


Fig. 14 Stiffness Index of the 2S-2S- U_H parallel mechanism

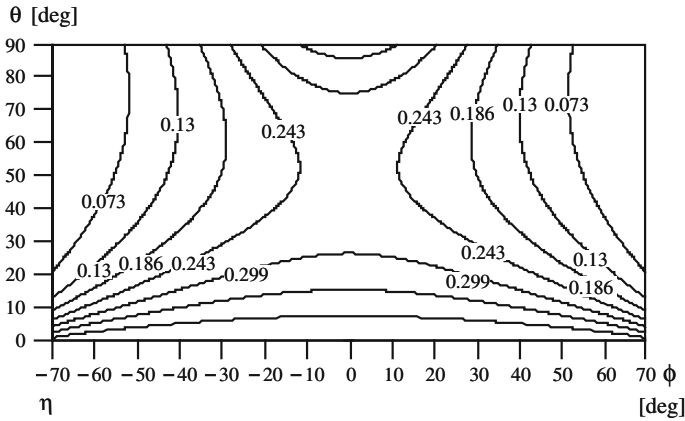


Fig. 15 Global Stiffness Index of the 2S-2S- U_V parallel mechanism

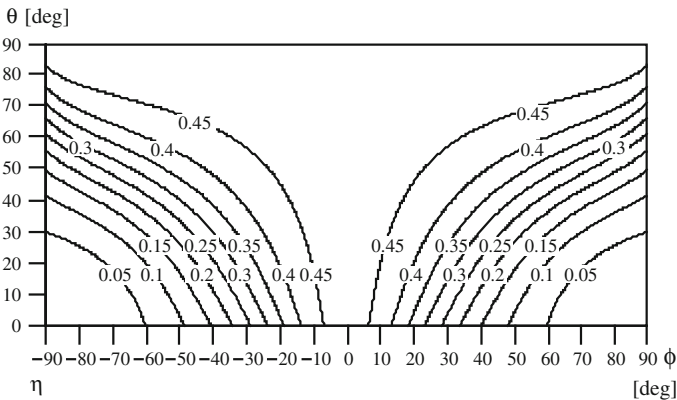


Fig. 16 Global Stiffness Index of the 2S-2S- U_H parallel mechanism

6 Conclusion

Two simple orientation parallel structures with two degrees of freedom have been analyzed in this paper, their kinematics, workspace, generalized driving forces have been evaluated under static conditions and the global stiffness index and global conditioning indices have been computed. The study consists in a structural optimization exercise. From the workspace point of view, the performances of the two mechanisms are similar. The values of the generalized static forces, the torque that loads the main universal joint, the conditioning and stiffness indices obviously show the performance of the 2S-2S- U_H mechanism. In both cases the stiffness decreases near the singularities curves of the first mechanism and in the areas of the workspace where the transmission angles are less than 20° in the case of the

second mechanism. The numerical results indicate that, in reachable workspace, the mechanisms are well conditioned, especially in the central area where the global conditioning index is 0.415 for 2S-2S- U_V and 0.492 for 2S-2S- U_H .

Acknowledgments The research work reported here was financed by the UEFISCDI project code PN-II-PT-PCCA-2011-3.2-0414, entitled “Robotic assisted brachytherapy, an innovative approach of inoperable cancers—CHANCE” and the project Scopes International Grant IZ74Z0-137361/1 entitled Creative Alliance in Research and Education focused on Medical and Service Robotics (CARE-Robotics).

References

- Arai T (1992) Analysis and synthesis of parallel link manipulator based on its statics. *J Robot Soc Japan* 10(4):526–533
- Carbone G, Ceccarelli M (2004) A procedure for experimental evaluation of cartesian stiffness matrix. 15th CISM-IFTToMM symposium on robot design. Dynamics and control, Montreal 04–24
- Carbone G, Ceccarelli M (2007) A comparison of indices for stiffness performance evaluation, 12th IFTToMM world congress, Besançon (France), June18–21, A831
- Ceccarelli M (2004) Fundamentals of mechanics of robotic manipulation. Kluwer Academic Publishers, Dordrecht
- Chakarov D (1998) Optimization synthesis of parallel manipulators with desired stiffness, *J Theor Appl Mech*, vol 28, no 4
- Gonçalves RS, Carvalho JCM (2008) Stiffness analysis of parallel manipulator using matrix structural analysis. 2-nd European conference on mechanism science, Cassino, Italy, 255–262
- Gosselin C (1990) Stiffness mapping for parallel manipulators. *IEEE Trans Robot Autom* 6(3):377–382
- Gosselin CM, Angeles J (1991) A global performance index for the kinematic optimization of robotic manipulators. *ASME J Mech Des* 113(3):220–226
- Gosselin CM, Zhang D (2002) Stiffness analysis of parallel mechanisms using a lumped model. *Int J Robot Autom* 17(1):17–27
- Hesselbach J, Kerle H, Kreft M, Plitea N (2004) The assessment of parallel mechanical structure for machines taking account of their operational purpose, Proceedings of the 11th world congress in mechanism and machine science, IFTToMM 11, Tianjin, China
- Itul T, Pisla D (2010) Kinematic-Dimensional Analysis of Parallel Robot used for Orientation. *Solid State Phenomena, Vol Robotics and Autom Syst* 166–167:229–234
- Itul T, Pisla D, Stoica A (2010) Kinematics and design of a simple 2-DOF parallel mechanism used for orientation, *New Trends in Mechanism Science. Analysis and Design*, Springer, 39–46
- Júnior GDLS, Carvalho JCM, Gonçalves RS (2011) Stiffness analysis of 6-RSS parallel manipulator. 13th world congress in mechanism and machine science, Guanajuato, México, 19–25 June, A12_381
- Liu X-J, Jin Z-L, Gao F (2000) Optimum design of 3-Dof spherical parallel manipulators with respect to the conditioning and stiffness indices. *Mech Mach Theor* 35(9):1257–1267
- Merlet J-P (2006) *Parallel robots*. Springer Verlag, Berlin
- Parenti-Castelli MCV (2004) A novel fully decoupled two-degrees-of-freedom parallel wrist. *Int J Robot Res*, 661–667
- Simaan N, Shoham M (2003) Stiffness synthesis of a variable geometry six-degrees-of-freedom double planar parallel robot. *Int J Robot Res* 22(9):757–775

Kinematic and Dynamic Modeling and Simulation of an Intelligent Adaptive CTLSO Brace

D. Mărgineanu, E.-Ch. Lovasz, L. V. Ciupe and L. Ciurdariu

Abstract Braces for scoliosis have to apply correction forces in a tolerable range and to allow some degree of movement for the patient. A type of adaptive intelligent CTLSO brace is proposed, with vertical, horizontal, lateral bending and twist compliance and correction with pneumatic muscles as actuators. The correlation between the patient's movements, acting commands, structure's compliance and corrective displacements and forces are studied analytically and numerically. The necessary acting forces and displacements are determined. Simulations for the brace behavior under load with compliance and corrective action are presented.

Keywords Braces · Scoliosis · Simulation · Pneumatics · Compliance

1 Introduction

Complex traditional medical management of scoliosis is determined by the severity of the curvature, skeletal maturity, and likelihood of progression (Thompson and Stephens Richards III 2008). The conventional options are, in order: observation, bracing, and surgery. As studies show that non-operative

D. Mărgineanu (✉) · E.-Ch. Lovasz · L. V. Ciupe · L. Ciurdariu
Politehnica University of Timisoara, Timisoara, Romania
e-mail: dan.margineanu@mec.upt.ro

E.-Ch. Lovasz
e-mail: erwin.lovasz@mec.upt.ro

L. V. Ciupe
e-mail: valentin.ciupe@mec.upt.ro

L. Ciurdariu
e-mail: loredana.ciurdariu@mat.upt.ro

treatment of adolescent idiopathic scoliosis with orthosis is effective (Smith and Harrigan 1998), a logical and appropriate treatment plan can be outlined for each patient. This will give control of curves with reduction in the need for surgery.

Bracing is only done when the patient has bone growth remaining, and is generally implemented in order to hold the curve and prevent it from progressing to the point where surgery is necessary (Wong and Evans 1998). Bracing involves fitting the patient with a device covering the torso and in some cases it extends to the neck. There are several types of braces depending on the individual's condition and type of curve.

The Cervico-Toraco-Lumbo-Sacral-Orthosis CTLSO (a.k.a. Milwaukee brace) is composed of metal bars extending around the shoulders to help against spine curvature. Elastic braces attempt to improve quality of wearer's life by allowing freedom of movement and improved compliance and can be worn by adults as postural support as well as treatment for Adolescent Idiopathic Scoliosis.

Compliant braces using less corrective force and pressure may be more effective than stronger ones, which can be uncomfortable and thus diminishing the daily wearing time, main factor in brace's efficiency.

Developing braces with higher compliance and intelligent supportive and corrective action is the task undertaken by the authors.

2 Proposed Solutions for Intelligent Adaptive Braces

The adaptive intelligent CTLSO is actually an exoskeleton composed of 2 parallel pre tensioned linkages consisting of rigid elements ("bones"), pneumatic actuators ("muscles") and traction springs ("tendons").

A first variant (Mărgineanu et al. 2008), shown in Fig. 1a, is composed of a main four-bar mechanism $A_1C_1C_2A_2$, with additional compliant and active supports B_1C_1 and B_2C_2 on both sides and the triangle MC_1C_2 on top. Pneumatic muscles, represented as pneumatic cylinders, form, along with traction springs, pre-tensioned acting elements with variable length.

On the horizontal element C_1C_2 , the tendon ensures the vertical compliance and the muscle delivers the main correction action. The lateral left and right compliant active elements BC stabilize the structure, allow lateral compliance and react to the lateral tilt in patient's posture by contracting the muscles.

This structure was built and tested. It has a good compliance but low correction action because of the large angles of bones to vertical, imposed by the limited height of the structure and the relative long pneumatic muscles. The total width of the structure results also larger as the patient's shoulders.

In order to reduce the horizontal size of the brace and to improve the correction force, a second variant with vertical main muscle and additional bones was developed (see Fig. 1b).

The vertical main muscle and tendon D_0D is linked to the left C_1 and right C_r "knees" through two inner bones CD . Thus the structure is much slimmer and

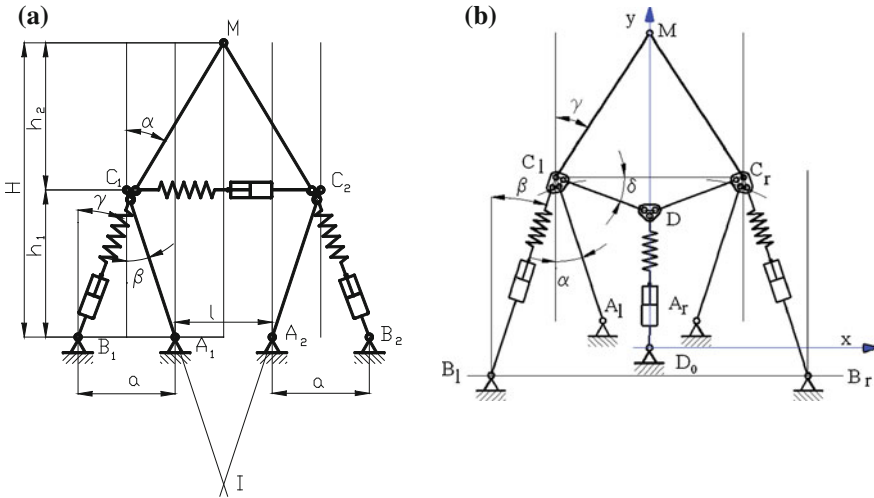


Fig. 1 Kinematic scheme of two CTLSO braces **a** with *horizontal* main muscle (Margineanu et al. 2008), and **b** with *vertical* muscle

stronger, maintaining some compliance as the angles α , β , and γ of the bones to vertical are larger as the self-locking angles of the knee mechanism.

The structure has knot plates in C_1 and C_r to avoid the presence of 3 super-imposed rotational joints, as in the following model.

The brace is provided with two pairs of proximity sensors, one pair for each linkage. Sensors activation detects compliant angular displacements of the lower bones under load. If the patient does not correct his/her posture, the control unit takes charge to impose the necessary correcting action. If, e.g., both sensors are activated i.e. a vertical displacement of the correction point M occurred, after a dwell the central main muscle contracts. Then, if the sensors are activated no more, after another dwell the main muscle relaxes.

3 Analytic Approach to Structure’s Kinematic

The calculus procedure follows the mounting steps for the structure.

First, the basic supporting structure $A_1C_1MC_rA_r$ and the side muscles with the tendons B_1C_1 and B_rC_r are mounted without pre-tension (see Fig. 2a) on the fixed element. The coordinates of the structure points and the angles of the bones to the vertical in this stage can be easily calculated in the coordinate system with the origin in $D_0(0,0)$, given the coordinates of the fixed points $A_{s,d}(x_{A_{s,d}},y_{A_{s,d}})$, $B_{s,d}(x_{B_{s,d}},y_{B_{s,d}})$, bones lengths $(AC)_{l,r} = a$, $(MC)_{l,r} = c$, $(DC)_{l,r} = d$, tendon lengths t_0 without pretension ($\Delta t = 0$) and non-contracted ($\Delta m = 0$) muscles lengths m_0 .

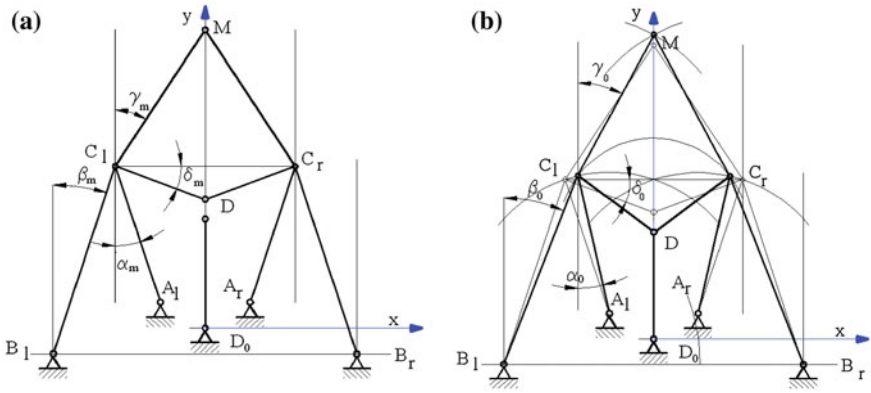


Fig. 2 Mounting the brace: **a** join the supporting structure and side muscles without pretension, and **b** pretension the structure by attaching the main muscle D₀D

Second, the structure is then pre-tensioned by attaching the main muscle D₀D (see Fig. 2b). The active and compliant elements BC and D₀D (Eq. 1) lengthen proportional with pretension load (1b). The muscles remain relaxed ($\Delta m_{s,l} = 0$). Structure's geometry can be calculated adding a deformation equation linking the central and the lateral tendons' deformation (Fig. 3).

$$(BC)_{l,r} = m_{l,r} + t_{l,r} \tag{1}$$

with

$$\begin{cases} m_{s_{l,r}} = m_{s_0} + \Delta m_{s_{l,r}} \\ t_{s_{l,r}} = t_{s_0} + \Delta t_{s_{l,r}} \end{cases} \text{ and } \begin{cases} m_c = m_{c_0} + \Delta m_c \\ t_c = t_{c_0} + \Delta t_c \end{cases} \tag{1a}$$

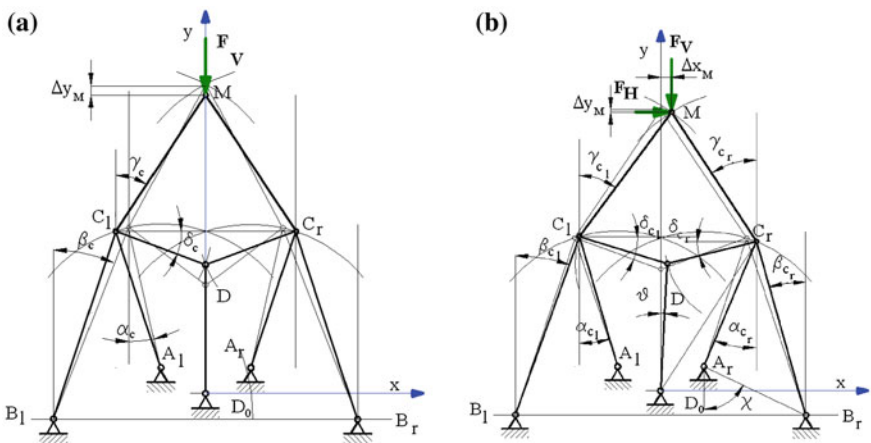


Fig. 3 Braces compliance: **a** vertical, and **b** combined (vertical and horizontal)

where

$$\Delta t_{sl,r} = \frac{F_{t_{l,r}}}{k_{sl,r}} \text{ and } \Delta t_c = \frac{F_{t_c}}{k_c} \tag{1b}$$

Third, as vertical or/and horizontal loads are applied on the correction point M, the structure deforms i.e. allows some mobility under increasing reaction. The geometry under load can be estimated by solving numerically the non-linear Equation system, composed of geometric dependencies (2–4) equilibrium Eqs. (5–7) (see Fig. 4a–c) of the knots and tendons deformation equations. In the first approach, friction in joints, damping effects and inertia are neglected.

$$\alpha = \arccos \frac{(m_s + t_s)^2 - (a^2 + \rho^2)}{2a\rho} - \chi \tag{2}$$

$$\beta = \chi - \arccos \frac{(m_s + t_s)^2 + \rho^2 - a^2}{2(m_s + t_s)\rho} \tag{3}$$

$$\theta = \arcsin \frac{(m_c + t_c)^2 + \rho_c^2 - d^2}{2\rho(m_c + t_c)} - \chi \tag{4}$$

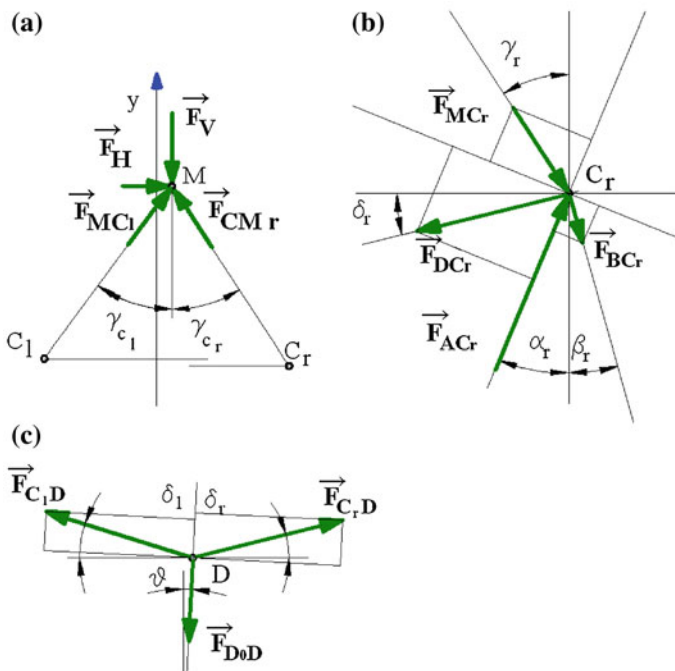


Fig. 4 Diagrams for knots equilibrium: **a** knot M, **b** knot C, and **c** knot D

where

$$\left\{ \begin{array}{l} \rho = \sqrt{(x_B - x_A)^2 + (y_B - y_A)^2} \\ \chi = \arctg \left| \frac{y_B - y_A}{x_B - x_A} \right| \end{array} \right. \text{ and } \left\{ \begin{array}{l} \rho_c = \sqrt{x_c^2 + y_c^2} \\ \chi_c = \arctg \frac{y_c}{x_c} \end{array} \right. \quad (4a)$$

$$\left\{ \begin{array}{l} F_V = F_{m_l} \cos \gamma_l + F_{CM_r} \cos \gamma_r \\ F_H = F_{CM_r} \sin \gamma_r - F_{CM_l} \sin \gamma_l \end{array} \right. \quad (5)$$

$$\left\{ \begin{array}{l} F_{CM} \sin(\alpha + \gamma) + F_H \sin(\alpha + \beta) - F_{DC} \cos(\alpha + \delta) = 0 \\ F_{AC} = \vec{F}_{MC} \cos(\alpha + \gamma) + \vec{F}_{t_l} \cos(\alpha + \beta) + \vec{F}_{DC} \sin(\alpha + \delta) - 0 \end{array} \right. \quad (6)$$

$$\left\{ \begin{array}{l} F_{CD_r} \cos(\delta_l + \theta) = F_{CD_l} \sin(\delta_r + \theta) \\ \vec{F}_{t_c} = \vec{F}_{CD_r} \sin(\delta_l + \theta) + \vec{F}_{CD_l} \sin(\delta_r - \theta) \end{array} \right. \quad (7)$$

The system with tendons' elongations as unknowns is solved in Matlab using the fsolve function. Then the coordinates of the knots are calculated and the structure can be drawn (see Fig. 5 for pre-tensioned mounting position and Fig. 6 for compliance under progressive vertical load).

Fourth, actions in muscles are imposed as contractions $\Delta m_{l,c}$ in Eq. 1a and b.

In this phase, the calculus may assess the corrective displacement of the point M at the same applied load F_V and/or F_H or the corrective force in M imposed by muscle contraction at a fixed position of M. The actual behavior depends greatly on the patient's response to correction.

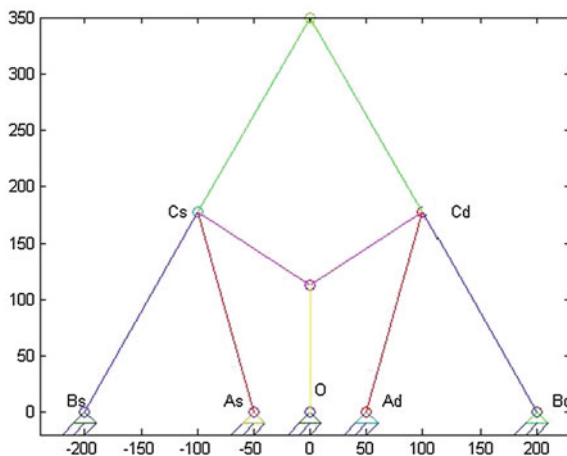


Fig. 5 Brace's structure by pre-tensioned mounting, calculated and drawn in Matlab

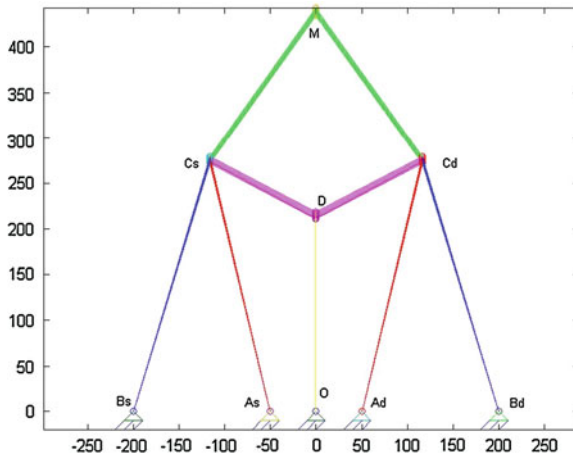


Fig. 6 Brace’s compliance, calculated and drawn in Matlab

Radial loads in joints and axial loads on bones are also estimated, allowing more accurate pre-dimensioning of brace’s structural elements.

For refining the solution, CAD models are developed next and simulation procedures are carried out, using the Multi Body Simulation (MBS) method. Structure’s weight, friction, damping and inertial forces are taken into account.

In Fig. 7a, an example of a brace model constructed in SolidWorks is presented; Fig. 7b shows a Motion Analysis procedure for compliance under vertical load using SolidWorks Motion.

The brace is composed of 200 mm long bones and 120 mm long inner bones. The pneumatic muscles with 20 mm stroke are in relaxed state 150 mm long between the attachment holes centers. The traction springs with 5 N/mm stiffness coefficient are pre-tensioned by 20 mm.

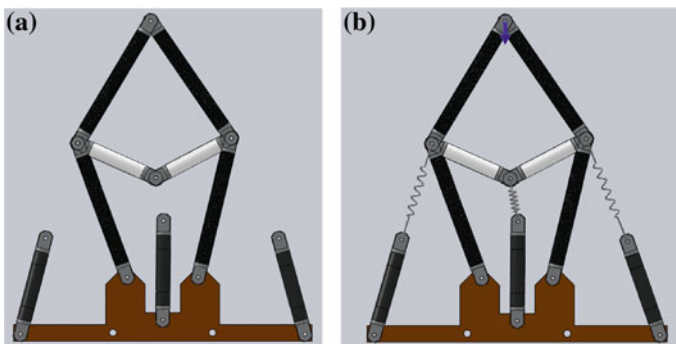


Fig. 7 Brace model in SolidWorks (a) and the simulation screen for vertical compliance in SolidWorks Motion, with pneumatic muscles, tendons and load (b)

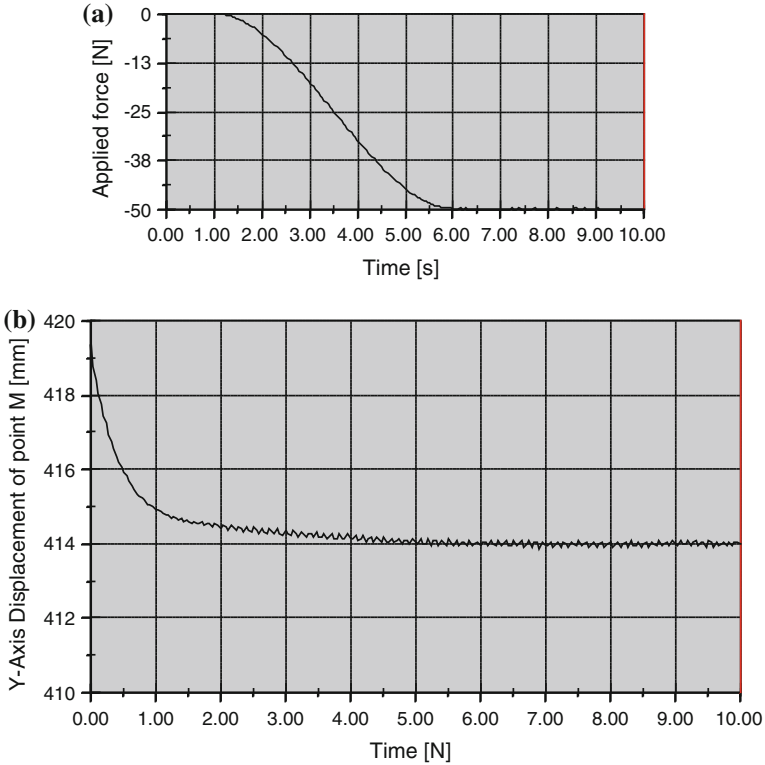


Fig. 8 Simulation results: **a** variation of applied load on correction point M, and **b** vertical displacement of the correction point M under load

In this procedure, a progressing vertical load applied 1 s after the simulation start increases from 0 to 50 N in 5 s, and then remains stable (see Fig. 8a).

The vertical displacement of the correction point M under load is shown in Fig. 8b. The designed brace is stiffer, with only 5 mm displacement under 50 N load.

4 Conclusions

The calculation, modeling and simulation procedure presented in the paper may be used for pre-dimensioning the brace's structural elements, assessing the compliance and corrective action, customizing and optimizing the structure for a given patient.

The structure with vertical main muscle and tendon provides stronger corrective action, but allows less compliance. The best compromise to solve this contradiction is to be achieved through optimization or by designing custom elastic elements with progressive stiffness or with limited deformation.

References

- Margineanu D, Perju D, Lovasz E-Ch, Văcărescu V, Ciupe V (2008) Consideration about one type of adaptive intelligent brace. In: Proceedings of the international conference ROBOTICS'08, vol 15(50), 13–14 Nov 2008, Series A, ISSN 123-9631. Buletin of the Transilvania University of Braşov, pp 213–218
- Smith BG MD, Harrigan TPT CO (1998) Bracing manual. Brace Scoliosis Research Society, Milwaukee
- Thompson GM, Stephens Richards III B (2008) In: Grivas TB (ed) Inclusion and assessment criteria for conservative scoliosis treatment. IOS Press
- Wong MS, Evans JH (1998) Biomechanical evaluation of the Milwaukee brace. *Prosthet Orthot Int* 22:54–67

Virtual Model for Kinematic Analysis of Human Upper Limb

Elena Mereuta, Marian Tudoran, Daniel Ganea
and Claudiu Mereuta

Abstract The paper presents a kinematic model of the linkage that models the human upper limb and which is used for the kinematic analysis. To achieve that goal Catia software and its features were used. The paper presents the steps to be followed and the results provided by the simulation of that spatial mechanical structure. We have been able to show the angles, the angular velocities, the angular accelerations for different input motions suitable to reveal the activity of the most important muscles of the human upper limb.

1 Introduction

Knowledge of mechanics and the behaviour of the musculoskeletal system is a prerequisite to designing systems to assist persons with disabilities, such as prostheses, orthosis and neuro-prostheses. Due to the complexity of skeleton of the hand the kinematics modeling is a challenge (Sancho-Bru et al. 2011).

This complexity compels researchers to develop simplifying assumptions in order to facilitate better understanding and model managing (Bullock et al. 2012). However, the assumptions have important implications regarding the accuracy of the final model (Valero-Cuevas 2003). These studies focus on kinematics analysis of human upper limb and simplifying assumptions are used in a wide range of models described in the literature as follows: descriptions on the biomechanics of the hand (Brand and Hollister 1999), kinematic models conceived for studying the neuromuscular control (Valero-Cuevas 2005), the techniques for identification of gestures analysis (Erol et al. 2007; Pavlovic et al. 1997) the fingers motion

E. Mereuta (✉) · M. Tudoran · D. Ganea · C. Mereuta
“Dunarea de Jos” University of Galati, Galati, Romania
e-mail: emereuta@ugal.ro

analyses in order to support the development of multiple fingers robots (Zhaojie and Honghai 2008), measurement of the active space of the human upper limb related to the rehabilitation and ergonomics (Kuo et al. 2009).

2 Modeling the Human Upper Limb

In order to create the kinematic model of human upper limb the environmental modelling program named CATIA was used. The kinematic model of the linkage which simulates the movement of the upper limb consists of five constraints and four kinematic elements (Tudoran 2013; Fig. 1). The shoulder is modelled using two rotational joints (Drăgulescu 2005). The rotational axes of joints are orthogonal. The following motions are allowed: abduction-adduction motion of the arm (joint A) (Fig. 4); flexion-extension motion of the arm is (joint B) (Fig. 1).

The elbow is modeled using joint C (Fig. 1) which allows the forearm flexion-extension motion. The joint D allows the pronation-supination motion of the forearm whose rotational axis is not coincident to the longitudinal axis of the forearm, in order to ensure the tipping of radius over the ulna during the pronation (Fick 1904). The wrist is modeled using joint E, which allows only the flexion-extension motion to palm (Drăgulescu 2005).

The geometrical model of the human skeleton was retrieved from the virtual library 3Dlancer,¹ as 3D surfaces in StudioMax. In order to get a realistic model of bones we have used a feature provided by AutoCAD that consists of refining the surface which was converted to a solid aiming to get automatically the bone mechanical properties (Tudoran 2013).

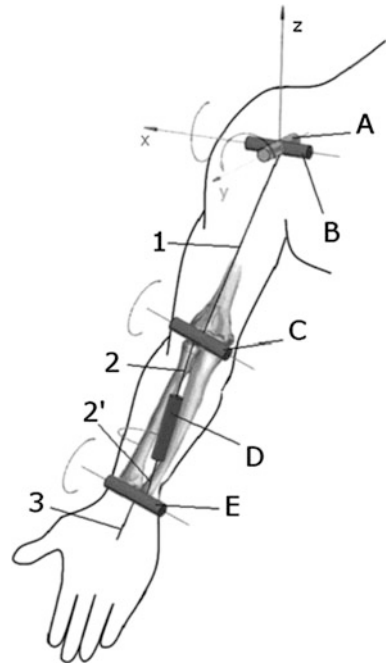
The joints of the human upper limb were modeled using rotational joints. The axis of rotation of the joint is oriented according to the anatomical consideration. Thus, the motion must be as closed as possible to real motion, and the distance between the joint surfaces must be constant throughout the motion. Using two geometric constraints, the elbow is modeled as a joint (Fig. 2), which allows the forearm flexion-extension motion.

The forearm joint must allow the pronation-supination and its rotational axis intersect the radius proximal head and ulna distal head (Fig. 3). The wrist is modelled using three cylindrical joints. In each of these joints, in addition to the rotations also translations are occurring. The translations are neglected due to small displacements. Thus, a rotational joint is used to model the motion toward the bones of the forearm, considering stiffened carpal bones (Fig. 4). The shoulder is modelled using two rotational joints. In order to achieve that goal we have used a universal joint (A) (Fig. 5).

To study muscle contraction in kinematic terms, the muscle is modelled through two semi couplings, corresponding to the proximal and distal end that translates one to another.

¹ <http://3dlancer.net/en/3dmodel-human-skeleton-4792.html>.

Fig. 1 Kinematic model of the human upper limb



The semi coupling is modelled using two lines at right angles, Δ_1 and Δ_2 and a plane. Because the longitudinal axis of the muscle is not in the motion plane (Fig. 6b) the connection between the muscle and the bone is carried out using an universal joint B (Fig. 6a; Tudoran 2013).

The biomechanical model of the human upper limb (Fig. 7b) comprises six muscle fibres (Fig. 7a) corresponding to the brachial muscle, with long and short head of the brachial biceps muscle, medial, lateral and long head of the brachial triceps muscle.

Fig. 2 Elbow model

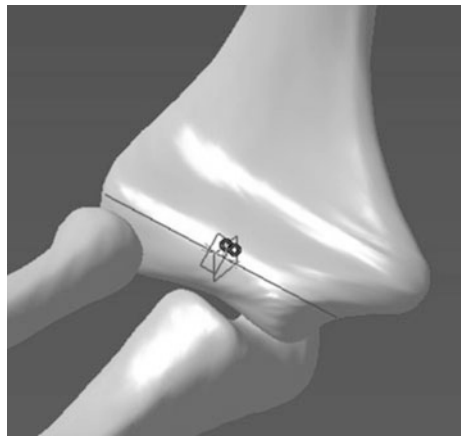


Fig. 3 Forearm joint model

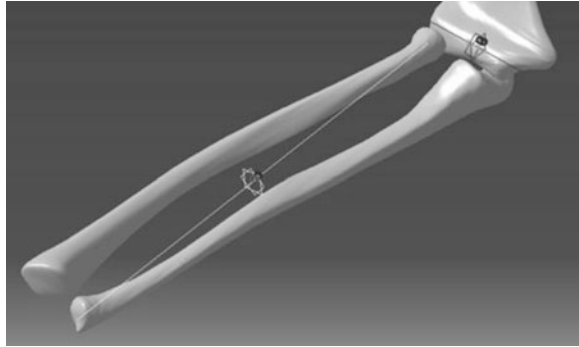


Fig. 4 Wrist joint model

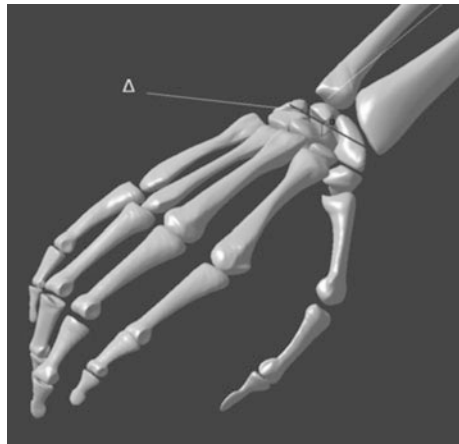
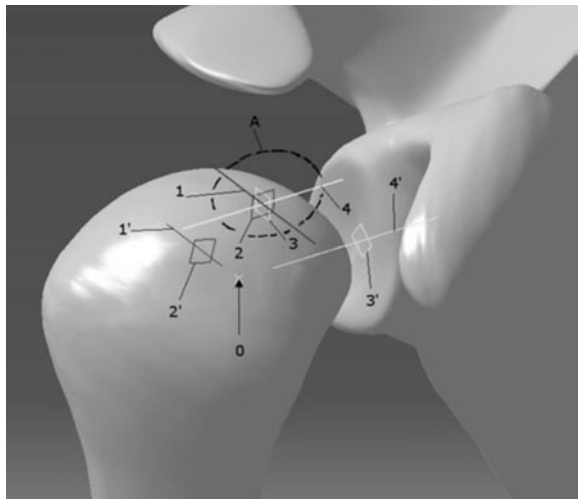


Fig. 5 Shoulder joint model



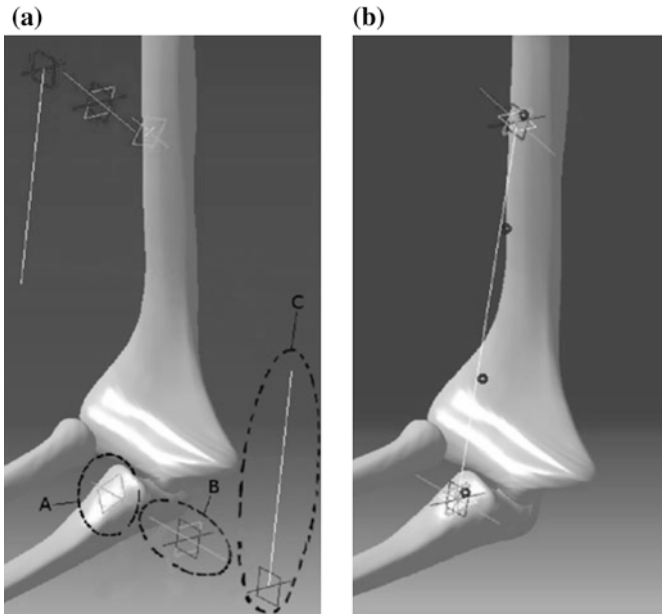


Fig. 6 Kinematic modelling of brachial muscle **a** insertion points of muscle **b** longitudinal axis of muscle

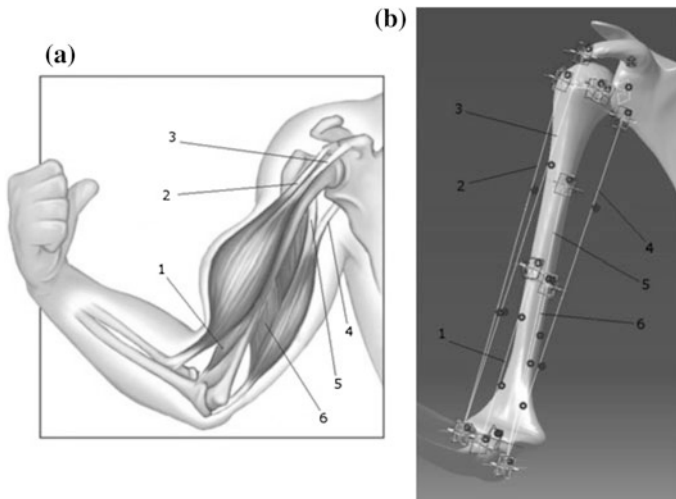


Fig. 7 Arm muscles: **a** anatomical model, and **b** biomechanical model

3 Simulation Results

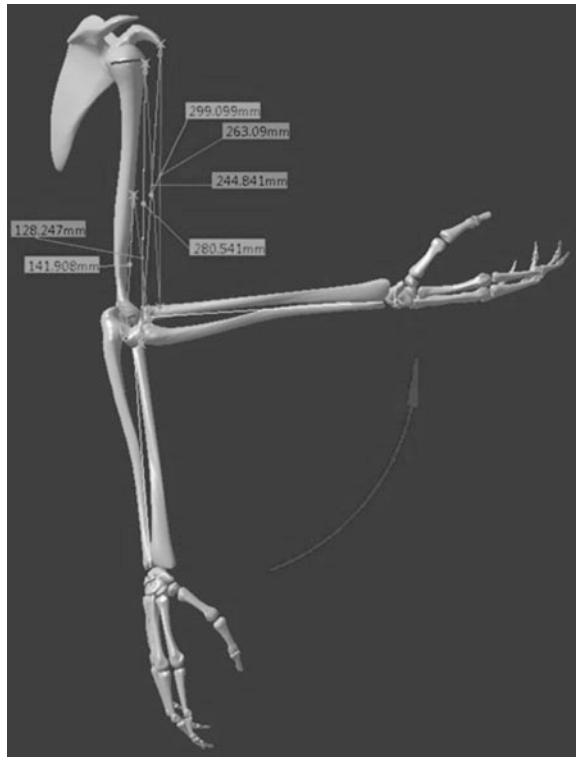
In order to perform the kinematic analysis of biomechanical model of upper limb we have chosen the following motions: the flexion of the forearm and the push-up. The flexion of the forearm highlights the brachial and biceps muscle activity, while the push-up emphasizes the triceps muscle activity. The spatial end-effector motion emphasizes the kinematic behaviour of the centres of gravity of the segments composing the skeleton of the upper limb.

The flexion motion consists of forearm motion within the range 0° – 90° (Fig. 8). The initial position of the forearm during flexion is the palm facing forward (Fig. 8).

The direct kinematic analysis has provided information on the muscles shortenings, velocities and accelerations of those contractions (Tudoran 2013). So, during flexion the brachial and biceps muscles are shortening. Their variation with respect to time has the same shape but different values (Fig. 9, Table 1).

The biceps long head shortens with 35.7 mm, which is a shortening of its length with 12.72 %. Values are close to those of the short head, 36.01 mm, 12.04 % respectively, but compared to the brachial muscle, are higher. The brachial muscle

Fig. 8 Forearm flexion



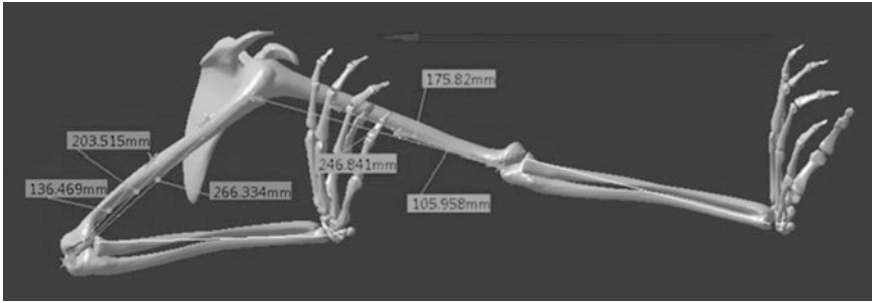


Fig. 9 Push-up motion

Table 1 Muscles shortening during flexion

Muscle	Initial length (mm)	Final length (mm)	Shortening	
			(mm)	(%)
Biceps—long head	280.54	244.84	35.70	12.72
Biceps—short head	299.09	263.09	36.01	12.04
Brachial	141.90	128.247	13.66	9.62

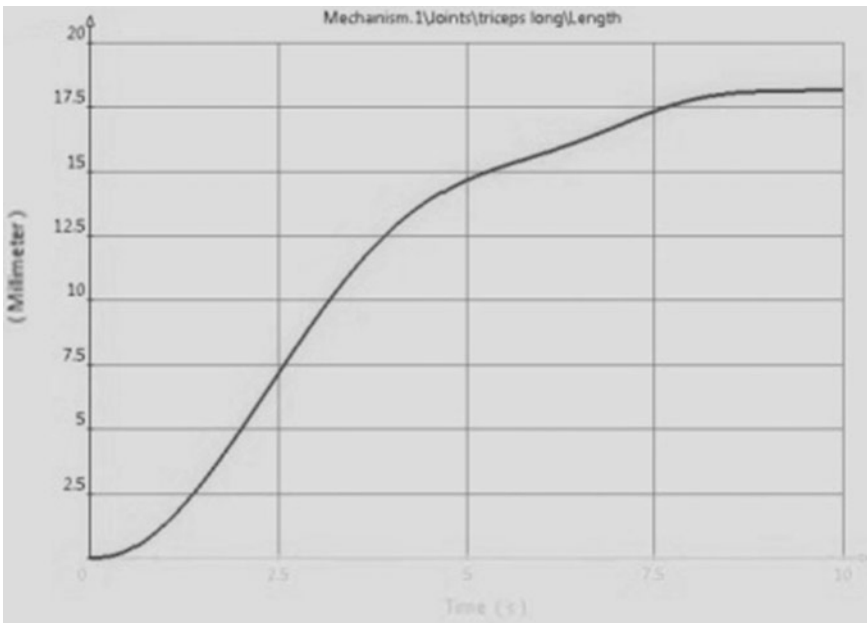


Fig. 10 Long head triceps lengthening

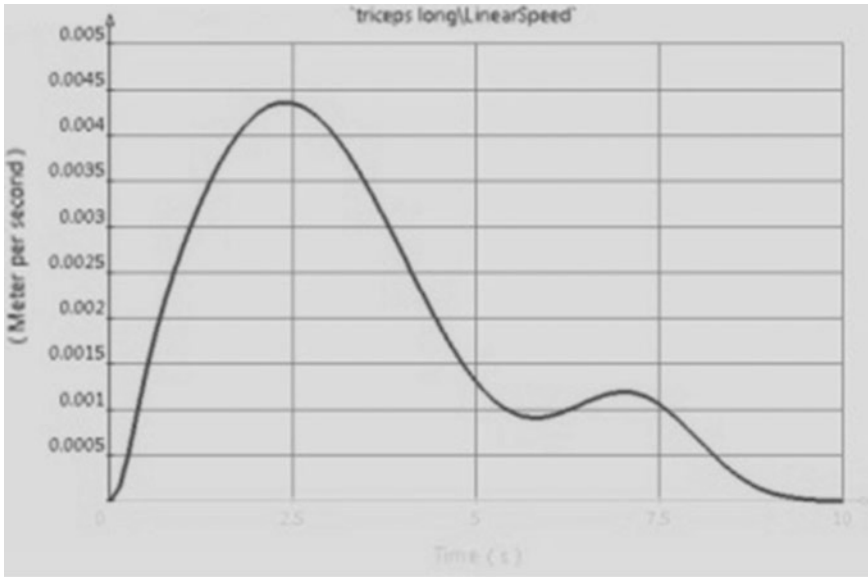


Fig. 11 Long head triceps lengthening velocity

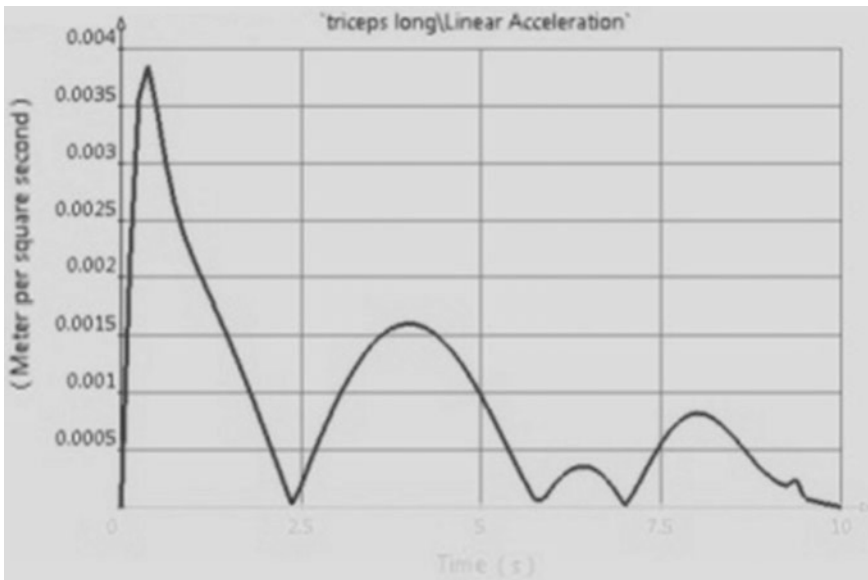


Fig. 12 Long head triceps lengthening accelerations

length recorded at the beginning a rise of 0.4 mm, corresponding to a rate of 0.28 % of the total length of the muscle fiber, followed by a emphasized shortening up to 9.62 %, i.e. 13.66 mm.

For the flexion the muscle contraction velocity has recorded an increase up to 7.71 m/s for long head and 7.95 m/s for short head, corresponding to the inflection point of the shortening curve variation. The velocity curve of the brachial muscle shows small differences in comparison with the other curves of variation as a result of the fact that this muscle is lengthening before the shortening phase.

The maximum values of the acceleration of the biceps, the long head and short head they are approximately equal to each other, 2.66 m/s^2 , respectively 2.69 m/s^2 . Instead, acceleration of brachial is smaller (1.46 m/s^2) due to the fact that the shortening is less than that of the biceps muscle.

For the kinematic analysis of triceps—long, lateral and medial head, the law of motion has been chosen to match the push-up motion (Fig. 9).

The inverse kinematic analysis has provided information on the lengthening, the velocities, and the accelerations of triceps muscle fibers. In this case, the end effector has to slide along x axis. During that push-up motion three of the triceps muscle fibers are lengthening. The time variation of these lengthens is shaped the same for the lateral and medial head, but the values are different.

The shape of the lengthening curve of the triceps long head (Fig. 10) is different from the other two fibers curve shape (lateral and medial), featuring an extended stretch since the insertion point of this fiber is on scapula and not on the humerus as in the case of the other two. The medial head of the triceps muscle is lengthening with 30.51 mm, which represents a percentage of 28.79 % of the initial muscle length. The long head of the triceps shows the lowest elongation, 19.49 mm or 7.89 %.

For the push-up motion, we have found that contraction velocities of the lateral and medial fibres of the triceps muscle have increased to 8.05 and 8.07 m/s corresponding to the inflection point of the lengthening curve. The triceps long head contraction speed (Fig. 11) has registered a smaller increasing compared to the other two fibres. This curve shows small differences in comparison with the other curves due to the fact that this muscle fibre has an extended elongation floor.

The analysis of accelerations shows that for the lateral head and the medial head the maximum values are similar, of 8.71 m/s^2 , respectively 8.59 m/s^2 . Instead, for the triceps long head the acceleration shows much lower values, 3.85 m/s^2 , due to the fact that the muscle shortening is bigger than the other two fibres (Fig. 12).

4 Conclusions

The kinematic model provides information about displacements, velocities and accelerations of bone segments composing the skeleton of the upper limb. This information can be used as input in the design of orthotic devices. So the most relevant conclusions are:

The brachial muscle has a slightly different behaviour than the biceps (long and short head) due to the fact that the input position is corresponding to the situation in which the forearm bones are prolonged to the arm bone and not in orthostatic position.

The forearm flexion stresses especially the long head and the short head of the biceps compared to the brachial muscle. To stress only the brachial muscle, either during medical rehabilitation programmes, either during sports training, the flexion should be in the range of 0° – 2.53° flexion of the forearm.

The push-up motion stresses the triceps medial head muscle compared to the other two fibres of the same muscles. To stress only the triceps long head, both in medical rehabilitation programs, and in sports training the push-up must be in the range of 380–450 mm sliding along O_y axis of end effector.

The proposed kinematic model is highly complex and allows the simulation of different and complex motions.

References

- Brand PW, Hollister A (1999) *Clinical mechanics of the hand*, 3rd edn. Mosby, St. Louis, Mo
- Bullock IM, Borràs J, Dollar AM (2012) Assessing assumptions in kinematic hand models: a review. In: *The fourth IEEE RAS/EMBS international conference on biomedical robotics and biomechatronics*, Roma, Italy, 24–27 June 2012, ISBN 978-1-4577-1200
- Drăgulescu D (2005) *Biomechanics modelling* (in Romanian). Didactică și Pedagogică, București
- Erol A, Bebis G, Nicolescu M, Boyle RD, Twombly X (2007) Vision-based hand pose estimation: a review. *Comput Vis Image Underst* 108(1–2):52–73
- Fick R (1904) *Handbuch der anatomie und der mechanik unter Berücksichtigung der bewegenden Muskeln*. Fischer Verlag
- Kuo LC, Chiu HY, Chang CW, Hsu H, Sun YN (2009) Functional workspace for precision manipulation between thumb and fingers in normal hands. *J Electromyogr Kinesiol* 19:829–839
- Pavlovic VI, Sharma R, Huang TS (1997) Visual interpretation of hand gestures for human-computer interaction: a review. *IEEE Trans Pattern Anal Mach Intell* 19(7):677–695
- Sancho-Bru JL, Perez-Gonzalez A, Mora MC, Leon BE, Vergara M, Iserte JL, Rotriguez-Cervantes PJ, Morales A (2011) Towards a realistic and self-contained biomechanical model of the hand. *Theor Biomech* 211–240
- Tudoran MS (2013) *Virtual biomechanical models for improving the positions of human upper limb* (in Romanian). PhD thesis
- Valero-Cuevas F (2003) Towards a realistic biomechanical model of the thumb: the choice of kinematic description may be more critical than the solution method or the variability/uncertainty of musculoskeletal parameters. *J Biomech* 36(7):1019–1030
- Valero-Cuevas FJ (2005) An integrative approach to the biomechanical function and neuromuscular control of the fingers. *J Biomech* 38(4):673–684
- Zhaojie J, Honghai L (2008) A comparison of grasp recognition methods for programming by demonstration. In: *Proceedings of the 2008 UK workshop on computational intelligence*

Estimating the Muscle Force Using a Kinematic Model of the Human Upper Limb

Elena Mereuta, Marian Tudoran, Daniel Ganea
and Claudiu Mereuta

Abstract The paper presents a kinematic model for a human upper limb that provides data for estimating the muscle force using Hill's model for the muscle force. In order to determine the force developed by human arm, we have measured the elongation and the contractions of the model of the muscle and the shortening velocities that are input data in the Hill model. The model enables to compare the magnitude of the muscle of a normal upper limb to a disabled one.

1 Introduction

Modeling the muscles has been a constant aim of researchers in biomechanics. They have desired either to anticipate the muscles behaviour under certain conditions, or to describe how they work and estimate the force that they develop. The planar models developed by Huijing and Woittiez (1984), have proved to be good enough for estimating the effect of muscle fibres slope on the force they develop. If we intend to use the muscle model for estimating the neuro-muscular control, we have to find out the link between the force they develop and their lengths or the contraction velocity (Winters and Stark 1985). Finite element models are useful when interaction between muscle fibres is taking into account (van der Linden 1998).

Basically, muscle models may be grouped into two categories: Hill-type models, which describe muscle functioning at macroscopic level using empirical relationships (Hill 1938), however confirmed by experiments, and advanced models that explain their behaviour at level (Winters and Stark 1987). A very simple model of

E. Mereuta (✉) · M. Tudoran · D. Ganea · C. Mereuta
“Dunarea de Jos” University of Galati, Galati, Romania
e-mail: emereuta@ugal.ro

muscle can be the result of surface observations and investigations and may lead to a reaction of the system other than the real. A too complex muscle model may lead to failure to achieve the expected results, owing to the large number of details.

2 Hill's Model for Muscle Force

The most used muscle model is the Hill's model. Assuming that the muscles are the actuators of the musculoskeletal system and that they are made up of fibres that generate forces and tendons that are connected to the bones, it is shown that there are factors that influence the developed force. As a result, the muscles can not be neglected when creating the biomechanical model of the human upper limb. The muscle force depends on the number of stimulated fibres and the of contraction velocity. The Hill's model is describing the relationship between maximum force developed a muscle fibre and its length (Fig. 1) or between the maximum force and contraction velocity (Fig. 2).

The force developed by a contracting muscle is:

$$f^{ce} = f^{ce}(a, v^{ce}, l^{ce}) \quad (1)$$

where: $a(t)$ describes the activation/deactivation state of the muscle; v^{ce} is the contraction velocity and l^{ce} is the muscle length.

For an isometric contraction of muscle the force maximum is corresponding to an optimal length l_{opt}^{ce} of elastic element (Fig. 1). For values greater than or smaller than this optimum value, the ability of the muscle to produce force decreases. Force–velocity relationship establishes a link between the developed muscle force of and muscle contraction velocity, at the optimal length of active fibres.

To study the kinematics of muscle contraction, we have modelled the muscle using two semi couplings, corresponding to the proximal end (the muscle origin) and distal end (the muscle insertion point), which are sliding each other.

Fig. 1 Force-length curve

$$\bar{f}^{ce} = \frac{f^{ce}}{f_{max}}$$

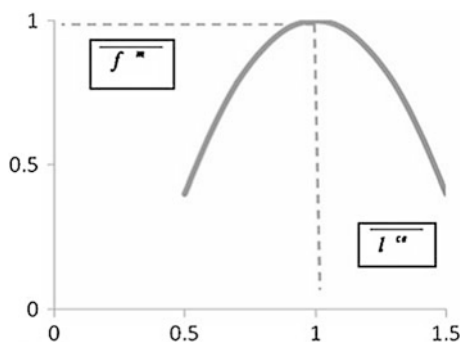
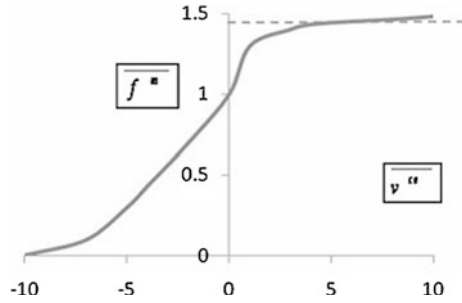


Fig. 2 Force-velocity curve

$$\overline{v}^{ce} = \frac{v^{ce}}{l_{opt}^{ce}}$$



3 Estimation of Muscle Force Using Hill’s Model

Estimation of a muscle force can be achieved using a muscle model and experimental measurements electromyography (EMG) type (Lloyd and Besier 2003). The method is not always effective because there are 38 muscles, and most of them are either small or are overlapping and their detachment in order to estimate the force developed is virtually impossible. The Hill’s model renders the possibility to estimate the force developed by the muscles, based on muscle contraction, respectively, on the muscle shortening/lengthening and on the contraction/stretching velocity. The muscle force—length curves (Chalfoun et al. 2005) highlight the fact that it is extremely important to know the length of the muscle fibre (l^M) and optimal length of the fibre (l_o^M). The muscle force is the sum of active and passive force (Fig. 3).

The maximum muscle force a can be determined as follows:

$$F_{max} = A \times \tau \tag{2}$$

where: A is the physiological cross-sectional area of the muscle; τ is the specific muscles tension.

For estimating the muscle forces parameters related to the physiology of muscles are required, such as cross-sectional area (A), the specific muscles tension (τ), the angle muscular fibre (α), the muscle length and its optimum length (Hale et al. 2011, Table 1).

The Hill’s model (Hill 1938) estimates the total force generated by the muscle–tendon unit as follows:

Fig. 3 The force–length relation (active/passive state)

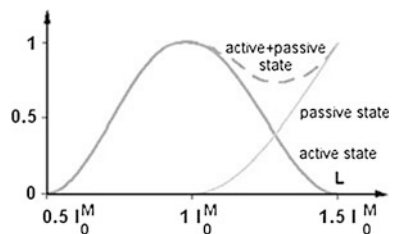


Table 1 Parameters for estimating the upper limb muscles forces

Muscle		A (cm ²)	τ (N/cm ²)	Fmax (N)	(α) (o)	(l ^M) (m)	(l _o ^M) (m)	(l _o ^M)/(l ^M)
Triceps	Long	40	58	2,320	9.1	0.246	0.099	0.402
	Lateral					0.175		0.566
	Medial					0.105		0.943
Biceps	Long	8.2		475.6	0	0.280	0.26	0.929
	Short					0.299		0.870
Brachial		14.4		835.2		0.141	0.064	0.454

$$F^M = F^{PE} + F^{CE} \tag{3}$$

where: F^M —muscle total force, F^{PE} —passive force, F^{CE} —active force.

A more general formula describing the force produced by the muscle–tendon unit was formulated by Audu and Davy (1985):

$$F^M = F^T = F^{\max} [a(t) \cdot f(l) + f_p(l)] \tag{4}$$

Walter (1999) sets out the relationship between the muscle force and its length:

$$f(\varepsilon) = \begin{cases} e^{-\left[\frac{0.9634 \times \left(1 - \frac{1}{i_a}\right)}{0.35327 \times (1 - i_a)} \right]^2} \dots i_a < 1 \\ e^{-[2.727277 \times \ln(\varepsilon + 1)]^2} \dots i_a = 1 \end{cases} \tag{5}$$

where:

$$\varepsilon = \frac{l^M - l_o^M}{l_o^M} \tag{6}$$

is the muscle relative lengthen; (l^M)—the length of muscle fibre; (l_o^M) the optimal length of the fibre corresponding to a maximum muscle force; i_a —the muscle constant (Walter 1999).

The passive elastic force of the muscles is determined using the relationship established in Walter (1999):

$$f_p(\varepsilon) = b_1 \cdot e^{b_2 \cdot \varepsilon} - b_1 \tag{7}$$

where: b_1, b_2 are muscle constants ($b_1 = 0.03; b_2 = 7$) (Hill 1938).

It has been proved (Garner and Pandy 2003) that the muscle acts efficiently within the range ($0.5 \cdot l_o^M \div 1.5 \cdot l_o^M$), meaning that $\varepsilon \in (-0.5; 0.5)$. Furthermore, starting with $1.2 \cdot l_o^M$ the muscle force is passive.

The kinematic model of the upper limb allows the estimation of the most important muscles forces, because the motion simulation has provided the length variation of the muscle fibre and thus, using data and formulas from literature we were able to assess its time variation, as well as its dependency on the contraction velocity of the muscle. We are now able to compare the motions for a normal

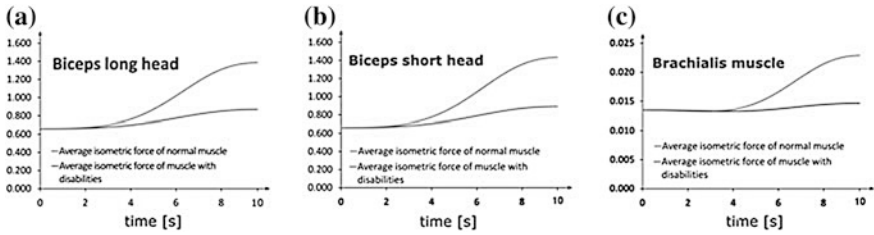


Fig. 4 Average isometric force: **a** biceps long head, **b** biceps short head, and **c** brachial

upper limb to those of a disabled one. Thus, considering the upper limb flexion, we have found that the muscles biceps long head, short head and brachial develops higher average forces (Fig. 4a–c) for a person who can perform the full motion (90°) versus a person with disabilities (45°).

We have concluded that for long head and short head biceps, at the input state of motion, there are no significant differences (Tables 2, 3). Thus, up to the 3.5 s, the difference is smaller than 5 % between the disabled and full mobility upper limbs. After this moment the differences grow to 37 % at the end of the stage.

As for the brachial muscle, we conclude that the flexion stresses a disabled upper limb 0.9 % more, after which the force is almost constant throughout the motion. Compared to the average force developed in a brachial muscles of the upper limb that can perform complete flexion, a 36 % lower force is revealed.

Similarly, the average force developed by the other muscles of the human upper limb can be determined.

Table 2 Average force in long head biceps

Time	Long head biceps		Relative shortening		Average isometric force	
	Normal	Disabled	Normal	Disabled	Normal	Disabled
0	0	0	0.079	0.079	0.661	0.661
0.125	0.000	0.000	0.079	0.079	0.661	0.661
...
10.000	-35.700	-13.814	-0.058	0.026	1.388	0.870

Table 3 Average force in short head biceps during flexion

Time	Long head biceps		Relative shortening		Average isometric force	
	Normal	Disabled	Normal	Disabled	Normal	Disabled
0	0.000	0.000	0.079	0.079	0.661	0.661
0.125	0.000	0.000	0.079	0.079	0.661	0.661
...
10.000	-37.221	-15.026	-0.064	0.021	1.436	0.891

4 Conclusions

The kinematic model is able to provide the kinematic parameters that describe the motion and the average forces developed by the most important muscles of the upper limb. The brachial muscle force can be assessed only using biomechanical models. Experimental measurement of this muscle activity using EMG cannot be done using non-invasive methods. Therefore, the kinematic model is an alternative to such invasive procedures. The muscle forces and their time variations are input data in dynamic models of the human upper limb. Starting from the average force, it is possible to determine the force magnitude, based on the maximum developed muscles force from literature (Chalfoun et al. 2005).

References

- Audu ML, Davy DT (1985) The influence of muscle model complexity in musculoskeletal motion modeling. *J Biomech Eng* 107:147–157
- Chalfoun J, Younes R, Ben-Ouezdou F (2005) Physiological muscle forces, activation and displacement prediction during free movement in the hand and forearm. *J Rob Syst* 22(11):2005
- Garner AB, Pandy MG (2003) Estimation of musculotendon properties in the human upper limb. *Ann Biomed Eng* 31:207–220
- Hale R, Dorman D, Gonzalez RV (2011) Individual muscle force parameters and fiber operating ranges for elbow flexion-extension and forearm pronation-supination. *J Biomech* 44:650–656
- Hill AV (1938) The heat of shortening and the dynamic constants of muscle. *Proc Roy Soc London* 126(B):136–195
- Huijing PA, Woittiez RD (1984) The effect of architecture on skeletal muscle performance: a simple planimetric model. *Neth J Zool* 34:21–32
- Lloyd GD, Besier FT (2003) An EMG-driven musculoskeletal model to estimate muscle forces and knee joint moments in vivo. *J Biomech* 36:765–776
- van der Linden BJJJ (1998) Mechanical modeling of skeletal muscle functioning. PhD-thesis, University of Twente, Enschede
- Walter M (1999) 3D modeling of the human upper limb including the biomechanics of joints, muscles and soft tissues. Ecole Polytechnique, Paris, p 182
- Winters JM, Stark L (1985) Analysis of fundamental human movement patterns through the use of in-depth antagonistic muscle models. *IEEE Trans Biomed Eng* 32(10):826–839
- Winters JM, Stark L (1987) Muscle models: what is gained and what is lost by varying model complexity. *Biol Cybern* 55:403–420

Formulations in Advanced Dynamics of Mechanical Systems

I. Negrean, C. Schonstein, K. Kacso and A. Duca

Abstract In the paper, in keeping with the fact that the robots are complex mechanical systems, on the basis of matrix exponentials, some notions applicable in advanced dynamics of mechanical systems, as well as variational principle from analytical mechanics will be analyzed. There will be presented the D'Alembert-Lagrange principle, written in the generalized form, and a few formulations on the Hamilton's variational principle. On the basis of these aspects, by using of important mass distribution parameters, there will be expressed the kinetic energy and first and second order of the acceleration energy, the last one into a new formulation.

Keywords Robotics · Matrix exponentials · Acceleration energy · Dynamics

1 Introduction

Within this paper the main objective consists in a few formulations about variational principle used to determine the moving differential equations for any mechanical system. But, at the beginning the geometry and kinematical equations followed by mass distribution must be established.

2 Forward Kinematics in Advanced Mechanics

On the basis of new formulations about the matrix exponentials, according to Negrean and Negrean (2001) and Negrean et al. (2008), in the following the equations of geometry and kinematical will be defined according to aspects from

I. Negrean (✉) · C. Schonstein · K. Kacso · A. Duca
Department of Mechanical Systems Engineering, Technical University of Cluj-Napoca,
Cluj-Napoca, Romania
e-mail: iuliu.negrean@mep.utcluj.ro

variational principles applied in the robot dynamics. So, the matrix exponentials and their associated transformations are included in the *MEK* algorithm, whose main steps are described in the following.

In keeping with the input data, is represented the kinematical structure of the robot, taking into study, as example the structure from Fig. 1. The matrix of the screw parameters is:

$$A_i = \begin{bmatrix} (\bar{k}_i^{(0)} \times) & \Delta_i & \bar{v}_i^{(0)} \\ 0 & 0 & 0 \end{bmatrix}; \tag{1}$$

The matrix of the nominal geometry, symbolized $M_{vn}^{(0)}$, according to Negrean et al. (2008) is defined:

$$M_{vn}^{(0)**} = \underset{(n+1) \times 9}{\text{Matrix}} \left[\bar{p}_i^{(0)T} \bar{k}_i^{(0)T} \bar{v}_i^{(0)} \right]^T, i = 1 \rightarrow n + 1 \tag{2}$$

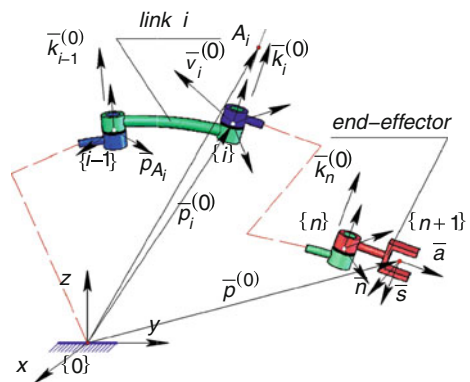
where $\bar{p}_i^{(0)T} = [x_i \ y_i \ z_i]^T$ is the position vector of the origin of the system $\{i\}$; $\bar{k}_i^{(0)} = \left(\frac{\bar{p}_{A_i}^{(0)}}{|\bar{p}_{A_i}^{(0)}|} \right)$ represents the unit vector corresponding to each driving axis (Negrean and Schonstein 2010) $i = 1 \rightarrow n$, and:

$$\bar{v}_i^{(0)} = \left(\bar{p}_i^{(0)} \times \right) \bar{k}_i^{(0)} \cdot \Delta_i + (1 - \Delta_i) \cdot \bar{k}_i^{(0)}, \tag{3}$$

where $\left(\bar{p}_i^{(0)} \times \right)$ is the skew-symmetric matrix associated to position vector $\bar{p}_i^{(0)}$ and $\Delta_i = \{1, \text{if } i = R\}; \{0, \text{if } i = T\}$ is an operator which highlights the type of the moving joint as R-rotation; T-prismatic joint.

The following notations are implemented $q_{i,j,k,m} \cdot \Delta_{i,j,k,m} = q_{i,j,k,m}^*$, $c(q_i^*) \equiv \cos(q_i^*)$; $s(q_i^*) \equiv \sin(q_i^*)$ and $\bar{\theta}_{(n+1)} = (q_i, \text{for } i = 1 \rightarrow n)^T$, representing the column vector of the generalized coordinates. The exponential of the rotation matrix is

Fig. 1 Sequence from a mechanical robot structure (MRS)



expressed, according to Negrean and Schonstein (2010), by means of the following expression as:

$$R(\bar{k}_i; q_i^*) = \exp \left[\left(\bar{k}_i^{(0)} \times \right) q_i^* \right] = I_3 \cdot c(q_i^*) + \bar{k}_i^{(0)} \times s(q_i^*) + \bar{k}_i^{(0)} + \bar{k}_i^{(0)T} [1 - c(q_i^*)] \quad (4)$$

where $\left(\bar{k}_i^{(0)} \times \right)$ is the skew-symmetric matrix associated to the unit vector belonging to every kinematical axis. In the study with matrix exponentials, to express the position, a new column vector, is established with:

$$\bar{b}_i = \left\{ I_3 \cdot s q_i + \left(\bar{k}_i^{(0)} \times \right) \cdot [1 - c(q_i^*)] + \bar{k}_i^{(0)} \cdot \bar{k}_i^{(0)T} \cdot [q_i - s(q_i^*)] \right\} \cdot \bar{v}_i^{(0)} \quad (5)$$

The exponentials for the homogeneous transformation matrix, which defining the position and orientation of frames $\{n\}$ and $\{n+1\}$ related to $\{0\}$, is:

$$T_{x0} = \prod_{i=1}^x T_{ii-1} = \begin{bmatrix} R_{x0} & \bar{p} \\ 0 & 0 & 0 & 1 \end{bmatrix}, \text{ where } x = (n; n+1) \quad (6)$$

where $R_{x0} = \exp \left[\sum_{i=1}^n \left(\bar{k}_i^{(0)} \times \right) q_i^* \right] \cdot R_{x0}^{(0)}$, and

$$\bar{p} = \sum_{i=1}^n \left\{ \left\{ \exp \left[\sum_{j=0}^{i-1} \left(\bar{k}_j^{(0)} \times \right) q_j^* \right] \right\} \cdot \bar{b}_i + \exp \left[\sum_{i=1}^n \left(\bar{k}_i^{(0)} \times \right) q_i^* \right] \bar{p}^{(0)} \delta_x \right\}, \quad (7)$$

where $\delta_x = \{(0; x=n), (1; x=n+1)\}$. The results above are used in determining the equations of forward kinematics for any robot structure, by:

$$ME(V_{i1}) = \exp \left[\sum_{j=0}^{i-1} \left(\bar{k}_j^{(0)} \times \right) q_j^* \right], \quad ME(V_{i2}) = \begin{bmatrix} I_3 & \Delta_i \cdot \left(\bar{k}_i^{(0)} \times \right) \end{bmatrix} \quad (8)$$

$$ME(V_{i3}) \equiv \{ME(V_{i31}^*) \quad ME(V_{i32}^*) \quad ME(V_{i33}^*)\} \quad (9)$$

The sub matrices from the matrix (9), according to Negrean et al. (2008, 2011), are:

$$ME(V_{i31}^*) = \begin{bmatrix} I_3 \\ [0]_{3 \times 3} \end{bmatrix}; \quad ME(V_{i33}^*) = \begin{bmatrix} [0]_{3 \times 3} \\ \exp \left[\sum_{k=i}^n \left(\bar{k}_k^{(0)} \times \right) q_k^* \right] \end{bmatrix}; \quad (10)$$

$$ME(V_{i32}^*) = \begin{bmatrix} [0]_{3 \times 3} \\ \exp \left[\sum_{m=i-1}^{k-1} \left(\bar{k}_m^{(0)} \times \right) q_m^* \cdot \delta_m \right] \end{bmatrix},$$

where $k=i \rightarrow n$, $\delta_m = \{(0; m=i-1); (1; m \geq i)\}$

In keeping with Negrean et al. (2008, 2011), the following exponential expressions are also obtained:

$$ME(J_{i1}) = \begin{bmatrix} ME(V_{i1}) & [0] \\ [0] & ME(V_{i1}) \end{bmatrix}; \quad (11)$$

$$ME(J_{i2}) = \begin{bmatrix} ME(V_{i2}) & [0] \\ [0] & I_3 \end{bmatrix}; \quad ME(J_{i3}) = \begin{bmatrix} ME(V_{i3}) & [0] \\ [0] & I_3 \end{bmatrix};$$

$${}_{[12+3(n-i) \times 1]} M_{iv\omega} = \left[M_{iv}^T \Delta_i \cdot \bar{k}_i^{(0)T} \right]^T, \quad M_{iv} = \left(\bar{v}_i^{(0)T} \bar{b}_k^T \bar{p}_n^{(0)T} \right) \quad (12)$$

The expression (12) is the column vector of screw parameters, as well as position and orientation parameters of the robot's end-effector.

The absolute values for angular and linear velocities and accelerations of first and second order, corresponding to any kinetic link ($i = 1 \rightarrow n$), are:

$$0_{\omega_i} \equiv \sum_{j=1}^i \left\{ \exp \left[\sum_{k=1}^{j-1} \left(\bar{k}_k^{(0)} \times \right) \cdot q_k^* \right] \cdot \bar{k}_j^{(0)} \cdot \dot{q}_j \cdot \Delta_j \right\} \quad (13)$$

$$0_{\sigma_i} = \sum_{j=1}^i [ME(V_{j1}) \cdot \dot{q}_j + ME(\dot{V}_{j1}) \cdot \dot{q}_j] \cdot \bar{k}_j^{(0)} \cdot \Delta_j \quad (14)$$

$$0_{\bar{v}_i} = \sum_{j=1}^i \left[\prod_{k=1}^3 ME(V_{jk}) \right] \cdot M_{jv} \cdot \dot{q}_j \quad (15)$$

$${}^0\dot{\bar{v}}_i = \sum_{j=1}^i \left\{ \prod_{k=1}^3 ME(J_{jk}) \cdot M_{jv} \cdot \dot{q}_j + \frac{d}{dt} \left\{ \left[\prod_{k=1}^3 ME(J_{jk}) \right] \cdot M_{jv} \right\} \cdot \dot{q}_j \right\} \quad (16)$$

$${}^0\ddot{\omega}_i = \sum_{j=1}^i [ME(V_{j1}) \cdot \ddot{q}_j + 2 \cdot ME(\dot{V}_{j1}) \cdot \dot{q}_j + ME(\ddot{V}_{j1}) \cdot \dot{q}_j] \cdot \bar{k}_j^{(0)} \cdot \Delta_j \quad (17)$$

$${}^0\dot{\bar{v}}_i = \sum_{j=1}^i \left\{ \prod_{k=1}^3 ME(J_{jk}) \cdot M_{jv} \cdot \ddot{q}_j + 2 \cdot \frac{d}{dt} \left\{ \prod_{k=1}^3 ME(J_{jk}) \cdot M_{jv} \right\} \cdot \dot{q}_j \right. \\ \left. + \frac{d^2}{dt^2} \left\{ \prod_{k=1}^3 ME(j_{jk}) \cdot M_{jv} \right\} \cdot \dot{q}_j \right\} \quad (18)$$

3 Fundamental Notions in the Advanced Dynamics of Robots

Among the notions in robot's advanced mechanics is the kinetic energy, which is compulsively included in the Lagrange—Euler equations devoted to the dynamic control functions, according to Negrean et al. (2008, 2011), Negrean and

Schonstein (2010), Ardema (2006), Romyantsev (2000). The dynamics equations for holonomic and nonholonomic mechanical systems can be also determined by means of the acceleration energy of first and second order. In the view of this, is taken into study a kinetic link from MRS, as presented in Fig. 2. The link contains an infinity of elementary mass, noted dm , which are continuously distributed, its position with respect to frame $\{i\}$ and $\{0\}$ is defined by the vector ${}^{(0)}i\bar{r}_i$.

Kinetic energy in explicit form. Performing a few transformations, the König's theorem for the kinetic energy is determined as presented below:

$$E_K^I = \frac{1}{2} \cdot M_j \cdot {}^j \bar{v}_{C_j}^T \cdot {}^j \bar{v}_{C_j} + \frac{1}{2} \cdot {}^j \bar{\omega}_j^T \cdot {}^j I_j^* \cdot {}^j \bar{\omega}_j. \tag{19}$$

where, the velocity of mass center is:

$${}^j \bar{v}_{C_j} = {}^j \bar{v}_j + {}^j \bar{\omega}_j \times {}^j \bar{r}_{C_j}; \tag{20}$$

and ${}^j I_j^*$ represents the inertial tensor in the mass center, ${}^j \bar{r}_{C_j}$ being the position vector of the mass center.

Kinetic Energy in the Matrix Form. After a few transformations, the matrix expression of the kinetic energy, finally, is defined as below:

$$E_k(\bar{\theta}; \dot{\theta}) = \frac{1}{2} \sum_{i=1}^n \sum_{j=1}^n M_{ij} \cdot \dot{q}_i \cdot \dot{q}_j = \frac{1}{2} \cdot \dot{\theta}^T \cdot M(\bar{\theta}) \cdot \dot{\theta} \tag{21}$$

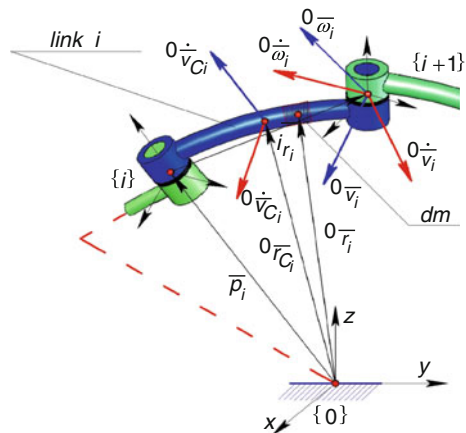
where the inertia matrix (mass matrix) is defined as:

$$M(\bar{\theta}) = \underset{(n \times n)}{\text{Matrix}} \{ M_{ij}, i = 1 \rightarrow n, j = 1 \rightarrow n \}. \tag{22}$$

and:

$$M_{ij} = \sum_{k=\max(i,j)}^n \text{Trace} \{ A_{ki} \cdot {}^k I_{psk} \cdot A_{kj}^T \}$$

Fig. 2 Sequence from a MRS



$$M_{ij} = M_{ji} = \sum_{k=\max(i;j)}^n Tr \left\{ A_{kj}^T = \left\{ \left\{ \exp \left\{ \sum_{i=0}^{j-1} A_i \cdot q_i \right\} \right\} \cdot A_j \left\{ \exp \left\{ \sum_{l=j}^k A_l \cdot q_l \right\} \right\} \cdot T_{k0}^{(0)} \right\}^T \right\} \quad (23)$$

Explicit form for the acceleration energy of first order. The dynamics equations for holonomic and nonholonomic mechanical system with (n) d.o.f., (Fig. 2) for example mechanical robot structure, can be also expressed by means of the acceleration energy of first order, developed in Negrean et al. (2008, 2011), Negrean and Schonstein (2010):

$$E_A^{(1)} = \frac{1}{2} \int \dot{v}_i^2 \cdot dm = \frac{1}{2} \int i\dot{v}_i^T \cdot i\dot{v}_i \cdot dm; \quad (24)$$

$$E_A^{(1)i} = \frac{1}{2} \cdot M_i \cdot i\dot{v}_{C_i}^T \cdot i\dot{v}_{C_i} + \frac{1}{2} \cdot i\dot{\omega}_i^T \cdot iI_i^* \cdot i\dot{\omega}_i + i\dot{\omega}_i^T \cdot (i\bar{\omega}_i \times iI_i^* \cdot i\dot{\omega}_i) + \frac{1}{2} \cdot i\bar{\omega}_i^T \cdot \left[i\bar{\omega}_i^T \cdot Trace \left(iI_{pi}^* \right) \cdot i\bar{\omega}_i - i\bar{\omega}_i^T \cdot iI_{pi}^* \cdot i\bar{\omega}_i \right] \cdot i\bar{\omega}_i \quad (25)$$

In the above equations can be remarked the mass distribution properties, where M_i is the mass corresponding to each kinetic link of the robot, iI_i^* which is the axial centrifugal inertia tensor and iI_{pi}^* the inertia tensor planar centrifugal that characterizes the entire kinetic assembly (i), relative to the frame $\{i\}$, applied in the mass center of each link C_i . In the same expression, $i\dot{v}_{C_i}$ and $i\ddot{v}_{C_i}$ are the velocity and the acceleration of mass center of the kinetic link (i).

The acceleration energy of second order. The mechanical displacements of the material system, which are including the robots, are characterized with higher order of accelerations, which are considered kinematically and dynamically fast motions. During this type of motions, obvious are appearing high order of accelerations. Therefore, the dynamic analysis is requiring higher order differential, having at least order three. Corresponding to those equations, in the following is presented the new formulation for the acceleration energy of second order:

$$E_A^{(2)} = \frac{1}{2} \cdot \int i\ddot{v}_i^T \cdot i\ddot{v}_i \cdot dm \quad (26)$$

$$E_A^{(2)} = \frac{1}{2} \cdot M \cdot i\ddot{v}_{C_i}^T \cdot i\ddot{v}_{C_i} + \frac{1}{2} \cdot i\ddot{\omega}_i^T \cdot iI_i^* \cdot i\ddot{\omega}_i + 2 \cdot i\bar{\omega}_i^T \cdot \left(i\ddot{\omega}_i \times iI_{pi}^* \cdot i\ddot{\omega}_i \right) + i\dot{\omega}_i^T \cdot \left(i\ddot{\omega}_i \times iI_{pi}^* \cdot i\bar{\omega}_i \right) - i\bar{\omega}_i^T \cdot \left(i\dot{\omega}_i^T \cdot iI_i^* \cdot i\bar{\omega}_i \right) \cdot i\bar{\omega}_i + 2 \cdot i\dot{\omega}_i^T \cdot \left(i\bar{\omega}_i^T \cdot iI_i^* \cdot i\bar{\omega}_i \right) \cdot i\bar{\omega}_i + i\bar{\omega}_i^T \cdot \left[i\dot{\omega}_i^T \cdot \left(i\dot{\omega}_i \times iI_{pi}^* \cdot i\bar{\omega}_i \right) \right] \cdot i\bar{\omega}_i + \frac{1}{2} \cdot i\bar{\omega}_i^T \cdot \left[i\bar{\omega}_i^T \cdot \left(i\bar{\omega}_i^T \cdot iI_i^* \cdot i\bar{\omega}_i \right) \cdot i\bar{\omega}_i \right] \cdot i\bar{\omega}_i; \quad (27)$$

where $i\ddot{v}_{C_i}$ is the acceleration of second order of mass center of the kinetic link (i), and $i\ddot{\omega}_i$ represents the angular acceleration of second order of the kinetic link.

4 Differential Equations of Motion

Considering aspects from Fig. 2, the D'Alembert-Lagrange's principle for multi-body systems, in which are included the robots, is according to:

$$\begin{aligned} & \sum_{i=1}^n ({}^i\bar{F}_i^* - M_i \cdot {}^i\dot{v}_{C_i}) \cdot \delta^i\bar{r}_{C_i} \\ & + \sum_{i=1}^n ({}^i\bar{N}_i^* + {}^i\bar{r}_{C_i} \times {}^i\bar{F}_i^* - {}^iI_i^* \cdot {}^i\dot{\omega}_i - {}^i\bar{\omega}_i \times {}^iI_i^* \cdot {}^i\bar{\omega}_i) \cdot \delta^i\bar{\Omega}_i = 0 \end{aligned} \quad (28)$$

where ${}^i\bar{F}_i^*$ and ${}^i\bar{N}_i^*$ are the active forces and theirs moments with respect to mass center. In the same expression, the virtual linear and angular displacements are:

$$\delta^i\bar{r}_{C_i} = \sum_{j=1}^k \frac{\partial \bar{r}_{C_i}}{\partial q_j} \cdot \delta q_j; \quad \delta^i\bar{\Omega}_i = \sum_{j=1}^k \frac{\partial \bar{\Omega}_i}{\partial q_j} \cdot \Delta_j \cdot \delta q_j \quad (29)$$

Applying differential transformations in (28), results:

$$\frac{d}{dt} \left(\frac{\partial E_K}{\partial \dot{q}_j} \right) - \frac{\partial E_K}{\partial q_j} + Q_g^j = Q_m^j + \sum_{i=1}^p \lambda_i \cdot a_{ij}, \quad (30)$$

where Q_m^j are generalized driving forces, which are characterizing every driving joint of the general robot structure and $\sum_{i=1}^p \lambda_i \cdot a_{ij}$ are the terms typical to differential constraints that characterizes the nonholonomic structures. In the same expression, the term Q_g^j represents the generalized gravitational force, defined as:

$$Q_g^j = \sum_{j=1}^k M_j \cdot \bar{g}^T \cdot A_{ji} \cdot {}^j\bar{r}_{C_j} \quad (31)$$

where M_j is the mass of kinetic element j , and A_{ji} is defined with:

$$A_{ij} = \left\{ \exp \left\{ \sum_{k=0}^{i-1} A_k \cdot q_k \right\} \right\} \cdot A_k \cdot \left\{ \exp \left\{ \sum_{l=1}^j A_l \cdot q_l \right\} \right\} \cdot T_{i0}^{(0)} \quad (32)$$

and $\bar{g}^T = (g \cdot \bar{k}_0^T \ 0)^T$, \bar{k}_0 being the unit vector of the vertical axis, belonging to the fixed frame $\{0\}$. The equations (30) are known as Lagrange-Euler's type equations.

The integral principle can be reformulated, based on acceleration energy $E_A^{(1)}$ as follows in the above expressions, for $j = 1 \rightarrow k$:

$$\int_{t_0}^{t_1} \left[\int_{t_0}^{t_1} \left(\int_{t_0}^{t_1} \delta E_A^{(1)} \cdot dt \right) \cdot dt + \sum_{i=1}^n [{}^i \bar{F}_i^* \cdot \delta \bar{r}_{C_i} + ({}^i \bar{N}_i^* + {}^i \bar{r}_{C_i} \times {}^i \bar{F}_i^*) \cdot \delta {}^i \bar{\Omega}_i] \right] \cdot dt = 0 \quad (33)$$

Performing some differential transformations, the integral principle from previous relation becomes:

$$\frac{\partial E_A^{(1)}}{\partial \ddot{q}_j} + Q_g^j = \frac{d}{dt} \left(\frac{\partial E_K}{\partial \dot{q}_j} \right) - \frac{\partial E_K}{\partial q_j} + Q_g^j = Q_m^j, j = 1 \rightarrow k \quad (34)$$

where the first term, for nonholonomic system, is equivalent with:

$$\frac{\partial E_A^{(1)}}{\partial \ddot{q}_j} + Q_g^j = Q_m^j + \sum_{i=1}^p \lambda_i \cdot a_{ij} \quad (35)$$

The expression (35), represents a generalization of the integral principle based on acceleration energy which is further used for determining the differential equations of motion for any type of mechanical structure (Negrean et al. 2008; Negrean and Schonstein 2010; Park 1994).

Having as starting equation the expression (34), after differential and integral transformations, there is obtained the new linkage relation between the acceleration energy of first order and kinetic energy, as:

$$E_A^{(1)}(\bar{\theta}; \dot{\theta}; \ddot{\theta}) = \frac{1}{2} \cdot \sum_{i=1}^n \frac{\partial^2 E_K}{\partial \dot{q}_i^2} \cdot \dot{q}_i^2 + \sum_{i=1}^{n-1} \sum_{j=i+1}^n \frac{\partial^2 E_K}{\partial \dot{q}_i \partial \dot{q}_j} \cdot \dot{q}_i \cdot \dot{q}_j + \sum_{i=1}^n \sum_{j=1}^n \frac{\partial^2 E_K}{\partial \dot{q}_i \partial q_j} \cdot \dot{q}_i \cdot \dot{q}_j - \sum_{i=1}^n \frac{\partial E_K}{\partial q_i} \cdot \dot{q}_i. \quad (36)$$

The third order differential expressions. Following to differential transformations, applied on D'Alembert-Lagrange principle, and considering the acceleration energy of first and second order, the new expressions are resulting:

$$\frac{\partial E_A^{(2)}}{\partial \ddot{q}_j} + \frac{\partial E_A}{\partial \dot{q}_j} + Q_g^j = \frac{dQ_m^j}{dt} = Q_m^j, j = 1 \rightarrow k \quad (37)$$

Applying the time derivative on (33), results:

$$\frac{d}{dt} \left(\frac{\partial E_A^{(1)}}{\partial \ddot{q}_j} \right) + Q_g^j = \frac{dQ_m^j}{dt} = Q_m^j, j = 1 \rightarrow k \quad (38)$$

In keeping with the previous expressions, there can be written the following equivalence:

$$\left(\frac{\partial E_A^{(2)}}{\partial \dot{q}_j}\right) = \frac{d}{dt} \left(\frac{\partial E_A^{(1)}}{\partial \dot{q}_j}\right) - \frac{\partial E_A^{(1)}}{\partial q_j}, \quad j = 1 \rightarrow k \tag{39}$$

The previous expressions are representing a system of third order of differential equations. In order to integrate these equations, the initial conditions are referencing to coordinates, velocities and accelerations.

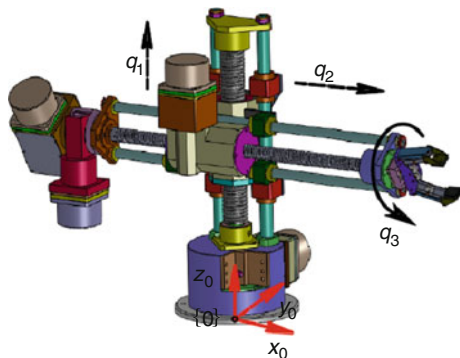
5 Applications

This section is devoted to establish the kinematic control functions, dynamics equations and driving torque corresponding to the rotational joint of a 2TR-type serial structure, belonging to a robot structure as shown in the Fig. 3.

It is considered that the main task of the 2TR-type structure is to handle a cylindrical piece, whose characteristics are known. The process consists by seven working sequences $j = 1 \rightarrow 7$, each being divided into three segments de noted $k = 1 \rightarrow 21$. The different phases of the technological process are representing seven configurations, in each one being observed the independent and distinct action of each driving joint $q_i, i = 1 \rightarrow 3$. Hence the study is oriented in determining of the driving force, to execute the task, knowing the parameters, as the numerical values for the time and the duration, which are characterizing the process. The analysis of the 2TR—type serial structure was extended in dynamics. Thus, the kinetic energy, the first and second orders acceleration energy, based on expressions (19), (25) and (27) for the 2TR studied structures are:

$$E_{Kjk}(\tau) = \frac{1}{2} \left[M_{10} \cdot \dot{q}_{1jk}^2(\tau) + M_{11} \cdot \left(\dot{q}_{1jk}^2(\tau) + \dot{q}_{2jk}^2(\tau) \right) + M_{12} \cdot \left(\dot{q}_{1jk}^2(\tau) + \dot{q}_{2jk}^2(\tau) \right) + I_x^* \cdot \dot{q}_{3jk}^2(\tau) \right] \tag{40}$$

Fig. 3 The 2TR serial structure



$$E_{Ajk}^{(1)}(\tau) = \frac{1}{2} \cdot \left[M_{10} \cdot \ddot{q}_{1jk}^2(\tau) + M_{11} \cdot \left(\ddot{q}_{1jk}^2(\tau) + \ddot{q}_{2jk}^2(\tau) \right) + M_{12} \cdot \left(\ddot{q}_{1jk}^2(\tau) + \ddot{q}_{2jk}^2(\tau) \right) + I_x^* \cdot \left(\ddot{q}_{3jk}^2(\tau) + \dot{q}_{3jk}^4(\tau) \right) \right]; \quad (41)$$

$$E_{Ajk}^{(2)}(\tau) = \frac{1}{2} \cdot \left[M_{10} \cdot \ddot{q}_{1jk}^2(\tau) + M_{11} \cdot \left(\ddot{q}_{1jk}^2(\tau) + \ddot{q}_{2jk}^2(\tau) \right) + M_{12} \cdot \left(\ddot{q}_{1jk}^2(\tau) + \ddot{q}_{2jk}^2(\tau) \right) + I_x^* \cdot \left(\ddot{q}_{3jk}^2(\tau) - 2 \cdot \ddot{q}_{3jk}^3(\tau) \cdot \dot{q}_{3jk}^3(\tau) + \dot{q}_{3jk}^6(\tau) \right) \right]. \quad (42)$$

where M_{10} , M_{11} and M_{12} are the mass of the kinetic elements, I_x^* represents the axial inertia moment on x axis, and (τ) being the actual value of the time parameter. Considering the aspects from (Negrean et al. 2008) concerning the generalized active and friction forces and by applying some transformations in the expressions (35) finally are obtained the differential equations of second order for 2TR serial robot, as:

$$\begin{cases} (M_{10} + M_{11} + M_{12}) \cdot (\ddot{q}_{1jk}(\tau) + g) = Q_m^{1jk}(\tau) \\ (M_{10} + M_{11}) \cdot (\ddot{q}_{2jk}(\tau) + \mu_1 \cdot g) = Q_m^{2jk}(\tau) \\ I_x^* \cdot \ddot{q}_{3jk}(\tau) + \frac{d_2}{2} \cdot \mu_2 \cdot M_{12} \cdot g = Q_3^{3jk}(\tau). \end{cases} \quad (43)$$

In the above equations, μ_1 , μ_2 and d_2 are the dry friction coefficients, respectively the diameter of the driving joints, and g is the absolute value of the gravitational acceleration. The expressions (43) are highlighting the generalized driving forces that are characterizing the dynamic behavior of the 2TR structure. On the basis of expressions or (38), for the 2TR robot, there are obtained the following:

$$\begin{cases} (M_{10} + M_{11} + M_{12}) \cdot \ddot{q}_{1jk}(\tau) = \dot{Q}_m^{1jk}(\tau) \\ (M_{11} + M_{12}) \cdot \ddot{q}_{2jk}(\tau) = \dot{Q}_m^{2jk}(\tau) \\ I_x^* \cdot \left(\ddot{q}_{3jk}(\tau) - \frac{1}{2} \cdot \dot{q}_{3jk}^3(\tau) \right) = \dot{Q}_m^{3jk}(\tau) \end{cases} \quad (44)$$

representing the generalized yank in each of the $i = 1 \rightarrow 3$ driving joint. They having a great signification when are taken into account the sudden motions, the reversing, or the suddenly stops, which conducts at higher order functions of the driving forces with deep implications upon the dynamic behavior of the mechanical robot structure.

6 Conclusions

In the paper, by using the matrix exponentials important notions in advanced dynamics of mechanical systems, as well as variational principle from analytical mechanics have been analyzed. An advantage of the exponentials is that are conducting to a compact representation of the necessary information for defining the direct geometry, kinematics and dynamics of a mechanical system with an

open or close chain. A few aspects about the mass distribution parameters have been also defined, essentially in expressing of kinetic energy and acceleration energy of first and second order, the last two into a new formulation. Considering these aspects and using the D'Alembert-Lagrange principle, written in the generalized form, a few new formulations on the integral principle based on the acceleration energy of first and second order, as well as the differential equations of third order have been described. In the final part of this paper the formulations have been applied on the 2TR serial robot structure, belonging to the hybrid robot, finally being determined the dynamics equations. For the same structure it's been analyzed the dynamic control functions, by expressing the kinetic energy and acceleration energy of first and second order. Also, in the paper have been presented, shortly a few advanced notions in mechanics as generalized jerk, or yank, having a great signification when are taken into account the suddenly motions. The example above shows the application of notions and principles demonstrated in the paper.

References

- Ardema MD (2006) Analytical dynamics theory and applications, ISBN 978-0-306-48681-4. Springer, US, pp 225–243, 245–259
- Negrean I, Negrean DC (2001) Matrix exponentials to robot kinematics. 17th international conference on CAD/CAM, robotics and factories of the future, vol 2. Durban, South Africa, pp 1250–1257
- Negrean I, Schonstein C (2010) Formulations in robotics based on variational principles. In: Proceedings of AQTR 2010 IEEE-TTTC, international conference on automation, quality and testing, robotics, ISBN 978-1-4244-6722-8. Cluj-Napoca, Romania, pp 281–286
- Negrean I, Duca A, Negrean DC, Kacso K (2008) Mecanică Avansată în Robotică, ISBN 978-973-662-420-9. UT Press, Cluj-Napoca. Available at <http://users.utcluj.ro/~inegrean>
- Negrean C, Schonstein C, Kacso K, Duca A (2011) Matrix exponentials and differential principles in the dynamics of robots. The 13th world congress in mechanism and machine science, Guanajuato, Mexico, 19–25 June 2011. http://somim.org.mx/conference_proceedings/pdfs/A12/A12_474.pdf
- Park FC (1994) Computational aspects of the product-of-exponentials formula for robot kinematics. IEEE Trans Autom Control
- Rumyantsev V (2000) Forms of Hamilton's Principle for nonholonomic systems. Mech, Autom Control Rob 2(10)

Gray-Box Modeling and Closed-Loop Temperature Control of a Thermotronic System

C.-R. Rad, O. Hancu and C. Lapusan

Abstract Accurate control of the temperature is essential in many modern applications like: medical devices, industrial plants, cars, office equipment's etc. The demands of high performances implies the use of new approaches in the designing process, which allow a better understanding of the design system and the development of more complex control strategies. In the paper is presented a new approach for modeling a thermotronic system using a gray-box modeling technique. The obtained model is used to develop a closed loop control strategy using MATLAB/Simulink environment. The simulation results are validated using dSPACE dS1104 platform. Finally, both simulation and experimental results are presented and discussed.

Keywords Thermotronics · Control · Simscape · Gray-box modeling

1 Introduction

Mechatronics is defined as the science of motion control (Van Brussel 1996) and its extension to other areas is known as: *hydronics* in the field of intelligent hydraulics, *pneutronics* in the field of intelligent pneumatics, *thermotronics*, in the field of thermal technique, *autotronics*, in the field of intelligent automotives, *agrotronic* in the field of intelligent agriculture, etc. These terms are the result of information integration in hydraulic, pneumatic, thermal, automotive, and agriculture products, leading to new research areas strongly related to mechatronics (Dumbrava 2009; Nicolae 2008).¹

¹ http://www.odelco.co/products/viewall_qpSi.html—thermotronics

C.-R. Rad (✉) · O. Hancu · C. Lapusan
Department of Mechatronics and Machine Dynamics, Technical University of Cluj-Napoca,
Cluj-Napoca, Romania
e-mail: ciprian.rad@mdm.utcluj.ro

Thermotronic system is the result of integration of three main fields in engineering: thermodynamics-heat transfer-fluid mechanics, electronics-control science and computer science. Thermotronics focuses on optimal design and control of thermal systems.

The term is well established in industry where many companies adopted it to describe: refrigeration systems, air conditioning systems, heating systems, compressed air thermodynamics systems, etc.

Temperature is one of the most important parameters in thermal systems and temperature controllers are found in many environments like: homes, cars, office equipment, and in many industrial processes. Accurate control of the temperature is essential in many applications. In some ones, an accuracy of around 5–10 °C may be acceptable, but there are also applications which require better than ± 1 °C accuracy. Accurate measurement of the temperature is not easy and to obtain accuracies better than 0.5 °C great care is needed. Errors occur due to several sources, such as: sensor nonlinearities, sensor time constant, sensor calibration errors, sensor self-heating, temperature gradients, poor thermal contact, and materials thermal properties (Dogan 2002). Taking this into account, it is clear that designing a good temperature controller requires a good mathematical model of the system.

Because the source of many errors is related to sensor, a good description of the sensor must also be taken into account. System modeling is a difficult task, since it requires experience, practice, and intuition (de Canete et al. 2011). A common approach to obtain the system model is by using system identification techniques. Two types of models are common in the field of system identification: gray-box and black-box models (Ljung 1999). Gray-box modeling is a combination of white-box and black-box modeling techniques, where the parameters of a first-principle mathematical model are estimated using experimental collected data.

In this paper, a practical grey-box modeling technique and a closed-loop temperature control of a thermotronic system is presented. The mathematical model is obtained using Simscape library from MATLAB/Simulink. Multi-domain modeling, simulation, and control can be performed using Simscape. Simscape technology lets you create a network representation of the system, based on the Physical Network approach,² which differs from the standard Simulink modeling approach and is particularly suited to simulating systems that consist of real physical components. According to this approach, any systems (electric, mechanic, hydraulic, pneumatic, thermic) is represented as consisting of functional elements that interact with each other by exchanging energy through their ports by a set of two variables: through and across variables, the product of both being power (de Canete et al. 2011). For thermotronic systems, this pair of two variables consists of: heat flow rate (through) and temperature (across). Moreover, Simscape models can be used to perform Hardware-in-The-Loop (HIL) simulations using a xPC Target (Alur 2005).

² http://www.mathworks.com/tagteam/63431_Physical_Networks_In_Simscape_PDF.pdf.

To be valid, the model response must match the real system response. In order to accomplish that, the model parameters are estimated using Simulink Design Optimization Tool (SDO)³ based on a set of experimental data. The parameters are then validated using a second set of experimental data. Also, the model is used for model-based control design to implement two control algorithms.

The rest of the paper is organized as follow: in part two the thermotronic system is presented, while in part three the mathematical model of the system is presented and implemented using Simscape block library; also the model parameters are identified using SDO tool. In part four, based on the obtained model, two controllers (ON-OFF and PI) are designed to meet the performance specifications. Both, simulation and experimental results are presented and discussed. Finally, part five ends up with the conclusion and further research investigations.

2 Thermotronic System

Figure 1 presents the studied system. The main components of the system are: a plastic chamber, a temperature sensor (NTC thermistor), a heat source (12 V, 5 W light bulb), a thermocouple for measuring ambient temperature, and a dS1104 DAQ board assembled in a PC. It's an electronic board specially designed to digital control development and data acquisition. The system will be interfaced with the board through ADC and DAC channels. Also the developed control algorithms will be tested using this board. Table 1 presents the main parameters of the system.

It is important to note that the chamber was considered to be from plastic, but inside and outside the plastic chamber there are also other elements made from different types of materials. This influences the thermal capacitance of the system. Next, the mathematical model of the system will be presented.

3 Mathematical Modelling

3.1 Chamber Mathematical Model

The chamber dynamics can be described starting from the conservation of energy principle:

$$\frac{dE_{in}}{dt} - \frac{dE_{out}}{dt} = \frac{dE_{stored}}{dt} \quad (1)$$

³ <http://www.mathworks.com/products/sl-design-optimization/index.html>.

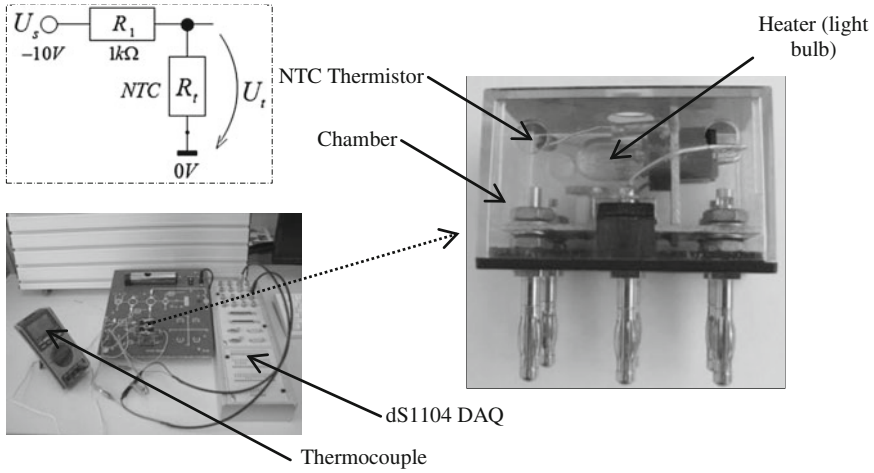


Fig. 1 Thermotronic system

Table 1 Thermotronic system parameters

Parameter	Value	Description
U_s (V)	-10	Voltage divider input voltage
R_1 (Ω)	1,000	Resistor R_1
R_t (Ω)	$f(\theta)$	Thermistor resistance as a function of temperature
R_{25} (Ω)	1,000	Thermistor resistance at 25 °C
β (K)	3,730	Thermistor β coefficient
τ_c (s)	20	Thermistor thermal cooling time constant (in air)
δ_{th} (W/K)	$7.5e-3$	Thermistor dissipation factor (in air)
U_h (V)	0-12	Heater input voltage

Energy entering the chamber can be described as:

$$q_{in}(t) = P_h \cdot \eta = U_h \cdot i_h \cdot \eta = U_h \cdot \frac{U_h}{R_h} \cdot \eta = \frac{U_h^2}{R_h} \cdot \eta \quad (2)$$

where:

$q_{in}(t)$ = thermal power entering the chamber (W), P_h = heater input electric power (W), U_h, i_h, R_h = heater input: voltage (V), current (A) and resistance (Ω), η = energy conversion efficiency.

Energy leaving the chamber can be described as:

$$q_{out}(t) = \frac{1}{R_{ch}}(\theta - \theta_{amb}) = k_2 \cdot A_{wall}(\theta - \theta_{amb}) \quad (3)$$

where:

$q_{out}(t)$ = thermal power leaving the chamber (W), R_{ch} = thermal resistance (K/W), k_2 = convective heat transfer coefficient (W/(m²*K)), A_{wall} = convective heat transfer area (m²).

Stored energy can be described as:

$$\frac{dE_{stored}}{dt} = C \frac{d\theta}{dt} = m_{wall} \cdot c_p \frac{d\theta}{dt} = \rho \cdot V \cdot c_p \frac{d\theta}{dt} \quad (4)$$

where:

C = chamber thermal capacitance (J*K), m_{wall} = material mass (kg), c_p = material specific heat (J/kg/K), ρ = density (kg/m³), V = volume (m³).

Introducing Eqs. (2–4) in (1), the dynamics of the chamber can be described as follows:

$$C \frac{d\theta}{dt} = [q_{in}(t) - q_{out}(t)] = \left[\frac{U_h^2}{R_h} \cdot \eta - k_2 \cdot A_{wall}(\theta - \theta_{amb}) \right] \quad (5)$$

3.2 Sensor Mathematical Model

The system has a NTC thermistor for measuring the temperature. NTC thermistors electrical resistance decreases with increasing temperature and the resistance–temperature relationship is very non-linear (Dogan 2002). Some thermistor manufacturers give the resistances of their devices at 25 °C and they also provide a thermistor temperature constant denoted by β (Dogan 2002). Taking this into account, two equations fully describe the dynamics of the sensor. Variation of the thermistor resistance vs. temperature is given by Eq. 6 and temperature variation is governed by the Eq. 7.

$$R_t(\theta) = R_{25} \cdot e^{(\beta(1/T_t - 1/T_{25}))} \quad (6)$$

$$q_{in} = m \cdot c \frac{d\theta}{dt} = \tau_c \cdot \delta_{th} \frac{d\theta}{dt} \quad (7)$$

where:

$q_{in} = \frac{1}{R_{th}}(\theta - \theta_{chamber}) = k_1 \cdot A_{th}(\theta - \theta_{chamber})$, R_t, R_{25}, T_t, T_{25} = thermistor resistance (Ω), thermistor resistance at 25 °C (Ω), thermistor actual temperature, temperature in (K) at 25 °C, R_{th}, k_1, A_{th} = thermal resistance, convective heat transfer coefficient (W/(m²*K)), convective heat transfer area (m²).

Equations (6–7) will be used to model the sensor. To calculate thermistor temperature from the real system, some extra steps need to be performed. Figure 1 presents the electric circuit of the thermistor. The circuit is a simple voltage

divider where the measured voltage U_t across the thermistor is used to calculate the resistance using Eq. 8. The temperature can be calculated rewriting Eq. 6 as 9.

$$U_t = U_s \frac{R_t}{R_1 + R_t} \Rightarrow R_t = \frac{U_t \cdot R_1}{U_s - U_t} \quad (8)$$

$$T_t = \frac{1}{1/\beta \cdot \ln(R_t/R_{25}) + 1/T_{25}} \quad (9)$$

3.3 Simscape Model

One way to obtain the mathematical model of the system is by implementing Eqs. (5–9) in Simulink using standard blocks. In this paper a more practical way to obtain the model will be presented by using physical blocks from Simscape library. This method is far more intuitive for engineers because the system can be described using physical components. The con between two components is not a mathematical connection, but a physical one. Figure 2a presents the Simscape model of the system implemented using thermal and electrical blocks from Simscape foundation library. Each block can be configured separately using his predefined parameters. For example, thermistor input voltage (U_s) is represented introduced in the model into the DC voltage source block while m_{wall} , c_p , θ_{amb} into the thermal mass block. The following assumptions were made:

- thermal capacitance of the system includes only the plastic material properties; it was considered that the plastic is the most important material that influences the system response;
- there is a free convection heat transfer;
- heater (light bulb) is modeled as an ideal flow source, the ambient temperature as an ideal temperature source, and the heat transfer between chamber interior-exterior and between chamber interior-thermistor as a convective heat transfer;

Sensor element (thermistor) can be found in SimElectronics library; thermal port of the sensor is connected to the interior chamber temperature, while electric ports to the voltage divider circuit. Thermistor voltage is measured through a voltmeter block and then converted into temperature through MATLAB function block (Eqs. 8–9). While some parameters of the system can be measured or approximated, other like: convective heat transfer coefficients, thermal mass, specific heat, thermistor and chamber convective areas, and efficiency conversion between heater electric input energy and thermal output energy must be estimated. Figure 2b presents the comparative response of Simscape model and analytical model (Eqs. 5–9) for a set of parameters. Next part presents the procedure for estimating the mentioned parameters for the real system.

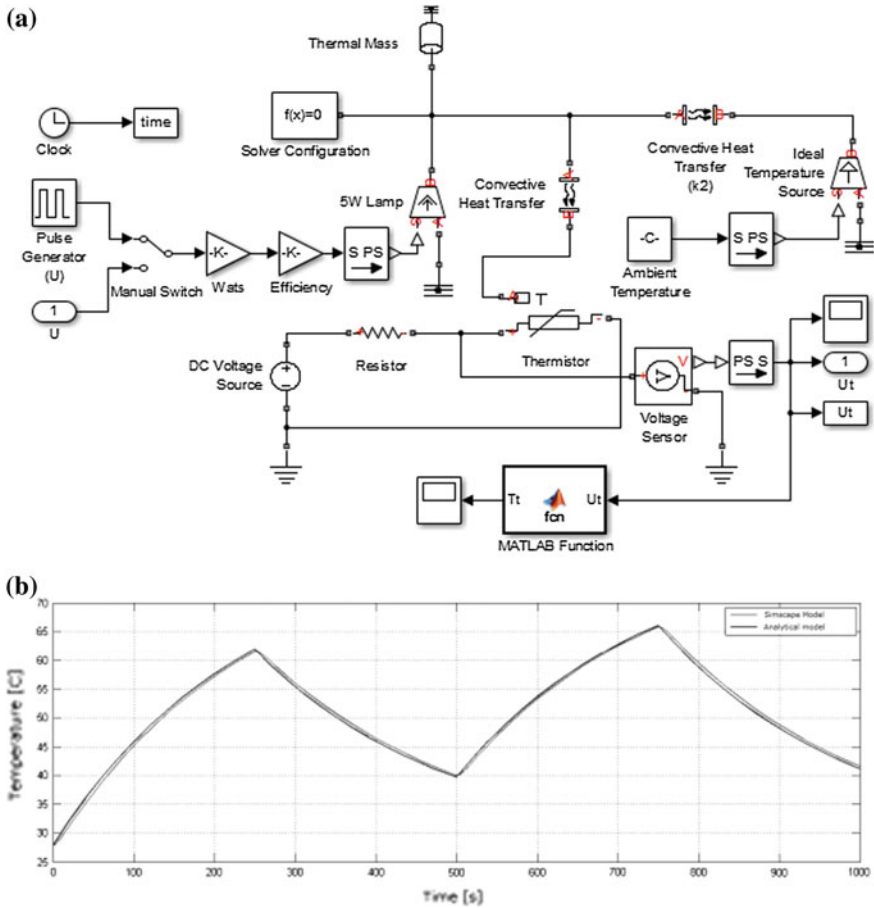


Fig. 2 Simscape model

3.4 Estimating Model Parameters

In this part, the procedure for estimating the model parameters is presented. The performance of the controller is directly influenced by the accuracy of the model. Figure 3a presents the model and the system response to a step and a square input signal. The response does not mach. To overcome this problem, the model parameters must be estimated. For this task SDO tool will be used. The estimation process works as follows:

- step input response of the real system (heater input voltage vs. thermistor output voltage) is measured using dS1104 DAQ board and then imported into MATLAB/Simulink;

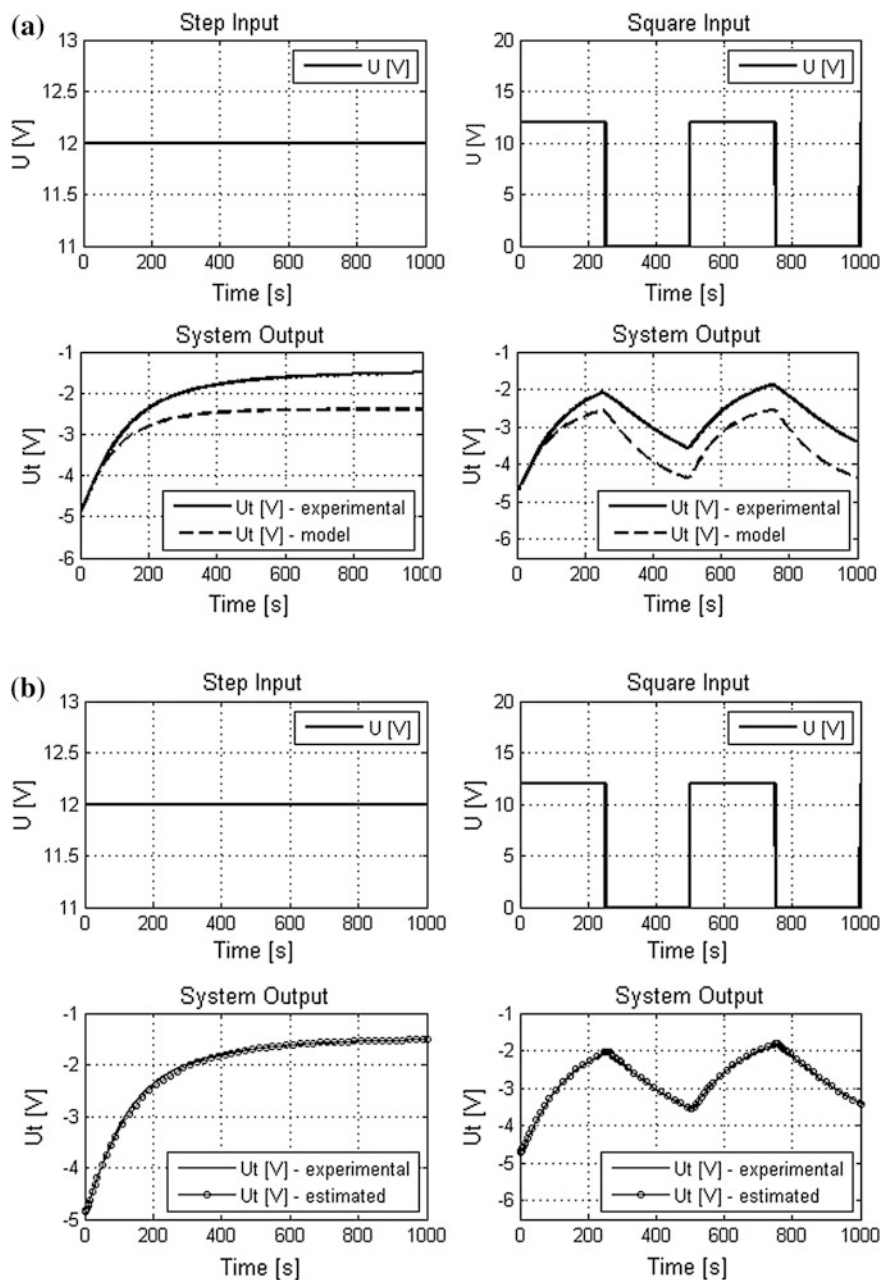


Fig. 3 Model response vs. system response: **a** without parameters identified **b** with parameters identified

Table 2 Model parameters

Parameter	Initial value	Estimated value
A_{wall} (m ²)	0.011	0.0116
m_{wall} (Kg)	0.0121	0.0129
c_p (J/kg/K)	1,670	1,670
k_1 (W/(m ² *K))	15	16.5587
k_2 (W/(m ² *K))	15	7.0977
$A_{thermistor}$ (m ²)	1.3554e-4	2.0475e-4
η (adimensional)	0.95	0.9501

- input–output values are then used in SDO for parameter estimation; heater input voltage will enter into the model through port U (Fig. 2a), while output U_t will plot the model response to that input signal;
- before starting the estimation process user must select the desired parameters for estimation (in our case parameters from Table 2);
- while estimation process is running, graphs with model response and parameter variation are shown; after few iterations the SDO will show the final results;
- to validate the estimated parameters, they are compared against a second set of collected input–output data (square input response); if the model response do match also the second set of data, then the model can be used for model-based controller design.

Table 2 presents the parameters initial values and estimated values. Figure 3a shows the model response with the initial values and Fig. 3b after parameter estimation process. It can be seen that both the experimental and model response are in agreement.

4 Model-Based Controller Design

Model based controller design can drastically improve the time needed for designing, verifying and validation of the controller. Using the proposed Simscape model, two controllers are designed and then tested and validated on the real system. Figure 4 presents the model and system response for an ON–OFF and PI controller. Controllers were implemented using dS1104 DAQ board and then compared with model results. The differences between simulated and experimental results can be explained by the nonlinear character of the system and the assumption made in Sect. 3.3.

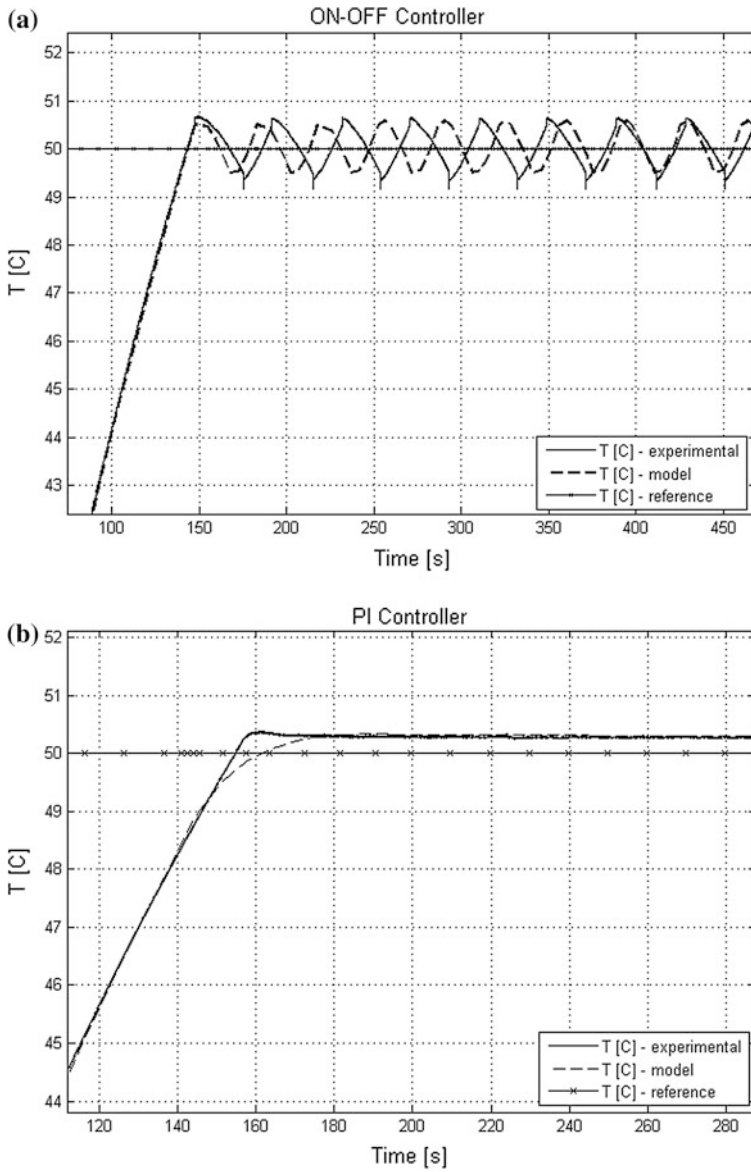


Fig. 4 a ON-OFF controller response; b PI controller response

5 Conclusion

Accurate control of the temperature is essential in many modern applications. The demands of high performances implies the use of new approaches in the design process, which allow a better understanding of the designed system and the development of more complex control strategies. The papers presented a new approach for modeling a thermotronic system using a gray-box modeling technique. The model was obtained using blocks from Simscape toolbox, while Simulink Design Optimization Tool was used to estimate the model parameters. Using Simscape is far more intuitive for engineers because the system can be described using physical components. The connection between two components is not a mathematical connection, but a physical one. It was shown that using Simulink Design Optimization Tool, the model parameters were correctly estimated and the model could be used for designing two closed-loop temperature controllers. The performances of the two controllers were directly influenced by the accuracy of the model and the presented results have shown that the model is good enough to design a temperature controller. The differences between simulated and experimental response can be explained by the nonlinear character of the system and the assumptions that were made when designing the Simscape model.

References

- Alur R et al (2005) Handbook of networked and embedded control systems, Birkhäuser
- de Canete JF, Galindo G, Moral IG (2011) System engineering and automation—an interactive educational approach, Springer-Verlag Berlin Heidelberg
- Dogan I (2002) Microcontroller based temperature monitoring and control, Elsevier Science & Technology Books
- Dumbrava V (2009) Analysis of the economic competitiveness increase for high-tech mechatronic products, The Romanian review precision mechanics, optics & mechatronics, 36
- Ljung L (1999) System identification: theory for the user 2nd edn, Prentice Hall
- Nicolae A (2008) Mechatronic technology in the area of pneumatics-pneutronics, international conference 6th workshop on European scientific and industrial collaboration on promoting advanced technologies in manufacturing, Bucharest, 25–26
- Van Brussel H (1996) Mechatronics, a powerful concurrent engineering framework. IEEE/ASMETrans Mechatronics 1(2):127–136

On the Eccentricity Effects in Solar Tracking Triangular Linkage with Eccentric Linear Actuator

Radu Saulescu, Olimpiu Munteanu, Mircea Neagoe
and Nadia Cretescu

Abstract Improving the efficiency of PV or solar-thermal platforms through the use of tracking systems including a triangle type mechanism with one variable link is the subject of many scientific papers and patents. The literature has emerged a new idea on improving the performance of tracking systems by introducing large eccentricity in the triangle linkage with eccentric linear actuator. It is known that, in a triangle type linkage, the output angular stroke is closely related to the minimum admitted transmission angle and reach a value of not more than 120° – 130° , for a linear actuator with null eccentricity. This paper deals with the study of the eccentricity influence on the actuator stroke, as well as on the forces generated into the tracking system and linear actuator by the moment of the tracked platform (under the wind load). The obtained results show that eccentricity does not modify the transmission angle, and increasing eccentricity reduces slightly the needed driving force, with the negative effect of generating a bending moment on the linear actuator.

1 Introduction

The study of improving the efficiency of PV panels or solar-thermal collectors using controllable tracking systems is the subject of many patents and scientific papers (Koussa et al. 2012; Kuan and Zhang 2012; Liao 2011, 2012; Visa et al. 2008; Visa et al. 2012). As a general rule, a tracking system characterized by simple architecture, easy maintenance, as well as minimal cost, imposes the use of a simple mechanical structure.

R. Saulescu · O. Munteanu · M. Neagoe (✉) · N. Cretescu
Faculty of Product Design and Environment, Product Design,
Mechatronics and Environment Department, Transilvania University of Brasov,
B-dul Eroilor no 29, Brasov, Romania
e-mail: mneagoe@unitbv.ro

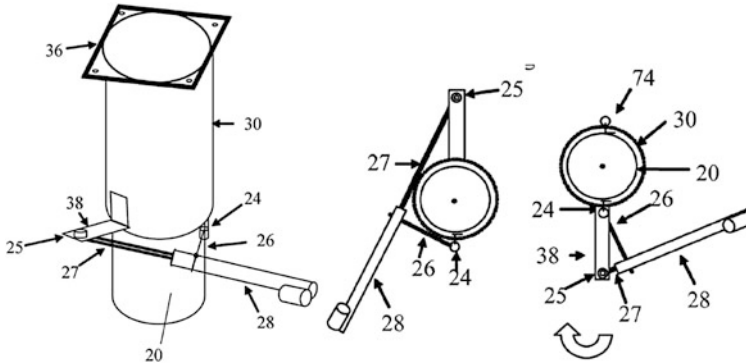


Fig. 1 Eccentric triangle linkage with one variable link, used in solar tracking systems (example taken from (Liao 2011))

Due to their simplicity and low cost, linear actuators are widely used in tracking systems (<http://www.degerenergie.de/en/open-land.html>; http://www.dobontech.com/tetra-track/eng/principal/index_tecnica.htm; <http://www.solar-trackers.com/specific-pv-applications/photovoltaic-systems>). They can accomplish in a triangle type linkage a maximum angular stroke of 120° – 130° , under the constraints of the transmission angle $\gamma_{\min} \geq \gamma_{\min \text{ adm}} = 25^{\circ}$ – 30° and of the actuator mounted without or with small eccentricity. As shown in (Burduhos et al. 2011; Visa et al. 2008; Visa et al. 2012), the triangle type linkage with one variable link needs increased actuator driving force while the transmission angle decreases.

New research (Liao 2011, 2012) shows that one way of increasing the output angular stroke of the solar platforms (angular stroke = 180° , Fig. 1), using a triangle type linkage with one variable link, is to increase the eccentricity of the linear actuator (Fig. 1).

Consequently, the modelling, simulation and identification of the main influences of eccentricity on the system's parameters are involved in this study. The purpose of the paper is to analyze the effects of the eccentricity on the transmission angles and implicitly on the output angular stroke, as well as on the forces and moments from tracking mechanical system.

2 Problem Formulation

According to Fig. 1, the general case of a triangle type linkage with variable link is considered (Fig. 2a), actuated through a linear actuator mounted eccentrically between the revolute joints A and C. The problem is to identify the influence of the eccentricity e on the kinematic and static behaviour of the mechanism. Therefore, further on the modelling of movements, forces and moments of the mechanism considered in the general case is performed, followed by numerical simulations on

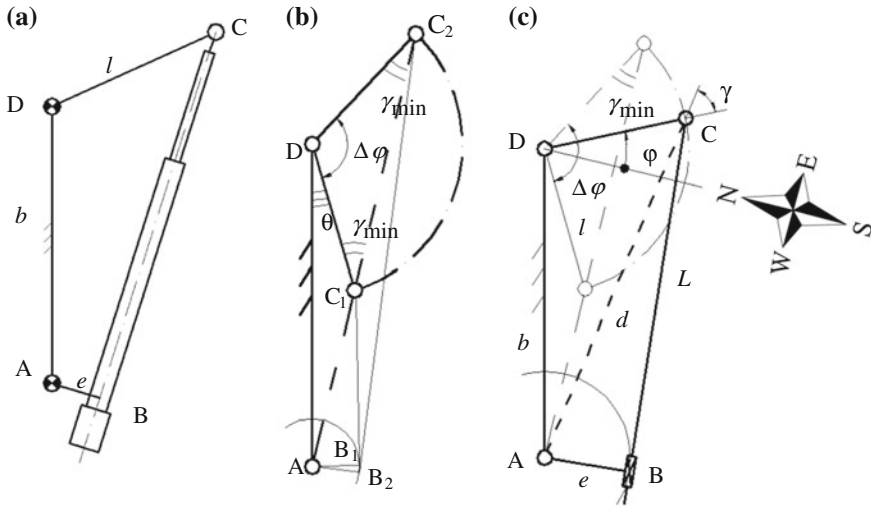


Fig. 2 Structural scheme (a) extreme positions (b) and current position (c) of a linkage with eccentric linear actuator

a particular relevant case. Assuming that the rocker length $CD = l$ and the output angular stroke $\Delta\varphi$ (Fig. 2) are known input data, the following notation and dimensionless factors used in kinematic and static modelling (see Fig. 2a, b) are introduced: the base length: $AD = b$, the output rocker length: $CD = l$, the eccentricity: $AB = e$, the current length of the variable side (as input size): $AC = d$, the current actuator length: $BC = L$, the output angular stroke: $\Delta\varphi$, the linear actuator stroke: $\Delta s = L_{\max} - L_{\min}$, $AC_2 = d_{\max}$, $AC_1 = d_{\min}$, $B_2C_2 = L_{\max}$, $B_1C_1 = L_{\min}$, $k_b = \frac{b}{l}$, $k_e = \frac{e}{l}$, $k_d = \frac{d}{l}$, $k_{\Delta s} = \frac{\Delta s}{l}$, $k_s = \frac{L - L_{\min}}{l}$, $k_{L\min} = \frac{L_{\min}}{l}$.

3 The Kinematic Modelling

The purpose of the kinematic modelling is to allow the determination of the linear actuator stroke coefficient ($k_{\Delta s}$), when the output angular stroke ($\Delta\varphi$) is known (Fig. 2). This modelling is done in the prerequisite that the transmission angle is the same at the both extreme positions of the linkage (γ_{\min} , Fig. 2b).

The scheme from Fig. 2b allows the determination of the needed geometrical parameters through the following relations:

$$\begin{cases} \gamma_{\min} = \frac{180 - \Delta\varphi}{2}, k_{d\min}^2 = k_L^2 \min + k_e^2, k_b^2 = 1 + k_{d\min}^2 + 2d_{\min} \cdot \cos(\gamma_{\min}), \\ \theta = \arccos \frac{1 + k_b^2 - k_{d\min}^2}{2 \cdot k_b}, k_{d\max}^2 = 1 + k_b^2 - 2 \cdot k_b \cdot \cos(\theta + \Delta\varphi) \\ k_{L\max} = \sqrt{k_{d\max}^2 - k_e^2}, k_{\Delta s} = k_{L\max} - k_{L\min}. \end{cases} \quad (1)$$

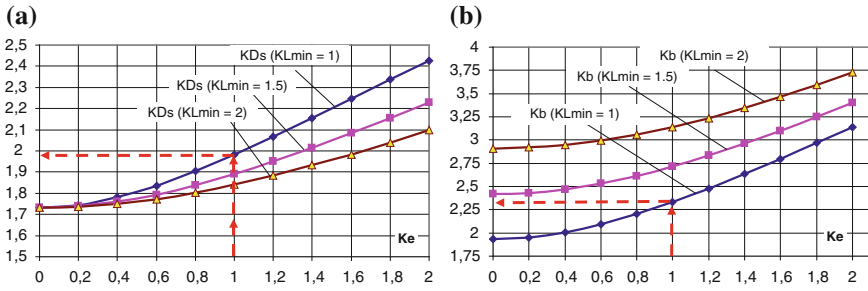


Fig. 3 Variations of the parameters k_b and $k_{\Delta s}$ for the case: $\Delta\varphi = 120^\circ$

For different values of k_{Lmin} coefficient, the linear actuator’s stroke coefficient $k_{\Delta s}$ can be determined as a function of the eccentricity coefficient k_e (Fig. 3).

In accordance with Fig. 3, the eccentricity increase (k_e) causes the increases of actuator’s stroke ($k_{\Delta s}$) and base length (k_b); also, for the same eccentricity (k_e), the k_{Lmin} increase generates a slightly decrease for the actuator stroke ($k_{\Delta s}$) and a significantly increase for the base length (k_b).

Case study: considering $k_{Lmin} = 1$ and $k_e = 1$ (see Fig. 3), the output sizes $k_{\Delta s} \cong 2$ and $k_b \cong 2.3$ are obtained. In accordance with Fig. 2c, the relations (2) can be written:

$$\begin{cases} k_d^2 = 1 + k_b^2 - 2b \cdot \cos\left(\theta + \frac{\Delta\varphi}{2} + \varphi\right), \text{ where } \varphi \in \left[-\frac{\Delta\varphi}{2}, \frac{\Delta\varphi}{2}\right] \\ k_L^2 = k_d^2 - k_e^2, k_s = k_L - k_{Lmin}; \gamma = \arccos((1 + k_d^2 - k_b^2)/(2d)). \end{cases} \quad (2)$$

According to Fig. 4, where dependencies between the linear actuator displacement (k_s), rocker angular displacement (φ) and transmission angle (γ) are represented, it can be shown that the eccentricity increase (k_e) causes the increase of the linear actuator stroke (for the same angular output stroke, Fig. 4a) and has no influence on the minimum transmission angle and implicitly on the angular output stroke; for a given eccentricity, the linear actuator position where the transmission angle achieves its maximum value ($\gamma = 90^\circ$) can be also established (Fig. 4b).

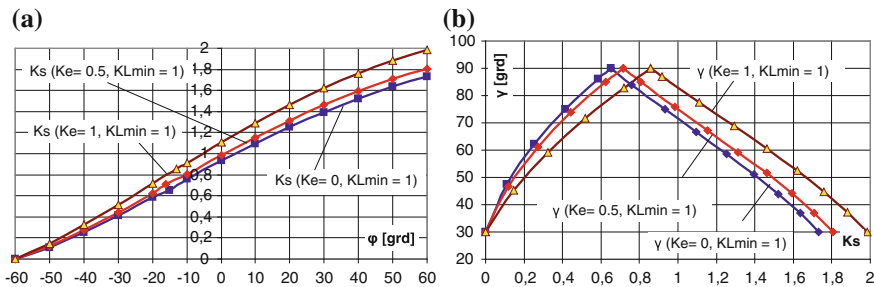


Fig. 4 Variations of the coefficient k_s versus rocker angular displacement φ (a) and variations of the transmission angle (γ) versus coefficient k_s (b)

4 The Static Modelling

The static modelling aims to establish the correlations between forces and moments from the tracking system, considering the previous geometric correlations of the triangle linkage. A known coefficient $k_T = T/l$ is also introduced, where T is the moment (generated by wind) that loads the output rocker CD.

On the basis of the schemes from Fig. 5a, b, the tracking system’s forces, as well as the necessary active force in the actuator can be determined. Also, the λ angle between the actuator axis and the actuator joints’ line can be established (Fig. 5b); the eccentricity increase causes the increase of the λ angle, and the decrease of the actuator’s forces (Fig. 5c and rel. (3)).

$$\begin{cases} P_t = k_T, P = \frac{k_T}{\sin \gamma}, \text{tg } \lambda = \frac{e}{L} = \frac{k_e}{k_l}, \\ P_a = \frac{k_T}{\sin \gamma} \cos \lambda, P_n = \frac{k_T}{\sin \gamma} \sin \lambda, F = P_a. \end{cases} \quad (3)$$

The forces in the tracking system (see Fig. 5b) induce transversal reaction forces (P_n) into the linear actuator (due to P_a active force), that generate a bending moment with negative effects on the actuator’s life. Considering, as example, an eccentric linear actuator [adapted after (<http://www.servomech.it/Pdf/prodotti/SERVOMECH-Linear-Actuators-2009.pdf>)], where l_{20} and l_{10} are known dimensions (Fig. 6), the transversal reactions inside the actuator can be computed, choosing the distance L_{min} where the actuator is articulated (Fig. 6). Others necessary dimensions can be thus calculated (see Figs. 6 and 7):

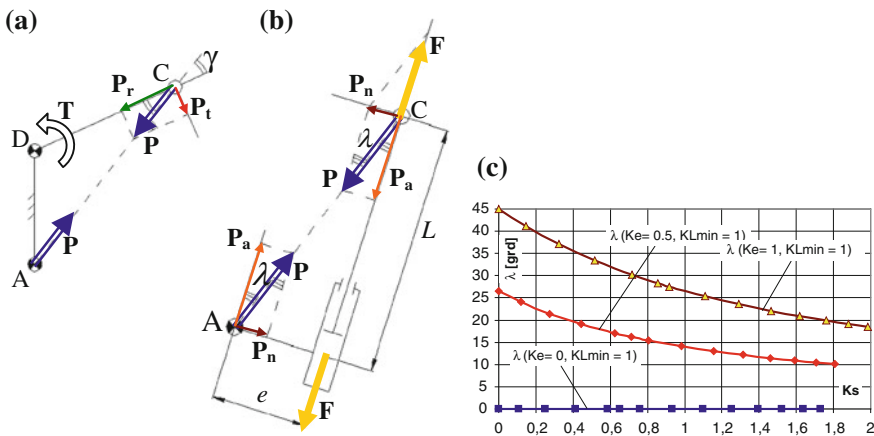


Fig. 5 Radial and tangential forces that stress the joint C (a), normal and axial forces applied on the linear actuator (b), variations of the λ angle between the actuator axis and the actuator joints’ line (c)

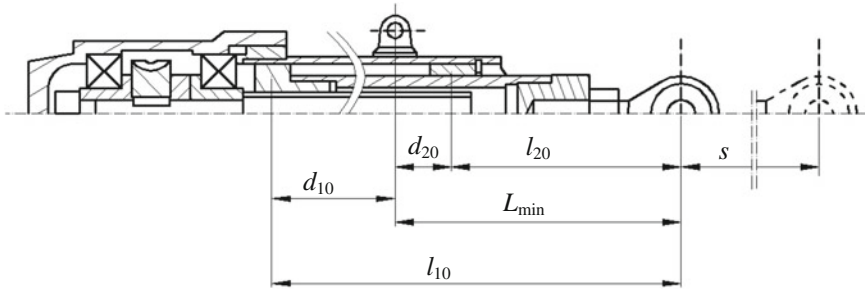
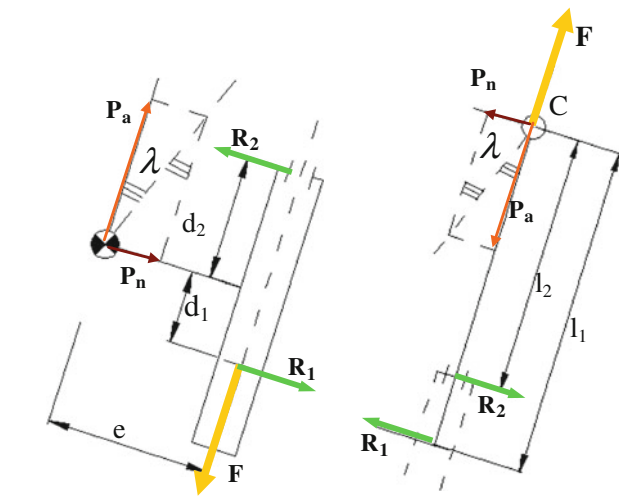


Fig. 6 Example of eccentric linear actuator [adapted after (<http://www.servomech.it/Pdf/prodotti/SERVOMECH-Linear-Actuators-2009.pdf>)]

Fig. 7 Forces' configurations for the two main components of the eccentric actuator



$$\begin{cases} d_{20} = L_{min} - l_{20}, d_2 = d_{20}, l_2 = l_{20} + s, \\ d_{10} = l_{10} - L_{min}, l_1 = l_{10}, d_1 = d_{10} - s. \end{cases} \quad (4)$$

Based on Fig. 7, the forces from actuator R_2 can be obtained:

$$R_1 = \frac{P_n \cdot l_2}{l_1 - l_2}, R_2 = \frac{P_n \cdot l_1}{l_1 - l_2}, R_2 = R_1 + P_n, F \cdot e = R_2 \cdot d_2 + R_1 \cdot d_1 \quad (5)$$

The relations (3), (4) and (5) allowed us drawing the diagrams from Fig. 8, and to highlight the following conclusions related to the system forces and moments:

- the forces P , P_a and P_n acting to the end C of the linear actuator (see Figs. 5b and 7c) have maximum values at the beginning and at the end of stroke, with minimum values at $k_s \approx 0.75$ (Fig. 8a, b);

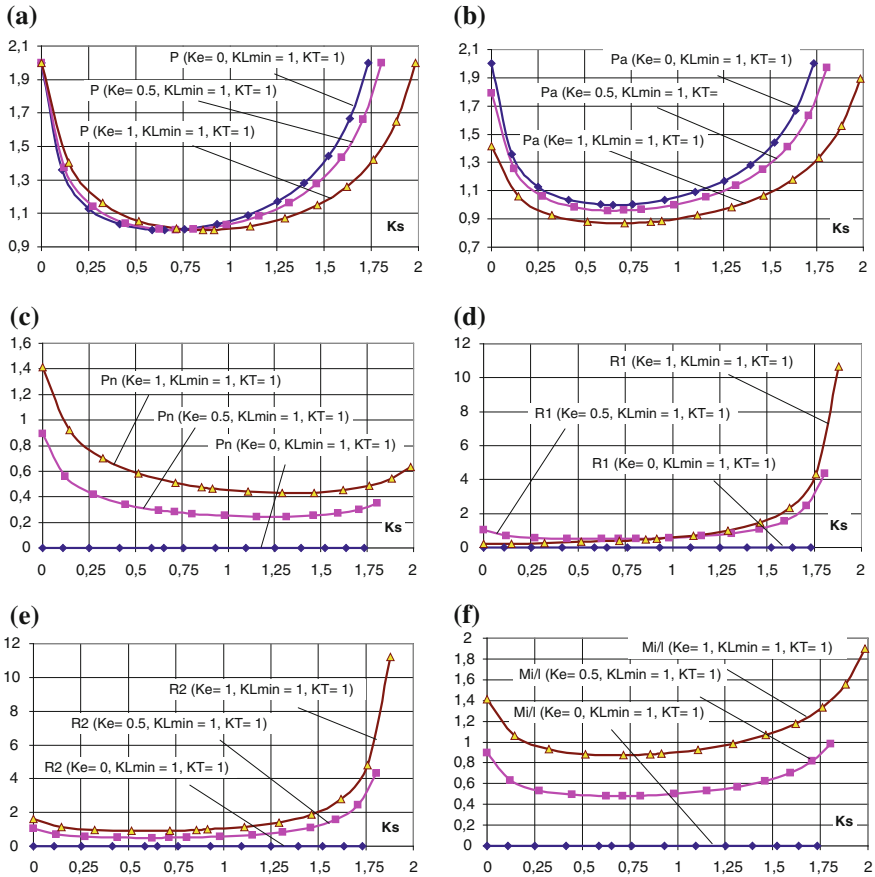


Fig. 8 Variations of tracking system’s forces, reactions and bending moment

- the eccentricity increase causes the decrease of the axial force P_a (Fig. 8b) and the increase of the transversal force P_n (Fig. 8c);
- the reactions forces R_1 and R_2 inside the linear actuator are maximum when the actuator is fully opened;
- when eccentricity increases, the reaction forces R_1 , R_2 (Fig. 8d and e) and the bending moment (M_i/l , Fig. 8f) increase too;
- the linear actuator operates in the worse conditions in maximum opening (maximum values of axial force P_a and of bending moment M_i/l). The best conditions are fulfilled at $k_s \approx 0.75$ and hence this position is recommended as safety stationary configuration.

5 Conclusions

Starting from the solar tracking system variants with eccentric triangle linkage presented in the literature, a resulting need was to model, simulate and identify the main influences of the actuator's eccentricity on the performance parameters of the system. Based on the performed modelling, simulations and interpretations, the following main influences are highlighted:

- the eccentricity increase does not change the minimum values of transmission angle (specific to the stroke ends), and implicitly it does not allow the increase of the tracking angular stroke ($\Delta\varphi$);
- the eccentricity increase causes a slightly decrease of the actuator axial active force (P_a) and an increase of the bending moment (M_i) that is extremely dangerous for the operation and reliability of the actuator.

As a result of this study, it is recommended to use *linear actuators without eccentricity or negligible eccentricity* in the tracking triangle linkages.

References

- Burduhos B, Diaconescu D, Vatasescu M, Saulescu R, Tatu I (2011) Energy Comparison of PV Systems with Mono- and Bi-axial Pseudo-equatorial Tracking Mechanisms. 13th world congress in mechanism and machine science, Guanajuato, México, 19–25 June 2011, IMD-123, CD Proceedings, ISBN: 978-84-614-7527-8
- Koussa M, Haddadi M, Saheb D, Malek A, Hadji S (2012) Sun tracker systems effects on flat plate Photovoltaic PV systems performance for different sky states. Energy Procedia 18:839–850
- Kuan J, Zhang W (2012) Design and implementation of tracking system for dish solar thermal energy based on embedded system. Knowl Discov Data Min, AISC 135:31–38
- Liao H (2011) Two-axle solar tracker system and apparatus for solar panel and likes. Brevet US2011/0041834 A1
- Liao H (2012) Two-axle solar tracking system device for solar panels, Brevet EP 2472197 A1
- Visa I, Diaconescu DV, Popa V, Burduhos B, Saulescu R (2008) The synthesis of a linkage with linear actuator for solar tracking with large angular stroke. Proceedings of EUCOMES 08. The second European conference on mechanism science, Casino, Italia, Sep 2008, ISBN Ed. Springer, ISBN 987-1-4020-8914-5, pp 457–464
- Visa I, Diaconescu DV, Moldovan MD (2012) A new solar tracking linkage with 2 actuators in parallel connected, The 2nd IFToMM asian conference on mechanism and machine science, Nov 7–10 2012, Tokyo, Japan, CD Proceedings, 2012

Influence of Mechanical Press Dimensions on its Kinematic Behavior

Iulian Tabără and Constantin Dogariu

Abstract This paper analyzes the influence of the links dimensions on the kinematics of the knuckle joint press. At the same time, depending on the results of the analysis, is accomplished the selection of the manufacturing operation for each considered structure. Modelling the knuckle joint press structures was performed using SolidWorks application while their operation simulation and determination of kinematic parameters variation diagrams of the ram was done using SolidWorks Motion model.

Keywords Knuckle joint press mechanism · Motion simulation · Suitable operation

1 Introduction

To achieve optimal technological conditions necessary for the development of plastic deformation, kinematic assembly of the presses must respect the specific characteristics of different processing methods. During operation of the press, the material is deformed under the action of the kinematic machine assembly and therefore the ram speed is obtained from the conditions imposed to its movement.

Ram speed has to be maintained in accordance with specific technological requirements of each operation, and towards the end of stroke race is necessary to ensure the transition from $v = v_{max}$ to $v = 0$, the system occur without significant dynamic loads.

I. Tabără (✉) · C. Dogariu
University Politehnica Bucharest, Bucharest, Romania
e-mail: iuliantabara@yahoo.com

C. Dogariu
e-mail: cdogariu@gmail.com

Processing procedures using mechanical presses are dependent on the temperature at which deformation occurs, the speed of the ram, thickness of material subjected to processing, dimensional and geometric characteristics of the shape of the finished piece, etc. (Al-Arifi et al. 2011; Osakada et al. 2011; Tabără and Tureac 1984; Tabără et al. 1976; Strano and Albertelli 2011; Der et al. 2007; Reid 1991; Oza and Patel 2011; Boerger 2000, 2012).

Kinematic parameters variation characteristics of the ram are very important for obtaining a high quality of machined parts. Also, depending on desired operation is imposed a certain interval of rams' kinematic parameters of variation as much as a certain aspect corresponding to the requirements of the imposed manufacturing process. In this paper it is determined which are the variants of the optimal structure of knuckle joint press depending on the operation which must be realized by the respective machines. It will have in view the minimal constructive modification of the schemes knuckle joint press schemes but with maximal impact on obtaining some diagrams of variation conform to the various imposed operations.

2 Content

Designing mechanisms for knuckle joint presses must be done taking into account processing media which it is intended. In this way are taken into account presses for operations such as: punching, stamping, forging, pressing powders etc. Kinematics of knuckle joint presses mechanisms determines the choosing of the optimal solution for each of the plastic deformation operations listed above.

This paper addresses only mechanical presses which contain knuckle joint mechanism. Kinematics of these mechanisms depends on their structure, the size of its components and in a large measure by their position in space. Next, we insist only on the last aspect, namely the influence of upper joint position on the kinematics knuckle joint mechanism.

For this we consider joint D located at the top (Fig. 1a) in three positions by translating it horizontally.

In the first version joints D and E are located on the same vertical and determine the direction of movement of the press ram. This is considered the classical structure of the knuckle joint press mechanism.

The second version (Fig. 1b) was made considering that D joint is moved opposite to the main shaft of the mechanical press with a distance.

The third version (Fig. 1c) was accomplished considering that D joint is moved and placed in a symmetrical position to the one presented in the previous case (Fig. 1b).

Kinematic analysis consisted in determining the displacement, velocity and acceleration of the ram of the mechanical press (specifically E joint).

Results are represented in Figs. 2, 3 and 4. Figure 2 shows the variation of displacement for a complete cinematic cycle in the three cases mentioned above and noted a , b , c .

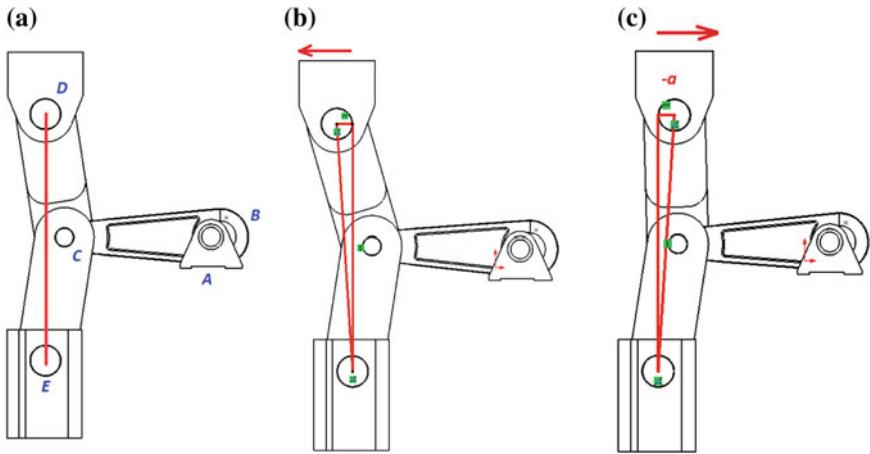


Fig. 1 Considered configurations of knuckle joint press mechanism

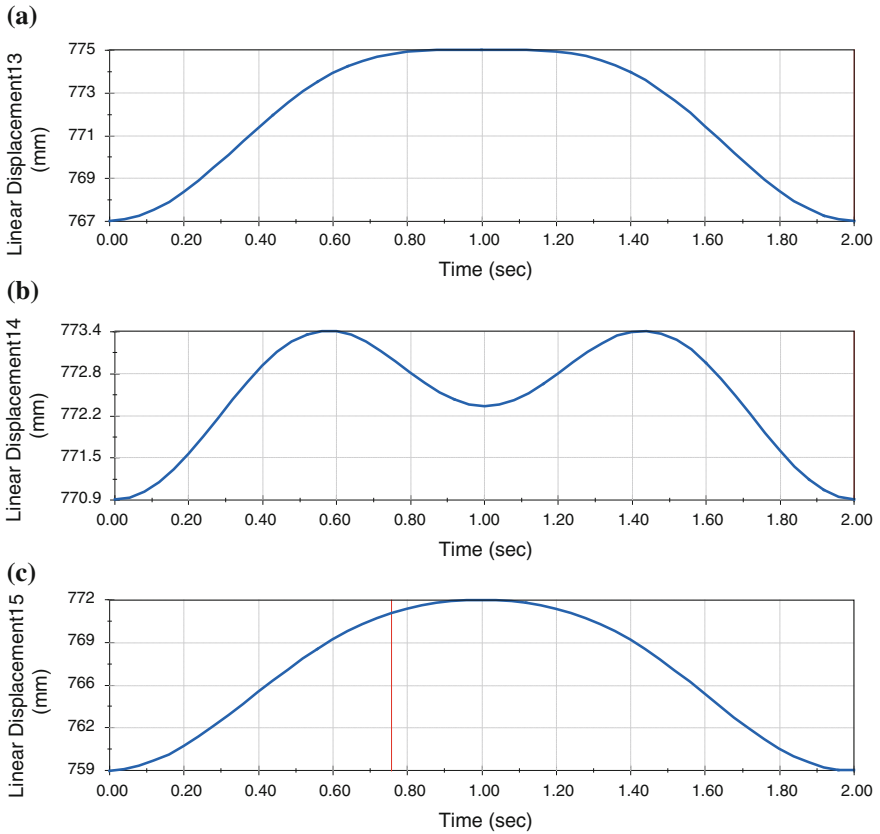


Fig. 2 Ram displacement function of time

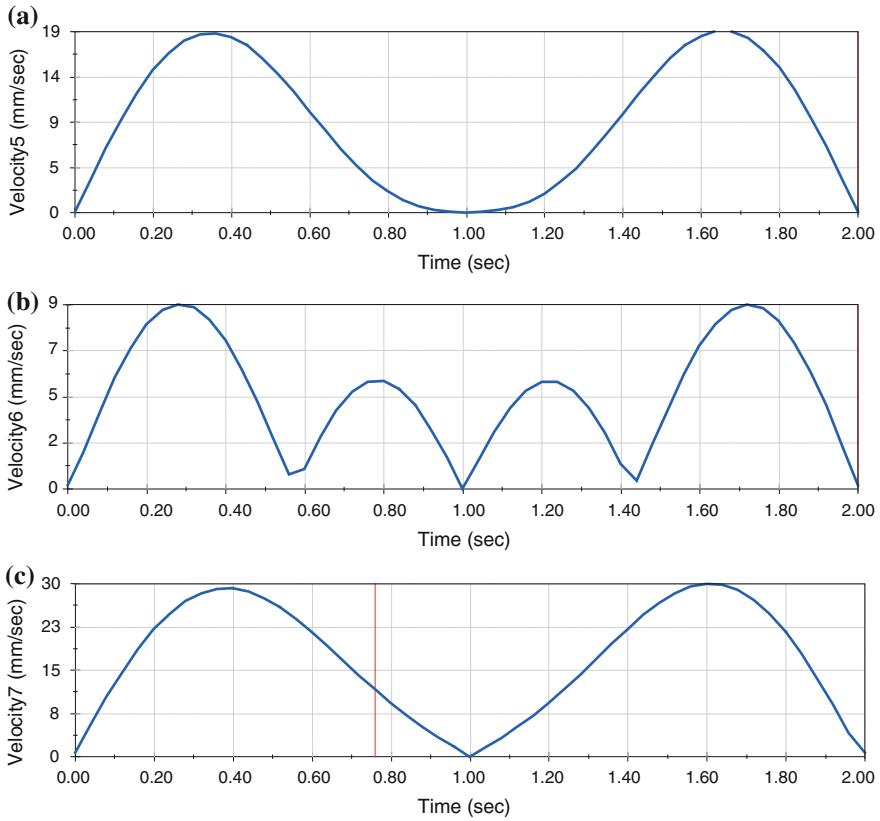


Fig. 3 Ram velocity function of time

Analyzing the diagrams of ram displacement variation depending on time is shown that the shortest stroke is done in the second case (Fig. 2b) and longest is presented in the first case (Fig. 2c). These schemes allow the selection of optimal kinematics depending on the operation to be executed by the mechanical press and the thickness of material to be deformed. Processing characteristic of each operation requires a certain size of the work stroke (deformation stroke) which is not identical with the entire descendent stroke of the mechanical press.

For a same active stroke length, it is found that the contact time between tool and material for processing is the longest in the second case and the shortest in the third case. Although the duration of contact between tool and work piece is higher in the second case, in this situation there is a noticeable reversal of the ram after reaching end of the stroke.

Note that speed limits vary between low limits (Fig. 3b) but with multiple variations during the same cycle cinematic which is another reason why this structure is recommended to press the pressing powders.

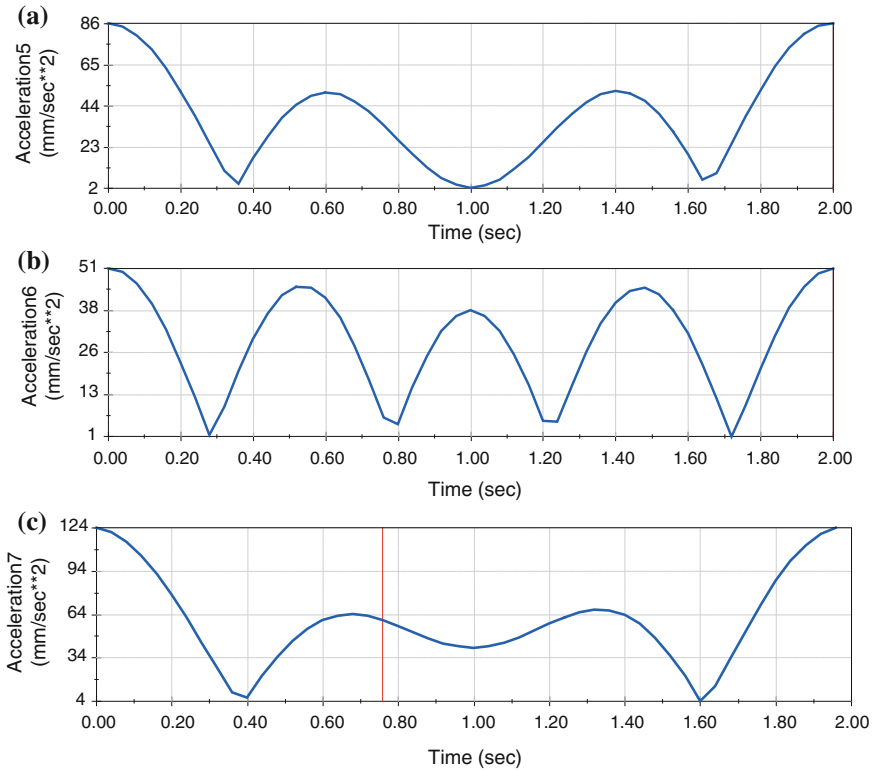


Fig. 4 Ram acceleration function of time

This solution can be adopted for presses that make pressing powders because the specificity of pressing powders consists in the fact that the speed should be low and the tool return allow stress relaxation and air removal from material particles which are pressed followed by a new compaction aimed to give the final shape of the product.

The third variant (Fig. 3c) shows that the contact between tool and work piece occurs in a very short time, in this situation, in this situation the press meant to be used for punching operations where displacement and speed are higher than in the previous case. Unlike the last version, the first version allows contact between tool and work piece over a longer period of time.

At the same time the range of velocities and accelerations is reduced with gentle changes of in velocity (Fig. 3a) and acceleration (Fig. 4a) in the first version in comparison with the third one (Figs. 3c and 4c). Smooth variation of acceleration leads to reduced dynamic shock, one of the most important goals pursued in the operation of mechanical presses. Therefore, this structure is suitable for drawing and assembly operations by plastic deformation.

3 Conclusions

It is noted that using very small changes of position of a joint are obtained important influence upon displacement, position, velocity and acceleration of the working ram. For this reason it is necessary for each project a detailed analysis to determine the optimal variant to satisfy the requirements of the machining process by plastic deformation. The press configuration modelling was fulfilled using SolidWorks software and their running simulation and determination of kinematic parameters variation diagrams of the ram was achieved using SolidWorks Motion model, which allow the selection of the optimal structure according to the kinematic requirements imposed by each operation performed by plastic deformation.

References

- Al-Arifi N, Zamani A, Khan J (2011) Billet optimization for steering knuckle using Taguchi methodology. *Int J Comp Theory Eng* 3(4)
- Boerger D (2000) The use of link motion on mechanical presses, AIDA-Tech. AIDA-America Corporation
- Der MT, Hsin PC, Wei CS, Chun YH, Tzuen LC (2007) Performance improvement of a punching mechanism for flexible printed circuit boards. In: *Proceedings of the 13th world congress in mechanism and machine science*, Guanajuato, A724, Besancon, France, pp 18–21 June 2007
- Flexible on the Job (2012) Knuckle-joint presses for the Non-Automotive Industry, Shuler Brochure, Netphen-Werthenbach
- Osakada KV, Mori K, Altan T, Groche P (2011) Mechanical servo press technology for metal forming. Elsevier Editorial System(tm) for CIRP, *Annals* 2011, vol 60/2
- Oza R, Patel SP (2011) Analysis and optimization of drive shaft in eccentric mechanical press. *Int J Eng Res Appl (IJERA)* 1(2):055–058
- Reid D (1991) *Fundamentals of tool design*, Society of manufacturing engineers. Publications development department
- Strano M, Albertelli P (2011) *Eco-design of forming machines*. Polytechnic University of Milan, Department of Mechanics
- Tabără V, Catrina D, Ganea V (1976) *Calculation, design and adjustment of presses*. Technical Publishing House, Bucharest
- Tabără V, Tureac I (1984) *Machines for plastic deformation*. Didactic and Pedagogical Publishing House, Bucharest

Nonlinear Analysis of Osteoarthritis Process in Virtual Human Knee Joint

D. Tarnita, M. Catana and D. N. Tarnita

Abstract The main objective of this paper is to present a study of the osteoarthritis phenomena based on a complex three-dimensional model of the human knee joint, using CT cross sections. For that purpose, we used Ansys Workbench software which allows defining models with a high level of difficulty including complex 3D shapes. The virtual biomechanical system of the human knee containing bones, ligaments, menisci, cartilage is studied using the finite elements method. To investigate the role of the articular cartilage in the developing of the osteoarthritis and to analyze and simulate the biomechanical behavior of knee joint, a non-linear analysis was performed. The non-linearities are due to the presence of the contact elements modeled between components surfaces. This paper shows the Von Mises stress distribution and the strain maps found in menisci, in femoral cartilage and in tibial cartilage, applying a load of 800 N, 0° in flexion for healthy knee and for three different cases of 10° physiological varus knee. The behavior of the virtual knee joint can give important information which can be used in the fields of medicine sciences and biomedical robotics.

Keywords Articular cartilage damage · Finite element analysis · Contact element · Knee joint · Osteoarthritis · Physiological varus

D. Tarnita (✉) · M. Catana
Department of Applied Mechanics, University of Craiova, Craiova, Romania
e-mail: tarnita.daniela@gmail.com

M. Catana
e-mail: marius_catana79@yahoo.com

D. N. Tarnita
University of Medicine and Pharmacy, Craiova, Romania
e-mail: dan_tarnita@yahoo.com

1 Introduction

Human knee joint is one of the most complex joints in the human body, taking into account the number of its components, their spatial geometry and their mechanical properties, the contacts between elements and the pressures acting on them. Different modeling techniques with the purpose to define more accurately the complex shape of each component of the human knee joint are developed. Authors of different studies have contributed for improving the quality of the geometric model of the knee joint (Bae et al. 2012; Fenning 2005; Bahraminasaba et al. 2011; Sandholm et al. 2011; Mohammad 2011; Kazemi et al. 2011; Hartley et al. 2009; Harrysson et al. 2007; Weiss and Gardiner 2001). In paper (Vidal-Lesso et al. 2011; Chung 2004; Moroni et al. 2007; Tichon 2011) the authors took into account the following components: the femur, tibia and bone cartilage, while in the articles (Fenning 2005; Hartley 2009; Kubicek and Zdenek 2009; Ramaniraka et al. 2005; Orsi et al. 2011; Randall 2011) was made a more complex modeling, considering the ligaments and cartilages. Finite element is a very powerful tool in predicting the behavior of human joints. However, the construction and validation of models is very difficult if one takes into account the complex behavior of components as well as their structure and mechanical properties. In the article (Moroni et al. 2007) the authors present a new technology solid free-form fabrication (SFF), which allows the fabrication of anatomical 3D scaffolds from computer tomography (CT) or magnetic resonance imaging (MRI) patients' dataset. In the article (Tichon 2011), a three-dimensional finite element model of the knee was used to determine the effect of various loads and torques imposed on the knee using the software FEBio. The results of the simulations show that several loading patterns can stress the medial meniscus to failure, especially if it was in a weakened state due to mechanical trauma or age.

Virtual models were analyzed with FEM, after previously achieving the network of nodes and elements such as tetrahedral finite element, hexahedral finite element, or using automatic meshing methods. Meshing algorithm using hexahedrons and bricks is intended to carry out a more rigorous analysis, with a much finer approximation for tibio-femoral contact area (Fenning 2005; Mohammad 2011; Kazemi et al. 2011; Kubicek and Zdenek 2009).

The general problems of interest in finite element analysis are the ones regarding the contacts, forces and pressures in the contact zones, the material properties used (Machado et al. 2011), and also the control of the contacts between the surfaces (Bredbenner et al. 2010). Mechanical stresses occurring in the knee joint also plays an essential role in the development of osteoarthritis, the existing literature on this topic being limited (Henderson 2009).

In his study, Bredbenner was demonstrated that quantitative differences in femur and tibia geometry were observed between surface models based on clinical MRI data for subjects at risk of developing osteoarthritis. The results suggest that variability in individual bone geometry may play a greater role in determining joint space geometry and related the real importance of considering geometry of

the individual bones and other structures in the knee joint in advancing the understanding of knee osteoarthritis.

The knee osteoarthritis is one of the major chronic diseases usually found in people of middle age and old age and also mainly causes various disabilities. Disorders of the musculoskeletal system are accompanied by pain, often an inflammatory response, and can lead to constraints on mobility, to longer-term disability and, in the extreme case, to an increased morbidity. It has a significant effect on patient quality of life, disability occurring in approximately 10 % of the population over 60 years. Knee osteoarthritis involves a degenerative process of cartilage in the knee joint leading to its loss (Lyu et al. 2012). It can also affect any or all three compartments of the knee joint (Checa and Taylor 2008). This degenerative process can be generally caused by obesity (Yang et al. 2007), by excessive physical activity, by joint trauma, immobilization and the hypermobility (Chantarapanich et al. 2009). Knee misalignment is considered one of the biomechanical key factors, factors that influence the progression of knee osteoarthritis (Yang et al. 2009).

The results presented by the authors in (Yang et al. 2009), demonstrated that the subject with varus alignment had the largest stresses at the medial compartment of the knee compared to the subjects with normal alignment and valgus alignment.

In (Vidal-Lesso et al. 2011), the authors present the stress distribution found in articular cartilage in femur and tibia, which were obtained applying a load range of 700–2,800 N, 0° in flexion and different cases with physiological valgus variation. A graphical model of stress prediction to the femur cartilage was created. The results show that different factors like overweight and misalignment could damage the articular cartilage.

The main objectives of our study are: to present a complex three-dimensional virtual model of the human knee joint, beginning from CT cross sections; to simulate a nonlinear analysis of the virtual model of healthy and osteoarthritic knee.

2 Modeling of Human Knee Joint

To obtain the geometric model of the healthy knee joint, CT images were processed using Space Claim integrated application and to obtain the 3D virtual model the integrated application DesignModeler was used. The virtual biomechanical system of the human knee contains femur, tibia and fibula bones, ligaments, medial and lateral menisci, femoral and tibial cartilages (Fig. 1) (Catana and Tarnita 2012).

Three distinct cases of osteoarthritis joint models with disease in *varus* of 10° were developed. The healthy joint is featured by a 176° angle between femur and tibia, while for the joint affected by osteoarthritis the analyzed geometry presented in this paper has an inclination of 186°. The osteoarthritis affects both medial and lateral compartment of the knee joint. Three distinct cases of progressive stages of

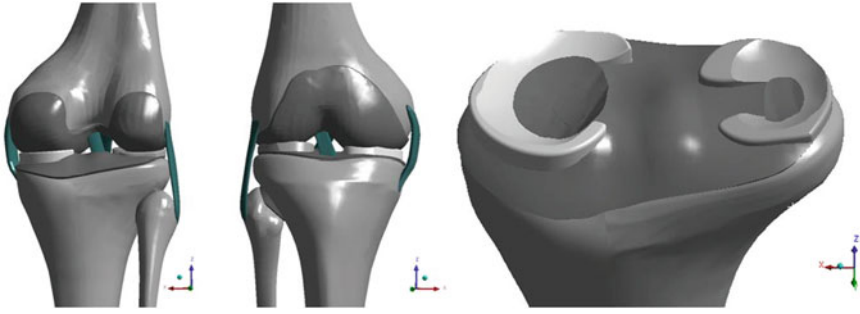


Fig. 1 Virtual model for the healthy knee joint (general views and details)

OA knee differ by the progressive increase of damage on the tibial cartilage, on the menisci and on the femoral cartilage in both compartments (Fig. 2). Note that the red areas represent the damaged area and the brown areas represent the affected parts.

For geometric discretization into nodes and elements, we used Solid 186 and Solid 187 tetrahedron elements, which are defined by 20 nodes and, respectively by 10 nodes, having three degrees of freedom per node: translations in the nodal x , y , and z directions. The elements support plasticity, hyperelasticity, creep, stress stiffening, large deflection, and large strain capabilities. The mesh of the geometric models for healthy knee joint and for the knee affected by osteoarthritis is shown in Fig. 3. For the areas of interest the elements dimension is 1 mm and for the adjacent areas is up to 4 mm. Advanced discretization methods such as “Sweep”, “HexDominant” and “Patch Conforming” were used.

For each studied case, the virtual model is discretized individually, the contact areas are readjusted and the analysis is run. In Table 1 there are presented the number of nodes and elements for all components of the healthy virtual knee.

The settings for the analysis and the boundary conditions are the following:

- taking into account the large number of nodes and elements but, also, the presence of nonlinear contacts, for solving the analysis it is necessary to implement a “smaller steps” system; solver was set as Preconditioned Conjugate Gradient level 2 iterative types. Boundary conditions for analysis are presented in Fig. 4.

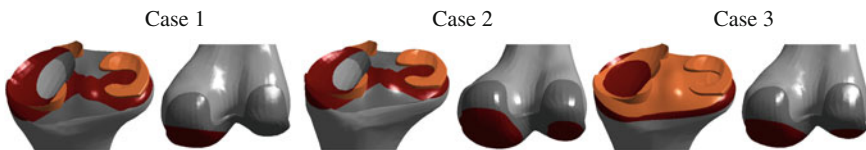


Fig. 2 Diseases areas and affected parts of OA knee for three different cases

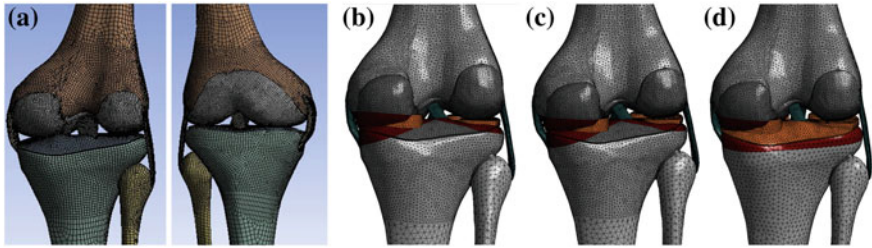


Fig. 3 The network nodes and elements for: **a** healthy knee; **b–d** the three OA stages (cases) of knee *varus* inclination of 10°

Table 1 Number of nodes and elements for all knee components

Case study	Number of nodes	Number of elements
Femur	185402	58604
Femoral cartilage	80036	22061
Tibia	127919	38401
Tibial cartilage	33787	8795
Medial menisci	8182	2596
Lateral menisci	7965	2519
Peroneu	39118	12876
Peroneu-tibie cartilage	6678	2365
LCM	6449	2223
LCL	7876	2747
LIA	1660	620
LIP	1885	679
Total	488092	148397

- on the proximal head of the femur bone there is applied a 800 N force in the -Z axis direction;
- on the same location it is applied the “Remote Displacement” that allows offset Z and RotY around the femur which allows movement of the hip;
- on the tibia distal head is applied “Remote Displacement”, which allows RotY (movement of the ankle around the tibia).

To better simulate the nonlinear contacts, “Bonded” and “NoSeparation” contacts type and “AugmentedLagrange” calculation algorithm were used. For a more efficient mathematical representation of these contact areas, the option “Pindball Region” with a radius of 0.1 mm was used.

Material properties used for knee geometric components are presented in Table 2.

During the progressive stages of the osteoarthritis, the menisci and the cartilage change their structures and their material properties. For an accurate virtual simulation of the process, the settings take into account these aspects.

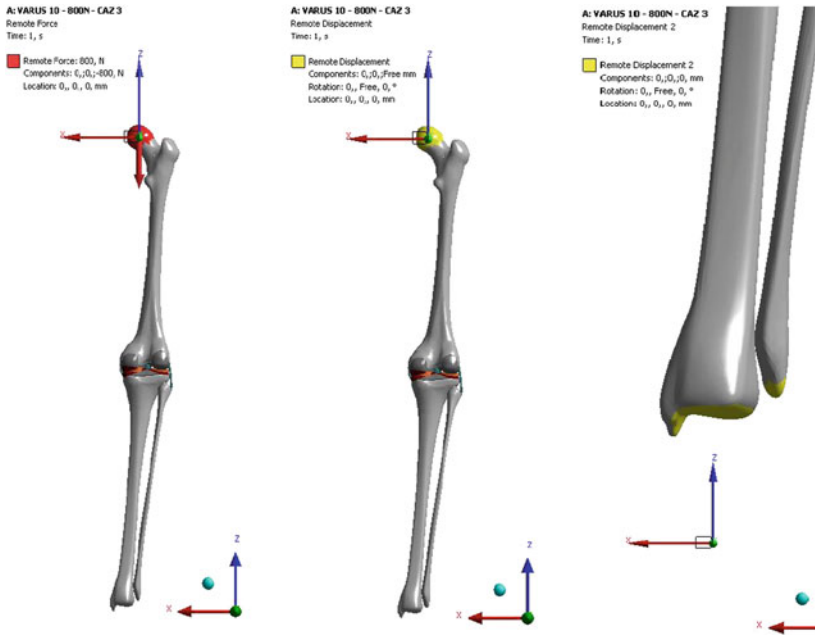


Fig. 4 Constraints and boundary conditions

Table 2 Material properties of knee geometric components (*Percentage of elasticity reduction)

Geometry	Young's modulus (MPa)	Poisson's ratio
Cortical–Femur bone	18600	0.3
Cortical–Tibia bone	12500	0.3
Trabecular bone	500	0.3
Cartilage	12	0.475
Meniscus	59	0.49
LCM–LCL	10	0.49
LIP–LIP	1	0.49
Meniscus affected	*50 %	0.49
Cartilage affected	*50 %	0.49

3 Results

To investigate the role of the articular cartilage in the developing of the osteoarthritis, and to analyze and simulate the biomechanical behavior of knee joint, a non-linear analysis with finite element method was performed. The non-linearities are due to the presence of the contact elements modeled between components surfaces. For each analysis there were extracted values for the maximum Von Mises stress and for the strain occurred due to compression on the femoral cartilage, on the tibial cartilage and on the menisci: healthy knee joint (Fig. 5) H-case

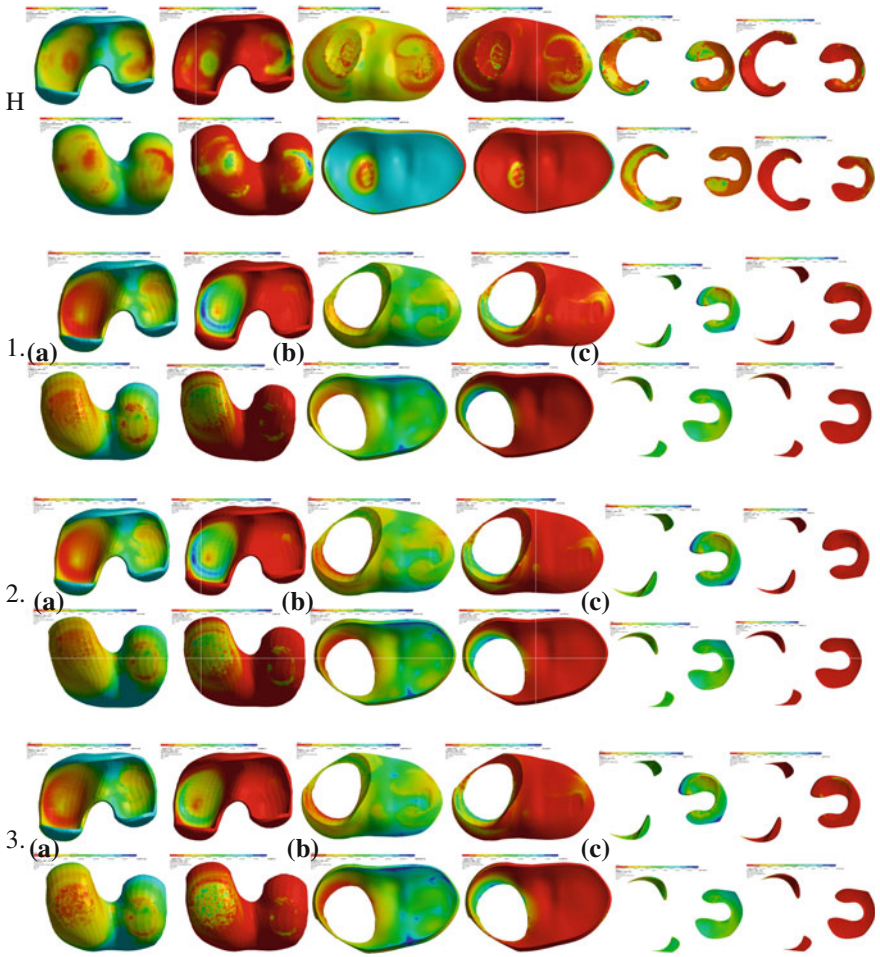


Fig. 5 Von Mises stress and strain due to compression on: **a** femoral cartilage **b** tibial cartilage; **c** menisci, for: *H* healthy knee, *1* Case 1 of OA knee, *2* Case 2 of OA knee, *3* Case 3 of OA knee

Table 3 Maximum Von Mises values and maximum strain obtained for analysis

Component geometry	Healthy knee	OA knee case 1	OA knee case 2	OA knee case 3
Femoral cartilage stress (MPa)	2.41	3.79	3.99	4.01
Tibial cartilage stress (MPa)	1.71	2.15	2.72	3.51
Menisci stress (MPa)	1.12	1.68	2.34	2.89
Femoral cartilage strain	0.197	0.102	0.106	0.168
Tibial cartilage strain	0.587	0.110	0.117	0.143
Menisci strain	0.487	0.107	0.088	0.119

1, 1-case 2, 2-case 3. Values resulted from this analysis are presented in Table 3. We can observe an progressively increase of the stress values in cartilage from healthy knee to case 1, then case 2 and case 3.

4 Conclusions

This paper presents advanced modeling and simulation methods, using the latest generation of CAD-CAE applications. For the geometric modeling of human knee joint there had been used embedded application as Ansys Workbench software package. The geometric model of the joint shows a 10^0 tilt in varus, the joint being affected by osteoarthritis in both lateral and medial compartment. Using Ansys simulation environment the virtual models of the healthy and affected knee joint has been subjected to a nonlinear analysis because of the used contacts areas. Finally a comparison is made between the results obtained from the performed analyzes. A finite element model of the knee is a powerful instrument in predicting the behavior of the healthy and affected knee joint which helps surgeons and biomechanical researchers to develop improved implants and treatment method for patients suffering bone loss and diseases. This paper shows the Von Mises stress distribution and the strain maps found in articular cartilage in femur and tibia, applying a load of 800 N, 0° in flexion and different cases with physiological varus. The values of the stress and the maximum strain due to compression forces found on the cartilages and menisci are in the limits reported by others authors. The results show that misalignment leads to an increase of stress value and this determines an articular cartilage damage and, finally, an augmenting of the osteoarthritis phenomenon.

Acknowledgments This work was supported by the strategic grant POSDRU/CPP107/DMI1.5/S/78421, Project ID78421 (2010), co-financed by the European Social Fund within the S O Program Human Resources Development 2007–2013.

References

- Bae YJ, Kyung SP, Jong KS, Dai SK (2012) Biomechanical analysis of the effects of medial meniscectomy on degenerative osteoarthritis. *Med Biol Eng Comput* 50:53–60
- Bahraminasaba M, Saharia BB, Roshdi H, Arumugamc M (2011) Finite element analysis of the effect of shape memory alloy on the stress distribution and contact pressure in total knee replacement. *Trends Biomater Artif Organs* 25(3):95–100
- Bredbenner T, Eliason T, Potter R, Masona R, Havillb L (2010) Statistical shape modeling describes variation in tibia and femur surface geometry between control and incidence groups from the osteoarthritis initiative database. *J Biomech* 43(9):1780–1786
- Catana M, Tarnita D (2012) The three-dimensional modeling of the complex virtual human knee joint. *Bulletin of the Polytechnic Institute of IASI, Tom LVIII (LXII) Fasc, vol. 3*, pp. 303–308
- Chantarapanich N, Nanakorn P, Chernchujit B (2009) A finite element study of stress distributions in normal and osteoarthritic knee joints. *J Med Assoc Thai* 92:S97–103

- Checa S, Taylor M (2008) Influence of an interpositional spacer on the behaviour of the tibio-femoral joint: A finite element study. *Clin Biomech* 23:1044–1052
- Chung LY (2004) Experimental evaluation of a natural knee contact model using response surface optimization. Degree of Master of Science, University of Florida
- Fenning SD (2005) The effects of meniscal sizing on the knee using finite element methods. In: Fritz J, Dolores H (ed.) A dissertation presented to the faculty of Russ College of Engineering and Technology of Ohio University
- Harrysson OL, Yasser AH, Nayfeh FJ (2007) Custom-designed orthopedic implants evaluated using finite element analysis of patient-specific computed tomography data: femoral-component case study. *BMC Musculoskelet Disord* 8:91
- Hartley YN (2009) The effect of the frontal plane tibiofemoral angle on the contact stress and strain at the knee joint. Mechanical engineering dissertations, Department of Mechanical and Industrial Engineering, Northeastern University
- Henderson C (2009) Use of the novel magnetic resonance based modeling technique to investigate differences in tibiofemoral articular cartilage contact area in subjects with moderate knee osteoarthritis. Master of Science in Mechanical Faculty of the University of Delaware
- Kazemi M, Li LP, Savard P, Buschmann MD (2011) Creep behavior of the intact and meniscectomy knee joints. *J Mech Behav Biomed Mater* 4(7):1351–1358
- Kubicek M, Zdenek F (2009) Stress strain analysis of knee joint. *Eng Mech* 16(5):315–322
- Lyu S, Liu D, Tseng C, Wang H, Chau L (2012) Knee health promotion option for osteoarthritic knee: Cartilage regeneration is possible. *Osteoarthritis—Diagnosis, Treatment and Surgery*, ISBN 978-953-51-0168-0
- Machado M, Flores P, Ambrosio J, Completo A (2011) Influence of the contact model on the dynamic response of the human knee joint. *Proc IMechE* 225(4):344–358
- Mohammad K (2011) A musculoskeletal model of a subject specific knee joint with menisci during the stance phase of a walk cycle. Dissertation in engineering and mathematics, University of Missouri-Kansas City
- Moroni L, Lambertsb F, Wilsonb W, Donkelaar C, Wijn JR, Huijskesb R, Blitterswijk C (2007) Finite element analysis of meniscal anatomical 3D scaffolds: implications for tissue engineering. *Open Biomed Eng J* 1:23–34
- Orsi A, Yang N, Vaziri A, Canavan P, Hashemi H (2011) Development of a failure locus for a 3-dimensional anterior cruciate ligament: a finite element analysis. In: Proceedings of the international mechanical engineering congress and exposition, Denver, Colorado, USA
- Ramaniraka NA, Terrier A, Theumann N, Siegrist O (2005) Effects of the posterior cruciate ligament reconstruction on the biomechanics of the knee joint: a finite element analysis. *Clin Biomech* 20:434–442
- Randall H (2011) Finite element analysis of knee articular cartilage. Thesis presented to Ryerson University, Master of Applied Science in the program of mechanical engineering Toronto, University of Waterloo, Ontario, Canada
- Sandholm A, Schwartz C, Pronost N, Zee M, Voigt M, Thalmann D (2011) Evaluation of a geometry-based knee joint compared to a planar knee joint. Virtual Reality Lab, École Polytechnique Fédérale de Lausanne, Lausanne, Switzerland
- Tichon DJ (2011) Finite element analysis of the effect of low-speed rear end collisions on the medial meniscus. Master's theses, University of Connecticut Digital Commons
- Vidal-Lesso A, Ledesma O, Lessa AR, Rodríguez C (2011) Dynamic response of femoral cartilage in knees with unicompartamental osteoarthritis. *J Appl Res Technol* 9(2):173–187
- Weiss JA, Gardiner JC (2001) Computational modeling of ligament mechanics. *Crit Rev Biomed Eng* 29(4):1–70
- Yang N, Hashemi N, Canavan P (2007) The effects of tibio-femoral angle and body weight on the stress field in the knee joint. In: Proceedings of the IMECE2007 international mechanical engineering congress and exposition, Seattle, Washington, USA
- Yang N, Hashemi H, Canavan P, Vaziri A (2009) Effect of frontal plane tibio-femoral angle on the stress and strain at the knee cartilage during the stance phase of gait. Published online in Wiley InterScience

Creating Artistic Curves with Planar Mechanisms

D. Tarnita, I. Popescu and D. Marghitu

Abstract The positions of closed and open kinematic chains can be obtain using symbolical and numerical Mathematica™. Rotating the mechanical systems with respect to different axis artistic curves can be obtained. Driving links and Assur groups can generate aesthetic curves that can be utilized for kinetic sculptures, fountains, or buildings. The driving links are elements with rotational motion and have complete rotation. The geometric curves are functions of the dimensions of the links and the type of kinematic pairs used for the closed kinematic chains. Curves generated using a bicorn mechanism are presented.

Keywords Aesthetic curve · Planar mechanisms · Dyads

1 Introduction

Mechanisms for obtaining solutions to geometrical problems, constructing different mathematical curves, are found in ancient Greece. The use of manipulators and robots in sculptures and buildings enable transformation to the natural world or to the aspiration of the designer and user. Mechanisms are used from machine design to kinetic art and the researchers are able to create new kinematic chains based on kinematic and dynamic analysis (Artobolevski 1977; Erdman and Sandor 1984).

D. Tarnita (✉)

Department of Applied Mechanics, University of Craiova, Craiova, Romania
e-mail: tarnita.daniela@gmail.com

I. Popescu

University of Craiova, Craiova, Romania

D. Marghitu

Auburn University, Auburn, US
e-mail: marghitu@auburn.edu

Hartenbarg (Hartenbarg 1971) presents a simple mechanical assembly for producing with a coupler plane non-circular trajectories of an infinite variety that are traversed at varying rates. The drive is moving at constant speed. The history of studies on light and the influence on artists of new knowledge about light including light produced by lasers can be found in (Doubek 1976). Kac (Kac 1997) has developed robotics into an art form to incorporated into performance, dance, and theater. Hoenich (Hoenich 1968) presented new techniques for robot-picture and robot-painter. Sculptures movement with control are presented in (Reas 2001). Jackson Pollock created fractal patterns by dripping paint onto horizontal canvases (Mandelbrot 1977; Taylor et al. 1999). Some form of nature have been shown to be chaotic and fractal (Gleick 1987; Mandelbrot 1977).

Case studies for linkage design and synthesis are presented (Hsu 2006). Analytical studies of the properties, classifications, critical examination and synthesis of coupler curves are presented in (Nolle 1974). Kinematics possibilities of mechanisms to generate complex curves are studied in (Popescu 1997; Popescu and Sass 2001; Popescu et al. 2011).

In this research we generate planar and spatial aesthetic curves and surfaces using mechanisms with dyads. The aesthetic curves and surfaces are visually pleasing curves and surfaces that allow emotional reactions. We present the coupler curves not as technical trajectories but as aesthetic forms that can be used for kinetic art.

2 Mechanisms for Generating Aesthetic Curves

For planar mechanisms the number of degrees of freedom is.

$$M = 3n - 2c_5 - c_4, \quad (1)$$

where n is the number of moving links, c_5 is the number of one degree of freedom joints, and c_4 is the number of two degrees of freedom joints.

A circle of radius AB is considered in Fig. 1 Two fixed points F and D are selected. The diameter BC and the segments DC and FB are considered. The length of the segments DC and FB is variable. The intersection point E of the segments DC and FB describes the “bicorn curve”.

For the synthesis of the mechanism the joints at B and C are build first. In this way the segments DC and FB have variable dimensions. At the intersection of the segments there is a dyad with two prismatic joints and a revolute joint.

The mechanism in Fig. 1 has seven links and ten one degree of freedom joints: $M = 3(7) - 2(10) = 1$. The structural diagram of the mechanism is shown in Fig. 2. The mechanism has a driving link with rotational motion a dyad BBF (RPR dyad), a dyad CCD (RPR dyad), and a dyad EEE (PRP dyad).

In Fig. 3 the slider-crank mechanism is rotated about an axis parallel to x -axis and situated at a distance h from the x -axis. With respect to the reference frame

Fig. 1 Mechanism that generates a bicorn curve

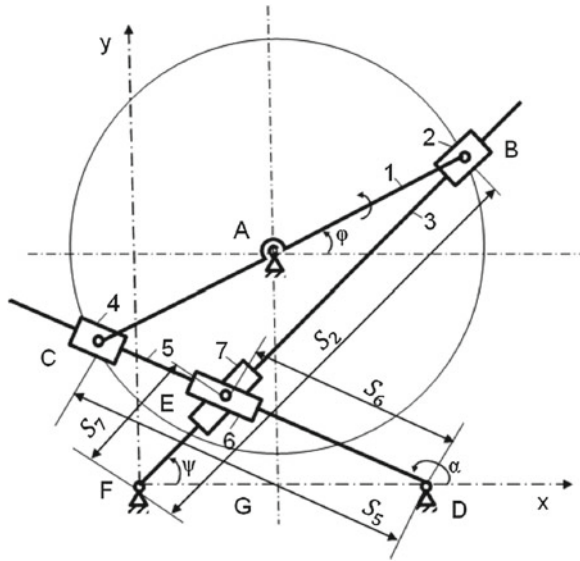
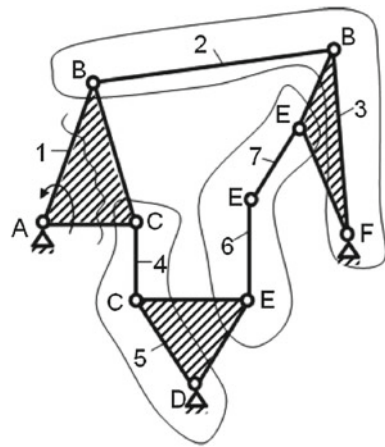


Fig. 2 Structural diagram for the mechanism



$x_Oy_Oz_O$ the coordinate x_E is constant and the coordinates y_E and z_E are changing. The rotation angle between the reference frame $x_Oy_Oz_O$ and reference frame xyz is ψ . The projection of the point E on the xy plane is M .

$$x_M = x_E, y_M = y_E, \text{ and } z_M = 0. \tag{2}$$

The coordinates of M with respect to $x_Oy_Oz_O$ are.

$$x_{M_O} = x_E, \tag{3}$$

$$y_{M_O} = y_M \cos\psi, \tag{4}$$

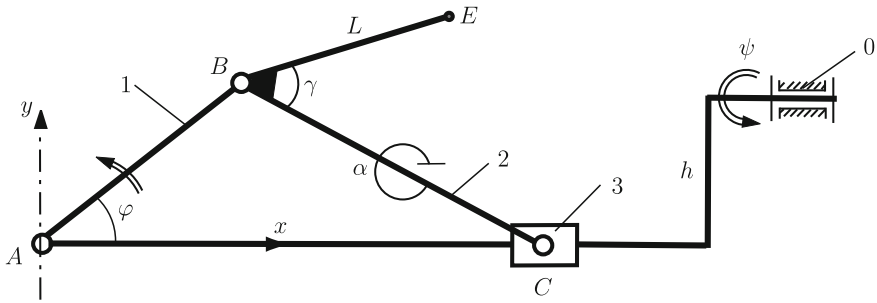


Fig. 3 Rotating slider-crank with respect to an axis parallel to x -axis

$$z_{M_O} = y_M \sin \psi. \tag{5}$$

The reference frame $x_W y_W z_W$ is located at a distance h from point A and the following relations can be written.

$$x_{M_W} = x_E, \tag{6}$$

$$y_{M_W} = y_{M_O} - h, \tag{7}$$

$$z_{M_W} = z_{M_O}. \tag{8}$$

The kinematic diagram for the mechanism with two driving links ($M = 2$) and one dyad shown in Fig. 4a has two driving links with rotational motion, links one and four, and one dyad RPR, links two and three. The kinematic joints for the dyad are revolute at B_R , prismatic at C_T , and revolute at C_R . The length of the connecting rod two is changing during the motion of the mechanism. The trajectory of the point

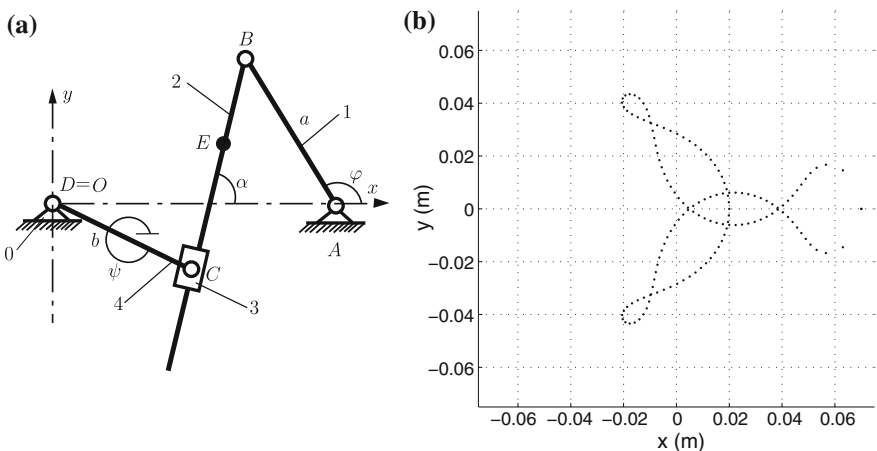


Fig. 4 Mechanism with two driving links

E located at the distance BE from joint B is studied. The geometric positions of point E will be calculated. The lengths of the driving links one and four are $AB = a$ and $CD = b$. The angle of the driving link one with the horizontal is φ and the angle of the driving link four with the horizontal is ψ . The coordinates of joint B are.

$$x_B = x_A + a \cos\varphi, y_B = y_A + a \sin\varphi, \tag{9}$$

and the coordinates of point C are.

$$x_C = x_D + b\cos\psi, y_C = y_D + b\sin\psi. \tag{10}$$

The variable length of the connecting rod BC is calculated with.

$$l_{BC} = \sqrt{(x_C - x_B)^2 + (y_C - y_B)^2}. \tag{11}$$

The changing angle α of the link two with the horizontal is given by the trigonometrical relations.

$$\cos\alpha = \frac{x_B - x_C}{l_{BC}}, \sin\alpha = \frac{y_B - y_C}{l_{BC}}. \tag{12}$$

The coordinates of point E on link 2 result from.

$$x_E = x_B + l_{BE}\cos(\alpha + \pi), y_E = y_B + l_{BE}\sin(\alpha + \pi). \tag{13}$$

The motion of the driving links 2 and 4 are correlated with the equation.

$$\varphi = c \psi. \tag{14}$$

For the initial numerical values $a = 0.03$ m, $b = 0.05$ m, $x_A = 0.015$ m, and $l_{BE} = 0.025$ m, and for a complete rotation of driving link four ($0 \leq \psi \leq 2\pi$) the angle of the driving link one is calculated with Eq. (14).

3 Results

For first mechanism, using the following initial data: $AB = 0.1$ m; $y_D = 0$; $y_A = AB$; $x_D = 5*AB$; $x_A = x_D/2$; the trajectory of the point E is shown in Fig. 5.

Changing the dimensions of the mechanism, different curves are obtained.

For the initial data: $AB = 0.1$ m; $y_D = 0$; $x_D = 5*AB$; $x_A = x_D/2$; $y_A = 0.3$ m; the curve in Fig. 6b is obtained.

For the initial data: $AB = 0.1$ m; $y_D = 0$; $x_D = 5*AB$; $x_A = x_D/2$; $y_A = 0.05$ m; the curve in Fig. 6b is obtained. For lower values of y_A there are extra loops for the curve and the curve is more flat.

For the initial data: $AB = 0.1$ m; $y_D = 0$; $x_D = 5*AB$; $x_A = x_D/2$; $y_A = -0.2$ m; the curve in Fig. 6c is obtained. For the initial data: $AB = 0.1$ m;

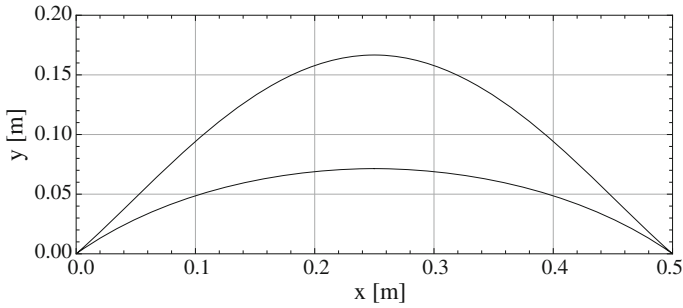


Fig. 5 Trajectory of point *E*

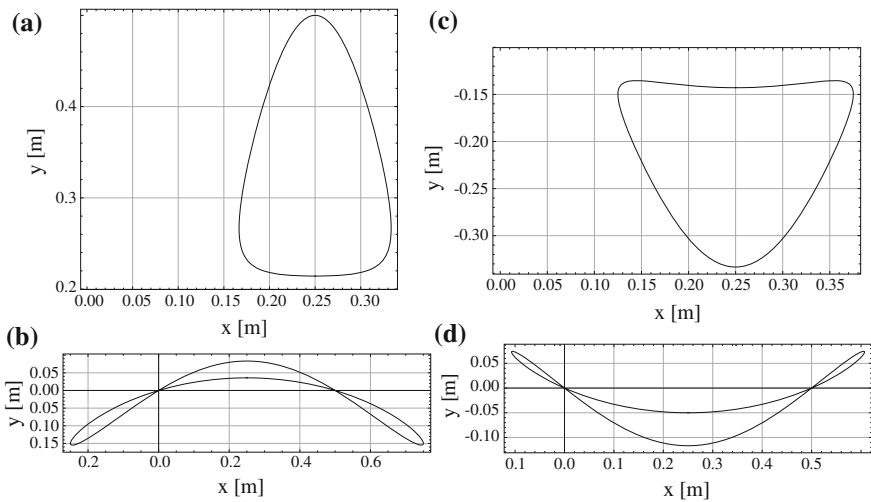


Fig. 6 Different trajectories for point *E*: **a** $y_A = 0.3$ m; **b** $y_A = 0.05$ m; **c** $y_A = -0.2$ m; **d** $y_A = -0.07$ m

$y_D = 0$; $x_D = 5 \cdot AB$; $x_A = x_D/2$; $y_A = -0.07$ m; the curve in Fig. 6d is obtained. For negative values of y_A the curve is under the x -axis.

Using the initial data: $AB = 0.1$ m; $y_D = 0$; $y_A = AB$; $x_D = 5 \cdot AB$; $x_A = x_D/2$; the planar curve is rotated about the y -axis and Fig. 7 is obtained. For the second mechanism, the Fig. 8a shows the trajectory of point *E* for $\psi = -5 \varphi$. The surface generated by the slider curve of *E* for $0 \leq \varphi \leq 2\pi$ and $0 \leq \psi \leq 2\pi$ is shown in Fig. 8b.

For the third mechanism, the trajectories of the point *E* are obtained for different values, positive and negative, of the parameter c . The driving links rotates in the same direction for positive values of c and in opposite directions for negative values of c .

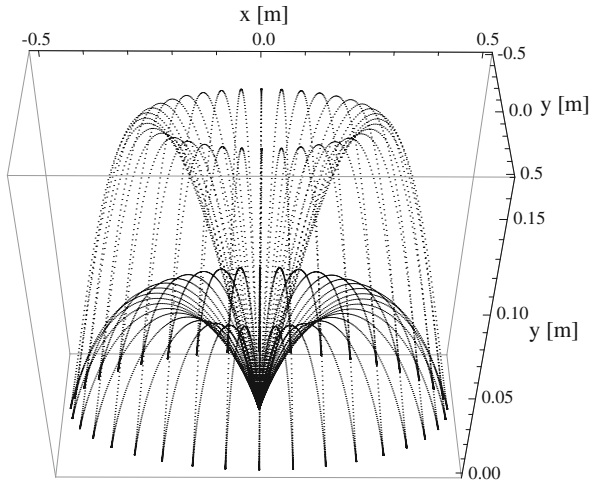


Fig. 7 Trajectories for point *E* in 3D after a rotation about *y*-axis

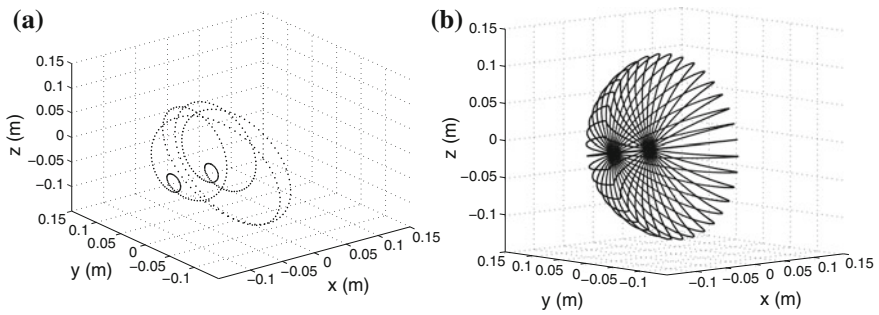


Fig. 8 **a** Trajectory of *E* for $\psi = -5\varphi$ and rotation about *x*-axis; **b** Spatial surface generated by rotating the slider curve of *E* about *x*-axis with $0 \leq \varphi \leq 2\pi$ and $0 \leq \psi \leq 2\pi$

The curve in Fig. 4b is obtained for $c = -2$. Rotating this curve along the *y*-axis a spatial surface is obtained and shown in Fig. 9. The increment for the rotation angle along the *y*-axis was selected as $\pi/6$. Rotating the planar curve along the *x*-axis the spatial surface shown in Fig. 10 is obtained. In this case the increment for the rotation angle along the *x*-axis was selected as $\pi/18$.

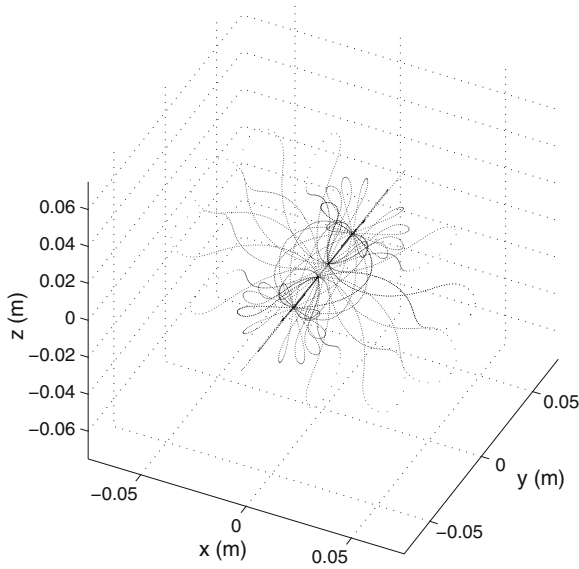


Fig. 9 Spatial surface generated by rotating the mechanism with two driving links about the y -axis

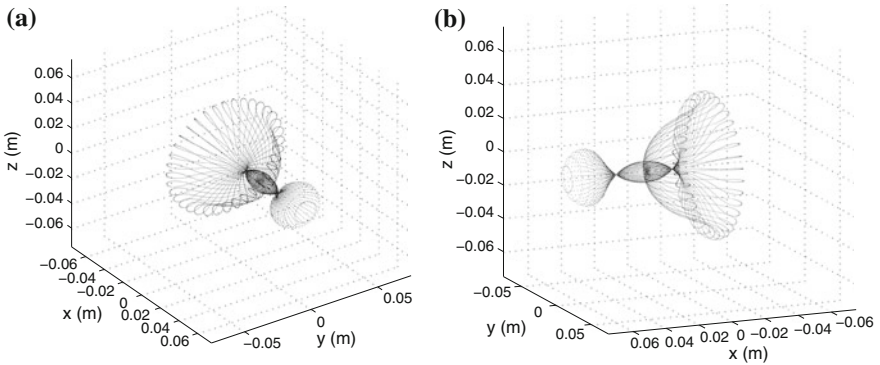


Fig. 10 Spatial surface generated rotating the mechanism with two driving links about the x -axis

4 Conclusions

We have obtained planar curves and spatial aesthetic surfaces using mechanisms with dyads. The output graphics depend on the geometry of the links. The paper presents the coupler curves not as necessary trajectories used in the technical field but the coupler curves can generate aesthetic curves and surfaces.

References

- Artobolevski II (1977) Mechanisms in modern engineering design. MIR, Moscow
- Doubek J (1976) Applications of lasers to kinetic art for the theatre and cinema. *Leonardo* 10:95–100
- Erdman AG, Sandor GN (1984) Mechanisms design. Prentice-Hall, Upper Saddle River, NJ
- Gleick J (1987) Chaos: making a new science. Penguin Books, New York
- Hartenbarg S (1971) Paths by coupler for kinetic art. *Leonardo* 4:125–128
- Hoenich PK (1968) Kinetic art with sunlight: reflections on developments in art needed today. *Leonardo* 1:113–120
- Kac E (1997) Digital reflections: the dialogue of art and technology. *Art Journal* 56(3):60–67
- Mandelbrot BB (1977) The fractal geometry of nature. W.H. Freeman, New York
- Hsu M.H.(2006) Planetary hypocycloid (epicycloid) mechanisms design, *Int J Appl Math* 38–44
- Nolle H (1974) Linkage coupler curve synthesis: a historical review II. Developments after 1875. *Mech Mach Theory* 9(3–4):325–348
- Popescu I (1997) Mechanisms. Reprography of the University of Craiova, New algorithms and programs
- Popescu I, Sass L, (2001) Mechanisms for curves generating, Edit. “Scrisul Romanesc”, Craiova
- Popescu I, Luca L, Mitsi S (2011) Geometry, structure and kinematics of some mechanisms. Edit. Sitech, Craiova
- Reas C (2001) Behavioral sculpture, Thesis Proposal for the Degree of Master of Science at the Massachusetts Institute of Technology, Thesis
- Taylor R P, Micolich A P, Jonas D (1999), ÖFractal analysis of Pollock’s Drip Paintings, Ó Nature, 399–1422

Optimal Design of the Front Suspension Mechanism Used for a Race Car

Vlad Țoțu and Cătălin Alexandru

Abstract The paper approaches the multi-criteria kinematic and dynamic optimization of the front suspension system used for a race car. The purpose of the kinematic optimization is to minimize the variations of the wheel track, wheelbase, castor angle and induced deflection, while the dynamic optimization targets to minimize the pitch and roll oscillations of the chassis. In the kinematic model, the chassis is fixed connected to ground. The dynamic model has the front suspension system mounted, while the rear suspension is replaced by a fictive spherical joint. The coordinates of the joints by which the suspension's arms are connected to the chassis are used as variables for the kinematic optimization, while for the dynamic study there are considered the coordinates of the connection points of the spring & damper. The optimization is based on design of experiments and regression models, the simulations being performed by using the software package ADAMS.

Keywords Race car · Front wheel suspension · Optimization · Regression model

1 Introduction

Kinematic analysis and optimization of the suspension mechanisms is a permanent concern and challenge. Important publications reveal a growing interest in analysis methods for multi-body systems (MBS) that may facilitate the self-formulating algorithms (Ceccarelli 2009; Haug and Choi 1995; Schiehlen 1997; Staicu 2011). Specific optimization algorithms are integrated in the commercial MBS software environments, the optimization process being based on the parameterization of the virtual model, selecting the design variables, and minimizing or maximizing the

V. Țoțu · C. Alexandru (✉)

Transilvania University of Brașov, 29 Eroilor Bvd 500036 Brașov, Romania
e-mail: calex@unitbv.ro

objective function over a selection of design variables. Generally, these methods are limited to a mono-objective optimization, or design constraints can be used as additional goals for optimization (Alexandru 2009).

This paper presents a multiple regression-based technique for the multi-criteria kinematic and dynamic optimization of the wheel suspension linkages. The optimization is approached through a screening experimental design. Based on the work space of the experiment, a linear regression model is developed, which is used to establish a relationship between the design variables and the design objectives. The application is for the front wheel suspension of a race car (Formula Student), using specific modules from the ADAMS package (Insight, View).

2 Kinematic Optimization of the Suspension Mechanism

This section approaches the multi-criteria kinematic optimization of the front wheel suspension mechanism. The suspension system is symmetrically disposed relative to the longitudinal axis of the car, so that the kinematic optimization is approached for a half-car model, considering a four-bar suspension mechanism. In kinematics, the chassis is fixed connected to ground, the vertical position of the wheel being controlled by a time-function kinematic restriction.

The half-car model contains five parts (bodies), as follows (Fig. 1): 1—chassis, 2—tie rod, 3—lower suspension arm, 4—upper suspension arm, 5—wheel assembly. Figure 2 indicates the spherical joints that connect the bodies: A & B—bodies 4/1; C & D—bodies 3/1; E—bodies 2/1 (considering that the steering rack is fixed connected to chassis); F—bodies 2/5; G—bodies 4/5; H—bodies 3/5. For the kinematic optimization, there will be considered the locations of the joints on chassis (A, B, C, D, E), resulting in this way 15 design variables (Table 1). The locations of the joints on wheel carrier (F, G, H) are established by constructive criteria.

Fig. 1 The suspension bodies

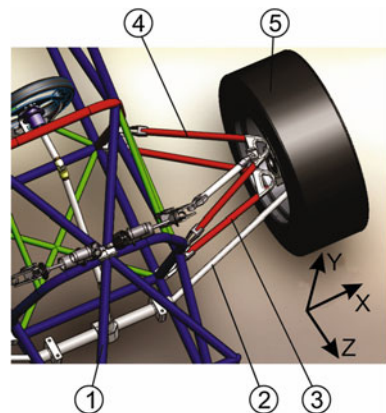


Fig. 2 The suspension joints

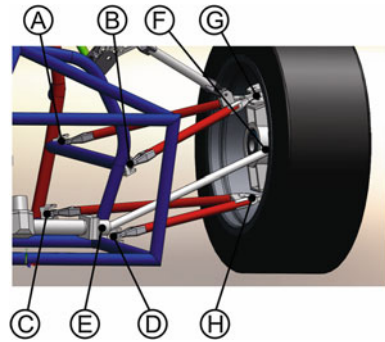


Table 1 The design variables for the kinematic optimization

Joint/point	X	Y	Z
A	DV_1	DV_2	DV_3
B	DV_4	DV_5	DV_6
C	DV_7	DV_8	DV_9
D	DV_10	DV_11	DV_12
E	DV_13	DV_14	DV_15

In the initial mechanism, the design variables have the following values (in mm): DV_1 = 259.43; DV_2 = 168.29; DV_3 = -856.9; DV_4 = 256.86; DV_5 = 167.17; DV_6 = -680.75; DV_7 = 219.71; DV_8 = 47.73; DV_9 = -878.41; DV_10 = 217.87; DV_11 = 47.42; DV_12 = -699.9; DV_13 = 272; DV_14 = 68.25; DV_15 = -546.77. For each variable, the variation field (domain) is [-15, +15] mm relative to the initial value.

The optimization goal is to minimize the variations of the wheelbase, wheel track, induced deflection and castor angle, the monitored value for each of them being the root mean square (RMS) during simulation, as follows: r_01—RMS of the induced deflection, r_02—RMS of the castor angle, r_03—RMS of the wheel track, r_04—RMS of the wheel base. The optimization is performed with ADAMS/Insight, which is a powerful design of experiments (DOE) software.

For the suspension system in study, there have been evaluated several DOE investigation strategies (Screening, Response Surface), and design types (Full Factorial, Plackett-Burman, D-Optimal). The best results, in terms of goodness of fit, have been obtained for the DOE Screening strategy with D-Optimal design (Grossman and Del Vecchio 2007).

Based on the design specifications, there have been created the design space and the work space, considering an experiment with 172 trials/runs. The design space is a matrix with the rows representing the runs, and the columns representing the design variables settings, which are in a normalized representation. The work space is a matrix with the rows indicating the trials and the columns identifying the design variables settings and resulting objectives values. There are combinations

with the minimum and maximum values of the design variables, in accordance with the variation field. For each trial, a simulation will be performed; after ADAMS/View completes the runs, the simulation results appear in the work space. As instant, a part from the work space is shown in Table 2, for the trials (runs) 1, 56, 112, 168, and 172. The analyses have been performed considering a sinusoidal vertical motion of the wheel, with the amplitude of 50 mm.

Afterwards, the work space matrix is used for fitting the results. The purpose is to establish a relationship between variables and objectives, by a multiple regression. The regression function captures the variable—objective relationship to a specified order. For this study, we have selected a linear model with interactions, whose effects are captured through special terms that consist of products of variables. The corresponding equation of the regression model has the form:

$$\begin{aligned}
 r_{0i} = & a_0 + a_1 \cdot DV_1 + a_2 \cdot DV_2 + \dots + a_{15} \cdot DV_15 + a_{16} \cdot DV_1 \cdot DV_2 \\
 & + a_{17} \cdot DV_1 \cdot DV_3 + \dots + a_{29} \cdot DV_1 \cdot DV_15 + a_{30} \cdot DV_2 \cdot DV_3 \\
 & + a_{31} \cdot DV_2 \cdot DV_4 + \dots + a_{42} \cdot DV_2 \cdot DV_15 + \dots \\
 & + a_{121} \cdot DV_14 \cdot DV_15 + e,
 \end{aligned}
 \tag{1}$$

where: r—the design objective (response), DV_1–DV_15—the design variables, a₀ to a₁₂₁—the coefficients computed by the regression analysis (a₀ being the constant term), e—the remaining error that is minimized by the regression analysis.

Table 2 Several trials from the work space (kinematic optimization)

	Trial 1	Trial 56	Trial 112	Trial 168	Trial 172
DV_1	249.43	269.43	249.43	269.43	249.43
DV_2	178.29	178.29	178.29	158.29	178.29
DV_3	-846.9	-846.9	-846.9	-846.9	-846.9
DV_4	246.86	266.86	266.86	266.86	246.86
DV_5	177.17	157.17	157.17	157.17	177.17
DV_6	-690.75	-690.75	-670.75	-670.75	-690.75
DV_7	209.71	229.71	209.71	229.71	209.71
DV_8	57.73	57.73	57.73	37.73	57.73
DV_9	-868.41	-888.41	-888.41	-868.41	-868.41
DV_10	207.87	227.87	227.87	207.87	207.87
DV_11	57.42	57.42	57.42	37.42	57.42
DV_12	-689.9	-709.9	-689.9	-709.9	-709.9
DV_13	262	282	282	262	282
DV_14	78.25	78.25	58.25	78.25	58.25
DV_15	-536.77	-536.77	-556.77	-536.77	-556.77
r_01	1.08482	1.32564	1.34152	1.17467	1.11867
r_02	0.320166	0.180598	0.813365	0.579429	0.877981
r_03	0.87579	0.863512	3.99151	1.66139	2.3862
r_04	4.81151	5.51243	5.3888	5.89829	4.80182

The goodness of fit is defined by the following measures (Manteiga and González 2006): R-squared (R2), R-squared-adjusted (R2adj), regression significance (P), range-to-variance (R/V), and F-ratio (F). R-squared indicates the variance in the predicted results versus the real data, a score of “1” indicating a perfect fit. R-squared-adjusted is similar to R2, but it is adjusted to account for the number of terms. Regression significance indicates the probability that the fitted model has no useful terms. Range-to-variance ratio indicates how well the model predicts values at the data points. F-ratio is used in the regression to test the significance of the regression, high values suggesting that the regression model is useful.

The results shown in Figs. 3, 4, 5, 6, 7 indicate that the regression models for the selected strategy (DOE Screening, D-Optimal, Interactions) matches the test data very well. The “green” indicator specifies that the entity is likely appropriate. The fit table contains also the number of independent variables that go into the estimation of a parameter (DOF), the sum of squares (SS), and the mean square (MS), for the statistical model parts: regression (model), residual (error), and total (Manteiga and González 2006).

In the final step, the effective optimization of the mechanism has been performed for minimizing the root mean squares of the responses. The method used in optimization is OptDes-GRG, which is a conventional gradient-based optimizer, provided with ADAMS/Insight. During optimization, the design variables are adjusted so that the resulting responses come as closely as possible to the specified target values. The results shown in Figs. 8, 9, 10, 11 present the variations of the interest kinematic parameters for the initial and final/optimal mechanism. There are the following values of the responses (in terms of RMS): r_01: 0.965 (initial) → 0.804 (optimal); r_02: 0.309 → 0.080; r_03: 0.835 → 0.209; r_04: 4.177 → 2.784.

Fig. 3 Goodness-of-fit summary for the kinematic responses

	r_01	r_02	r_03	r_04
R2	1 ●	1 ●	1 ●	1 ●
R2adj	1 ●	1 ●	1 ●	1 ●
P	0 ●	0 ●	0 ●	0 ●
R/V	1e+020 ●	1e+020 ●	1e+020 ●	1e+020 ●

Fig. 4 Fit regression for the induced deflection

	DOF	SS	MS	F	P
Model	171	4.49	0.0262	1e+020	0 ●
Error	0	5.1e-026	0		
Total	171	4.49			
R2	1 ●				
R2adj	1 ●				
R/V	1e+020 ●				

Fig. 5 Fit regression for the castor angle

	DOF	SS	MS	F	P
Model	171	31.3	0.183	1e+020	0 ●
Error	0	1.12e-023	0		
Total	171	31.3			
R2	1 ●				
R2adj	1 ●				
R/V	1e+020 ●				

Fig. 6 Fit regression for the wheel track

	DOF	SS	MS	F	P
Model	171	178	1.04	1e+020	0 ●
Error	0	4.49e-022	0		
Total	171	178			
R2	1 ●				
R2adj	1 ●				
R/V	1e+020 ●				

Fig. 7 Fit regression for the wheelbase

	DOF	SS	MS	F	P
Model	171	19.2	0.112	1e+020	0 ●
Error	0	5.02e-026	0		
Total	171	19.2			
R2	1 ●				
R2adj	1 ●				
R/V	1e+020 ●				

Fig. 8 Induced deflection

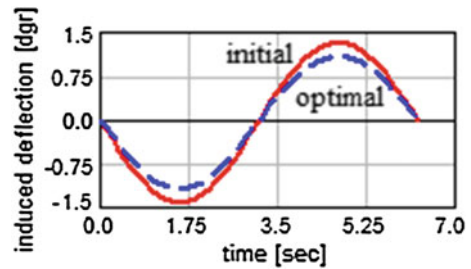


Fig. 9 Castor angle deviation

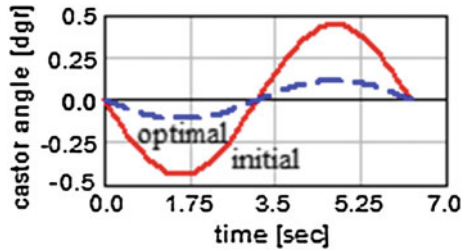


Fig. 10 Wheel track deviation

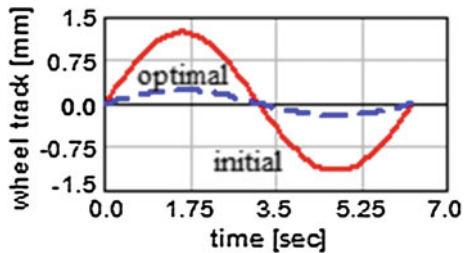
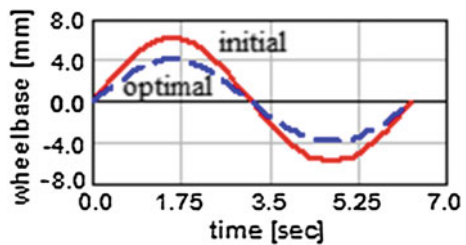


Fig. 11 Wheelbase deviation

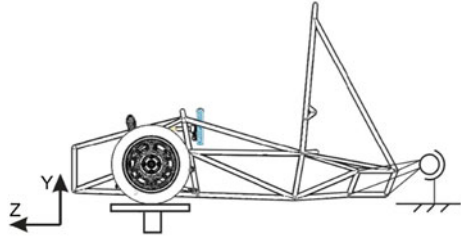


There can be observed substantial reductions of the wheel track and castor angle variations, and only a small decrease of the wheel base and induced deflection (to achieve greater reductions, there are necessary larger variation fields of the design variables). Nevertheless, the obtained optimal variant is a good one, the variations being in the acceptable domains for the Formula Student suspensions.

3 Dynamic Optimization of the Suspension System

The dynamic optimization is performed for a half-car model that corresponds to the guiding—suspension system of the front axle. In the lack of the rear suspension, modeling a fictive spherical joint between chassis and ground ensures the car equilibrium (Fig. 12). The spherical joint is disposed at the rear axle level, in the vertical—longitudinal (YZ) plane.

Fig. 12 The half-car dynamic model



The dynamic model is analyzed in the passing over bumps regime. The wheels are anchored on driving actuators, which can execute vertical motions (to simulate the road profile). The motion for the right actuator/wheel corresponds to a sinusoidal profile bump with the amplitude of 50 mm, which is passed in 0.18 s, while the left actuator is fixed maintained (as though the left wheel runs on smooth surface), thus generating roll and pitch oscillations of the chassis.

In the dynamic model, the spring & damper group is mounted between the rocker (7) and chassis (Fig. 13). The rocker has a revolute joint to the chassis, and it takes the motion from the upper suspension arm (4) through the transversal arm (6), which is connected by spherical joints to the adjacent parts (see Figs. 1, 2). The locations of the attaching points of the spring and damper groups are used as variables for the dynamic optimization. Considering the symmetry of the suspension system relative to the longitudinal axis (Z), there will result 6 design variables, as shown in Table 3. In the initial suspension, before the optimization, the design variables have the following values (in mm): $DV_{16} = 17.2$, $DV_{17} = 512.6$, $DV_{18} = -606.4$, $DV_{19} = 210.27$, $DV_{20} = 520.0$, $DV_{21} = -637.87$. The each of them, the variation field is $[-15, +15]$ mm relative to the initial value.

The optimization goal is to minimize the variations of the roll and pitch oscillations of the chassis, the monitored value for each of them being the root mean square (RMS) during simulation. The design objectives (responses) are noted in following way: r_{05} —RMS of the roll angle, r_{06} —RMS of the pitch angle.

The experimental design has been performed with the same investigation strategy as in the kinematic optimization (see Sect. 2), namely DOE Screening, with D-Optimal design and Interactions model. There is an experiment with 22 trials/runs, which are used to create the design and work spaces. A part of the work space is shown in Table 4, considering the trials 1, 7, 12, 20 and 22.

Fig. 13 The spring & damper connections

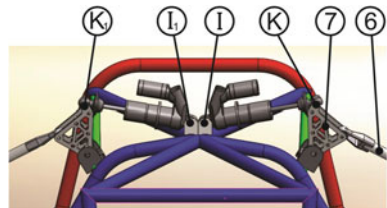


Table 3 The design variables for the dynamic optimization

Point	X	Y	Z
I/I ₁	DV_16/-DV_16	DV_17	DV_18
K/K ₁	DV_19/-DV_19	DV_20	DV_21

Table 4 Several trials from the work space (dynamic optimization)

	Trial 1	Trial 7	Trial 12	Trial 20	Trial 22
DV_16	2.2	32.2	32.2	2.2	32.2
DV_17	527.6	527.6	497.6	527.6	497.6
DV_18	-621.4	-621.4	-591.4	-591.4	-621.4
DV_19	225.27	195.27	225.27	225.27	225.27
DV_20	505	505	505	535	505
DV_21	-652.87	-652.87	-622.87	-622.87	-652.87
r_05	0.820589	0.800775	2.51156	0.710741	0.777014
r_06	0.171662	0.153685	0.486113	0.089821	0.115884

The corresponding equation of the regression model for the dynamic optimization (linear regression with interactions) has the following form:

$$\begin{aligned}
 r_{0i} = & b_0 + b_1 \cdot DV_{16} + b_2 \cdot DV_{17} + \dots + b_6 \cdot DV_{21} + b_7 \cdot DV_{16} \cdot DV_{17} \\
 & + b_8 \cdot DV_{16} \cdot DV_{18} + \dots + b_{11} \cdot DV_{16} \cdot DV_{21} + \dots \\
 & + b_{21} \cdot DV_{20} \cdot DV_{21} + e,
 \end{aligned}
 \tag{2}$$

where the terms' significance is similar to those in Eq. (1).

The results shown in Figs. 14, 15, 16 indicate that the regression model for the dynamic optimization matches the test data very well.

During the dynamic optimization, the design variables are adjusted so that the responses (roll and pitch oscillations) are minimized much as possible. Figures 17 and 18 show the time-history variations of the roll and pitch angles, in the initial and optimal system. There are the following values of the responses (in terms of RMS): r_05: 0.905 (initial) → 0.668 (optimal); r_06: 0.162 → 0.079. To achieve greater reductions, larger variation fields of the variables are required, or to address an optimization with more variables in the suspension system.

Fig. 14 Goodness-of-fit summary for the dynamic responses

	r_05	r_06
R2	1	1
R2adj	1	1
P	0	0
R/V	1e+020	1e+020

Fig. 15 Fit regression for the roll angle

	DOF	SS	MS	F	P
Model	21	5.71	0.272	1e+020	0
Error	0	1.08e-024	0		
Total	21	5.71			
R2	1				
R2adj	1				
R/V	1e+020				

Fig. 16 Fit regression for the pitch angle

	DOF	SS	MS	F	P
Model	21	0.268	0.0127	1e+020	0
Error	0	2.01e-026	0		
Total	21	0.268			
R2	1				
R2adj	1				
R/V	1e+020				

Fig. 17 Roll oscillations of the chassis

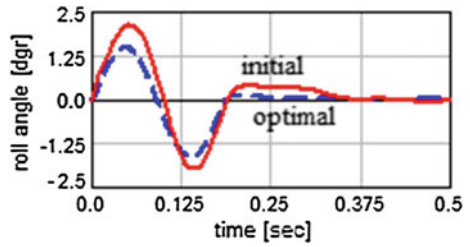
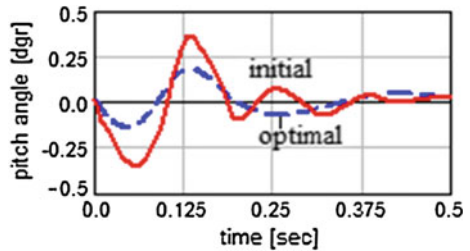


Fig. 18 Pitch oscillations of the chassis



4 Final Remarks

The modeling, simulation and optimization in virtual environment precede the development of the physical prototype, targeting the evaluation and improvement of the kinematic and dynamic behavior. The proposed optimization strategy leads to an efficient suspension, without developing expensive hardware prototypes. Thus, the behavioral performance predictions are obtained much earlier in the design cycle, thereby allowing more effective and cost efficient design changes. The obtained suspension will be implemented on the Formula Student race car of the Transilvania University, and the data sets achieved by measurements will be compared with the results of the virtual prototype analysis (for reciprocal validation).

References

- Alexandru C (2009) Software platform for analyzing and optimizing the mechanical systems. Proceedings of the 10th IFToMM international symposium on science of mechanisms and machines—SYROM, Springer, pp 665–677
- Ceccarelli M (2009) Challenges for mechanism design. Proceedings of the 10th IFToMM international symposium on science of mechanisms and machines, Springer, pp 1–13
- Grossman R, Del Vecchio R (2007) Design of experiments, John Wiley & Sons, New Jersey
- Haug EJ, Choi KK (1995) Virtual prototyping simulation for design of mechanical systems. Transact ASME 117:63–70
- Manteiga WG, González AP (2006) Goodness-of-fit tests for linear regression models with missing response data. Canadian J Stat 34(1):149–170
- Schiehlen WO (1997) Multibody systems dynamics: roots & perspectives. Multibody Syst Dyn 1(2):149–188
- Staicu S (2011) Dynamics of the 6-6 Stewart parallel manipulator. Rob Comput-Int Manuf 27(1):212–220

Educational Pneumatic Engine for a Small Size Vehicle

Tiberiu Vesselenyi, Alexandru Rus, Mircea Bogdan Tătaru
and Tudor Mitran

Abstract The paper presents the design and testing of a pneumatic engine built from standard cylinders. The engine, designed as a centric inverted slider-crank mechanism, had been modeled and simulation results are presented together with some test results used to validate the model.

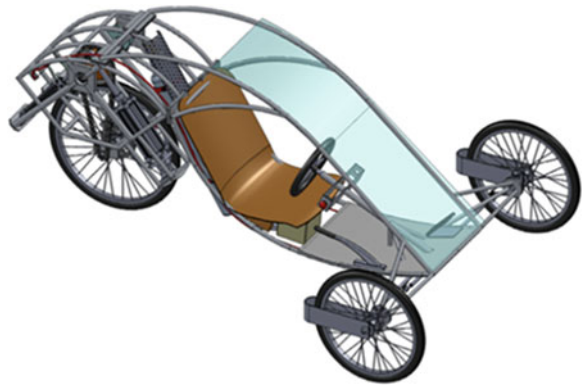
1 Introduction

The educational pneumatic engine is used on a compressed air powered experimental vehicle, designed to participate at the “PNEUMOBIL 2012” race, organized by the BOSCH-REXROTH Company. The vehicle’s engine is made up by standard pneumatic cylinders and valves supplied by the BOSCH-REXROTH company. The control of the vehicle engine is made with a IndraLogic L10 PLC. The design of the vehicle is presented in Fig. 1. The compressed air in the tank has a pressure of 200 bars which is then reduced to an operating pressure of 10 bars.

The basic idea of this project is to design the engine so that it can use as much energy as possible from the compressed air (Marghitu 2009; Williams 1994). The engine itself is in fact a centric inverted slider-crank mechanism. By completing this project, students have learned important concepts regarding mechanical and pneumatic systems design.

T. Vesselenyi (✉) · A. Rus · M. B. Tătaru · T. Mitran
University of Oradea, 410087 Oradea, Romania
e-mail: vtiberiu@uoradea.ro

Fig. 1 Small size educational vehicle



2 Basic Concept of the Pneumatic Engine

The engine of the vehicle is composed by 4 Rexroth cylinders driven by electric valves and controlled by PLC. Transmission of motion from the engine axle to the driven wheel axle is made with a chain and sprockets. The piston rods of the cylinders are coupled to a special crankshaft shown in Fig. 2 where the two arms of the shaft are rotated at 90° . In this figure only one pair of cylinders is represented. The other pair of cylinders is coupled in a similar way.

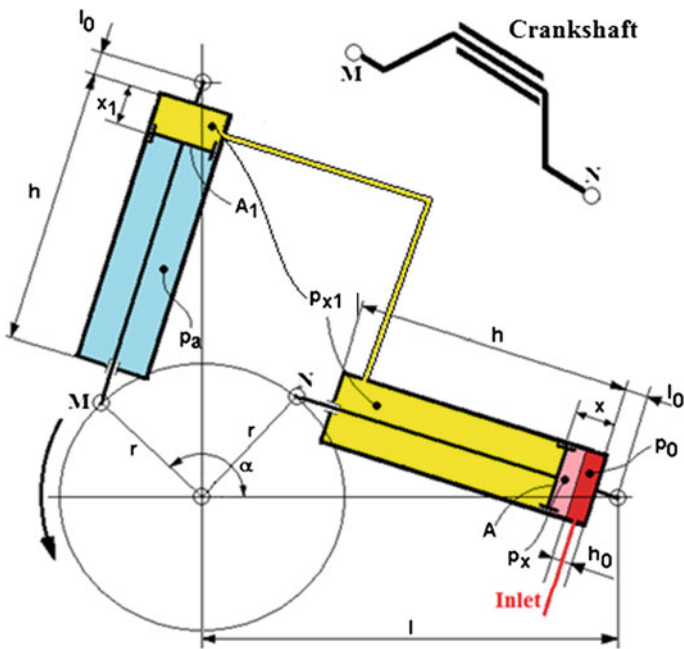


Fig. 2 Engine operation diagram

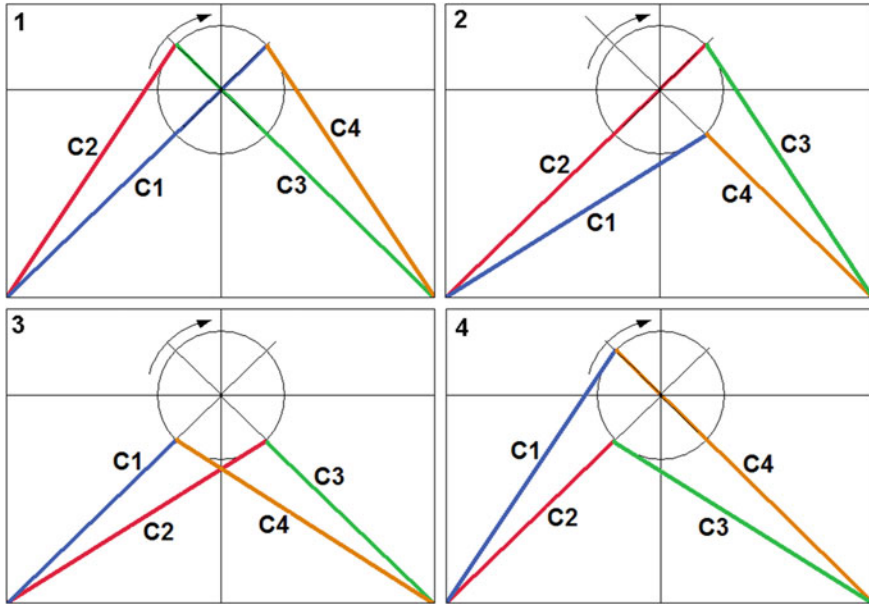


Fig. 3 Phases of operation cycles

One pair of cylinders is composed by a smaller diameter cylinder having the piston area of A and a larger cylinder having the area of A_1 . The small cylinder can be filled with compressed air in a part of the stroke (h_0) and then the air can expand from p_0 having a variable decreasing pressure p_x .

The large cylinder is powered by the air which is exhausted from the small cylinder and will expand in both two chambers having a variable, decreasing pressure p_{x1} .

The purpose of this design is to use all the energy given by the compressed air. In our design the air expands (with a reduction of pressure) and will be released in the atmosphere at a much lower pressure which means that the engine had used a greater amount of energy. A complete cycle of motion of the engine is shown in Fig. 3. In Fig. 3 the smaller, fully powered cylinders are denoted with C1 and C2 while the larger cylinders which are powered by the air received from the smaller cylinders are denoted C3 and C4.

3 Experimental Measurements for Air Expansion Estimation

In order to estimate the expansion parameters in the large cylinder we have made an experimental setup as shown in Fig. 4. The load G was given by a weight and the experiment was repeated for loads from 30 to 140 daN in steps of 5 daN.

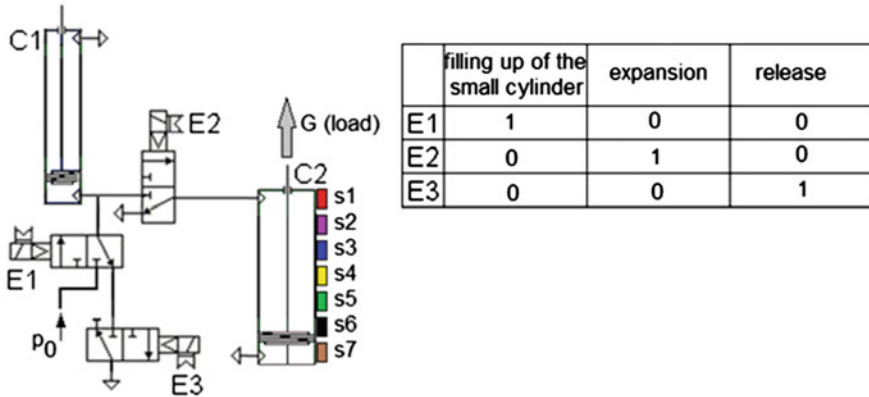


Fig. 4 Experimental device pneumatic diagram

On the large cylinder, where the expansion occurs, a set of 7 Reed relays had been placed coupled to a data acquisition board.

After data processing the diagrams in Fig. 5 could be obtained.

The diagrams clearly show that the expansion of air can give a significant boost to the engine using only the compressed air exhausted from the small cylinder (which usually is lost) at least up to a load of 80 daN.

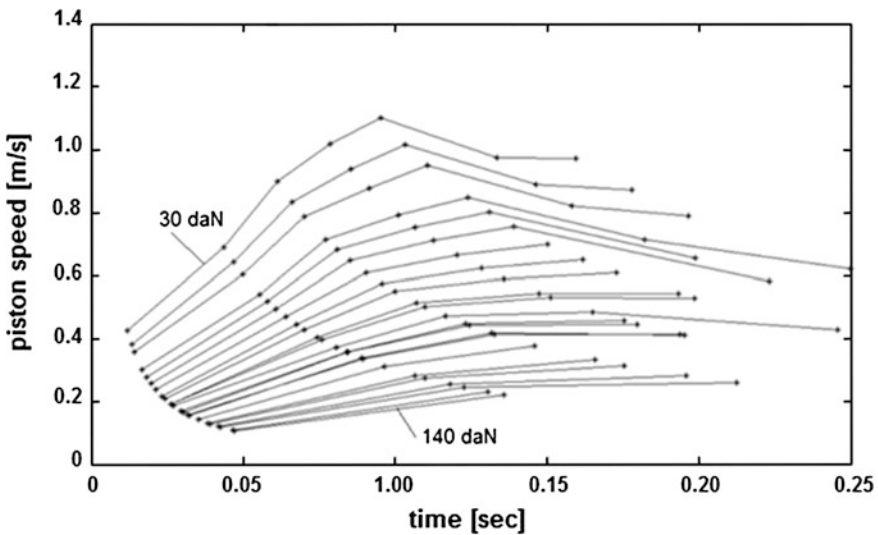


Fig. 5 Experimental results: piston speed versus time, for different loads

4 Torque Computation Program

For engine torque calculations the geometrical notations are shown in Fig. 6. In order to choose the proper cylinder diameters we have developed a program which computes the engine torque as function of large cylinder and small cylinder area ratio and the length of stroke on which the small cylinder is under p_0 pressure (10 bars).

Parameters used in computation of torque are as follows:

$h = 0.192$ m—total length of piston stroke; $k = p_0/p_a$; h_0 —fill length;
 $k_1 = h_0/h$; $k_v = h_0/x$; $A_1 =$ large cyl. area; $A = 0.025$ m²—small cyl. area;
 $k_a = A_1/A$; $n = 1.2$ —polytropic coefficient; $r = 0.1$ m.

We then compute the torque of the engine for a range of values of $k_a = 1 \dots 10$ and also for a range of fill lengths $h_0 = h/10 \dots h$. For every pair of values of k_a and h_0 we compute the values of engine torque on a whole cycle, according to the following relations:

$$k_1 = \left(\frac{h_0}{h}\right)^n \tag{1}$$

Given α in the range of $1 \dots 360^\circ$ for one cycle, the engine parameters are:

$$c = \sqrt{l^2 - 2lr \cos(\alpha) + r^2} \tag{2}$$

The length of the current lever arm is given by (3):

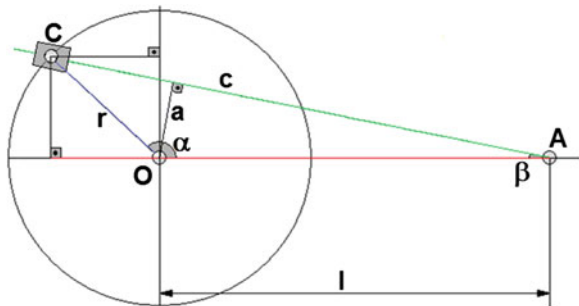
$$a = \frac{lr \sin(\alpha)}{c} \tag{3}$$

In order to compute the current pressure in the cylinders we defined the following parameters:

$$x = c - (h + l_0) \tag{4}$$

$$k_v = \begin{cases} 1; & x < h_0 \\ \left(\frac{h_0}{x}\right)^n; & x \geq h_0 \end{cases} \tag{5}$$

Fig. 6 Schematic of centric inverted slider-crank mechanism



$$k_{v1} = \left(\frac{h}{h - x + k_a x} \right)^n \tag{6}$$

Torque given by 2 cylinders has the expression:

$$T = A[(p_x - p_{x1})a + (p_{x1} - p_a)k_a a] \tag{7}$$

where $p_x = p_a \cdot k \cdot k_v$ and $p_{x1} = p_a \cdot k \cdot k_l \cdot k_{v1}$.

Representing the mean torque of the engine (computed using relation (7)) as function of h_0 and the rate of large cylinder and small cylinder area (k_a) we obtain the diagram in Fig. 7.

As it can be observed from this diagram, the best option is to use a radius rate of approximately 1.6–1.8. So the large cylinder radius will be of 0.040 m. The diagram also shows that the pressure p_0 must be applied to the smaller piston at least for half the stroke. In order to have a reserve of torque, we can choose transmission ratios (engine axle torque/wheel axle torque) of 3. The schematic of the drive chain is also presented in Fig. 8. Operational parameters of the vehicle, considering computed torque and transmission rate as well as pneumatic parameters are presented in Table 1.

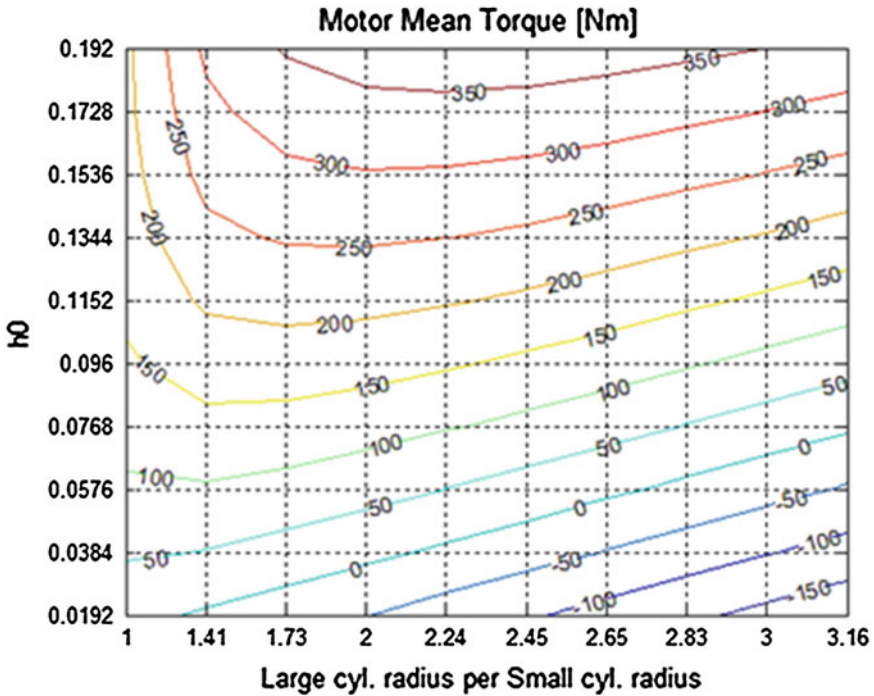


Fig. 7 Engine mean torque as function of h_0 and the A_1/A ratio

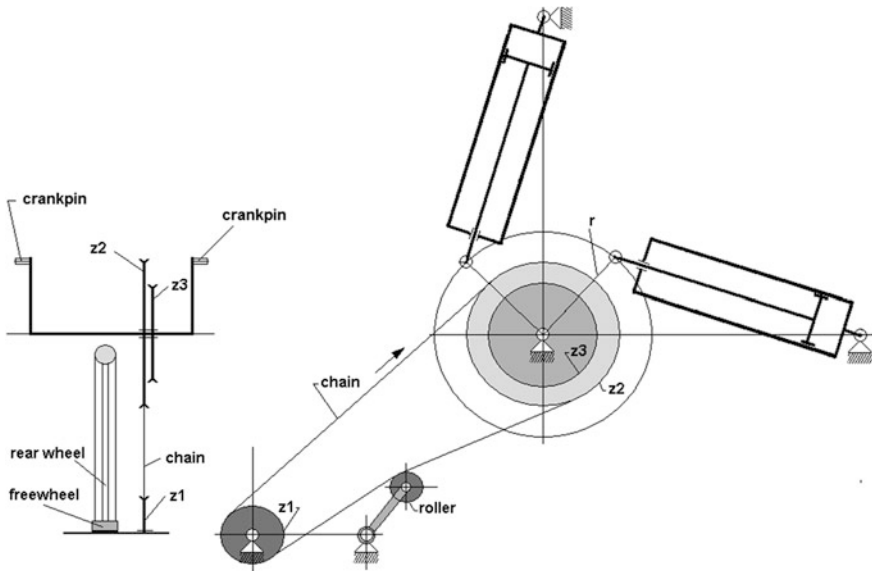


Fig. 8 Drive mechanism of the vehicle

Table 1 Pneumatic parameters

Vehicle speed [km/h]	Transmission rate	Flow rate [l/min]	Engine axle rotation speed [RPM]	Wheel axle rotation speed [RPM]	Piston speed [m/s]
45	3	563	120.5	361.5	0.8033

5 Conclusions

The engine presented in this paper had been designed and tested by the authors. As far as we know systems using compressed air expansion had not been used yet in a way presented in our paper (Cundiff 2002; Graebel 2007; King 2002; Parr 2011).

Our experimental results show that air expansion can produce significant surplus of actuating force, enhancing the engine efficiency. This expansion based operation is only possible if the engine, designed by the authors, is a central inverted slider-crank mechanism with two pins at 90° to couple the 4 cylinders. We also developed a computer program which includes the mathematical model of the mechanism and which generates torque diagrams in order to support an optimal solution for cylinder diameter selection. Based on this design the vehicle was built and tested having a maximal speed of 38 km/h.

References

- Cundiff JS (2002) Fluid power circuits and controls, fundamentals and applications. CRC Press LLC, United States
- Graebel WP (2007) Advanced fluid dynamics. Academic Press, Elsevier Inc, Massachusetts
- King RP (2002) Introduction to practical fluid flow, Butterworth-Heinemann
- Marghitu DB (2009) Mechanisms and robots analysis with matlab, Springer Dordrecht Heidelberg London New York, Springer—Verlag London ltd, ISBN 978-1-84800-391-0
- Parr A (2011) Hydraulic and pneumatics, a technician's and engineer's guide, Butterworth-Heinemann, Oxford
- Williams II RL (1994) Mechanism kinematics & dynamics and vibrational modeling. Mechanical Engineering, Ohio University. Notes book supplement for ME 3011 kinematics & dynamics of machines, © 2013 Dr. Bob Productions

A Structural Synthesis of a New Leg Mechanism

I. Dugaesescu, M. Ceccarelli and A. Comanescu

Abstract This paper presents a procedure for the structural synthesis of a new planar leg mechanism. Several new kinematic schemes of a planar leg mechanism have been created by composing Evans mechanism and the pantograph mechanism. In order to identify a new leg mechanism for walking robots with low-cost easy-operation features a procedure of the structural analysis has been also introduced and applied.

Keywords Structural analysis · Leg mechanisms · Design · Planar mechanisms

1 Introduction

The structural synthesis of mechanisms is also used to design mechanical systems which can generate a given trajectory.

The biped robots have characteristics with path generation issues, such as their capacity of displacement to avoid obstacles, to ascend and to descend stairs (Li and Ceccarelli 2011). The motion of legged robots is achieved by actuating motors. Each leg of a mobile robot has generally three actuating motors. There are also legged robots with a complex structure and a special control system.

I. Dugaesescu (✉) · A. Comanescu
Department of Machines and Mechanisms Theory, Politehnica University of Bucharest,
Bucharest, Romania
e-mail: ileana_d1@yahoo.com

A. Comanescu
e-mail: adrianacomanescu@yahoo.com

M. Ceccarelli
LARM: Laboratory of Robotics and Mechatronics, DICEM, University of Cassino and
South Latium, Cassino, Italy
e-mail: ceccarelli@unicas.it

There are many types of mechanisms which can be used to actuate a robot leg. The four-bar mechanism with its variants and the pantograph mechanism may be used and indeed they widely implemented.

Several walking robots were designed at LARM in Cassino (Ottaviano et al. 2004). They are based on a Chebyshev mechanism and a pantograph one. The Chebyshev mechanism generates an approximate trajectory with a very accurate straight part (Ottaviano et al. 2004). An important parameter for a leg mechanism is the degree of mobility. The degree of mobility is determined by the number of the independent parameters of the system according its number of active joints. If the number of the active joints is limited at few motors, advantages such as low-cost and easy-operation may be achieved. These planar mechanisms generate a suitable curve of the leg extremity and reduce the motion control complexity.

This paper presents a structural analysis procedure for a new planar leg mechanism. This new leg is based on a pantograph mechanism and Evans four-bar mechanism.

2 A Structural Synthesis Procedure

In order to obtain certain trajectories of the end-effector the structural synthesis of leg mechanisms has the following objectives: to identify the degree of mobility, the number of the kinematic links and pairs, the pair types.

A structural analysis is aimed to obtain structural models from a kinematic scheme included in the mechanical system data basis (Comănescu et al. 2010). The structural solutions for kinematic linkages are mentioned in the literature (Comănescu et al. 2010) and then the kinematic schemes are deduced.

A proposed procedure for obtaining kinematic schemes follows seven steps marked in Fig. 1:

Step 1: The degree of mobility determination [$M = 0, M = 1, M = 2$]. This means to choose the number of simple movements that determines the motion degree of all kinematic elements.

Step 2: The determination of the number of independent contours.

The number N of the independent contours shows the number of the independent vectorial equations for that mechanism (Chu et al. 1998; Comănescu et al. 2010).

Step 3: The following equations give the links and pairs numbers.

$$\begin{aligned} m &= 2N + M \\ c &= 3N + M \end{aligned} \tag{1}$$

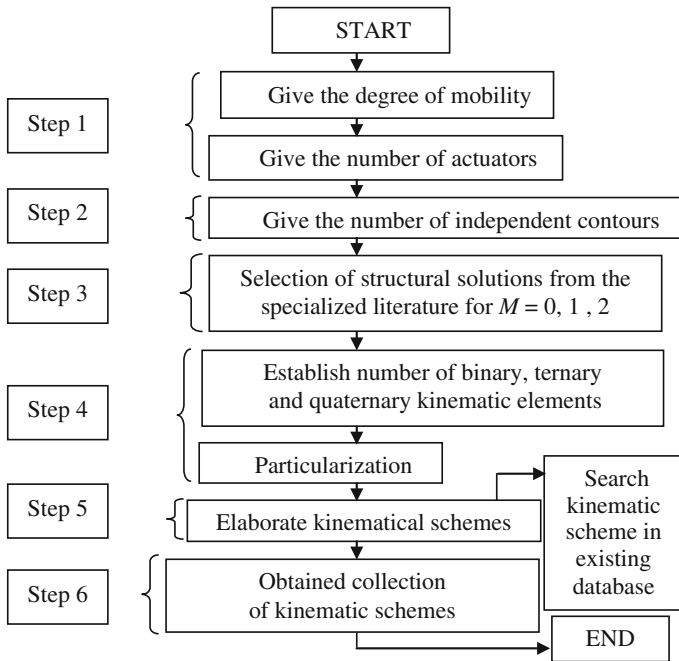


Fig. 1 A proposed procedure for the kinematic structure synthesis

By using them one may select kinematic linkages with M and N parameters from a planar linkages data base (Comănescu et al. 2010).

In Eq. (1) m represents the number of mobile kinematic elements and c is the total number of lower pairs (revolute and prismatic pairs).

Step 4: The structural solutions in Fig. 2 may be chosen for planar mechanisms obtained from kinematic chains with one degree of mobility.

Step 5: From the chosen structural solutions one may establish the number of links as follows: the binary link number (n_2), the ternary link number (n_3), the quaternary link number of (n_4) etc.

Step 6: Determination of the kinematic schemes.

A kinematic scheme is the representation of a system with shape and geometrical dimensions of the kinematic elements, nature and position of the pairs. This is a drawing scale valid for a single position system (Comănescu et al. 2010).

Step 7: The kinematic scheme can be identified from existing kinematic schemes in specialized literature.

In the specialized literature (Comănescu et al. 2010) all structural solutions for kinematic chains with one degree of mobility and two and three independent loops mentioned in Fig. 2 are given.

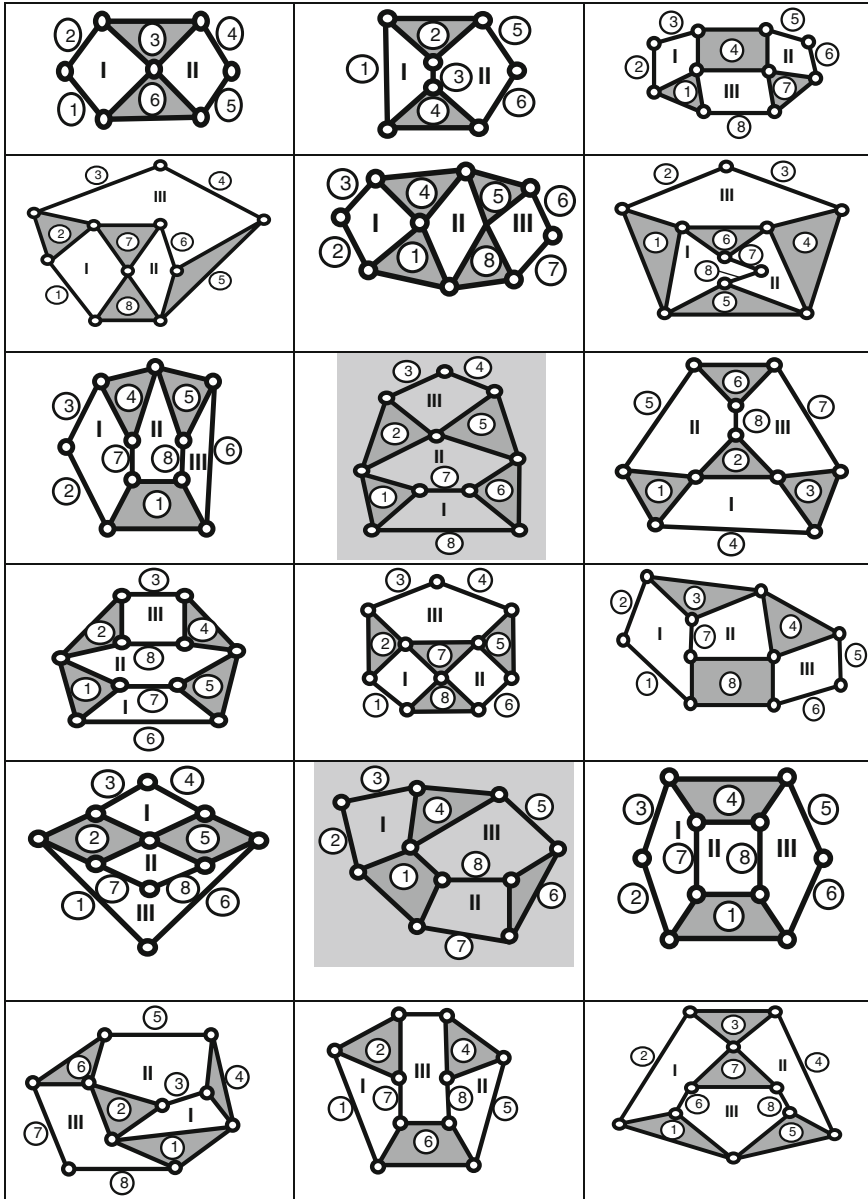


Fig. 2 The structural solutions for planar kinematic linkages with one degree of mobility and two and three independent loops

3 A Structural Analysis Procedure

In order to obtain solutions for mechanisms with one degree of mobility a linkage can be selected from Fig. 2. A structural analysis may follow the next steps (Fig. 3).

- Step 1: Selection of actuators. The actuators are placed in the active kinematic pairs. Their number is equal to the degree of mobility of the mechanism.
- Step 2: Identification of the structural groups. In the structure of a planar mechanism there are passive and active groups. The passive groups are open linkages with zero degree of mobility (dyads, triads etc.). The active groups have positive degree of mobility.
- Step 3: Identification of the associated graph for the structural scheme. The kinematic elements are represented by vertices (nodes) and the lower joints by edges.
- Step 4: The adjacency matrix (A) for the graph. In this matrix the elements may be 0 or 1 in function of the existing connections between links. The value of the A^k matrix is used¹ to determine the paths of length k ($k = 1, 2, 3, \dots$).
- Step 5: Identification of the modular groups connection.

4 A Procedure for the Leg Mechanism Design

In this paper the proposed procedure is applied to design a new leg mechanism with one degree of mobility composed by a pantograph mechanism and a four-bar mechanism.

One of the objectives of this paper is to find a proper structural analysis based on a kinematic scheme for a walking legged robot. A suitable kinematic chain can be obtained by using Evans straight-line mechanism and a pantograph structure.

The Evans straight-line mechanism in Fig. 4 is a four-bar linkage (Liang et al. 2008; Li and Ceccarelli 2011) with AB as a crank and the joints A and D are the connections with the frame. The links AB, BC and EB are all equal. The point E describes an approximate straight-line.

For a new leg mechanism it is possible to have one degree of mobility ($M = 1$) and three independent contours ($N = 3$). Based on Eq. (1) seven mobile kinematic elements and ten joints can be used.

The Evans linkage has $n_2 = 2$, $n_3 = 1$ or $n_2 = 2$, $n_4 = 1$. The pantograph linkage has $n_2 = 2$, $n_3 = 2$ or $n_2 = 3$, $n_4 = 1$.

Two variants of linkages with one degree of mobility and three independent contours (marked in Fig. 2) are identified and presented in Fig. 5.

Some mechanism solutions are presented in Fig. 6.

¹ <http://www.math.cornell.edu/~mec/Winter2009/RalucaRemus/Lecture2/lecture2.html>. Accessed on 14 July 2012.

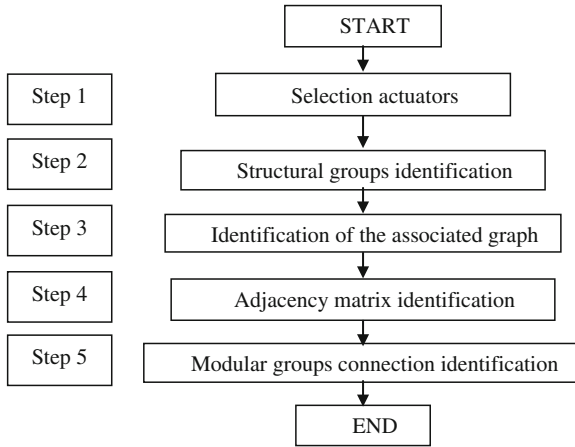


Fig. 3 A proposed procedure for the structural analysis

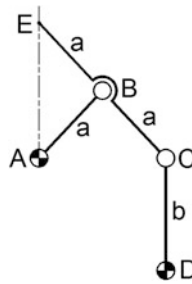


Fig. 4 An Evans straight line mechanism

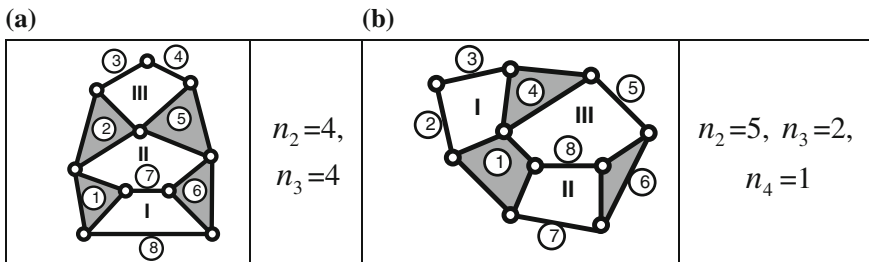


Fig. 5 The chosen structural solutions: a variant 1; b variant 2

4.1 The Structural Analysis of the Planar Leg Mechanism

The proposed procedure in Fig. 3 is applied to the case in Figs. 5 and 6 for two possible solutions. A graph can be represented by a square matrix of size equal to its number of nodes (Comănescu et al. 2010).

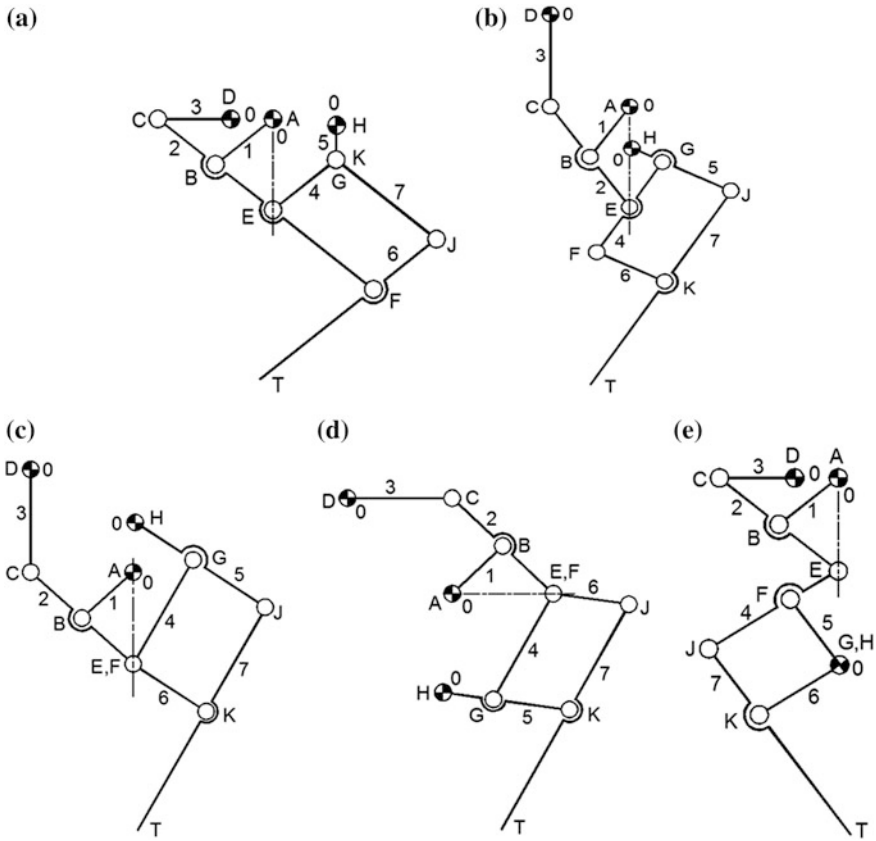


Fig. 6 Leg mechanisms based on the kinematic chains in Fig. 5

In the first case there are four binary elements and four ternary elements (Fig. 6b, c). The structural scheme which corresponds to this situation is presented in the Fig. 7. The actuating pair is drawn as a black dot.

The structural model in Fig. 7 is composed by one active modular group (GMAI(A,1)) and three passive groups of the RRR dyad type (Comănescu et al. 2010). The modular groups connection for the scheme presented in Fig. 7 is given in Fig. 8.

The associated graph of the structural model is given in Fig. 9. It is composed by 7 mobile links, 10 lower pairs and three independent contours.

This graph has eight nodes, ten edges and three independent contours. The adjacent matrix A is built with all direct connections between nodes (1 if there is an edge and 0 otherwise). The matrix is a square and symmetric one its elements of the principal diagonal being null, because an element can not be connected to itself.

Fig. 7 The structural model for mechanisms in Fig. 6b, c

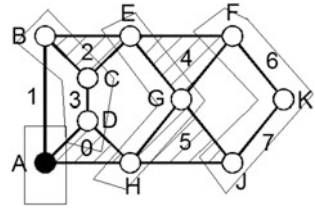


Fig. 8 The modular groups connection for the structural model in Fig. 7

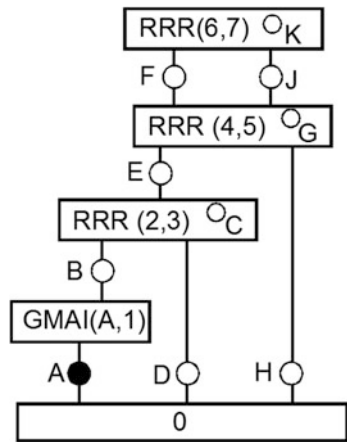
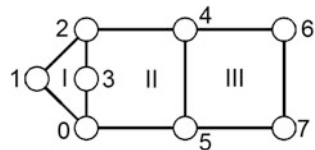


Fig. 9 The associated graph for the model in Fig. 7

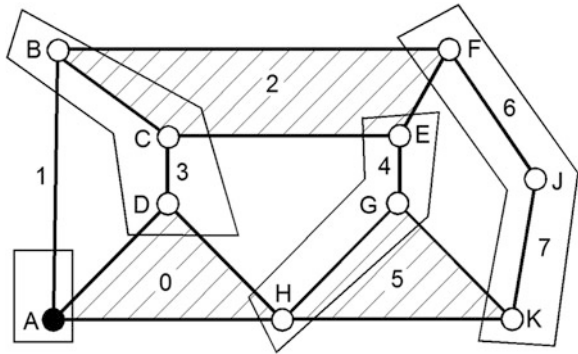


$$A = \begin{pmatrix} 0 & 1 & 0 & 1 & 0 & 1 & 0 & 0 \\ 1 & 0 & 1 & 0 & 0 & 0 & 0 & 0 \\ 0 & 1 & 0 & 1 & 1 & 0 & 0 & 0 \\ 1 & 0 & 1 & 0 & 0 & 0 & 0 & 0 \\ 0 & 0 & 1 & 0 & 0 & 1 & 1 & 0 \\ 1 & 0 & 0 & 0 & 1 & 0 & 0 & 1 \\ 0 & 0 & 0 & 0 & 1 & 0 & 0 & 1 \\ 0 & 0 & 0 & 0 & 0 & 1 & 1 & 0 \end{pmatrix} \tag{1}$$

The rank of the i link is $\sum_j a_{ij} = \sum_i a_{ji}$.

In the second case there are five binary elements, two ternary elements and one quaternary element (Fig. 6a, d and e). Any link may be chosen as the frame.

Fig. 10 The structural model of mechanisms in Fig. 6a, d



The structural model given in the Fig. 10 has a ternary element for the frame (see the Fig. 6a, d). It is composed by active modular group and three passive groups of RRR dyad type (Fig. 11).

The associated graph of the kinematic scheme is given in Fig. 12.

The adjacent matrix B in this case is given as follows:

$$B = \begin{pmatrix} 0 & 1 & 0 & 1 & 0 & 1 & 0 & 0 \\ 1 & 0 & 1 & 0 & 0 & 0 & 0 & 0 \\ 0 & 1 & 0 & 1 & 1 & 0 & 1 & 0 \\ 1 & 0 & 1 & 0 & 0 & 0 & 0 & 0 \\ 0 & 0 & 1 & 0 & 0 & 1 & 0 & 0 \\ 1 & 0 & 0 & 0 & 1 & 0 & 0 & 1 \\ 0 & 0 & 1 & 0 & 0 & 0 & 0 & 1 \\ 0 & 0 & 0 & 0 & 0 & 1 & 1 & 0 \end{pmatrix} \quad (2)$$

The adjacent matrix B given in (2) shows all direct connections between nodes.

Fig. 11 The modular groups connection for the structural model of Fig. 6a, d

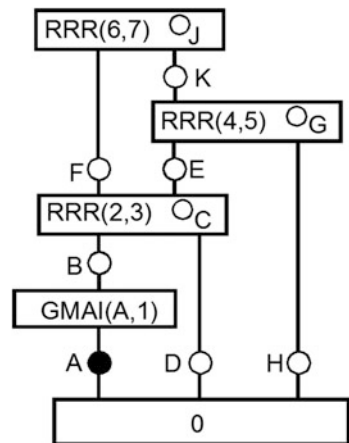


Fig. 12 The associated graph for the model in Fig. 10

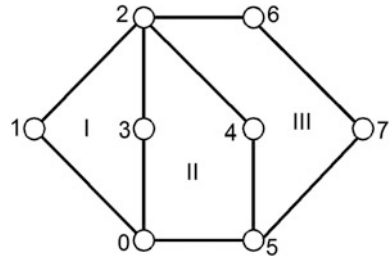
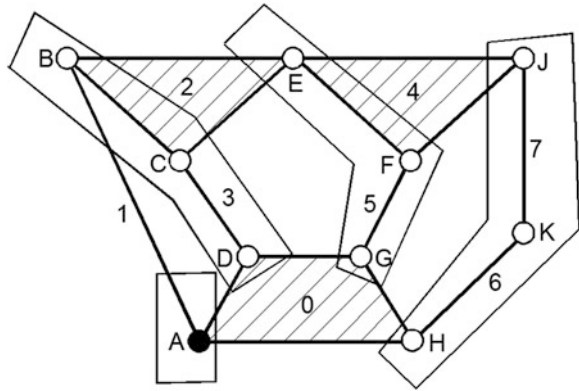


Fig. 13 The structural model of mechanisms in Fig. 6e



If the fixed element has four pairs (see Fig. 6e) the structural model is given in Fig. 13 and corresponds to the graph connection identified in Fig. 14.

The associated graph (Fig. 15) of the kinematic scheme is given in the Fig. 16. The adjacent matrix C in this case is given as follows:

$$C = \begin{pmatrix} 0 & 1 & 0 & 1 & 0 & 1 & 1 & 0 \\ 1 & 0 & 1 & 0 & 0 & 0 & 0 & 0 \\ 0 & 1 & 0 & 1 & 1 & 0 & 0 & 0 \\ 1 & 0 & 1 & 0 & 0 & 0 & 0 & 0 \\ 0 & 0 & 1 & 0 & 0 & 1 & 0 & 1 \\ 1 & 0 & 0 & 0 & 1 & 0 & 0 & 0 \\ 1 & 0 & 0 & 0 & 0 & 0 & 0 & 1 \\ 0 & 0 & 0 & 0 & 1 & 0 & 1 & 0 \end{pmatrix} \quad (3)$$

Consequently a specific adjacent matrix characterizes each structural solution given in Fig. 5.

New solutions can be identified in the leg mechanisms in Fig. 6a, b, d and e, but the most feasible ones looks to be Fig. 6c, e.

Fig. 14 Connection for the structural model of Fig. 6e

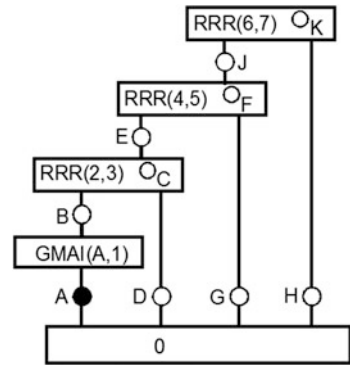


Fig. 15 The associated graph for the model in Fig. 13

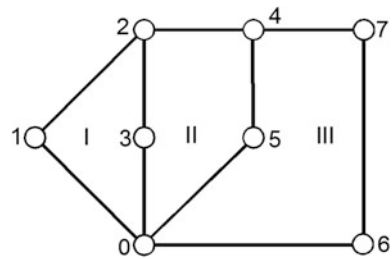
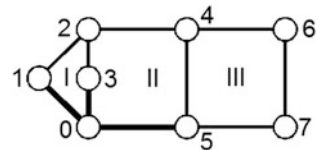


Fig. 16 Three kinematic elements connected to the fixed element (base)



4.2 The Analysis Through Adjacent Matrix

By using the graph theory more characteristics of structural solutions are put into evidence, such as the relation between the adjacency matrix and the paths of length k ($k = 1, 2$).

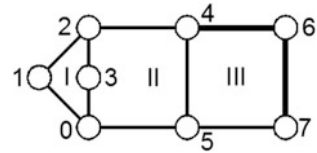
In an adjacency matrix given in (1-3) two nodes x_i and x_j of graph are taken. The existence of a path of length 2 between them implies the existence of a node k in the graph, where $x_i x_k$ and $x_j x_k$ are edges.

To describe the existence of a path between two nodes is enough to calculate the square power of the adjacent matrices A , B and C .

In the first case the analysis can be carried out by means of the adjacent matrix.

The calculation of the matrix $A^2 = A \cdot A$ gives

Fig. 17 The connection of the kinematic element 6



$$A^2 = \begin{pmatrix} 3 & 0 & 2 & 0 & 1 & 0 & 0 & 1 \\ 0 & 2 & 0 & 2 & 1 & 1 & 0 & 0 \\ 2 & 0 & 3 & 0 & 0 & 1 & 1 & 0 \\ 0 & 2 & 0 & 2 & 1 & 1 & 0 & 0 \\ 1 & 1 & 0 & 1 & 3 & 0 & 0 & 2 \\ 0 & 1 & 1 & 1 & 0 & 3 & 2 & 0 \\ 0 & 0 & 1 & 0 & 0 & 2 & 2 & 0 \\ 1 & 0 & 0 & 0 & 2 & 0 & 0 & 2 \end{pmatrix}$$

For example in first row and first column the element is 3 which correspond to the fact that at the base element there are three connections. It means at the base element are connected three kinematic elements (1, 3 and 5) that can be shown in the Fig. 11.

In seventh row and seventh column the element is 2. This means the kinematic element 6 has two connections (with 4 and 7 kinematic elements) (Fig. 17).

The matrix diagonal elements reveal the number of connections of each corresponding link.

5 Conclusions

This paper presents a structural synthesis that is based on structural analysis and adjacent matrices. New distinct solutions for mechanisms with one degree of mobility may be obtained by using the adjacent matrix and its square.

New designed solutions were obtained by combining Evans straight-line mechanism with a pantograph mechanism.

From the structural point of view and in order to avoid the aberrations in function an optimal model with one degree of mobility must have a minimum number of passive modular groups (Comănescu et al. 2010).

Acknowledgments The work was partially supported by for the project “Exploitation of Cultural Identities in global processes” co financed by the European Union and the Government of Romania from European Social Fund through the Operational Sectorial Program for the Human Resources Development, POSDRU/89/1.5/S/59758.

References

- Chu J, Cao W, Yang T (1998) Type synthesis of Baranov truss with multiple joints and multiple joint links. Proceedings of ASME design engineering technical conference, Atlanta, Georgia
- Comănescu Adr, Comănescu D, Dugaesescu I (2010) Bases of the mechanisms modeling. Editura Politehnica Press, București (in Romanian). ISBN 978-606-515-115-47
- Li T, Ceccarelli M (2011) A topology search for a new LARM leg mechanism. Proceedings of MUSME 2011, the international symposium on multibody systems and mechatronics, Valencia, Spain, 25–28 Oct 2011
- Liang C, Ceccarelli M, Takeda Y (2008) Operation analysis of a one-DOF pantograph leg mechanisms. Proceedings of the RAAD 2008, 17th international workshop on robotics in Alpe-Adria-Danube region, Ancona, Italy, 15–17 Sept 2008
- Ottaviano E, Lanni C, Ceccarelli M (2004) Numerical and experimental analysis of a pantograph-leg with a fully-rotative actuating mechanism. Proceedings of the 11th world congress in mechanism and machine science, Tianjin, 1–4 April 2004

Regression Model for Optimizing the Thin Films Deposition on Planar Photovoltaic Cells

Monica Enescu and Cătălin Alexandru

Abstract The paper puts forward the optimization of the thin films deposition using spray pyrolysis. The application is for the photovoltaic cells, considering the deposition on a planar surface, by using a robotic system. A solution to optimize the characteristic parameters of the spray pyrolysis deposition using design of experiments (DOE) and multiple regression is proposed. The optimization purpose is to improve the thin film uniformity. The study is based on DOE Response Surface investigation strategy with Fractional Factorial design and Interactions model. The work space contains 32 trials, which have been used for fitting the results to a regression model. The numerical values of the film thickness are obtained by experimental measurements, using Ultraviolet/Visible spectroscopy. The optimization is conducted in ADAMS/Insight by a conventional gradient-based optimizer.

Keywords Thin film deposition · Experimental design · Regression model

1 Introduction

The photovoltaic (PV) systems convert solar energy into electric energy, their efficiency depending on the degree of use and conversion of the solar radiation. Titanium Dioxide (TiO₂) is frequently used in the PV systems due to its optical properties. Conditions for obtaining TiO₂ and the specific properties are presented in the literature (Okuya et al. 1999; Suciu et al. 2011). Besides being a cheap and simple technique, spray pyrolysis allows deposition on large areas and on complex surfaces. This deposition technique is being used in various applications, such as

M. Enescu · C. Alexandru (✉)

Transilvania University of Braşov, 29 Eroilor Bvd, 500036 Braşov, Romania
e-mail: calex@unitbv.ro

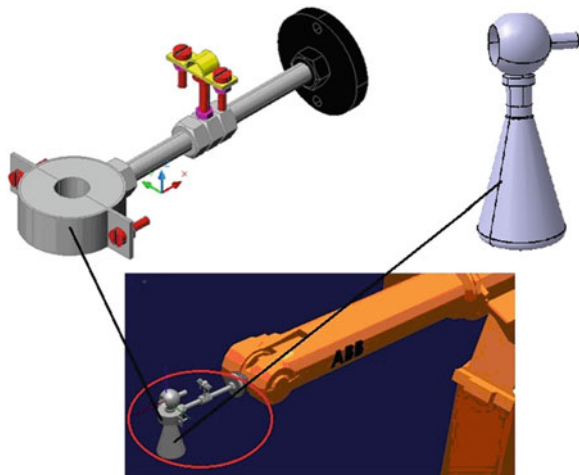
hydrogen or solar cells technology. Spraying angle, height of spraying cone, trajectory step, time between two passes, carrier gas pressure, substrate temperature, spraying velocity and solvent concentration must be controlled in order to obtain uniform thin films (Enescu and Alexandru 2011; Perendis and Gauckler 2005; Senthilnathan and Ganesan 2010). The advantage of the proposed spraying process consists in its potential use for larger planar surfaces (e.g. $500 \times 500 \text{ mm}^2$) in comparison with traditional processes and instead other technologies that allow the spraying of maximum $100 \times 25 \text{ mm}^2$.

The purpose of this paper is to develop an optimal algorithm to obtain uniform thin films by using spray pyrolysis technology. For beginning, the characteristic parameters of the trajectory and the automatic spray pyrolysis methodology are introduced and explained. Then, the optimal algorithm for the spray pyrolysis deposition, which is based on DOE (Design of Experiments) technique, is presented. Response Surface investigation strategy, with Fractional Factorial design and Interaction model, was used to obtain the appropriate regression model. The optimization was conducted by using a powerful DOE software solution (ADAMS/Insight).

2 Designing the Spraying System

The uniformity of the thin films depends on the input data referring to the specific parameters of spray pyrolysis, and for this reason in the design process of the spraying system the following parameters have been considered: substrate temperature, height of spraying cone, spraying angle, carrier gas pressure, trajectory step, time between two passes, and the number of consecutive passes on the substrate.

Fig. 1 The virtual model of the robotic system for spray pyrolysis deposition



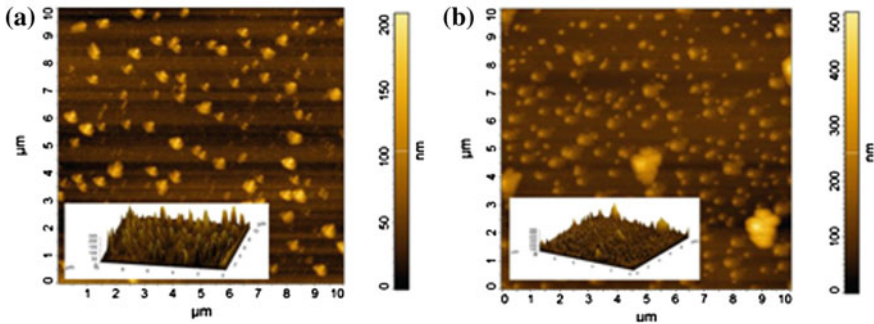


Fig. 2 AFM micrograph films

The deposition is performed by using a robotic system. Mechanical versatility and programming flexibility are fundamental characteristics of robots (Ceccarelli 1999; Neagoe et al. 2005). By using a robot in the spray pyrolysis deposition, the errors made by the human operator on the manual deposition can be eliminated (or at least minimized).

The virtual model of the robotic system is shown in Fig. 1. The system contains an ABB IRB 2400L robot, equipped with spray nozzle, heating plate, and microcomputer. Commercial CAD environment (CATIA) was used to design the virtual model, while the off-line programming was performed with RobotStudio. On the obtained solid models from the CAD environment, there is implemented the program that will be simulated and then imported on the physical robot.

Significant morphology changes of TiO_2 films can be obtained in different deposition conditions. Such results are shown in Fig. 2, considering the deposition with two spraying angles (a— 75° , b— 45°). The micrograph films are obtained with AFM (Atomic Force Microscopy).

3 Optimization Strategy

The paper is focused on the optimal design of the characteristic parameters (factors) for the spraying system described in Sect. 2. To perform this study, we used a design of experiments (DOE) method. DOE is a procedure to plan experiments, analyzing the results, having as goal to identify which combinations of factors most affect the behavior of the SPD system.

Response Surface method with Fractional Factorial design and Interactions model was used as investigation strategy. This method fits polynomials to the results of the trials in the experiment, the fitting functionality giving an approximation of the SPD system performance. Fractional Factorial designs are referred to as reduced factorial designs, being used principally for screening factors with

two-levels (Grossman and Del Vecchio 2007). Interaction effects are captured through special terms in the model that consist of products of factors. This strategy was chosen in order to evaluate the effect of the factors and of their interactions on the thin film uniformity, as well as the levels of the factors needed to produce an optimal uniformity.

Seven factors (variables) are used in the optimization, as follow: spraying angle—X1 [degrees], height of spraying cone—X2 [mm], trajectory step —X3 [mm], number of consecutive passes on the substrate—X4, time between two passes—X5 [seconds], carrier gas pressure—X6 [bar], and substrate temperature—X7 [°C]. The following responses (objectives) are used to evaluate the SPD system performance (see Fig. 3): Y1 [nm]—the film thickness in a point P₁, Y2 [nm]—the thickness in another point P₂, Y3 [nm]—the difference in thickness between the two points.

Based on the design specifications (Response Surface—Fractional Factorial—Interactions), there have been created the design & work spaces, considering an experiment with 32 trials. The design space is a matrix with the rows representing

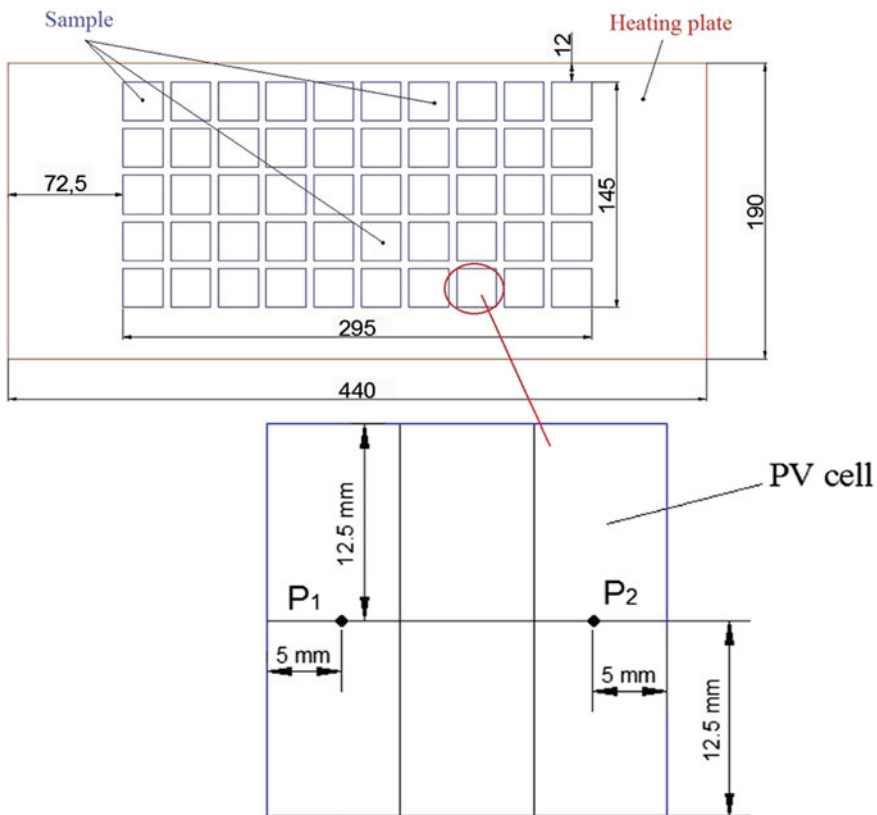


Fig. 3 The locations of the interest points on the PV cell

the trials, and the columns representing the factors settings. Then, considering the minimum and maximum values of the factors, the work space has been created (Table 1). This is a matrix with the rows indicating the experiments and the columns identifying the factors setting and resulting responses values. There have been considered the following fields of the factors: $X1 \in [45, 75]$, $X2 \in [150, 300]$, $X3 \in [20, 30]$, $X4 \in [5, 40]$, $X5 \in [5, 75]$, $X6 \in [1, 1.5]$, $X7 \in [300, 450]$.

The values of the responses Y1 and Y2 have been obtained by experimental measurements (using Ultraviolet/Visible Spectrophotometers), while Y3 has been determined as the difference in absolute value between Y2 and Y1, $Y3 = |Y2 - Y1|$. The work space was used for fitting the results to a response surface. The purpose was to establish a relationship between factors and responses, as follows:

Table 1 The work space of the experiment

	X1	X2	X3	X4	X5	X6	X7	Y1	Y2	Y3
Experiment 1	45	150	30	40	5	1.0	300	275.82	305.60	29.78
Experiment 2	45	150	20	40	75	1.0	300	241.34	271.27	29.93
Experiment 3	75	150	30	5	5	1.0	300	103.43	153.39	49.96
Experiment 4	75	150	20	5	75	1.0	300	68.95	119.06	50.11
Experiment 5	45	300	20	5	5	1.0	300	155.15	151.90	3.25
Experiment 6	45	300	30	5	75	1.0	300	17.24	34.33	17.09
Experiment 7	75	300	20	40	5	1.0	300	362.01	374.57	12.56
Experiment 8	75	300	30	40	75	1.0	300	224.10	257.00	32.90
Experiment 9	45	150	20	5	5	1.5	300	155.15	161.00	5.85
Experiment 10	45	150	30	5	75	1.5	300	17.24	43.43	26.19
Experiment 11	75	150	20	40	5	1.5	300	362.01	383.66	21.65
Experiment 12	75	150	30	40	75	1.5	300	224.10	266.09	41.99
Experiment 13	45	300	30	40	5	1.5	300	310.29	298.94	11.35
Experiment 14	45	300	20	40	75	1.5	300	275.81	264.61	11.20
Experiment 15	75	300	30	5	5	1.5	300	137.91	146.73	8.82
Experiment 16	75	300	20	5	75	1.5	300	103.43	112.40	8.97
Experiment 17	45	150	20	5	5	1.0	450	189.62	186.61	3.01
Experiment 18	45	150	30	5	75	1.0	450	51.72	69.04	17.32
Experiment 19	75	150	20	40	5	1.0	450	396.48	409.27	12.79
Experiment 20	75	150	30	40	75	1.0	450	258.58	291.70	33.12
Experiment 21	45	300	30	40	5	1.0	450	344.77	324.55	20.22
Experiment 22	45	300	20	40	75	1.0	450	310.29	290.21	20.08
Experiment 23	75	300	30	5	5	1.0	450	172.38	172.34	0.04
Experiment 24	75	300	20	5	75	1.0	450	137.91	138.01	0.10
Experiment 25	45	150	30	40	5	1.5	450	344.77	333.64	11.13
Experiment 26	45	150	20	40	75	1.5	450	310.29	299.31	10.98
Experiment 27	75	150	30	5	5	1.5	450	172.38	181.43	29.78
Experiment 28	75	150	20	5	75	1.5	450	137.91	147.10	29.93
Experiment 29	45	300	20	5	5	1.5	450	224.00	179.95	49.96
Experiment 30	45	300	30	5	75	1.5	450	86.19	62.38	50.11
Experiment 31	75	300	20	40	5	1.5	450	430.96	402.61	3.25
Experiment 32	75	300	30	40	75	1.5	450	293.05	285.04	17.09

$$\begin{aligned}
 Y_i = & a_0 + a_1 \cdot X_1 + a_2 \cdot X_2 + a_3 \cdot X_3 + a_4 \cdot X_4 + a_5 \cdot X_5 + a_6 \cdot X_6 + a_7 \cdot X_7 + a_8 \cdot X_1 \cdot X_2 \\
 & + a_9 \cdot X_1 \cdot X_3 + a_{10} \cdot X_1 \cdot X_4 + a_{11} \cdot X_1 \cdot X_5 + a_{12} \cdot X_1 \cdot X_6 + a_{13} \cdot X_1 \cdot X_7 + a_{14} \cdot X_2 \cdot X_3 \\
 & + a_{15} \cdot X_2 \cdot X_4 + a_{16} \cdot X_2 \cdot X_5 + a_{17} \cdot X_2 \cdot X_6 + a_{18} \cdot X_2 \cdot X_7 + a_{19} \cdot X_3 \cdot X_4 + a_{20} \cdot X_3 \cdot X_5 \\
 & + a_{21} \cdot X_3 \cdot X_6 + a_{22} \cdot X_3 \cdot X_7 + a_{23} \cdot X_4 \cdot X_5 + a_{24} \cdot X_4 \cdot X_6 + a_{25} \cdot X_4 \cdot X_7 + a_{26} \cdot X_5 \cdot X_6 \\
 & + a_{27} \cdot X_5 \cdot X_7 + a_{28} \cdot X_6 \cdot X_7, i = 1 \dots 3.
 \end{aligned}
 \tag{1}$$

where Y_i is the measured response, X_1 to X_7 —the factors, and a_0 to a_{28} — the coefficients calculated by multiple regression (a_0 being the constant term coefficient).

There are several statistical measures that define the goodness-of-fit (Manteiga and González 2006). R-squared (R^2) indicates the variance in the predicted results versus the real data, being the proportion of total variability in the data which is explained by the regression model. R-squared-adjusted (R^2_{adj}) is similar with R-squared but is adjusted to account for the number of terms. Regression significance (P) indicates the probability that the fitted model has no useful terms. Range-to-variance ratio (R/V) indicates how well the model predicts values at the data points. F-ratio (F) defines the significance of the regression.

The optimization goal is to minimize the difference in thickness between two interest points (P_1, P_2) on the cell. Thus, a mono-objective optimization will be approached, focusing on the regression model that describes the response Y_3 . The fit table (Fig. 4) shows that the regression matches the test data very well, the “green” bullets indicating the results soundness (entity is likely appropriate). The fit table contains also the number of variables that go into the estimation of a parameter (DOF), the sum of squares (SS), and the mean square (MS), for the three parts of the statistical model: regression (model), residual (error), and total (Manteiga and González 2006).

The residuals for the response Y_3 are presented in Fig. 5. Residual is the difference between the predicted and actual values of the response. Studentized residuals are residual values that are scaled to make them independent of the magnitude of the actual residuals. For a good model, the studentized residuals should be between -3 and 3 . Cook’s statistics measure the influence of each trial on

Fig. 4 The fit table for the response Y_3

	DOF	SS	MS	F	P
Model	28	6.11e+003	218	64.5	0.0027
Error	3	10.2	3.38		
Total	31	6.12e+003			
R^2	0.998				
R^2_{adj}	0.983				
R/V	28.6				

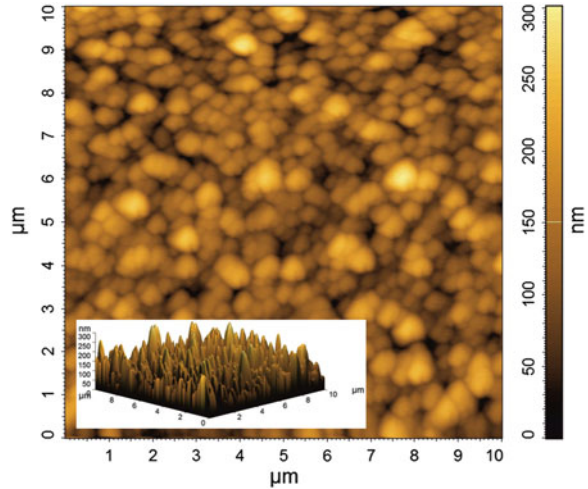
Fig. 5 The residuals for the response Y3

	Actual	Estimate	Raw Residual	Studentized	Cook's
1	29.78	29.83	-0.050125	-0.063418	0.00060097
2	29.93	29.88	0.050125	0.063418	0.00060097
3	49.96	49.91	0.050125	0.063418	0.00060097
4	50.106	50.156	-0.050125	-0.063418	0.00060097
5	3.25	2.4019	0.84813	1.073	0.17205
6	17.096	17.944	-0.84812	-1.073	0.17205
7	12.56	13.408	-0.84813	-1.073	0.17205
8	32.9	32.052	0.84812	1.073	0.17205
9	5.85	6.6256	-0.77563	-0.98132	0.14389
10	26.191	25.415	0.77563	0.98132	0.14389
11	21.65	20.874	0.77562	0.98132	0.14389
12	41.99	42.766	-0.77563	-0.98132	0.14389
13	11.35	11.324	0.025875	0.032737	0.00016014
14	11.2	11.226	-0.025875	-0.032737	0.00016014
15	8.82	8.8459	-0.025875	-0.032737	0.00016014
16	8.97	8.9441	0.025875	0.032737	0.00016014
17	3.01	2.2809	0.72913	0.92249	0.12716
18	17.322	18.051	-0.72912	-0.92249	0.12716
19	12.79	13.519	-0.72913	-0.92249	0.12716
20	33.12	32.391	0.72913	0.92249	0.12716
21	20.22	20.219	0.000875	0.001107	1.8313e-007
22	20.08	20.081	-0.000875	-0.001107	1.8313e-007
23	0.04	0.040875	-0.000875	-0.001107	1.8313e-007
24	0.1	0.099125	0.000875	0.001107	1.8313e-007
25	11.13	11.107	0.023375	0.029574	0.00013069
26	10.98	11.003	-0.023375	-0.029574	0.00013069
27	9.05	9.0734	-0.023375	-0.029574	0.00013069
28	9.19	9.1666	0.023375	0.029574	0.00013069
29	44.05	44.852	-0.80162	-1.0142	0.1537
30	23.815	23.013	0.80163	1.0142	0.1537
31	28.35	27.548	0.80162	1.0142	0.1537
32	8.01	8.8116	-0.80162	-1.0142	0.1537

the fit; the values should be between 0 and 1. As shown in Fig. 5, the residuals are in the recommended fields, so that the regression model is useful (viable).

Finally, the optimization was performed for obtaining a better uniformity of the film, by minimizing the response Y3. The algorithm used in optimization is OptDes-GRG, which requires that factors have range limits, since it works in scaled space. Thus, the optimal values of the factors and the corresponding responses were obtained, as follows: X1 = 75°, X2 = 300 mm, X3 = 29 mm, X4 = 6 passes, X5 = 12 s, X6 = 1 bar, X7 = 450 °C, Y1 = 172.9 nm, Y2 = 172.89 nm, Y3 = 0.01 nm. An area from the micrograph film obtained with

Fig. 6 The optimal AFM micrograph film



these data is shown in Fig. 6, which demonstrates the high quality of the obtained film (there are agglomerated nanostructured porous crystal films, and the roughness is very small).

4 Conclusions

The spray pyrolysis technology is one with low costs, but it allows obtaining homogeny thin film with rigorously controlled and reproducible properties. These properties require robotized depositions and a flexible control, adaptable to different applications. In this study, the usage of the robot in the covering and optimization process has allowed to easy obtain the optimal values of the main factors for the SPD process. Future development is needed to adapt the spraying program for the deposition on non-planar surfaces. A multi-objective optimization will be also approached from the structural properties and film purity point of view.

Acknowledgments This paper is supported by the Sectoral Operational Programme Human Resources Development (SOP HRD), financed from the European Social Fund and by the Romanian Government under the contract number POSDRU/89/1.5/S/59323.

References

- Ceccarelli M (1999) A manipulation analysis for robot programming. *Robotica* 17(5):529–541
- Enescu M, Alexandru C (2011) Virtual prototyping of a spraying robotic system. *Environ Eng Manage J* 10(8):1197–1205
- Grossman R, Del Vecchio R (2007) *Design of experiments*. Wiley, New York

- Manteiga WG, González AP (2006) Goodness-of-fit tests for linear regression models with missing response data. *Can J Stat* 34(1):149–170
- Neagoe M et al (2005) High degree accuracy modelling and calibration of serial robots with large errors. *Prod Eng* 4:397–408
- Okuya M et al (1999) TiO₂ thin films synthesized by the spray pyrolysis deposition (SPD) technique. *J Electrochem Soc* 19:903–906
- Perendis D, Gauckler LJ (2005) Thin film deposition using spray pyrolysis. *J Electroceram* 14:103–111
- Suciu RC et al (2011) Fe₂O₃–TiO₂ thin films prepared by sol-gel method. *Environ Eng Manage J* 10:187–192
- Senthilnathan V, Ganesan S (2010) Novel spray pyrolysis for dye-sensitized solar cell. *J Renew Sustain Energy* 2(6):063102

About Speed Breaker Synthesis with No Deterioration of the Car Suspension

V. Mesaros-Anghel, E. Ianosi, I. Carabas and L. Madaras

Abstract On the roads, near pedestrian crossings or other areas of the road where cars speed reduction is required (schools, hospitals, markets, and dangerous curves), rectangular, trapezoidal or circular speed breaker shapes are placed. The paper analyzes the kinematics of vehicles passing over the speed breaker appreciating qualitatively/quantitatively the influence on vehicle dynamics. We use the analogy of the car in motion as cam follower in oscillation and the speed breaker as flat cam in translation. The authors propose a configuration of the speed breaker section to protect the car (especially the suspension) from unwanted shocks, without affecting the original purpose of speed reduction.

Keywords Speed breaker · Cam · Synthesis · Car suspension

1 Introduction

Moving a car with speed V on a road before a natural or artificial barrier (but known) can be treated as a planar cam mechanism in translation with a roller plunger, as shown in Fig. 1. Oscillating plunger length L is the wheelbase of the

V. Mesaros-Anghel (✉) · E. Ianosi · I. Carabas · L. Madaras
Politehnica University of Timisoara, Timisoara, Romania
e-mail: voicu.mesaros@mec.upt.ro

E. Ianosi
e-mail: andre.ianosi@mec.upt.ro

I. Carabas
e-mail: iosif.carabas@mec.upt.ro

L. Madaras
e-mail: lucian.madaras@mec.upt.ro

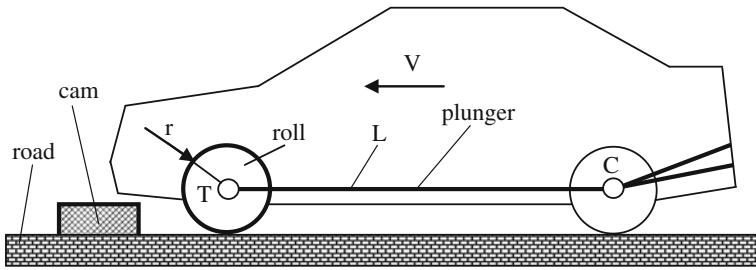


Fig. 1 The analogy of the car and the cam mechanism

car, the radius r is the radius of the wheel and the cam in translation can have a form type as shown in Fig. 2a, b, c.

The goals of these artificial obstacles (speed breakers) are:

- (A) their observation by the driver and reduce speed to prevent the hypothetical negative effects on the car or driver (acceleration, additional inertial forces);
- (B) climbing, descending has quite significant negative consequences (as will be demonstrated below) due to the shape and size, somehow inappropriate for these types of obstacles.

The authors are considering keeping purposes (A) and elimination of the (B) considering rigid mechanism elements.

The narrow nature of speed breakers often allows vehicles to pass over them at high speed while only perturbing the wheels and suspension, hardly affecting the vehicle cab and its occupants. For many who travel on cars or buses on the bumpy roads, spinal injuries could soon be a cause for worry. The spine surgeons are seeing a sharp increase in the number of youngsters with complaints of back pain,

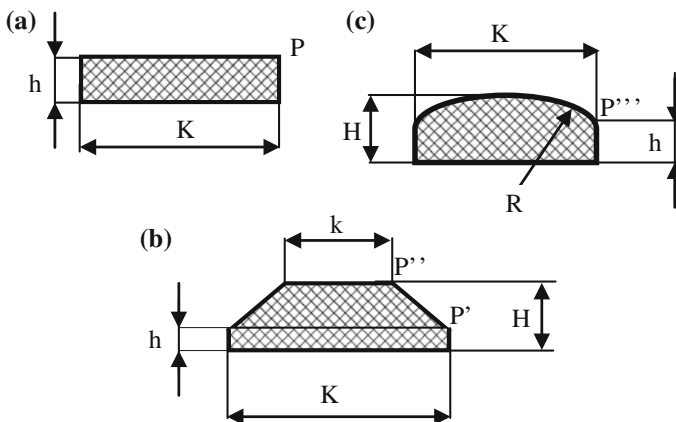


Fig. 2 Usual speed breaker types **a** rectangular, **b** trapezoidal, **c** curved

and the age group varies from 20 to 45 years. They also see an increase in the number of patients suffering from Spondylosis. If severe, it may cause pressure on nerve roots with subsequent sensory and motor disturbances, such as pain, paresthesia, or muscle weakness in the limbs (Anders Brandt 2008).

Due to these considerations the authors consider that it is recommended to realyse an analysis of the existing speed breaker types.

The usual section types for the speed breakers are presented in Fig. 2.

2 Calculus for Rectangular Speed Breakers

The contact of the car wheel (the roll) with the rectangular speed breaker (the cam) will be analysed in three positions, as shown in Fig. 4:

- (a) one point of the wheel on the road (R), and another point of the wheel (P) in contact with the speed breaker;
- (b) the wheel climbing of the speed breaker and a single contact point (P);
- (c) the wheel on the corner of the speed breaker (P).

For the moving car to a rectangular speed breaker (like the one from Fig. 2a) the first phase is the roll-wheel contact with the road in the point P (Fig. 3a), the initial space can be calculated with the relation (1).

$$s_0 = L + \sqrt{r^2 - (r - h)^2} \tag{1}$$

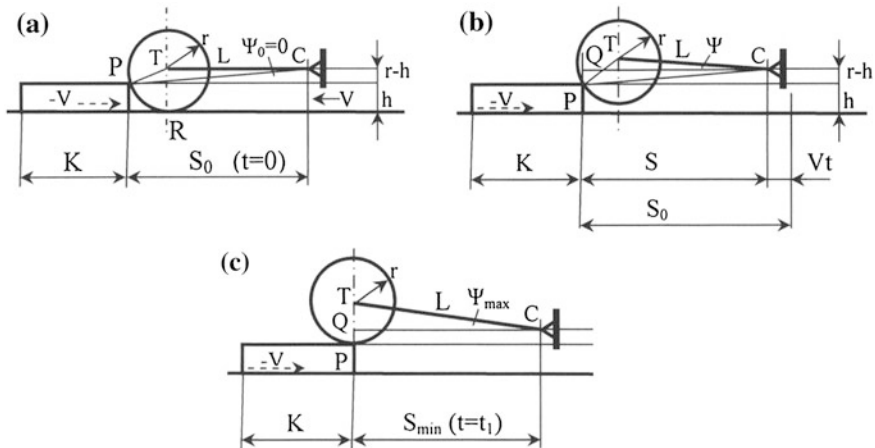


Fig. 3 The three positions of the wheel

In Fig. 3b the roll-wheel escalates the corner P which gives as result the growing of the position angle ψ of the plunger, which can be calculated with relations (2–6).

$$s = s_0 - V \cdot t \quad (2)$$

$$\overline{CP} = \sqrt{s^2 - (r - h)^2} \quad (3)$$

$$\angle PCT = \arccos \frac{-r^2 + L^2 + \overline{CP}^2}{2 \cdot L \cdot \overline{CP}} \quad (4)$$

$$\angle PCQ = \arctg \frac{r - h}{s} \quad (5)$$

$$\Psi = \angle PCT - \angle PCQ \quad (6)$$

In Fig. 3c the roll-wheel starts moving on the rectangular obstacle and the maximum angle position remains constant as the roll-wheel are moving on the distance K. Dimensions and time for escalation can be determined by relations (7–10).

$$\overline{TQ} = r - (r - h) = h \quad (7)$$

$$s_{\min} = \sqrt{L^2 - h^2} \quad (8)$$

$$t_1 = \frac{s_0 - s_{\min}}{v} \quad (9)$$

$$tg \Psi_{\max} = \frac{h}{L} \quad (10)$$

$$\Psi_{\max} = \arctg \frac{h}{L} \quad (10')$$

Variation of the position angle ψ is the angular velocity of the plunger $\dot{\Psi}$ and $\ddot{\Psi}$ is its angular acceleration, when $\Delta t \rightarrow 0$.

$$\dot{\Psi} = \lim_{\Delta t \rightarrow 0} \frac{\Delta \Psi}{\Delta t} \quad (11)$$

$$\ddot{\Psi} = \lim_{\Delta t \rightarrow 0} \frac{\Delta \dot{\Psi}}{\Delta t} \quad (12)$$

If the time interval Δt is small enough then the results are technically acceptable without the necessity to derive the relation (6).

3 Numerical Examples, Discussions

We will consider a Logan car with $m = 1,100$ kg/wt, $r = 310,75$ mm and $L = 2,630$ mm (see Fig. 1) and a rectangular speed breaker of the type shown in Fig. 2a., with dimensions $h = 16$ mm and $K = 200$ mm, and the car moving speed $V = 18$ km/h. Using the relation (9) we can calculate the time t_1 and t_2 for the displacement during the distance K :

$$t_1 = 0,019695 \text{ s} \tag{13}$$

and

$$t_2 = K/V = 0,04 \text{ s} \tag{14}$$

The roll-wheel will descend from the speed breaker at $t_3 = t_1$, the space law of angle ψ is axially symmetric to the middle of the obstacle and the laws of speed/acceleration angle $\dot{\Psi}/\ddot{\Psi}$ is punctually symmetric to the same middle.

Discrediting the calculation (in 5,000 divisions during t_1) the graphics presented in Fig. 4 was obtained. The angular velocity $\dot{\Psi}$ varies almost linearly, resulting a nearly parabolic variation of the angle ψ , and an almost constant angular acceleration $\ddot{\Psi}$.

As given in (Tesar and Matthew 1976) for the start of climbing on the speed breaker and for the end of descent in the velocity jump points (the cusp point of the space) a velocity shock/impact/hammer blow is appearing as also indicated “hard shock” in (Kovacs et al. 1978; Mesaros-Anghel et al. 1997; Perju 1990), the corresponding acceleration is theoretically infinite, leading to moments or inertial forces theoretically infinite.

As given in (Tesar and Matthew 1976) at the end of the speed breaker climb and for the start of descent (the cusp point of the velocity) an early shock acceleration/dropped weight/amplitude amplification appears, as also indicated “soft shock” in (Kovacs et al. 1978; Mesaros-Anghel et al. 1997; Perju 1990), the corresponding acceleration presents a finite jump, generating moments or finite inertial forces that appear suddenly.

In (Tesar and Matthew 1976) the derivate $j = \ddot{\Psi}$ is named jerk, but the authors consider that rad/s^3 is a not enough palpable measurement unit, preferring units of force.

For the given the car presented at point 3.1 can be considered that approximately $m/2 = 550$ kg will be allocated on the front car deck (max. 880 kg with load).

The moment of inertia M_i , mass moment J , the inertial force on the front car deck F_{ip} and the inertial force of one telescope F_{it} will be:

$$M_i = J \cdot \ddot{\Psi}; \quad J = \frac{m}{2} L^2; \quad F_{ip} = \frac{M_i}{L}; \quad F_{it} = \frac{F_{ip}}{2} \tag{15}$$

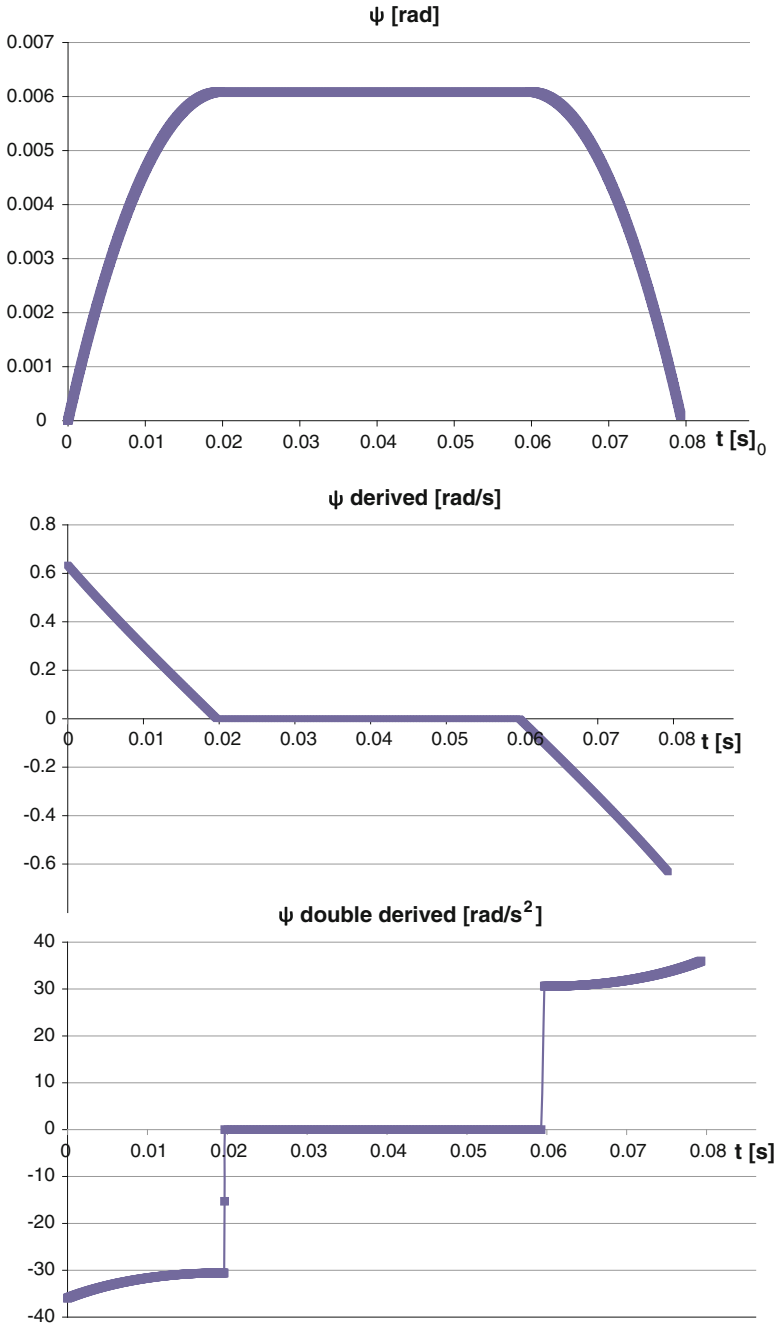


Fig. 4 The variation of the angle, the angular velocity and acceleration (for $h = 16$ mm)

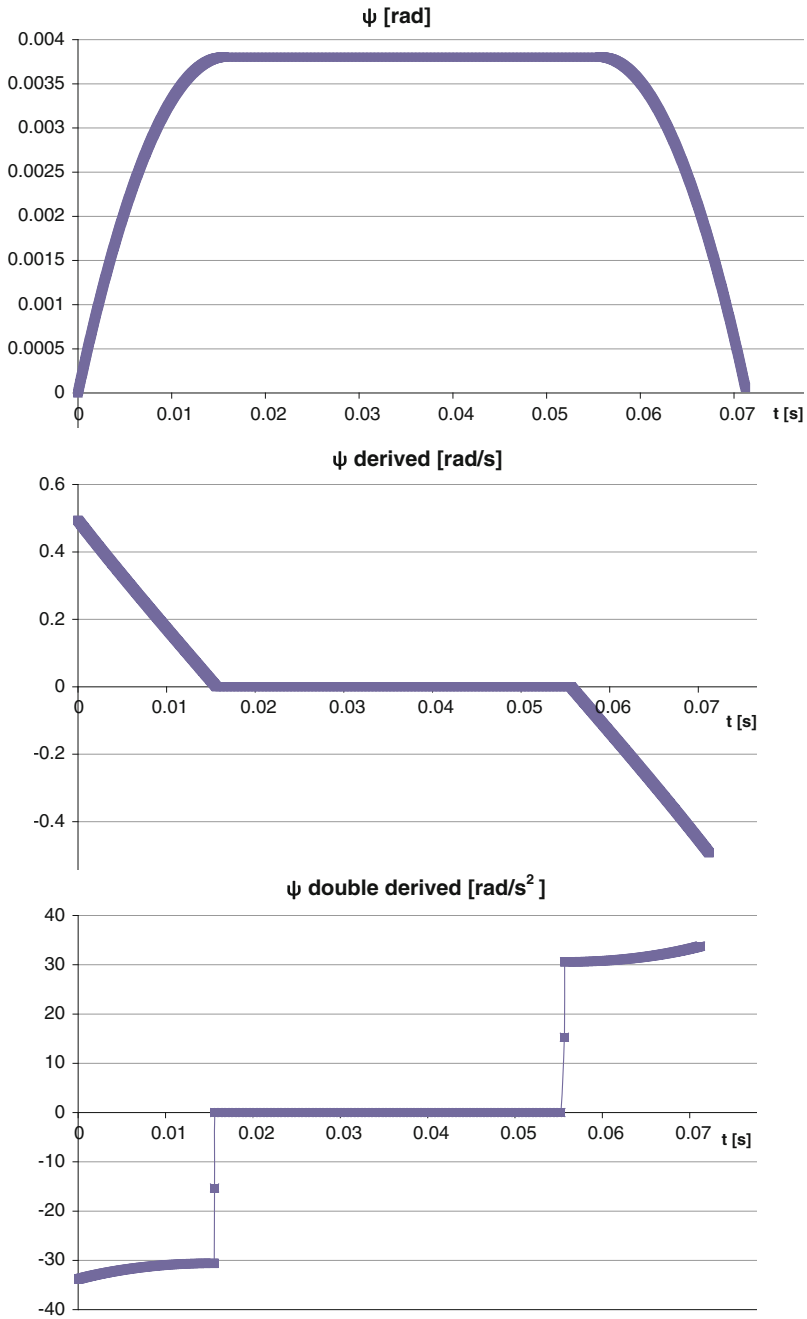


Fig. 5 The variation of the angle, the angular velocity and acceleration (for $h = 10$ mm)

If we have $\ddot{\Psi} \approx 30 \text{ rad/s}^2$ and $L = 2,63 \text{ m}$, it will result:

$$\begin{aligned} J &= 3804,3 \quad (\text{max. } 6086,9) \text{ kgm}^2, \\ M_i &= 114129 \quad (\text{max. } 182607) \text{ Nm}, \\ F_{ip} &= 43395 \quad (\text{max. } 69432) \text{ N}, \\ F_{it} &= 21697,5 \quad (\text{max. } 34716) \text{ N}. \end{aligned}$$

That means that theoretically only the finite shock (soft shock) produce suddenly approx. 2,17 (max. 3,47) tf (t force) on a telescope for a rectangular speed breaker with height of 16 mm.

In the same conditions as presented at point 3.1 if we consider $h = 10 \text{ mm}$ the height of the speed breaker, we obtain:

$$t_3 = t_1 = 0,015643 \text{ s} \tag{13'}$$

and

$$t_2 = 0,04 \text{ s} \tag{14'}$$

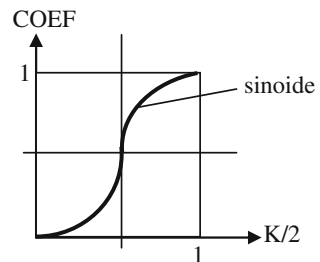
Doing similar calculus as in point 3.1 the graphics from Fig. 5 are resulting, together with the same conclusions, but surprisingly the effect of shock is approximately the same in values as those calculated with relations (15), despite the speed breaker height decreased from 16 to 10 mm.

4 Authors Proposals, Conclusions

Due to the fact that in the points P', P'', P''' from Fig. 2 are producing similar dynamic effect's as in point P the authors consider that the trapezoidal/curved speed breaker's (Fig. 2b, c) produces the same harmful effect on the car/driver/passenger as the rectangular speed breaker (verifiable also in practice, because the dimension $H = 50\text{--}60 \text{ mm}$ and $h = 10 \text{ mm}$).

The authors propose a comparative study with the above presented (also for determination of h_{min}) and an extrapolation of the K for different values of r for

Fig. 6 The proposed graphic



different vehicles. For the moment they propose a graphical solution given in Fig. 6 (sinoide) for the variation of the height of the speed breaker.

From this proposed graphic the speed breaker manufacturers can extract the coefficients (COEF) which will multiply the dimension H when the height of the speed breaker is increasing from the ideal value $h = 0$, that will give as result a transversal profile of the speed breaker which may be producing the elimination of the shock's (fine variation of the angular acceleration), as indicated in (Kovacs et al. 1978; Mesaros-Anghel et al. 1997; Perju 1990; Tesar and Matthew 1976).

This effect may be benefic for the car/driver/passenger keeping the aim from point A) presented in the Introduction.

References

- Brandt A, Granlund (2008) Bus driver's exposure to mechanical shocks due to speed bumps. Society for experimental mechanics, IMAC XXVI conference and exposition on structural dynamics
- Kovacs FW, Perju D, Crudu M (1978) Mecanisme, vol 1,2. Lito IP Traian Vuia Timisoara
- Mesaros-Anghel V, Carabas I, Lovasz E-C (eds) (1997) Manual pentru proiectarea mecanismelor, Mirton, Timisoara
- Perju D (1990) Mecanisme de Mecanica Fina, vol 1,2. Litografia IP Traian Vuia Timisoara
- Tesar D, Matthew G-K (1976) The dynamic synthesis, analysis, and design of modeled cam systems. Lexington Books, Lexington, Massachusetts-Toronto

Structural Systematization and Kinematic Analysis of Redundant Kinematic Chains with 7 and 8 Axes for Robots

Ionel Staretu

Abstract Initially it was considered that redundant kinematic chains are not desirable because they lead to unnecessary increase of the complexity, to a longer time to calculate trajectories and costs. In recent years (2–4 years), concerns to promote and even make industrial robots with redundant kinematic chains, especially for those with 7 axes, have emerged. This paper presents the most possible structures with 7 or 8 axes, which correspond to non-degenerate workspaces of which one can choose other variants than existing ones, to be manufactured. Representation of workspace helps the designer to choose structures that may have a high degree of functionality for a given range of applications. Kinematic analysis based on the method of homogeneous operators exemplifies the possibility to resolve this issue in the case of these redundant robots too.

Keywords Redundant robot · Structural systematization · Kinematic chain · Kinematic analyse

1 Introduction

Traditionally, it was agreed that an industrial robot kinematic chain must have 6 axes (3 axes corresponding to the positioning kinematic chain and 3 axes corresponding to the orientation kinematic chain), any additional axes (monomobile kinematic coupling), leading to a certain redundancy. Initially it was considered that redundant kinematic chains are not desirable because they increase complexity unnecessarily, leading to more time to calculate trajectories and costs. In recent years (2–4 years) however, concerns to promote and even make industrial robots with redundant

I. Staretu (✉)
Transilvania University of Brasov, Brasov, Romania
e-mail: staretu@unitbv.ro

kinematic chains have emerged, especially those with 7 axes, as Qirox Cloos robot and Denso didactical robot or 8 axes like Qirox Cloos robot with additional translation (Brell-Cokcan et al. 2009; Qi et al. 2011; Wang et al. 2010).^{1,2,3,4,5,6}

They have proven that they have larger workspaces and increased possibilities for maneuvering in these areas. Mentioned disadvantages have significantly reduced their importance through increasing the speed of trajectories calculation due to the explosive growth of the active processors computational power, reducing design and production costs, and the complicated structure became practically an important functional advantage. To provide a useful working basis, including promoting new redundant structures, others than those already applied, in the paper there is a systematization of kinematic chains structures with 7 and 8 axes. It is given an example of calculating direct kinematics for a kinematic chain of 7 axes and for a kinematic chain with 8 axes applying the uniform operators method.

2 Structural Systematization of Kinematic Chains with 7 Axes for Robots

According to (Dudita 1987), there are some structures of kinematic chains with 6 axes for robots, which have nondegenerate workspaces (reduced to a line or surface) and which are usable. They were obtained by identifying the possible combinations of 3 axes (monomobile joints) of rotation, translation, respectively (RRR-TTT). It was possible taking into account only the situations when two successive joints are perpendicular or parallel for positioning kinematic chains, with consideration of possible eccentricities equal or not to zero, and of 3 axes (monomobile joints) of rotation (RRR), corresponding to the kinematic orientation chain. There were retained only the structures that correspond to nondegenerate workspaces. We took into account only the structures with relative positions of successive couplings that are perpendicular or parallel, because these structures are the most frequently applied to industrial robots, and have been validated as the most functional in practice. Structures with 7 axes (monomobile kinematic couplings) are obtained from 6-axis ones, adding a kinematic monomobile coupling of rotation (R) or translation (T), also in a relative position perpendicular or parallel to the front or rear coupling. Obviously for each structure it is generated the appropriate

¹ <http://www1%253awww.foodengineeringmag.com/%25e2%2580%25a6/seven-ax>.

² www2:www.motoman.com.

³ <http://www3%253awww.yaskawa.co.jp/en/%25e2%2580%25a6/robotics/01.html>.

⁴ http://www4%253awww.ragroup.com.au/robots/%25e2%2580%25a6/sda_sia_seri%25e2%2580%25a6.

⁵ www5%253awww.cloos.de/QIROX/%e2%2580%25a6/roboter/%25e2%2580%25a6/index.p%25e2%2580%25a6.

⁶ www6:www.densorobotics.com/news/34.

workspace and are retained only those that correspond to nondegenerate workspaces. Basic versions are obtained if the eccentricity between two successive couplings is zero and derivative versions where eccentricity is not zero, developed by an axis, two axes, or three axes. Thus, according to (Dudita 1987), there are 20 distinct trimobile positioning structures of kinematic chains, which create nondegenerate volume-workspaces and 8 trimobile orientation structures of kinematic chains. In Fig. 1a and b I give two examples of positioning kinematic chains (R, T-kinematic monomobile of rotation or translation joints, a_1, a_2, d, r, S_0, S -kinematic dimensions, M-characteristic point of the robotic kinematic chain (Dudita 1987).

In Fig. 1c I give one examples of orientation kinematic chains (a,b-kinematic dimensions, l-longitudinal or n-normal orientation of the gripper (Dudita 1987). Connecting in a row a sitioning kinematic chain and an orientation kinematic chain, we obtain the guiding kinematic chain, in this case with six axes (six kinematic rotation or translation monomobile couplings) in which two successive axes-couplings are perpendicular (\perp) or parallel (\parallel).

Guiding kinematic structures with seven axes (seven monomobile kinematic couplings of rotation or translation, positioned relatively perpendicular or parallel) are obtained from the six axes by adding a monomobile kinematic coupling (an additional axis) of rotation (R) or translation (T). This coupling can be added at the beginning, at the end of the guiding kinematic chain or between these two kinematic chains. To obtain all possible combinations without losing the functionality of the positioning and orientation kinematic chains, we consider the positioning kinematic chain, a distinct kinematic module called positioning module (PM) and the orientation kinematic chain, an orientation kinematic module called orientation kinematic module (OM).

The relative position of the seventh coupling (axis) against the first or the last coupling of one of the two modules can be perpendicular (\perp) or parallel (\parallel). The result means 12 possible combinations: $R\perp(PM)(OM), R\parallel(PM)(OM), T\perp(PM)(OM), T\parallel(PM)(OM), (PM)\perp R(OM), (PM)\parallel R(OM), (PM)\perp T(OM), (PM)\parallel T(OM), (PM)(OM)\perp R, (PM)(OM)\parallel R, (PM)(OM)\perp T, (PM)(OM)\parallel T$. In Fig. 2 are represented 4 kinematic versions with seven axes (T,R-monomobile translation

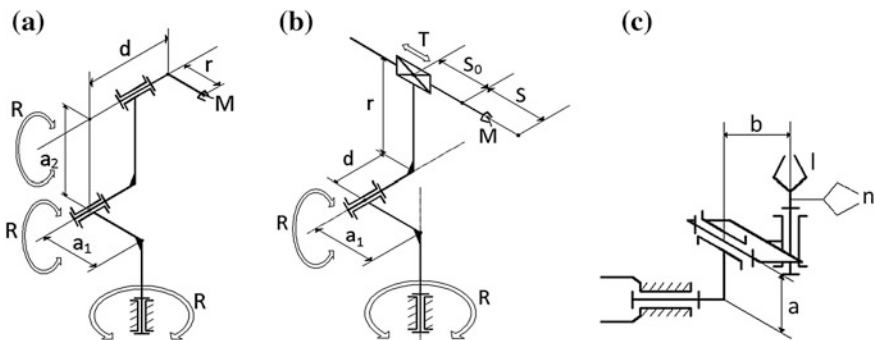


Fig. 1 Two examples of positioning trimobile kinematic chains (a and b) and one examples of trimobile orientation kinematic chains (c)

or rotation joints; a,b,c,d,e,f and r are kinematic dimensions and M-characteristic point of the robotic kinematic chain), with representation in detail of the positioning module and brief representation of the orientation module (OM).

The structural diagram of the positioning module corresponds to version b in Fig. 1.

In Fig. 3 for structures a, b and c in Fig. 2, apart from the orientation module (OM—which does not affect the volume, shape, and size of the workspace-volume of the kinematic chain) are the kinematic schemes (T,R-monomobile joints of translation or rotation; a, b, c₁, d, d₁, d₂, e₁ and e₂ are kinematic dimensions and M is the characteristic point).

3 Structural Systematization of Kinematic Chains with 8 Axes for Robots

Structures of kinematic chains with 8 axes can be obtained from 6-axis ones, by adding two axes (two monomobile kinematic couplings) of rotation or translation or combined RT, respectively, TR. They can be both at one end of the 6-axis kinematic chain, or one at one end and the other at the other end of the said kinematic chain, or by adding R or T axes to 7-axis structures. This additional axis is added similarly to the case of obtaining structures with 7 axes out of 6-axis ones. Therefore, we obtain a number of distinct structures corresponding to nondegenerate workspaces. Thus, by adding a rotation (R) or translation (T) coupling, perpendicular (\perp) or parallel (\parallel) to the first four structures (R/T)(\perp/\parallel)(PM)(OM) of the seven-axis kinematic chain, we obtain 16 8-axis kinematic chain structures: $R\perp R\perp(PM)(OM), \dots, T\parallel T\parallel(PM)(OM)$. Similarly, we obtain structural variants with eight axes based on 7-axis structures such as: (PM)(\perp/\parallel)(R/T)(OM) and (PM)(OM)(\perp/\parallel)(R/T). There are 96 final versions, 16 for each combination: (R/T)(\perp/\parallel)(R/T) (\perp/\parallel)(PM)(OM), (R/T)(\perp/\parallel)(PM) (\perp/\parallel)(R/T)(OM), (R/T) (\perp/\parallel)(PM)(OM) (\perp/\parallel)(R/T), (PM) (\perp/\parallel)(R/T)(OM) (\perp/\parallel)(R/T), (PM) (\perp/\parallel)(R/T) (\perp/\parallel)(R/T)(OM) and (PM)(OM)(\perp/\parallel)(R/T) (\perp/\parallel)(R/T). In Fig. 4 are two kinematic structures with 8 axes with representation in detail of the positioning module structure and brief

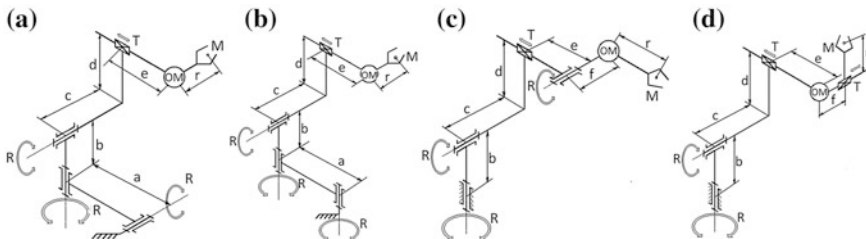


Fig. 2 Examples of guiding kinematic chains with seven axes: $R\perp(PM)(OM)$ -a, $R\parallel(PM)(OM)$ -b, $(PM)\perp R(OM)$ -c and $(PM)(OM)\parallel T$ -d

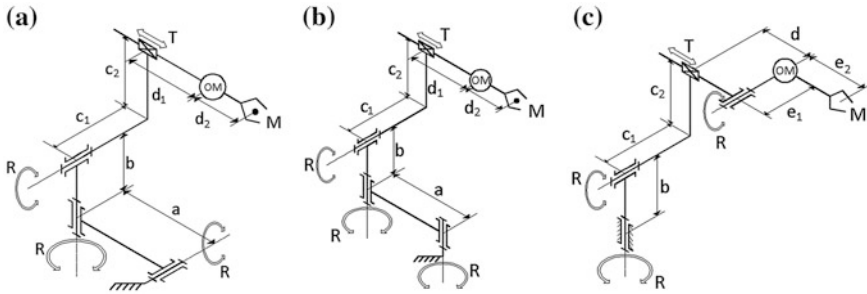


Fig. 3 Kinematic schemes for robots with seven axes: $R \perp (PM)(OM)$ -a, $R \parallel (PM)(OM)$ -b and $(PM) \perp R(OM)$ -c

representation of the orientation module. Corresponding structural diagrams can be represented for all the 96 different possible combinations.

In Fig. 5 for the structures in Fig. 4, apart from the orientation module, there are kinematic diagrams indicating significant dimensional parameters ($a_0, a, b, c_1, c_2, \dots$). It is noted that in a similar way you can obtain redundant structures that can be used in industrial robots with more than 8 axes: 9, 10, 11 or even 12 axes. Some of these structures may have specific functional advantages in certain situations, which will be validated for sure by future practical applications. A number higher than 12 axes already approaches the robotic trunk like structure formed by linking in a row several identical or similar constructive modules (Dutita 1987).

4 Kinematic Analysis of Kinematic Chains with 7 Axes

Kinematic analysis problem is solved with homogeneous operators' method (Dutita 1987). You can apply both direct and inverse kinematics problem. We give as example the application of the homogeneous kinematic operators direct kinematics structure with 7 axes, considered representative. The method

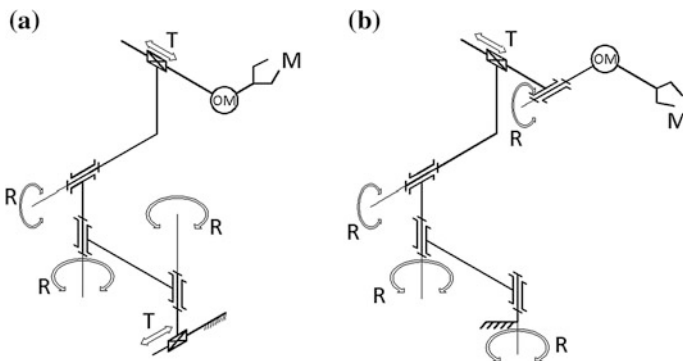


Fig. 4 Structural diagrams of two types of kinematic chains with 8 axes

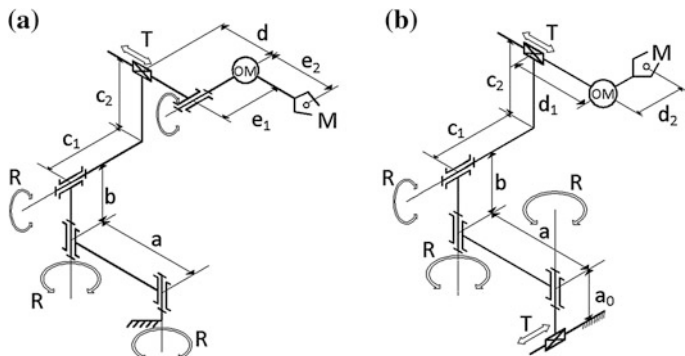


Fig. 5 Kinematics diagrams of two structures with 8 axes

application involves the use of homogeneous operators, of rotation, translation, and rotation-translation, respectively, translation-rotation. According to Fig. 6a, the form of the elementary homogeneous translational operator from the reference system $O_m x_m y_m z_m$ to the reference system $O_n x_n y_n z_n$, by $x_m = x_n$ axis is:

$$A_{mn} = T_{mn}^x = \begin{bmatrix} 1 & 0 & 0 & 0 \\ d_{nm} & 1 & 0 & 0 \\ 0 & 0 & 1 & 0 \\ 0 & 0 & 0 & 1 \end{bmatrix}. \tag{1}$$

Matrix forms of rotation elementary homogeneous operators by axes x, y and z, according to Fig. 6b, c and d are:

$$A_{mn} = R_{mn}^x = \begin{bmatrix} 1 & 0 & 0 & 0 \\ 0 & 1 & 0 & 0 \\ 0 & 0 & C_{nm} & -S_{nm} \\ 0 & 0 & S_{nm} & C_{nm} \end{bmatrix}; A_{mn} = R_{mn}^y = \begin{bmatrix} 1 & 0 & 0 & 0 \\ 0 & C_{nm} & 0 & S_{nm} \\ 0 & 0 & 1 & 0 \\ 0 & -S_{nm} & 0 & C_{nm} \end{bmatrix}; A_{mn} = R_{mn}^z = \begin{bmatrix} 1 & 0 & 0 & 0 \\ 0 & C_{nm} & -S_{nm} & 0 \\ 0 & S_{nm} & C_{nm} & 0 \\ 0 & 0 & 0 & 1 \end{bmatrix}. \tag{2}$$

In these matrices, $S_{nm} = \sin\phi_{nm}$, and $C_{nm} = \cos\phi_{nm}$ are cosine and sine of rotation angles around those axes between m and n reference systems. Using two elementary homogeneous operators of rotation and translation, respectively translation and rotation, we can obtain mixed homogeneous operators corresponding to matrices resulting from multiplying matrices corresponding to elementary homogeneous operators. Mixed operators simplify to some extent, kinematic calculation by reducing the number of multiplication operations of

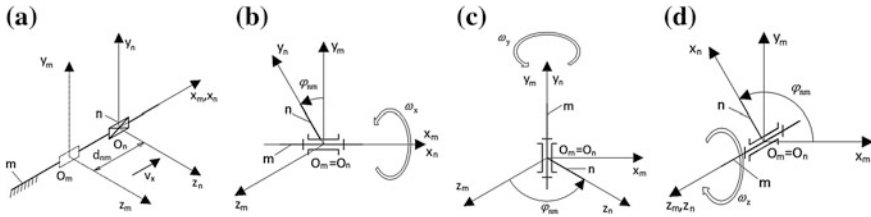


Fig. 6 Kinematic diagrams corresponding to elementary homogeneous operators: translational-**a**, rotational by axis **x-b**, rotational by axis **y-c**, rotational by axis **z-d**

matrices corresponding to rotations around axes in kinematic couplings and to translations between two axes in two successive couplings. It is given as example the direct kinematic problem solving for the kinematic structure with 7 axes of Fig. 7a and b, corresponding to the combination R||**(PM: R⊥R⊥T)**(OM: R⊥R⊥R). 1, ..., 7 are kinematic elements.

To obtain $O_7 x_7 y_7 z_7$ reference system coordinates against $O_0 x_0 y_0 z_0$ reference system (direct kinematics problem) we write the matrix form of rotation or translation operators successively passing from the reference system m to the reference system n : $m = 0, \dots, 6$; $n = 1, \dots, 7$.

These matrices are:

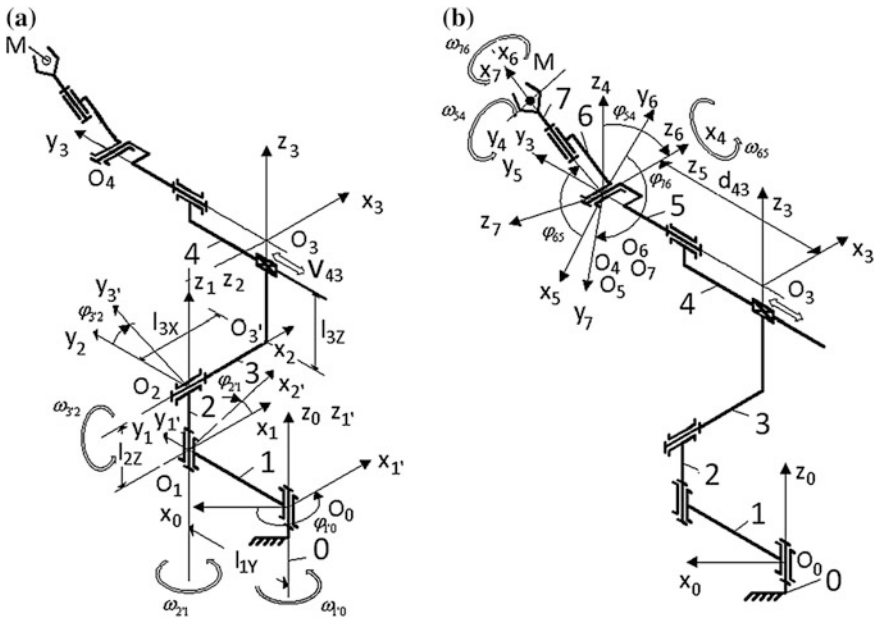


Fig. 7 Kinematic homogeneous coordinates of the kinematic chain with 7 axes:**PM : R⊥R⊥T-a**, **OM : R⊥R⊥R-b**

$$\begin{aligned}
A_{01'} = R_{01'}^z &= \begin{bmatrix} 1 & 0 & 0 & 0 \\ 0 & C_{1'0} & -S_{1'0} & 0 \\ 0 & S_{1'0} & C_{1'0} & 0 \\ 0 & 0 & 0 & 1 \end{bmatrix}; A_{1'1} = T_{1'1}^y = \begin{bmatrix} 1 & 0 & 0 & 0 \\ 0 & 1 & 0 & 0 \\ l_{1y} & 0 & 1 & 0 \\ 0 & 0 & 0 & 1 \end{bmatrix}; \\
A_{12} = R_{12}^z &= \begin{bmatrix} 1 & 0 & 0 & 0 \\ 0 & C_{21} & -S_{21} & 0 \\ 0 & S_{21} & C_{21} & 0 \\ 0 & 0 & 0 & 1 \end{bmatrix}; A_{2'2} = T_{2'2}^z = \begin{bmatrix} 1 & 0 & 0 & 0 \\ 0 & 1 & 0 & 0 \\ 0 & 0 & 1 & 0 \\ l_{2z} & 0 & 0 & 1 \end{bmatrix}; \\
A_{23'} = R_{23'}^x &= \begin{bmatrix} 1 & 0 & 0 & 0 \\ 0 & 1 & 0 & 0 \\ 0 & 0 & C_{3'2} & -S_{3'2} \\ 0 & 0 & S_{3'2} & C_{3'2} \end{bmatrix}; A_{3'3} = T_{3'3}^x T_{3'3}^z = \begin{bmatrix} 1 & 0 & 0 & 0 \\ l_{3x} & 1 & 0 & 0 \\ 0 & 0 & 1 & 0 \\ l_{3z} & 0 & 0 & 1 \end{bmatrix}; \quad (3) \\
A_{34} = T_{34}^y &= \begin{bmatrix} 1 & 0 & 0 & 0 \\ 0 & 1 & 0 & 0 \\ d_{43} & 0 & 1 & 0 \\ 0 & 0 & 0 & 1 \end{bmatrix}; A_{45} = R_{45}^y = \begin{bmatrix} 1 & 0 & 0 & 0 \\ 0 & C_{54} & 0 & S_{54} \\ 0 & 0 & 1 & 0 \\ 0 & -S_{54} & 0 & C_{54} \end{bmatrix}; \\
A_{56} = R_{56}^z &= \begin{bmatrix} 1 & 0 & 0 & 0 \\ 0 & C_{65} & -S_{65} & 0 \\ 0 & S_{65} & C_{65} & 0 \\ 0 & 0 & 0 & 1 \end{bmatrix}; A_{67} = R_{67}^x = \begin{bmatrix} 1 & 0 & 0 & 0 \\ 0 & 1 & 0 & 0 \\ 0 & 0 & C_{76} & -S_{76} \\ 0 & 0 & S_{76} & C_{76} \end{bmatrix}.
\end{aligned}$$

In these matrix:

$C_{1'0} = \cos \phi_{1'0}^z$; $S_{1'0} = \sin \phi_{1'0}^z$; $l_{1y} = \overline{O_0 O_1}$; $C_{21} = \cos \phi_{21}^z$; $S_{21} = \sin \phi_{21}^z$; $l_{2z} = \overline{O_1 O_2}$; $l_{3x} = \overline{O_2 O_3}$; $C_{3'2} = \cos \phi_{3'2}^x$; $S_{3'2} = \sin \phi_{3'2}^x$; $l_{3z} = \overline{O_3 O_3}$; $d_{43} = \overline{O_3 O_4}$; $C_{54} = \cos \phi_{54}^y$; $S_{54} = \sin \phi_{54}^y$; $C_{65} = \cos \phi_{65}^z$; $S_{65} = \sin \phi_{65}^z$; $C_{76} = \cos \phi_{76}^x$; $S_{76} = \sin \phi_{76}^x$; the angles ϕ_{ij}^k are the angles between the reference systems i and j ($i, j = 0, 1', 1, 2', 2, 3', 3, 4, 5, 6, 7$ and k the axis x, y or z) and l_{ik} or d_{ij} are the distances between the reference systems with parallel axes.

The matrix of the coordinates of $O_7 x_7 y_7 z_7$ reference system against $O_0 x_0 y_0 z_0$ reference system results as a product of the transfer matrices above, namely:

$$A_{07} = A_{01'} A_{1'1} A_{12} A_{2'2} A_{23'} A_{3'3} A_{34} A_{45} A_{56} A_{67}. \quad (4)$$

The kinematic analysis presented can be extrapolated to any other structure with 7 axes.

5 Kinematic Analysis of Kinematic Chains with 8 Axes

This problem is solved similarly as in the kinematic chain with 7 axes, exemplifying for a structure with 8 axes considered significant. Of the 96 possible configurations we analyzed cinematically the structural kinematic variant in Fig. 8, appropriate for the combination: $R||(\text{PM}: R \perp R \perp T)(\text{OM}: R \perp R \perp R)||T$.

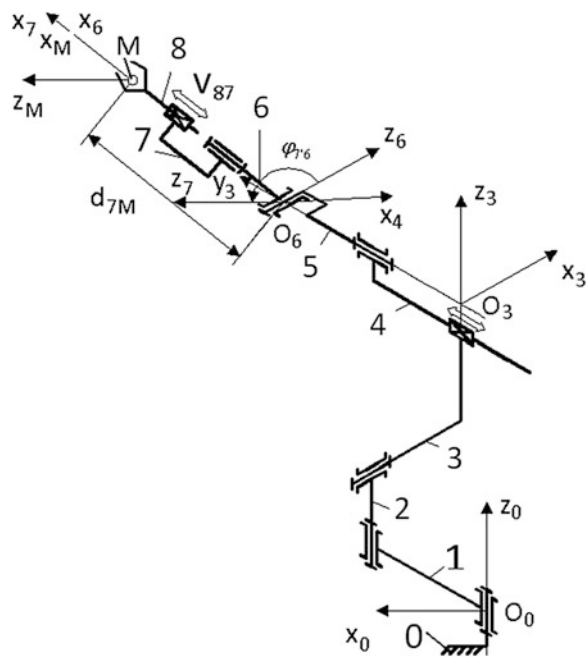
Since the kinematic chain consisting of the first 7 axes (rotation or translation kinematic couplings) is the same as the one analyzed in the previous point, the matrix of the characteristic M point coordinates against the origin of the reference system $O_0 x_0 y_0 z_0$ (direct kinematics solution) is obtained as a product of the matrix A_{07} with the A_{7M} transfer matrix:

$$A_{0M} = A_{07}A_{7M}, \tag{5}$$

where A_{07} is obtained according to relation (4), and A_{7M} is the matrix corresponding to the elementary homogeneous translation operator along the x_7 -axis, over the distance $d_{7M} = O_7 M$:

$$A_{7M} = T_{7M}^x = \begin{bmatrix} 1 & 0 & 0 & 0 \\ d_{M7} & 1 & 0 & 0 \\ 0 & 0 & 1 & 0 \\ 0 & 0 & 0 & 1 \end{bmatrix}. \tag{6}$$

Fig. 8 Structural kinematic scheme of a robotic structure with 8 axes



6 Conclusions

Redundant kinematic chains with 7 or 8 axes (7 or 8 monomobile rotation or translation couplings) have proved useful and some variants are already applied in some industrial robots already in use. This paper presents an original work regarding a method for obtaining the most possible structures with 7 or 8 axes, which correspond to nondegenerate workspaces of which you can choose other options than those known, to be achieved.

The representation of the structural/kinematic schemes and of the workspaces, in the next papers, helps the designer to choose structures that may exhibit maximum functionality for a range of given applications. Kinematic analysis based on the homogeneous operators' method illustrates the possibility of resolving this problem in the case of these redundant robots too.

References

- Brell-Cokcan S, Reis M, Schmiedhofer H, Braumann J (2009) digital design to digital production: flank milling with a 7-axis robot and parametric design. In: Computation: the new realm of architectural design—proceedings of the 27th eCAADe conference, Istanbul, pp 323–330
- Dudita FI (1987) Linkages mechanisms (in Romanian). Bucharest, Tehnica Press, Romania
- Qi R, Lam TL, Qian H, Xu Y (2011) Arc tracking on an eight-axis robot system. In: ROBIO 2011, pp 678–683
- Wang J, Li Y, Zhao X (2010) Inverse kinematics and control of a 7-DOF redundant manipulator based on the closed-loop algorithm. *Int J Adv Robot Syst* 7(4):1–9

A Method for Experimental Identification of Nonlinear Mechanical Systems

Adina Bălan, Mihai Petru Draghici, Radu Donca, Alin Pleșa
and Vistrian Mătieș

Abstract The paper presents a method for experimental identification of nonlinear mechatronic systems. The method uses a parametric nonlinear model and a search algorithm in the parameter space. It compares the behavior of the process and the model, and then, based on a performance index the parameters of the model are up-dated. The method is applied to an inverted pendulum on a cart. There are presented some possible strategies to raise the pendulum, simulation results and aspects regarding the experimental setup using LEGO Mindstorms components.

Keywords Nonlinear systems · Inverted pendulum on a cart · Identification

1 Introduction

The mechatronic systems are mainly nonlinear systems. To apply linear specific methods it is required that the system to work around an operating point where the process can be considered linear. Choosing multiple operating points for each point an approximate model can be obtained. This technique called multiple-model approach (Dougherty and Cooper 2003) can be applied for systems with small nonlinearities. However, in case of strong nonlinearities other methods must be used. This paper presents a method based on on-line simulation and minimization of a performance index. The structure of the nonlinear model is considered known, defined by the nonlinear state equations. As a result, this method permits to obtain the model parameters. The method is applied to the well-known problem of inverse pendulum on a cart (Åström et al. 1996). Due to the particular

A. Bălan (✉) · M. P. Draghici · R. Donca · A. Pleșa · V. Mătieș
Technical University of Cluj-Napoca, B-dul Muncii 103-105, Cluj-Napoca, Romania
e-mail: adinabalan@yahoo.com

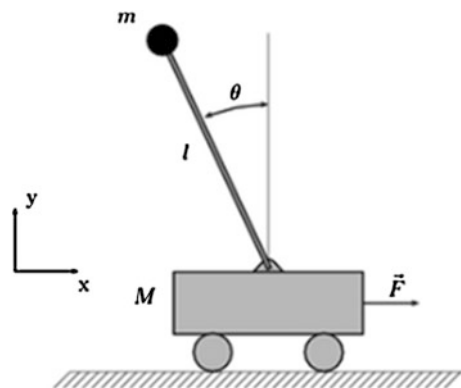
characteristics of each nonlinear system, in the past numerous identification techniques have been developed. Many of these techniques are presented in (Kerschena et al. 2006).

2 The Model of Inverted Pendulum on a Cart

Consider a pendulum-cart system similar to the one in Fig. 1, where the cart can move on a finite length rail. The pendulum is represented as an m mass point attached to an l length rod. It is considered that the rod has no mass and the pendulum can swing 360° and unconstrained. The main purpose of the problem is to get the pendulum in an inverted vertical position (the m mass point is up) and to maintain it, starting from the initial position of stable equilibrium (pendulum of mass m is below). This is achieved by applying variable horizontal forces, obtained through an advanced control algorithm, forces that move the pendulum-cart system along the rail in one way or the other. The applicability of the problem is broad: robotics (biped robots), aviation, astronautics, military field, etc.

To study the inverted pendulum on a cart problem, a mathematical model is needed. This model is represented by a set of differential equations describing as accurately as possible the system behavior. Choosing the appropriate model is very important, especially if the model is used to design a controller that stabilizes the system. The state space model can be written as (Balan et al. 2005):

Fig. 1 Inverted pendulum on a cart¹



¹ http://en.wikipedia.org/wiki/Inverted_pendulum.

$$\begin{aligned}
\dot{x}_1 &= x_2 \\
\dot{x}_2 &= \frac{(M+m)g \sin x_1 - (mlx_2^2 \sin x_1 - bx_4 + u) \cos x_1}{l(M+m \sin^2 x_1)} \\
\dot{x}_3 &= x_4 \\
\dot{x}_4 &= \frac{-mg \sin x_1 \cos x_1 + mlx_2^2 \sin x_1 - bx_4 + u}{(M+m \sin^2 x_1)}
\end{aligned} \tag{1}$$

where: $x_1 = \theta$ represents the angular position of the pendulum, $x_2 = \dot{\theta}$ represents the angular velocity of the pendulum, $x_3 = x$ represents the cart position, $x_4 = \dot{x}$ represents the cart velocity, M is the cart mass, m is the pendulum mass, l is the pendulum length, $g = 9.81$ represents the g-force, b is the viscous friction and u is the force applied to the cart.

For the model (1) to be used, it has to be discretized. A simple relation to approximate the derivate function is used:

$$\dot{x} = \frac{x(t+T) - x(t)}{T} \tag{2}$$

where t is the time, T is the sampling period. Of course, the above relation can be an acceptable approximation only in several situations. Using the above relation, the equivalent discrete equations are obtained (1):

$$\begin{aligned}
x_1(t+T) &= x_1(t) + T \cdot x_2(t) \\
x_2(t+T) &= x_2(t) + T \cdot \frac{(M+m)g \sin x_1(t) - (mlx_2^2(t) \sin x_1(t) - bx_4(t) + u(t)) \cos x_1(t)}{l(M+m \sin^2 x_1(t))} \\
x_3(t+T) &= x_3(t) + T \cdot x_4(t) \\
x_4(t+T) &= x_4(t) + T \cdot \frac{-mg \sin x_1(t) \cos x_1(t) + mlx_2^2(t) \sin x_1(t) - bx_4(t) + u(t)}{(M+m \sin^2 x_1(t))}
\end{aligned} \tag{3}$$

Considering the approximation based on relation (2) as well as the fact that the model can be used to implement the model based control or for other purposes, it is necessary to verify the effects of such discretization. The value of T must be proper chose. In the experimental applications a too low value of the sampling time may lead to a large prediction horizon, which inevitable leads to high calculus time. On the other hand, a too high value may lead to faulty control signal generation. After appropriately choosing the sample time, a solution to increase the model precision is to make a supplementary discretization of the process model. To verify the functionality of it the following methods can be implemented:

- The initial position of the pendulum should be very close to the up vertical position, the control signal and friction coefficient are null. If the model is correct and the sampling time is properly chosen then the pendulum will oscillate without getting to full and continuous rotation or to significant damping of it;

- A high value of the cart mass is chosen, as well as null values for the control signal and friction coefficient b . Initially, the pendulum is positioned at a small deflection from the vertical, stable equilibrium position. The oscillation period to be measured when the pendulum is set free must be close to $2 \cdot \pi / \sqrt{l/g}$;
- The discretized system functionality is compared (pendulum's angular position and velocity, cart's position and velocity) with the normal functioning of the system (for instance the Matlab/Simulink model).

The previous tests allow the proper choosing of the sampling time and the supplementary discretization interval.

3 Swing Up Strategies

Raising the pendulum to a vertical position can be achieved by many methods. A widely used method is based on the energy approach (Åström et al. 1996). Based on the corresponding variation of the applied force, the pendulum's energy will rise up to the value where the superior unstable equilibrium position can be achieved. Around this position the system can be controlled by other various control strategies, including linearizing the nonlinear system. Moreover, in (Åström et al. 1996) the “energy control” strategy to raise the pendulum is compared with the “minimum time control” strategy.

If the movement limit of the cart is taken into consideration, a simple algorithm to raise the pendulum can work like this:

- initialization step, the maximum value of the control signal will be used;
- if the estimation determines that the movement limits are exceeded, then the control signal sign is changed;
- if the pendulum passes through the inferior stable equilibrium position, the control signal sign is changed;
- if the pendulum is near the superior unstable equilibrium position and it is estimated that the system has gathered sufficient energy so that the system to be stabilized in this position, then the stabilization algorithm will take over.

Another possibility to raise the pendulum is presented in (Balan et al. 2005). At each sampling time a set of control sequences to simulate future behavior of the system is used, based on the following sequences (u_{\max} , u_{\min} are the limits of control signal):

$$\begin{aligned} u_1(t) &= \{u_{\min}, u_{\min}, \dots, u_{\min}\}, & u_2(t) &= \{u_{\max}, u_{\min}, \dots, u_{\min}\}, \\ u_3(t) &= \{u_{\min}, u_{\max}, \dots, u_{\max}\}, & u_4(t) &= \{u_{\max}, u_{\max}, \dots, u_{\max}\} \end{aligned} \quad (4)$$

The control sequences are chosen in such way (or maybe even reconfigured) so that the cart position will not exceed its imposed limits. The output sequences (cart position and velocity) are analyzed and the current value of the control signal is

chosen as the first element of the sequence to lead to the unstable equilibrium position. This method has the advantage that it uses the nonlinear model directly and can be used both to raise and to stabilize the pendulum. Moreover, the method has the advantage that it does not need a prior analysis of the model process particularities. A disadvantage is that usually the control sequence is not optimal.

4 Parameter Identification

Considering the nonlinear model of a mechatronic system to be similar to:

$$y(k) = f(y(k-1), \dots, y(k-n), u(k-1), \dots, u(k-m), s(k-1), s(k-2), \dots, s(k-r), p) \quad (5)$$

where y is the output, u is the control signal, s is the measurable perturbation signal, p are the model parameters and y, u, s, p are vectors of the lengths n, m, r , correspondingly. Using the inputs (u, s) and the outputs (y) for a n_{sim} number of prior sampling steps (process history), in (Balan et al. 2011) an efficient algorithm to permit the accurate estimation of p_1, p_2, \dots, p_q model parameters is developed. A simple method can be the following: for each sampling step the process evolution is simulated, starting with the $(t - n_{sim} \cdot T)$ moment of time. The model will use the current values of the \hat{p} estimated parameters. A cost index is set, to compare the evolution of the measured output with the simulated values, based on the estimated parameters. A key aspect is the quantification through an index of the state at a certain time. By obvious reasons, some parameters will not be estimated in steady state.

Regarding the parameter identification it is considered that most of the time the friction coefficient is unknown, the cart mass, the pendulum mass and the pendulum length are known. However, in the following section, for testing purposes, these parameters will be considered unknown. Two situations were simulated: without measurement noise on the output (angular position of the pendulum) (Fig. 2) and with measurement noise (Fig. 3). Note that without parameter identification, the control system is not capable to get the pendulum in a vertical position. The results obtained in the two situations are presented in these figures. Even if the noise is present and visible on the output, the system identification performances are good enough to achieve a proper control. For the experiments, the sample period was 0.01 s. The ratio between estimated and real parameter (e.g. el is the estimate of length) is represented. In Figs. 2, 3, 4, *only* for graphical representation, the angle of the pendulum can vary between -80 and 280° (else 360° are added or subtracted).

If the applied force is dependent by unknown parameters, the identification process will try to estimate the parameters that fit the best to the given situation, which will lead to an estimation of parameters different than the real ones. In Fig. 4 the force can vary between 50 and 100 % of supposed force.

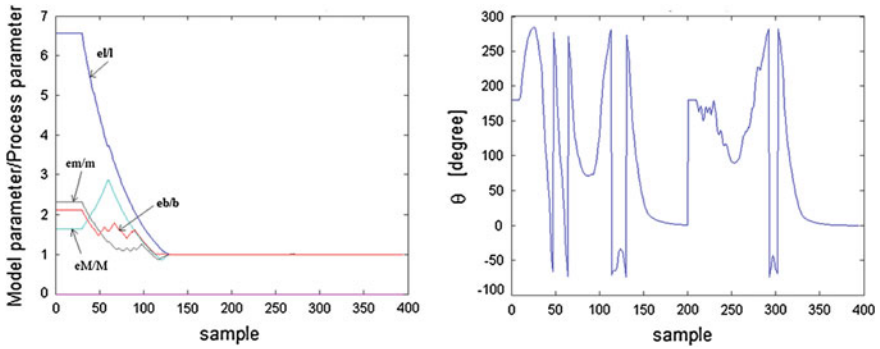


Fig. 2 Parameter identification and theta angle variation—zero noise case

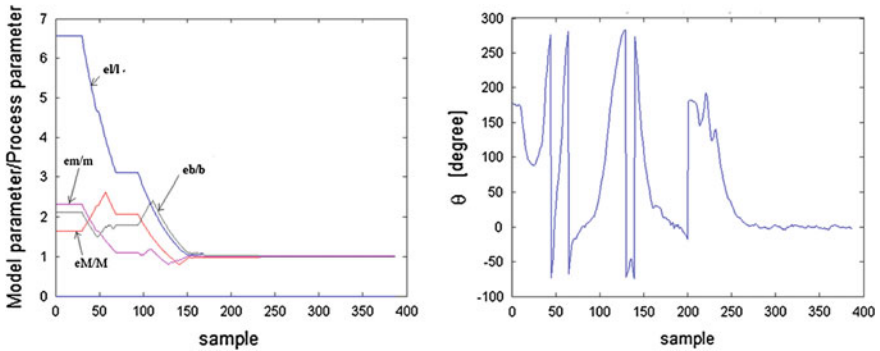


Fig. 3 Parameter identification and theta angle variation—noise on the output

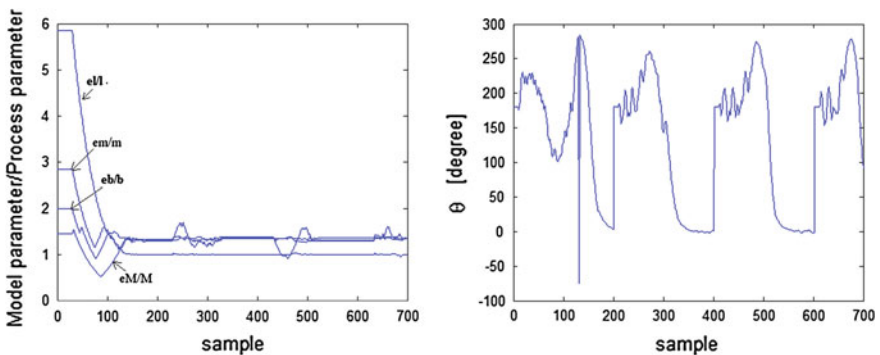


Fig. 4 Parameter identification and theta angle variation—different model/process structure

This will lead to a poor performance of the control system comparing to the ideal case, but the control system has a good behavior and the on-line algorithm application necessity is proven. In this case the identified parameters may not have a physical interpretation.

However, taking into account that some of the parameters are known, the proposed method can lead to tests that validate the proposed model.

5 LEGO Based Experimental Setup

Using LEGO components to create a good mechanical structure is a challenge because of the low precision of the components, fixed length of the elements, high friction and wear. First important step was to create a small size cart, one to weigh less, to have minimum friction with the path and to be able to encapsulate the rotation sensor where the pendulum is inserted. Thus, using LEGO train chassis we developed a cart small enough but that can hold the sensor, allowing us to use LEGO train tracks for the path, to minimize friction between the cart and the path.

The second step was to create the path for the cart. As shown in Fig. 5, two rows of tracks were used, one suspended above the cart to keep it on the right path. A platform to put the FPGA board was created, as well as a crane to hold the sensor connectors above the track, avoiding the entanglement.

A problem that occurred during the development of the mechanical structure was regarding the way of transmitting the force from the motor to the cart. First solution was to use chain drive platform but because of the forces needed, the chain broke so another solution was to be considered. Using 5 mm nylon wire, the force is transmitted entirely and there is no stretching in the wire. The wire is hooked up to the cart and using a pulley system, the force is transmitted from the engine to the cart. The actuator used to move the cart is a LEGO motor.²

Using an approximate model and a model based control algorithm, the LEGO pendulum was raised in the unstable vertical equilibrium position. Input and output data acquisition was conducted and then based on an offline procedure, the model parameters were obtained. Thus obtained parameters were used to determine the system response (curve 2, Fig. 6) for the same control signal. In Fig. 6 the control signal is proportional with the value of motor voltage.

To be noted that the experimental output and the calculated output are similar thus validating the identification method for the model parameters.

² <http://mindstorms.lego.com/en-us/default.aspx>



Fig. 5 Experimental application

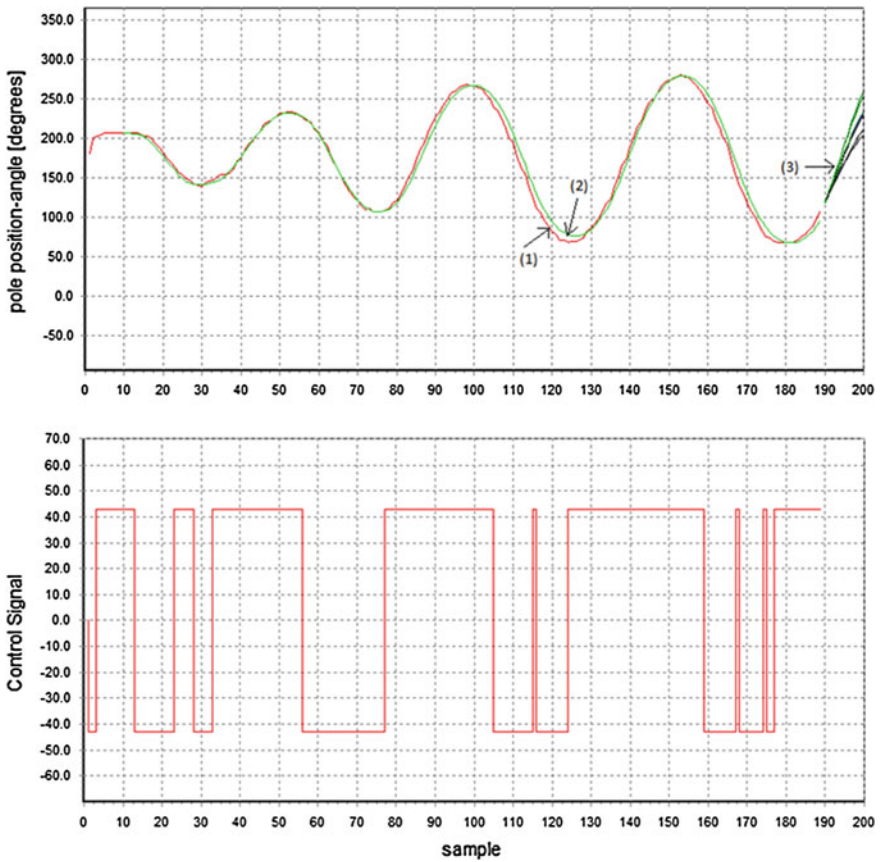


Fig. 6 Control signal, process output (1), model output (2), predictions (3)

6 Conclusions

Stabilizing the inverted pendulum on a cart in a vertical position of instable equilibrium is a difficult control problem. Using LEGO components to implement the solution is a bigger challenge because these components raise more difficulties compared to other solutions. The difficulties are mainly due to lack of precision, wear and fixed component dimensions (which leads to acceptance of various inconveniences), frictions etc. The tests show that model based solutions lead to good results if parameters identification models are used also. Both simulation and experimental tests were made. In the practical experiments, testing and tuning of the system parameters is difficult due to the process instability. The experiments allowed to obtain the data needed for the off-line process identification. Several algorithms to raise and stabilize the pendulum in a vertical position were developed, tested and implemented. As future research, on-line identification algorithms will be implemented, to get better control performance.

Acknowledgments This work has been supported by the project “Q-DOC- Creșterea calității studiilor doctorale în științe inginerești pentru sprijinirea dezvoltării societății bazate pe cunoaștere” contract no. POSDRU/107/1.5/S/78534 and by the project Flexform, contract no. POSDRU/87/1.3/S/64069, projects co-funded from European Social Fund through Sectorial Operational Program Human Resources 2007–2013.

References

- Åström KJ, Furuta K (1996) Swinging up a pendulum by energy control. In: Proceedings of IFAC 13th world congress, San Francisco, California, pp 37–42
- Balan R et al (2005) A predictive control approach for the inverse pendulum on a cart problem. IEEE ICMA 4:2026–2031
- Balan R, Cooper J, Chao CM, Stan S, Donca R (2011) Parameter identification and model based predictive control of temperature inside a house. Energy Buildings 43(2011):748–758. doi:10.1016/j.enbuild.2010.10.023
- Dougherty D, Cooper D (2003) A practical multiple model adaptive strategy for multivariable model predictive control. Control Eng Pract 11:649–664
- Kerschen G, Worden K, Vakakis AF, Golinval JC (2006) Past, present and future of nonlinear system identification in structural dynamics. Mech Syst Sign Proces 20:505–592

Innovative Tracking System for Parabolic Dish Solar Collector

Daniela Ciobanu and Codruta Jaliu

Abstract The efficient conversion of the direct solar radiation into heat by using concentrating solar collectors involves a biaxial tracking system. Usually, the tracking systems use linkages, gears or chain transmissions, the actuation being achieved by geared motors. Thus, the tracker complexity increases (mainly in the linkage type case), the system is expensive, and the collector's orientation is made continuously. In order to overcome these disadvantages, an innovative tracking system of chain/cogged belt type, driven by a linear actuator is proposed in the paper. The simulations performed in the paper prove that this tracking system can assure the concentrating collector rotation by angles up to 180° . The size and complexity of the innovative tracking system are reduced, and, in case of using a step-tracking program, the power consumption is reduced as well. In order to avoid/limit the chain transmission disadvantages (like the supplementary load on the chain or actuator), the tracking system will undergo a process of optimization.

Keywords Solar energy · Parabolic dish collector · Tracking system · Chain transmission

1 Introduction

The growing use of fossil fuels and, simultaneously, the increase in greenhouse gas emissions lead to an agreement among 191 countries within the Kyoto Protocol in implementing renewable energy systems in a more accelerated manner. Solar energy represents the main renewable energy source nowadays, being used either

D. Ciobanu (✉) · C. Jaliu
Transilvania University of Brasov, 29 Eroilor Bvd, 500036 Brasov, Romania
e-mail: daniela.ciobanu@unitbv.ro

to generate electric energy by means of photovoltaic panels, or heating by means of solar collectors.

Thermal energy for domestic hot water or heating can be produced on solar basis by using planar solar collectors, while electric energy can be generated by means of thermal energy obtained by concentrated solar collector that heat the working fluid at high temperatures (Shuang-Ying et al. 2010). So far, the main types of concentrating solar collectors that are implemented contain: parabolic trough collector (Fig. 1a), central receiver (Fig. 1b), and parabolic dish collector (Fig. 1c). According to the technical literature, the most efficient concentrator system is the parabolic dish collector (Reddy and Veershetty 2013).

The parabolic dish solar collector contains the following components (see Fig. 2): reflector, receiver and tracking mechanism. Thus, in order to follow the sun path on the sky, these collectors are equipped with biaxial trackers, which allow simultaneous rotations on two orthogonal axes: an elevation motion (α), and a diurnal motion (ψ) (Fig. 2).

The main types of biaxial tracking systems are equatorial and azimuthal. The equatorial trackers are systems whose rotation axes are arranged to remain parallel to the Earth's polar axis, and to the rotation axis that determines the sun seasonal position on the sky, respectively. This type of tracking systems has the following main advantages: it ensures an accurate orientation, and the two motions are decoupled, lowering, thus, the energy consumption. The disadvantage brought by the equatorial tracking systems consists in a lower stability than in the azimuthal systems case.

The azimuth trackers are systems that have one rotational axis normal to the location surface, while the second rotation axis is given by the seasonal position of the sun on the sky. They are the most stable tracking systems due to diurnal rotation axis arrangement, having also a very good accuracy. In this case, it is necessary to synchronize the two tracking motions, which leads to high power consumption and high complexity of control algorithms. So far, the azimuthal trackers are the most used in the case of parabolic dish collectors, which need to achieve high orientation accuracy (Chong and Wong 2009). According to the

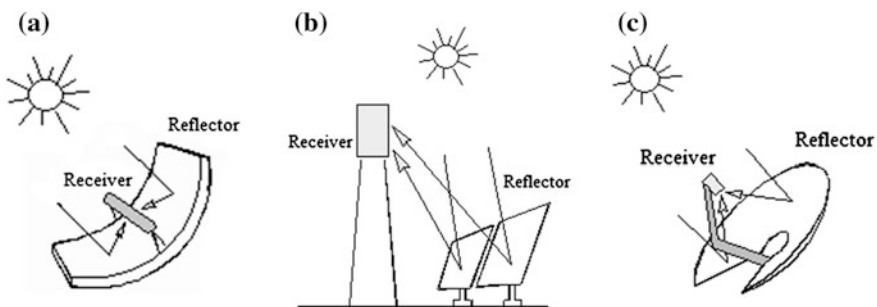
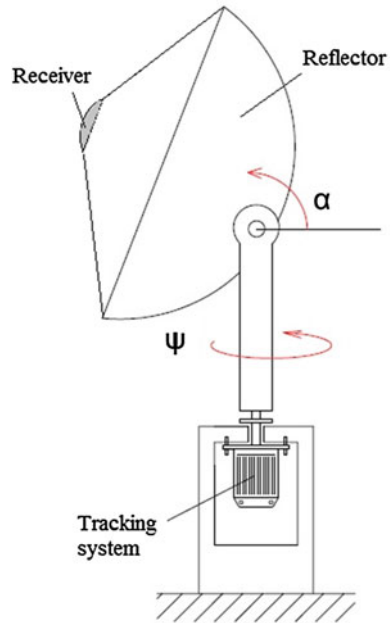


Fig. 1 Concentrating solar collector. **a** Parabolic trough collector. **b** Central receiver. **c** Dish collector

Fig. 2 Parabolic dish solar collector



technical literature, the errors that are allowed in system orientation must fit into the range 0.5–10 mrad (Bonanos 2012).

In order to overcome the trackers disadvantages and to limit the orientation errors, an innovative solution of tracking system of chain/cogged belt type connected to a linear actuator is presented in the paper. Thus, the cost and complexity of the entire system decrease, while maintaining the same tracking accuracy.

2 Tracking System Description

The increase of the amount of thermal energy produced by the solar collectors is achieved, on one hand, by focusing the radiation with optical devices, and on the other hand, by minimizing losses occurred in the collecting process, which can be achieved by reducing the receiver’s surface. The quantity of solar thermal energy produced by solar collectors depends on the number of daylight hours, and, therefore, on the sun position on the sky, which involves the following factors:

- the change in the Sun–Earth distance, given in the number of days (N);
- the tilt of Earth’s rotation axis, namely the declination angle ($\delta[^\circ]$);
- the latitude of the observer ($\varphi[^\circ]$).

Thus, the elevation angle (α [°]) that must be achieved by the tracking system is given by the following relation (Hermenean and Visa 2011) and can be obtained using linkages or gears:

$$\alpha = \sin^{-1}(\sin \delta \sin \varphi + \cos \delta \cos \varphi \cos \omega). \tag{1}$$

In case of diurnal motion, the diurnal angular stroke (ψ [°]) must be at least of 180° and can be calculated by means of relation (2) (Vatasescu et al. 2010):

$$\psi = (\sin \omega) \cos^{-1} \left(\frac{\sin \alpha \sin \varphi - \sin \delta}{\cos \alpha \cos \varphi} \right) \tag{2}$$

Due to the Earth’s spin rotation, the diurnal angle of the dish collector shall not exceed an angular step of 15°/h (Ciobanu 2011). In practice, the mechanisms used to ensure the accurate diurnal orientation are based on gears or chain transmissions, which are actuated continuously, involving high power consumption and cost (Ciobanu 2011).

The proposed variant (Fig. 3a) solves the complexity and cost problems, consisting of a parabolic dish collector (1), an elevation tracking mechanism (2), a diurnal tracking system containing a driving gear (3), a driven gear (4) attached to the dish solar collector, and a chain/cogged belt (5). The linear actuator is connected to the chain through a special link (Fig. 3b). The diurnal tracking system is driven by the linear actuator (6), providing the solar dish collector’s rotation angle of 180°. To ensure the diurnal angle accuracy, the dimensioning of the chain transmission is based on the speed ratio (i_{34}), given by relation (3) (Lateş 2012):

$$i_{34} = \frac{r_4}{r_3} \tag{3}$$

where r_3 , r_4 are the radiuses of the driving/driven wheels.

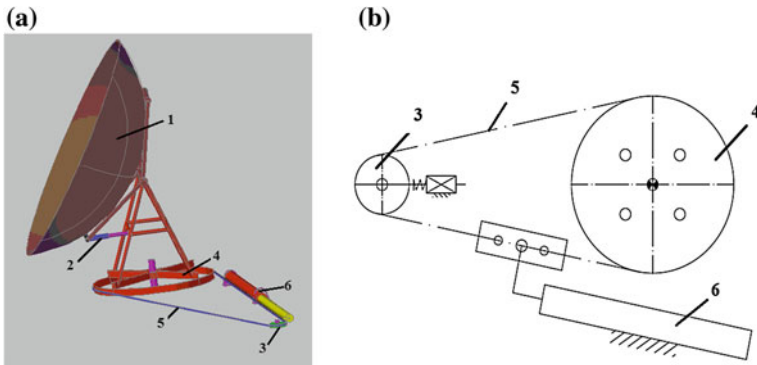


Fig. 3 The biaxial tracking system used in parabolic dish collector. **a** 3D model. **b** Structural scheme for the proposed transmission

The technical literature indicates the values of the speed ratio for chain transmissions working at speeds below 7 m/s, which are greater than 6, and, also, the number of teeth of the wheel z_3 , in the range 11–17 Vatasescu et al. 2010.

To find out the radius of wheel (3) r_3 the following relation is used (Lateş 2012):

$$r_3 = 2 \frac{p}{\sin\left(\frac{180}{z_3}\right)} [\text{mm}], \tag{4}$$

where p is the standardized pitch of chain link [mm].

The radius r_4 is calculated based on relations (3) and (4):

$$r_4 = i_{34} \frac{2 \cdot p}{\sin\left(\frac{180}{z_3}\right)} [\text{mm}], \tag{5}$$

Relation (6) presents the relationship between the stroke of the linear actuator and the tracking system accuracy for a parabolic dish collector (Lateş 2012):

$$L_{act.} = \frac{\pi \cdot r_4 \cdot \psi}{180} [\text{mm}]. \tag{6}$$

For a diurnal angle of $\psi = 180^\circ$, the maximum linear actuator stroke ($L_{act.}$ [mm]) is given by

$$L_{act.} = \pi \cdot r_4 [\text{mm}]. \tag{7}$$

In order to reduce the power consumption for the actuation of the azimuthal tracking system, a step orientation is further considered; the step duration between two actions is considered to be up to 8 min (Ciobanu 2011). In this case, the parabolic dish collector should focus with an angle equal to 2° , which leads to the minimum linear actuator stroke that is necessary to be ensured (rel. 6).

3 Results and Discussion

The implementation of the solar collectors in the built environment imposes certain restrictions in terms of size. Thus, in order to verify if the proposed tracking system can provide the necessary orientation accuracy of the concentrating collectors, the following data are considered: a declination angle $\delta = 23.45^\circ$; the latitudinal angle $\varphi = 45.68^\circ$ (Brasov latitude); the diameter of the collector reflector of 3,000 mm, and the receiver dimension of 200 mm. The diagrams for the variation of elevation angle for the summer solstice ($N = 172$), winter solstice ($N = 355$) and for spring and vernal equinox ($N = 82$, $N = 265$) in Brasov location are presented in Fig. 4, while the simulations from Fig. 5 present the diurnal angle values. The diagram for elevation and diurnal angles where obtained from rel. (1) and (2), by using the above mentioned values for

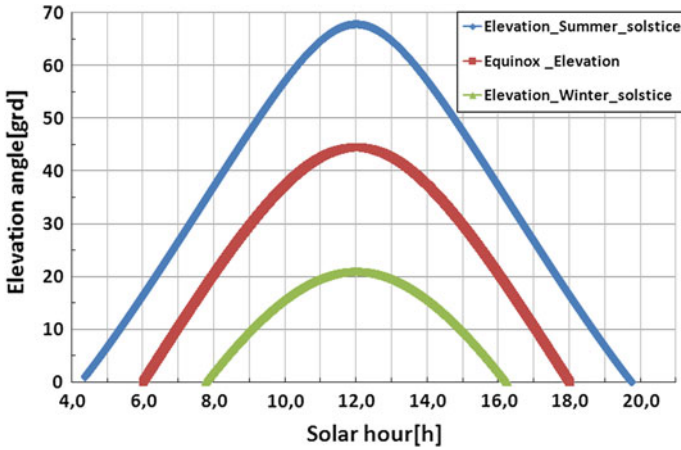


Fig. 4 The elevation angle for Brasov area

declination and latitudinal angle and for the day number. The values for the elevation angle ($22\text{--}69^\circ$) can be easily ensured with a tracking system of linkage type (Ciobanu 2011).

According to Fig. 5, the azimuth angle extreme values are $\pm 123^\circ$. These values can be assured with gear mechanisms, complex linkages or chain transmissions. In all these cases, the actuation is performed either by a geared motor, which involves a higher price for the tracking system, or by a linear actuator that increases the mechanism complexity (Creanga et al. 2011). To decrease the mechanism complexity and cost, the paper presents an innovative solution that uses a special link to drive the chain (see Fig. 3b).

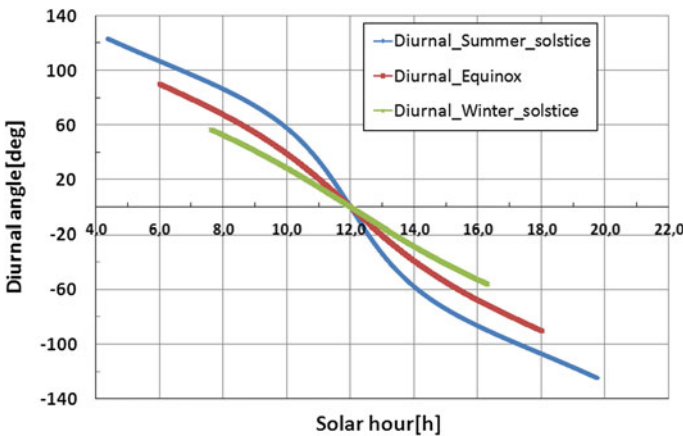


Fig. 5 The diurnal angle for Brasov area

Since the solar radiation intensity is low during morning and evening, an angle of 180° is considered to be enough for the diurnal orientation of the parabolic dish collector.

Numerical simulations are performed in order to verify the range in which the diurnal angle takes values. The nomograms from Figs. 6, 7, 8, 9 are obtained for the following values: the speed ratio $i_{34} = 6, 8, 10$; the teeth number of wheel (3) $z_3 = 11-17$; the chain pitch $p = 9.525; 38.1; 50.8$ mm Vatasescu et al. 2010.

The numerical simulations for the influence of the driven wheel teeth number on the speed ratio are presented in Fig. 6, while the influence of the chain pitch (p) on the driven wheel radius r_4 is presented in Fig. 7. Considering a roller chain transmission, the value for the teeth number of the driven wheel is recommended to be up to $z_{4max} = 120$ teeth (Lateş 2012). The dimensions of the chain transmission can be chosen from the numerical simulations, part of them being presented in Figs. 6 and 7: the maximum numbers of teeth of the driving/driven wheels z_3/z_4 are 17/102 for a speed ratio $i_{34} = 6$, 12/112 for $i_{34} = 8$, and 11/111 for a speed ratio $i_{34} = 10$ (Fig. 6).

Under the condition that the driven wheel teeth number must not exceed 120 teeth (due to the transmission size and chain type), the simulations from Fig. 7 present the dependence between the dimensions of wheel 4 (r_4), the speed ratio (i_{34}) and the chain pitch (p). The diagram highlights the increase of the driven wheel dimensions with the chain pitch; thus, for a low pitch value ($p = 9.25$ mm), the driven wheel size changes in a 50 mm limit, while in the case of a pitch equal to 50.8 mm, the dimensions are increasing by 166 mm. Due to the fact that the speed ratio increases with the decrease of the driven wheel dimensions, the tracking system diurnal mechanism containing a chain with a higher pitch value ($p = 38.1$ or 50.8 mm), has a reduced size if the speed ratio is 6. In this case, the radius of the driven wheel can be either $r_4 = 622$ or 829.5 mm (Fig. 7).

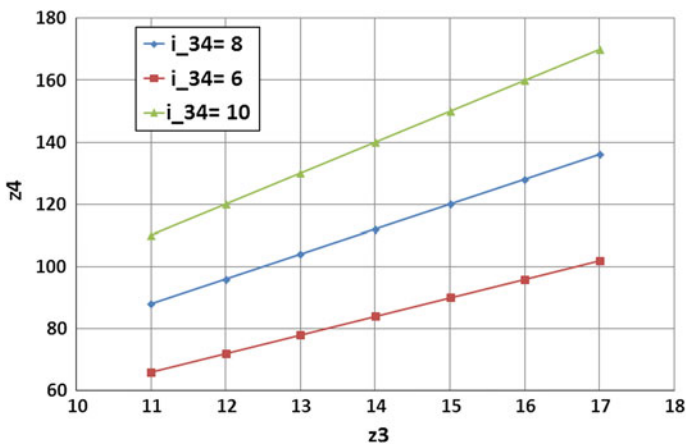
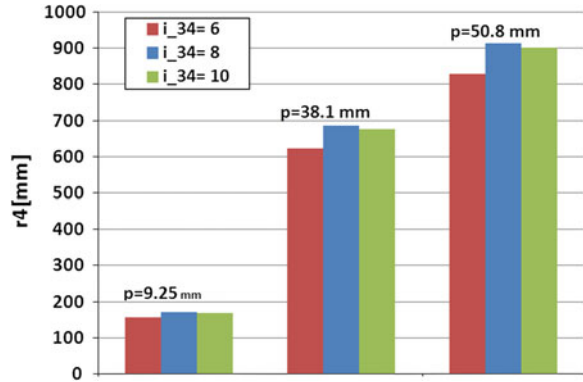


Fig. 6 Simulations for the dimensions of wheels 3 and 4 vs. the speed ratio (i_{34})

Fig. 7 The driven wheel dimensions (r_4) vs. the chain pitch (p) and the speed ratio (i_{34})



The next step is to check if the motion of the chain/cogged belt transmission can be obtained using a linear actuator for solar platforms www.eler-linear.com. The ranges in which the actuator overall dimensions and stroke take values are given in catalogues (size 2,084–2,884 mm, and strokes of 600, 800 and 1,000 mm www.eler-linear.com).

In order to determine if the actuator can ensure the diurnal angular stroke of 180° for the solar dish collector, numerical simulations were performed based on rel. (7), for different values of speed ratio (i_{34}) and chain pitch (p). The analysis of the diagrams from Fig. 8 allows highlighting the following conclusion: the diurnal angular stroke of 180° can be achieved only for a chain pitch $p = 9.25$ mm, and for all the values of the speed ratio.

A way to reduce the energy consumption is by using a step orientation of the solar collector, at every 8 min. This actuation involves a rotation of the solar collector with $2^\circ/\text{step}$. The corresponding stroke of the linear actuator can be obtained by replacing the value of the diurnal angle in relation (6). The diagrams for the stroke variation, presented in Fig. 9, confirm the accomplishment of a 2° diurnal angle by using the linear actuator, regardless of the values of pitch and

Fig. 8 The actuator maximum stroke vs. the speed ratio (i_{34}) and the chain pitch (p)

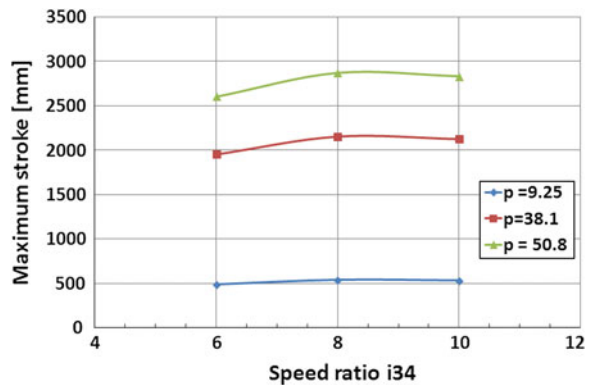
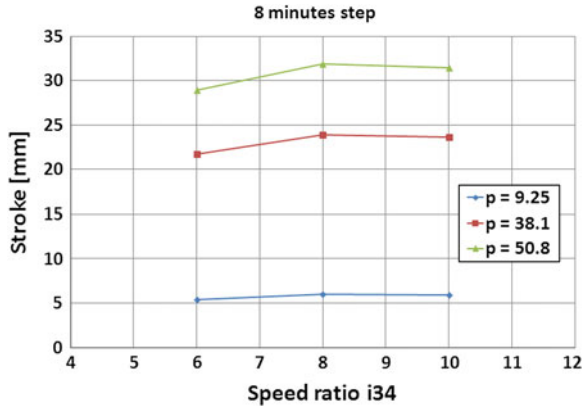


Fig. 9 Linear actuator stroke vs. the speed ratio (i_{34}) and chain pitch (p)



speed ratio (as the minimum stroke provided by the linear actuator is 1.5 mm www.eler-linear.com). Thus, it can be concluded that the tracking mechanism from Fig. 3, containing a linear actuator for PV platforms, allows the orientation of the solar dish collector with a diurnal angular stroke of 180° . Low power consumption is obtained by driving the linear actuator every 8 min, the collector rotation being of $2^\circ/\text{step}$. Thus, by using the proposed diurnal mechanism, consisting of the linear actuator and a chain transmission, the tracking system complexity, cost and power consumption are very much reduced.

The disadvantage brought by the proposed mechanism is the supplementary load on the chain and on the actuator, due to the way the linear actuator drives the chain transmission. Therefore, the next step in the diurnal tracking system development is the transmission optimization, meant to eliminate the additional loads. Four of the eight optimized solutions proposed by the authors to avoid the supplementary loads, are presented in the paper. The proposed variants for the chain transmission used in the orientation of the parabolic dish solar collector are object of a patent request.

Thus, in the mechanism from Fig. 10a, the stator of the linear actuator is not fixed, being articulated to the base; this structure can take over any deviations that may occur during installation or operation. But in this driving situation, the eccentricity between the actuator articulation and the chain axes, introduces additional loads. Their values can be reduced by ensuring the collinear position of the actuator articulation and the chain axis (Fig. 10b).

Other two solutions to avoid the supplementary loads in the diurnal tracking mechanism are proposed in Figs. 11 and 12. The chain transmission from Fig. 11, consisting of the driven wheel (1) that is attached to the parabolic dish solar collector, the driving wheel (2) and the chain pre-tensioning system (8, 8a), is driven by the linear actuators (4) and (4a), articulated to the base. The actuators are connected to the special chain link (6) through spherical joints, an intermediate element (5), and a revolute joint.

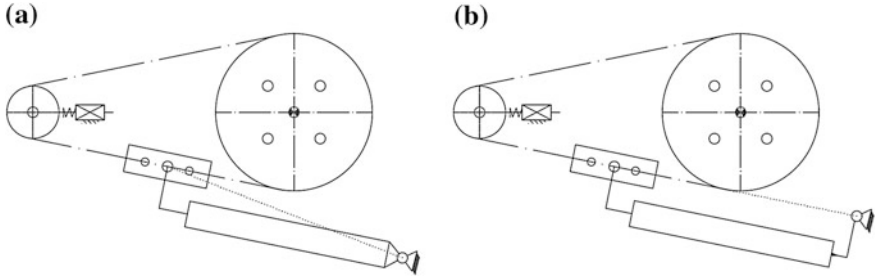
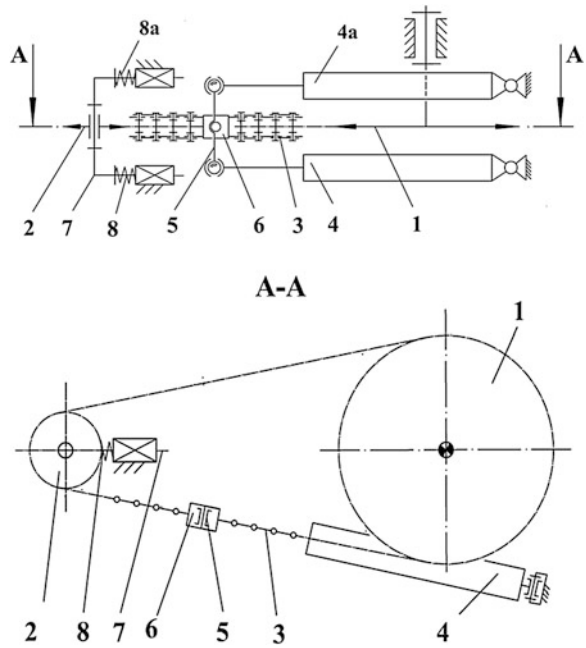


Fig. 10 Structural variants of the diurnal tracking mechanism containing: an eccentrically articulated actuator (a), and a coaxially articulated actuator (b)

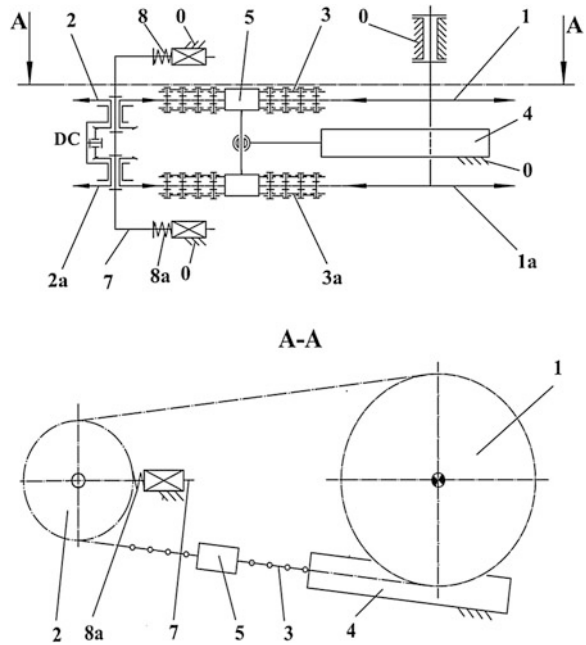
Fig. 11 Structural scheme of the chain transmission driven by two linear actuators



The solution proposed in Fig. 12 uses one fixed linear actuator (4) for the orientation of the parabolic dish collector that is connected to the double wheel (1, 1a). The actuator is articulated to a special element (5), mounted on both chains (3) and (3a), for dynamic reasons. The errors that can occur in the chain transmission during assembling and functioning are taken over by a planetary gear (DC) (Fig. 12).

The concept of the chain transmission, which will be further developed, will be selected among the proposed variants, based on multi-criteria analysis. The prototype of the optimized tracking system will be manufactured and implemented in a demonstrator to be tested in the Transilvania University Research Institute.

Fig. 12 Structural scheme of the chain transmission with one actuator and a planetary gear



4 Conclusions

In order to follow the sun path on the sky, the parabolic dish solar collectors use biaxial tracking system for orientation. For these collectors, the elevation movement is typically generated by using linkage mechanisms driven by linear actuators. For the collector diurnal motion, the paper proposes three new variants of tracking systems consisting of a chain transmission driven by a linear actuator, the solutions being proposed to be patented. By using the linear actuator connected to the chain through a special link, the mechanism has a reduced complexity, a low price, and reduced energy consumption when using a step tracking. The case study developed for Brasov area proves that the proposed mechanism ensures a rotation of the parabolic dish with a total angle of 180°, and, in case of step tracking, the linear actuator stroke allows a rotation with 2°/step. In order to overcome the disadvantages related to the supplementary loads that occur in the chain and actuator due to the way the components are assembled to each other, an optimization is performed and eight innovative solutions are proposed. The next steps in the research consist in building the virtual model, manufacturing the prototype and implementing it in the built environment.

Acknowledgments This paper is supported by the Sectoral Operational Programme Human Resources Development (SOP HRD), financed from the European Social Fund and by the Romanian Government under the contract number POSDRU/89/1.5/S/59323.

References

- Bonanos AM (2012) Error analysis for concentrated solar collectors. *Renew Sustain Energ J* 4. doi:[10.1063/1.14768546](https://doi.org/10.1063/1.14768546)
- Chong KK, Wong CW (2009) General formula for one-axis sun tracking system and its application in improving tracking accuracy of solar collector. *Sol Energ J* 83(3):298–305
- Ciobanu D (2011) Conceptual design of a solar thermal system with dish solar collector. *Environ Eng Manage J* 10(8). ISSN 1582-9596
- Creanga N, Diaconescu D, Hermenean I (2011) 4-bar geared linkage used for photovoltaic azimuth orientation. *Environ Eng Manage J* 10(8):1139–1148
- Hermenean I, Visa I (2011) Step tracking synthesis of an azimuth tracked concentrating photovoltaic (CPV) system. *Environ Eng Manage J* 10(9):1225–1234
- Lateş MT (2012) Bush chains design process. *Annals of Oradea University, Management and Technological Engineering Fascicle, vol XI (XXI), 2*, Oradea University Publishing House, ISSN 1583–0691, pp 2.51–2.55
- Reddy KS, Veershetty G (2013) Viability analysis of solar parabolic dish stand-alone power plant for Indian conditions. *Appl Energ J* 102:908–922
- STAS 4075-53, 4076-53
- Vatasescu MM, Visa I, Diaconescu D, Hermenean IS, Creanga NC (2010) New solar angles and their corresponding tracking systems efficiency. *Renew Energ Power Quality J* 8. Online at: <http://www.icrepq.com/icrepq'10/511-Vatasescu.pdf>
- Technical documentation ATON 3. Online at www.elero-linear.com
- Wu S-Y, Xiao L, Cao Y, Li Y-R (2010) A parabolic dish/AMTEC solar thermal power system and its performance evaluation. *Appl Energ J* 87:452–462

Interactive Animation Production by Means of Advanced Image Processing

V. Ciupe, E.-Ch. Lovasz, M. Reessing, V. Henkel, C. M. Gruescu
and E. S. Zabava

Abstract The paper describes an application developed within the European project thinkMOTION. The project aims to post online, within a digital library, heterogeneous content regarding mechanisms science and related fields. Special systems were developed in Ilmenau, Germany and in Timisoara, Romania, in order to actuate and take photographs of the physical models of the mechanisms to be digitized. The systems consist of a motor mechanically connected to the mechanism by means of a coupling device and electrically connected to a PC or a PLC. A digital still camera is connected to the same computer/controller. The logic of this system is to take a photograph after each rotational increment of 0.9° , thus obtaining a complete 400 images set that can be further processed via software in order to obtain an interactive animation which can be uploaded on the project's dedicated web portal and used in this way as an educational or informational content tool.

Keywords Interactive animation · Mechanisms · Physical models · Stepper motor · Servo motor · Java applet

V. Ciupe (✉) · E.-Ch. Lovasz · C. M. Gruescu · E. S. Zabava
Politehnica University of Timisoara, Timisoara, Romania
e-mail: valentin.ciupe@mec.upt.ro

E.-Ch. Lovasz
e-mail: erwin.lovasz@mec.upt.ro

C. M. Gruescu
e-mail: corina.gruescu@mec.upt.ro

E. S. Zabava
e-mail: eugen.zabava@mec.upt.ro

M. Reessing · V. Henkel
Technische Universität Ilmenau, Ilmenau, Germany
e-mail: michael.reessing@tu-ilmenau.de

V. Henkel
e-mail: veit.henkel@tu-ilmenau.de

1 Introduction

The current availability of computer-type devices and of the internet provides a great tool for information and knowledge spreading in all fields of human activity and in particular in the technical fields. The European project thinkMOTION <http://www.thinkmotion.eu/> is intended to offer knowledge in the field of mechanisms and machine science through a specialized site called DMG-Lib www.dmg-lib.org which is a digital library that provides content originating from a wide range of sources such as universities, libraries, patent offices, museums etc. (Lovasz et al. 2012).

One of the content categories posted on the DMG-Lib site (aside books, articles, images, biographies etc.) is represented by the interactive animations. These animations have the role of bringing the users closer to the real functioning mode of the mechanisms (physical or CAD models) listed on the portal, by allowing to virtually “drive” those models with the mouse or with the touch of a finger (Fig. 1).

The partners in the project are Ilmenau University of Technology (Germany), University of Basque Country (Spain), University “Politehnica” of Timisoara (Romania), RWTH Aachen University (Germany), French Institute of Advanced Mechanics (France) and University of Cassino (Italy). The partners put together content from national sources and from providers in their neighborhood areas, willing to collaborate. No matter what the original source is, it requires digitization and preparation of high-quality web-compliant files to be posted online (Brix et al. 2011; Lovasz et al. 2012). Similar projects aiming at the teaching of mechanisms (Barej et al. 2013) or at the research and development (Lonij et al. 2012) proved to

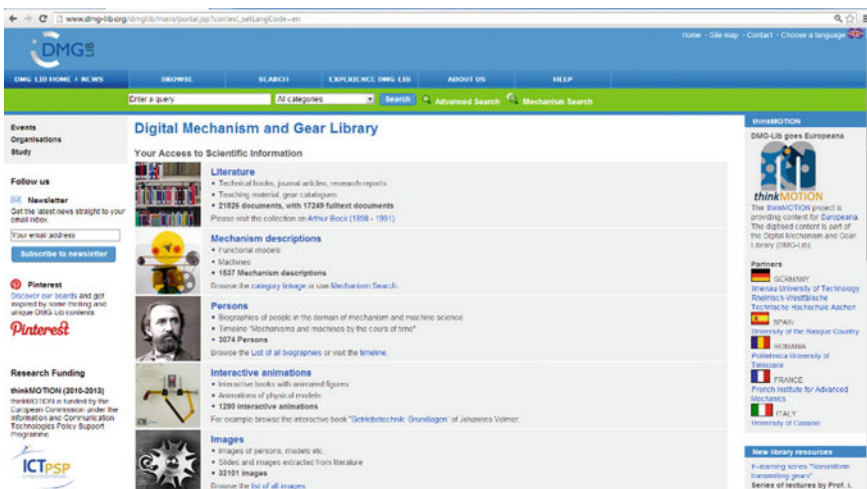


Fig. 1 The web-site of DMG-Lib, with 1,290 interactive animations available www.dmg-lib.org

be successful among their users and further strengthen the need for a new online library able to provide content from multiple source types (including sources where the users benefit from the physical contact, for study) in the field of mechanisms and machine science.

2 The TU-Ilmenau Digitizer

Content sources as the basis for mechanism descriptions are physical demonstration models (Fig. 2, left), pictures, movies and animations but also figures in literature such as technical books, journal articles, research reports, patent specifications or mechanism catalogues. A lot of these literature sources contain design solutions or structures of mechanisms in form of technical drawings, solution principles or images (Fig. 2, right) for creating mechanism descriptions.

Interactive animations can be produced for all these content sources, and in the case of drawings or images an image sequence can be generated from some CAD software and then further processed using the AIS generator software.

For the case of physical models a digitization workstation was developed at the Ilmenau University of Technology, Germany which works with a digital (photo) camera, a variable lighting system and a PC-controlled stepper motor (Fig. 3). For each series of models an individual adapter between the motor and the model input and an invisible fixing for the model must be designed. A customized lighting position for each series and sometimes for each model is necessary to get contrasty and nearly shadowless images.

The stepper motor drives the model step by step and the camera takes a photo after each step. The stepper motor and the camera are controlled by a PC. The controlling software (Fig. 4) allows different settings depending on the



Fig. 2 Physical demonstration models from the University of Hannover (*left*) and figures and descriptive texts in books (*right*) as examples for content sources for mechanism descriptions

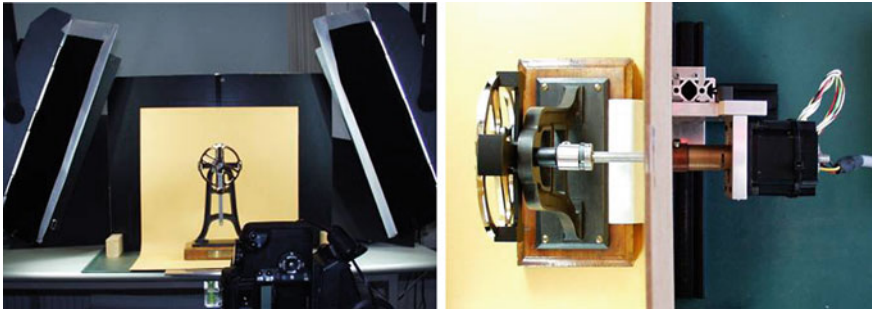


Fig. 3 Workstation at the Ilmenau University of Technology for digitalization of the physical demonstration models (*left front view, right top view*)

peculiarities of the models. In this way, from each model a sequence of usually 400 images per turn is recorded.

With the image sequence recorded, the next step consists of processing these images inside the AIS generator software.

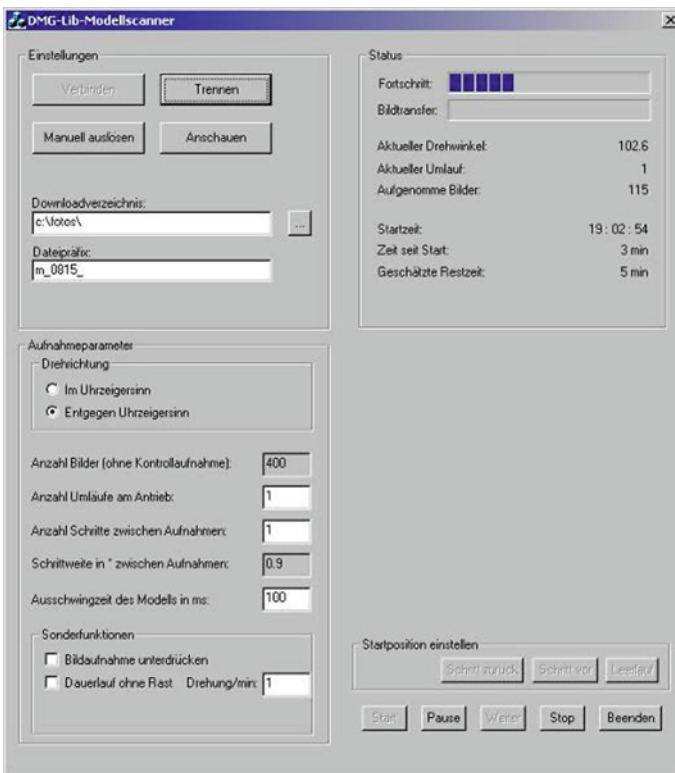


Fig. 4 PC software for controlling stepper motor and camera

3 The UPT Digitizer

The method approached at UPT for digitizing the physical mechanisms models is to use a compact system that can be easily carried around and can be set up in a few minutes. This compact PC-less option is preferred due to the fact that is more difficult to bring a bunch of physical models into a digitizing lab especially when they are in a large number and/or in sparse locations (multiple universities). In order to achieve this goal the system uses a programmable logic controller http://www.festo.com/net/SupportPortal/Files/142497/FEC-Standard_0609_EN.pdf connected to a digital servo-motor http://www.festo.com/cat/ro_ro/products_MTR_DCI and also to a digital photo camera (Fig. 5, left).

The chassis of the system supports the motor, the controller, the power source and also the user interface buttons. The servo-motor can be positioned on its vertical axis in order to accommodate the coupling to different mechanisms (which can have their driving element at different heights).

In order to solve the mechanical coupling to the driven mechanisms, the motor benefits from a standard chuck attached to its driving shaft via an elastic element. In this way, mechanisms having their driving axle with a diameter between 2 and 10 mm can be driven by this digitizing system.

From an electric point of view the controller is connected to the motor's electronics and is also connected to a digital camera that takes the pictures of the mechanism between each movement increment, and to the user buttons board. A schematic of the electrical assembly is represented in Fig. 6.

Beside the aforementioned components the digitizing system also benefits from a led lamp for illuminating the digitizing scene. The advantage of this lamp is its high light output combined with very low heat emissions, thus making it suitable for placing it very close to the photo camera or to the physical model of the mechanism.

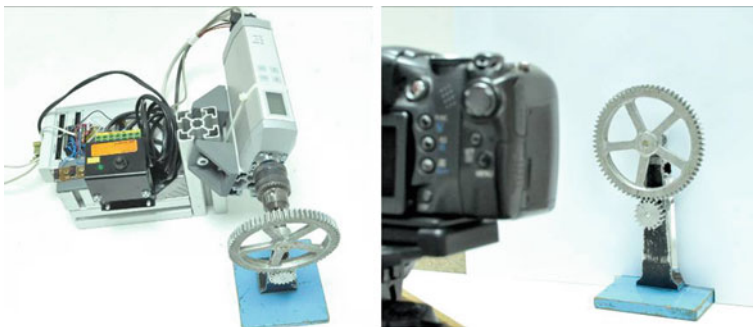


Fig. 5 General view of the digitizing stand, coupled to a physical model (*left*) and the physical model being digitized (*right*)

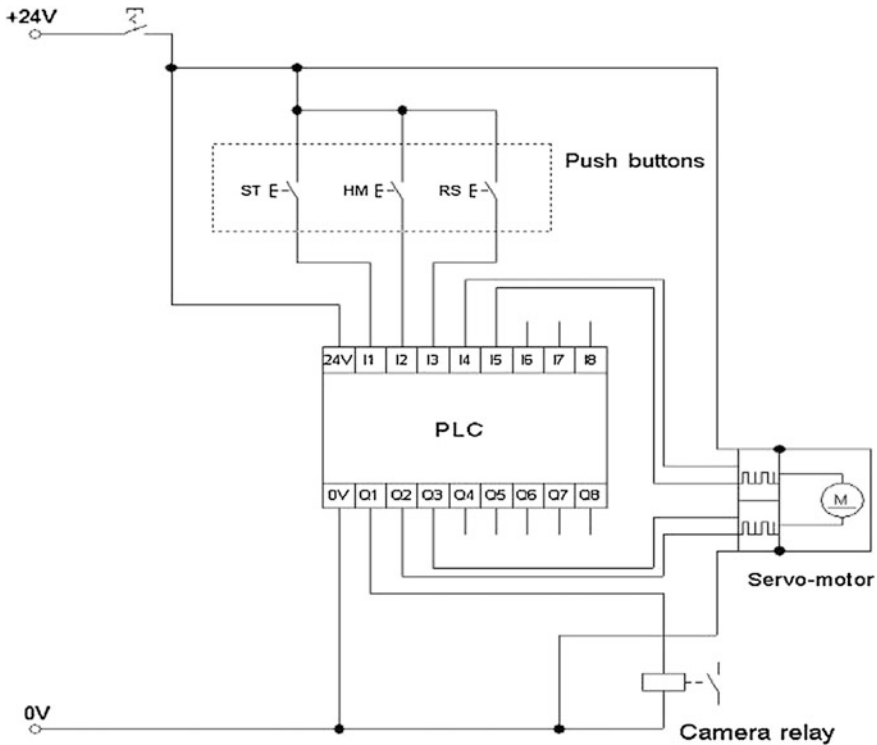


Fig. 6 Electrical assembly schematic for the digitizing stand

Figure 5 right, presents the model being photographed, having a cardboard sheet (with an appropriate cut-out) placed between the model and the motor's chuck in order to hide the stand behind it from being captured by the camera.

From the software point of view, the image capturing sequence can be regarded as event-driven loop. After the mechanism is securely affixed to the motor's shaft, the lights are arranged and the camera is set up, the user pushes the homing (HM) button in order to define the current position of the motor as "home" and then the start (ST) button to begin the process. The motor is then commanded to rotate to its next relative stored position (CCW, 0.9°) and the controller waits for the "motion complete" signal from the motor. After receiving this signal the controller sends a low voltage pulse (via a relay and a voltage divider) to the photo camera through its USB port. The camera uses a modified firmware <http://www.stereo.jpn.org/eng/sdm/index.htm> that allows for remote shooting when its USB interface detects a rising edge pulse on the cable power lines. After the time delay reserved for taking the photograph expired, the process repeats and the controller commands another 0.9° rotational increment of the motor.

In the event of a motion error or a motion watchdog catch (e.g. after commanding an increment it takes more than 1 s. for the motor to send the "motion

complete” signal) the process is paused and the user can either eliminate the cause of the malfunction and continue (press ST button) or reset (RS button) the system and start the process again from the current location.

When the mechanism inched a full rotation (400 increments/360°) the controller commands the motor to return the model to its initial position and with this motion completed the process ends. The 400 pictures can now be downloaded from the SD card to a PC and then further processed using the AIS-Generator software.

4 The AIS-Generator Software

Producing the interactive animation requires the processing of the image sequences. For this, “thinkMOTION” uses an interactive web video technology called AIS which originated from project DMG-Lib. <http://www.dmg-lib.org/dmglib/main/portal.jsp?mainNaviState=browsen.manim> and has been improved since. AIS stands for Augmented Image Sequence and consists of three essential parts: the generator software, the data format and the web player software.

The generator software uses videos or image sequences as input data. Some manual preparation steps are necessary before automatic processing can begin. At first, the user needs to specify a crop region to select the part of the image to be used in the interactive animation. Then a logo and its position may be selected. The software also allows adding information for linking the created animation to existing content in the DMG-Lib database (e.g. description of the mechanism featured in the animation).

The last and most important preparation step is the specification of the driving element and its parameters. The user interactively draws lines that represent the position and orientation of the driving element at the beginning and at the end of the animation. This information is necessary to map user interactions to video frames in the finished animation. Currently, the AIS generator and player support rotational and translational driving motions.

Once these manual steps are completed, the generator software processes the input data and creates the AIS animation. In addition to the actual video content and a preview image it contains an XML file that holds the interaction-related parameters to be interpreted by the AIS player software. Typically, a finished AIS animation will be uploaded to the DMG-Lib database. There it will be listed and may be loaded into the AIS player.

The player is a Java applet that can be embedded into web pages. It features play controls like a normal, non-interactive video player. Still, the most interesting mode of interaction is to directly “grab” the driving element with the mouse and move it. The video content in the player will react accordingly (Figs. 7 and 8). This creates the illusion of actually touching and operating the mechanism. It brings the user closer to the real demonstration model that has been digitized. That

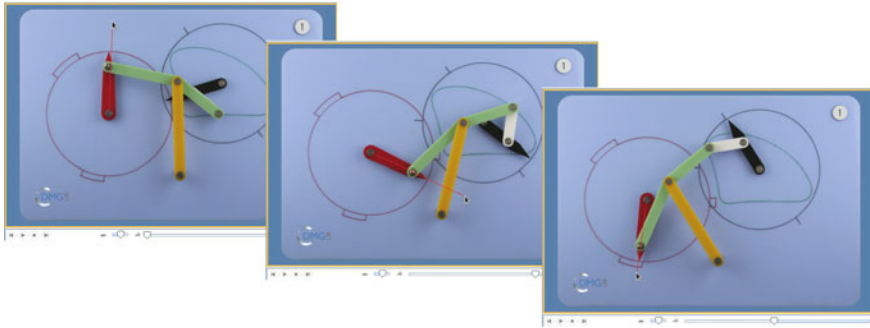


Fig. 7 Digitized and processed mechanism in the AIS Player. The mouse cursor controls the motion of the mechanism in the animation. <http://www.dmg-lib.org/dmglib/main/portal.jsp?mainNaviState=browsen.mecdesc.viewer&id=1305025>



Fig. 8 Interactive animation for a digitized physical model (*left*) and for a CAD generated model (*right*), on the DMG-Lib portal. <http://www.dmg-lib.org/dmglib/main/portal.jsp?mainNaviState=browsen.mecdesc.viewer&id=2711025>, <http://www.dmg-lib.org/dmglib/main/portal.jsp?mainNaviState=browsen.mecdesc.viewer&id=2730025>

way, the interactive animation facilitates to understand the mode of operation and the kinematic properties of the mechanism.

5 Conclusions

Physical demonstration models (and mechanism figures in literature) are the basis for creating mechanism descriptions in the DMG-Lib.

The physical working models of the mechanisms are digitally recorded as a sequence of images, usually covering a full rotation of the input (driving) element.

With further handling steps, these image sequences are composed to interactive animations, which can be started inside the DMG-Lib Internet portal with a special player or can be downloaded as video files for local use. By digitizing these content sources as interactive animations, the working principles and kinematic properties of these mechanisms can be observed much easier and with a greater impact on the information quantity and quality for the user of the web site.

The mechanisms and physical models presented in this paper, and many more, can be viewed and interactively animated by accessing the DMG-Lib portal, available at www.dmg-lib.org.

References

- Barej M, Husing M, Corves B (2013) Teaching in mechanism theory—from hands-on analysis to virtual modeling, new trends in mechanisms and machine science, ISBN 978-9400749016. Springer, pp 703–710
- Brix T, Doering U, Brecht R, Reessing M, Lovasz E-Ch (2011) ThinkMOTION—Europeanas Tor in die Welt der Getriebe. In: Proceedings of Kolloquium Getriebetechnik, Chemnitz 2011, ISBN 978-3941003408, MV Verlag, pp 57–72
- DMG-Lib: Mechanism ID: 1305025. <http://www.dmg-lib.org/dmglib/main/portal.jsp?mainNaviState=browsen.mecdesc.viewer&id=1305025>
- DMG-Lib: Mechanism ID: 2711025. <http://www.dmg-lib.org/dmglib/main/portal.jsp?mainNaviState=browsen.mecdesc.viewer&id=2711025>
- DMG-Lib: Mechanism ID: 2730025. <http://www.dmg-lib.org/dmglib/main/portal.jsp?mainNaviState=browsen.mecdesc.viewer&id=2730025>
- DMG-Lib: Digital mechanism and gear library. www.dmg-lib.org
- DMG-Lib: interactive animations. <http://www.dmg-lib.org/dmglib/main/portal.jsp?mainNaviState=browsen.manim>
- FESTO: FC640 FEC standard controller. http://www.festo.com/net/SupportPortal/Files/142497/FEC-Standard_0609_EN.pdf
- FESTO: MTR-DCI-32S-VCSC-EG7-H2IO motor unit. http://www.festo.com/cat/ro_ro/products_MTR_DCI
- Lonij G, Corves B, Reessing M, Razum M (2012) Application of the research environment e-kinematics in mechanism development, advances in mechanisms design. In: Proceedings of TMM 2012, ISBN 978-9400751257. Springer, pp 27–33
- Lovasz E-Ch et al (2012) Advanced digitization techniques in retrieval of mechanism and machine science history, advances in mechanisms design. In: Proceedings of TMM 2012, ISBN 978-9400751257. Springer, pp 36–41
- Stereo data maker: USB remote triggering firmware for Canon PS Cameras (v1.60). <http://www.stereo.jpn.org/eng/sdm/index.htm>
- ThinkMOTION: DMG-Lib goes Europeana. <http://www.thinkmotion.eu/>

Vibrations Concerning with Safety in Vehicle Rolling Conditions

Mircea Diudea, Victor Hodor, Radu Balan and Mircea Bara

Abstract This paper is intended as a study of the composition of existing vibrations in the rear of a car, while it is running in order to increase traffic safety. The main factors that cause the occurrence of these vibrations are related to runway irregularities, imperfections of the elements that compose the system running, and the vibrations caused by aerodynamic (CFD predictions) of the shell –as it runs at high speed (i.e. in-between legal limits). Accuracy in terms of the gas-dynamics behavior, implies a CFD analysis with LES model. Predicting the distinct characteristics in relation to sources, follows the influence related to the wheel and respective to body motion. These analyses were done by the use of FFT method, and with the classic procedures in processes controlling–using MATLAB-Simulink. These are analyzed in order to face a common risk of resonance in certain specific conditions, to prevent safety running conditions.

Keywords Safety · Vehicle running · Vibrations · Shell CFD aerodynamic · Rolling-path irregularities · Control Simulink

List of Symbols and Units

CFD Computational fluid dynamics
LES Large eddy simulation
FFT Fast Fourier transform

M. Diudea (✉) · V. Hodor · R. Balan · M. Bara
Department of Mechanisms, Precision Mechanics and Mechatronics,
Technical University of Cluj-Napoca, Cluj-Napoca, Romania
e-mail: mircea_diudea@yahoo.com

1 Introduction

Over the last two decades, developments in vehicle suspension design have focused on increased level of safety and comfort. Choi et al. (2008) investigated vibration control responses of a full-vehicle installed with ER dampers. They demonstrated that vibrations under bump and random road conditions can be effectively suppressed by the activation of electrorheological (ER) dampers associated with the sliding mode controller. More recently, Rosenfeld and Wereley (2004) proposed an optimisation methodology for performance improvement of magnetorheological (MR) damper. M. Canale et al. (2005) proposed analysis of a control strategy, for semi-active suspensions in road vehicles, based on Model Predictive Control (MPC) strategies.

The vibrations that occur when running is due to the constructive elements of the vehicle, the aerodynamic forces acting on the body, but also those caused by the rolling track. In order to perform the study were to taken into account the elements constructive wheels, them having a significant role in the development of vibrations. The composition of these vibrations can be dangerous in case of certain resonances that could have a critical influence on the adherence to the rear wheels. That is the case where the appearance of side drafts (depending on weather conditions) is unhappily associated with any of asphalt compositions.

In this paper we present the use of new concepts constructive-functional of modern vehicles, by studying their virtual simulation methods.

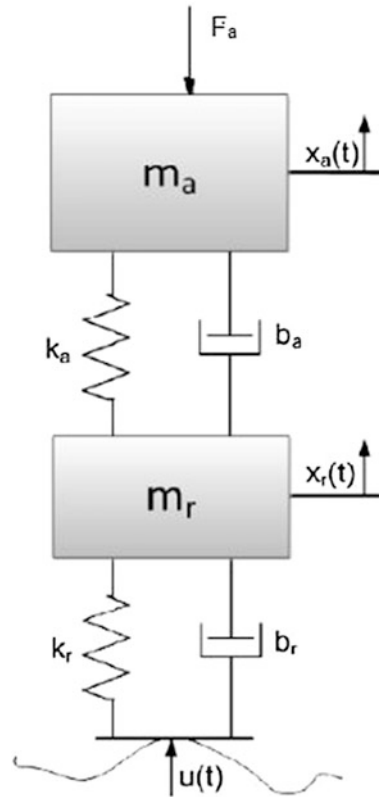
The ultimate goal of this study is to identify resonance vibrations that may appear because of vibrations caused by the composition of the three elements presented above.

2 Method of Study

The study method is based on analyzing the behavior of the rear suspension of a car at the appearance of vibrations, using MATLAB-Simulink. Suspension modeling and simulation of the dynamic behavior of a car when the car goes over a bump or another variant of the road. Body movements are studied in case of various external stimuli and can be done using a generic model introduced to behavioral analysis in MATLAB-Simulink. A car can be representations in a simplified form as the schematic in Fig. 1.

The resulted effect is due to vibrations of its constructive elements and those due to other external factors such as the quality of the track, or turbulence occurred in the rear of the vehicle at relatively high speeds. Among the building blocks that produce significant vibration during running, the most important are car wheels. They are mainly due to errors in geometry and mass errors. These occur due to imperfections in the manufacturing process or due to the time operating conditions. In order to determine their frequencies and amplitudes used tires or features

Fig. 1 Generic model of the dynamic analysis



provided by tire manufacturers for a tow but falling average running speed study, and for those due to the runway or used ISO 8608:1995, which characterizes each category of road roughness coefficient based on classifying them into eight categories. Such models have been developed in MATLAB/Simulink and were generated different types of roads. It was found that for a constant speed of travel of the vehicle, depending on the category of road roughness amplitudes (ZQ)—caused by the roughness parameter ($GQ (\Omega)$) increase in exponential manner and their frequencies remain constant. Thus, for a given frequency amplitudes were calculated maximum amplitudes and amplitudes of road roughness average for the five standard categories of roads. The results are presented in the Table 1.

Own wheel vibrations arise mainly because tires and which occur due to the manufacturing process, different density materials, operability, condition, etc. They arise from the manufacturing process and are a source of excitation for vibration wheel.

Mass variation can lead to static and dynamic imbalance. Static weight imbalance occurs when there is a change table in one plane in circumference. This leads to variations in radial force and tangential forces. These forces are a function of running speed and increases with it. Dynamic imbalance is due to change in

Table 1 Road roughness amplitude characteristic

Category of road	Amplitude [mm]	
	Zq, max	Zq, med
A (very good)	± 5.4	± 1.2
B (good)	± 10.8	± 2.3
C (medium)	± 21.8	± 4.6
D (bad)	± 43.4	± 9.3
E (very bad)	± 87	± 18.6

mass in different planes, circular and results in the changes of torque perpendicular to the axis of rotation.

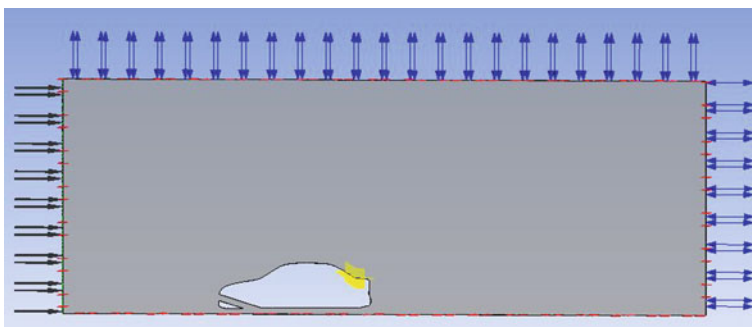
ANSYS CFX code was used for CFD prediction of the aerodynamic influences.

The computational domain has two space dimensions and time. The present flow problem is inherently unsteady, not only because of the flow turbulence, but also because of the large scale vortex shedding present in the separated wake behind the truck and another car. The turbulence away from the boundaries was modeled by a constant eddy viscosity of 1,000 times the molecular value for air under standard conditions.

Consequently, all solutions presented were calculated using the constant eddy viscosity model of turbulence (Figs. 2, 3, 4, 5, 6, 7, 8).

Analyzing the values obtained in simulations monitoring points were determined requirements due to aerodynamic forces acting on the rear of the vehicle, and their variation over time in different running speeds. After determination of the stresses that occur during runtime, it was started to implement the model and motion simulation using MATLAB-Simulink. Application developed will take into account one of the four suspension of the car. The model will include both elements of the suspension (spring, damper) as well as the tires (Table 2).

Next, the wheel was analyzed (xr) to see if in certain circumstances, there may be a resonance phenomenon, which is a significant increase of the vibration wheel,

**Fig. 2** Simulation conditions

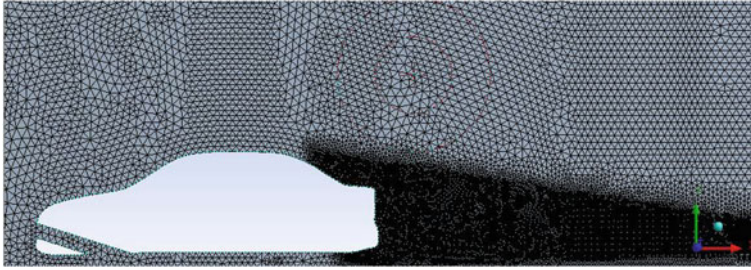


Fig. 3 The overall mesh

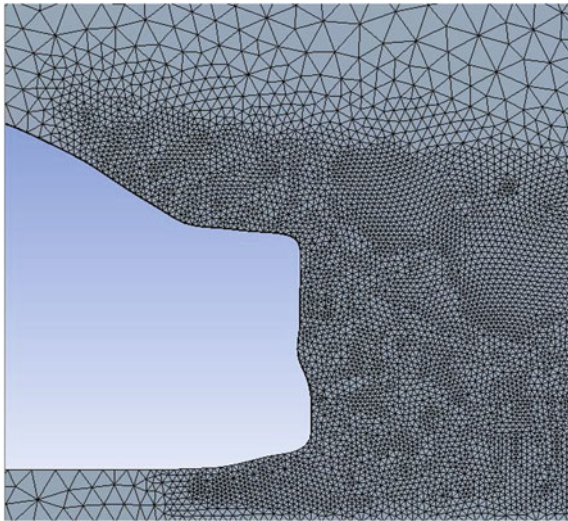


Fig. 4 Mesh detail

allowing loss of contact with the road surface. The following laws has created a study that have been introduced previously presented initial data (Fig. 9).

To continue this study, data runs were made corresponding to several categories of road for different speeds between 90 and 130 km/h, as well as car body mass variations around the initial value (Figs. 10, 11, 12).

Thus for several sets of values (126 km/h, $I = 244$ kg, $m_a = 31$ kg) showed an increase in the amplitude of vibration of the wheel, leading to lower adherence to the rear axle path (Fig. 13).

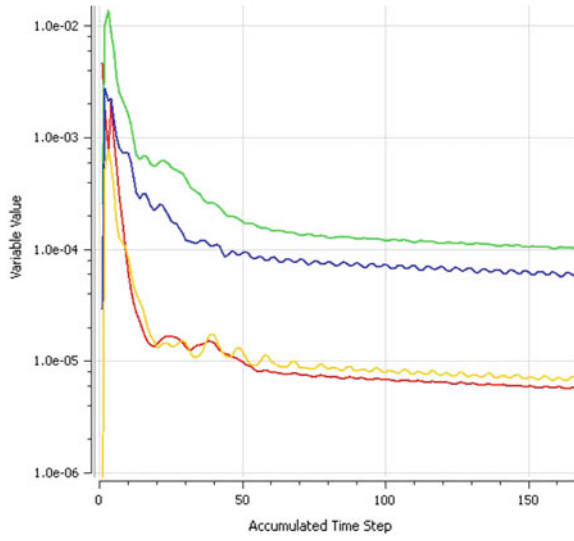


Fig. 5 Root mean square

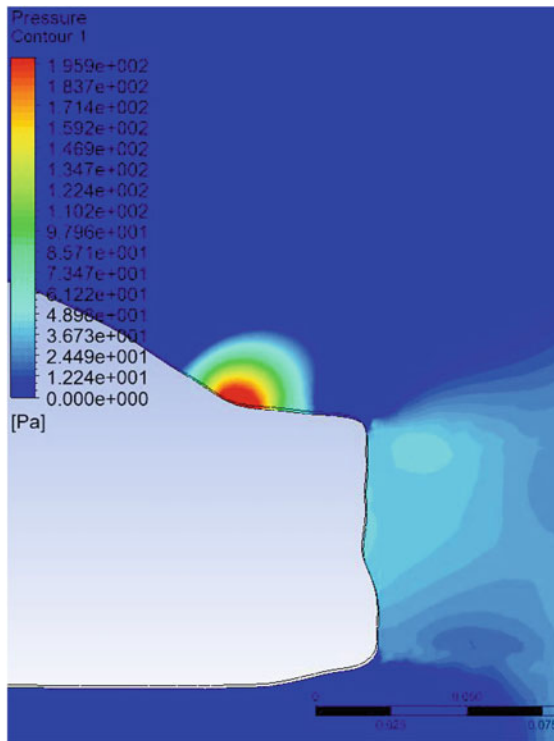


Fig. 6 Pressure on the bodywork

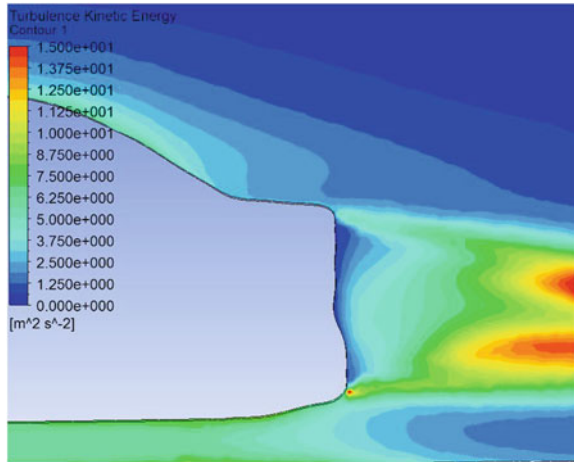


Fig. 7 Turbulence kinetic energy

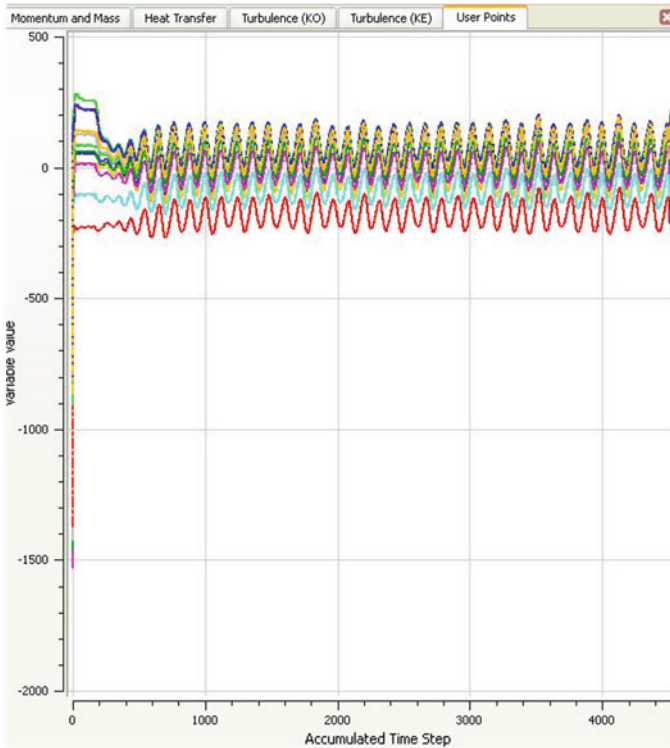


Fig. 8 Pressure at the monitoring points

Table 2 MATLAB initial data

Name	Notation	Value	UM
Mass cas	ma	250	[kg]
Mass wheel	mr	30	[kg]
Suspension damper coefficient	ba	1,500	[Ns/m]
Wheel damping coefficient	br	200	[Ns/m]
Constant spring suspension	ka	16,000	[N/m]
Constant wheel arch	kr	160,000	[N/m]

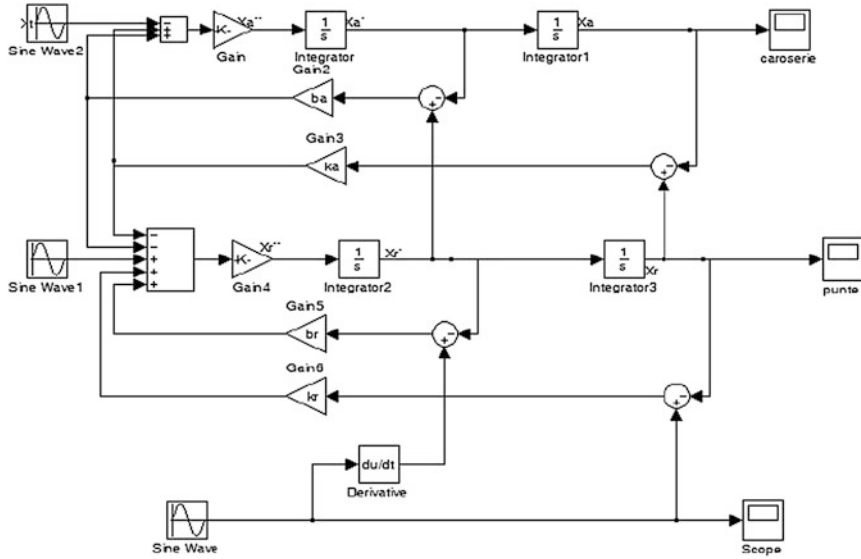


Fig. 9 Schematic Simulink model

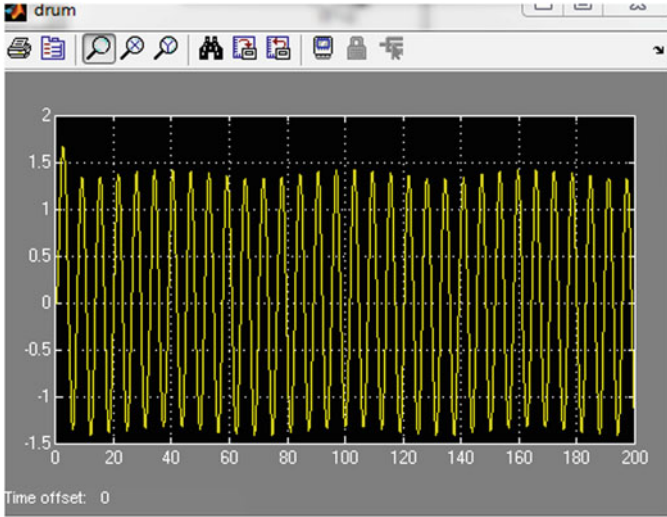


Fig. 10 Signal rolling track

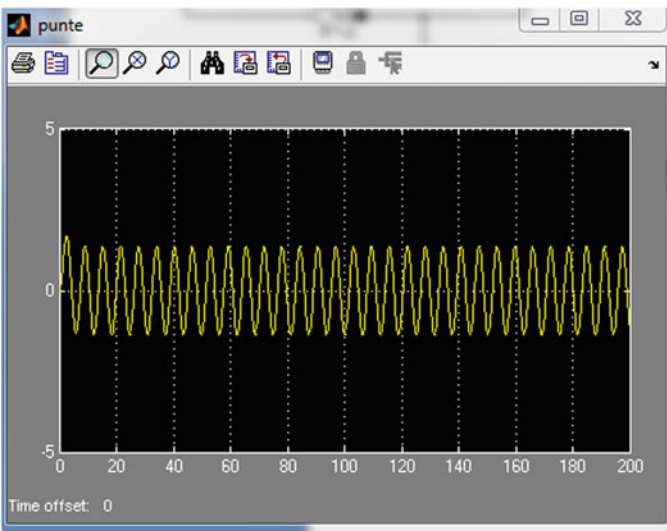


Fig. 11 Away rear axle

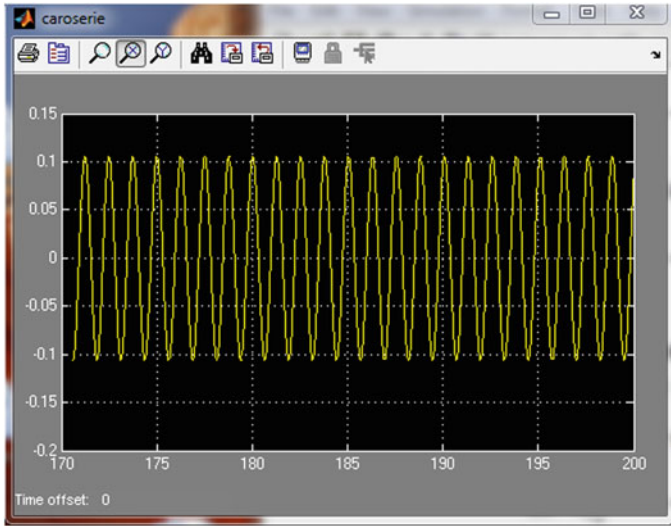


Fig. 12 Bodywork away

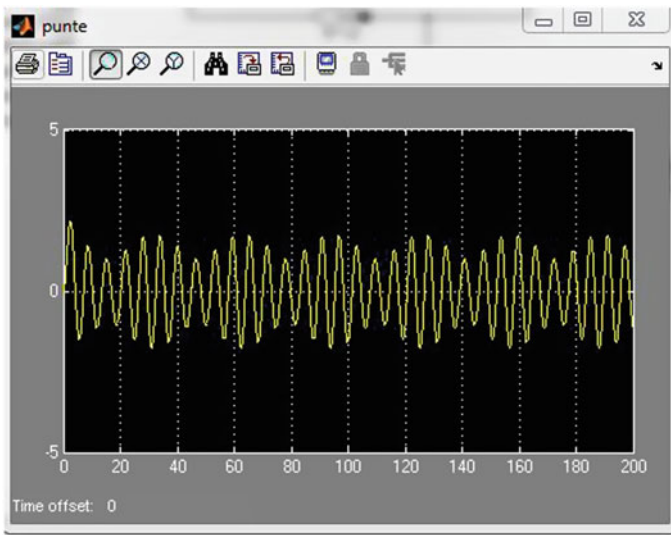


Fig. 13 Away rear axle

3 Conclusion

From the above results, it can be concluded that, during the running of a vehicle, there may be times in which grip the ground behind the car train can decrease dangerous.

In real driving conditions, the occurrence of this phenomenon is difficult to estimate, because the factors taken into consideration may significantly change.

This study is especially important in terms of how relationships can occur running and other factors that may amplify this phenomenon, such as tire wear, or dampers or other road conditions.

In conclusion, damper design should be done taking into consideration appearance of the phenomenon of resonance of the system, in order to counteract.

Acknowledgments Authors gratefully acknowledge the financial support of the National PN-II-PT-PCCA 2011-3.2.0512, 2012–2015 for the “EQUATOR” “Advanced strategies for high performance indoor Environmental Quality in Operating Rooms”.

References

- Canale M et al (2005) Semi-active suspension control using “Fast” Model Predictive Control, Am Control Conf Portland, OR, USA
- Choi S et al (2008) Vibration control of magnetorheological damper system subjected to parameter variations. *Int J Vehicle Design* 46(1)
- Rosenfeld NC and Wereley NM (2004) Volume constrained optimization of magnetorheological and electrorheological valves and dampers. *Smart Mater Struct* 13:1303–1313

Control Method Comparison for Pneumatic Artificial Muscle Actuators

Mihai Petru Draghici, Calin Rusu, Alin Plesa, Radu Balan
and Sorin Besoiu

Abstract The artificial muscles are pneumatic actuators that have similar characteristics as the human ones. Major applications for the artificial muscles are haptic devices, as well as robotic hands. One of the important part in developing such mechanisms is the actuator control. Many control methods were applied to these muscles, but there are few comparisons between the efficiency of each method. This paper will present the implementation of PID control theory as well as On/Off with hysteresis methods to position an end effector using artificial muscles. The control method will be implemented in LabView environment, using a Compact Rio acquisition board. We will show that using PID control the positioning will be more accurate and done faster than using the On/Off controller.

Keywords McKibben muscles · Hysteresis control · PID control · LabView data acquisition

1 Introduction

In the past years several applications regarding haptic devices were developed by companies worldwide. The Shadow Robot Company developed state-of-the-art anthropomorphic robot hands, and for actuation they used “air muscles” (Shadow Hand 2013), pneumatic McKibben muscles. McKibben invented the muscles back in 1950s, to help disabled individuals and in 1980 Bridgestone Company improved the design and extent their use to painting robots.

In definition, pneumatic artificial muscles (PAM) are devices operated by air flow through a pressurized pneumatic rubber enclosure that can contract or extent

M. P. Draghici (✉) · C. Rusu · A. Plesa · R. Balan · S. Besoiu
Technical University of Cluj-Napoca, 103-105 Muncii blvd, Cluj-Napoca, Romania
e-mail: mihai.draghici@mdm.utcluj.ro

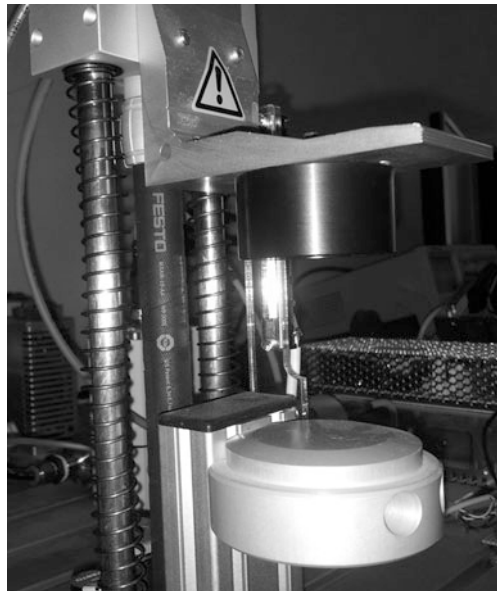
(Fig. 1). Usually, like the human muscles, they are antagonistic grouped in pairs. The major advantages of the PAM are high power to weight ratio and the inherent compliant behavior (Van Ham et al. 2001). The compliance is due to air compressibility and can be influenced by controlling the pressure. It is an important tool for delicate human and machine interaction, mainly used as actuator for haptic devices (handling fragile objects etc.).

Thanks to compliance, soft touch of the object as well as safe interaction can be achieved. By contrast, rigorous feedback laws have to be applied to achieve same compliance using hydraulic or electric actuators (Daerden and Lefeber 2002).

In order to satisfy control performance, a lot of intelligent control strategies were proposed and tried, due to the nonlinearities of the pneumatic artificial muscle. In (Thanh and Ahn 2006) a nonlinear PID controller is proposed, mixed with a neural control, to predict and adapt the controller to the nonlinearities of the system. A sliding mode control was applied to the air muscle and presented in (Shen 2010), where the system model was thoroughly defined and the dynamic model was well defined. However, simple control methods can have good response as well, and this paper presents a comparison made between the simplest control methods, on–off control method and PID control method.

In the first part of the paper, the experimental setup is described, as well as a short theory behind the control systems applied to the PAMs. Description of the on/off controller, the first mean of control used in engineering and the PID control method, along with the ways of tuning the controller. The second part presents the experimental results and the conclusions regarding the efficiency of the two controllers, comparing one with the other.

Fig. 1 Festo McKibben muscle



2 Experimental Setup

In Fig. 2 you can see the main components of the physical system. The system contains the McKibben muscle as well as a pressure sensor and a valve from FESTO Didactic (FESTO DIDACTIC), a position sensor (a linear side potentiometer, up to 10 k Ω). To power up the system we use a protected current source generating 24 and 9 V and a current up to 4 A. For data acquisition we use a Compact Rio 9,074 with several modules.

One of the key features of this board is the fact that it has LAN port and protocol installed, allowing the user to connect remotely to it. This way, students are being able to use the system as well, as part of an online educational laboratory. Another feature is the DAC/ADC module (digital-to-analog and analog-to-digital converter respectively), the module used for data acquisition. The potentiometer and the pressure sensor send analog data to the cRIO board. Using the ADC component of the board, the signal is interpreted and the result can be used in data processing. Similar to this process, the result of the data processing and calculus is passed through a DAC and the analog signal is given afterwards to the pressure valve.

2.1 On-off Controller

An on-off controller (or hysteresis controller) is a feedback controller that changes unexpectedly sudden between two states of the signal. It can be used as a mean of control for the plants that accept an all or nothing input, like an incubator, that is either completely on (heat turn on) or off. Thermostats are also a good example of on-off controllers, and they can be found in almost every residential building that has central heating (Balan 2006).

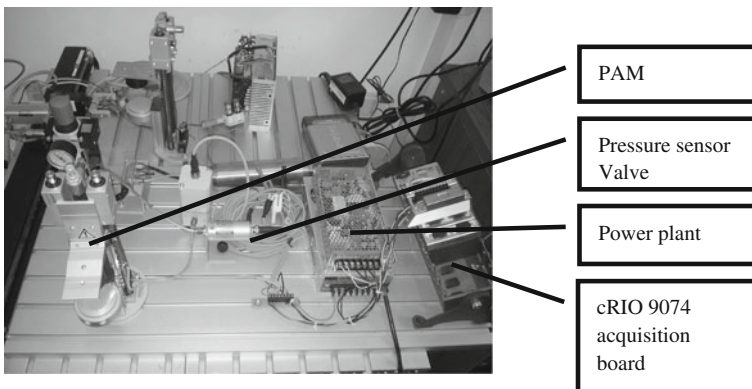


Fig. 2 Experimental setup

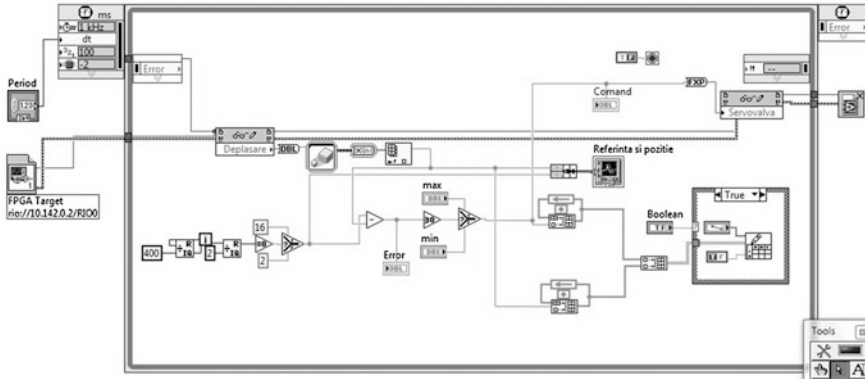


Fig. 3 On-off algorithm in LabView

One of the solutions where this kind of control can appear is the minimum-time problem. This is to be wanted when we want maximum and minimum commands. Heating water to the boiling point then stop the heat is an example. Many controllers are relays that can wear in time, thus the hysteresis appear. This allows the controller to oscillate around the set point, turning off when exceeds a set limit and turning on when it goes below another set limit. In Fig. 3 you can see the On-Off algorithm developed in LabView environment (Sárosi et al 2009).

2.2 PID Controller

The proportional-integrative-derivative controller is one of the most spread controllers in the industry (Ogata 2002). The wide spread dues to the generality of the controller. Usually it applies when the mathematical model is unknown, thus being unable to apply analytical control methods (Fig. 4).

$$u(t) = kp * e(t) + ki * \int e(\tau)d\tau + kd * \frac{d}{dt}(e(t)) \tag{1}$$

The controller consists in three components:

The proportional component P consists in the multiplication of the error with a kp coefficient.

The integral component I is calculated using the accumulation of the errors and then multiplication by a ki coefficient. This component eliminates the stationary error specific to P control.

The derivative component D applies a differential to the error and multiplies it by a kp coefficient. The effect of this component is a predictive behavior of the system.

Applying the Eq. 1 the output of the plant can be determined. The 3 parameter correlation is necessary for the system to be stable. The correlation process is called tuning the controller.

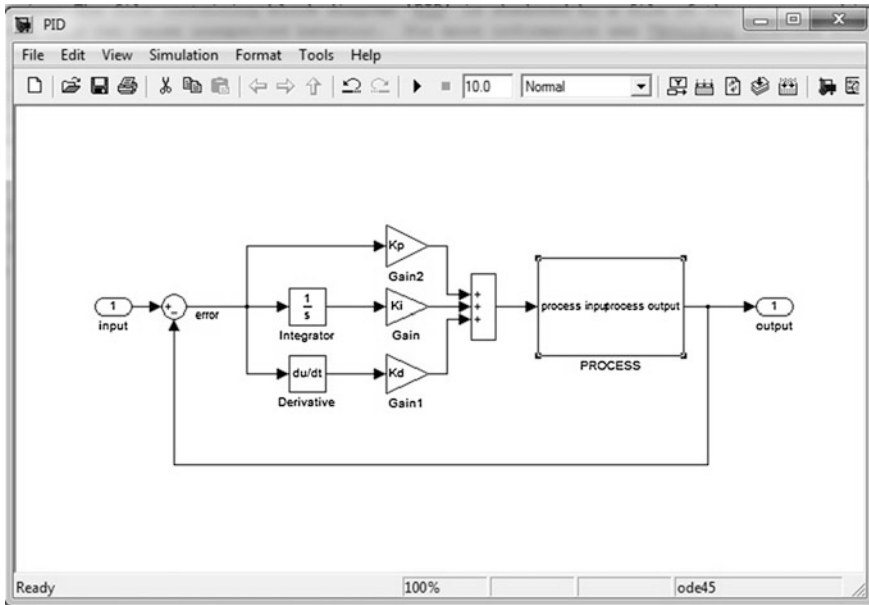


Fig. 4 PID controller in Matlab

In Fig. 5 the application in LabView is presented, where the PID tuning is made automatically.

Tuning the PID controller can be done in multiple ways. The first and easiest method is the manual tuning, but the engineer must be experienced in these practices. Another method is the empirical method called Ziegler-Nichols. First step in this method is to increase the value of the Kp parameter until the system output displays sustained oscillations. This value is called Kcr and for this signal, a period

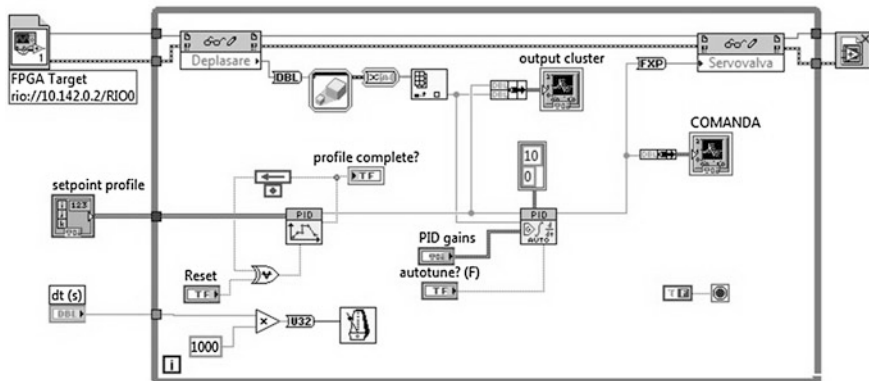


Fig. 5 PID controller in LabView

Table 1 PID tuning values

Controller type	K_p	T_i	T_d
P	$0.5K_{cr}$	∞	0
PI	$0.45K_{cr}$	$0.83P_{cr}$	0
PID	$0.6K_{cr}$	$0.5P_{cr}$	$0.125P_{cr}$

called P_{cr} is determined. After this, using Table 1 the parameters k_p , T_i , T_d are determined, and inserted in the Eq. 2.

$$G(s) = kp(1 + \frac{1}{T_i}s + T_d s) \tag{2}$$

3 Experimental Data

For the on-off controller we used a square signal input, to be the system positioning reference. In the first experiments, where the power is set to maximum, we can observe the slow answer of the system, as well as the bad response of it and the controller's flaws (Fig. 6).

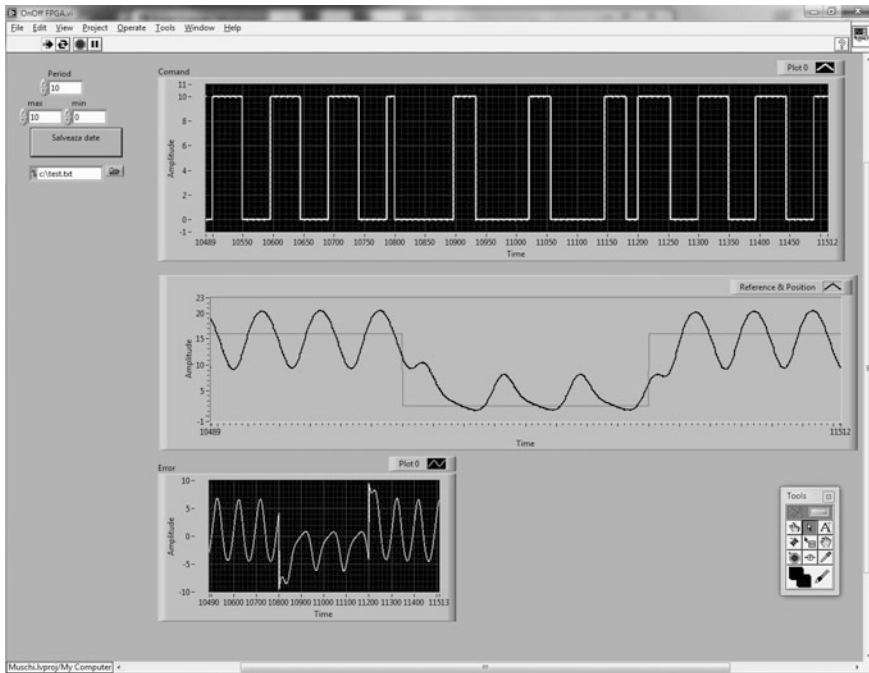


Fig. 6 On-off commands on the valve

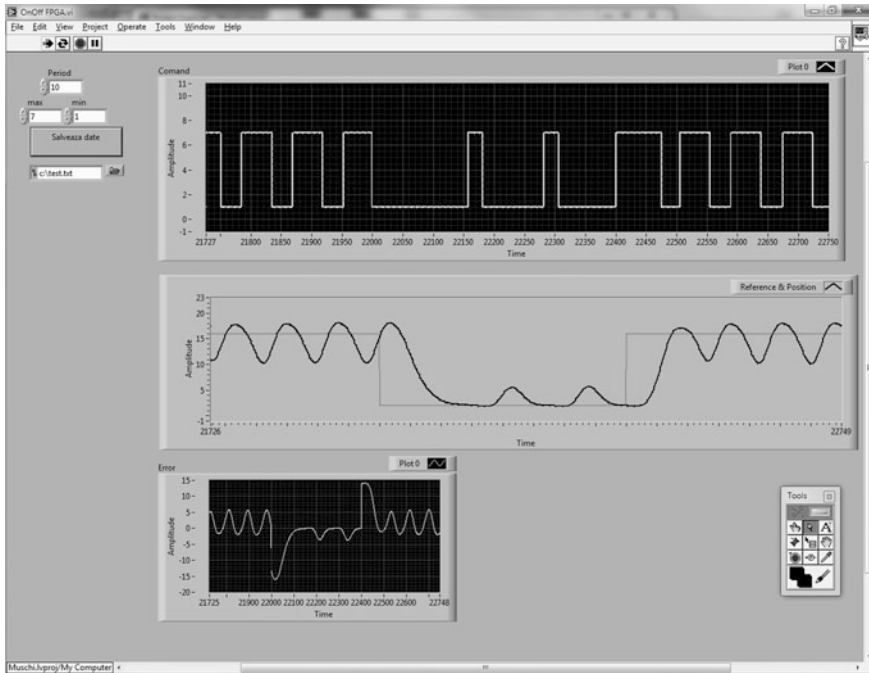


Fig. 7 Command constraint for the on-off controller

As we manually decrease the maximum command, in Fig. 7 it can be observed how the system response is getting closer to the setpoint, the oscillation's amplitude decreases and the system delay is getting lower. The error is shown in the bottom left graphic. As it can be seen, pure on-off controllers have big errors, especially on this type of systems. However, on the tuned on-off controller, the error decreased, as shown in the Fig. 7. It is clearly that on-off controllers are not a good way to control pneumatic systems but in several cases where precision is not that important, but the repeatability of the movement, the on-off controller is more suitable than the PID controller as it is faster and cheaper to implement it. From the two figures we can conclude that if the command on the actuator is constricted to a proper value, the on-off controller behaves satisfactory as the overshoots are lower and the response time is higher.

When using the PID controller, the system response is improved. As we can see, there are practically no oscillations near the setpoint, and the system responds faster. In Fig. 8 it can be seen the response for a square signal using auto tuned PID controller.

On the left side the reference signal generator is presented, as well as the tuned PID parameters. On the top right part of the figure we can see the setpoint and system response and on the bottom, the command value for the valve. The response time is faster than for on-off controller and there are no overshoots if the PID controller is tuned properly. It is clear that the PID controller is better than the on-off controller in positioning systems using pneumatic actuators.

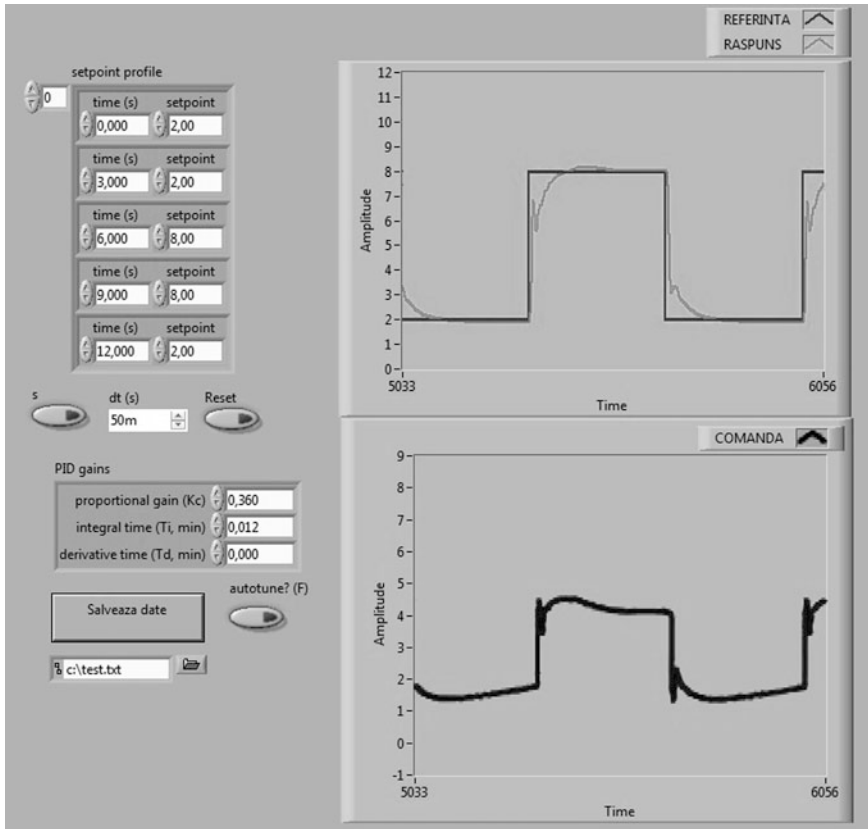


Fig. 8 System response using PID controller

4 Conclusions

The artificial muscles are the future in haptic devices and in human prosthetics for their human like characteristics. It is important to have a good control system for the precise positioning of the end effectors or of the robotic hand. Due to the compliance of the muscles, this actuating system is good for fine manipulation.

The on-off controller is a basic type of controller, which introduces in the system high oscillations and delays, and is not suit for this kind of actuation. However, if the command is constricted to a certain value, the system response can be satisfactory, thus having a cheap and sufficient control, especially if the precision is not that important.

The PID controller is good for this kind of actuation, as it provides high response time for the system as it was proven by the experimental applications. If the task of the actuator involves precision positioning, it is preferable to use this kind of control instead of on-off, as it has better performances.

References

- Balan R (2006) Delphi * Aplicatii in Mecatronica, ed. Todesco, Cluj-Napoca, pp 225–228
- Daerden F, Lefeber D (2002) Pneumatic artificial muscles: actuators for robotics and automation. *Eur J Mech Environ Eng* 47(1):11–21
- FESTO DIDACTIC, <http://www.festo-didactic.com/int-en/services/printed-media/data-sheets/sensor-technology/analogue-pressure-sensor-150556.htm>
- Ogata K (2002) Modern control engineering. 4th edn, 0130432458
- Sárosi J et al (2009) Accurate position control of PAM Actuator in LabVIEW environment. In: 7th international symposium on intelligent systems and informatics, SISO '09
- Shadow Hand (2013) Shadow Robot Company, <http://www.shadowrobot.com/>
- Shen X (2010) Nonlinear model-based control of pneumatic artificial muscle servo systems. *Control Eng Pract* 18(3):311–317
- Thanh TU, Ahn KK (2006) Nonlinear PID control to improve the control performance of 2 axes pneumatic artificial muscle manipulator using neural network. *Mechatronics J* 16(9):577–587
- Van Ham R et al (2001) Pressure control with on-off valves of pleated pneumatic artificial muscles in a modular one-dimensional rotational joint. In: Proceedings of international conference on advanced intelligent mechatronics

Advances in Optomechanical Scanning Technologies for High-End Biomedical Applications

V.-F. Duma

Abstract The paper presents an overview of our main contributions on optomechanical scanners used especially for biomedical applications with high requirements—with a focus on Optical Coherence Tomography (OCT). Rotating polygon scanners (pyramidal or prismatic, normal or inverted) are approached, in their kinematic, kinetostatic and dynamic aspects—with requirements of OCT systems. Oscillatory, galvanometer-based scanners are approached in their optomechanical aspects, with a focus on their dynamical aspects. Their optimal scanning functions were demonstrated—to produce the highest duty cycle (i.e., time efficiency) of the device: linear on the active portions with parabolic non-linear stop-and-turn portions. This result contradicts what was previously considered in the literature, that linear plus sinusoidal scanning functions were optimal. 2D (bi-dimensional) scanning systems with Risley prisms on which we are currently working are also pointed out.

Keywords Optomechanics · Optomechatronics · Optical devices · Scanners · Polygons · Galvanometers · Risley prisms · Scanning functions · Optimization

1 Introduction

Optomechanical scanners can be (Bass 1995) rotational and oscillatory. They can be built with mirrors or with refractive elements (i.e., prisms or lenses). The most utilized devices are (Marshall 2004) with monogon/plane mirrors [rotational (Duma 2001) and galvanometer-based (Duma 2009, 2010; Duma et al. 2010; Montague 2003)], polygonal (normal or inverted, prismatic or pyramidal)

V.-F. Duma (✉)
Aurel Vlaicu University of Arad, Arad, Romania
e-mail: duma.virgil@osamember.org

(Duma 2001, 2005, 2007; Duma et al. 2010; Duma and Rolland 2010; Duma and Podoleanu 2013; Oh et al. 2005; Oldenburg et al. 2003; Sweeney 1997; Walters 1995; Wojtkowski 2010), and refractive [with Risley prisms/optical wedges (Bass 1995; Duma et al. 2010; Marshall 1999; Tao et al. 2010; Warger and DiMarzio 2007) or with cylindrical lenses]. Other interesting scanning solutions also exist, but they are more rarely used: holographic, electro- and acousto-optical (Marshall 2004). Other configurations are still continuously developed, some of them surprising, such as an endoscopic probe with two orthogonal translational lens.

We have approached in the last two decades several of the above devices.¹ Because of the large area of applications of the scanning technologies (especially for high-end systems) in the last three decades, this topic is of high interest for various communities, from optomechanical to electrical engineering, and from photonics to biomedical imaging. We have reviewed these applications (Duma et al. 2010; Duma and Podoleanu 2013), as well as the related scanning systems and techniques developed in close relationship with the most demanding applications. The most dynamic of these is probably Optical Coherence Tomography (OCT) (Huang et al. 1991; Wojtkowski 2010), and we shall point out its impact on the scanning systems in this paper as well.

The scope of this presentation is to provide a very brief overview of our contributions in the context of the scanners development in relationship with high-end applications, especially OCT, but also other biomedical imaging systems, such as confocal microscopy. Other fields, such as optical metrology, printing and remote sensing are also benefit traditionally from the development of scanners, and they have greatly influenced it.

2 Polygonal Mirror and Monogon Scanners

A classification of the PM scanners (Bass 1995) is made in Fig. 1. The *regular, normal and prismatic PM* (Duma and Podoleanu 2013; Marshall 2004; Sweeney 1997) is by far the most used type of scanners with rotating mirrors. *Normal pyramidal PMs* are more rarely used, because they are more difficult to manufacture at the precisions required, and the number N of facets that can be obtained is smaller than for the prismatic. *Inverted PMs*, although interesting, are even less utilized, because of the structural integrity issues at the high rotational speeds required by most applications.

Combinations of normal and inverted PMs have been developed (Fig. 1), both prismatic (Dierking and McCormick 1994) and pyramidal (Liu et al. 2007), in double configurations—the former for a continuous wave (cw) laser, to generate high frequency laser impulses, and the latter for confocal microscopy. *Irregular PMs* (Fig. 1) are only used in special applications, by example to generate

¹ www.3omgroup.appspot.com/.

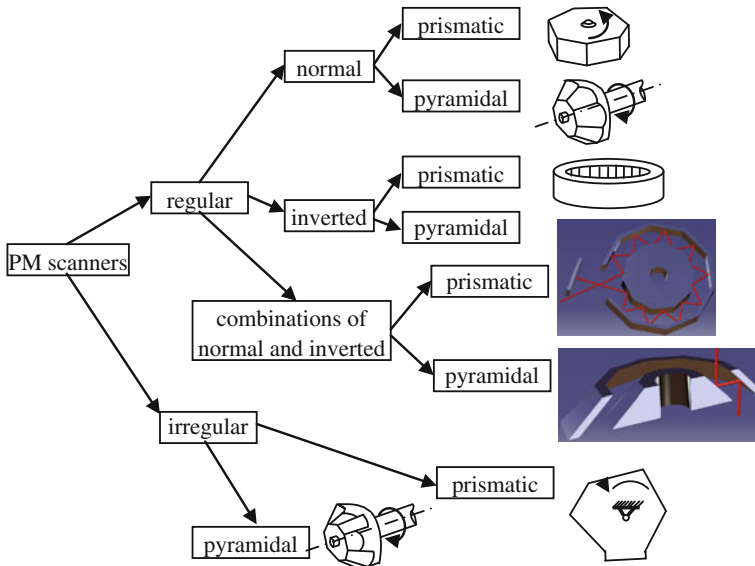


Fig. 1 Classification of polygonal mirror (PM) scanners

irregular, mobile grids of laser lines (in infrared) for safety systems, by example in museums.

The study of PM scanners implies all the aspects known—from the Theory of Mechanisms (Eckhardt HD 1998; Perju D 1990)—for a very fast rotating shaft (with rotational speeds ω of up to 60 krpm—Fig. 2) and for a cam—and much more, as optical aspects also have to be taken into account. Thus, considering the PM as a rotating cam and the laser beam as a follower, we have developed a kinematic analysis of the reflected beam (Duma 2001, 2005, 2007) that is different (exact, yet simpler) than the one in the literature (Bass 1995; Marshall 2004). The study has been performed with regard to the rotational speed ω and to the constructive parameters of the PM scanning head: R , inner radius of the PM; e , eccentricity of the incident beam with regard to the pivot O; N , number of facets ($\alpha = \pi/N$ —Fig. 2a); f , distance from the fixed beam to the lens L (to its principal object plane), equal to the focal length of L. The following characteristic functions were deduced and analysed (for an optimal design of the PM heads and of their related setups, by example for broadband laser sources scanned in frequency (Oh et al. 2005; Yun et al. 2003) for OCT):

- $h(\theta)$, scanning function—current position of the beam emergent parallel to the O.A. (optical axis) after the lens L;
- v , scanning velocity, not constant. From Fig. 2b $h(\theta)$ is non-linear and therefore only the central part of its graph can be used—with a certain level of precision—for the scanning process. F-theta lenses are designed (Marshall 2004) to further linearize $h(\theta)$ and to achieve a constant velocity of the emerging beam.

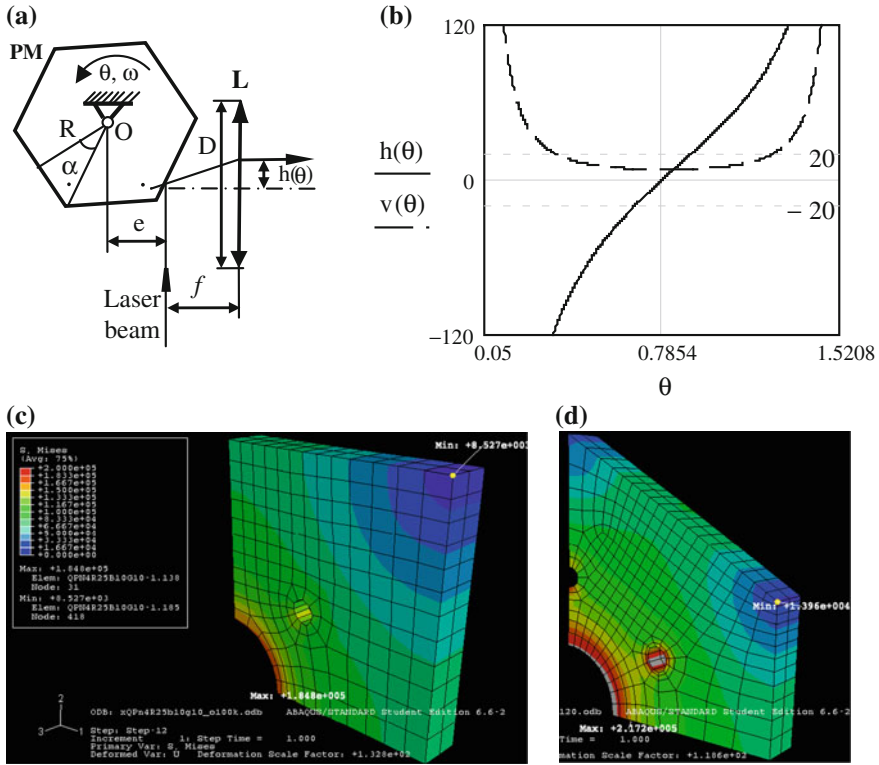


Fig. 2 a Polygon mirror (PM) scanner; b Scanning function $h(\theta)$ and reduced velocity $v(\theta)/10^4$, for a PM with $R = 25$ mm, $e = 3$ mm, $L = 100$ mm, $\omega = 400$ rad/s and $D = 120$ mm. Extreme values of the mechanical stress (with ABAQUS™) for $\omega = 120$ krpm c $N = 4$; (d) $N = 6$

- *Characteristic pairs of angles* in the scanning process: θ_1, θ_2 are the angles for which the margins of the lens L are reached: $h(\theta_1, \theta_2) = \pm D/2$, where D is the diameter of L and it defines the useful scanning domain; θ_1, θ_2 are the angles for which the scan of a PM facet begins, respectively ends. From the study in (Duma 2005),

$$\theta_{\min, \max} = \arcsin \frac{e \cdot \cos \alpha}{R} \mp \alpha \tag{1}$$

- *Duty cycle η* , defined as the time efficiency of the scanning process, i.e. the amount of time used for the scan is (Duma 2007), using Eq. (1):

$$\eta = \frac{\theta_2 - \theta_1}{\theta_{\max} - \theta_{\min}} = N \frac{\theta_2 - \theta_1}{2\pi}. \tag{2}$$

Kinestatics of PMs imply two essential aspects: bearings (aerodynamic for the rotational speeds used, of 10–60 krpm) and windage torques—significant at these speeds and produced by the polygonal shaped of the rotating piece. This windage torque, although it decreases when N is higher (as it is the case of high-end applications) has to be reduced. Solutions for this include a cage for the PM (as we use in our lab) or—for lower ω —only PMs with rounded margins and placed between two plates (Marshall 2004).

Dynamics of PMs have to analyze two aspects: structural integrity and deformation of the PM and of its facets with ω . Finite Element Analysis (FEA) is necessary for these aspects, as shown in the two examples in Fig. 2c, d. Both aspects are critical for the maximum values of ω (60 krpm, but motors have now evolved towards 120 krpm): the mechanical stress has to be lower than σ_a (Duma 2010), while—even more difficult—the facet-to-facet deformation has to be less than $\lambda/10$, where λ is the wavelength of the laser radiation utilized (roughly between 400 and 1,400 nm). These requirements impose the use of beryllium alloys for the construction of the most demanding PMs.

The rotating monogon scanner, plane or polygonal (Fig. 3) is a particular case of the PMs which is used for diverse applications, from fast printers (on cylindrical interior surfaces) to remote sensing—as their field-of-view may reach (Fig. 3b) even 360°.

We have studied monogons for on-line dimensional measurements for industrial applications (Duma 2001, 2005). Their characteristics functions are much simpler than for the PM, because $R = 0$ for the monogon; thus the beam can be incident on the pivot O and therefore $h(\theta) = f \tan(2\theta)$. This is a slight disadvantage, as one has thus less degrees of freedom in the scanning process, but it is also a major advantage, as the pivot O can thus be placed in the focal point of the lens L, which is an essential requirement for the interferometric setups for OCT by example: it allows for the control of the variation of the Optical Path Difference (OPD) with the angle θ . While rotating monogons do have their niche, oscillatory plane mirrors (galvanometer or resonant) are the most important device of this type (Sect. 3).

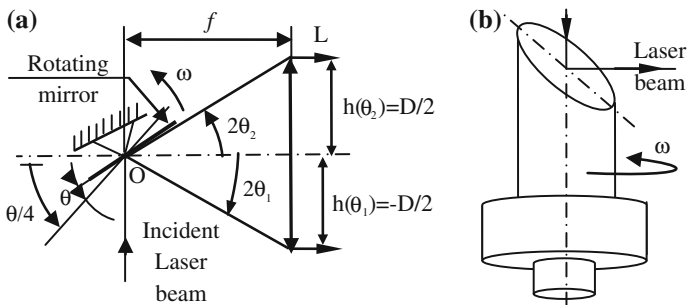


Fig. 3 Monogon scanners (Duma 2005): **a** plane rotating mirror (M); **b** inclined rotating mirror/pyramidal configuration

3 Galvanometer-Based Scanners

GSs (Fig. 4a) are the most used scanning devices since the early 90 s, both as 1-D (uni-dimensional) and as 2-D (bi-dimensional) setups, the latter with two galvo-scanners with orthogonal axes. The 1-D GSs (Montague 2003) have to be optimized with regard to their command/input functions in order to maximize their duty cycle η . We have studied experimentally the most utilized types of input functions for GSs: sawtooth, sinusoidal and triangular (Fig. 4b), and demonstrated (Duma et al. 2011) that the triangular provides the highest η and the most artefact-free images in OCT. The complex study achieved in (Duma et al. 2011) also determined the practical limits of use of this type of devices and provided the optical community with the necessary optomechatronic optimization of the different scanning regimes in terms of scan frequencies, amplitudes and function profiles (including the programmed η for the sawtooth).

This optimization was also done theoretically for the most convenient profiles of the signal, i.e. with linear portions (to scan a sample, by example in OCT, with constant speed) and with as fast as possible non-linear stop-and-turn portions. We demonstrated that the maximum η is obtained for the linear plus parabolic functions (Duma 2010), while previously it has been considered (Montague 2003) that the best function was linear plus sinusoidal. Differences of 4 % were obtained in η for the practical values (of 60–70 %) that can be achieved technologically for this time efficiency parameter of the scanning process. One must take into account that η has to be maximized, especially for high-end applications like OCT, to obtain real time in vivo biomedical imaging capabilities.

Passing from 1-D to 2-D scanners, another major direction of research is related to optimal scanning algorithms and protocols for 2-D scanners. We derived such an optimized algorithm (Duma 2009) to eliminate the distortion produced otherwise by the distance between the oscillatory orthogonal galvomirrors (Marshall 2004).

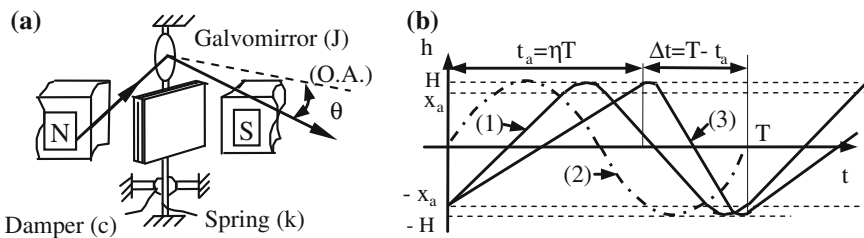


Fig. 4 **a** General structure of a GS with characteristic parameters: J , axial mass inertia moment of the mobile element; c , damping coefficient; k , elastic coefficient; **b** scanning functions: (1) optimal triangular (linear plus parabolic); (2) sinusoidal; (3) sawtooth

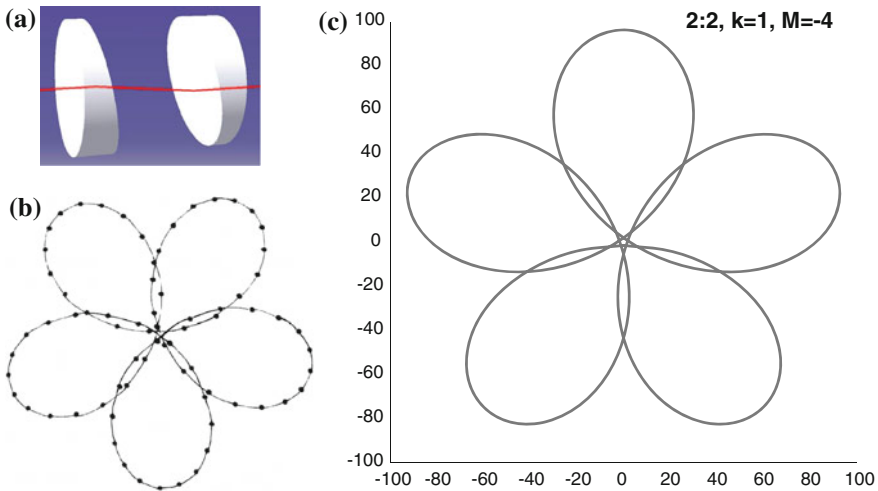


Fig. 5 a Example of modeling in CATIA of a Risley prisms scanner (with *two identical wedges*) (Schitea et al. in print, 2013); scan pattern determined **b** experimentally; **c** by modeling—with the ratio of the wedges angles $k = \theta_2/\theta_1 = 1$, and with the ratio of the rotational speeds $M = \omega_2/\omega_1 = -4$

4 Risley Prisms Scanners

There are several types of scanners with refractive elements—lenses or prisms (Bass 1995), but the most utilized, especially for biomedical imaging are the Risley prisms (Warger and DiMarzio 2007). They consist of two or three optical wedges (Fig. 5a) or doublets that can be rotational, tilting, translational, or their combinations. Their optical aspects have been studied analytically and approximately (Marshall 1999), and constructive solutions were developed—the latter with regard to the dimensions of the prisms (for sub-millimeter to tenths of cm in diameter). We approached scanners with Risley prisms in a different way, using (Schitea et al. 2013) mechanical design programs (Fig. 5c) to obtain their exact scan patterns for cases of interest with regard to their functioning parameters (Marshall 1999): k and M . Our experimental studies confirm the simulation part (Fig. 5b). As a remark, combinations of 1-D GSs and 2-D Risley prisms have also become of interest lately (Tao et al. 2010) to achieve 3-D scanning.

5 Conclusions

We presented briefly our main directions of research and some of our contributions on the most utilized types of optomechanical scanners, in relation to their issues and challenges for highly demanding applications. Our studies have been thus

focused on the most rapidly evolving biomedical field today, OCT, where scanning is an essential technology to provide the fast acquiring data (video frame) capability necessary for real time in vivo imaging. While in this presentation we have considered polygonal mirror, monogon, galvanometer-based, and Risley prisms scanners, there are several other types of devices that we have in study, especially for the micro-scanners necessary in endoscopic heads for OCT. Specific setups with macro-scanners (especially GSs) for handheld heads for clinical applications of OCT (Sinescu et al. 2008; Podoleanu and Rosen RB 2008) are also in development in our current project.

Acknowledgments This work was supported by a grant of the Romanian National Authority for Scientific Research, CNDI-UEFISCDI project number PN-II-PT-PCCA-2011-3.2-1682.

References

- Bass M (ed) (1995) Handbook of optics. McGraw-Hill, New York
- Dierking MP, McCormick WS (1994) High-bandwidth laser-pulse generator using continuous-wave lasers. *Appl Opt* 33(24):5657–5664
- Duma VF (2001) Contributions to the analysis and the design of scanning systems. Ph.D. thesis, Polytechnics University of Timisoara
- Duma VF (2005) On-line measurements with optical scanners: metrological aspects. *Proc SPIE* 5856:606–617
- Duma VF (2007) Novel approaches in the designing of the polygon scanners. *Proc SPIE* 6785:67851Q
- Duma VF (2009) Mathematical functions of a 2-D scanner with oscillating elements. In: Awrejcewicz J (ed) Modeling, simulation and control of nonlinear engineering dynamical systems. Springer, Berlin, pp 243–253
- Duma VF (2010) Optimal scanning function of a galvanometer scanner for an increased duty cycle. *Opt Eng* 49(10):103001
- Duma VF, Podoleanu AGH (2013) Polygon mirror scanners in biomedical imaging: a review. *Proc SPIE* 8621:8621V
- Duma VF, Rolland JP (2010) Mechanical constraints and design considerations for polygon scanners. In: Pisla D, Ceccarelli M, Husty M, Corves B (eds) Mechanisms and machine science, vol 5(8). Springer, Berlin, pp 475–483
- Duma VF, Rolland JP, Podoleanu AGH (2010) Perspectives of scanning in OCT. *Proc SPIE* 7556:7610
- Duma VF, Lee K-S, Meemon P, Rolland JP (2011) Experimental investigations of the scanning functions of galvanometer-based scanners with applications in OCT. *Appl Opt* 50(29):5735–5749
- Eckhardt HD (1998) Kinematic design of machines and mechanisms. McGraw-Hill, New York
- Huang D, Swanson EA, Lin CP, Schuman JS, Stinson WG, Chang W, Hee MR, Flotte T, Gregory K, Puliafito CA, Fujimoto JG (1991) Optical coherence tomography. *Science* 254(5035):1178–1181
- Liu L, Chen N, Sheppard CJR (2007) Double-reflection polygon mirror for high-speed optical coherence microscopy. *Opt Lett* 32(24):3528–3530
- Marshall GF (1999) Risley prisms scan patterns. *Proc SPIE* 3787:74–86
- Marshall GF (ed) (2004) Handbook of optical and laser scanning. Marcell Dekker, New York
- Montague J (2003) Scanners—galvanometric and resonant. In: Driggers RG (ed) Encyclopedia of optical engineering. Taylor & Francis, New York, pp 2465–2487

- Oh WY, Yun SH, Tearney GJ, Bouma BE (2005) 115 kHz tuning repetition rate ultrahigh-speed wavelength-swept semiconductor laser. *Opt Lett* 30:3159–3161
- Oldenburg AL, Reynolds JJ, Marks DL, Boppart SA (2003) Fast-fourier-domain delay line for in vivo optical coherence tomography with a polygonal scanner. *Appl Opt* 42:4606–4611
- Perju D (1990) *Mecanisms of fine mechanics*. Politehnica, Timisoara
- Podoleanu AGh, Rosen RB (2008) Combinations of techniques in imaging the retina with high resolution. *Prog Retinal Eye Res* 27:464–499
- Schitea A, Tuef M, Duma VF (2013) Modeling of Risley prisms devices for exact scan patterns. *Proc SPIE* 8789:8789–8840
- Schitea A, Kaposta I, Tuef M, Jurca S-C, Duma VF (2013) Risley prisms scanners: Analysis with mechanical design programs. In: *Proceedings of SYROM*, Springer
- Sinescu C, Negrutiu ML, Todea C, Balabuc C, Filip L, Rominu R, Bradu A, Hughes M, Podoleanu AGh (2008) Quality assessment of dental treatments using en-face optical coherence tomography. *J Biomed Opt* 13(05):054065
- Sweeney MN (1997) Polygon scanners revisited. *Proc SPIE* 3131:65–76
- Tao X, Cho H, Janabi-Sharifi F (2010) Optical design of a variable view imaging system with the combination of a telecentric scanner and double wedge prisms. *Appl Opt* 49:239
- Walters CT (1995) Flat-field postobjective polygon scanner. *Appl Opt* 34:2220–2225
- Warger WC II, DiMarzio ChA (2007) Dual-wedge scanning confocal reflectance microscope. *Opt Lett* 32:2140
- Wojtkowski M (2010) High-speed optical coherence tomography: basics and applications. *Appl Opt* 49:D30
- Yun SH, Boudoux C, Tearney GJ, Bouma BE (2003) High-speed wavelength-swept semiconductor laser with a polygon-scanner-based wavelength filter. *Opt Lett* 28:1981–1983

Mechatronic System with Applications in Medical Robotics

Nicolae Dumitru and Violeta Cristina Dumitru

Abstract This paper studies the dynamic analysis of a multi-articulated mechanical system actuated by elastic cables, for a complete cycle of operation. The multi-articulated mechanical system consists of two kinematic chains, one interior and the other one exterior. The kinematic chains build a mechanical structure for a multi-articulated robotic system. The robot tended to be used in minimally invasive surgery. The motion of the system is obtained by overlapping the rigid body movement with the elastic one. The dynamic analysis was made possible by building a model and virtual prototyping model.

Keywords Dynamic analysis · Multi-articulated mechanical system

1 Introduction

In recent years it became a major concern developing miniature robots for inspection and exploration in minimally invasive environments with many restrictions and difficult access (positioning operation, skillful manipulation of objects, actions behind barriers or inaccessible spaces). Multi-articulated mechanical systems, among others, identify three major technology trends: making multi-articulated robotic arms with very small diameters; multiple bending sections snake like; mechanical system with high bandwidth actuators (MPP). The analysis and modeling of these mechanical systems are complex. The architecture of miniature surgical robots is described in (Davies 2000). Due to the large number of degrees of freedom, solving kinematics and dynamics of these devices has been one of the main problems that have delayed their use. For inverse kinematics

N. Dumitru (✉) · V. C. Dumitru
Faculty of Mechanics, Applied Mechanics Department, University of Craiova, Craiova,
Romania
e-mail: nicolae_dtru@yahoo.com

analysis, remarkable results were achieved by Han and Rudolph (2006), Chirikjian and Burdick (1995), Gravagne and Walker (2000), who founded the theory of inverse kinematics of robots hyper-redundant discrete elements by using variation calculation methods.

2 Multi-articulated System Structure

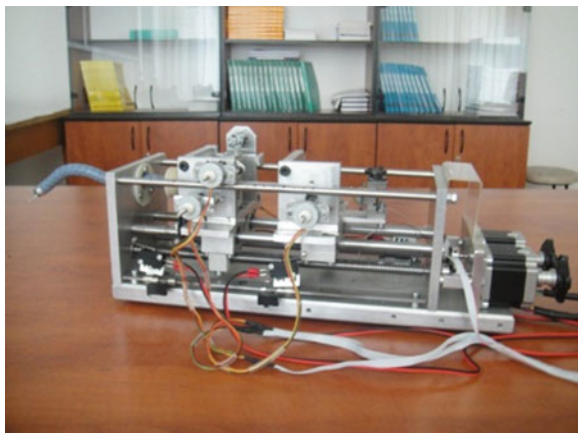
Figure 1 shows an experimental stand developed for testing a compact and modular mechanical system, capable of operating in environments with many restrictions and difficult access (operator positioning, inspection and minimally invasive explorations), under the direct control of the human operator. The multi-articulated mechanical system consists of two subsystems, a robotic arm and a drive system (Dumitru and Dumitru 2011).

Multi-articulated robotic arm (Fig. 2) is composed of two mechanisms, one inner and one outer mechanism, with the relative motion between them. Each device contains adjacent elements, like rigid vertebrae interspersed with cables (wires). Each vertebra is made with single or double curved elements (spherical surface). The vertebrae are held in contact by 3 wires for outer mechanism arranged at 120° between them and a central cable for the inner mechanism.

3 Dynamic Analysis

ADAMS dynamic analysis program has the theoretical foundation the method described by Craig and Bampton (1968). It considers only small deformations, linear bodies, relative to a local reference system. Flexible body is discretized into

Fig. 1 Experimental stand for testing the multi-articulated mechanical system



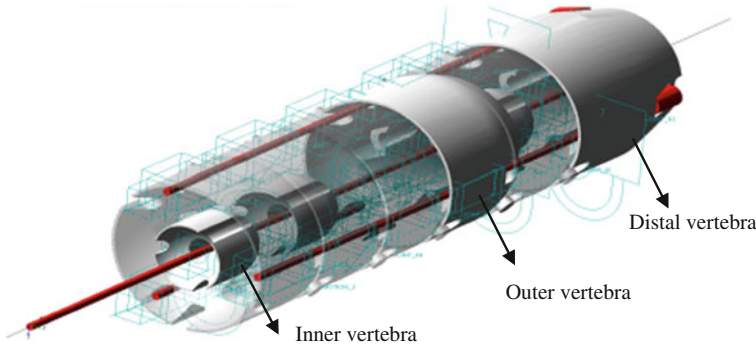


Fig. 2 Kinematic model of the robotic arm

finite elements. The linear deformations of finite element nodes u can be approximated as a linear combination of a small number of form vectors (or forms modal), ϕ :

$$u = \sum_{i=1}^M \phi_i \cdot q_i \tag{1}$$

where: M , the number of modal forms (vibration modes); q , modal coordinates. Equation (3.1) is often presented in a matrix form, $u = \phi \cdot q$ where: q is the vector of modal coordinates and modes ϕ_i will be on the columns of matrix functions. Flexible body kinematics can be defined by markers. Instantaneous position of a marker that is attached to a node P , on a flexible body, consists of three vectors:

$$r_p = \vec{x} + \vec{s}_p + \vec{u}_p \tag{2}$$

where: \vec{x} is the position vector from the origin of the fixed reference system at the origin of the local reference system of the flexible body; \vec{s}_p is the position vector of the undeformed location of point in relation to the local reference system attached to the body, \vec{u}_p is the translation of the strain vector of point P , the position vector from the location of unaltered point to deformed location, deformation vector u_p is an overlap of shape functions: $u_p = \Phi_p q$, where: Φ_p is the portion of the shape function matrix corresponding translational degrees of freedom of the node P . Matrix size Φ_p is $3 \times M$ where M is the number of shape functions. Generalized coordinates of the flexible body are:

$$\xi = \{x, y, z, \psi, \theta, \phi, q_i, (i=1...M)\}^T \tag{3}$$

As the body deforms, the marker rotates through angles relatively small compared to the reference system. As translational deformations, these angles are obtained using modal overlap, as follows: $\theta_p = \Phi_p^* q$, where: Φ_p^* is the part from the shape functions matrix which corresponds to the rotational degrees of freedom of the node. Matrix size Φ_p^* is $3 \times M$ where M is the number of shape functions.

For dynamic analysis of multi-articulated mechanical system, we started from the virtual 3D model of the robotic arm designed in Solid Works 2010 software, model which was then imported into the program Automatic Dynamic Analysis of Mechanical Systems (ADAMS) for analysis and optimization of dynamic mechanical multi-body systems. Dynamic modal analysis includes the following steps: construction of the geometrical model, construction of the markers as interest points to define correctly the kinematic joints, construction of the kinematic model, launching the procedure to transform from solid rigid into deforming solids of the three actuating elements and of the central one, having as basis the method of the finite element, digitization with finite elements of tetrahedral type, redefinition of the kinematic joints.

Mechanical system was treated in ADAMS as a collection of objects connected by mechanical links (joints), elastic and amortization elements. On bodies, besides the conditions of position and orientation the velocity conditions were imposed (at $t = 0$), in the rotation or translation movement.

For the motion analysis of the robotic system in coupled regime (translation of outer vertebra, flexible cable actuation, translation of inner vertebrae) were determined the laws of variation over time for generalized coordinates of elements considered rigid (outer and inner vertebrae) $\{x \ y \ z \ \psi \ \theta \ \phi\}^T$ and a modal-dynamic analysis was performed with determination of the laws of variation in time for generalized coordinates of the flexible elements, $\{x \ y \ z \ \psi \ \theta \ \phi \ q_i\}^T$. The analysis of rigid body movement is done when studying changes of position vector components of mobile reference system together with flexible element, respectively the variation of element orientation by the three Euler angles. Motion analysis as deformable solid is performed when studying variation of translation vector components of a point (node) or the vector orientation given by the Euler angles.

In Fig. 3 the variation time of the position vector in (mm) of node 2,142 is shown in relation to the global reference system in the movement of the solid deformable flexible element 3. In Fig. 4 is shown the variation law of displacement of an engine coupler to drive a bending elastic vertebra of the robotic arm, and in Fig. 5 is shown the variation law of displacement for outer chain actuation.

Input data for the dynamic modal analysis were established experimentally and are: variation in time of the displacement slide of the outer mechanism, variation in time of the displacement slide of the inner mechanism, variation in time of displacement of one of the elastic cables.

For a cycle of the multi-articulated mechanical system, sequence of motions is done step by step (Degani et al. 2006):

- Step 1. Both mechanisms (inner, outer) coupled in rigid mode;
- Step 2. Advance the distal vertebra (Fig. 6);
- Step 3. Orientation of the distal vertebra (Fig. 7);
- Step 4. Advance the inner mechanism (Fig. 8);
- Step 5. Keep the previous configuration.

The movement continues with second step, as is shows in Fig. 9.

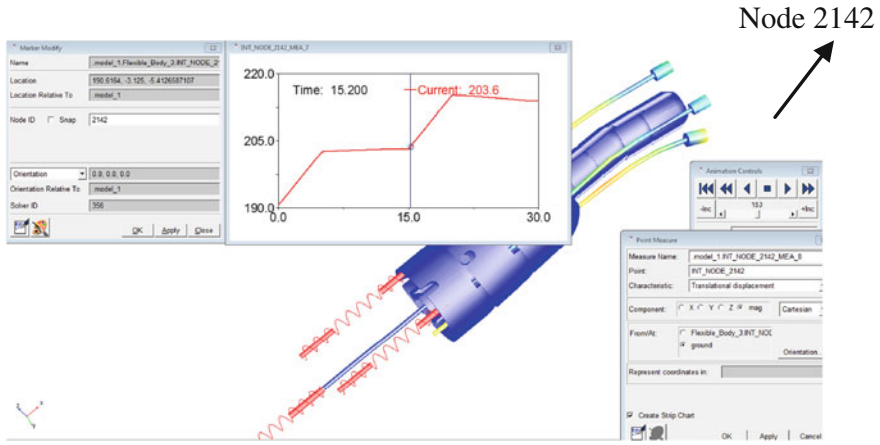


Fig. 3 Variation in time of the node 2,142 position vector magnitude (mm)

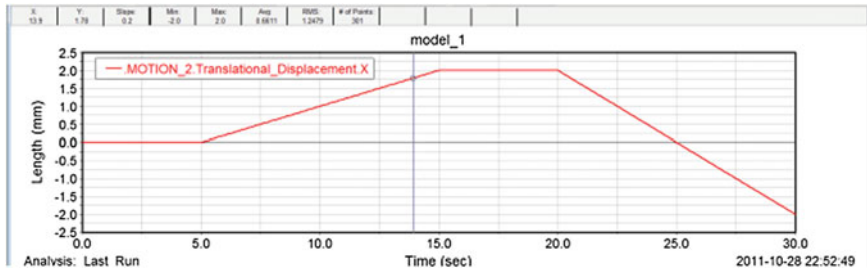


Fig. 4 Variation law of displacement for a vertebra actuation

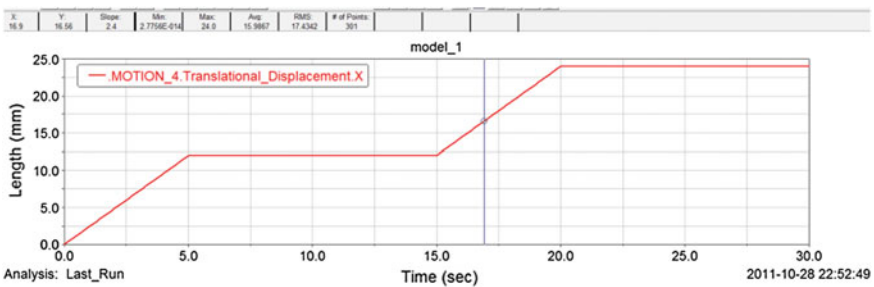


Fig. 5 Variation law of displacement for outer chain actuation

The geometrical model and especially the kinematic and dynamic model made in ADAMS, with the correct definition of the connections between flexible and rigid elements, with the definition of the markers and the nodes of interest for each

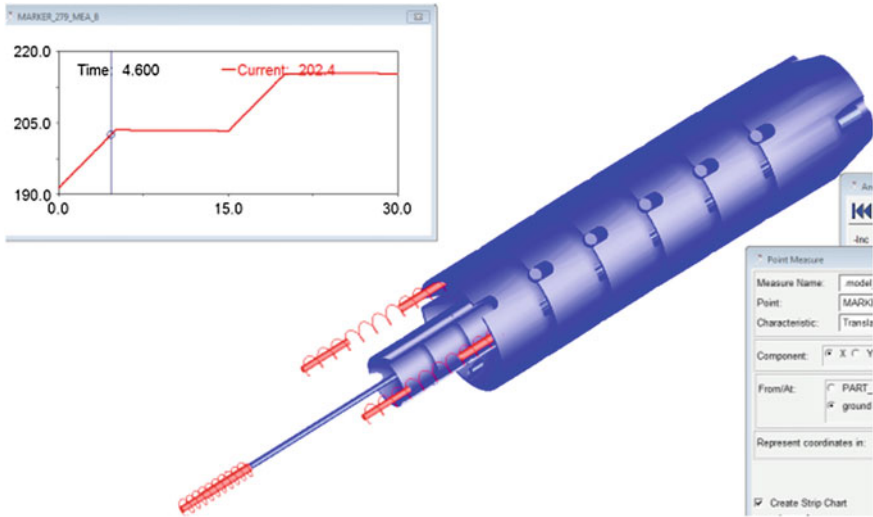


Fig. 6 First sequence movement of the robot (outer vertebra displacement)

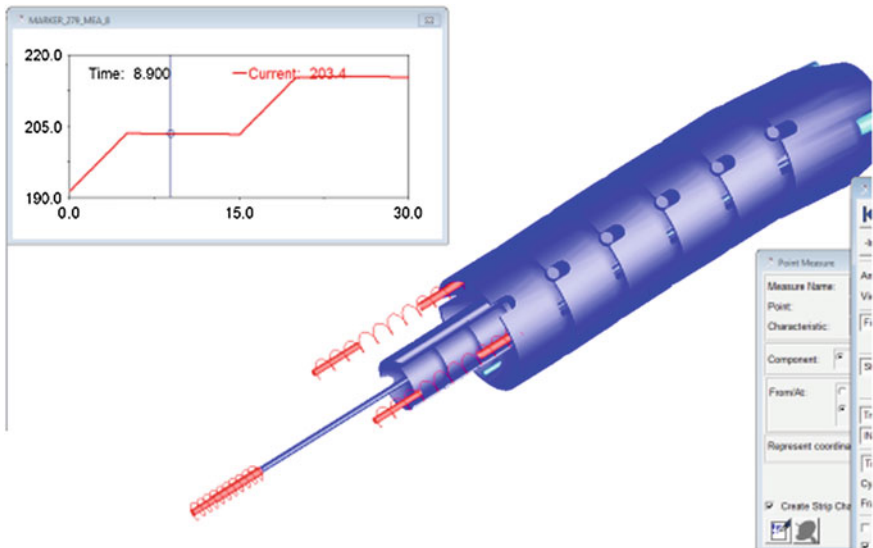


Fig. 7 Second sequence movement of robot (orientation distal vertebra)

kinematic element of the system, with the introduction as initial information of the variation connections of the displacements from the engine coupling, established experimentally, allows the correct and complete monitoring of the dynamic response of the mechanical system at any moment in time and for any loading conditions.

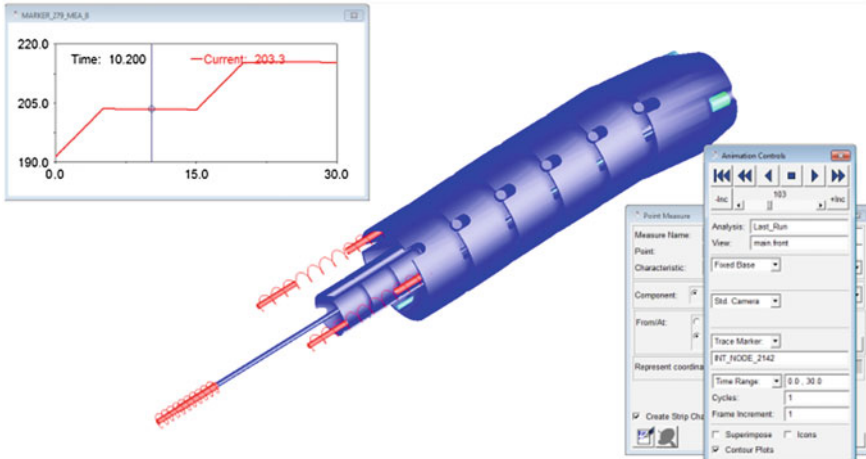


Fig. 8 Third sequence movement of robot (inner vertebra displacement)

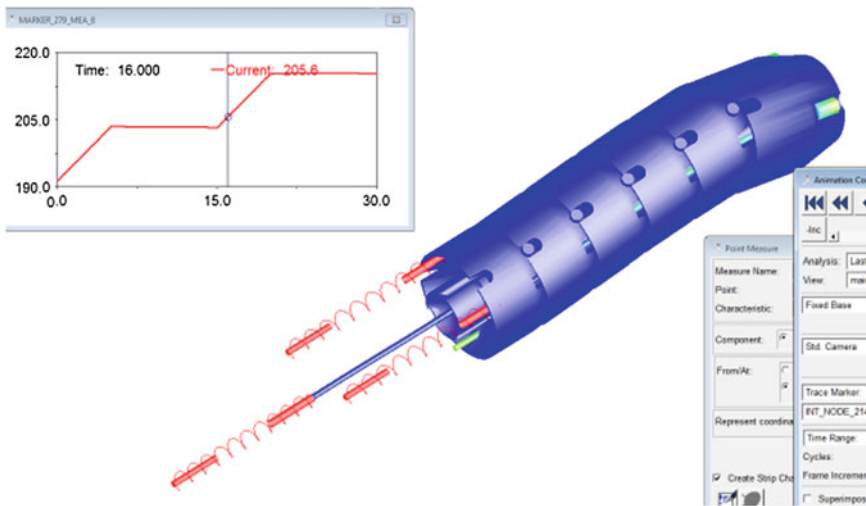


Fig. 9 Fourth sequence movement of robot (outer vertebra displacement)

4 Experimental Modeling

In this paper, using multi-articulated mechanical system prototype architecture designed for experiments, we have planned some experiments on the dynamic behavior of the system under the action of external disturbances, repeatability trajectories. To analyze and evaluate the dynamic behavior of the mechanical

system we developed a virtual instrument “DimamicaRobot.tst” under Test Point programming environment.

For experiments were used two types of interference signals, impulse and step. The first experiment possible was to determine the tension force of cable (wire) inside the central mechanism for preserving space curve shape 3D robotic arm. Next experiment will address the capability of the robotic arm movement as a function of the forces.

We studied the dynamic behavior responses to perturbation like impulse measured in force, respectively, displacement for three distinct cases, namely: (a) one wire tensioned wires 2, 3 tension-free (Fig. 10b) wire 2 tensioned wires 1, 3 tension-free, (c) wire 3 tensioned wires 1, 2 tension-free. Perturbation amplitude was considered uniform and the values of the characteristic parameters were varied in terms of size, around unit. Negative force means that we have traction force in the tension cable. At the weakening of the cable, is a jump in the traction force due to a rotation with a small angle of the grip cable system.

Figure 10 presents the variation diagrams of the kinematic and dynamics parameters to impulse signal, (only for case a).

The significance notations of Fig. 10 is the following: XSL2 (mm) is the linear sled 2 course, F(N) (mm) is the force of wire actuator; XB (mm) is the displacement in the direction OX of distal vertebra, YB (mm) is the displacement in the direction OY of the distal vertebra, ZB (mm) is the displacement in the direction OZ of the distal vertebra.

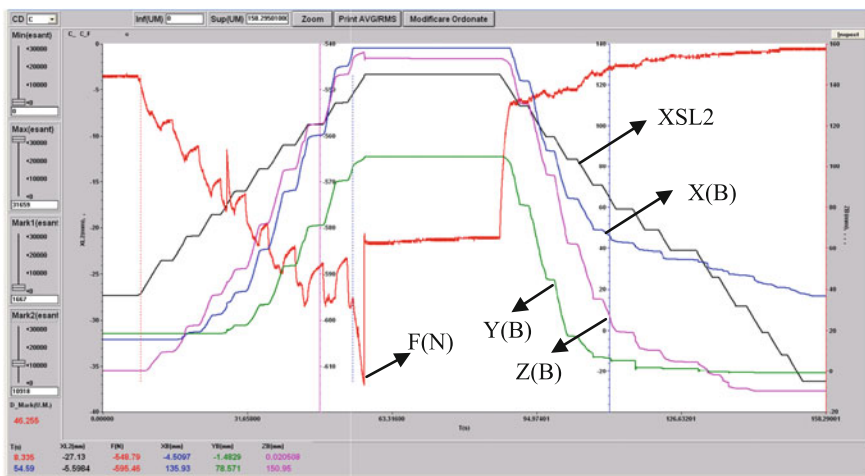


Fig. 10 Dynamics of the robotic arm at the step by step sequential displacement ($p = 12$ mm)

5 Conclusions

The dynamic analysis procedure, performed with ADAMS software, enabled a comprehensive study of the dynamic response of the multi-articulated mechanical system for a complete operating cycle (advance mechanism outside, orientation distal vertebra; advance mechanism inside, keeping the previous configuration) or on sequences, depending on operating conditions and rules.

The input data (time variation of outer mechanism displacement, time variation of inner mechanism displacement, the time variation of cable displacement) for dynamic modal analysis were established experimentally. For experimental determinations was designed a virtual instrument “DimamicaRobot.tst” under Test Point programming environment for analysis and evaluation of the dynamic behavior of the mechanical system multi-articulated. We identified the laws of variation for the generalized coordinates that define the displacement and orientation in space of each of the four flexible cables by overlapping rigid solid movement on the deformable solid movement and settled laws of variation for kinematic elements considered solid rigid or specific points of interest along with them. We also analyzed movements of kinematics flexible elements from the mechanical system structure.

Geometrical model, especially kinematic and dynamic model built in ADAMS, with correct definition of the relationship between flexible and rigid elements, with setting markers and nodes of interest for each element of the kinematic system, with the introduction of the laws of variation, allows accurate and complete monitoring of the dynamic response of the mechanical system in any time and for any load conditions. The system is designed in modular construction and can be used for minimally invasive explorations.

References

- Chirikjian G, Burdick J (1995) Kinematically optimal hyper-redundant manipulator configurations. *IEEE Trans Robot Autom* 11:794–806
- Craig RR, Bampton MC (1968) Coupling of substructures for dynamics analyses. *AIAA J* 6(7):1313–1319
- Davies B (2000) A review of robotics in surgery. *Proc Inst Mech Eng Part H J Eng Med* 214(1):129–140
- Degani A, Choset H, Wolf A, Takeyoshi O, Zenati M (2006) Percutaneous intrapericardial interventions using a highly articulated robotic probe. *International Conference on Biorobotics and Biomechatronics*, pp 112–121, Pisa, Italy
- Dumitru V, Dumitru S (2011) Computer-aided modeling for a poly articulated robotic arm with spherical joints. *World Congress on Engineering*, 6–8 Iulie, London
- Gravagne I, Walker I (2000) Kinematics transformations for remotely actuated planar continuum robots. *IEEE International Conference on Robotics and Automation*, pp 19–26
- Han L, Rudolph L (2006) Inverse kinematics for a serial chain with joints under distance constraints, pp 177–184, <http://www.roboticsproceedings.org/rss02/p23.pdf>

Low-Speed Actuator Used in Solar Tracking Systems

Codruta Jaliu, Mircea Neagoe, Radu Săulescu
and Edith-Bianca Dobre

Abstract This paper presents a geometric and kinematical modelling of a new variant of low speed actuators for the accurate orientation of solar concentrators. The panels' orientation must be done in small angular steps, which requires the use of actuators capable of ensuring the necessary accuracy. For this reason, the authors propose a new actuator variant consisting of a classical DC/AC motor, an intermediate speed reducer of crank-rocker type, foreseen at its output with a backstopping clutch and an irreversible final reducer. The proposed system is characterized by a reduced design complexity, easy maintenance and low friction losses due to the replacement of the intermediate gear reducer in one or more steps with an intermittent articulated reducer that can ensure high transmission ratio, either constant or with a continuous or discrete adjustment.

Keywords Concentrating solar tracking · Accurate orientation · Low speed actuator · Intermittent articulated reducer · Crank-rocker mechanism

1 Introduction

In tracking systems (trackers) for solar concentrators' orientation, an important role is played by actuators, and it is crucial that their movement to be done at very low speeds so that these systems can track accurately the sun trajectory, in order to maximize the amount of solar radiation captured by the conversion systems (Rizk and Chaiko 2008; <http://en.wikipedia.org/wiki/Actuator>). Actuators are

C. Jaliu (✉) · M. Neagoe · R. Săulescu · E.-B. Dobre
"Transilvania" University of Brasov, Faculty of Product Design and Environment,
Product Design, Mechatronics and Environment Department, 1 Colina Universitatii Street,
500068 Brasov, Romania
e-mail: cjaliu@unitbv.ro

devices frequently used in mechanisms to control angles, distances, repeatability of motion.

There are two types of tracking systems by means of action: passive systems (without actuators) and active systems (containing actuators) (Burduhos 2009).

The passive trackers achieve the movement of the solar concentrators by using a low boiling point liquid, which is vaporized by the added solar heat while the centre of mass is shifted, until the system reaches a new equilibrium position (Cabanillas 2009).

The active systems use linear or rotary actuators, controlling the orientation on one or two axes (Burduhos 2009; Diaconescu et al. 2009; Northrup 2010; Visa et al. 2012c). This type of systems can be divided into single-axis and dual-axis solar trackers.

A single-axis tracker can only pivot in one plane—either horizontally, performing the azimuthal (diurnal) movement, which describes the angular movement of the sun from East to West,—or vertically, performing the elevation movement, which is the angular movement of the sun on local vertical axis (Jesus et al. 2008; Kalogirou 2009). This kind of operation makes it less complex, and, generally, with a lower cost than a dual axis tracker, but also less effective in capturing the available solar radiation.

Dual-axis solar trackers, as their naming suggests, can rotate simultaneously on two orthogonal axes, being able to track the sun at any time, in any location. According to the sun movements on the sky, four types of dual-axis solar trackers are reported in literature: equatorial (Goswami et al. 2000), pseudo-equatorial (Burduhos 2009), azimuthal (Cabanillas 2009; Diaconescu et al. 2009; Jesus et al. 2008), and pseudo-azimuthal solar systems (Vatasescu et al. 2011).

The development and implementation of dual-axis trackers have a disadvantage in terms of economics (Verhelst 2010), but a significant energy gain (Bakos 2006; Serhan and El-Chaar 2010) is obtained compared to single-axis systems.

The energy advantages of dual-axis systems have increased the interest in research, innovation, implementation and optimization of these types of trackers (Kalogirou 2009; Kvasznicza and Elmer 2006). Obviously, dual-axis tracking systems are suitable in high precision applications, like the orientation of solar concentrators, their performance being directly related to the mechanical system driven by low speed actuators.

Linear actuators are mainly used for small angles in the elevation movement, while rotary actuators are designed for large angles, usually over 180° for diurnal orientation (Diaconescu et al. 2009; Sclater 2011).

Actuators used in solar trackers consist of a DC or AC electric motor that sets in the motion of an intermediate planetary or fixed axes gear reducer, serially connected with an irreversible final reducer: screw-nut type mechanism, in case of linear actuators (Fig. 1a), and worm gear type, in case of rotary actuators (Fig. 1b), (Vatasescu et al. 2011; <http://www.tradekorea.com>; <http://www.ultramotion.com/products>).

Due to technical and economical advantages, linear actuators are the most used in solar systems orientation. The low speed linear actuators on the market

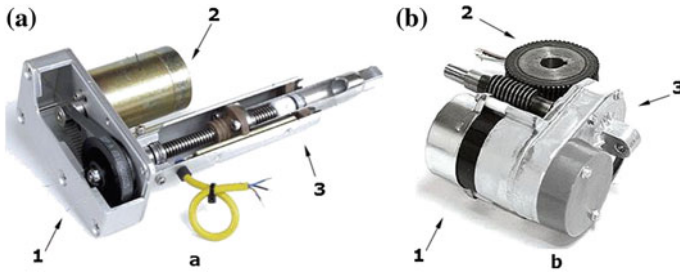


Fig. 1 Examples of actuators. **a** Linear actuator with screw-nut, and DC motor, 1—speed reducer, 2—DC electric motor, 3—screw-nut mechanism (<http://www.ultramotion.com/products>). **b** Rotary actuator with worm gear, 1—AC electric motor, 2—worm gear, 3—planetary gearbox (<http://www.tradekorea.com>)

nowadays provide a speed in the range 1.5–2.7 mm/s at an operating DC voltage of 24 V and 1–2 mm/s for AC motors.¹ A main disadvantage of nowadays actuators refers to the high structural complexity of the intermediate gear reducer and its relatively low efficiency due to the high transmission ratio, which depends on orientation accuracy.²

In order to overcome the previous disadvantage, the paper proposes a new solution for low speed linear actuators used in solar trackers (Alava 2008; Cabanillas 2009; Neff 2007), which are able to achieve at least similar functional performances as the best known solutions, but in a more energy efficient and economical alternatives.

2 New Low-Speed Actuator Design

A classical actuator for solar tracking achieves a low angular/linear speed by using an irreversible final reducer, an intermediate gear reducer with high transmission ratio, and a classical AC/DC motor.

The new actuator design simplifies the structural and technological complexity of the intermediate gear reducer, positioned between motor and irreversible final reducer, by replacing it with an intermittent crank-rocker type linkage connected to the output by backstopping clutches (Visa et al. 2012b).

The classical variants of low speed actuators used in solar trackers (Fig. 2a) usually consist of a stepping motor that can be easily controlled, a gearbox with a low transmission ratio and an irreversible reducer, usually a worm gear or screw-nut mechanism, for the self-locking of the solar panel in case of disturbances.

The proposed system operates on the principle shown in Fig. 2b.

¹ Elero-Linear—Product Catalogue.

² Framo-Morat—Product Catalogue.

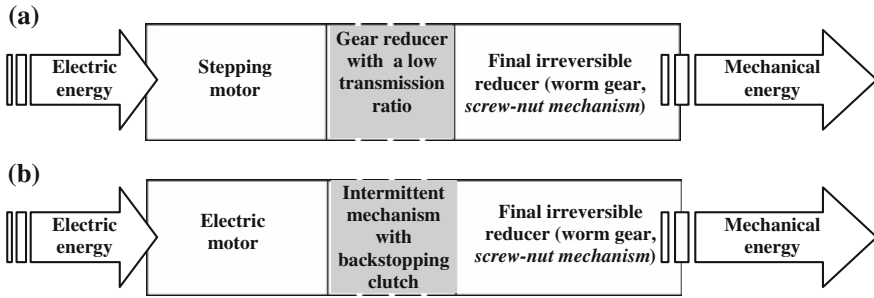


Fig. 2 Working principle of low speed actuators. **a** A classical variant. **b** The proposed variant

The working principle presented in Fig. 2b for a rotary low speed actuator has two mounting options, which are highlighted in Fig. 3a and b.

The structural scheme of the concept presented in Fig. 3b is detailed in Fig. 4, in which the principal solution of the intermediate reducer is a four-bar linkage of crank-rocker type.

The motion in the rotary actuator with four-bar linkage (Fig. 4) is transmitted from the electric motor (M) to a crank-disc (1) on which is eccentrically articulated a connecting rod (2) that drives the rocker (3) in an oscillating motion. From here, the motion is intermittently transmitted via a backstopping clutch, modelled by a ratchet wheel (4) and a latch (5) (see also Fig. 6) to the worm (7) of the final irreversible reducer that engages the worm wheel (8).

In the side view of Fig. 4 it is represented the four-bar type linkage (0-1-2-3) proposed in the new actuator design, which is able to achieve a low angular output stroke (ψ) (see Fig. 5) (Dudiță Fl et al. 1989; Neagoe et al. 2010; Vatasescu et al. 2011; Visa et al. 2012a).

In the construction of the rotary actuators with one-way output motion, a single backstopping clutch is needed to allow the output element to return to its original position.

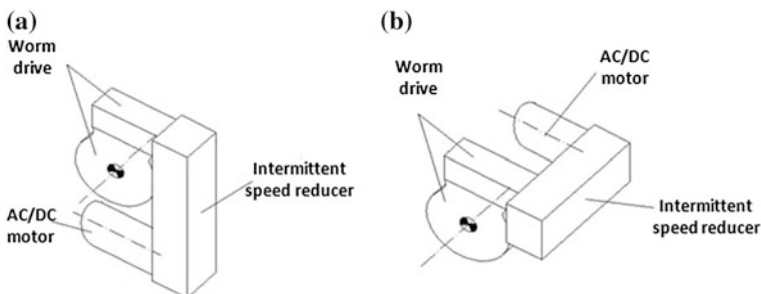


Fig. 3 Conceptual schemes for the new low speed rotary actuator. **a** Planar variant. **b** Spatial variant

Fig. 4 Structural scheme of the proposed low-speed rotary actuator (Diaconescu et al. 2009)

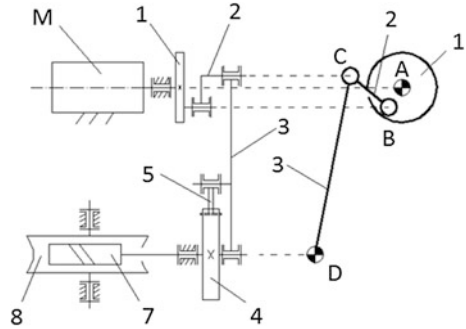
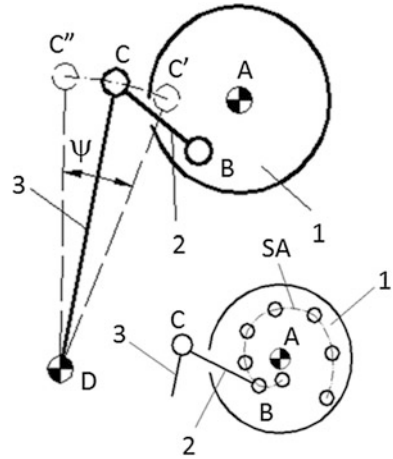
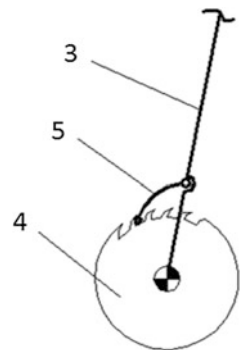


Fig. 5 Angular output stroke of the four-bar linkage with short crank, and a proposed stepped solution for crank radius adjustment



The backstopping clutch (Fig. 6) consists of a ratchet wheel (4), articulated at the base and, effectively, part of the final gearbox input, and a latch (5) articulated to the rocker (3); the clutch transmits motion to the final gear reducer only in the active stroke of the rocker (3), while in the rocker idle stroke, the ratchet wheel (4) remains at rest (Burduhos 2009).

Fig. 6 Conceptual scheme of a one-way backstopping clutch



In order to determine the rocker angular stroke (ψ), the following notations and relations are considered (Fig. 7):

$$AB = r, BC = l, CD = b, AD = B; \tag{1}$$

$$\frac{r}{l} = k_r, \frac{b}{l} = k_b, \frac{B}{l} = k_B; \tag{2}$$

$$\psi = \sphericalangle ADC_2 - \sphericalangle ADC_1 \tag{3}$$

Thus, the rocker angular stroke (ψ) can be determined based on Eq. (4):

$$\psi = \arccos \frac{k_b^2 + k_B^2 - (1 + k_r)^2}{2 \cdot k_b \cdot k_B} - \arccos \frac{k_b^2 + k_B^2 - (1 - k_r)^2}{2 \cdot k_b \cdot k_B}. \tag{4}$$

Numerical simulations for the rocker angular stroke (ψ) were performed considering the values set $k_b = k_B = (1, 2.5, 5, 7.5, 10)$; implicitly, a kinematical ratio for the intermediate reducer i_R is obtained for a known ψ [rad] value:

$$i_R = 2PI/\psi. \tag{5}$$

The nomograms from Fig. 8 allow setting the k_r and $k_b = k_B$ ratios. By adopting values for the base length (B), the values for the lengths of the other links from the four-bar mechanism can be obtained from (Eq. 2).

Considering an intermediary intermittent linkage reducer implemented into a rotary actuator consisting of a classic electric motor with the rotational speed $n_1 = (750, 1000, 1500, 3000)$ [rpm] and a final worm drive with the transmission ratio $i_{78} = 20$ (see Fig. 4), for a given rocker angular stroke (ψ), the output speed n_8 is obtained from relation (6), and it is graphically represented in Fig. 9.

$$n_8 = n_1 / (i_R \cdot i_{78}) [\text{rpm}]. \tag{6}$$

Fig. 7 Kinematical scheme for determining the rocker angular stroke (ψ)

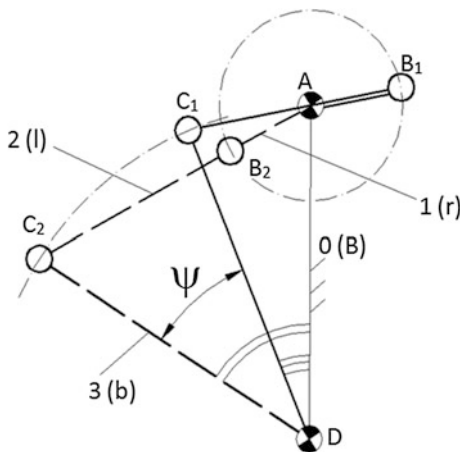


Fig. 8 The nomograms of the rocker angular stroke (ψ) depending on k_r

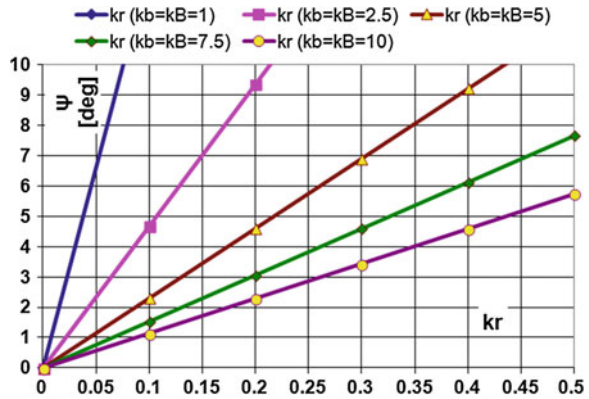
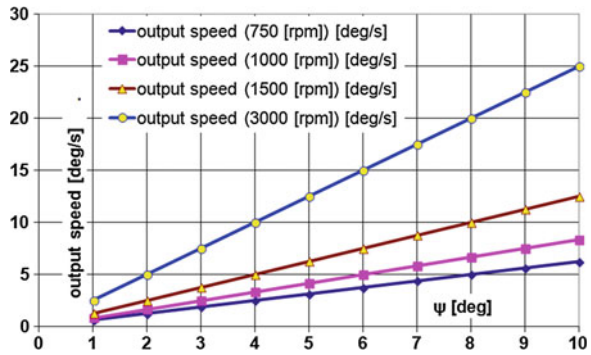


Fig. 9 The nomograms of the output speed n_s depending on the rocker angular stroke (ψ)



3 Discussions and Conclusions

The proposed low speed actuator variant, containing an intermittent mechanism with a single backstopping clutch, can be used in accurate solar stepwise orientation in order to achieve small angular displacements.

Reducing the structural complexity, the proposed solution can be implemented for rotary or linear actuators, by replacing the intermediate gear reducer with two or more planetary gear stages with an intermittent linkage reducer, yielding to high quality solutions with affordable prices and higher efficiencies.

The low speed actuator solution presented in the paper, using a four-bar linkage of crank—rocker type as intermediate reducer, is able to achieve small output angular strokes and, implicitly, low output speeds. For instance, using the nomograms from Figs. 8 and 9, it can be easily stated that, for an accurate solar orientation where the output speed should be adjusted between (0...8) [deg/s], the rocker angular stroke (ψ) of the proposed four-bar mechanism will be adjusted between (0...3) [deg], considering a classical motor of 3000 rpm.

The new low speed actuator can be designed in a flexible approach of *stepped* or *continuous* adjustable kinematical ratio i_R and, implicitly, adjustable output speed, by using a single back-stopping clutch in case of one-way rotary actuators or two counter-phase back-stopping clutches for the two-way rotary actuators.

The next steps in the development process of the proposed low speed actuator consist in the embodiment design, optimization and validation by virtual prototyping, followed by physical prototype development and implementation in a concentrating solar tracking system.

Acknowledgments The authors would like to acknowledge the support provided through the project EST IN URBA and the technical support provided by the RTD Institute, Centre for Renewable Energy Systems and Recycling, within *Transilvania* University of Brasov, Romania.

References

- Alava O (2008) Two axis solar tracker. Patent no. EP 1 998 122 A1
- Bakos C (2006) Design and construction of a two-axis Sun tracking system for parabolic trough collector (PTC) efficiency improvement. *Renew Energy* 31:2411–2421
- Burduhos BG (2009) Optimization of pseudo-equatorial orientation of the mechanisms used to increase the conversion efficiency of individual photovoltaic panels, Doctoral Thesis, Transilvania University of Brasov, Romania
- Cabanillas J (2009) The wind and the Panacea of the stow position in the solar trackers. Article accessible on-line at: www.pvresources.com
- Diaconescu DV, Visa I, Vatasescu M, Hermenean I, Saulescu R (2009) Synthesis of a bi-axial tracking spatial linkage with a single actuator. In: Proceedings of SYROM 2009, the 10th IFToMM international symposium on science of mechanisms and machines, pp 632–617. Springer, Berlin, ISBN: 978-90-481-3521-9; e-ISBN: 978-90-481-3522-6
- Dudiță FI, Diaconescu DV, Gogu Gr (1989) Articulated mechanisms. *Inventics Kinematics București*, Tehnical Publishing House, Romanian
- Goswami DJ, Kreith K, Kreider JF (2000) Principles of solar engineering. CRC, USA, ISBN 978-1560327141
- Jesus A et al (2008) Solar tracker with movement in two axes and actuation in only one of them. Patent WO2008/000867 A1, 18 June 2008
- Kalogirou S (2009) Solar energy engineering: processes and systems. Elsevier, UK
- Kvasznicza Z, Elmer G (2006) Optimizing solar tracking systems for solar cells. In: 4th Serbian-Hungarian joint symposium on intelligent systems, pp 167–180
- Neagoe M, Diaconescu D, Jaliu C, Munteanu O, Saulescu R, Cretescu N (2010) Linkage accuracy modelling. Transilvania University of Brasov, Brasov, ISBN 978-973-635-921-7
- Neff K (2007) Tracking systems for solar units, Brevet nr: WO 2007/025618 A, 08 Mar 2007
- Northrup LL (2010) Solar tracking systems. 2nd edn. ISBN: 978-0-470- + 44633-1
- Rizk J, Chaiko Y (2008) Solar tracking system: more efficient use of solar panels. *World Acad Sci Eng Technol* 31:314–316
- Sclater N (2011) Mechanisms and mechanical devices sourcebook, 5th edn. McGraw-Hill Co., NY
- Serhan M, El-Chaar L (2010) Two axes sun tracking system: comparison with a fixed system. In: Proceedings of international conference on renewable energies and power quality (ICREPQ'10), Granada, Spain
- Vatasescu M et al (2011) Linkages for solar tracking. Transilvania University Press, Brasov (in Romanian)

- Verhelst B et al (2010) Technical and business economic study of photovoltaic systems. International Conference on Renewable Energies and Power Quality (ICREPQ'10), Granada Spain
- Visa I, Diaconescu DV, Moldovan M (2012a) A new solar tracking linkage with 2 actuators in parallel connected, The 2nd IFToMM Asian conference on mechanism and machine science, 7–10 Nov 2012, Tokyo, Japan
- Visa I, Diaconescu DV, Neagoe M, Jaliu CI, Alexandru C, Dobre EB, Botoman MA, Saulescu R, Moldovan M, Proca Vatasescu M (2012b) Low speed actuator with gear reducer articulated intermittent. Patent pending RO 128120 A0, no. a 2012 00664, 2012
- Visa I, Diaconescu DV, Eftimie E, Serban C, Moldovan M, Saulescu R, Vatasescu Proca M, Burduhos B, Totu I (2012c) Single axis linkage with two linear actuators. Patent pending no. A/00467, 2012

WiSeIn: Wireless Sensor Network Used for Data Acquisition from Indoor Locations

Marius C. Luculescu, Sorin C. Zamfira and Luciana Cristea

Abstract One of the most modern technologies for monitoring environmental parameters is the autonomous sensor networks. Network nodes communicate through interfaces wired or wireless connected. This paper presents a solution based on a performance Wireless Sensor Network (WSN) to provide real-time tracking of temperature and humidity. WSN was implemented in locations from distant buildings where the wired connection was not possible. Network nodes based on Waspnote modules have a flexible configuration that allows connecting additional type of sensors to solve any kind of applications. The system highlights take into account the low power consumption, a wide variety of communication protocols, the possibility of local storage (memory cards) or remote information transmission and GPS positioning of network nodes.

Keywords Wireless sensor network · Waspnote · Wired sensor network · ZigBee

1 Introduction

One of the key topics for the 21st century is the networked sensors technology. The research on sensor networks is related to the variety of applications, from environmental monitoring—which involves air, soil and water, to habitat monitoring, seismic detection, military applications, medical healthcare, industrial applications, smart spaces, smart cities etc.

A Sensor Network (SN) is described as a collection of sensor nodes which communicate each other or with a gateway, using different protocols, to perform

M. C. Luculescu (✉) · S. C. Zamfira · L. Cristea
Transilvania University of Braşov, 29 Eroilor Bvd, 500036 Braşov, Romania
e-mail: lucmar@unitbv.ro

the data acquisition task (Smart Sensor Networks 2009). Usually each sensor node consists in one or more sensors connected to a microcontroller board ready to send data (temperature, moisture, pressure etc.) and receive configuration information (Lotf and Nazhad Ghazani 2011).

Very important in designing the structure and the architecture of the sensor network are factors as: topology, error endurance, scale adjustment, hardware limitations, production cost, operation environment, connection tools and energy consumption. The main advantage of a sensor network is flexibility, in terms of scalability and dynamical adaptation to changes in node density and topology (Puccinelli and Haenggi 2005).

During the time, due to technological progress, the wired network solution was replaced by wireless communication and the number of nodes significantly increased.

A Wireless Sensor Network (WSN) represents a special type of sensor network which includes a set of small sensing self-powered nodes which are able to gather information from their surroundings with a certain goal, to process and store information and to exchange data with other nodes or with a base station in a wireless mode.

Additionally to a SN, a WSN design may take into account important aspects related to the fault tolerance, distances, security, location and transmission media and has to pay a special attention to scalability and power consumption (Akyildiz et al. 2002; Boaventura and Carvalho 2013).

One of the applications that can be efficiently solved using SN or WSN in many areas is the environmental parameters monitoring. It enables a long-term data collection at different scales and resolutions (Abed et al. 2011; Tsang-Chu et al. 2011).

2 Problem Formulation

The paper presents an integrated flexible solution for indoor data acquisition, taking into account specific conditions regarding the number and type of locations, distances between nodes and gateway, domain for the monitored values, power consumption and security. The problem can be solved using a wired Sensor Network (wSN) if only one room has to be monitored or using a WSN for multiple rooms in the same location or in different buildings, no matter distances between them. Information obtained from the network nodes by a central gateway are processed by a management system that can rise alarms and also control the parameters within certain limits.

3 Wireless Sensor Network Structure

For monitoring physical and environmental conditions, spatially distributed autonomous sensors are needed and a WSN is the most used solution to collect data.

For the nodes of the WSN, Wireless Sensor Network Used for Data Acquisition from Indoor Locations (WiSeIn) system works with Wasp mote modules (Fig. 1), due to their high flexibility and lot of advantages (Wasp mote 2013). These modules can be attached as required by the applications and will communicate with a Wasp mote configured as a gateway, or with a Meshlium multiprotocol router with wireless (2.4, 5 GHz), ZigBee, GPRS, Bluetooth and Ethernet (Meshlium 2013).

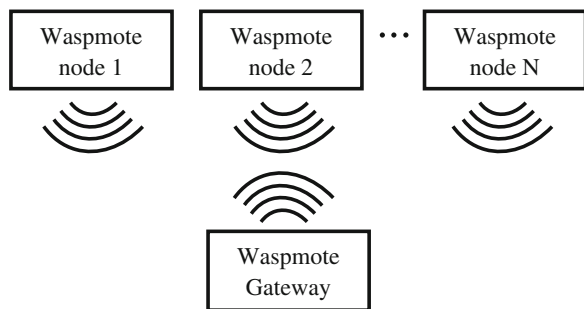
Wasp mote, a modular electronic board from Libelium, is based on ATmega 1281 microcontroller and offers 7 analogue inputs, 8 digital Inputs/Outputs, 1 Pulse Width Modulation (PWM) output, 4 interfaces (2 × UART, 1 × I2C and 1 × USB), a built-in Real Time Clock—RTC, 2 build-in sensors (temperature and accelerometer) and all microcontroller facilities (Fig. 2).

Different sensors shields can be connected on the Wasp mote board and also different communication modules (Bluetooth, XBee, ZigBee), covering distances until 12 km. A GSM/GPRS module is also available, so that the information to be transferred no matter of distance, but depending only on the presence of a GSM/GPRS network. If no network is available, data can be stored on a microSD card. Each sensor node can be located using a GPS module ready to give information about latitude, longitude, height, speed, direction, date/time and ephemerids management. Using shields, the node can deal with more than 50 types of sensors.

Low power consumption is one of the most important advantages of the board. To save energy a common programming technique supposes to block the program until some events appear and this can be accomplished by using interrupt methods. There are 4 operational modes available for Wasp mote:

- ON—normal mode with a 9 mA current consumption;
- Sleep—a latent state with a time interval between 32 ms and 8 s;

Fig. 1 WiSeIn WSN



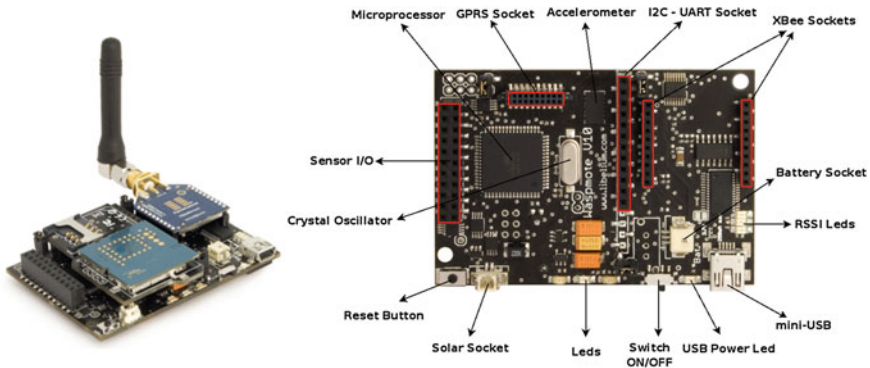


Fig. 2 Waspote module (Waspote 2013)

- Deep Sleep—also a latent state with a time interval from 8 s to minutes, hours, days, in which all asynchronous and synchronous interrupts interruption triggered by RTC can awake the microcontroller;
- Hibernate—a mode when main program is stopped and all Waspote modules are disconnected. To reactivate the device from this state with a time interval from 8 s to minutes, hours, days, RTC (synchronous interrupt) must be programmed.

Low power consumption is assured because in Sleep and Deep Sleep modes the current has the value of $62 \mu\text{A}$ while in Hibernate mode only $0.7 \mu\text{A}$ are consumed. For version 1.2 of Waspote the current for Sleep and Deep Sleep modes decreases at $55 \mu\text{A}$ while for Hibernate mode only $0.07 \mu\text{A}$ are used. Unfortunately, in ON mode the current rises at 15mA .

For external data storage Waspote uses a microSD (Secure Digital) card up to 2 GB with FAT16 file system which can be accessed by different operating systems such as Linux, Windows or Mac-OS. Information are transferred on the microSD card using a SPI interface.

Built-in sensor for temperature ($-40, +85 \text{ }^\circ\text{C}$, with $0.25 \text{ }^\circ\text{C}$ accuracy) is embedded in Waspote RTC. In version 1.1 of Waspote, the STMicroelectronics acceleration sensor works at $\pm 2 \text{ g}$ (1024 LSB/g) / $\pm 6 \text{ g}$ (340 LSB/g) $40/160/640/2560 \text{ Hz}$, while in version 1.2 the sensor is changed and works at $\pm 2/ \pm 4/ \pm 8 \text{ g}$, in low power ($0.5/1/2/5/10 \text{ Hz}$) or normal mode ($50/100/400/1000 \text{ Hz}$). These two built-in sensors transfer data on I2C interface.

Different type of sensors for indoor environment monitoring can be connected to the Waspote board, as it can be observed in Fig. 3.

In storage locations, for example, where the temperature need to be monitored at different heights from the floor level, WiSeIn system uses a network of DS18B20 sensors coupled by OneWire bus, each of them with its own address.

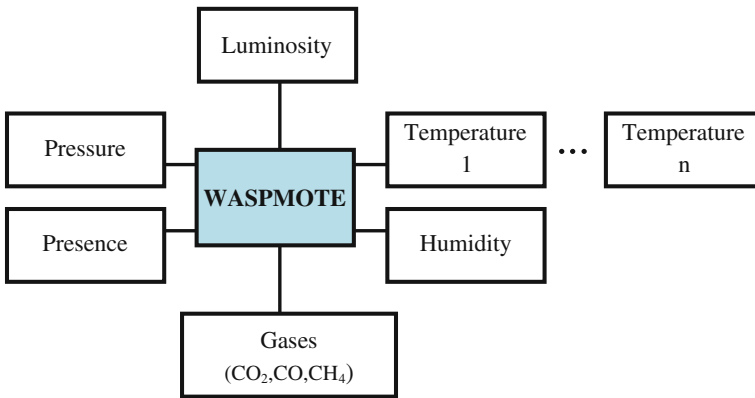


Fig. 3 Sensors that can be connected to the Waspote node

4 Wireless Sensor Network Implementation

WiSeIn system is implemented in 4 locations positioned in 4 different buildings situated at distances below 100 m, namely one central room and three storage rooms and the aim is to monitor temperature and humidity in real time (Fig. 4).

WiSeIn is integrated with WiSeManS, a **Wireless Sensor Network Data Management System for Indoor Climatic Control** which is capable to keep temperature and humidity in certain limits.

The number of nodes in each location is different and it mainly depends on the area of the room (Fig. 5).

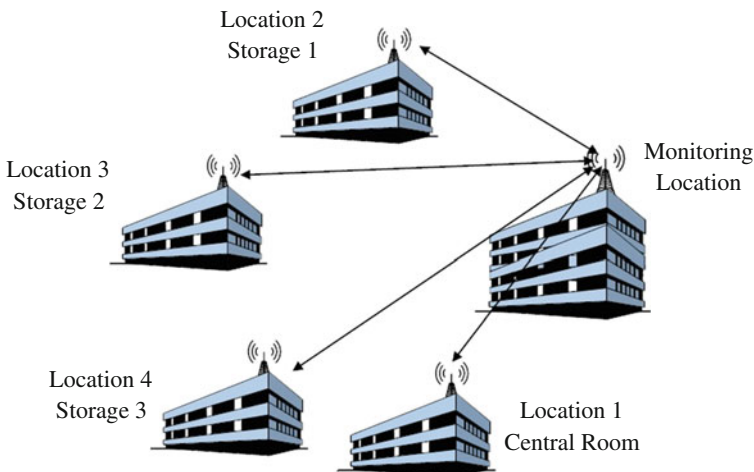


Fig. 4 Locations monitored by WiSeIn system

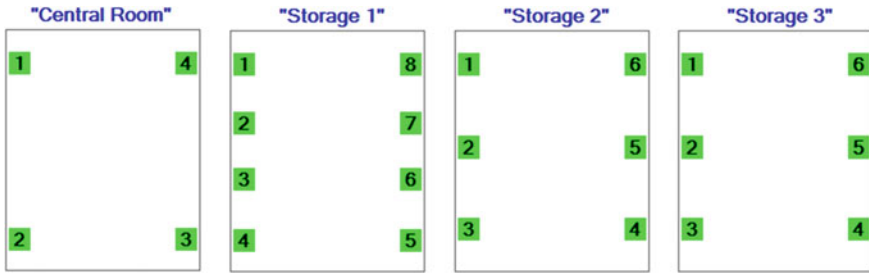


Fig. 5 WiSeIn Wasp mote nodes distributed in monitored locations

Each node acquires information about temperature from 3 sensors DS18B20 from Maxim, using the dedicated OneWire protocol and from another supplemental sensor for humidity that offers also temperature information (SHT15 from Sensirion). The DS18B20 sensors are vertically distributed so that to measure temperature at different height levels. Data from DS18B20 are serially transmitted to the Wasp mote.

Temperature and humidity information are then sent by Wasp mote nodes, at a certain time interval, to a gateway connected to a computer on which WiSeManS system is running.

Average temperature is computed for each node and for each location and is displayed in real time.

To make the communication possible, each Wasp mote board has attached on it an XBee Pro S1 module working with 802.15.4 protocol. For receiving data a Wasp mote Gateway having also an XBee Pro module with a standard USB port is connected to the computer.

Node parameters for the WSN are:

- MAC Address—a 64-bit number that identifies uniquely a node inside a network. It cannot be modified and it is given by the manufacturer.
- Network Address—a 16-bit number that identifies a node inside a network, but that it can be modified at running time.
- PAN ID—a 16-bit number representing the name of the network, which must be unique to differentiate a network. All the nodes in the same network should have the same PAN ID.
- Node Identifier (NI)—a max 20-character ASCII string which identifies the node in a network, used also to search a node in a network.
- Channel—a parameter that defines the frequency channel used by the module to transmit and receive. 802.15.4 defines 16 channels to be used (from $0 \times 0B$ to $0 \times 1A$). XBee module works in 2.4 GHz band, having 16 channels with a 5 MHz bandwidth per channel (2.40–2.48 GHz).

To create a network only two parameters are necessary: channel and PAN ID. These parameters are the base of a network and have to be carefully chosen. There

are also other parameters used to create and connect to a network like security parameters, baud rate etc.

To configure the XBee modules for data transmission and reception, X-CTU software can be used (Fig. 6). More details about these aspects can be found in (Zamfira et al. 2011).

Data is transferred between nodes and gateway in ASCII format. A sample of information generated by one of the nodes is presented in Fig. 7.

It can be observed the addresses of each DS18B20 temperature sensor and the values for temperature (first 3 values on each row). The fourth and the fifth values representing temperature and humidity were obtained from the SHT15 Sensirion sensor. Time interval for sending values was set to 60 s.

The entire management process starting from WSN configuration, with number of locations, number of nodes per location, node settings, temperature and humidity limits, data receiving, processing and displaying in real time, risen

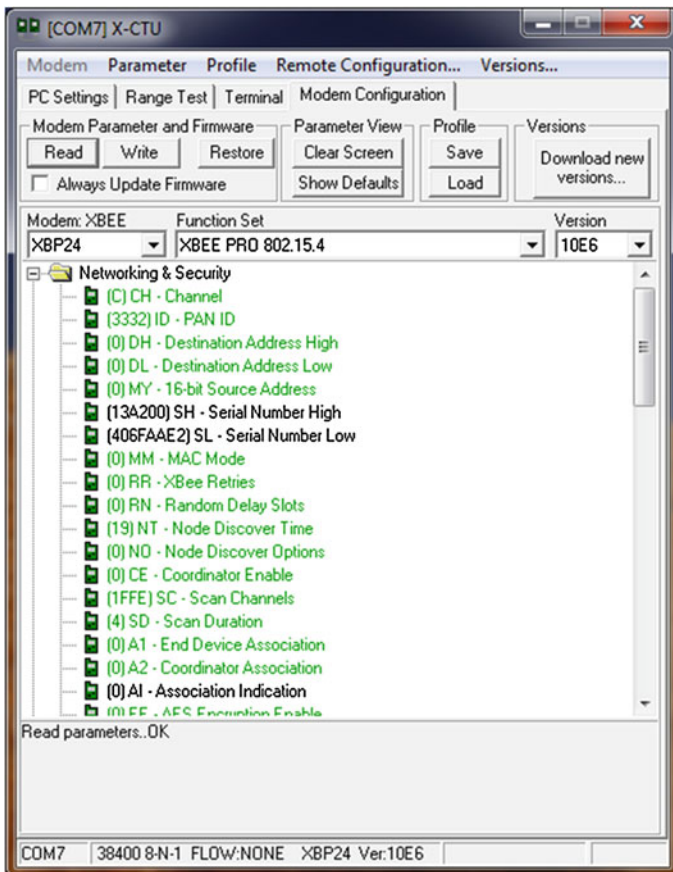


Fig. 6 X-CTU software used for XBee modules configuration

```

Central Room - Node 2 - Notepad
File Edit Format View Help
Locating devices...Found 3 devices.
Found device 0 with address: 10B05376020800BF
Found device 1 with address: 10C4567602080029
Found device 2 with address: 100C497602080004

20.37 20.56 20.56 21.350 51.119
20.37 20.62 20.56 21.220 51.823
20.37 20.62 20.56 21.240 50.904
20.37 20.56 20.50 21.220 51.277
20.44 20.62 20.56 21.230 50.973
20.37 20.62 20.50 21.240 50.868
20.37 20.56 20.50 21.210 51.821
20.37 20.62 20.56 21.140 51.168
20.37 20.62 20.56 21.200 52.058
20.44 20.62 20.56 21.250 52.168
20.37 20.62 20.56 21.240 52.166

```

Fig. 7 Temperature and humidity information acquired by a WSN node

alarms and parameters control is made by WiSeManS, which is a special software described in another paper.

5 Conclusions

Using the WiSeIn system for indoor data acquisition from different locations the following advantages were obtained:

- Flexible nodes that can be configured for different type of sensors (temperature, humidity, gases, pressure, luminosity) and also, if it is necessary, for events as presence or intrusion
- Low-power nodes
- Different communication protocols (XBee, ZigBee, GSM/GPRS)
- Local (microSD card) and remote information storage
- GPS location for each node.

Further development will include smart sensors that already contain the communication interfaces.

WiSeIn system is integrated in WiSeManS—Wireless Sensor Network Data Management System for Indoor Climatic Control presented in another paper.

References

- Abed AA, Ali AA, Aslam N (2011) Building an HMI and demo application of WSN-based on industrial control systems. *Iraqi J Electric Electron Eng* 7(1):107–111
- Akyildiz IF, Su W, Sankarasubramaniam Y, Cayirci E (2002) Wireless sensor networks: a survey. *Comput Netw* 38(4):393–422
- Boaventura A, Carvalho N (2013) A low-power wakeup radio for application in WSN-based indoor location systems. *Int J Wirel Inform Netw* 20(1):67–73. doi: [10.1007/s10776-012-0183-3](https://doi.org/10.1007/s10776-012-0183-3)
- Lotf JJ, Nazhad Ghazani SHH (2011) A survey of wireless sensor networks. *Aust J Basic Appl Sci* 5(8):1496–1503
- Meshlium (2013) <http://www.libelium.com/products/meshlium/>. Accessed in 20 Mar 2013
- Puccinelli D, Haenggi M (2005) Wireless sensor networks: applications and challenges of ubiquitous sensing. *IEEE Circ Sys Mag New Ser* 5(3):19–29
- Smart Sensor Networks (2009) Technologies and Applications for Green Growth. Dec 2009
- Tsang-Chu Y, Chung-Chih L et al (2011) Wireless sensor networks for indoor air quality monitoring. *Med Eng Phy*. doi: [10.1016/j.medengphy](https://doi.org/10.1016/j.medengphy.2011.10.011). 2011.10.011
- Waspnote (2013) <http://www.libelium.com/products/waspnote/>. Accessed in 20 Mar 2013
- Zamfira SC, Cadareanu R, Luculescu MC (2011) Low data rate wireless network, 8th international association of online engineering (IAOE) conference, remote engineering and virtual instrumentation—REV, 28 June 2011–1 July 2011, Brasov, Romania, pp 415–417. ISBN 987-3-89958-555-1

WiSeManS: Wireless Sensor Network Data Management System for Indoor Climatic Control

Marius C. Luculescu, Sorin C. Zamfira and Luciana Cristea

Abstract Used in a large diversity of scientific, military, medical, commercial and educational applications, Wireless Sensor Networks are one of the top today topics. With sizes becoming smaller due to technological progress of semiconductor manufacturing, providing special techniques to reduce power consumption, autonomous sensors transmit data about the physical world using high-performance communication interfaces. Networking, sensor configuration, data acquisition, processing and storage are all operations carried out by specialized data management systems. This paper presents a data management system called WiSeManS, used for indoor climatic control in different type of locations from distant buildings. The system offers high flexibility due to a parametric design that allows adding locations, setting the number of nodes in each location and configuring node parameters (number of sensors per node, type, position and address of them, range of monitored values, communication channel, network ID, destination ID). The software is also an instrument for identifying connectivity problems and finding solutions, showing information about received signal strength, managing sensor nodes time synchronization, querying the node status and configuration, authentication and security. The values from the sensors are displayed in real-time, compared with preset values or ranges of values and each exceeding generates alarms and causes the system to intervene in order to keep parameters within prescribed limits.

Keywords Wireless sensor network · Management system · Waspnote · Climatic control

M. C. Luculescu (✉) · S. C. Zamfira · L. Cristea
Transilvania University of Braşov, 29 Eroilor Bvd 500036 Braşov, Romania
e-mail: lucmar@unitbv.ro

1 Introduction

Monitoring and control systems based on Wireless Sensor Networks (WSNs), bridge the cyber-world of computing and communications with the physical world, whose processes need to be continuously digital supervised (Yuanyuan et al. 2012).

Combining the capabilities of low-power processors with different wireless communication modules and protocols, WSNs consist of portable and multifunctional sensor nodes that communicate each other or with a gateway (Ma et al. 2010).

For the data management system there are two main possibilities to obtain information from WSN. The first one supposes that network nodes send data continuously to a gateway module connected to a PC that store them in a database. The second possibility deals with a local storage approach that means data are managed locally by sensor nodes that will send information to the gateway only when they are queried (Diallo et al. 2012). For a real-time data management, time constraints are to be taken into account.

Factors as energy consumption, fault tolerance, data routing, security, distances, location, error endurance are mandatory in designing the structure and the architecture of the sensor network and also in network operation (Znaidi and Minier 2012; Fersi et al. 2013).

Such a WSN can be used together with wireless control modules so that to obtain not only data acquisition for monitoring, but also control for keeping parameters within certain limits. For all of these, a special data management system is necessary.

The main issues in WSN data management system are: to identify the connectivity problems and find solutions; technologies used for data acquisition have to guarantee performance such as accuracy, timeliness, reliability, scalability and energy efficiency; to assure the monitoring and process control by using sensors and actuators together. Management protocols have to introduce rules for the sensor nodes related: to data aggregation, attribute-based naming, clustering, time synchronization, position changes, turning on and off, querying the configuration and status, authentication, key distribution and security (Akyildiz et al. 2002).

2 Problem Formulation

Indoor climatic control is a wide spread application implemented with a large diversity of solutions. Starting from specific home environmental comfort and ending with more stringent requirements for storage of products, data management and control systems have a major contribution in keeping temperature and humidity within certain limits or conditioning their evolution corresponding to certain variation curves. Such a system has to be designed and implemented, taking into account important aspects regarding monitored locations (number, position, area and distances between them), energy consumption, transmission media,

transmission security, flexibility in connecting additional sensors, parametric configuration for each location, real time tracking of the values, risen alarms and last but not least the indoor climatic control.

An integrated flexible solution, fully parametrized, was called WiSeManS—Wireless Sensor Network Data Management System for Indoor Climatic Control and is presented in this paper.

3 Structure of the Data Acquisition and Control System

The general structure of the data acquisition and control system is presented in Fig. 1 and it contains wireless sensor modules and wireless control modules configured to work in the same network.

All modules communicate with a gateway connected to the PC from the central monitoring and control location, where WiSeManS software is running.

Four locations positioned in four different buildings situated at distances below 100 m, have to be monitored regarding temperature and humidity. Data from one central room and three storage rooms are sent to a different building where the monitoring and control centre has been located. Environment parameters are tracked and kept within prescribed limits in real time using wireless control modules. Each exceeding of the values raises an alarm in the management software that will send commands to the control nodes. The preset values for the

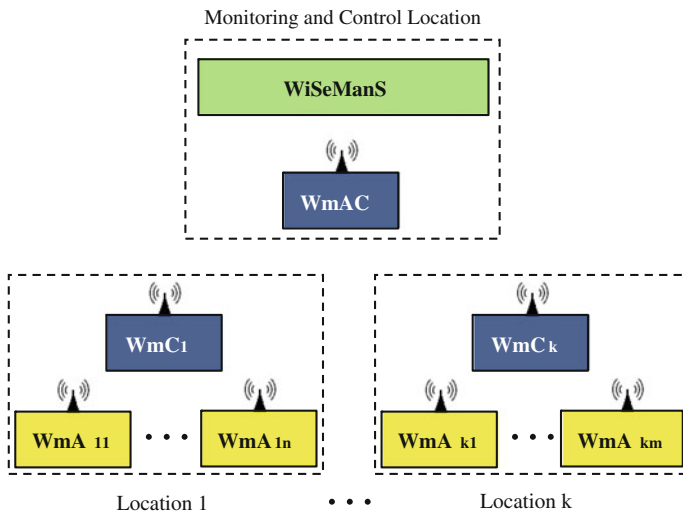


Fig. 1 General structure of the data acquisition and control system, *WmA*—Waspnote node for data acquisition, *WmC*—Waspnote node for control, *WmAC*—Waspnote gateway for data acquisition and control

temperature and humidity for the monitored locations, in our application, in winter, are: for central room, $T_{\max} = 22\text{ }^{\circ}\text{C}$, $H_{\min} = 40\%$, $H_{\max} = 55\%$, for storages 1–3, $T_{\min} = 3\text{ }^{\circ}\text{C}$, $T_{\max} = 4\text{ }^{\circ}\text{C}$, $H_{\min} = 70\%$, $H_{\max} = 72\%$.

3.1 WSN for Data Acquisition

For all the nodes of the wireless network, Wasp mote modules were used (Fig. 2), due to their high flexibility (Wasp mote 2013). Even those modules are not so cheap, they have a lot of advantages: they communicate using different wireless interfaces and protocols (ZigBee, GPRS, Bluetooth), they contain built-in sensors, one for temperature ($-40, +85\text{ }^{\circ}\text{C}$, with $0.25\text{ }^{\circ}\text{C}$ accuracy) and one for acceleration that works at $\pm 2\text{ g}$ (1024 LSB/g)/ $\pm 6\text{ g}$ (34 0LSB/g) $40/160/640/2560\text{ Hz}$ and over 50 types of sensors can be connected to them: gases (CO_2 , CO , CH_4), presence, pressure, luminosity etc. (Wasp mote 2013).

Each node acquires temperature information from three DS18B20 sensors, using a dedicated OneWire protocol and from a SHT15 supplemental sensor for humidity and temperature, communicating on I2C bus. The DS18B20 sensors are connected in a wired subnet, vertically positioned to measure temperature at different height levels. Data from them are serially transmitted to the Wasp mote.

Figure 3 presents the location map with nodes distribution in each monitored location. Wasp mote node communicates with the gateway through an XBee Pro S1 module using 802.15.4 protocol. Node parameters for the WSN are: MAC address, network address, PAN ID (name of the network), node identifier—NI, communication channel (from $0x0B$ to $0x1A$). Only channel and PAN ID are necessary to create the network. All these parameter have to be configured on each node. For XBee modules configuration, X-CTU software is used.

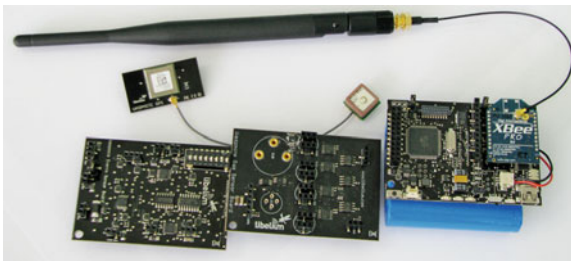


Fig. 2 Wasp mote used in data acquisition node, Wasp mote with XBee module and battery (*right side*), Gases sensor board (*center*), Events sensor board (*left*), GPS module (*up*)

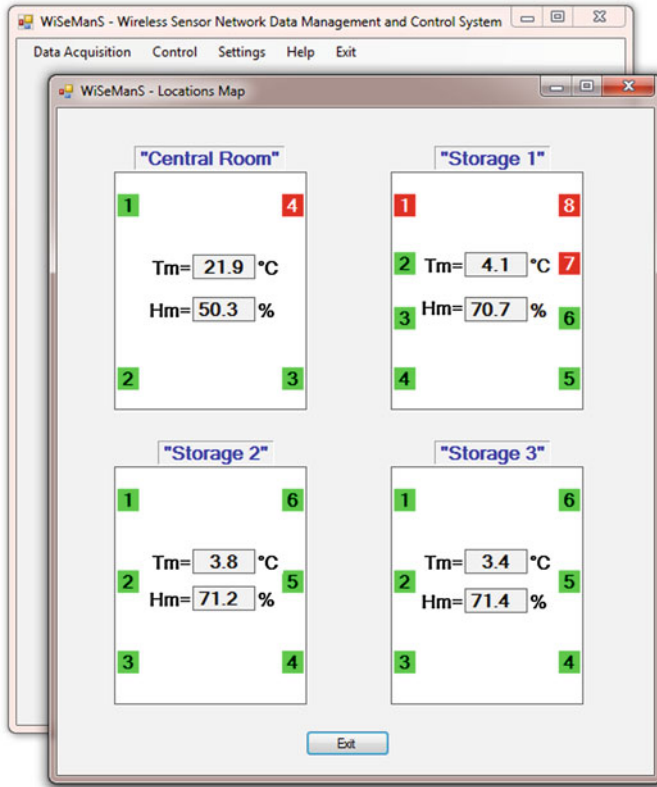


Fig. 3 WiSeManS—location map

3.2 Climatic Control

If the values for temperature and humidity exceed the preset domain, the WiSeManS sends commands to a Heating, Ventilation and Air Conditioning (HVAC) system through a Wasmote control module, existing in each location, to adjust the values to the required range.

Taking into account that the control modules communicate wireless, it is very important to be always valid and the command protocol to verify periodically their status.

3.3 WiSeManS Software

Wireless sensor network management differs from traditional network management due to the failures that can occur in a WSN. Energy shortages, connection

interruptions, physical equipment damage, security violation and environmental changes can lead to nodes failures. Thus, a sensor network must be robust, and must function even when individual nodes, networks, or even services fail (Ma et al. 2010).

WiSeManS software is a powerful package having the main aim to control the indoor temperature and humidity, based on information obtained by querying the WSN. Due to a parametric concept, users can easily design the structure and architecture of networks. This can be done step by step using a recommended wizard option included by the software, or in a custom mode for advanced users (Fig. 4).

The steps to be completed for the network design refer to:

- Adding locations. For each location a name can be assigned.
- Specifying the number of network nodes existing in selected location.
- Setting the ranges for temperature and humidity for the entire location. These preset values are monitored and any overflow will trigger an alarm in the

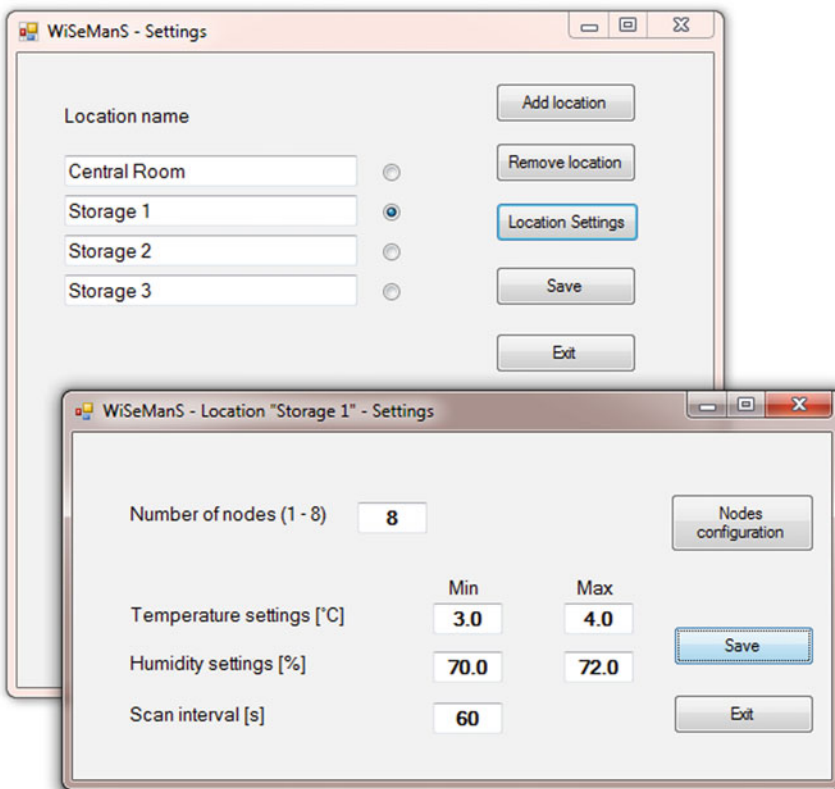


Fig. 4 Settings for location “Storage 1”

software and will determine the system to intervene so that the parameter value to return to desired range.

- Setting the nodes scanning time interval. If it is necessary, this interval can be different for different locations, but in actual version of software, user can define only one interval for the entire location. As each node can contain multiple sensors of the same type (in our application there are four temperature sensors per node, for example), information will be first processed at the node level with respect to compute an average of the monitored parameter. The feature for node scanning interval will be improved in next software version in the context in which the system will offer a degree of generality in terms of parameters that will be monitored and sensors that will be used. Thus, in a location different nodes may contain different types of sensors and scanning time can be customized on each node.
- Configuring node parameters. Each node has a default number and a name can be assigned. If user want to benefit the capability to monitor multiple networks, the PAN ID and communication channel have to be specified for selected node. These values together with destination ID, baud rate and information about security are stored in each Waspote module. Using the network scanning option, information about MAC address, Node Identifier, Received Signal Strength Indicator (RSSI) are obtained and assigned with a certain node. Position of the node inside location (left, right, center, up, down) have also to be specified.
- Configuring network(s). Selected nodes are assigned to a network. Parameters as communication channel, PAN ID, baud rate, authentication, encryption type have to be specified for the entire network.

After the network design is finished, monitoring and control process can start. The average values for each location can be observed on the location map (Fig. 3). If parameters exceed the preset values, the node colour is red, otherwise colour is green. With a double-click on the location name, detailed information can be obtain (Fig. 5).

The values received from the nodes in the querying phase are displayed in real-time. They are compared with preset ranges and each exceeding generates alarms and causes the system to intervene in order to keep parameters within prescribed limits.

For each monitored parameter a chart can be displayed at the node level or at the location level (Fig. 6).

Information is observed for different periods of time and a parameter history option is available.

Optional, monitored locations position can be identified using GPS modules connected to Waspote nodes, but this depends on the GPS signal visibility, taking into account that we are dealing with indoor nodes. Due to the fact that software can be used for a large type of applications, GPS location facility was provided.

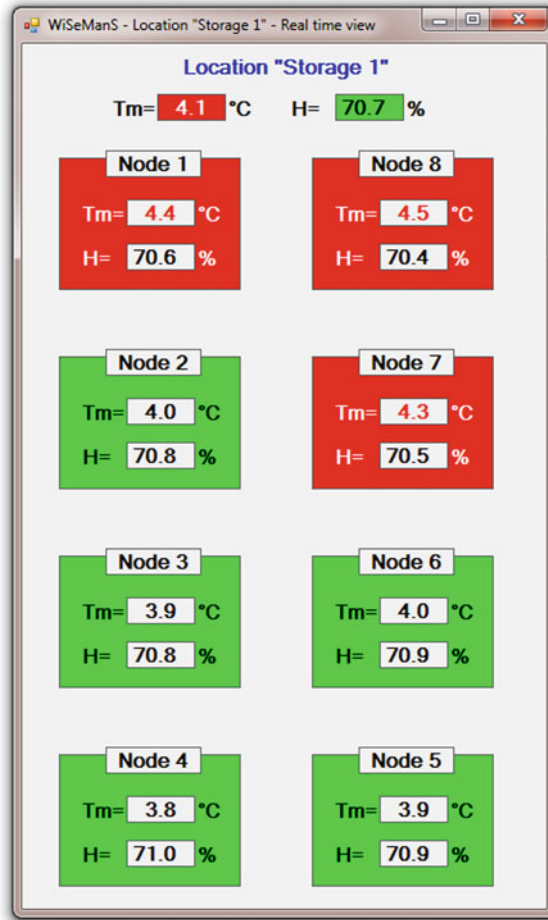


Fig. 5 Details for location "Storage 1"

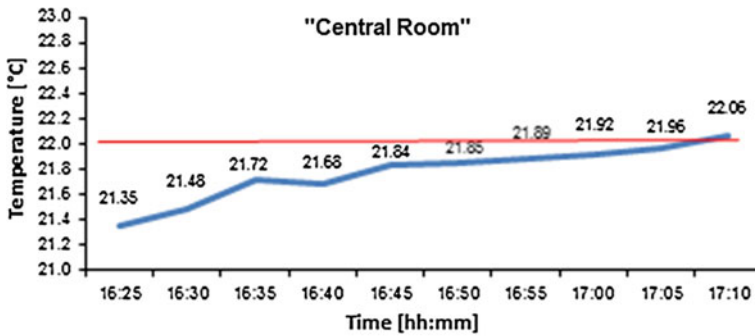


Fig. 6 Temperature chart for central room location

4 Conclusions

WiSeManS, a powerful parametric software package for indoor climatic control, based on Wireless Sensor Network data management, assures high flexibility starting with the design of network structure and architecture, till detailed environment parameters monitoring and process control. Waspnote modules, even they are not so cheap, offer a lot of advantages regarding: the number and type of sensors that can be connected or that are built-in, the available wireless protocols and interfaces for short, medium and long distances, and the low power consumption. The developed software allows identifying connectivity problems, offering smart solutions, optimizing the communication with wireless modules.

For the next version, a series of improvements will be taken into account. Each node will be also organized as a subnet for the same sensors used for a certain parameter, in order to receive each value, not an average. Doing this will be possible to track temperature on vertical levels inside location using one node that contains a subnet of wired sensors. The type and the number of sensors per node have to be specified for assigning received values.

References

- Akyildiz IF, Su W, Sankarasubramaniam Y, Cayirci E (2002) Wireless sensor networks: a survey. *Comput Netw* 38:393–422
- Diallo O, Rodrigues JJPC, Sene M (2012) Real-time data management on wireless sensor networks: a survey. *J Netw Comput Appl* 35(3):1013–1021
- Fersi G, Louati W, Ben Jemaa M (2013) Distributed Hash table-based routing and data management in wireless sensor networks: a survey. *Wirel Netw* 19(2):219–236. doi: [10.1007/s11276-012-0461-0](https://doi.org/10.1007/s11276-012-0461-0)
- Ma YW, Chen JL, Huang YM, Lee MY (2010) An efficient management system for wireless sensor networks. *Sens J* 10:11400–11413. doi:[10.3390/s101211400](https://doi.org/10.3390/s101211400)
- Waspnote (2013) <http://www.libelium.com/products/waspnote/>. Accessed in 15 Mar 2013
- Yuanyuan Z, Kai X, Deshi L (2012) Monitoring technologies in mission-critical environment by using wireless sensor networks: cap 11. In: Matin MA (ed) *Wireless sensor networks: technology and applications*. ISBN 978-953-51-0676-0. <http://dx.doi.org/10.5772/1100>
- Znaidi W, Minier M (2012) Key establishment and management for WSNs. *Telecommun Sys* 50(2):113–125. doi: [10.1007/s11235-010-9391-2](https://doi.org/10.1007/s11235-010-9391-2)

Four-Bar Linkages with Linear Actuators Used for Solar Trackers with Large Angular Diurnal Strokes

Macedon Dumitru Moldovan, Ion Visa, Radu Saulescu
and Mihai Comsit

Abstract The paper presents a detailed analysis on four-bar linkages, driven by linear actuators, used in solar tracking systems with large diurnal strokes. Based on the analysis of representative solutions in literature, a dimensional synthesis algorithm is proposed for a four-bar linkage, actuated by a linear actuator, linked with the connecting rod and with the base. The results are supporting the design of efficient, tracked solar energy conversion systems.

Keywords Solar tracking systems · Solar thermal collector · Photovoltaic platform · Four-bar linkage · Large angular stroke · Synthesis algorithm · Pressure angle

1 Introduction

Solar tracking systems maximize the normal component of the solar direct radiation captured by solar thermal collectors or photovoltaic modules. Depending on the number of tracking axes (single- or dual-axis), an energy gain up to 45 % can be obtained (Eke and Senturk 2012; Abu-Khader et al. 2008).

Solar tracking systems can be divided in azimuthal, pseudo-azimuthal, equatorial and pseudo-equatorial type (Mousazadeh et al. 2009; Vatasescu et al. 2011). The tracking system must adjust the orientation of the solar thermal collectors or of the photovoltaic modules, continuously or step-wise, for following the apparent path of the sun in the sky. The current position of the sun is characterized by a pair of solar angles: the diurnal and respectively the elevation angle. The stroke range of these angles depends on the type of the tracking system. This paper discusses

M. D. Moldovan (✉) · I. Visa · R. Saulescu · M. Comsit
Transilvania University of Brasov, 29 Eroilor Bvd 500036 Brasov, Romania
e-mail: macedon.moldovan@unitbv.ro

the case of an azimuthal solar tracking system, defined by the *azimuthal angle* ψ^* (corresponding to the azimuthal—diurnal—solar angle ψ) and by the *altitude angle* α^* (corresponding to the solar altitude—elevation—angle α). In Fig. 1a, an example of such a tracking system is presented, (Visa et al. 2008), while Fig. 1b presents the variations of the solar angles during the summer solstice (N = 172) in Brasov/Romania location.

The angular stroke of the solar altitude, α , varies between 0° and 90° , depending on the geographic location (e.g. $0^\circ \dots 67.8^\circ$ in Brasov, Romania); the solar azimuthal angle, ψ , has a much higher maximum stroke, between $+180^\circ$ and -180° , depending on the geographic location (e.g. between $+125^\circ \dots -125^\circ$ in Brasov, Romania).

The elevation of a solar tracking system can be obtained using triangle linkages with linear actuator (Fig. 2a) while the diurnal tracking can use a gear reducer with rotary actuator. Linear actuators have usually lower costs as compared to the rotary ones; supplementary, gear reducers have lower efficiencies and a more difficult clearances' control. Therefore, research focuses on designing relatively simple linkages that use linear actuators, able to reach large angular strokes and favourable values of the pressure angles.

In Fig. 2a a triangle linkage with reduced angular stroke, $\Delta\psi^*$, is presented; the minimum accepted values for pressure angles ($\beta = 60^\circ \dots 65^\circ$) are limiting the stroke at $120^\circ \dots 130^\circ$, thus this linkage is not well suited for getting large angular strokes for the diurnal tracking angle. When the linear actuator is connected with a four-bar (planar or spatial) linkage, Fig. 2b, the actuator drives one of the rockers and the four-bar linkage works as angular amplifier, for reaching a large angular stroke ($\phi \geq 130^\circ$), (Visa et al. 2009). Using the linkage described in Fig. 2b, an azimuthal stroke of 190° was obtained, for a minimum transmission angle $\gamma_{min} = 38^\circ$ and an amplification ratio of $\phi/\varphi = 190^\circ/86^\circ = 2.20$. The same azimuthal angular stroke was reached by a spatial linkage with $\gamma_{min} = 20^\circ$ and an amplification ratio of $\phi/\varphi = 190^\circ/72^\circ = 2.64$, (Visa et al. 2009).

A linkage with linear actuator and large angular stroke is presented in Fig. 3 (McNeil-Yeckel and Kaido 2010). It is used to control the position of a solar

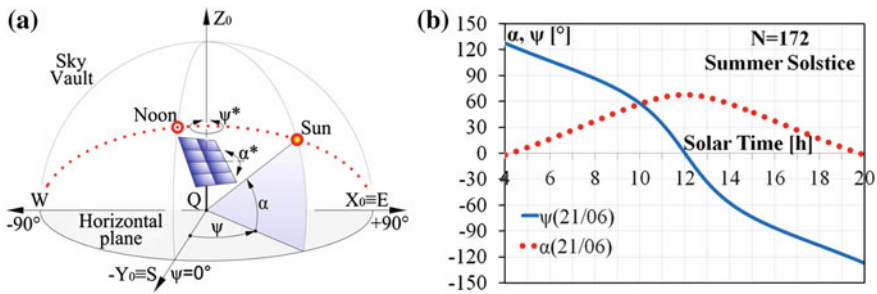


Fig. 1 a Azimuthal dual-axis tracker (Visa et al 2008); b Sun-ray azimuth and altitude angles and their variations during the Summer Solstice (day no. 172) in Brasov/Romania

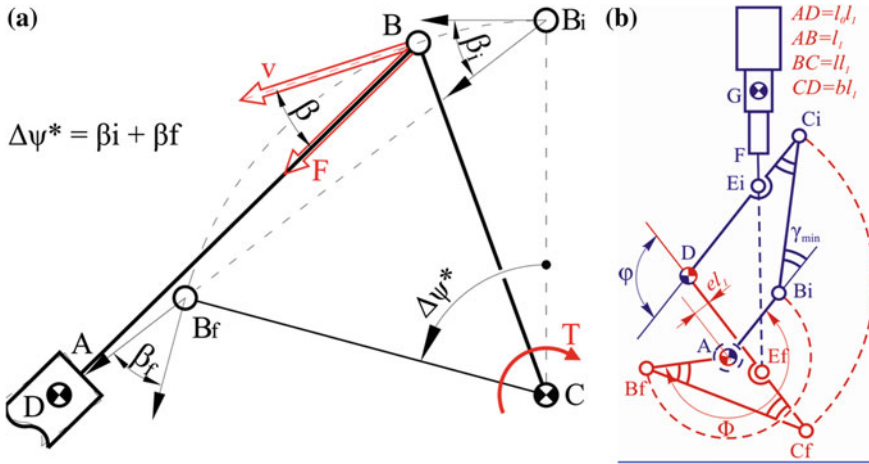
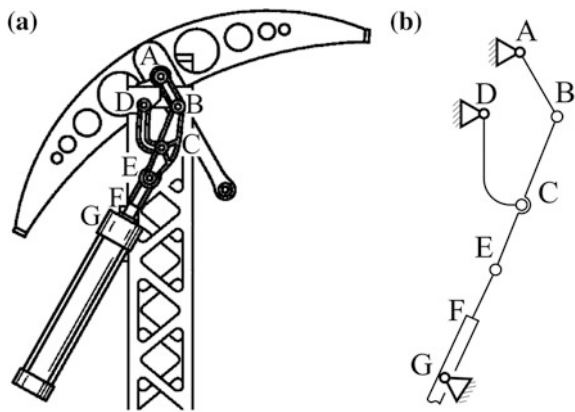


Fig. 2 a Triangular and b four-bar (Visa et al. 2009) linkages driven by a linear actuator

Fig. 3 Four-bar linkage with a linear actuator jointed to the connecting rod (a) constructive detail (McNeil-Yeckel and Kaido 2010) and (b) structural scheme



parabolic trough collector. The rocker-rocker four-bar solar tracking linkage is driven by a hydraulic cylinder connected through revolute joints to the base and to an extension of the linkage connecting rod BC. The angular stroke of the solar collector is 240°, out of which 180° for solar tracking and the difference for maintenance and service. The four-bar linkage and the actuator have a high torque resistance under normal operation conditions (normal wind and its own weight), and under peak loads caused by massive snowfall or extreme wind.

The paper presents the kinematical synthesis of an azimuthal tracking linkage using a linear actuator positioned between the basis and the connecting rod of the linkage in the general case. An optimisation algorithm is presented and also the numerical simulations done for a linkage that can achieve large angular stroke (up to 235°) maintaining pressure angles under the maximum admissible value (60°...65°).

2 Problem Formulation

This study aims at designing a four-bar planar linkage (Fig. 4) driven by a linear actuator, for the diurnal movement of an azimuthal solar tracking system of a solar thermal collector or a photovoltaic platform attached in joint A to the rocker AB. For an azimuthal solar tracking system following requirements need to be considered:

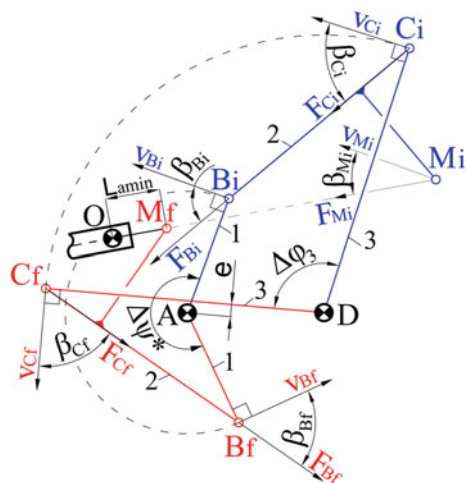
- the diurnal angular stroke $\Delta\psi^*$ should be larger than 180° ;
- the pressure angles are limited to $60^\circ \dots 65^\circ$ for avoiding excessive forces in the linear actuator and in the linkage's elements.

To reduce the complexity of the linkage, an additional condition is imposed: the crank CD should not interfere with the rotating pole from joint A. Thus, an eccentricity, e , defined as the distance between joint A and the crank CD, should be considered.

The position of the revolute joints of the linear actuator (O on the basis and M on the connecting rod of the linkage) are subject of optimisation to provide a minimal linear stroke. In Fig. 4, L_{amin} is a constructive length of the linear actuator describing the closest position of the joint M relative to joint O.

Following rule governs the linkage synthesis: for the complete angular stroke of the crank AB ($\Delta\psi^*$), the pressure angles β_B (between the crank AB and the connecting rod BC), β_C (between the connecting rod BC and the crank CD), and β_M (in the revolute joint M of the actuator with the connecting rod) must be lower than β_{max} (usually $60^\circ \dots 65^\circ$).

Fig. 4 Initial, *i*, and final, *f*, position of the four-bar linkage



3 Geometrical Synthesis of the Four-Bar Linkage

The geometrical algorithm is designed to set the linkage constructive parameters: $l_0 = AD$, $l_2 = BC$, $l_3 = CD$ and $\Delta\varphi_3 = C_iDC_f$ (Fig. 5d), considering an imposed angular stroke $\Delta\psi^*$, at maximum accepted pressure angles for $\beta_{Bf} = \beta_{Cf} = \beta_{Bi} = \beta_{max}$ and $\beta_{Ci} \leq \beta_{max}$; the algorithm follows four stages (Fig. 5):

- the initial and the final positions of the crank 1, AB_i and AB_f , (Fig. 5a) are drawn with the length l_1 to describe the imposed angular stroke, $\Delta\psi^*$;
- the directions of the connecting rod B_fC_f and B_iC_i (Fig. 5b) result by considering the pressure angles $\beta_{Bi} = \beta_{Bf} = \beta_{max}$ in the joint B;

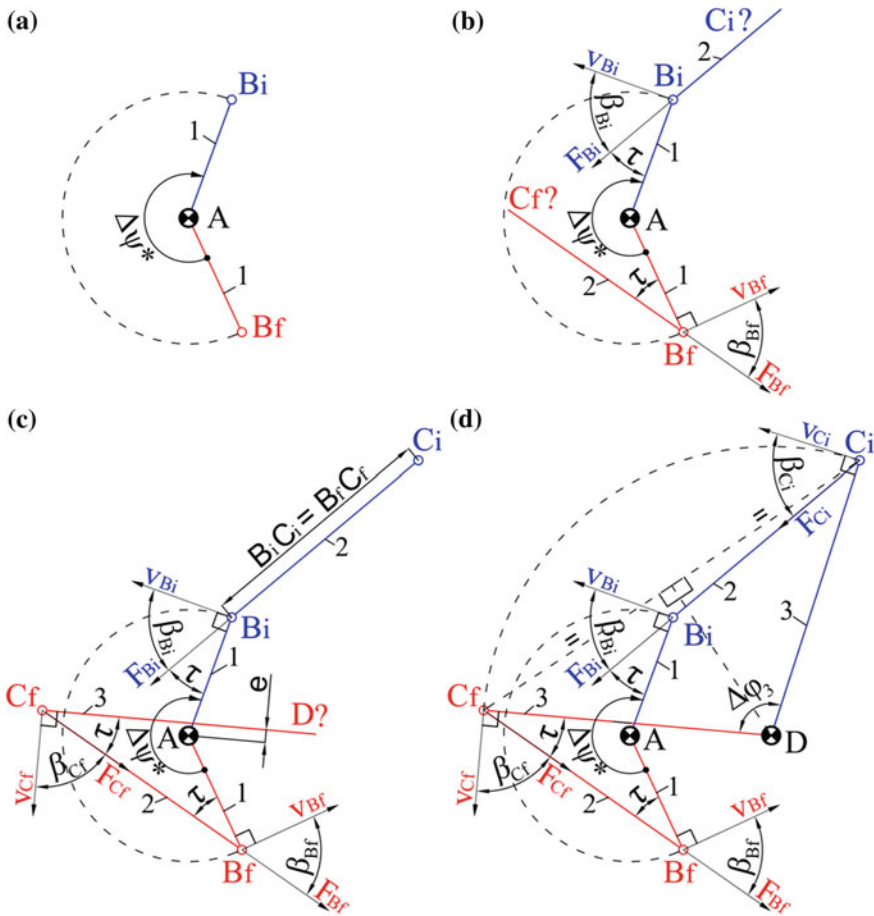


Fig. 5 The geometrical algorithm to set the linkage constructive parameters

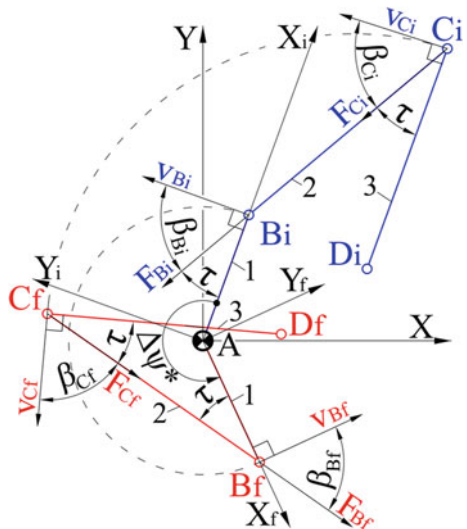
- c. the direction of the crank C_fD (Fig. 5c) is defined by a line forming the τ angle ($\tau = 90^\circ - \beta_{max}$) with the direction of the connecting rod B_fC_f and is tangent to a circle with radius e and center in A; the position of the C_f joint (and thus the length l_2 of the connecting rod BC) result at the intersection between the crank C_fD direction and the direction of the connecting rod B_fC_f ; the position of the C_i joint results based on the length of the connecting rod BC (l_2) and the direction of B_iC_i , before defined;
- d. the position of the joint D (Fig. 5d) results at the intersection between the crank C_fD direction and the straight line passing through the midpoint of the C_iC_f line segment; thus, the length l_3 , the angular stroke $\Delta\varphi_3$ of the crank CD, and the length l_0 of the base AD are geometrically defined.

4 Analytical Synthesis of the Azimuthal Solar Tracking Linkage

The analytical synthesis of the azimuthal solar tracking linkage has as input parameters: the AB crank length, l_1 ; the eccentricity, e ; the maximum admitted pressure angle β_{max} (usually $60^\circ \dots 65^\circ$). Using these values, the goal is to obtain the main parameters of the linkage: l_0 , l_2 , l_3 and $\Delta\psi^*$, using Fig. 6 where $\beta_{Bi} = \beta_{Bf} = \beta_{Ci} = \beta_{Cf} = \beta_{max}$. The angle $\tau = 90^\circ - \beta_{max}$ will be further used.

$$l_2 = 2 \cdot l_1 \cdot \cos \tau + \frac{e}{\sin \tau}; \tag{1}$$

Fig. 6 Geometrical scheme for the analytical synthesis



$$[AD_i^{(i)}] = \begin{bmatrix} l_1 + l_2 \cdot \cos \tau - l_3 \\ -l_2 \cdot \sin \tau \end{bmatrix}; \quad (2)$$

$$[M_{if}] = \begin{bmatrix} \cos \Delta\psi^* & -\sin \Delta\psi^* \\ \sin \Delta\psi^* & \cos \Delta\psi^* \end{bmatrix}; \quad (3)$$

$$[AD_f^{(f)}] = \begin{bmatrix} l_1 - l_2 \cdot \cos \tau + l_3 \cdot \cos 2\tau \\ -l_2 \cdot \sin \tau + l_3 \cdot \sin 2\tau \end{bmatrix}; \quad (4)$$

$$[AD_i^{(f)}] = [M_{if}]^T \cdot [AD_i^{(i)}]; \quad (5)$$

$$D_i \equiv D_f \equiv D \Leftrightarrow [AD_i^{(f)}] = [AD_f^{(f)}]. \quad (6)$$

Following the condition (6) it results:

$$\begin{cases} \Delta\psi^* = \arcsin\left(\frac{c}{a} \cdot \cos \varepsilon\right) - \varepsilon; \\ l_3 = \frac{l_1 \cdot \sin \Delta\psi^* - l_2 \cdot \sin \tau + \sin(\Delta\psi^* + \tau)}{\sin \Delta\psi^* - \sin 2\tau}; \\ l_0 = \sqrt{l_1^2 + l_2^2 + l_3^2 + 2 \cdot l_1 \cdot l_2 \cdot \cos \tau - 2 \cdot l_1 \cdot l_3 - 2 \cdot l_2 \cdot l_3 \cdot \cos \tau}, \end{cases} \quad (7)$$

where:

$$\begin{cases} a = -l_1 + l_2 \cdot \cos \tau - l_1 \cdot \cos 2\tau - l_2 \cdot \cos 3\tau; \\ b = l_2 \cdot \sin \tau - l_1 \cdot \sin 2\tau - l_2 \cdot \sin 3\tau; \\ c = 2l_2 \cdot \sin \tau - l_1 \cdot \sin 2\tau; \\ \varepsilon = \arctg(b/a). \end{cases} \quad (8)$$

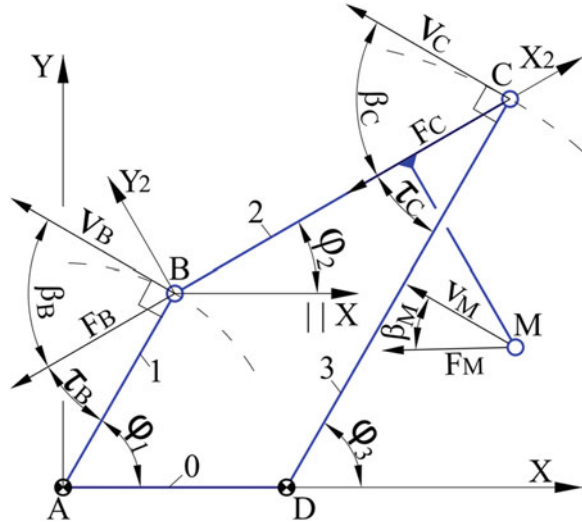
Once the main parameters of the linkage (l_0 , l_2 , l_3 and $\Delta\psi^*$) are obtained, the analytical expression of the pressure angles β_B , β_C can be calculated as function of the angular stroke φ_I of the AB crank, based on Fig. 7.

$$\begin{cases} \begin{bmatrix} X_B \\ Y_B \end{bmatrix} = \begin{bmatrix} l_1 \cos \varphi_1 \\ l_1 \sin \varphi_1 \end{bmatrix}; \\ \begin{bmatrix} X_C \\ Y_C \end{bmatrix} = \begin{bmatrix} l_0 + l_3 \cos \varphi_3 \\ l_3 \sin \varphi_3 \end{bmatrix}; \\ [BC] = \begin{bmatrix} l_0 + l_3 \cos \varphi_3 - l_1 \cos \varphi_1 \\ l_3 \sin \varphi_3 - l_1 \sin \varphi_1 \end{bmatrix}; \end{cases} \quad (9)$$

$$\begin{cases} \tau_B = \arccos\left(\frac{\overrightarrow{AB}}{l_1} \cdot \frac{\overrightarrow{BC}}{l_2}\right); \\ \tau_C = \arccos\left(\frac{\overrightarrow{BC}}{l_2} \cdot \frac{\overrightarrow{CD}}{l_3}\right); \end{cases} \quad (10)$$

$$\beta_B = 90 - \tau_B, \beta_C = 90 - \tau_C. \quad (11)$$

Fig. 7 Geometrical scheme for the kinematical synthesis



The joint M defined in the coordinate system BX_2Y_2 of the connecting rod, can be described in the AXY coordinate system by:

$$\begin{bmatrix} X_M \\ Y_M \end{bmatrix} = \begin{bmatrix} X_B \\ Y_B \end{bmatrix} + [M_2] \begin{bmatrix} X_M^{(2)} \\ Y_M^{(2)} \end{bmatrix}, \text{ where } [M_2] = \begin{bmatrix} \cos \varphi_2 & -\sin \varphi_2 \\ \sin \varphi_2 & \cos \varphi_2 \end{bmatrix}. \quad (12)$$

Based on Eq. (12), the initial M_i and the final M_f positions of the joint M (Fig. 4) are calculated and consequently, the linear stroke of the actuator:

$$L_a = \sqrt{(X_{M_i} - X_{M_f})^2 + (Y_{M_i} - Y_{M_f})^2}. \quad (13)$$

Based on these values and on the constructive length L_{amin} of the actuator (Fig. 4), the position of the joint O (X_O, Y_O) is calculated using:

$$\begin{bmatrix} X_O \\ Y_O \end{bmatrix} = \begin{bmatrix} X_{M_f} \\ Y_{M_f} \end{bmatrix} - L_{amin} \begin{bmatrix} (X_{M_i} - X_{M_f})/L_a \\ (Y_{M_i} - Y_{M_f})/L_a \end{bmatrix}. \quad (14)$$

The pressure angle β_M in the revolute joint M is calculated using:

$$\beta_M = \arccos(\overrightarrow{M_i M_{i+1}} \cdot \overrightarrow{OM_i}), \quad (15)$$

where M_i and M_{i+1} are two intermediate position of the point M, determining the direction of its absolute velocity, and OM_i the direction of the actuator's force.

For the optimal positions of the linear actuator's joints M (X_M, Y_M) and O (X_O, Y_O) a numerical optimisation algorithm is further presented.

5 Numerical Optimisation of the Solar Tracking Linkage

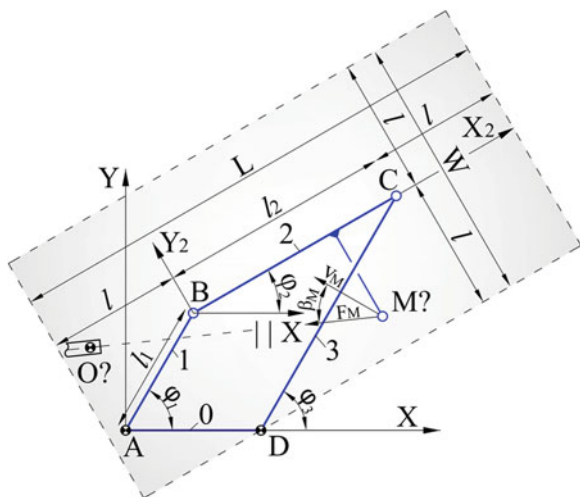
The prerequisites set for the optimal positions of the joints $M (X_M, Y_M)$ and $O (X_O, Y_O)$ of the linear actuator are: the variable length of the linear actuator should be a monotonic function of the angular displacement ϕ_I of the crank AB, and the pressure angle β_M should be lower than β_{max} , both for the entire angular stroke $\Delta\psi^*$ of the crank AB, (Fig. 8).

The proposed method to find the optimal joints' positions consists in numerical simulations incrementally done for different positions of the joint M defined into the BX_2Y_2 coordinate system, relative to the connecting rod BC. The highlighted area in Fig. 8 is explored to find the optimal position of the joint M. It consists in a rectangle centred on the connecting rod BC, having the length $L = l_2 + 2 \cdot l$, and width $W = 2 \cdot l$, where l_2 is the length of the connecting rod BC and l is arbitrary chosen.

For each selected position of the joint M, the variation of the actuator's length is calculated for the entire angular stroke $\Delta\psi^*$ of the crank AB. If the actuator's length has not a continuous increase or decrease (monotonous variation) on the entire angular stroke $\Delta\psi^*$ of the AB crank, the position is not further considered.

For the positions of the joint M matching the monotony condition, the pressure angle β_M is calculated as function of the angular displacement ϕ_I of the AB crank. Further on, there are considered only the positions of the joint M when the pressure angle is smaller than the admitted pressure angle β_{max} . For these positions, the average pressure angle for the entire angular stroke $\Delta\psi^*$ is calculated. Finally, the optimal position of the actuator's joints is selected as for the lowest linear stroke. If there are several solutions closely matching this condition, the choice runs towards the solution with the lowest average value of the pressure angle.

Fig. 8 Area explored to find the optimal position of the joint M



6 Results and Discussions

Based on these steps, a four-bar planar linkage was designed (Fig. 4) for the diurnal movement of an azimuthal tracking system for a solar thermal collector or photovoltaic platform, to be installed in Brasov, Romania (latitude 45.65° N).

The analytical model was used to evaluate the maximum angular stroke $\Delta\psi^*$ of the crank AB for an eccentricity $e = 0.1 \cdot l_1$, where l_1 is the length of the rocker AB, and for pressure angles of 60° both in the initial and final positions of the linkage. A maximum diurnal angular stroke $\Delta\psi^* = 235^\circ$ was obtained, along with the main linkage parameters: the angular stroke of the crank CD $\Delta\varphi_3 \approx 118^\circ$, resulting an amplification factor of 1.99, the reduced length of the connecting rod BC/AB = $l_2/l_1 \approx 1.93$, the reduced length of the crank CD, CD/AB = $l_3/l_1 \approx 2.17$, and the reduced length of the base AD/AB = $l_0/l_1 \approx 1$ (Fig. 4).

Next, the position of the joints M and O are calculated through numerical simulations, done for different positions of the joint M defined into BX_2Y_2 coordinate system, relative to the connecting rod BC. The area explored to find the optimal position of the joint M consists in a rectangle centred on the connecting rod BC, having the length $L = l_2 + 2 \cdot l$, and width $W = 2 \cdot l$, where l_2 is the length of the connecting rod BC and $l = l_1$, where l_1 is the length of the rocker AB (Fig. 8). An increment of $0.01 \cdot l_1$ in choosing the positions of the joint M was used. For example, the first considered position of the point M into the BX_2Y_2 coordinate system was $M(-l_1, -l_1)$, the second was $M(-0.09 \cdot l_1, -0.09 \cdot l_1)$ and so on, until the last one $M(l_2 + l_1, l_1)$. The first three solutions, corresponding to the shortest linear actuator's strokes are: $M_1(1.17, -1.12)$ with $L_{a1} = 1.98$, $M_2(1.06, -0.52)$ with $L_{a2} = 2.00$ and $M_3(1.19, -0.90)$ with $L_{a3} = 2.03$. The trajectories of the joint M are plotted in Fig. 9, for the three best solutions (M_1, M_2 and M_3), along with the cases when the joint M is positioned on the connecting rod BC: $M_4(0, 0)$, $M_5(l_2, 0)$, $M_6(0.4 \cdot l_2, 0)$ and $M_7(0.8 \cdot l_2, 0)$. The graphs plotted in Fig. 9 allow a qualitative description of the joint M trajectory. These trajectories should be as close as possible to straight lines and with minimum distance between the initial, M_i , and the final, M_f , positions, to obtain the minimum strokes of the linear actuator.

The positions corresponding to most of the smallest strokes of the linear actuator are in the half-plane of the rod containing the basis. By positioning the joint M on the connecting rod or on its extension, no improvements are obtained; similarly, by increasing the area of the explored surface (Fig. 8) to $l > l_1$, no better solutions were obtained.

As previously explained, the variation of the actuator's length, L_a , should be a monotonic function. Thus, in Fig. 10 there are plotted the variations of reduced length, L_a/l_1 , for the three best solutions (M_1, M_2 and M_3), along with the cases when the joint M is positioned on the connecting rod BC (M_4, M_5, M_6 and M_7). It can be observed that the actuator's length for $M_4 = B$ does not fulfil the imposed condition: the reduced length increases from 1.77 ($\varphi_1 = 0^\circ$) to 1.97 ($\varphi_1 = 50^\circ$) then begins to decrease. Therefore, the connection of the linear actuator's joint M

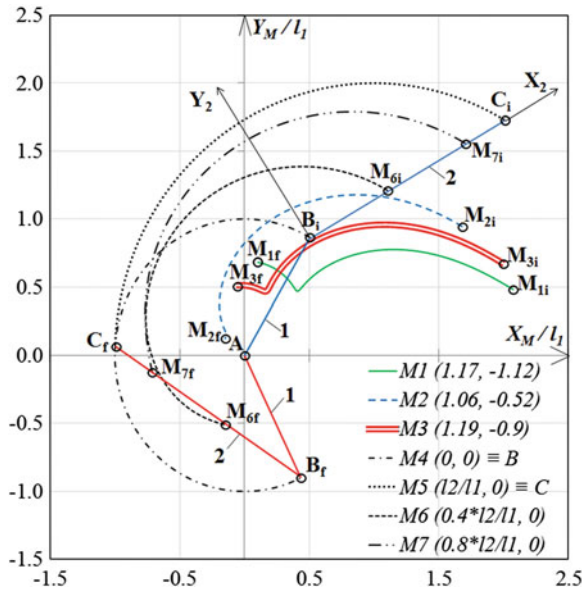


Fig. 9 The trajectories of the actuator's joint M

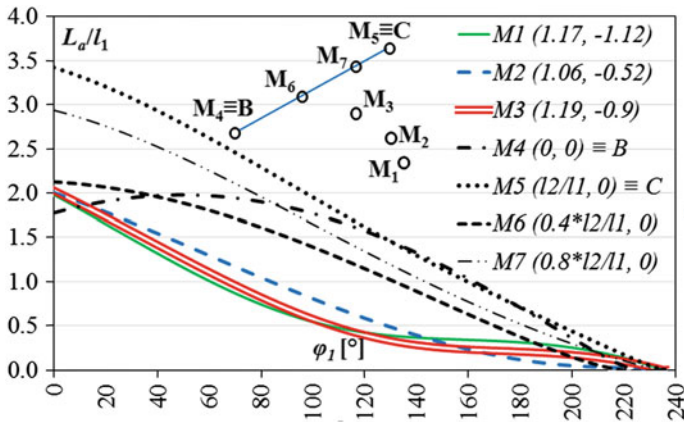


Fig. 10 The variation of the linear actuator's reduced length

in joint B will allow only an angular stroke of $\Delta\psi^* = 50^\circ$, much smaller than the expected one ($\Delta\psi^* = 235^\circ$). The other cases are all monotonic functions.

Quantitative results are also outlined in Fig. 10: the best three solutions were obtained for M₁, M₂ and M₃, with actuator's reduced strokes of about 2. Hence, the optimal position of joint M does not belong to the connecting rod BC. When M belongs to the connecting rod BC (M₅, M₆ and M₇) the actuator's reduced stroke is

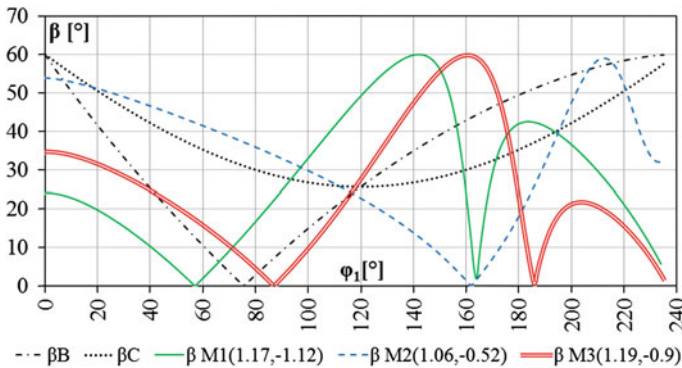


Fig. 11 The variation of the pressure angles β_B , β_C , and β_M

Table 1 Average pressure angles for the entire angular stroke of the crank AB

Solution	M ₁	M ₂	M ₃
Average pressure angle	28.26°	33.65°	25.25°

in the range 2.1... 3.5. Only for M₄ = B the stroke is lower than 2 but the variation of the actuator’s length is not monotonic.

The three solutions (M₁, M₂ and M₃) have close values therefore, to choose the optimal position of joint M, the pressure angles β_B , β_C , and β_M were evaluated as functions of the angular displacement φ_1 of the AB crank, for the entire angular stroke, and the results plotted in Fig. 11.

The variations of the pressure angles β_B , in joint B, and β_C , in joint C, (Fig. 4) are lower than the imposed value of 60° for the entire angular stroke of the AB crank. These angles are depending only on the angular displacement φ_1 of the AB crank and are not depending on the position of the M joint. The pressure angles β_{M1} , β_{M2} , and β_{M3} reach the admitted value of 60°, only once, at different angular displacement φ_1 of the AB crank, otherwise all the values are below, for all three solutions (M₁, M₂ and M₃). Thus, these solutions are valid and the average pressure angles for the entire angular stroke of the AB crank were calculated and are presented in Table 1. The lowest average pressure angle (β_M is 25.25°) corresponds to M₃ (1.19, -0.9), so this represents the optimal position of the linear actuator’s joint with the connecting rod. For this solution, the lowest average load of the linear actuator will be reached and also the lowest energy needed to drive the linkage.

7 Conclusions

The geometrical and analytical synthesis of a four-bar linkage, used to track a solar thermal collector or a photovoltaic platform with large azimuthal angular stroke, driven by a linear actuator, allow the following conclusions:

1. The use of a linear actuator, replacing a rotary actuator, represents a viable option when a four-bar linkage is used for the azimuthal movement of the platform;
2. The four-bar linkage allows a maximum angular stroke $\Delta\psi^* = 235^\circ$, wherever the linear actuator is connected (on the crank or on the connecting rod), when considering an imposed maximum pressure angle of $60^\circ \dots 65^\circ$ and an eccentricity that simplifies the mechanism;
3. If the four-bar linkage is driven by a linear actuator positioned between the basis and the connecting rod, the optimal positions of its revolute joints were identified in the half-plane of the connecting rod containing the basis; thus, the overall sizes of the mechanism decrease, as compared to the case of the linkage actuated on the rocker;
4. The optimal positions of the linear actuator's joints depend on the average pressure angle for the entire stroke of the crank, and correspond to the minimal average load of the linear actuator and the minimal energy needs;
5. The four-bar linkage driven by a linear actuator positioned between the basis and the connecting rod can be used as efficient amplifier mechanism, in the specific application of solar tracking systems, being able to output an amplifying factor up to 2, while maintaining the pressure angles lower than maximum admitted pressure angle of $60^\circ \dots 65^\circ$.

Acknowledgments This work was done in the frame of the Program: Cooperation in Priority Fields - PNII, developed with the support of ANCS, CNDI-UEFISCDI, Romania in the project EST IN URBA, PN-II-PT-PCCA-2011-3.2-051.

References

- Abu-Khader MM, Badran OO, Abdallah S (2008) Evaluating multi-axes sun-tracking system at different modes of operation in Jordan. *Renew Sustain Energy Rev* 12:864–873
- Eke R, Senturk A (2012) Performance comparison of a double-axis sun tracking versus fixed PV system. *Sol Energy* 86:2665–2672
- McNeil-Yeckel CD, Kaido PF (2010) Actuator-based drive system for solar collector. US Patent 2010/0300429 A1, Int. Cl. F24 J 2/38, 2010
- Mousazadeh H, Keyhani A, Javadi A, Mobli H, Abrinia K, Sharifi A (2009) A review of principle and sun-tracking methods for maximizing solar systems output. *Renew Sustain Energy Rev* 13:1800–1818
- Vatasescu M, Moldovan M, Burduhos B (2011) Linkages for solar tracking. Transilvania University Press, Brasov
- Visa I, Diaconescu D, Popa V, Burduhos B, Saulescu R (2008) The synthesis of a linkage with linear actuator for solar tracking with large angular stroke. In: *Proceedings of EUROMEC 08*, 457–464
- Visa I, Diaconescu DV, Popa V, Burduhos B (2009) Synthesis of linkages for tracking systems with increased angular stroke. In: *International Symposium on Science of Mechanisms and Machines*, Brasov-Romania, 193–206, Springer, 2009

Study of the Contact Between Toothed Chains and Guides

Radu Papuc, Radu Velicu and Mihai Lates

Abstract This paper is dealing with the bases of the design and optimization of the chain guide system with practical application on the toothed chains for the timing mechanism of combustion engines. The main purpose of the present analysis is to determine the contact normal reactions which will be used for subsequent analysis on the tribological chain-guide contact. Equivalent stresses will also be analyzed in order to have an input for chain-guide contact pressures.

Keywords Chain guide · Friction · Contact · FEM

1 Introduction

In toothed chain transmissions, the contact between the sprockets teeth and the chain is made through links and not through rollers or bushings like in the case of other chain transmissions. Based on this fact, the dynamic loads may be reduced, and the toothed chains could be used at high speeds (Jula et al. 2005). The chain load capacity is increased by the possibility of using bigger bolts (Jula 1989).

The kinematic and dynamic functioning features of the toothed chains highlight the possibilities of vibrations apparition. There can be mentioned transversal, longitudinal and twist vibrations. Chain functioning in vibration conditions reduces the durability performances due to specific dynamics. From this reason the presence of chain guide is imposed. Chain tensioning is also compensating the initial pitch errors and wear effects leading to extension of the length of the chain (Gafitanu 1983).

R. Papuc (✉) · R. Velicu · M. Lates
Transilvania University of Braşov, 29 Eroilor Bvd, 500036 Braşov, Romania
e-mail: radu.papuc@unitbv.ro

2 Preliminary Calculus Procedure of the Geometrical and Functional Parameters of the Chain–Guide Contact

Figure 1a presents the chain–guide components: guide (1); exterior toothed links (2); interior toothed links (3); sprocket guiding links (4); bolts (5). The interior and exterior toothed links engage with the sprockets teeth and the guiding links have the purpose of not allowing the chain to slide off the sprocket. The guiding links and the interior toothed links are fixed on the bolts and the exterior toothed links are articulated on the bolts. Figure 1b presents the geometrical parameters of the toothed chain. The chain–guide contact is achieved, in one phase, between exterior toothed links and guide and in the other phase between interior toothed link together with guiding links and guide.

Figure 2 presents the geometrical diagram of the tensioning guide and toothed chain defining the following elements: $R_{r1,2}$ —sprockets radii; A —center distance; R —guide radius; l —guide length; N —normal force; F —force along the chain branch.

In order to exemplify the calculus method it was considered a reference chain transmission having the following parameters: chain pitch $P = 9.525$ mm; number of chain links $w = 64$; number of teeth of sprockets $z_{1,2} = 16$; width of the interior and exterior toothed links $b_i = b_e = 2.2$ mm; width of the sprocket guiding links $b_s = 1$ mm; tensioning guide radius $R = 150$ mm; angle of guide-chain contact $\alpha = 26^\circ$; Force along the driving branch $F = 1000$ N.

Table 1 presents the proposed preliminary calculus procedure of the geometrical and functional guide-chain contact parameters with numerical examples for the considered transmission. It considers a circular shape guide and uniform distribution of normal loads on length of contact.

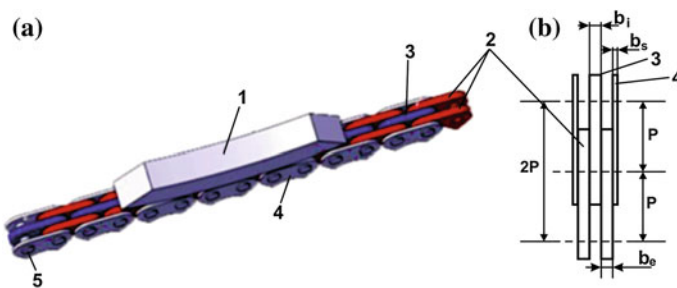


Fig. 1 Toothed chain–guide model

Fig. 2 Geometry of the tensioning guide and chain

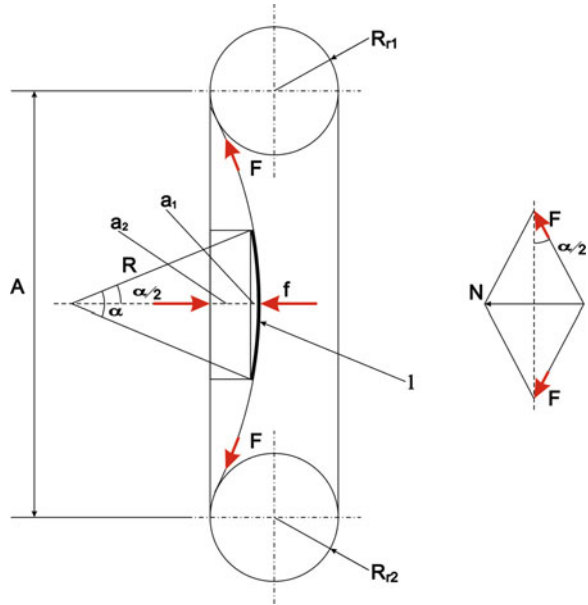


Table 1 Preliminary calculus method of the geometrical and functional guide-chain contact parameters

No.	Parameter	Calculus relation	Calculated values
1	Sprockets radii $R_{r1,2}$	$R_{r1,2} = \frac{p}{\sin\left(\frac{180}{z_{1,2}}\right)}$	49 mm
2	Center distance A	$A = \frac{L - 2 \cdot \pi \cdot R_r}{2}$	305.85 mm
3	Guide length l	$l = R \cdot \frac{26}{180} \cdot \pi$	70 mm
4	Chain length L	$L = p \cdot w$	800 mm
5	Normal force N	$N = 2 \cdot F \cdot \sin\frac{\alpha}{2}$	450 N
6	Component of the guide displacement a_1	$a_1 \cong \frac{L_2 - l}{2} \cdot \sin\frac{\alpha}{2}$	26.415 mm
7	Guide deviation a_2	$a_2 = R \cdot (1 - \cos\frac{\alpha}{2})$	3.9 mm
8	Total guide displacement f	$f = a_1 + a_2$	30.315 mm
9	Number of link pitches in contact with the guide n_z	$n_z = \frac{l}{p}$	7.35
10	Average normal force on a pitch link N_{za}	$N_{za} = \frac{N}{n_z}$	61.2 N
11	Number of exterior links z_E (for a pitch)	See Fig. 1	2
12	Number of interior and guide links z_{IG} (for a pitch)	See Fig. 1	3
13	Average normal force on an exterior pitch link N_{Ea}	$N_{Ea} = \frac{N_{za}}{z_E}$	30.6 N
14	Average normal force on an interior + guide pitch link N_{IGa}	$N_{IGa} = \frac{N_{za}}{z_{IG}}$	10.2 N

3 Elastic Characteristic of the Guide Material

The elastic characteristic is one of the mechanical properties of a material. In technique, hardness is defined as being the resistance opposed by a material when another, more hard, mechanically penetrates the material.

The elastic characteristic of the materials is determined through standard methods. According to the force exerted on the indenter, the laboratory methods can be: static or dynamic. The testing equipment for Vickers hardness (CETR UMT 2009) determination is presented in Fig. 3. For this test pin holder, indenter, specimen (guide material), suspension, sensor capacitor.

The pressing force overcomes first the material elastic deformations, then passing small plastic deformations finally reaching important plastic deformations. The experimental measurements of the time dependent applied force F_z and indenter penetration depth δ are presented in Fig. 4.

Figure 5 presents the experimental elastic characteristic (deformation depending on force) of the guide material. The first stage with direct depending deformation—force is useful in FEM further modeling. The elastic characteristic can be considered as determining the same mechanical material property, like, for example, the traction resistance, but in other requirement conditions. By numerical method and experiments it was found a proportionality relation between hardness and traction resistance. The elastic characteristic is considered one of the material properties with significant contribution in tribology processes.

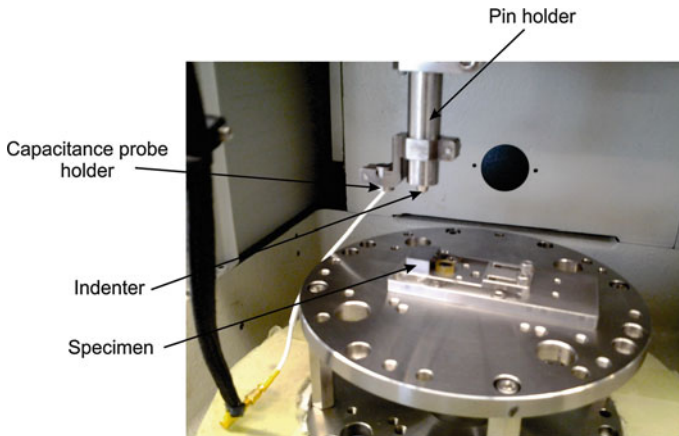


Fig. 3 Vickers method- tribometer

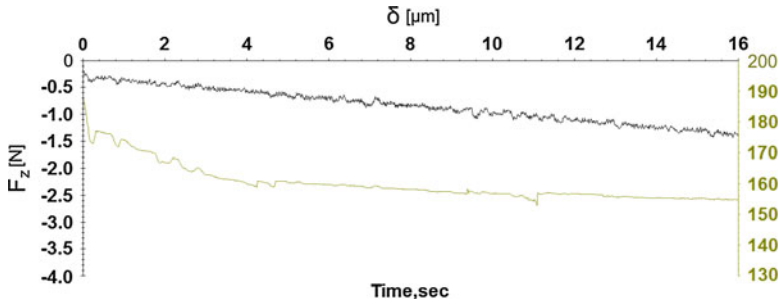


Fig. 4 Graphical determination of the guide material elasticity

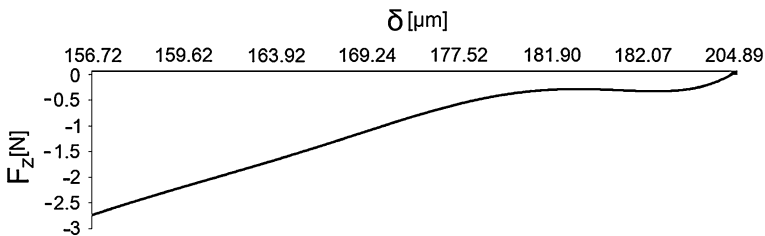


Fig. 5 Elastic characteristic of the guide material

4 Stresses and Normal Reactions in Guide–Chain Contact Using FEM

Bases In practice, the mechanical systems are met frequently in situations when, due to form and connections, their elements become instable, thus a guide-chain contact. Removing the functionality of some mechanical systems elements can have serious consequences on the entire system. Thus, after finite element analysis of these structures, which assume identifying the displacement and tensions fields, post processing is mainly aimed at determining the displacements, rigidities, contact reactions, either for or comparison with the admissible limits for use in subsequent calculus (Mogan 2007). In the case of chain-guide contact, the main purpose of the present analysis is to determine the contact normal reactions which will be used for subsequent analysis on the tribological chain-guide contact. Equivalent stresses will also be analyzed in order to have an input for chain-guide contact pressures.(Lates 2008).

Application description and purpose The geometry of the model is based on the inputs and preliminary calculations presented in Chap. 2. The ends of the chain are fixed and the load is created through a force distributed on the guide surface, acting upon the chain with $N = 450 \text{ N}$ (Fig. 6).

The analysis method FEM procedure starts with definition of the geometrical model and continues with materials definition: longitudinal elasticity module,

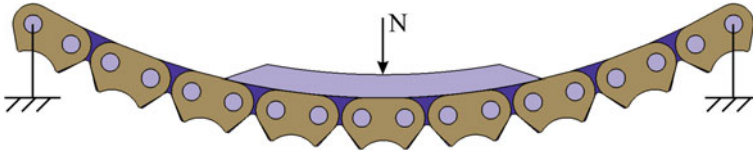


Fig. 6 The geometrical form at detailed level of the guide–chain contact

Poisson transversal contraction coefficient and density (chain links and guide). The meshing is made with tetrahedron finite elements, and the constraints are modeled as follows:

- clamp: restriction of all the displacements regarding the global coordinate system at both chain ends;
- pressure fitting: using this constraint was established the assembly fixed type link by pressing the bolts and plates;
- user-defined restrain: another essential element for the two elements contact analysis is referred to the restrains that can define the restriction of some motions. At the guide-links contact there were restricted the other motions less the z axis translation and at the links the translation is made on yz axes and the solution about x axis is allowed;
- Slider connection: the connections between guide and links are associated with a finite element mobile contact.

The loads are represented by distributed forces. Generating a distributed force normal to a surface, practically the guide acts with a force resulted from the preliminary calculus of the contact $N = 450 \text{ N}$, on the chain all over the contact surface.

Results Fig. 7 presents the Von Mises stress distribution. It shows that the maximum stresses appear on the links ($\sigma = 300 \text{ MPa}$) with acceptable values. The pressures between links and guide reach a maximum of approximately 0.5 MPa , which is also acceptable.

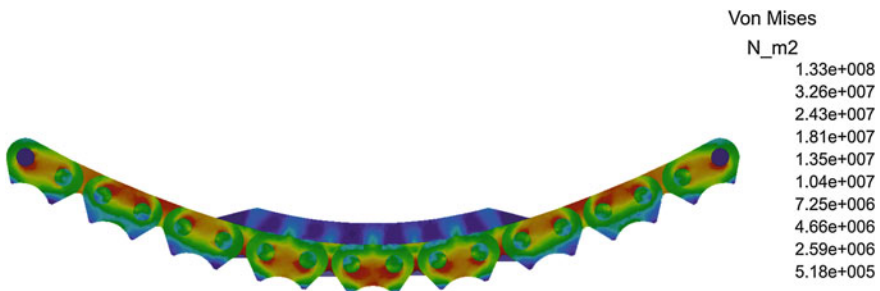


Fig. 7 Von mises stress

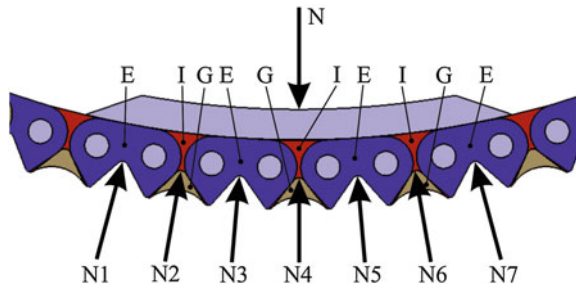


Fig. 8 Graphic representation of links and links normal reactions

Figure 8 presents the position of links relative to the guide with the following notations: E—exterior link, I—interior link, G—sprocket guiding link and normal reactions N_x ($x = 1...8$). The normal reactions can be separated as: on exterior links $N_{E1,3,5,7}$; on interior links $N_{E2,4,6}$; on sprocket guiding links $N_{G2,4,6}$. Figure 9 presents the resulted normal reaction distribution on links: a—normal reactions on exterior links, b—added normal reactions on interior and sprocket guiding links, c—total reaction distribution. There is a reduced normal reaction on exterior links at the ends of the guide due to the higher elasticity of guide coming from the thinner end shape.

As an average, the results are according to the values calculated in Table 1. However, it shows a variable normal reaction along the guide, which can be translated also in variable pressures.

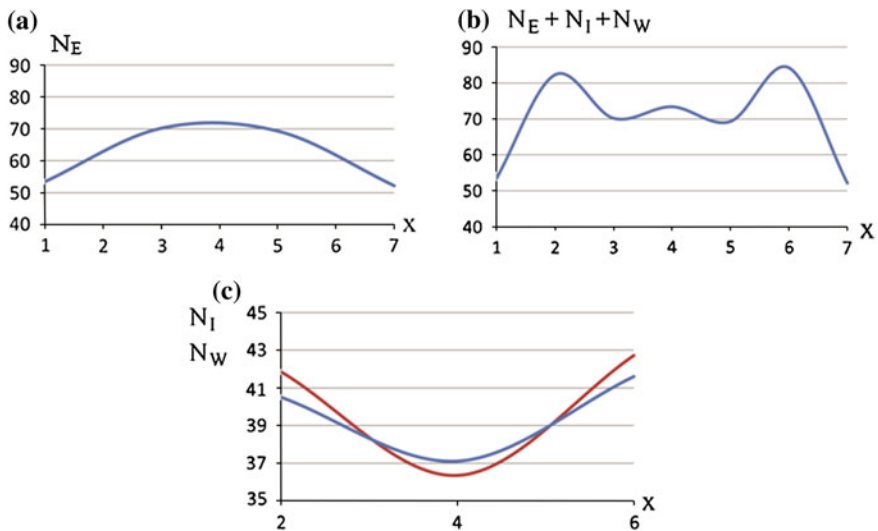


Fig. 9 Distribution of normal loads on link–guide contact

5 Conclusion

The distribution of normal reactions between chain link and guide are the start for the tribological analysis of this type of contact. The final purpose is the material and shape optimization with the goal of friction reduction and durability improvement. Further research must focus on sequential movement of the chain along the guide and effect on resulted normal reactions and pressure distribution.

References

- CETR UMT (2009) Multi-specimen test system hardware installation & applications manual, Centre for Tribology, USA
- Gafitanu M, a.o (1983) Machine elements (in Romanian), Ed. Tehnica, Bucuresti. ISBN 973-31-1400-6
- Jula A, a.o (1989) Machine elements, Vol. 2 (in Romanian), Ed. Universitatii din Brasov
- Jula A, Chisu E, Lates M (2005) Mechanical transmissions (in Romanian), Ed. Universitatii Transilvania, Brasov. ISBN 973-635-444-1
- Lates M (2008) The method of finite element (in Romanian) Ed. Universitatii Transilvania, Brasov. ISBN 948-973-635-659-9
- Mogan G, a.o (2007) The analyse with finit element in engineering domain, Ed. Universitatii Transilvania, (in Romanian) Brasov. ISBN 978-973-589-154-4

Study of the Curved Plate Spring Behavior for Small Displacements

Hariton Poparad

Abstract This paper presents the results of the study performed on curved plate springs used in flexible coupling systems. Through the modeling of the elastic curved bar element using finite element techniques with the series constituted by two elements in circular arc and a straight bar element, the rigidity influence of the entire structure will be established. The conclusions obtained in this paper allow the accurate estimation of the structure response.

Keywords Elastic response • Deformed structure • Displacement • Coupling

1 Introduction

The flexible coupling system with curved plate springs is framed in the class of the permanent elastic couplings with metallic intermediary elements; they serve for the transmission of the motion, compensation of the deviations caused by the arrangement of the coupled shafts, and the absorption of the shock and torsion vibrations (Jula et al. 1989; Gafitanu et al. 1983).

The properties of the flexible couplings are highlighted by the torsion rigidity parameter, which determine the semi-couplings rotation angle φ_n at applied torsion force M_m (Draghici et al. 1978, 1983; Silveira et al. 2013). With this in consideration, the dimensioning of the coupling must begin from the design of the curved plate springs-elements that define the work of the studied elastic couplings with constructive parameters and form represented in Fig. 1.

The study of the induced stress and the state of deformation of the elastic elements involves the necessity to find correlations between the geometrical

H. Poparad (✉)

Transilvania University of Brasov, 29 Eroilor Bvd 500036 Brasov, Romania
e-mail: hariton.poparad@unitbv.ro

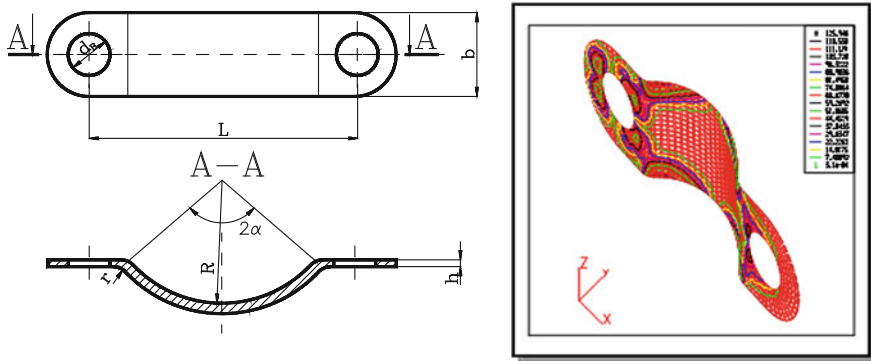


Fig. 1 Elastic coupling elements

parameters (the radius of curvature R , the radius of connection r , central angle 2α , height h , width b , the number of elastic elements z) and the working conditions of the elastic couplings with curved plate springs (M_m, φ_n).

2 Modeling and Simulation of Elastic Structure for Small Displacements

The concept of the *elastic finite element* is defined in (Courbon 1971; Tofan et al. 1995). The unloaded elastic element (EF), simulated as a finite kinematic link, comprises a series of infinitesimal elastic elements (EI) Fig. 2. The infinitesimal elastic element (EI) is normal defined for a cylindrical symmetrical bar with respect to the Frenet local frame as $\mathbf{FR} = [\mathbf{t} \mid \mathbf{n} \mid \mathbf{b}]$.

In the absence of the cylindrical symmetry, the definition is made locally with respect to a main reference frame that differs from the frame \mathbf{FR} due to a tensional

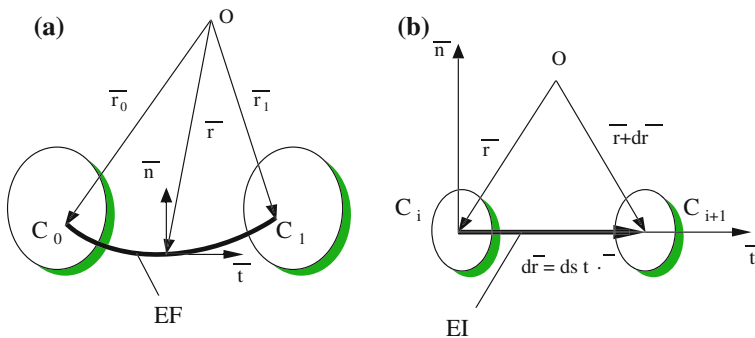


Fig. 2 The model for the infinitesimal elastic finite element

rotation around the tangent \mathbf{t} . Considering the cylindrical symmetry for an infinitesimal curved bar element that has the length ds (see Fig. 2b), the flexibility will be represented by a diagonal matrix with respect to the local frame \mathbf{FR} :

$$DE = \backslash \frac{1}{EA_t} \quad \frac{1}{GA_n} \quad \frac{1}{GA_b} \quad \frac{1}{GI_t} \quad \frac{1}{EI_n} \quad \frac{1}{EI_b} \backslash \cdot ds \tag{1}$$

This will determine the linearity and the separation of all patterns of the elastic response due to the elongation, shearing, torsion and bending. The elastic deformation of the element \mathbf{EI} will result due to the relative displacement between the two rigids attached to the extremities and will define the deformation screw:

$$\hat{\delta \mathbf{e}} = \mathbf{DE} \cdot \hat{\mathbf{F}}\mathbf{I} \tag{2}$$

We denoted $\hat{\delta \mathbf{e}}$ to be the elastic relative displacement screw and $\hat{\mathbf{F}}\mathbf{I}$ the force screw that loads the \mathbf{C}_{i+1} rigid attached to the end of the transversal of section $r + dr$:

$$\hat{\delta \mathbf{e}} = \left\{ \begin{matrix} \delta \mathbf{e} \\ \delta \theta \end{matrix} \right\}, \quad \hat{\mathbf{F}}\mathbf{I} = \left\{ \begin{matrix} \mathbf{F} \\ \mathbf{M} \end{matrix} \right\}, \tag{3}$$

According to the Sommerfeld considerations, the displacement and force screws are dual screws. $\hat{\delta \mathbf{e}}$ contains the linear displacement vector in the upper position, and the angular displacement vector in the lower position. $\hat{\mathbf{F}}\mathbf{I}$ contains the force vector in the upper position, without dependence on the pole, and the lower position represents the moment with respect to the pole. The first screw is a field generator in the entire rigid space. The second represents the reduction of the resultant action of the mechanical communication through the force of the rigid space (Tofan et al. 1995).

In the specific case of planar bars (without torsion), the local base is positive, where $\mathbf{FR} = [\mathbf{t} \ \mathbf{n} \ \mathbf{k}]$ and the relation (1) will be reduced to:

$$DE = \backslash \frac{1}{EA_t} \frac{1}{GA_n} \frac{1}{EI_z} \backslash \cdot ds \tag{4}$$

Considering bending the main strain, the first two components of the elongation and shearing will be neglected, so that the bending flexibility associated to element \mathbf{EI} has activated only one diagonal component, Eq. (4).

We will employ the numerical applications developed through the software MathCAD. We will use the homogeneous screws' representation for linear displacement and force, and Eqs. (5) for planar circular arcs. Superimposing the relative elementary displacements screws $\hat{\delta \mathbf{e}}$ is done in a global reference system. This composition will connect the displacement of the \mathbf{EI} elements series and the relative displacement of the rigid attached to the end "1" with respect to the rigid from the end "0", Fig. 2.

$$\hat{\delta \mathbf{e}} = \left\{ \begin{matrix} \delta \mathbf{e} \\ r \cdot d\mathbf{q}_z \end{matrix} \right\}, \quad \hat{\mathbf{F}}\mathbf{l} = \left\{ \begin{matrix} \mathbf{F} \\ \frac{M_z}{r} \end{matrix} \right\}, \quad \mathbf{DE} = \begin{bmatrix} 0 & 0 & 0 \\ 0 & 0 & 0 \\ 0 & 0 & \frac{r^3}{E I_z} \end{bmatrix} \cdot ds \quad (5)$$

By setting \mathbf{TD}_{Or} as the linear transformation of the displacement screw at the tip of vector \mathbf{r} in pole O , we can define the image of the rigid displacement screw induced by the screw of \mathbf{r} in O ,

$$\hat{\delta \mathbf{e}}_O = \mathbf{TD}_{Or} \cdot \hat{\delta \mathbf{e}}_r, \quad \mathbf{TD}_{Or} = \begin{bmatrix} \mathbf{E}(3) & \tilde{\mathbf{r}} \\ \mathbf{0} & \mathbf{E}(3) \end{bmatrix}, \quad \mathbf{E}(3) = \text{identity}(3), \quad (6)$$

where $\tilde{\mathbf{r}}$ is the product vector attached to the positioning of the $d\theta$ as elementary rotation vector along the axis.

Similarly the transformation of \mathbf{TF}_{rO} is introduced based on the torque theorem and it conveys the force screw applied in O to the section in the tip of vector \mathbf{r} .

$$\hat{\mathbf{F}}\mathbf{l}_r = \mathbf{TF}_{rO} \cdot \hat{\mathbf{F}}\mathbf{l}_O, \quad \mathbf{TF}_{rO} = \begin{bmatrix} \mathbf{E}(3) & \mathbf{0} \\ \tilde{\mathbf{r}} & \mathbf{E}(3) \end{bmatrix} = \mathbf{TD}_{Or}^T \quad (7)$$

In the Sommerfeld sense, the duality of the screws works at a translation level and insures invariance of the elementary mechanical work:

$$\hat{\mathbf{F}}\mathbf{l}_r^T \cdot \hat{\delta \mathbf{e}}_r = \hat{\mathbf{F}}\mathbf{l}_O^T \cdot \hat{\delta \mathbf{e}}_O = \delta L \rightarrow \mathbf{TF}_{rO}^T \cdot \mathbf{TD}_{rO} = \mathbf{E}(6) \quad (8)$$

The image of the constitutive local law in the global reference system, Eq. (2), results from the rotation of the local base \mathbf{FR} due to active translations in the global reference.

$$\begin{aligned} \hat{\delta \mathbf{e}}_O &= \mathbf{TD}_{Or} \cdot [\mathbf{R}(\mathbf{r})] \cdot \mathbf{DE} \cdot (\mathbf{TD}_{Or} \cdot [\mathbf{R}(\mathbf{r})])^T \cdot \hat{\mathbf{F}}\mathbf{l}_O, \\ [\mathbf{R}(\mathbf{r})] &= [\mathbf{FR}(\mathbf{r})] = \begin{bmatrix} [\mathbf{FR}(\mathbf{r})] & \mathbf{0} \\ \mathbf{0} & [\mathbf{FR}(\mathbf{r})] \end{bmatrix}. \end{aligned} \quad (9)$$

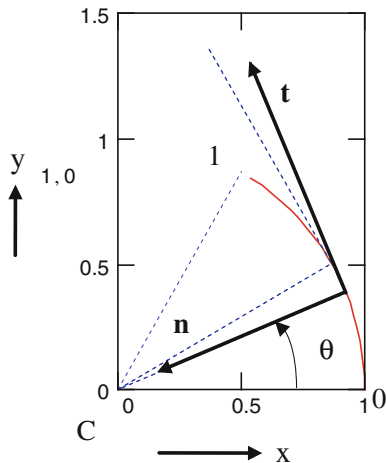
According to the sequence imported from MathCAD Fig. 3, the total flexibility of the curved plate spring corresponds to a half angle $\alpha = \pi/6$ at pure bent form, and is defined by the translation operator, $\mathbf{TD}(\theta)$, in the current position O ,

$$\mathbf{TD}(\theta) = \begin{bmatrix} 1 & 0 & -s(\theta) \\ 0 & 1 & c(\theta) \\ 0 & 0 & 1 \end{bmatrix}, \quad (10)$$

$$\text{where : } c(\theta) \underline{\underline{=}} \cos(\theta), \quad s(\theta) \underline{\underline{=}} \sin(\theta),$$

which supports the rotation θ around the normal vector \mathbf{n} of the Frenet base in respect to the global reference system:

Fig. 3 The MathCAD model for the curved plate springs element



$$\mathbf{R}(\theta) = \begin{bmatrix} c(\theta) & -s(\theta) & 0 \\ s(\theta) & c(\theta) & 0 \\ 0 & 0 & 1 \end{bmatrix}. \tag{11}$$

The variables from the MathCAD sequence are dimensionless and they are r^3/EI_z excepted. By integration of the elementary flexibility \mathbf{D} from relation (5), the analytical representation of the flexibility matrix will be:

$$\mathbf{Dcc}(\alpha) = \int_0^{2\cdot\alpha} \mathbf{TD}(\theta) \cdot \mathbf{R}(\theta + \frac{\pi}{2}) \cdot \mathbf{D}(\theta) \cdot \mathbf{R}(\theta + \frac{\pi}{2})^T \cdot \mathbf{TD}(\theta)^T ds, \tag{12}$$

$$\mathbf{Dcc}(\alpha) = \begin{bmatrix} \alpha - \frac{s(4\alpha)}{4} & \frac{s(2\alpha)^2}{2} & 1 - c(2\alpha) \\ \text{SIMM} & \alpha + \frac{s(4\alpha)}{4} & -s(2\alpha) \\ \text{SIMM} & & 2\alpha \end{bmatrix} \rightarrow \mathbf{Dcc}(\frac{\pi}{6}) = \begin{bmatrix} 0.307 & -0.375 & -0.5 \\ \text{SIMM} & 0.74 & 0.866 \\ \text{SIMM} & & 1.047 \end{bmatrix}.$$

The two indexes of \mathbf{Dcc} flexibility marks:

- The first point of displacement on the rigid attached to the end 1
- The point of loading force on the same rigid.

We note the fact that in the flexibility representation from relation (12) there is only the component that amplifies the uniformly distributed flexibility of arc bending, r^3/EI . The application for the curved plate spring is developed for the elastic element made by two arcs with equal central angles $2\alpha = \pi/3$, $(0 - a; a - b)$. The first plate spring segment is fix in 0, the second plate spring is extended in b using a straight bar element $(b - c)$.

Fig. 4 Curved plate spring radius $r_{al} = 1$

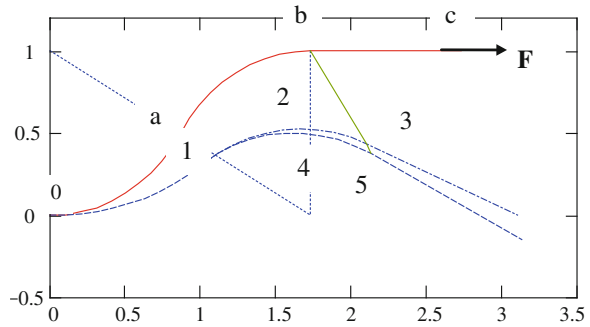
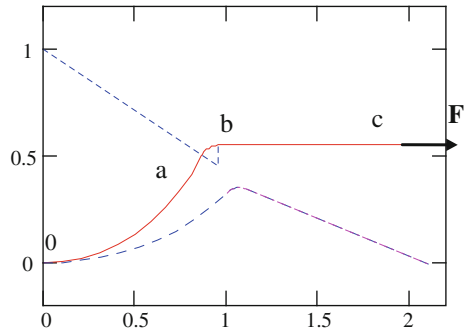


Fig. 5 Curved plate spring radius $r_{al} = 1/10$



Figures 4 and 5 represents the deformed structures for different geometry of the curved plate spring under applied horizontal force, $\mathbf{F} = F \mathbf{i}$ in the endpoint c. This superposition can be observed in the following results from Math CAD sequence (13):

$$\begin{aligned}
 D_{33} &= \begin{pmatrix} 0.173 & -0.62 & -0.394 \\ -0.62 & 2.35 & 1.546 \\ 0.394 & 1.546 & 1.048 \end{pmatrix} & K_{33} &= D_{33}^{-1} & K_{33} &= \begin{pmatrix} 284.99 & 160.48 & -129.609 \\ 160.48 & 104.981 & -94.542 \\ -129.609 & -94.542 & 91.7 \end{pmatrix} \\
 K_{3j} &= (D_{33_{0j}})^{-1} & K_{330} &= \begin{pmatrix} 248.99 \\ 160.48 \\ -129.609 \end{pmatrix} & K_3 &= \begin{pmatrix} 5.77 \\ -1.613 \\ -2.538 \end{pmatrix} & K_3 &= \begin{pmatrix} 5.77 \\ -1.613 \\ -2.538 \end{pmatrix} \times EI/r_0^3
 \end{aligned}
 \tag{13}$$

The numerical example shows the feasibility of the proposed mathematical model to predict the flexible element behavior as a subcomponent of flexible couplings. Also, it highlights the suitable practical solutions for the assembly as a flexible coupling between random axes.

The FEA results using specialized programs (e.g. NASTRAN, Fig. 1) did not satisfy the curved plate spring behavior research objectives. Constrains induced by these specialized softwares were overcome by creating a more flexible mathematical model using MathCAD. The proposed model allows for obtaining consistent results and easy transition between small and large displacements as well as a better approximation of the non-linear elastic structure response.

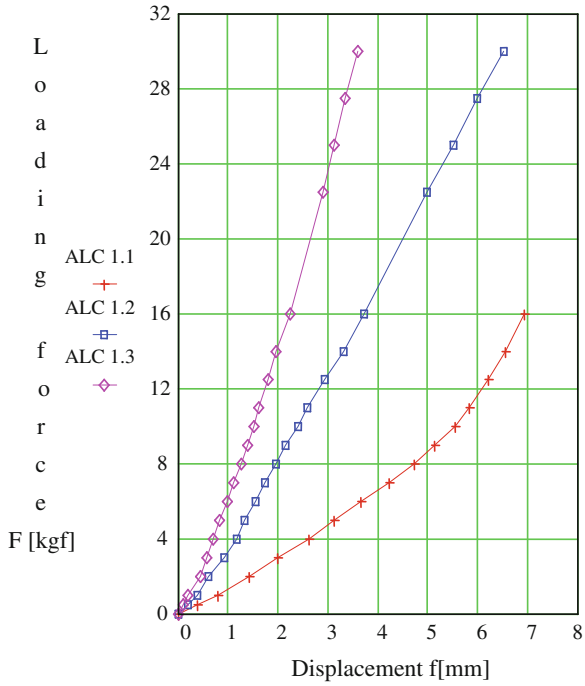


Fig. 6 Curved plate spring radius

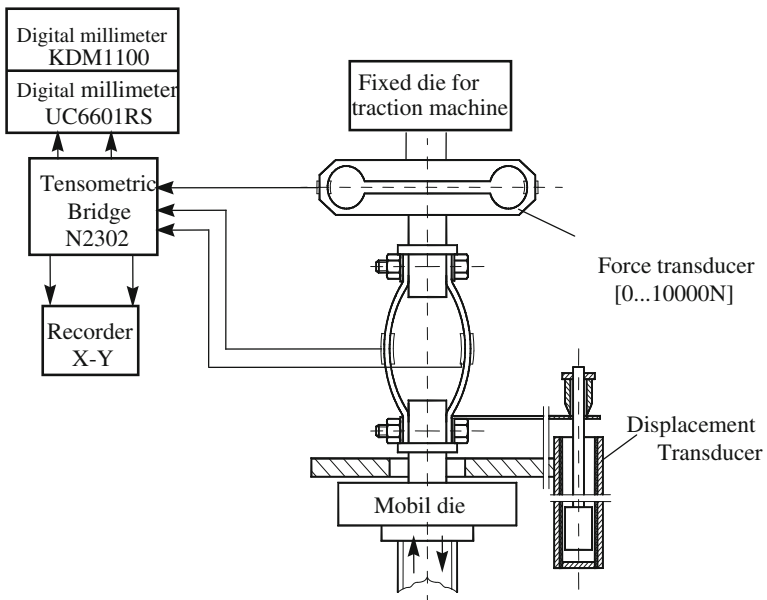


Fig. 7 The block diagram of the bench test installation

3 Bench Test Results

In Fig. 6 is represented the elastic characteristic for the curved plate springs from bench test experiments.

In Fig. 7 is represented the block diagram of the bench test equipment used to estimate the stress level and the elastic characteristic for the curved plate springs.

The *stress–deformation* transducer *TER* was attached to the curved plate springs to record the stress level for the most deformed spring segment. The correlation of loading force F [kgf] and the elastic deformation f [mm] is highlighted in the Fig. 6 by the points collected on the bench test for different curved spring plates geometry (type ALC1.1, ALC1.2 and ALC1.3).

The loading–unloading structure was performed using a traction machine type AWPMA.

4 Conclusion

- To the best of our knowledge, this is first time when the integral flexibility of the curved plate springs used as coupling element was estimated.
- For high curved plate radius $r_{a1} = 1$:
 - the spring segment (a c) is displaced as rigid following the blue-dot line (1–2–3)
 - the spring segment (a–c) is displaced as an elastic element following the blue dashed line (1–4–5), slightly different due to the elastic deformation of the (a–b) segment.
- For the small radius of the curved plate spring, ($r_{a1} = 1/10$), the sector is stiffened and the elastic displacement disappears. The linear element (a–c) in the small displacements case, is not bent.

The application with the results comprised within the limits of the small displacements is a challenge for further expanded study. Only a representation in large displacements can approximate the image of the non-linear response, the one on which the dynamic response of the coupling endowed with such elements can develop.

References

- Courbon J (1971) Calcul des structures (in French). Dunod, Paris
- Draghici I et al (1978) Coupling systems design (in Romanian). Ed. Tehnica, Bucuresti
- Draghici I et al (1983) Machine elements (in Romanian), vol 3 (in Romanian). Ed. Universitatii din Brasov

- Gafitanu M et al (1983) Machine elements (in Romanian). Ed. Tehnica, Bucuresti, ISBN 973-31-1400-6
- Jula A et al (1989) Machine elements, vol 2 (in Romanian). Ed. Universitatii din Brasov
- Silveira RAM, Nogueira CL, Goncalves PB (2013) A numerical approach for equilibrium and stability analysis of slender arches and rings under contact constrains. Int J Solids Struct 50(1):147–159
- Tofan M et al. (1995) Deformed structures (in Romanian). Ed. LUX LIBRIS, Brasov

Study of the Motion of Random Axes Using the Coupling with Curved Plate Springs

Hariton Poparad

Abstract This paper presents the results of the modeling of an elastic shaft as an equivalent to a flexible coupling between two random axes using FEM. Calculus models are presented for the distorted structures of the elastic elements of two couplings—the universal coupling, known as the cardan joint, and the coupling with curved plate springs disposed on the contour.

Keywords Coupling · Elastic structure · Curved springs · FEM

1 Introduction

An elastic coupling performs transmission of the power between two random axes and suffers structural elastic deformations which simulate what a hypoid rigid gear achieves through rolling with slipping motion (Draghici 1983; Tofan 1995). The behaviour of the elastic coupling is in fact the same as the behaviour of a flexible element complexly stressed, subjected not only to torsion but also to bending, shearing and tension as shown in Fig. 1.

The elastic coupling changes the uniform rotation of the input shaft into a non-uniform rotation of the output shaft. The coupling is loaded only in the point 0 and 1, connecting nodes to the two fixed random axes. The equilibrium of this connecting sub-system is described in equations:

$$\begin{aligned}\hat{\mathbf{F}}_0 + \mathbf{TF}_{01} \cdot \hat{\mathbf{F}}_1 &= \hat{\mathbf{0}}_0, \\ -\mathbf{TF}_{10} \cdot \hat{\mathbf{F}}_0 - \hat{\mathbf{F}}_1 &= \hat{\mathbf{0}}_1,\end{aligned}\tag{1}$$

H. Poparad (✉)

Transilvania University of Braşov, 29 Eroilor Bvd 500036 Braşov, Romania
e-mail: Hariton.paparad@unitbv.ro

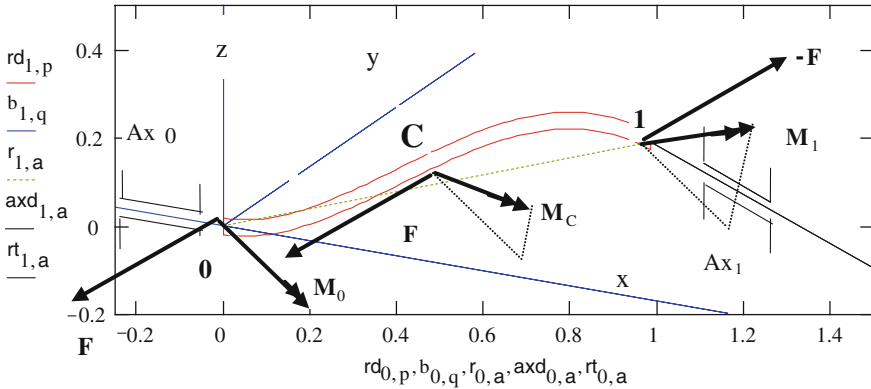


Fig. 1 The elastic image of the coupling as a flexible element complexly stressed: A_{x_0} —input shaft; A_{x_1} —output shaft; C —flexible element loaded in node 0 and 1 by force \mathbf{F} and torque \mathbf{M}

and by the equilibrium of the two force screws in a pole C , respectively:

$$\mathbf{TF}_{C0} \cdot \hat{\mathbf{F}}_0 + \mathbf{TF}_{C1} \cdot \hat{\mathbf{F}}_1 = \hat{\mathbf{0}}_c \tag{2}$$

\mathbf{TF}_{01} represents the translation operator of the force screw $\hat{\mathbf{F}}_1$ from point 1 to 0

$$\mathbf{TF}_{01} = \begin{bmatrix} \mathbf{E} & \mathbf{0} \\ \tilde{\mathbf{r}}_1 - \tilde{\mathbf{r}}_0 & \mathbf{E} \end{bmatrix}, \mathbf{E} = \mathbf{identity}(3), \tilde{\mathbf{r}}_1 - \tilde{\mathbf{r}}_0 \underline{\underline{\tilde{\mathbf{01}}}} = (\mathbf{r}_1 - \mathbf{r}_0)x, \tag{3}$$

with the sign Tilde (\sim) denoting the non-symmetrical positioning operator (the vectorial product). The dynamic equilibrium of the coupling is more complex, involving terms of inertia and considering offsets (Khanlo 2013).

The two screws in static equilibrium are decomposed in local bases \mathbf{R}_i , which are associated to the endings in all 6 coordinates of which only one represents the torque of the transmission (Tofan 1995).

$$\hat{\mathbf{f}}_i = \left\{ \begin{matrix} \mathbf{f} \\ \mathbf{m} \end{matrix} \right\}_i = \begin{bmatrix} \mathbf{R} & \mathbf{0} \\ \mathbf{0} & \mathbf{R} \end{bmatrix}_i^T \cdot \left\{ \begin{matrix} \mathbf{F} \\ \mathbf{M} \end{matrix} \right\}_i, \quad i = 0..1, \tag{4}$$

In the linear simulation, the transversal components are linear in the instantaneous image of the offsetting coordinates and also in the one caused by the axial load due to torsion.

The study of the distorted structure response is very complex. The first experience in which we used 3D binodal elastic elements for models, yielded the conclusion that even at static equilibrium, simplifications will significantly alter the results, which will lead to loss of stability and even significance.

2 Model of the Couplings with Binodal Elements

The properties of the flexible couplings are defined by the torsion rigidity parameter, which determines the input and the output shaft rotation angle φ_n at applied torsion M_n (Draghici 1978). With this in consideration, Fig. 2 presents the components of the flexible coupling with curved plate springs.

Figure 3 shows two models of couplings with binodal constitutive elements developed using MathCAD software. We have employed the simplest elements, proving their sufficiency in the assembled structures, which are homomorphous with the analysed couplings. They help to immediately establish the accurate forces in the joints and to develop the elastic image of these couplings. Yet, their reaction in terms of displacements remains at the qualitative level, as a first approximation.

The binodal element used is a cylindrically symmetric **BEAM**. In addition, another **BEAM** element was employed as the special curved plate element to which bending and traction stresses were applied by linking a series of three elements (curved and straight bars) within a single element (Mogan 2007).

The universal coupling model has a planar input fork with 5 elements, supporting elastic elements 3 and 4, restrained in central node 4, as the the universal joint cross origin.

The curved plate on the countor coupling has the same input shaft incident in nodes 3 and 5. The elastic connection with the output fork blocked in nodes 4 and 6 is achieved by the four elastic elements 3 through 6 placed on the contour. The plane yOz was chosen to make the connection between the two shafts. For the universal coupling, the incidence of the input shaft in nodes 3 and 5, will be achieved by a finite rotation of angle β_0 around the Oy axis, which is compatible with the kinematic coupling in nodes 3 and 5. Similarly, the finite rotation β_1 of the secondary shaft around the Oz axis is compatible with the kinematic coupling in the cross vertical elements.

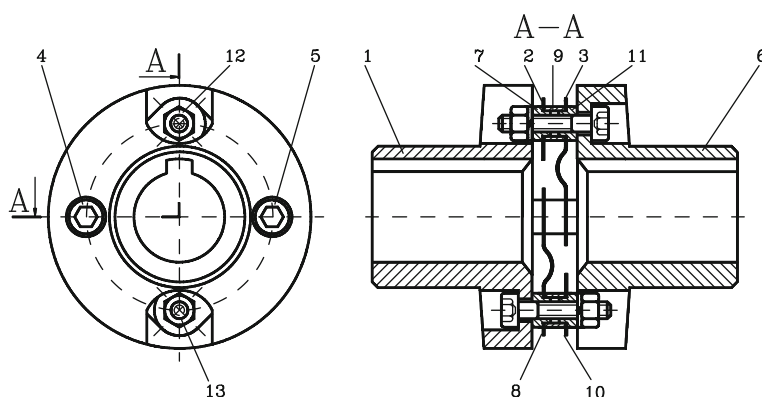


Fig. 2 Flexible coupling with curved plate springs geometry: 1—input shaft; 2, 3, 8, 10—curved plate springs; 6—output shaft; 4, 5, 12, 13—bolt; 7, 11, 9—spacer

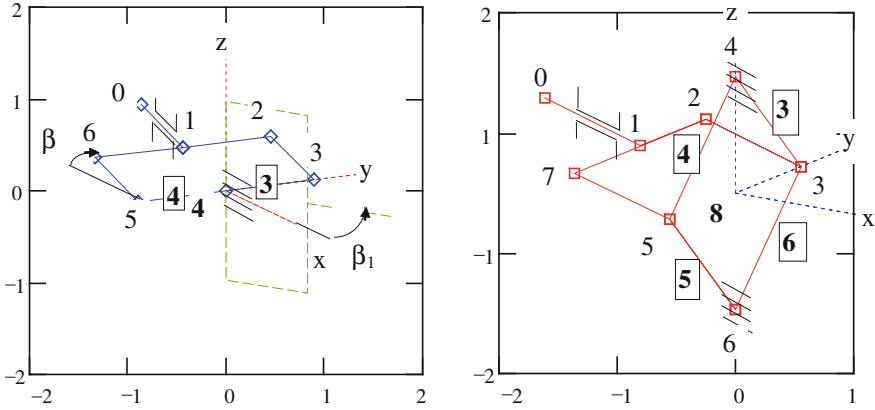


Fig. 3 Input models for the universal coupling (3 and 4 flexible elements), and curved plate springs coupling (3, 4, 5, 6 flexible elements)

For the curved plate on counter coupling, the incidence of the input fork around nodes 3 and 5 axis of β_0 elementary angle and that of the exit fork are achieved through the elastical rotation of the elementary rotation of angle β_1 around the axis of nodes 4 and 6.

By developing an analysis on this class of models, we can directly project images of the disorted coupling structures. The distorted structure of the universal coupling was plotted in Fig. 4, by blocking exit node1's six degrees of freedom. The applied load of the coupling will be introduced in input node 0, either by torque M_0 , or by elementary rotation θ_0 , on the input axis direction by blocking the other coordinates corresponding to the input node. Thus, the similitude of the retransmission of both loading modes is confirmed.

The similar distorted states of the couplings with elastic elements on the contour are presented in the Fig. 5.

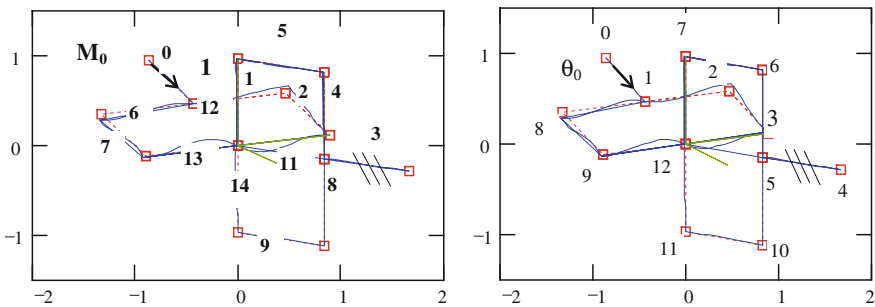


Fig. 4 The model of deformed universal coupling

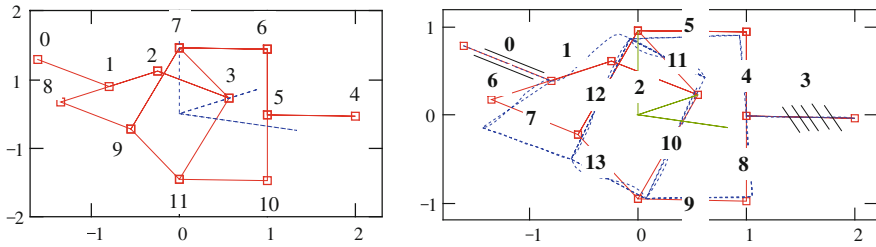


Fig. 5 MathCAD model for deformed curved plate spring coupling

The analysis, conducted on the coupling of Fig. 5, was carried out by blocking the nodes corresponding to the last element of the exit fork (i.e. element 3) and introducing the load through the input torque on the direction of element 0. The nodal displacements (the base of the performed representations) and subsequently the internal and external linking forces were established. **BEAM** elements were placed on this structure's incident by enclosure in afferent nodes. A coupling with ball jointed elements will be analyzed likewise, using **TRUSS** elements (Mogan 2007; Tofan 1995).

The introduction of the freedom specific to the kinematic couples of the universal coupling in Fig. 4, the slip in node 3 and 7, and the torsion unloading of the cross elements were all achieved by cancelling the rigidity associated with the degree of freedom of the element compatible with the kinematic couple. In order to maintain the degree of mobility released in the unloaded couple, there exists a coupling operator that is adequate for every existing kinematic link.

Figure 6 presents a special element, the curved plate spring with a non-linear (NL) characteristic, locally linearized by rigidity **KS**. This element generates a strong joining of tension and bending stresses.

The study associated with this special element is completely developed on FEM in the reduced models below.

3 Reduced Models

Considering the rigid forks, we reduce the coupling only to its own linking elements between the two axes: the cross for universal coupling and the contour for the coupling with spring plates, Fig. 7.

By introducing into the nodes of the two forks the rigid displacements induced in the coupling origin and eliminating the static condensation node O of the universal coupling, the rigidities of the elastic coupling between the two rigid shafts written in C can be obtained directly.

We introduce the rigid movements by translation **TC**, built as a dual operator for the translation operator of force screw **TF**, Eq. (3), conducting in the Sommerfeld sense.

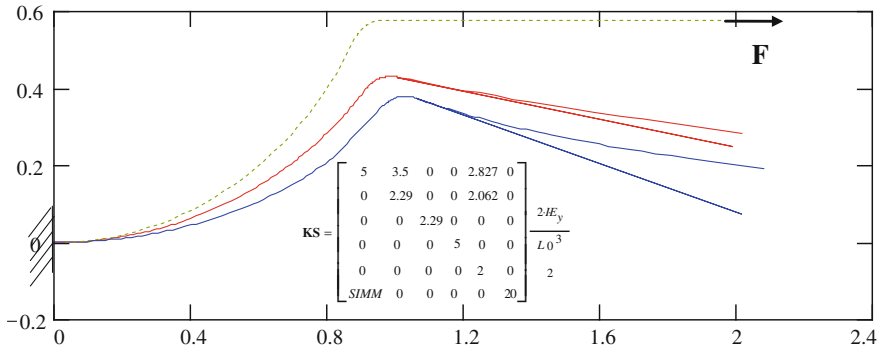


Fig. 6 The curved spring plate with a nonlinear characteristic and **KS** rigidity

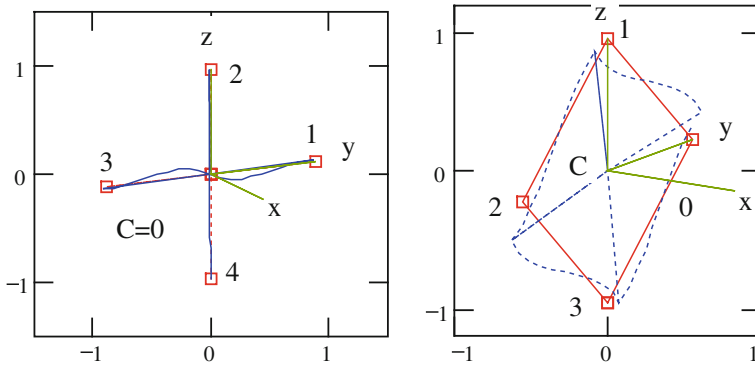


Fig. 7 Reduced models to the flexible elements

$$\mathbf{TC} = \begin{bmatrix} \mathbf{EE} & 0 & 0 \\ 0 & \mathbf{TD}_{C0} & 0 \\ 0 & 0 & \mathbf{TD}_{C1} \\ 0 & \mathbf{TD}_{C2} & 0 \\ 0 & 0 & \mathbf{TD}_{C3} \end{bmatrix} \cdot \begin{Bmatrix} \hat{\delta}_0 \\ \hat{\delta}_1 \\ \hat{\delta}_2 \end{Bmatrix}, \mathbf{K1} = \mathbf{TC}^T \cdot \mathbf{K} \cdot \mathbf{TC}, \quad (5)$$

K is the rigidity of the assembled cross elements through positional incidence. The expanded incidence Σ matrix is for the universal coupling from the Fig. 8 (the expansion of the identical matrix 4×4 with the connecting line of the 4 elements to node 0 to the origin of the cross).

The rigidity matrix **K11** (12,12) results from eliminating the unloaded node **O** \equiv **C** as the structural origin of the universal coupling cross. This is the equivalence of the elastic link between the two rigid crosses, both having the dual displacement screws $\delta_{i,i} = 1, 2$, (Tofan 1995).

$$\hat{\delta}_i = \{ \delta^T \quad \theta^T \}_i = \{ u \quad v \quad w \quad \theta_x \quad \theta_y \quad \theta_z \}_i^T, \tag{6}$$

In global reference, the translation is represented at top and the generator of rotator at bottom Eq. (6). The elementary displacement δ is naturally decomposed in the oblique base $\{\mathbf{a}_0, \mathbf{a}_1, \mathbf{a}_0 \times \mathbf{a}_1\}$, built on the versors of the input and respectively output axes. If the two axes are not aligned, the term $\delta_n \neq \mathbf{0}$ will describe the directory circle in the transversal plane, which is orthogonal on the input axis \mathbf{a}_0 in the relative motion with respect to the reference system fixed on the input fork. It is clear that the center of the flexible cross is no longer a fixed point with respect to this reference system, although it remains fixed in the absolute system.

The rigidity matrix **K11** is built as a singular matrix, and it has in fact the representations of the two responses associated to the coupling as an unloaded rigid. By extracting the first diagonal cell (6,6) we identify the rigidity of the elastic link of the input shaft to the fixed output shaft **KEC** from relation (7), regardless of the uniform bending rigidity factor 2 ($E \cdot I_y/L^3$).

The diagonal structure should not surprise us, because the origin **C** coincides with the *elastic center*, and the global reference system is *principal* to the coupling rigidity along which the flexibility is uniformly distributed. We find also the compatibility with rotations θ_y, θ_z , in convergence with the universal coupling in the finite as observed in the elementary reference system.

Rigidity is the elastic operator in the screw space, and is the one kept in **KE**, as shown in relation (7).

$$\mathbf{KEC} = \begin{bmatrix} 6 & 0 & 0 & 0 & 0 & 0 \\ 0 & 9.7 & 0 & 0 & 0 & 0 \\ 0 & 0 & 9.7 & 0 & 0 & 0 \\ 0 & 0 & 0 & 2 & 0 & 0 \\ 0 & 0 & 0 & 0 & 0 & 0 \\ 0 & 0 & 0 & 0 & 0 & 0 \end{bmatrix}, \quad \mathbf{KE} = \begin{bmatrix} 6 & 0 & 0 & 0 \\ 0 & 9.7 & 0 & 0 \\ 0 & 0 & 9.7 & 0 \\ 0 & 0 & 0 & 2 \end{bmatrix}. \tag{7}$$

Relation (8) highlights the matrix of rigidity for elements in which compatibility was achieved to link the spherical joints.

$$\mathbf{Ke}(0, 1) = \begin{bmatrix} 0 & 0 & 0 & 0 & 0 & 0 \\ 0 & 6 & 0 & 0 & 0 & 3 \\ 0 & 0 & 6 & 0 & -3 & 0 \\ 0 & 0 & 0 & 0 & 0 & 0 \\ 0 & 0 & -3 & 0 & 2 & 0 \\ 0 & 3 & 0 & 0 & 0 & 2 \end{bmatrix}, \quad \mathbf{Ke}(2, 3) = \begin{bmatrix} 50 & 0 & 0 & 0 & 0 & 0 \\ 0 & 6 & 0 & 0 & 0 & 3 \\ 0 & 0 & 6 & 0 & -3 & 0 \\ 0 & 0 & 0 & 0 & 0 & 0 \\ 0 & 0 & -3 & 0 & 2 & 0 \\ 0 & 3 & 0 & 0 & 0 & 2 \end{bmatrix}, \tag{8}$$

The coupling with standard **BEAM** elements displayed on the contour is very rigid due to the dominant tension–compression stress (8).

$$\mathbf{KL}(0) = \begin{bmatrix} 50 & 0 & 0 & 0 & 0 & 0 \\ 0 & 6 & 0 & 0 & 0 & 3 \\ 0 & 0 & 6 & 0 & -3 & 0 \\ 0 & 0 & 0 & 0.386 & 0 & 0 \\ 0 & 0 & -3 & 0 & 2 & 0 \\ 0 & 3 & 0 & 0 & 0 & 2 \end{bmatrix}, \tag{9}$$

$$\mathbf{KE} = \begin{bmatrix} 24 & 0 & 0 & 0 & 0 & 0 \\ 0 & 112 & 0 & 0 & 0 & 0 \\ 0 & 0 & 112 & 0 & 0 & 0 \\ 0 & 0 & 0 & 103 & 0 & 0 \\ 0 & 0 & 0 & 0 & 8 & 0 \\ 0 & 0 & 0 & 0 & 0 & 8 \end{bmatrix}.$$

The flexibility achieved by using the curve plate element will introduce the traction and bending stresses, and will increase the tension of the tangent flexibility as showed in relation (9). But, this increased tangent flexibility is not sufficient for the flexibility required by the system!

$$\mathbf{KL}(0) = \begin{bmatrix} 5 & 0 & 0 & 0 & 2.8 & 0 \\ 0 & 6 & 0 & 0 & 2 & 3 \\ 0 & 0 & 6 & 0 & 0 & 0 \\ 0 & 0 & 0 & 0.5 & 0 & 0 \\ 2.8 & 2 & 0 & 0 & 2 & 0 \\ 0 & 3 & 0 & 0 & 0 & 20 \end{bmatrix}, \tag{10}$$

$$\mathbf{KE} = \begin{bmatrix} 24 & 0 & 0 & 0 & 0 & 0 \\ 0 & 22 & 0 & 0 & 0 & 0 \\ 0 & 0 & 22 & 0 & 0 & 0 \\ 0 & 0 & 0 & 14 & 0 & 0 \\ 0 & 0 & 0 & 0 & 44 & 0 \\ 0 & 0 & 0 & 0 & 0 & 44 \end{bmatrix}.$$

The equivalent rigidity in \mathbf{C} , as the origin of the coupling with elastic curved plate elements is reduced to the Jordan quasi-diagonal canonic form. The associated shaft has no elastic center in the real.

The numerical example shows the feasibility of the proposed mathematical model in order to predict the flexible coupling with curved plate springs behavior for practical solutions for the assemblies between random axes. The FEM results' using specialized programs sows limitations. Constrains induced by these specialized softwares were overcome by creating a more consistent and flexible mathematical model presented in this paper.

4 Conclusion

In conclusion, we state that:

- To the best of the authors' knowledge, no work has been presented on coupling modeling with curved plate springs behavior performing transmission of the power between random axes.
- In this work the four elastic curved plate springs of the coupling were simulated as equivalent elastic shafts.
- The equivalent shaft of the universal coupling is perfectly flexible, finitely torsional, and flexible in axial and cross offsetting.
- The shaft associated with the coupling with elastic curved plate elements displayed on the contour is finitely flexible on any direction of the offsetting screw, with a crooked curve as a distorted version permanently coupled with torsion and tension.
- The wise technical solution is the one with two couplings, with a free connecting shaft it allows for axial pumping.
- If technical reasons impose the use of a single elastic couple, the limits of the offsetting's support by this couplings must be known, or the coupling must be dimensioned to take over known offsetting. In these cases the elastic shaft attached to the coupling becomes an instrument for analysis.
- The analysis is not fully completed. The model has only instantaneous positional applicability. The attached shaft varies with the relative position of the shafts along a rotation, and a dynamic study offers a more complex understanding.

References

- Draghici I (1978) Coupling systems design. Tehnica, Bucuresti (in Romanian)
- Draghici I (1983) Machine elements, vol 3. Universitatii din Brasov, Brasov (in Romanian)
- Khanlo HM (2013) The effects of lateral–torsional coupling on the nonlinear dynamic behavior of a rotating continuous flexible shaft–disk system with rub–impact. Communications in Nonlinear Science and Numerical Simulation 18(6):1524–1538 (Science Direct. Web)
- Mogan G (2007) The analyses with finite element in engineering domain. Universitatii Transilvania, Brasov (in Romanian). ISBN 978-973-589-154-4
- Tofan M (1995) Deformed structures. LUX LIBRIS, Brasov (in Romanian). ISBN 948-973-635-659-9

Scanners with Risley Prisms: Modelling with Mechanical Design Programs

A. Schitea, I. Kaposta, M. Tuef, S.-C. Jurca and V.-F. Duma

Abstract Opto-mechanical scanners with Risley prisms (double optical wedges) are one of the most used scanning systems for applications that range from micro-mechanical endoscope probes to large optics for satellite positioning. The paper presents an exact modelling of the scan patterns produced using such systems, in a dedicated program for mechanical design—CATIA V5R20. This approach utilizes the characteristic parameters of scanners with Risley prisms: the ratio of the rotation velocities of the two wedges $M = \omega_2/\omega_1$ and the ratio of their apex $k = \theta_2/\theta_1$. The advantages of this method with regard to analytical solutions and with regard to approximate methods are pointed out. The similarities of this exact modelling of this type of scanners with the theory of mechanisms are highlighted. An experimental part validates the theoretical results. Driving solutions at the precision level required by these devices are presented.

Keywords Optomechatronics · Mechatronics · Scanners · Risley prisms · Modeling · Simulations · Experiments · Constructive solutions

1 Introduction

Optomechatronics is a blend of Optics and Mechatronics, the latter being itself a mixture of Mechanical, Electrical Engineering and IT. Laser scanners (Bass 1995; Marshall 1999) are one of the main devices approached in Optomechatronics, as they imply all these multi-disciplinary aspects.

A. Schitea · I. Kaposta · M. Tuef · V.-F. Duma (✉)
Aurel Vlaicu University of Arad, Arad, Romania
e-mail: duma.virgil@osamember.org

S.-C. Jurca
S.C. OK Tehnic Consult S.R.L, Arad, Romania

There are several types of scanners in use nowadays, while others, developed in the last 4 decades, are only utilized for niche applications. The most important laser scanners are thus (Marshall 1999): galvanometer (GS) (Duma 2001, 2009; Duma et al. 2011; Marshall 2004; Montague 2003), polygonal (Duma 2001; Marshall 1999), refractive (Cheng and Chang 1998; Duma and Nicolov 2009; Garcia-Torales et al. 2002, 2007; Kaposta et al. 2012; Li et al. 2003; Li 2011a, b; Marshall 1999, 2004; Rosell 1960; Warger and DiMarzio 2007; Yang 2008), holographic, acousto- and electro-optical. Their applications range (Bass 1995) from commercial (e.g., barcode scanning) to industrial (e.g., for dimensional measurements (Duma 2001)), and to high-end biomedical imaging (Duma et al. 2010). For the latter, one of the most dynamic applications is Optical Coherence Tomography (OCT) (Huang et al. 1991; Wojtkowski 2010), for which we have approached different types of scanners that are or may become of interest (Duma et al. 2010), especially GSs and polygons.

OCT is an interferometric technique that has non-destructive imaging capabilities with millimeters depth and micrometer resolution—both for tissue and for non-metallic materials. The different types of OCT (Wojtkowski 2010) benefit nowadays from the development of handheld and endoscope probes, to be able to move the technique from lab to clinic. Other applications of OCT besides the classical imaging of the retina (Podoleanu and Rosen 2008), such as art conservation or dentistry (Sinescu et al. 2008) also require handhelds.

Mostly GSs and Micro-Electrical–Mechanical Systems (MEMS) were applied so far in handhelds. Our approach implies refractive scanners, with Risley prisms, which have the major advantage of a small axial dimension, adjustable scan patterns and the possibility of miniaturization—as off-the-shelf optical prisms with sub-millimeter diameters exist. Their main disadvantage is the complicated scan pattern that has to be followed exactly to reconstruct the image after the lateral scan of the sample—for both handheld and fixed devices (Tao et al. 2010; Warger and DiMarzio 2007). Studies exist on approximate (Marshall 1999) and exact analytical approaches (Li 2011a, b; Yang 2008) to determine these scan patterns. The scope of the present paper is to present our approach to obtain the exact patterns (of the laser spot after the successive refractions in the two prisms) by using general mechanical design programs (Schitea et al. 2013)—in this study, CATIA V5R20. The simulations achieved have been completed by experimental validations and by constructive solutions of the scanning device. Due to space limitation, in this paper only examples of these three aspects will be presented.

2 Scanner with Risley Prisms

In Fig. 1a, b the path of the central laser ray that is refracted in the device with two Risley prisms is presented, for two positions rotated with 180° of the prisms. In Fig. 1b the modeling made in CATIA V5R20 is presented: the direction of the central ray of the laser beam is simulated considering the refraction laws—with the

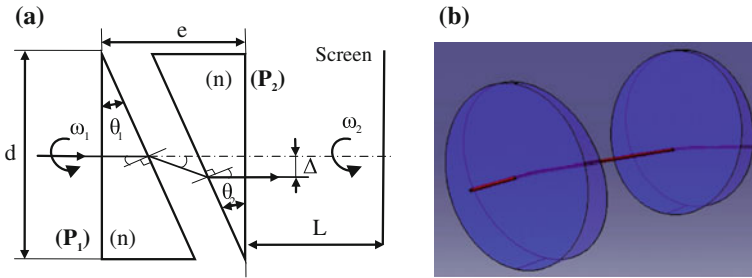


Fig. 1 Scanner with Risley prisms: **a** optical scheme; **b** modeling with CATIA V5R20

refracted ray in the plane determined by the incident ray and by the normal to the specific surface of the prism. The reciprocal movement of the prisms is made in the same or in the opposite sense, with incremental angles that are different to simulate the various rotational speeds ω_1 and ω_2 . The position of the laser spot on a screen situated at an adjustable distance L from Prism 2 is obtained. The prisms are placed with the facets perpendicular on the optical and rotational axis (O.A.) placed on the exterior, at the distance “ e ” from each other. Other configurations, with at least one of these facets on the interior (Li 2011a, b) can also be modelled.

Besides L and e , the constructive parameters of the device are the angles θ_1 , θ_2 of the prisms (which may be identical or not), and the refractive index n (usually identical). With these angles, the parameter $k = \theta_2/\theta_1$ has been defined by Marshall, who studied (Marshall 1999) approximately (as Lissajoux figures) the scan patterns produced by the two prisms—considered as optical wedges, with an approximate deviation $D_i = (n - 1)\theta_i$, $i = 1, 2$. The second parameter is—similar to the Theory of Mechanisms—the ratio $M = \omega_2/\omega_1$ of the two rotational speeds of the prisms, P_1 and P_2 .

3 Modeling of the Scan Patterns

In Fig. 2 an example of such a modeling is presented, for the following pairs of prism angles (on each column): (a) 10° with 6° , (b) 6° with 6° , (c) 4° with 6° , and with two equal but opposite values of M (on each row): (1) $M = 4$ and (2) $M = -4$. For $M > 0$, as k is increased, the trajectory of the beam no longer covers the entire scanned space. It is actually reduced to a circular crown with an increasing circular open space in the centre. While this is convenient for some applications, by example in manufacturing, it may not be favourable in other processes, by example in scanning a sample—in imaging. There are actually several issues that need to be addressed through the modelling of the scan patterns: (1) the area of the outer disc scanned; (2) the area of the inner that is not scanned (which may appear

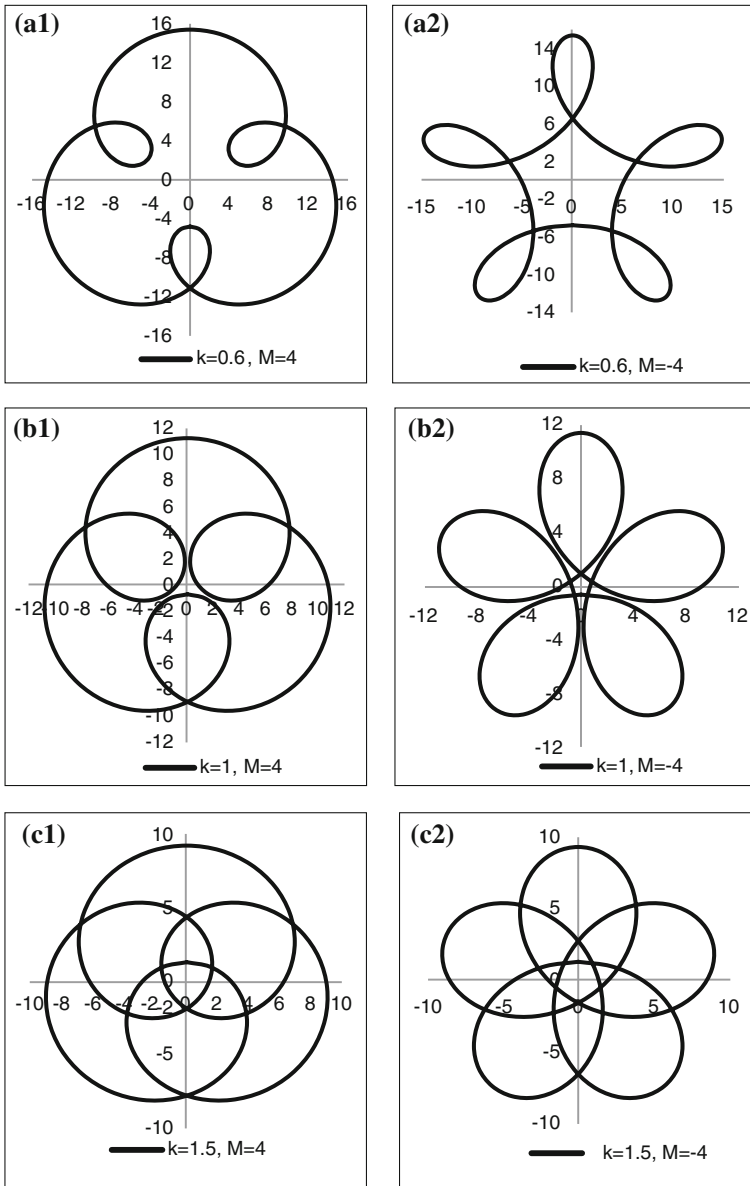


Fig. 2 The modeling of the scan pattern of Risley prisms with CATIA (details in the text)

or not); (3) the density of the scanning paths, which represent a “spatial duty cycle” of the process; (4) the number of intersection points of the path.

One must also take into account that the scanning paths are in reality not simple lines, but curves with a width that depends on the diameter of the laser beam. We

may therefore define a parameter, the cover ratio, that represents the area covered by the scan pattern over the total area (of the circular disc or crown) defined by the envelope of the scan pattern. An entire discussion can be made regarding the process starting with this parameter and with N —the number of intersection points of the scan paths. From the analysis of the patterns, rules-of-thumb may be thus obtained with regard to the requirements of a certain application to derive the parameters of the device: k —therefore the angles θ_1 and θ_2 of the prisms to be used; M —therefore the rotational speeds ω_1 and ω_2 of the prisms.

The distance L influences the diameter of the outer disc—the one that inscribes a pattern. In Fig. 3 a study on L and e is shown—to compare the way the patterns are modified when changing one of these two parameters (while the other remains constant). One may see that the diameter of the outer circle increases proportional with L (for $e = \text{cst.}$), while the diameter of the inner circle increases—but not proportional—with e (for $L = \text{cst.}$).

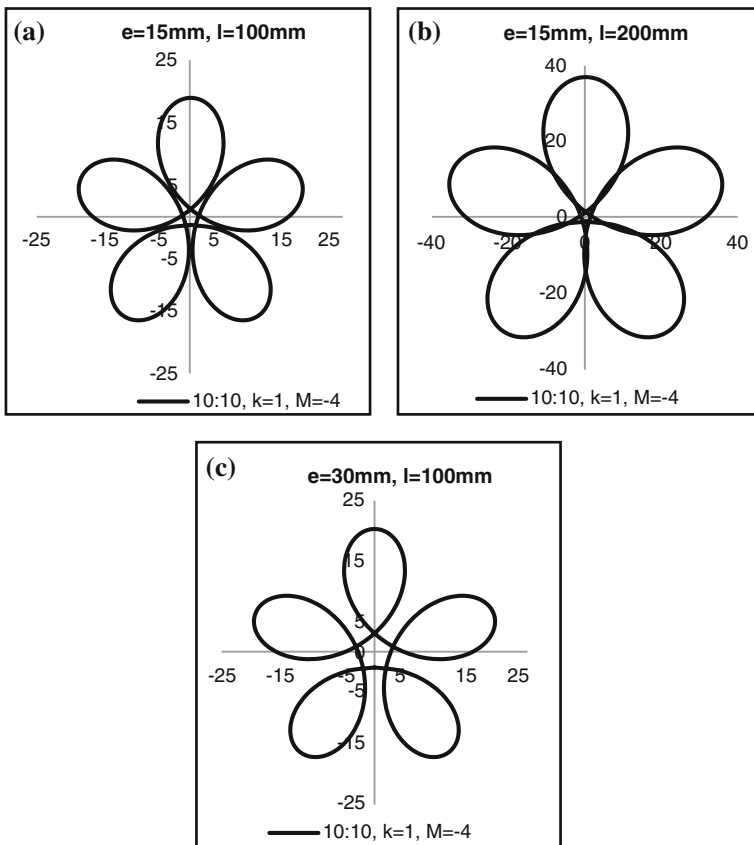


Fig. 3 a Scan pattern for $k = 1$ (identical wedges with the angles of the prisms equal to 10°) and $M = -4 < 0$; b $e = \text{cst.}$ and L is double; c $L = \text{cst.}$ and e is double

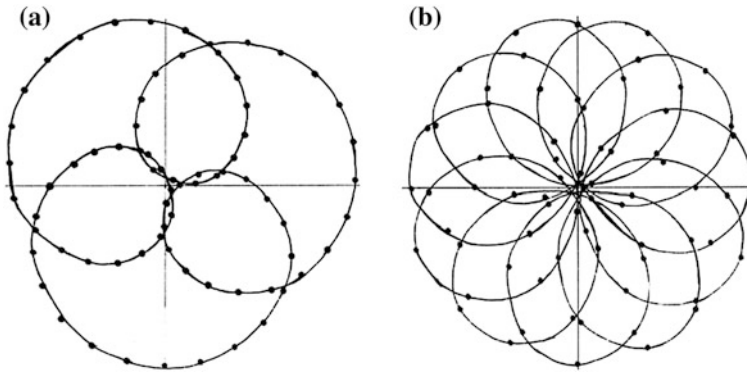


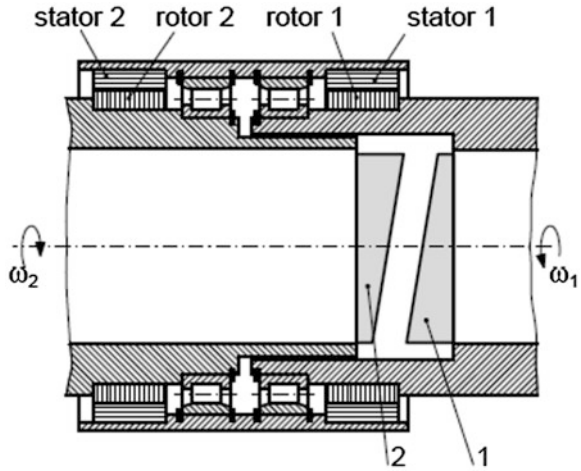
Fig. 4 Experimental scan patterns for $k = 1$ (prisms with 2°) and **(a)** $M = 4$; **(b)** $M = -10$

We made the experimental validations of the modeling presented and obtained a good match. Due to space limitations, in Fig. 4 only two patterns thus obtained are presented—for identical prisms, but for different (and opposite) values of M .

Table 1 Characteristics of some of the possible driving solutions of Risley prisms scanners (Kaposta et al. 2012)

Parameters	Units	Pinions	Worm gears	Harmonic	Synchronous belts
Efficiency	[%]	85	70	82	83
Number of gears	[-]	10	2	2	4
Number of bearings	[-]	14	6	5	6
Contact pressure	[MPa]	350	350	42	–
Number of teeth in the gearing	[-]	7	2	50	–
Dimensions: Height	[mm]	331	584	152	
Length		381	482	252	
Width		331	356	152	
Clearance at twist	[-]	Yes, adjustable	Yes, adjustable	Yes, adjustable	Yes/No adjustable
Positioning error		$<3'$	$<3'$	$<1'$	$<6'$
Theoretical efficiency of the gear	[%]	98	97	97	96
Mass inertia moment of the input shaft	[kg·m ²]	0.01	Dependent on structure	≤ 0.055	Dependent on gear diameter
The working life is limited by	[-]	Teeth rupture	Teeth rupture	Flexible gear	Teeth rupture
Design pattern	[-]	Coaxial	Crossed axes	Coaxial	Crossed axes
Driving moment/Mass	[Nm/kg]	78	120	128	–

Fig. 5 Rotational electric special motor for the precise driving of Risley prisms (Kaposta et al. 2012)



4 Constructive Solutions

There are diverse solutions to drive the two Risley prisms. These aspects depend on the type of relative movement of the prisms [rotation (Li et al. 2003; Li 2011a, b), translation (Duma and Nicolov 2009) or tilt (Li et al. 2003)] and on the dimension of the device: miniaturized (even sub-millimeter)—for endoscopes, or with diameter up to half a meter—for positioning system for satellite monitoring. Table 1 presents the main parameters of the mechanical driving gears used for the new driving systems, highlighting their precision, dimensions and dynamics. All data refer to reduction gears with a $i = 100$ reduction ratio on a reduction step, an input power $P = 1.36$ at an angular speed $\omega_2 = 20$ rad/s. A solution developed (Kaposta et al. 2012) for the precise driving of the prisms is shown in Fig. 5.

5 Conclusions

We presented the modeling we are performing on the scanners with Risley prisms. A few examples of the scan patterns (spiral-shaped) obtained were shown, in the analysis carried out using Marshall's parameters: the ratios of the angles and of the rotational speeds of the prisms. The latter parameter ($M = \omega_2/\omega_1$) is similar to the transmission ratio from the Theory of Mechanisms. Several parameters were also introduced to characterize the scan patterns.

Future work refers to the development of these parameters and to the approach of other scanning devices with Risley prisms, by example with tilting parts (Li et al. 2003). Solutions of GSs and Risley are also of interest (Tao et al. 2010), as well as scanners with three prisms, that may provide more degrees of freedom in the inverse problem of the beam positioning (Li 2011). The driving of the prisms

with appropriate mechanisms for different applications (and, as pointed out, for different diameters of the prisms) is another issue of interest (Garcia-Torales et al. 2007; Kaposta et al. 2012). Delicate problems arise, especially in the case of large prisms, because of the deformations of the prisms due to the mechanical part and due to temperature variations (which require a Finite Element Analysis).

Acknowledgments This work was supported by a grant of the Romanian National Authority for Scientific Research, CNDI-UEFISCDI project number PN-II-PT-PCCA-2011-3.2-1682.

References

- Bass M (ed) (1995) Handbook of optics. Mc. Graw-Hill
- Cheng Y-S, Chang R-C (1998) Characteristics of a prism-pair anamorphic optical system for multiple holography. *Opt Eng* 37:2717
- Duma VF (2001) Contributions to the analysis and the design of scanning systems. Ph.D. Thesis, Polytechnics University of Timisoara
- Duma VF (2009) Mathematical functions of a 2-D scanner with oscillating elements. In: Modeling, simulation and control of nonlinear engineering dynamical systems. Springer, pp 243–253
- Duma VF, Nicolov M (2009) Neutral density filters with Risley prisms: analysis and design. *Appl Opt* 48:2678
- Duma VF, Rolland JP, Podoleanu AGh (2010) Perspectives of scanning in OCT. *Proc SPIE* 7556:7556–7610
- Duma VF, Lee K-S, Meemon P, Rolland JP (2011) Experimental investigations of the scanning functions of galvanometer-based scanners with applications in OCT. *Appl Opt* 50(29):5735–5749
- Garcia-Torales G, Strojnik M, Paez G (2002) Risley prisms to control wave-front tilt and displacement in a vectorial shearing interferometer. *Appl Opt* 41:1380
- Garcia-Torales G, Flores JL, Muñoz RX (2007) High precision prism scanning system. *Proc SPIE* 6422, 64220X
- Huang D, Swanson EA, Lin CP, Schuman JS, Stinson WG, Chang W, Hee MR, Flotte T, Gregory K, Puliafito CA, Fujimoto JG (1991) Optical coherence tomography. *Science* 254(5035):1178–1181
- Kaposta I, Jurca S, Duma VF (2012) Driving solutions of Risley prisms scanners. In: Proceedings of 4th ISREIE symposium, series: engineering (in print)
- Li Y (2011a) Third-order theory of the Risley-prism-based beam steering system. *Appl Opt* 50:679
- Li Y (2011b) Closed form analytical inverse solutions for Risley-prism-based beam steering systems in different configurations. *Appl Opt* 50:4302
- Li A, Liu L, Sun J, Zhong X, Wang L, Liu D, Luan Z (2003) Research on a scanner for tilting orthogonal double prisms. *Appl Opt* 45:8063
- Marshall GF (1999) Risley prisms scan patterns. *Proc SPIE* 3787:74–86
- Marshall GF (ed) (2004) Handbook of optical and laser scanning. Marcell Dekker
- Montague J (2003) Scanners—galvanometric and resonant. In: Driggers RG (ed) Encyclopedia of optical engineering. Taylor & Francis, NY pp 2465–2487
- Podoleanu AGh, Rosen RB (2008) Combinations of techniques in imaging the retina with high resolution. *Prog Retinal Eye Res* 27:464–499
- Rosell FA (1960) Prism scanner. *J Opt Soc Am* 50:521

- Schitea A, Tuf M, Duma VF (2013) Modeling of Risley prisms devices for exact scan patterns. Proc SPIE 8789:8789–8840
- Sinescu C, Negrutiu ML, Todea C, Balabuc C, Filip L, Rominu R, Bradu A, Hughes M, Podoleanu AGh (2008) Quality assessment of dental treatments using en-face optical coherence tomography. J Biomed Opt 13(05):054065
- Tao X, Cho H, Janabi-Sharifi F (2010) Optical design of a variable view imaging system with the combination of a telecentric scanner and double wedge prisms. Appl Opt 49:239
- Warger WC II, DiMarzio ChA (2007) Dual-wedge scanning confocal reflectance microscope. Opt Lett 32:2140
- Wojtkowski M (2010) High-speed optical coherence tomography: basics and applications. Appl Opt 49:D30
- Yang Y (2008) Analytic solution of free space optical beam steering using Risley prisms. J Lightwave Technol 26:3576

Applications of the Ackerman Steering and Electronic Differential in Modern Electric Drive Automotive Systems

A. Szilagyi, V. Ciupe and I. Maniu

Abstract Because the rise of the gas prices worldwide cannot be neglected, hybrid and electric vehicles are becoming a more viable alternative to the combustion engine vehicle. This article explores the possibility of using an Ackerman steering system together with an electric drive that uses one motor per wheel. Wheel-hub motors allow electric drive units to be located where their torque is needed: at the wheel. Here, they can also be used as brakes. In combination with a new system architecture, these motors not only enhance efficiency and safety, but also open the door to personalized cars through software upgrades. One advantage of the system is scalability, which means it can be adapted also for 4 wheel drive vehicles and the arrangement allows for the incorporation of every possible type of electronic assistance system. As a result, an experimental stand was built in order to check the capabilities of the system.

Keywords Steering mechanism · Differential · Electric drive · Hub motor

1 Introduction

The present tendency in the automotive industry regarding the electric vehicles is to replace the internal combustion engines from an existing model, with an electric one. While this is a cheap solution, it is not the best and is not using the full capabilities of an electric drive system.

A. Szilagyi (✉) · V. Ciupe · I. Maniu
“Politehnica” University of Timisoara, Timisoara, Romania
e-mail: andrei.szilagyi@mec.upt.ro

V. Ciupe
e-mail: valentin.ciupe@mec.upt.ro

I. Maniu
e-mail: inocentiu.maniu@mec.upt.ro

The success of a technical solution has to follow some basic rules:

- Simplicity
- Low costs
- Modular solution
- Structural robustness
- Facile and cheap maintenance
- Reduced environmental impact.

Many private companies are funding research in this area and, as one of the leaders of this market, Protean Electric Inc. has proved with its prototype vehicles that there are many benefits in using wheel hub motors. Although in this configuration the mass of the vehicle's powertrain is moved from the chassis to the hubs and this can cause unwanted problems in the vehicle dynamics by increasing the unsprung mass, Lotus Engineering together with Protean Electric has proved in the research called "The Effect of the Hub Motor on Vehicle Dynamics" that most of these problems "could be largely recovered through design changes to suspension compliance bushings, top mounts, PAS characteristics and damping, all part of a typical new vehicle tuning program" (Lotus Engineering and Protean Electric Inc. 2013).

Using individual electric motors for each wheel is a solution that needs to be considered also because of the bigger level of control, higher torque values achieved in comparison with single motor configurations and simplicity in adding new safety layers through software upgrades.

As big companies push the research in this direction, it opens a new field of research possibilities. The steering system studied here is based on a bachelor diploma project and it is only the beginning of a broader research. The objective was to build a platform on which different software algorithms can be further studied.

2 Models

Consider a front wheel steering vehicle that is turning to the right, as shown in Fig. 1. "When the vehicle is moving very slowly, there is a kinematic condition between the inner and outer wheels that allows them to turn slip-free. The condition is called the Ackerman condition and is expressed by Eq. (1)" (Jazar 2008).

$$\cos \beta - \cos \alpha = \frac{e}{a} \quad (1)$$

"where, α is the steer angle of the *inner wheel*, and β is the steer angle of the *outer wheel*. The inner and outer wheels are defined based on the turning center O.

The distance between the steer axes of the steerable wheels is called the *track* and is shown by e . The distance between the front and rear axles is called the *wheelbase* and is shown by a . Track e and wheelbase a are considered as kinematic width and length of the vehicle.

To have all wheels turning freely on a curved road, the normal line to the center of each tire-plane must intersect at a common point. This is the Ackerman condition” (Jazar 2008).

As reminded in (Alexandru and Alexandru 2010), Eq. (1) can be modified to take into account the lateral deviations of the elastic tires. Although in some cases these forces can be significant, their influence is ignored here and is reserved for further research including feedback from the TPMS (Tire Pressure Monitoring System) (Dielacher et al. 2013) and accelerometers for X and Y axes.

As a basis for the study, wheel speeds of a real world vehicle were recorded. In this case a Ford Sierra 1989 was used to read the ABS sensors and plot the wheel speeds in different conditions as seen in Fig. 2. The data was collected using an Arduino Duemilanove development board.

As expected, even at low speeds of the vehicle a difference between inner and outer wheel speeds (Fig. 2b) was observed while cornering. Also in normal driving conditions the bumps in the road induced perturbations in the system. This information is useful in designing future control and safety algorithms by comparing real world wheel feedback with the feedback acquired from the experimental stand.

To check if the same effect can be reproduced for electric vehicles, an experimental stand was built. The stand simulates a front wheel drive vehicle powered by a direct drive electric system. In the absence of a mechanical differential, the effect needed to be implemented by software in order to obtain the different wheel speeds while cornering. As inputs there have been considered the angle of the steering wheel and the wheel speed, ignoring the friction in the system or the situations where the tire pressure is not equal in all tires, or one wheel loses adherence. In this case the functioning of the system is strongly influenced. These

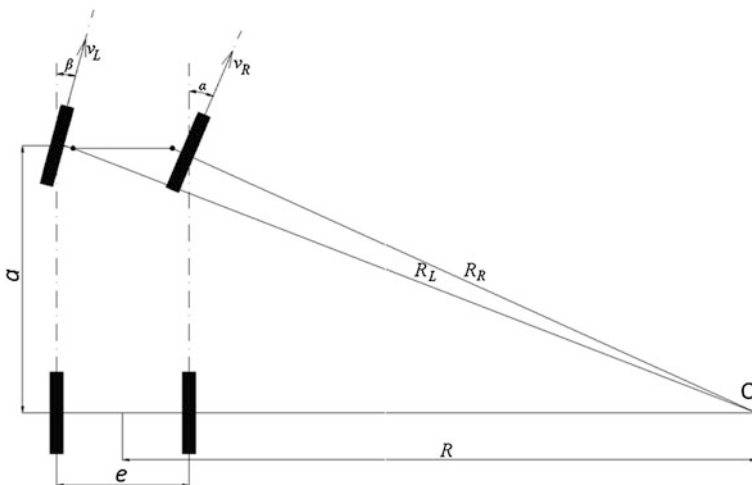


Fig. 1 Ackerman steering geometry

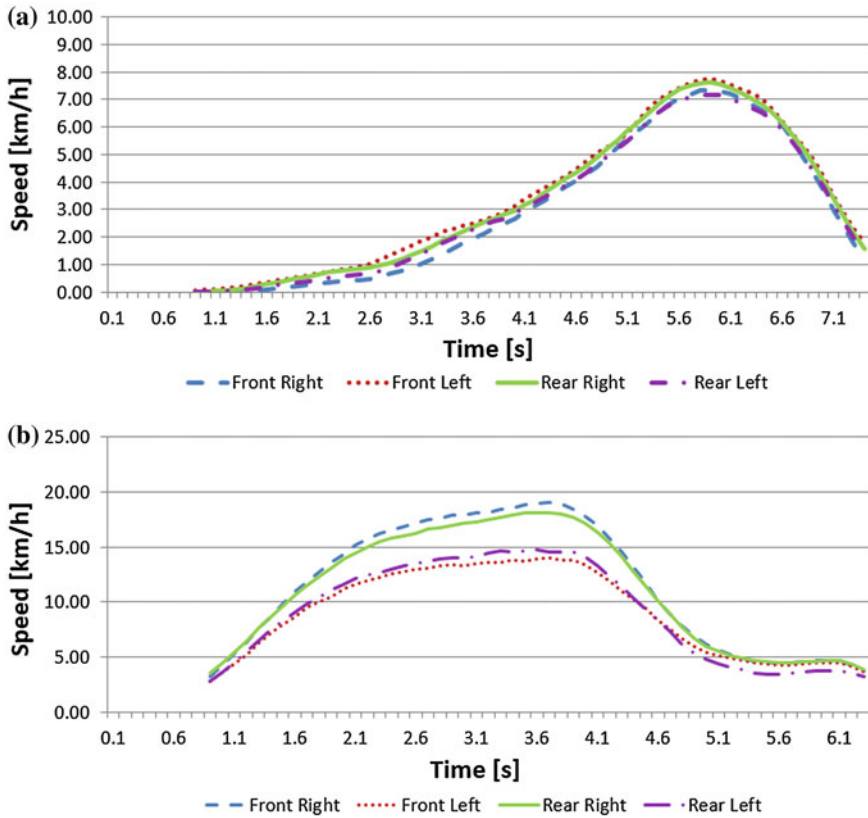


Fig. 2 a Driving in strait line—accelerating from standing still and braking. b Making a 360° left turn

situations can be avoided by adding a safety layer in the software that constantly monitors the torque of each wheel.

The steering system respects the *Ackerman condition* and it was designed with a track of 200 mm and a theoretical wheelbase of 400 mm. Starting from these restrictions, the angle of the steering arm and the length of the steering rack were calculated.

In Fig. 3, after drawing the theoretical lines that join the steering pivot, front wheel rotation center and rear axle center, the following theoretical values were obtained:

- Length of the steering rod (a): 30.92 mm
- Total length of the steering rack (b*2): 185 mm
- Angle of the steering rod (c): 14.04°
- Ackerman angle (c*2): 28.08°.

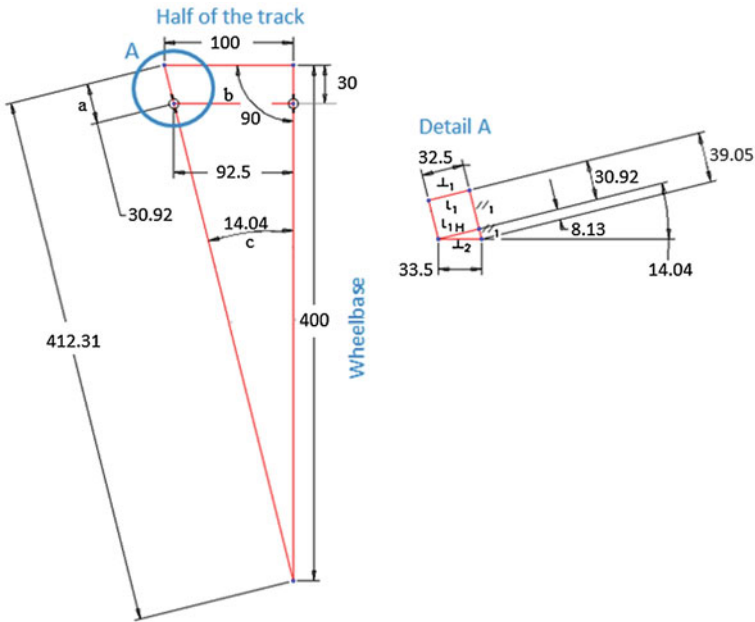


Fig. 3 Geometric calculus of the Ackerman steering for the experimental stand

Detail A describes the customized geometry used in the experimental stand where some restrictions were imposed by the mounting holes of wheel support. Calculus of the instant circle radius of the front wheels:

- Radius of the circle described by the right wheel:

$$R_R = \frac{a}{\sin \alpha} \tag{2}$$

$$R = l * ctg \alpha + \frac{e}{2} \tag{3}$$

- Radius of the circle described by the left wheel:

$$R_L = \frac{a}{\sin \beta} \tag{4}$$

$$\beta = atg \frac{\alpha}{R + \frac{e}{2}} \tag{5}$$

- Speed of right wheel:

$$v_R = \omega_v \cdot R_R \tag{6}$$

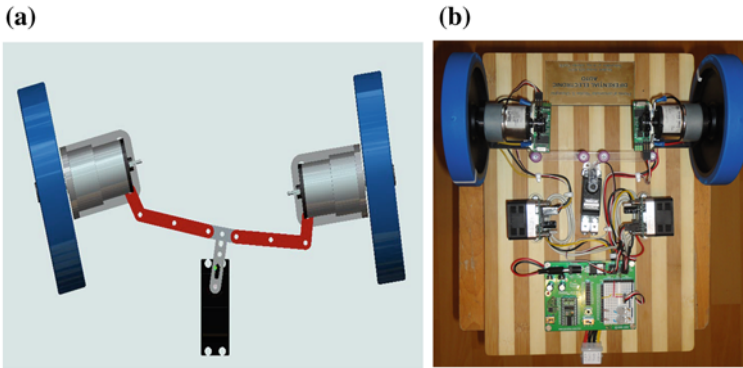


Fig. 4 **a** Top view of the ProEngineer simulation, **b** Top view of the experimental stand

- Speed of left wheel:

$$v_L = \omega_v \cdot R_L \tag{7}$$

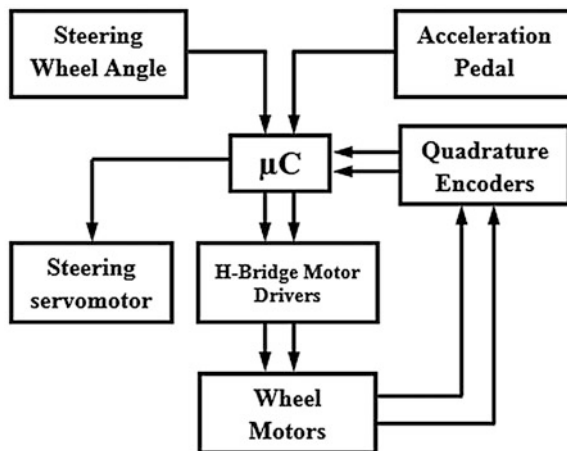
$$\omega_v = \frac{v}{R} \tag{8}$$

In Eq. (8) ω_v represents the vehicle speed in the plane of motion.

To verify the geometry calculated in Fig. 3, a kinematic simulation of the steering mechanism was made using ProEngineer software package (Fig. 4a). Through this simulation the maximum steering angle of the steering mechanism could be determined and used as a restriction in the steering algorithm.

The experiment was build using off-the-shelf parts from Parrallax Inc. The microcontroller was a PIC16C56. It sends PWM signals to a servomotor that controls the steering and also to the motor drivers (Fig. 5). The motors used were

Fig. 5 Block diagram of the control system; μC Microcontroller



two 7.2 V DC motors coupled with two quadrature encoders, and the steering mechanism was laser cut from plexiglas for a precise fit. As inputs for the system, the resistance of 2 variable resistors was recorded and they represented the steering wheel and the acceleration pedal.

3 Conclusions

The present experimental stand proves that this setup of individual motors for each driving wheel and a mechanical steering system based on the Ackerman principle is a feasible solution. While the direct drive eliminates the energy losses through friction from the mechanical transmission, the mechanical steering system assisted by an electric motor is offering a safe way to control the vehicle in case of a power failure.

The system is also scalable and the experimental stand can be used to study other active safety features.

The experimental stand has opened future research opportunities by adding feedback from a Tire Pressure Monitoring System and accelerometers and improving the control algorithm by taking in consideration forward and lateral forces and even tire deformation using improved Pacejka equations (Soubakhsh and Eskandarian 2012).

References

- Alexandru P, Alexandru C (2010) Correlating requirements regarding the command and the mechanical structure of the automotive steering system. Syrom 2009, Springer, Netherlands, pp 217–226. ISBN 978-90-481-3522-6
- Dielacher M, Flatscher M, Herndl T, Lentsch T, Matischek R, Prainsack J, Weber W (2013) A robust wireless sensor node for in-tire-pressure monitoring. In: MEMS-based circuits and systems for wireless communication, Springer, United States, pp 313–328. ISBN 978-1-4419-8798-3
- Jazar RN (2008) Vehicle dynamics: theory and application. Springer, United States, pp 379–454. ISBN 978-0-387-74244-1
- Lotus Engineering, Protean Electric Inc. (2013) The effect of hub motors on vehicle dynamics. <http://www.proteanelectric.com/wp-content/uploads/2012/10/The-Effect-of-Hub-Motors-on-Vehicle-Dynamics.pdf>. Accessed 10 May 2013
- Soubakhsh D, Eskandarian A (2012) Vehicle lateral and steering control. In: Handbook of intelligent vehicles, Springer, London, pp 209–232. ISBN 978-0-85729-085-4

Geometric Modeling of Power Joints from Bush Chain Drives

A. Todi-Eftimie, R. Velicu, R. Saulescu and C. Jaliu

Abstract The chapter presents a comparison between the geometry of chain sprockets for bush chains, described in American and ISO standards. The differences between the two chain sprockets designs and influence of the behavior have been graphically analyzed. The chain sprocket geometry is a starting point to establishing the contact between the sprocket and the bush chain during rotation. The evolution of the contact angle between the engagement and disengagement points is analyzed for different pitches.

1 Introduction

A high-speed chain drive is a transmission consisting of sprockets, a chain and various tensioning, lubrication and safety systems. The basic components of the chain drive are the sprockets and the chains. Due to chain gearing on the sprocket, sliding is non-existent, leading to constant transmission ratio. Chain transmissions are preferred when the system demands high torques with constant transmission ratio Tsubakimoto Chain Co. (1997). Chains are flexible kinematic elements consisting of articulated links. The operation of a chain transmission is based on the engagement of chain with sprockets provided with special teeth. Bush chains

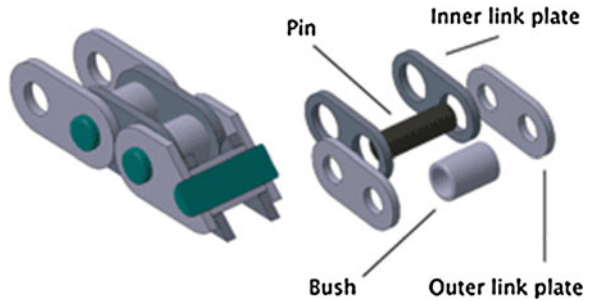
A. Todi-Eftimie (✉) · R. Velicu · R. Saulescu · C. Jaliu
Transilvania University of Brasov, Brasov, Romania
e-mail: alina.eftimie@unitbv.ro

R. Velicu
e-mail: rvelicu@unitbv.ro

R. Saulescu
e-mail: rsaulescu@unitbv.ro

C. Jaliu
e-mail: cjaliu@unitbv.ro

Fig. 1 Bush chain. Assembled chain elements and components identification (Tsubakimoto Chain Co. 1997)



are assemblies of link plates, pins and bushings (Fig. 1). The outer link plates are pressure fitted on pins, and the inner link plates are pressure fitted on bushings. When moving, the two couples of elements form two distinct articulated kinematic elements. Due to the increased contact surface between pins and bushings, bush chains are recommended to work in conditions of medium loads and values of velocities under 3 m/s Tsubakimoto Chain Co. (1997). The chain used in this study is a short pitch transmission precision bush chain, as found in the standard ISO 606:2004 ([Short pitch transmission precision bush chains and chain wheels](#)).

The link plates are elements which support the tension applied to the chain. Therefore, the plate must have great static tensile strength, and must hold up to dynamic loads and shocks. The pin is subjected to shearing and bending forces transmitted by the link plate. At the same time, it forms a bearing, together with the bushing, when the chain flexes during sprocket engagement. Therefore, the pin needs high tensile and shear strength, resistance to bending, and also must have proper strength against shocks and wear. The bushing is subject to bending stresses transmitted by link plates, and is also a subject to impact load as it strikes sprocket teeth during chain engagement with the sprocket. After engagement, the bushing changes its point of contact and balance. It is held between the sprocket teeth and pin, and moves on the tooth face while receiving a compression load. Being in contact with the sprocket teeth, it must be resistant to wear with strength against contact fatigue.

The normal function of a chain sprocket is not only to drive or to be driven by chain, but also to guide and support the chain in its intended path. When the chain engages on the sprocket, it forms polygons instead of circles, which is causing a periodic fluctuation of linear and transversal velocity, together with periodic transverse displacements at both ends of the chain (Pedersen 2005). The result is in transversal and longitudinal vibrations, known as the polygonal effect. Due to this polygonal effect, the velocities of the driven sprockets will fluctuate even if the velocity of the driving sprocket is constant (Constantin and Palade 2004; Pfeiffer 2008). In order to define a realistic model of the contact forces between chains and sprockets, special attention must be paid to a correct engagement and disengagement description. The chapter establishes the bushing-sprocket position at engagement and disengagement and the evolution of the contact angle with influence on contact forces.

2 Sprockets Geometry

The chain sprocket geometry is a starting point to establish the static forces in the contact between the sprocket and the bush chain, and for the kinematics of the friction couples bushings—chain sprocket and bushings—pins, respectively.

The sprocket profile geometry studied in this chapter has been chosen from ISO 606:2004 ([Short pitch transmission precision bush chains and chain wheels](#)). The chosen tooth profile is divided in three contact areas, with circular shapes, as shown in Fig. 2a. As a term of comparison, the American standard provides a more complex construction of the tooth profile. According to the sprocket tooth profile ASME B29.100–2011 ([Precision power transmission roller chains, attachments and sprockets](#)), the tooth profile can be divided using its construction elements, as shown in Fig. 2b. Thereby, we can obtain seven areas in which the bushing-sprocket contact can occur.

The ASME tooth profile standard defines explicit values of the dimensional parameters, from which only one tooth profile can be designed. The ISO 606:2004 standard allows the tooth profile to diversify between minimum and maximum values. For the future calculus, we have chosen a medium tooth profile (Fig. 3).

The study is made for vertical single row chain transmission, with parameters as following: transmission ratio 1:1; teeth number $z = 16$; pitch $p = 9.525$ mm; pitch diameter $D_d = 48.824$ mm; bush diameter $d_r = 5.08$ mm. These parameters were introduced in the calculus for both ASME and ISO sprocket profiles.

The comparison between the minimum and maximum ISO 606:2004 tooth profile and the American tooth profile can be observed graphically, in Fig. 4.

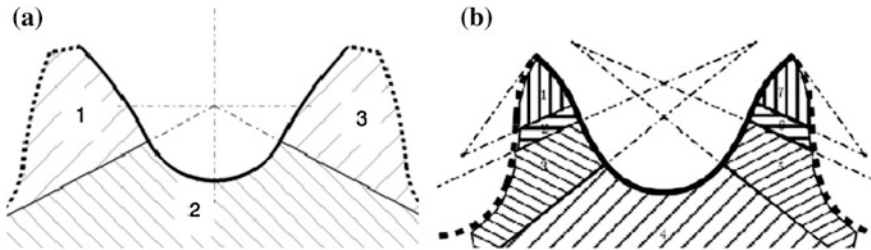
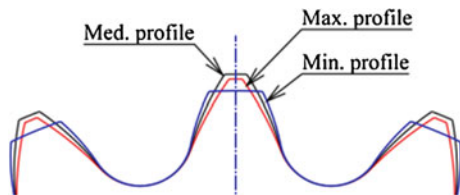


Fig. 2 Real tooth profiles separated in contact areas **a** ISO 606:2004 ([Short pitch transmission precision bush chains and chain wheels](#)); **b** ASME B29.100–2011 ([Precision power transmission roller chains, attachments and sprockets](#))

Fig. 3 Comparison between ISO 606:2004 minimum, medium and maximum tooth profile



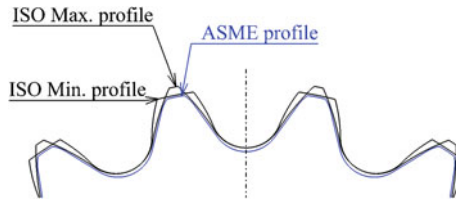


Fig. 4 Comparison between precision power transmission sprocket ASME B29.100–2011 and ISO 606:2004 minimum and maximum tooth profile

There is a clear difference between the two profiles and not just in the height of the tooth.

The ASME tooth profile is slightly smaller than the ISO tooth profile. The ASME tooth profile is closer to the maximum ISO tooth profile. Transition from area 2 to area 1 and 3 of the ISO profile (see Fig. 2a) is more sudden than transition from area 4 to area 3 and 5 of the ASME profile (see Fig. 2b). This may influence the engagement and disengagement of the bushing—tooth contact. The presence of the seven areas of the ASME tooth profile may provide better instruments in the optimization of contact between tooth and bushing.

3 Contact Points Between Bushing and Sprocket

The medium sprocket profile of the ISO standard, for the same chain size with three pitch values was used in order to analyze the tooth-bushing contact angles while engaging and disengaging the sprocket (Fig. 5). The chain used for this study (Short pitch transmission precision bush chains and chain wheels, ISO 606:2004 ([Short pitch transmission precision bush chains and chain wheels](#))) can admit a pitch

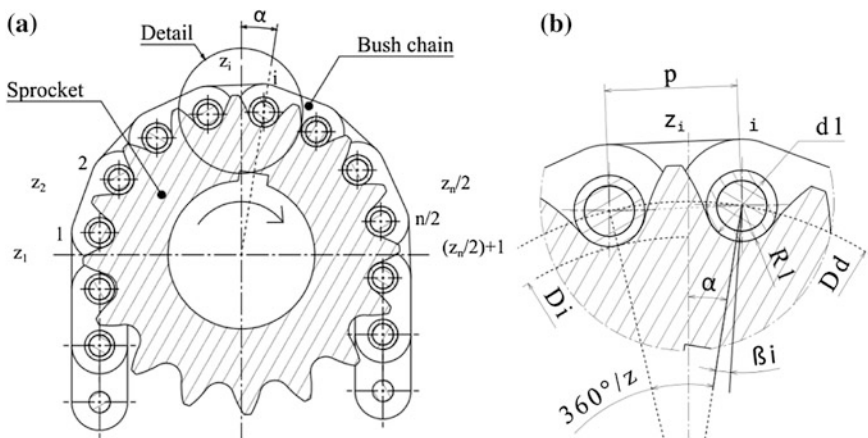


Fig. 5 Contact angles between bushing and sprocket. **a** General view, **b** detail view

deviation up to 0.2 % of the normal pitch. This deviation is due to inaccurate execution, due to elongation coming from wear during functioning. The dimensions for this chain were chosen to be: pitch of 9.525 mm and bushing diameter of 5.08 mm. Therefore, the three pitch variations for this chain are: minimum chain pitch—9.525 mm, medium chain pitch—9.535 mm, maximum chain pitch—9.544 mm.

It is recommended that the chain used in transmissions to have even number of links, and also the sprocket to have even number of teeth. The positioning of the chain on the sprocket was considered as starting with the bushing-tooth contact on the vertical axis of the sprocket (Fig. 5a). The contact angle β on this contact point, for angle $\alpha = 0^\circ$ is equal to 0° . This positioning is normal for a contact point with no tangential force.

The contact point is situated on the line that connects the centers of the bushing and the bushing seat (Fig. 5b). The contact angle β_i represents the angle between the line connecting the center of the sprocket with the center of the bushing seat and the line that connects the center of the bushing seat and the contact point bushing–bushing seat. It is calculated for each i numbered bushing seat. This angle is similar for the same positive or negative value of the sprocket rotation α angle.

In the first theoretical case, the bush chain pitch is equal with the sprocket pitch. This means that for a 1:1 transmission ratio and a total number of teeth z_n , the number of teeth in possible contact with the chain in all the sprocket angle of rotation α is $(z_n/2) + 1$. Also, in this case, all the contact points between bushings and sprocket teeth have the same contact angles β , equal to 0. In this theoretical case, the transmission does not fulfill geometrical conditions to transmit torque; the tangential forces are only resulting from friction.

The second case considered is the one in which the medium profile sprocket is assembled to the medium pitch chain. This leads to a variation of the contact angle from 0° to 24.9° . The graphical representation from Fig. 6a shows the points of contacts and contact angles points for all bushings starting with the bushing-tooth contact on the vertical axis of the sprocket. As the bushing moves away from the vertical position, contact angles increase as shown in the diagram from Fig. 6b.

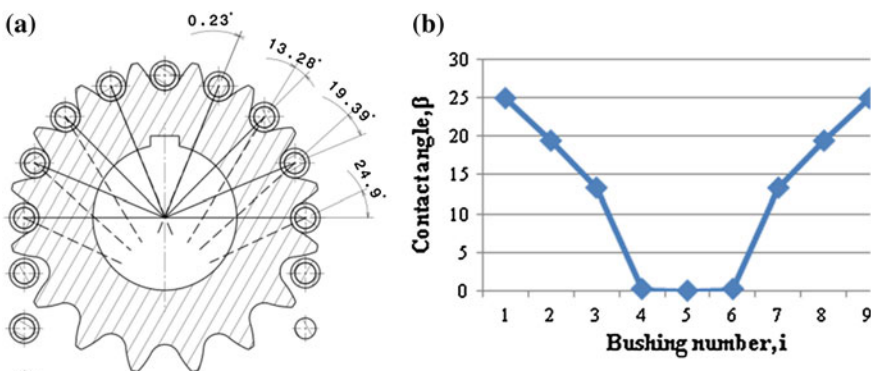


Fig. 6 Contact angle for medium profile sprocket and medium pitch chain. a Drawing, b graphic

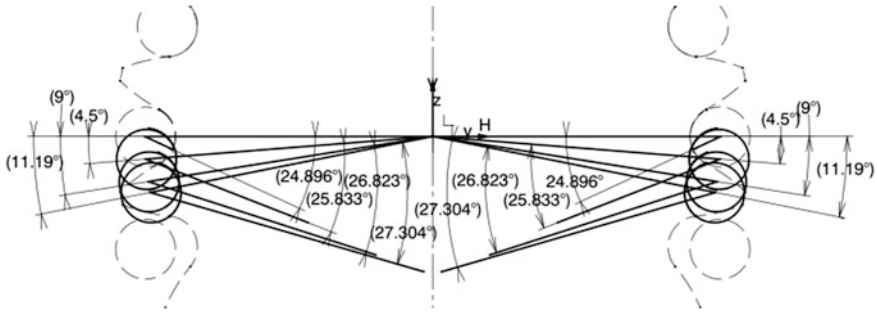


Fig. 7 Contact angle for medium profile sprocket and medium pitch bush chain for the first and last bushing-tooth contact

The engagement and disengagement of bushing—tooth contact are the most important stages defining the behavior of a chain drive. The drawing from Fig. 7 was developed in order to find the position at which the chain enters the contact and leaves the contact with the sprocket. It illustrates the position of the first and last bushing in contact with the sprocket teeth. The sprocket was rotated with positive α values, up to almost half of the pitch angle of 11.25° , until the contact condition is satisfied.

It is important to know how the bushing moves on the sprocket profile while engaging with the sprocket, in order to determine the maximum contact angle (the position of engagement and disengagement). The sprocket angle of rotation, α , relative to the horizontal axis—in which the first bushing comes in contact and the last bushing leaves the contact with the sprockets profile, while rotating—is 11.19° , for which the contact angle is maximum 27.304° (Fig. 7).

The graphic from Fig. 8 represents the evolution of the contact angle while rotating the sprocket with 4.5° , 9° and 11.19° clockwise and counterclockwise in respect to the vertical position of the sprocket.

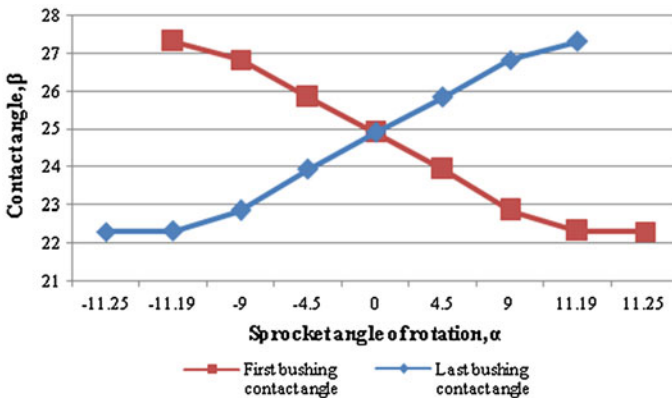


Fig. 8 First and last tooth contact angle for medium profile sprocket and medium pitch chain

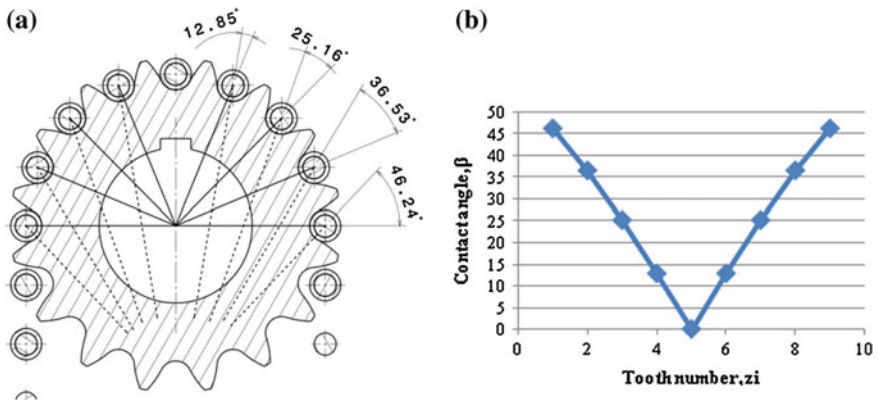


Fig. 9 Contact angle for medium profile sprocket and maximum pitch chain. **a** Drawing, **b** graphic

The third case, in which a medium profile sprocket is assembled to a maximum pitch chain, leads to the variation of the contact angle from 0° to 46.24° . The graphical representation from Fig. 9a shows the points of contacts and contact angles for all bushings starting with the bushing-tooth contact on the vertical axis of the sprocket. As bushing moves away from vertical position, the contact angle increases as shown in the diagram from Fig. 9b.

For the assembly between the medium profile sprocket and the maximum pitch chain, Fig. 10 illustrates the position of the first and last bushing in contact with the sprocket teeth. The sprocket was rotated with positive α values, up to almost half of the pitch angle, which is 11.25° , until the contact condition is satisfied.

The sprocket angle of rotation, α , relative to the horizontal axis—in which the first bushing comes in contact and the last bushing leaves the contact with the

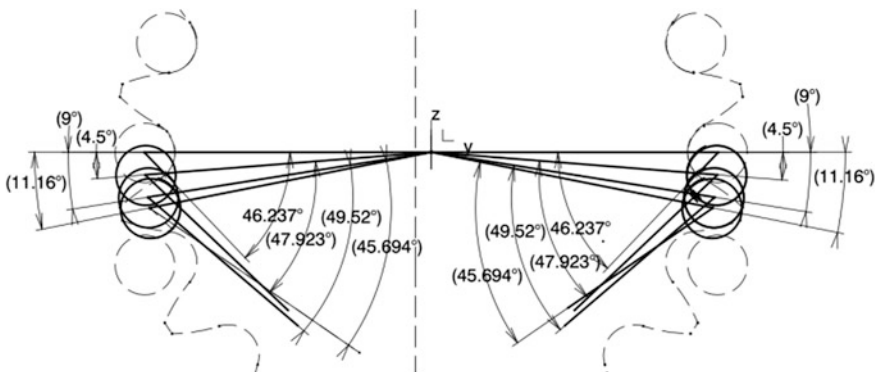


Fig. 10 Contact angle for medium profile sprocket and maximum pitch bush chain for the first and last bushing-tooth contact

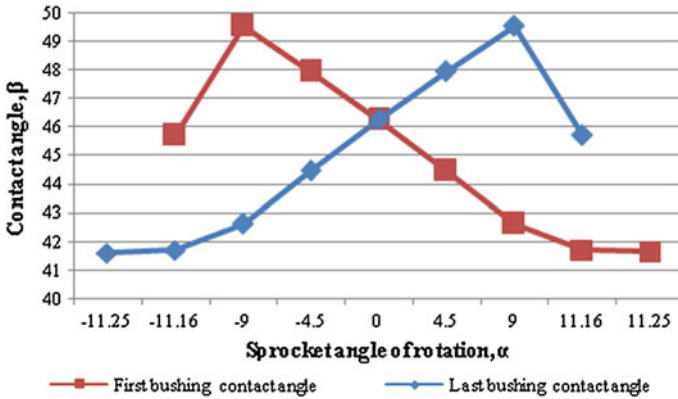


Fig. 11 First and last tooth contact angle for medium profile sprocket and maximum pitch chain

sprockets profile, while rotating—is 11.16° , for which the contact angle is at a maximum value of 45.694° (Fig. 10).

The graphic from Fig. 11 represents the evolution of the contact angle while rotating the sprocket with 4.5° , 9° and 11.16° clockwise and counterclockwise in respect to the vertical position of the sprocket. The evolution of contact angles for bushings situated in the negative sprocket rotation angle is symmetric to contact angles from the positive side. Comparing the graphical representations of contact angles of medium and maximum pitch chains, we can observe that the maximum pitch chain leads to higher values and higher variations for the contact angles.

The sprocket rotational angles for the first and last contact between bushings and sprocket (the engagement and disengagement positions) are bigger for the maximum pitch chain. This means that engagement and disengagement contact angles increase together with the increase of chain pitch.

4 Conclusions

The bushing-sprocket positions at engagement and disengagement, their contact angles and also the evolution of contact angles with sprocket angles of rotation are the main results of this chapter. The reduction of engagement and disengagement contact angles as a meaning of reducing engagement and disengagement shocks is a common sense measure. This possibility will be subject of further research after computing reaction forces in the bushing-sprocket contact point and establishing their evolution during rotation.

References

- Tsubakimoto Chain Co. (1997) The complete guide to chain (U.S., ed.). Accessed 20 May 2012, on <http://chain-guide.com/toc.html>
- Precision power transmission roller chains, attachments and sprockets, ASME B29.100–2011
- Short pitch transmission precision bush chains and chain wheels, ISO 606:2004
- Constantin V, Palade V (2004) Organe de mașinișimecanisme (Machine elements), vol. 1, (ed) FundațieiUniversitatea “Dunărea de Jos”, Galati
- Pedersen SL (2005) Model of contact between rollers and sprockets in chain-drive systems. In: Archive of applied mechanics 74, (ed) Springer, pp 489–508. DOI [10.1008/s00419-004-0363-4](https://doi.org/10.1008/s00419-004-0363-4)
- Pfeiffer F (2008) Mechanical system dynamics. Lecture notes in applied and computational mechanics, vol. 40, (ed) Springer, Berlin. ISBN: 978-3-540-79435-6, ISSN 1613-7736

One-DOF Mechanisms for Dual-Axis Solar Tracking

Ion Visa, Monica Vatasescu, Mircea Neagoe
and Bogdan Gabriel Burduhos

Abstract This paper presents a comparative study of one DOF mechanisms with one input and two correlated outputs connected to both diurnal and elevation orientation movements from dual-axis solar tracking systems. Based on known solutions from the literature, the paper provides a systematization of the existing one DOF mechanism variants; thus, there were identified two main categories: (a) four-bar spatial linkage, with or without adjusting link lengths, and (b) planar linkage serially connected with a cam mechanism. The comparative kinematical studies of two representative one DOF mechanism variants allow highlighting the advantages and drawbacks each category, the compound mechanism with cylindrical cam and 4R planar linkage being the most recommended for tracking small PV systems. Considering applications based on location Brasov, Romania, there are drawn useful conclusions for researchers, designers and specialists to set the best orientation solution suitable to a given location.

Keywords Dual-axis azimuth solar tracking · One DOF mechanism · Spatial linkage · Four-bar linkage · Slider-rocker linkage · Cam mechanism · Transmission angle

1 Introduction

The recently tendency in developing solar tracking systems is building up mechanisms which can move on two axis by introducing a single independent motion. The existing solutions of one DOF dual-axis tracking systems are of azimuth type and, using an intermediate mechanism, generate the elevation motion

I. Visa · M. Vatasescu · M. Neagoe (✉) · B. G. Burduhos
Faculty of Product Design and Environment , Product Design, Mecatronics and Environment
Department, Transilvania University of Brasov, Bd Eroilor no 29, Brasov, Romania
e-mail: mneagoe@unitbv.ro

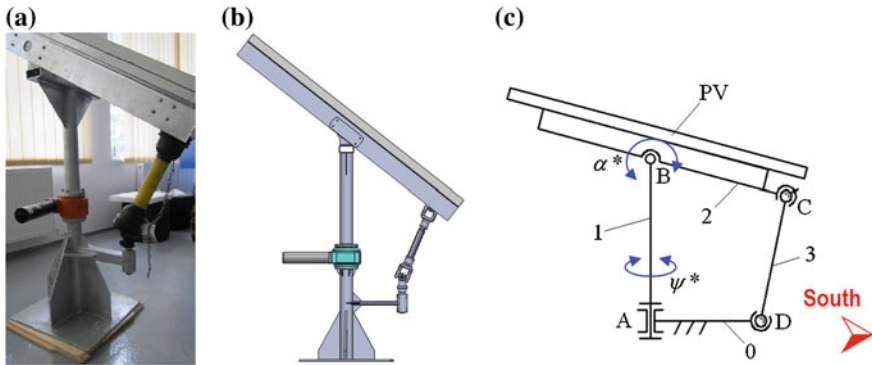


Fig. 1 The one DOF dual-axis azimuth solar tracking solution with four-bar spatial linkage (a) the 7R prototype built and implemented at *Transilvania* University of Brasov, (b) the 3D model of the 7R PV system on its noon position and (c) the generalized structural scheme on its noon position

(α^*) as a function depending on the azimuth motion (ψ^*) (Vatasescu et al. 2011b; Fragkiadakis 2009; Stanestanislavo and Soler 2009; Jesus et al 2008; Mavromatakis and Franghiadakis 2008; Niessing Anlangenbau GmbH 2007; Linder 2006; Berger 1998)¹ (Figs. 1, 3, 6).²

There are two directions in developing one DOF dual-axis tracking mechanisms:

1. Using a *four-bar spatial linkage* (Vatasescu et al. 2011b; Stanestanislavo and Soler 2009; Jesus et al. 2008; Niessing Anlangenbau GmbH 2007; see footnote 1):
 - (a) without adjusting elements, when the system can perform the solar elevation motion according to a single orientation program (Fig. 1) (Vatasescu et al. 2011; Niessing Anlangenbau GmbH 2007);
 - (b) with adjusting elements for some lengths of the linkage links, which make possible the implementation of different tracking laws during a year (Diaconescu et al. 2009; Stanestanislavo and Soler 2009; Jesus et al. 2008).
2. Using a *compound mechanism*: a **planar linkage** serially connected with a **cam mechanism** (in which a fixed cylindrical cam is used); the planar linkage can be:
 - (a) a **four-bar 4R linkage** (R = rotation), in which the input motion is the output rotation from the cam-mechanism (Figs. 3 and 4a) (Linder et al. 2006; see footnote 2);

¹ MECAPISA, Spain, <http://www.mecapisa.com/en/>.

² TechnoSunSolar: EcoChamp-ST 3000-Dual-Axis Tracking Systems, www.environmental-expert.com/products/ecochamp-st-3000-dual-axis-tracking-systems-211552.

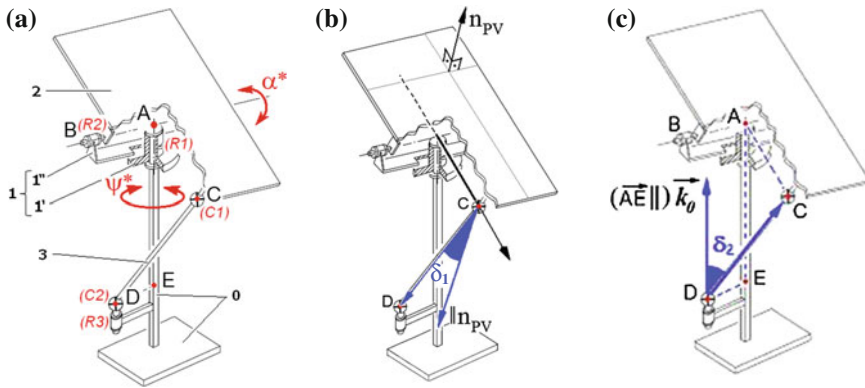


Fig. 2 (a) The structural scheme of the one DOF dual-axis azimuth 7R spatial linkage, and its operating angles along with the correspondent moving limits, (b) $\delta_1 \leq 55^\circ$ and (c) $\delta_2 \leq 65^\circ$ (Vatasescu et al. 2011a, b; Visa et al. 2011; Diaconescu et al. 2009, 2010)

(b) a **slider-rocker 3RT linkage** (T = translation) in which the input motion is the output translation (T) from the cam-mechanism (Fig. 6) (Fragkiadakis 2009; Mavromatakis and Franghiadakis 2008; Berger 1998).

The main drawbacks and advantages of these solutions are:

- Even though the four-bar spatial linkage solution is suited for large PV platforms, it has severe limitations on the angular strokes in order to avoid the interference and blocking of mechanism elements at the extreme positions (Fig. 2) (Vatasescu et al. 2011a, b; Visa et al. 2011).
- This weak point of the four-bar spatial linkage solutions is solved by the compound mechanism variants in which the planar linkage is always on a vertical plane (Fig. 3) (Fragkiadakis 2009; Mavromatakis and Franghiadakis 2008; Linder et al. 2006; Berger 1998).
- When considering the compound mechanism category, the 4R variant (Fig. 4) is preferred to the 3RT variant (Fig. 6) due to the prismatic joint (T), which leads to high constructive and technological complexity.

2 The Four-Bar Spatial Linkage Analysis

A known solution for one DOF dual-axis azimuth solar tracking systems is the 7R spatial linkage (Figs. 1a, b and 2) (Vatasescu et al. 2011a), which represents the derived and improved solution of the 2R2ST (S = spherical joint) spatial linkage with adjusting element, described in (Diaconescu et al. 2009, 2010), similar to the Spanish solution described in (Jesus et al. 2008). Moreover, the 7R solution

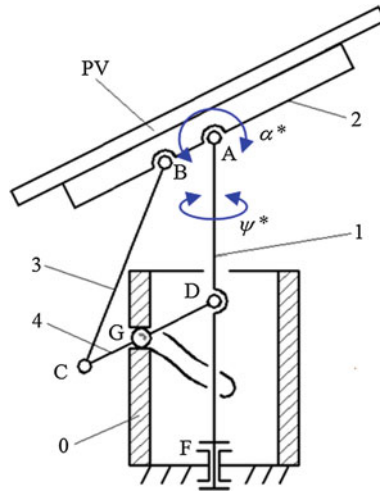


Fig. 3 The equivalent structural scheme of the compound one DOF dual-axes azimuth mechanism with planar 4R linkage

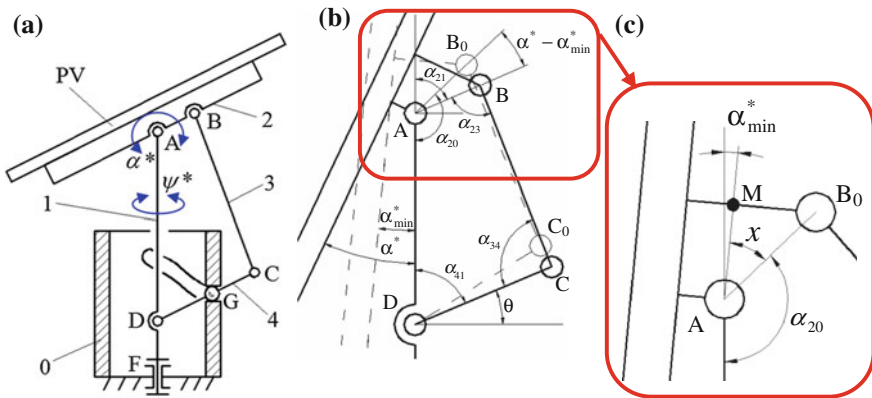


Fig. 4 (a) The compound mechanism with 4R linkage, with connecting rod mounted on the back of the PV platform (in regard to the noon position, when the PV platform is positioned toward South), (b) the detailed kinematic scheme of the 4R linkage, (c) detail for the parameters of the rocker AB in the initial position

(Figs. 1a, b and 2) eliminates the drawback of the passive motion on the S–S chain from the 2R2ST mechanism, by replacing it with a universal Hook transmission.

The generalized solution for the one DOF four-bar spatial linkage category (Fig. 1c) consists of a vertical revolute joint A which spins the pole 1 around its own vertical axis; the pole 1 is joined with the PV platform 2 by the horizontal revolute joint B; the rocker 3 is linked one end with the PV platform 2 by the spherical joint C and the other end to the base 0 by the spherical joint D.

The passive rotation of the crank 3 around its own axis is eliminated by the pin introduced in the spherical joint C. Thus, the mobility degree M for this mechanism solution is:

$$M = 6 \cdot n - \sum_{i=1}^4 c_i = 6 \cdot n - (c_A + c_B + c_C + c_D) = 6 \cdot 3 - (5 + 5 + 4 + 3) = 1, \tag{1}$$

where n represents the number of kinematical elements (mobile links) and c_X – the constrains’ number of the joint X ($X = A, B, C, D$).

The solutions of the one DOF four-bar spatial linkage category (Figs. 1 and 2) (Vatasescu et al. 2011a, b; Diaconescu et al. 2010, 2009; Jesus et al. 2008; see footnote 1) have the major drawback of the limited angular strokes due to the fact that, for the sunset and sunrise positions when the elevation angle α^* tends to become 0° and the diurnal angle ψ^* has its maximum absolute values, the rocker 3 tends to become parallel with the PV platform.

To avoid the 7R linkage blocking tendency in the critical operation positions of the rocker 3, specific to the sunrise and sunset PV platform orientations (the pressure angle in the universal joint C is limited to a maximum values, e.g. 65°) and, on the other hand, to comply the relative angular displacements in the universal joints with its angular capacity, angular restrictions are imposed as shown on Fig. 2 and detailed in (Vatasescu et al. 2011a, b).

Considering the limit values of the operating angles (δ_1, δ_2) specified in Fig. 2, with the aim to capture at least 96 % of the annual available direct solar radiation, in the real sky assumption for Brasov location, the optimal values of the specific geometrical parameters were obtained (Vatasescu et al. 2011a, b): $H = AE/ED = 2.58$, $R = AC/ED = 2.04$ and $L = CD/ED = 1.33$, along with the following limit values: $\delta_{1max} = 55^\circ$, $\delta_{2max} = 62^\circ$, allowing the azimuth angle $\psi^* = \pm 90^\circ$ and the maximum elevation angle $\alpha^* = 48^\circ$. On the basis of this limited values of the tracking angles (ψ^*, α^*) allowed by the 7R spatial linkage, can be underlined that this solution is not advantageous for low latitudes (under 45°) and during summer season, when the Sun describes extended angular trajectories, characterized by large diurnal strokes $\Delta\psi^* > 180^\circ$ (Vatasescu et al. 2011a).

3 The Compound Mechanism Analysis

Considering the one DOF dual-axis azimuth compound mechanism category, the existing solutions include a cam mechanism (with a fixed cylindrical cam), which converts the azimuth motion ψ^* into an intermediate rotation or translation motion, and a simple planar linkage, serially connected to the cam mechanism, which converts the intermediate motion into the elevation motion α^* (Figs. 3, 4, 6) (Linder 2006; see footnote 2).

In the first case, a four-bar linkage of 4R type is used as planar mechanism (Fig. 3) with the advantages given by revolute joints, this variant is recommended to track only small PV platforms due to the incongruent contact between the cam profile and its follower (Visa et al. 2011; Neagoe et al. 2010). The equivalent generalized solution (Fig. 3) of the compound mechanism presented in (Linder 2006), includes a cylindrical cam mechanism with oscillating follower consisting of the elements 0-1-4 and the planar four-bar linkage composed by the interconnected elements 1-2-3-4.

The composed mechanism from Fig. 3 has the mobility degree M :

$$\begin{aligned}
 M &= M_1 + M_2 - L_c = \{3 \cdot n_1 - [(c_A - 3) + (c_B - 3) + (c_C - 3) + (c_D - 3)]\} \\
 &+ \{6 \cdot n_2 - [(c_D - 0) + (c_F - 0)] + (c_G - 0)\} - L_c = (3 \cdot 3 - [(5 - 3)]) \\
 &+ \{6 \cdot 2 - [2 \cdot (5 - 0)] + (1 - 0)\} - 1 = 1 + 1 - 1 = 1,
 \end{aligned}
 \tag{2}$$

where $n_1 = 3$ and $M_1 = 1$ are the number of kinematical elements (with 1 \equiv reference element) and respectively the mobility degree of the planar 4R linkage (ABCD), $n_2 = 2$ and $M_2 = 1$ are the number of kinematical elements and respectively the mobility degree of the cam mechanism (FDG), c_X is the restrictions' number of the joint X and $L_c = f_D = 1$ represents the number of active mobility of the common revolute joint D of the two previous mechanisms.

Considering the previous aspects, the kinematical analysis of the solution proposed in Fig. 4a is based on the parameterization from Fig. 4b and c, and the relations' set (3).

The relations (3) are useful for setting up the variation of the main compound mechanism parameters (Fig. 5), considering $AB = 500$ mm, $AB = 1389.2$ mm, $CD = 1052$ mm, $AD = 1503.8$ mm, $DG = DC/2$ (see Fig. 4a), $R_{med} = 479.28$ mm, and the annually equivalent day $N = 110$ (Vatasescu et al. 2011b), only for the time interval from noon to sunset (negative values of the diurnal angle ψ^*), due the symmetrical variations of the parameters with respect to the noon position (Visa et al. 2011; Vatasescu et al. 2011b; Diaconescu et al. 2010).

$$\left\{ \begin{aligned}
 &AB = l_2, BC = l_3, CD = l_4, AD = l_1, \alpha_{20} = 180 - \alpha_{min}^* - x, x = \arcsin \frac{MB_0}{l_2} \\
 &\alpha_{21} = 180 - [\alpha_{20} - (\alpha^* - \alpha_{min}^*)], \alpha_{41} = 2 \arctg \frac{A_{41} + \sqrt{A_{41}^2 + B_{41}^2 - C_{41}^2}}{B_{41} - C_{41}}, \\
 &A_{41} = 2l_1l_4 \sin(\alpha_{21}), B_{41} = 2l_1l_4 \cos(\alpha_{21}) + 2l_1l_4, \\
 &C_{41} = l_3^2 - l_2^2 - l_4^2 - l_1^2 - 2l_2l_1 \cos(\alpha_{21}), \\
 &\alpha_{34} = \arccos \frac{l_3^2 + l_4^2 - l_1^2 - l_2^2 - 2l_1l_2 \cos(\alpha_{21})}{2l_3l_4}, \\
 &\alpha_{23} = 180 - (\alpha_{34} + \alpha_{41} - \alpha_{21}), \theta = 90 - \alpha_{41}, \\
 &\gamma_{23} = \alpha_{23} \text{ for } \alpha_{23} \leq 90^\circ, \gamma_{23} = 180 - \alpha_{23} \text{ for } \alpha_{23} > 90^\circ, \\
 &\gamma_{34} = \alpha_{34} \text{ for } \alpha_{34} \leq 90^\circ, \gamma_{34} = 180 - \alpha_{34} \text{ for } \alpha_{34} > 90^\circ, \\
 &\cos(\beta_{40G}) = \cos(\alpha_{40G}) \cdot \cos(\theta) \Leftrightarrow \sin(\gamma_{40G}) = \cos(\alpha_{40G}) \cdot \cos(\theta),
 \end{aligned} \right.
 \tag{3}$$

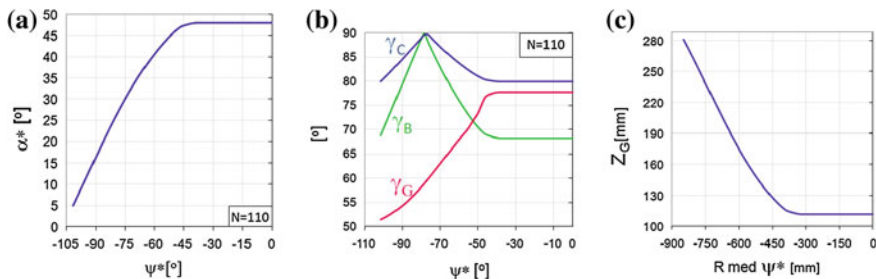


Fig. 5 (a) the elevation α^* as a function of ψ^* variation, (b) the transmission angles ($\gamma_B = \gamma_{23}$, $\gamma_C = \gamma_{34}$, $\gamma_G = \gamma_{40G}$) on B, C and G joints of the system from Fig. 4, (c) the pitch curve amplitude Z_G , determined on the medium cam radius R_{med} , depending on the length $R_{med} \cdot \Psi^*$

where γ_{xy} represents the transmission angle in the joint composed by the pair elements x and y , β_{40G} is the pressure angle cam-follower (in the cam joint G), α_{40G} is the inclination angle of the pitch curve of the cylindrical cam (on a medium cylinder of radius R_{med}).

The compound mechanism from Fig. 4a achieves the elevation angle variation as show on Fig. 5a, where the elevation angle is limited to the value $\alpha^*_{max} = 48$ (the same value was considered as well for the four-bar spatial 7R linkage, presented in the Sect. 2).

For the motion law of the dependent variable angle $\alpha^*(\psi^*)$, graphically depicted in Fig. 5a, the compound mechanism with 4R plane linkage develops the transmission angles in B, C and G joints, plotted on Fig. 5b; according to their variations within the range $[50^\circ-90^\circ]$, it is thus proved that this variant represents a feasible mechanism solution, with advantageous transmission angles (Neagoe et al. 2010).

In Fig. 5c is plotted the variation of the vertical position of the G contact point between the follower and the cam profile (pitch curve), while the transmitting angle γ_G (Fig. 5b) between cam and follower is maintaining into a favorable value range (over 50°).

A second case of the compound mechanism category introduces a 3RT linkage used as planar mechanism (Fig. 6) (Fragkiadakis 2009; Mavromatakis and Franghiadakis 2008; Berger 1998); it consists of a revolute joint F which spins the vertical pole 1 around its own axis, simultaneously generating the linear relative displacement on joint D due to the contact of the translation follower 4 on the cam profile, and the spin of the planar chain ABCD around the vertical axis (AD). The 3RT linkage (ABCD) transforms the input motion from the prismatic joint D to the horizontal rotational motion of the PV platform through the joint A, where the elevation α^* is performed.

The generalized solution of dual-axis one DOF azimuth mechanism with a 3RT linkage is represented in Fig. 7a. The 3RT linkage variant with the connecting rod 3 mounted on the back of the PV platform (Fig. 7a) can be designed to develop better transmission angles than the variant from Fig. 6.

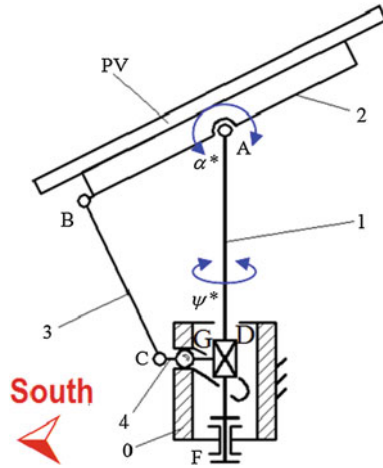


Fig. 6 The one DOF azimuth solar tracking system with fixed cylindrical cam and 3RT planar linkage: the structural scheme

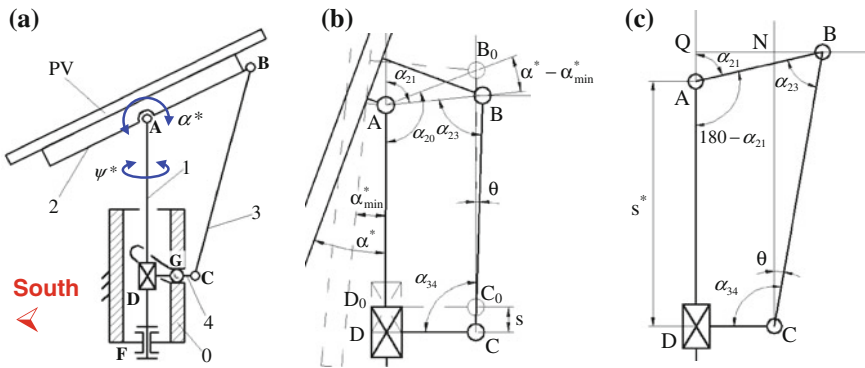


Fig. 7 (a) The compound mechanism with 3RT planar linkage, where the connecting rod is mounted on the back of the PV platform; (b), (c) the kinematic parameterization schemes of the 3RT linkage

The composed mechanism with 3RT linkage (Fig. 6) has the mobility degree $M = 1$, determined also with rel. (2) as in the previous 4R linkage case.

Based on the 3RT linkage parameterization proposed in Fig. 7b and c, the relations' set (4) is derived and used in a numerical approach to identify the kinematical characteristic features of the conceptual solution presented in Fig. 7a:

$$\left\{ \begin{array}{l} AB = r, BC = l, CD = e, \\ NB = QB - QN = r \cdot \sin \alpha_{21} - e, \\ \theta = \arcsin \frac{r \cdot \sin \alpha_{21} - e}{l}, s^* = l \cdot \cos \theta - r \cdot \cos \alpha_{21}, \\ \alpha_{23} = \alpha_{21} - \theta, \alpha_{34} = 90 + \theta, \\ \gamma_{23} = \alpha_{23} \text{ for } \alpha_{23} \leq 90^\circ, \gamma_{23} = 180 - \alpha_{23} \text{ for } \alpha_{23} > 90^\circ, \\ \gamma_{34} = \alpha_{34} \text{ for } \alpha_{34} \leq 90^\circ, \gamma_{34} = 180 - \alpha_{34} \text{ for } \alpha_{34} > 90^\circ, \end{array} \right. \quad (4)$$

where γ_{23} is the transmission angle in the joint B and γ_{34} – the transmission angle in the joint C.

Aiming to compare the main features of both compound type mechanisms, let consider for the 3RT linkage case a similar numerical example as used previously for the 4R linkage, based on the same dependence $\alpha^*(\psi^*)$, as shown in Fig. 5a, and $r = 500$ mm, $l = 1229.82$ mm, $e = 459.52$ mm, $DG = R_{med} = 420$ mm (see Fig. 7a).

The obtained variations of the transmission angles in B, C and G joints for the compound mechanism with 3RT linkage (Fig. 8a), by applying rel. (4) and comparing with the results from Fig. 5, highlight a significant improvement of the transmission angle γ_{34} in joint C (γ_C), but accompanied by a significant worsening of the transmission angle γ_G in the cam-follower contact at the angular stroke ends.

The variation of the vertical position Z_G of the G contact cam-follower point (the pitch curve) is plotted in Fig. 8b; in this case of the compound mechanism with 3RT linkage, the characteristic cam profile results with a higher amplitude (~ 350 mm) comparing with de 4R case (~ 170 mm, see Fig. 5c), leading to negative effects on the minimum value of transmission angle in cam joint. Due to the prismatic joint D, the compound mechanism with 3RT linkage becomes constructively more complex than the 4R linkage case.

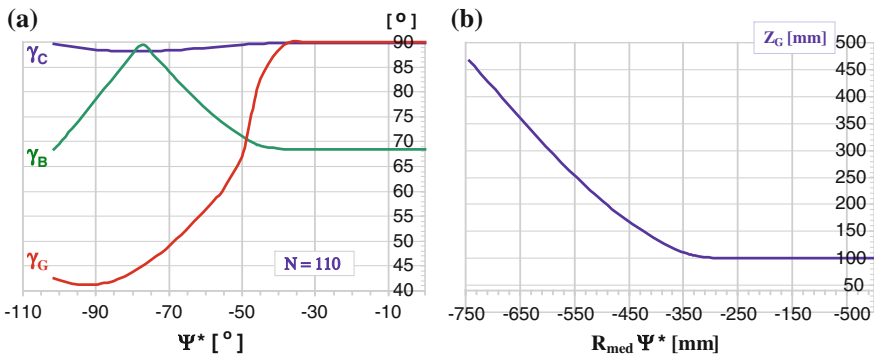


Fig. 8 (a) the transmission angles ($\gamma_B = \gamma_{23}$, $\gamma_C = \gamma_{34}$, $\gamma_G = \gamma_{40G}$) on B, C and G joints (Fig. 7), (b) the pitch curve amplitude Z_G depending on the length $R_{med} \cdot \Psi^*$

4 Conclusions

The authors developed an extended comparative research on the geometric-kinematic synthesis of two representative classes of one DOF mechanisms for dual-axis solar tracking: four-bar spatial linkage versus compound mechanism with cylindrical cam. Specific synthesis algebraic models, algorithms and monograms were developed and used for optimally design the selected representative mechanisms considering the pressure/transmitting angles as main optimization parameter, useful to design reliable low energy solutions avoiding the blocking tendency in real operational conditions. The analysis of the one DOF dual-axis solar tracking representative mechanisms allows us to draw the following conclusions:

1. The existing solutions use an **azimuth type** orientation system, where an intermediate mechanism generates the elevation motion α^* dependent on the diurnal motion ψ^* .
2. The existing solutions can be systematized in **two main categories**:
 - (a) **four-bar spatial linkages**, characterized by a robust and easy to build structure, season adapted motion programs when adjustments are allowed, suited for tracking large PV platforms. In order to avoid the low transmission angles, specific to the angular stroke ends, there are severe limitations on the diurnal and elevation strokes (e.g. for Brasov: $\Delta\psi^* \leq 180^\circ$, $\Delta\alpha^* \leq 33^\circ$ (Vatasescu et al. 2011a; Vatasescu et al. 2011b))
 - (b) **compound mechanisms**, including a simple planar linkage (4R or 3RT type) serially connected with a cam mechanism (with fixed cylindrical cam), have the advantage of allowing large diurnal and elevation strokes. The incongruent contact between the cam follower and the cam profile makes the compound mechanisms suitable only for small PV platforms, usually tracked upon on a single annual tracking program. Comparing with the 4R solution, the 3RT variant is characterized by least favorable transmission angles in the cam-follower incongruent contact at pitch curve ends and by a higher level of constructive complexity due to the prismatic joint.

Considering all the above aspects, the paper highlights that the optimum reliable solution, able to perform large diurnal and elevation tracking strokes and develops a safe operating, is the **compound mechanism with fixed cylindrical cam and 4R planar linkage**, used especially for tracking small PV platforms.

Acknowledgments This work was supported by the Romanian research program Cooperation in Priority Fields - PNII financed by CNDI-UEFISCDI through the project EST IN URBA, PN-II-PT-PCCA-2011-3.2-051, and by the Sectoral Operational Programme Human Resources Development (SOP HRD) - Post Doctoral School POSDRU/89/1.5/S/59323.

References

- Vatasescu MM, Moldovan MD, Burduhos BG (2011a) Articulated systems for solar tracking. Transilvania University Press, Braşov. ISBN: 978-973-598-946-0
- Visa I, Diaconescu D, Saulescu R, Vatasescu MM, Burduhos B (2011) A new linkage with linear actuator for tracking PV systems with large angular stroke. *Chinese J Mech Eng* 4(5):1000–9345. doi:[10.3901/CJME](https://doi.org/10.3901/CJME)
- Vatasescu M, Visa I, Diaconescu D, Saulescu R (2011b) Synthesis of a RRSS linkage for tracking a two axis photovoltaic system, 13th World Congress in Mechanism and Machine Science. Guanajuato, México
- Diaconescu D, Visa I, Vatasescu M, Saulescu R, Burduhos B (2010) The optimization of a bi-axial adjustable mono-actuator PV tracking spatial linkage. In: Pisla D, Ceccarelli M, Husty M, Corves B (eds) *New trends in mechanism science. Analysis and design*, vol 5. Springer, Berlin, pp 181–188. ISBN 978-90-481-9689-0
- Neagoe M, Diaconescu D, Jaliu C, Munteanu O, Saulescu R, Cretescu N (2010) Linkage accuracy modelling, Transilvania University Press, Braşov. ISBN 978-973-635-921-7
- Diaconescu D, Visa I, Vatasescu MM, Hermenean I, Saulescu R (2009) Synthesis of a bi-axial tracking spatial linkage with a single actuator. In: *Proceedings of SYROM*, Springer Science and Media, pp 617–632. ISBN: 978-90-481-3522-6_52
- Fragkiadakis I (2009) Innovative azimuthal solar tracker, Patent: GR1006107B1, Espacenet
- Stanestanislavo C, Soler M (2009) Patent WO 2009/087252 A1, Espacenet
- Jesus A et al (2008) Solar tracker with movement in two axes and actuation in only one of them. Patent: WO2008/000867 A1., Espacenet
- Mavromatakis F, Franghiadakis Y (2008) A highly efficient novel azimuthal heliotrope Solar Energy. *Sol Energy* 82:336–342
- Niessing Anlangenbau GmbH (2007) Patent DE202006015917U1, Espacenet
- Linder B et al (2006) Patent EP1710651A1, Espacenet
- Berger A (1998) Sun tracker, US patent No. WO94128360, Espacenet

Findings on Italian Historical Developments of Machine Technology in 19th Century Towards Industrial Revolution

Yibing Fang and Marco Ceccarelli

Abstract The chapter deals with a study to stress main characteristics of Italian industrial developments in machine technology during 19th century. Main aspects are outlined and discussion is focused on two cases of study on company developments and personality achievements.

1 Introduction

The evolution of Italian frames during the Industrial Revolution is more complex than in other European countries not only for the heavy cultural backgrounds from the past but mainly for the intriguing situations due to the history of nation unification in those years and the influences of the other European nations from several perspectives. In addition the variety of conditions made possible a variety of different evolutions both in term of geographical locations and in machine developments. Most of previous studies were focused mainly on political changes and their influences in order to reconstruct a national plan of political and social developments. Only recently specific scholars have been concentrated on the study of local evolution and even on technological developments with engineering insights, like for example in (Angotti et al. 2010; Ansaldo 1910; Bachelier et al. 1818; Cardone and La Mantia 2006). Thus, there is still a fertile field of studies for understanding the technological developments in Italy in 19th century, but in different parts of it as due to a past tradition and stimulating conditions

Y. Fang (✉)

Institute for the History of Natural Science, Chinese Academy of Sciences, Beijing,
People's Republic of China
e-mail: yibing@ihns.ac.cn

M. Ceccarelli

Laboratory of Robotics and Mechatronics, University of Cassino and South Latium,
Cassino, Italy

because of the unification and impulse of the emerging Industrial Revolution. Indeed, the unification for an Italian Kingdom gave the possibility of accelerated development of some regions and technologies but at the same time it was the cause of braking of developments in other areas.

This chapter is an attempt to clarify those contradictory evolutions in the Italian territory by outlining main aspects from technical viewpoints more than from political aspects. The study is presented with some emblematic examples as referring to the case of industrial companies and engineering productions of common values through contribution from university. The proposed findings show that South Italy was not undeveloped and academic activity was professionally oriented, with evidences that outline a view of the Italian industrialization which was usually ignored in some other literature, (Cafagna 1972; Lacaita and Poggio 2011).

2 General Considerations

The competitions among small states and kingdoms in Italy evolved from a stimulating environment of Renaissance to a frozen puzzle at the beginning of 19th century, as imposed by influence of the powerful European nations. The political situation at the beginning of Industrial Revolution is summarized in the existence of different states as indicated in Fig. 1 as related to previous situations too.

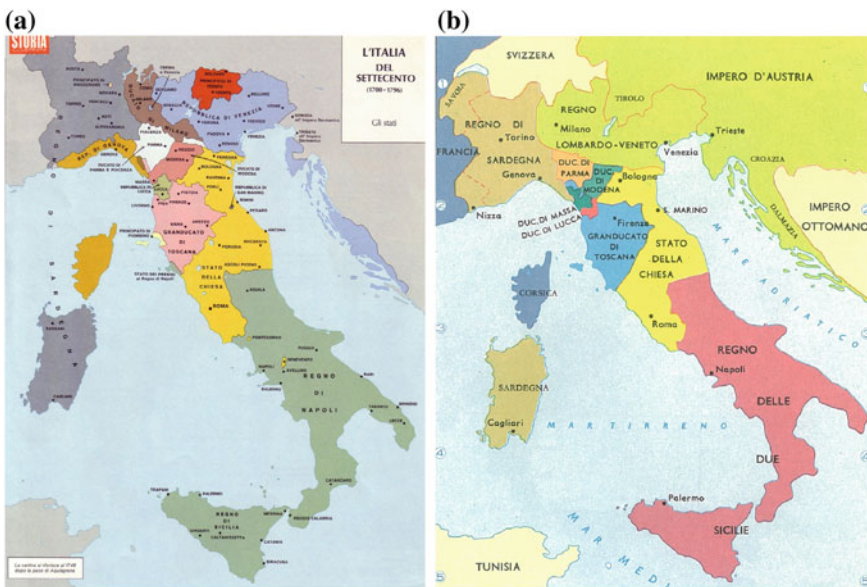


Fig. 1 States and Kingdoms in Italy in: a 1720; b 1820

This fragmentation of the territory produced also a fragmentation but a differentiation of conditions both for formation and evolution of technological frames. In general universities were organized differently not only in terms of curricula but even for professional perspectives. The emerging industrial environments were structured differently as referring not only to local market and needs, but also as function of the possibilities supported by the influencing European leader nations.

After the reunification under the Italian Kingdom that was completed in 1871, national efforts were planned to achieve common formation frames producing professionals with skills useful in whole nation territory and at the same time a common industrial infrastructure was planned that could generate a generally well distributed improvement in terms of growth of the economic, social conditions and technological capabilities. But the situations with their long-time background were so different in different areas in general culture and technological activities that even today Italy suffers of non homogenous environment for technological developments. Most influent aspects can be considered as historical backgrounds both in terms of external influences and internal traditions as well as governmental strategic plans for development and formation after reunification. University frames were very active but with differentiation and limitation in vision and result circulation. But considerable achievements were obtained even in engineering practice.

3 Handbooks by Giuseppe A. Borgnis and Giuseppe Colombo

Giuseppe Antonio Borgnis, Fig. 2a, was born on April 15, 1781 in Craveggia from a well established family since the father Giovanni was banker in Paris. He was well educated with special interest on mathematical disciplines and although the revolution time affected the family he was able to graduate as engineer. He got a position as naval engineer in Venice and because of gained expertise he wrote his first book on machines on 1809. This gave him a good reputation and got the possibility to attend the Ecole Polytechnique in Paris. During this period he deepened his expertise on machine design both on theoretical studies and practical applications, by evolving views from the Monge's approach. He published ten books from 1818 up to 1823, (Bachelier et al. 1818), as a handbook on machine designs and applications, with a new classification for an overall view, Fig. 2b, (Ceccarelli 2004). Once returned in Italy he got the position of professor at the University of Pavia where he became also rector in 1848. Because of his interests and activities in theory and engineering designs, during the first period of industrial revolution he was well reputed professor of applied mathematics and civil transportation architecture, all around Italy, although he was in the north east state within in the Austrian-Hungarian Empire.

The encyclopaedic handbook is organized by Borgnis from a clarification overview up to specific studies of category of machines by discussing design and



Fig. 2 Giuseppe Antonio Borgnis (1781–1863): **a** portrait; **b** a title page; **c** example of a machine description. (Massimo Borgnis is thankfully acknowledged for portrait and biographical notes)

operation characteristics as in Fig. 2c. The last book is on terminology with synthesis of concepts and understanding of terms that are related to design, operation, and manufacturing of machines.

Giuseppe Colombo, Fig. 3a, was born on December 3, 1836 in Milan from a middle-class family that permitted him to graduate in mathematics at the University of Pavia in March 1857. He was attracted to engineering application and he started to teach in Milan with a position of a professor of Mechanics applied to



Fig. 3 Portrait of Giuseppe Colombo (1836–1921): **a** portrait; **b** title page; **c** example of machine descriptions

Industry in 1864 and just afterwards in 1865 he got the position of a full professor at the just founded Politecnico di Milano. During his teaching he was always interested to look at the developments abroad also with the aim to stimulate similar experiences and new initiatives in the frames of the Milan society. He dedicated efforts in research and publications, with several articles in the journal Politecnico and other Italian publication frames up to work the milestone hand book for engineers in 1877, Fig. 3b. He was attracted also to implement expertise in industrial activities with foundation of companies by his former students and even with his personal participation, like for example in the case of Pirelli started in 1872. Emblematic is the initiative that he promoted and supported personally for the installation of the first electricity network in Milan with construction and operation of the first European power plant in Santa Ragedonda in the center of Milan in 1883.

After those experiences he was involved in government activities from local frames up to national positions in the Italian Parliament with increasing influence mainly in aspects linked to technological developments up to reach the role of minister and Head of the Parliament. While he run an intense political activity mainly in the last decade of the 19th century, he continued to teach and spend efforts for developing proper technical formation of engineers. After reducing the politics activity he came back with great attention to the academy and design of industrial machinery up to his death in Milan on 16 January 1921.

Colombo can be recognized as a modern engineer, who applied his activity for technological developments of society benefits up to be an influential actor of governing politics. From technical viewpoints, historical significance of his personality can be summarized in having well defined a technical formation of industrial engineers, Fig. 3b and c, with practical skills up to the publication of the milestone handbook of engineers and in having stimulated even with personal participation initiatives for industrial activities both in new emerging fields and in expanding local enterprises.

Borgnis worked out his encyclopaedic work of machine handbook as an evolution of both the tradition of *Theatrum Machinarum* and new analytical analysis of mechanisms. The handbook shows a considerable descriptive approach that is justified and indeed motivated by the fact that there was not yet a consolidated community of industrial engineers. The handbook can be also understood as a basis for an establishment of such a community. In this respect emblematic is the volume for the dictionary of technology as a need of standardization, probably also due to the fragmentation that he continuously experienced even from Italy fragmentation.

Colombo worked out his engineering handbook as inspired by a similar work by Reuleaux in Germany with the aim of providing a means for facilitating the practice of engineering. The handbook was thought as a synthesis of practical information that can help a practitioner (engineer or not) to get a first insight of a problem and a solution. It was accepted immediately with great success and several editions were published year after year up today.

In only fifty years, although Borgnis encyclopaedic work was still used even at the end of 19th century, the needs of summary of references were evolved considerably towards a more technical specialization as produced by the industrial revolution. The specificity of differentiated situations in Italy and Europe make also a great differentiation of the work and aim in the milestones by Borgnis and Colombo. The first gave handbook contribution at the beginning of the industrial revolution with common views on machine design over Europe, even with the purposes for early teaching frames. The latter worked his handbook for the Italian community of engineers and practitioners as oriented to a practical engineering with only technical contents.

4 Industrial Developments at Pietrarsa Workshop in Napoli and Ansaldo Company in Genova

Pietrarsa Workshop was originated from a small mechanical factory that was founded by William Robinson (a captain of Bourbon navy) in Torre Annunziata. The factory was part of a renovation process implemented by Ferdinando II, King of the Two Sicilies, who wished to emancipate the kingdom from the dependence on foreign military and technology. The factory was transferred to the Palace of Napoli in 1837, which was the birth place of the first Italian locomotive, Fig. 4, that served on the first railway from Napoli to Portici, inaugurated on 3 October 1839. In order to meet the development of railway, the young king decided to construct a larger workshop on the seaside of Pietrarsa. From technological view points the first two locomotives were not a real Italian output. They were designed by French engineer Armand Bayard, based on a prototype by George Stephenson. Due to the lack of capability of producing steam locomotives in Italy, the essential parts of the locomotives were built by British company and then were shipped to Napoli, where they were reassembled by local works under the guidance of British technicians.

Fig. 4 The Locomotive Bayard, one of the first locomotives built in Napoli, 1839. (Preserved in the national railway museum of Pietrarsa)



Successively, the workshop underwent a period of expansion from 1843 to 1853 by a direct interest of Ferdinando II, who planned the factory for manufacturing locomotives as well as for their repair and maintenance. A school for training machinists was also opened at Pietrarsa in April of 1841, but it was closed in 1848 since there were not enough students with employment opportunities. However, the expansion made Pietrarsa Workshops the largest industrial pole in Italy in 1853. Between 1845 and 1860, 20 locomotives were made in Pietrarsa as based on the license of Stephenson’s model, (Puca 2011). The first seven locomotives were produced under the direction of Robertson between 1845 and 1850, with materials partially stored in the military warehouse or bought in England, and partially made at Pietrarsa factory itself. The production of the second batch of 10 locomotives was completely designed and made at Pietrarsa Workshop with the exception of axles. The final three locomotives with doubled power capability were finished before the fall of the kingdom.

The origins of the Ansaldo Company may be traced back to 1846 when the English engineer Philip Taylor and the Piedmontese Fortunato Prandi established a workshop for the construction and repair of railroad machinery in Sampierdarena near Genova with a state loan. In 1853, the workshop was taken over by four new Italian entrepreneurs, namely Giovanni Ansaldo, Carlo Bombrini Raffaele Rubattino and Giacomo Penco. The new company was founded under the name Giovanni Ansaldo & C because Ansaldo was the only person who had specific technical skills for company management.

The Ansaldo Company was the first locomotive manufacturer in north Italy. In 1854 Ansaldo began to produce its first two locomotives, Fig. 5a. They were designed by Giovanni Ansaldo himself with a number of design adjustments to increase speed and reduce fuel consumption or to solve new problems in the mountain railway routes. All the essential parts of the locomotive were made at Ansaldo workshops with original solutions for steam generator, motor and mechanism system (consisting of a cylinder with piston engines linked to the apparatus for the transmission of motion and the mechanism for steam

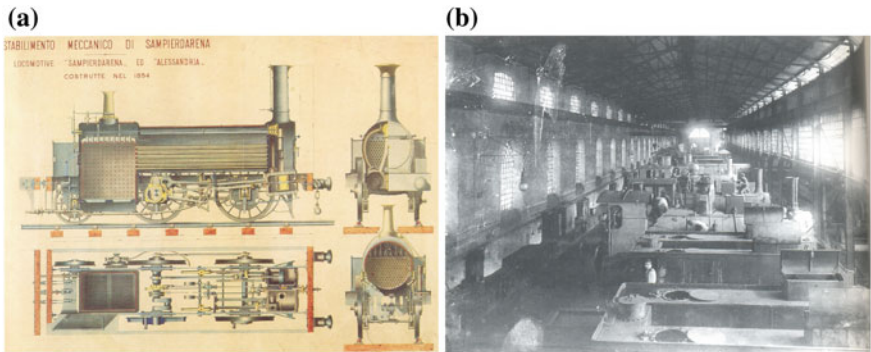


Fig. 5 Locomotives by Ansaldo company: **a** design of the locomotive Sampierdarena, in 1855; **b** construction of locomotive FS290 and FS870 in 1907

distribution), and locomotive wagon, (Lacaita 1994). These two locomotives were completed at the end of 1855 and immediately started the service in Torino-Rivoli railway. The two locomotives were successful so that Ansaldo were committed for construction of many more. 20 locomotives were produced in Ansaldo up to 1895 when Giovanni Ansaldo died. Because of the support of Italian government within strategic plans for industrial developments and military updates after the unification of Italy, the company increased the industrial capability up to be a competitor of large European companies, as demonstrated by a contract made in 1910 for a destroyer ship with the Chinese emperor Navy, (Ansaldo 1910). By the end of the First World War, the company was developed into one of Italy's largest industrial corporation that was engaged in railroad machinery, Fig. 5b, shipbuilding, armaments manufacturing and steel making.

PiETRAsarsa Workshops can be regarded as a prime effort by a monarch in Italy toward industrialization. It was a personal initiative of the king without real industrial infrastructures. Nevertheless, this made south Italy to be the first area where Italian engineering industrialization occurred. But the King's project was based on foreign technology not only in construction of the factory but also in production of locomotives. However, although the limitation of market success due to the territory fragmentation, the initiative was relevant as a successful experience of technology transfer into a local production with independent capabilities.

Ansaldo can be regarded as a typical successful case of a national plan for Italian industrialization. At its foundation Ansaldo was very limited but thanks to Italy re-unification it could benefit of strategic plans that were mainly based on North Italy. The more consistent academic technical frames in North gave support to the rapid growth of Ansaldo with well educated professionals and engineers. In South Italy Pietrasarsa Workshop was a brilliant isolate initiative that because of lack of surrounding professional frames and governmental support after re-unification, very strongly reduced the activity with a loss of a promising regional development up to a minimum in 1875. The two companies show remarkable developments on mechanical industry that beside their difference can indicate the potentiality and reality of the emerging Italian Industrial Revolution.

5 Conclusions

A survey is attempted to discuss the evolution of Italian frames towards a successful period of industrial revolution while nation re-unification. This period is characterised by considerable changes in organization and engineering approach both for design and manufacturing. Reported cases of study are emblematic examples of differences, efforts, and evolution of Italian frames towards industrial revolution.

Acknowledgments The first author acknowledges thankfully the support of Chinese Academy of Sciences for a period of study in Cassino A.Y. 2012-13.

References

- Angotti F, Pelosi G, Soldani S (eds) (2010) *At the roots of modern engineering: expertise and opportunities in Florence at 19th century*. Firenze University Press, Firenze (in Italian)
- Ansaldo (1910) *Specifications: destroyer ship for Chinese state navy*. Gio. Ansaldo Armstrong & C, Genova (in Italian)
- Borgnis GA (1818–1821) *Traité complet de mécanique appliquée aux arts*. Bachelier, Paris, vol 9
- Cafagna L (1972) *The industrial revolution in Italy 1830–1914*. In: Cipolla CM (ed) *The Fontana economic history of Europe: the emergence of industrial societies part 1*, vol 4. Glasgow, Gollins/Fontana, pp 279–328 (in Italian)
- Cardone V, La Mantia FP (eds) (2006) *The history of engineering and engineering study in Palermo and in Italy*. CUES, Salerno
- Ceccarelli M (2004) *Classifications of mechanisms over time*. Proceedings of international symposium on history of machines and mechanisms HMM 2004, Kluwer, Dordrecht, pp 285–302
- Lacaita GC (1994) *Technical and enterprise cultures*. In: *History of Ansaldo, 1: the origins 1853–1882*. Editori Laterza, Bari (in Italian)
- Lacaita C-G, Poggio PP (eds) (2011) *Science, technology and industry in the 150 years of unity of Italy*. Jaca Book SpA, Milano (In Italian)
- Puca A (2011) *The impossible industrialization in at the origin of triumphant Minerva*, vol III. Tipografia Gutenberg, Fisciano (in Italian)

Considerations Regarding the Process of Integration the Mechanisms in the Structure of the Mechatronic Systems

V. Maties, O. Hancu, C.-R. Rad and L. Dache

Abstract Mechatronic systems are the result of integration the modules belonging to mechanical engineering, electrical engineering and information-automation engineering. The paper presents the fundamentals of the integration process in the nature and technology, and the role of information in that process. Information is the basic component of the mechatronic technology. Mechatronic knowledge is the result of information structuring and integration. The concept of information links, information carriers, and information kinematic chains in the study of the mechanisms for mechatronics are outlined too. The modern concepts in engineering education like transdisciplinarity, complexity and integral education are detailed based on the educational potential of mechatronic platforms. The basic approaches in the field are detailed too.

Keywords Mechatronics · Mechanisms · Integration · Information · Education

1 Introduction

The evolution and development of the human society is closely related to the technology evolution. This connection is easily understandable if we take into account the fact that starting from the Stone Age technology we are now in the information technology age.

The term mechatronics was coined by Japanese in the mid-70s last century, to define the technology fusion: mechanics—electronics—informatics. Its meaning has been continually enriched as a natural consequence of the technology development and, step by step, mechatronics has become a philosophy, the science of

V. Maties (✉) · O. Hancu · C.-R. Rad · L. Dache
Department of Mechatronics and Machine Dynamics, Technical University of Cluj-Napoca,
Cluj-Napoca, Romania
e-mail: vistrian.maties@yahoo.com

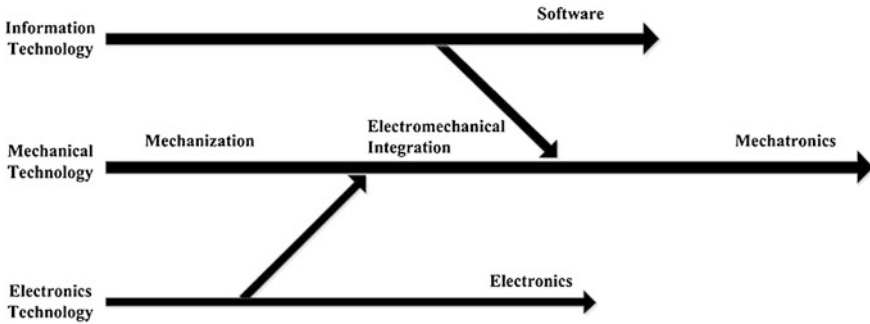


Fig. 1 Technological flow towards mechatronic integration

intelligent machines and the educational environment for integration thinking development in the knowledge based society. The flow to mechatronic integration is suggestively highlighted in the Fig. 1 (Maties et al. 2001, 2009; Nicolescu 1999; Peters et al. 1989).¹

Traditionally, mechanical technology dealt mainly with the problems of energy and material. The progress of semiconductors, especially integrated circuits, made it possible the integration of machines and electronics in one body. However, at this stage, the system could not have intelligence yet. Next revolution began with the appearance of microcomputers. Small and cheap microprocessors have been integrated into machines, and permitted machines to think and take decisions. Then, mechanical technology has changed to mechatronics by merging information-processing functions.

Integration is mechatronics paradigm (Berian and Maties 2011; Maties et al. 2009; Nicolescu 1999) and knowledge is the result of structuring and integrating information. As integronics is the science of integration processes and hyperintegrated systems (Maties et al. 2001; Nicolescu 1999), it deals with integration levels, integration degrees, hyperintegrated systems and the benefits of integration.

Integration is not a useless process. Contrary, integration gives new possibilities to control the systems. Integration gives the possibility of association to complementary elements, the possibility of connecting, of forming cycles and networks. But integration also gives the possibility to obtain a surplus of elements, a structural redundancy. In the case of hyperintegrated systems, where everything is linked to everything, the structural redundancy results in a fantastic combinatory redundancy (human body is a very representative as a hyperintegrated system). Integration therefore gives the systems larger possibilities to maintain their identity despite the second principle of thermodynamics.

In the integration process a special role is attached to information, since elements have to recognize one another in order to be able to unite in increasingly organized systems. For this reason, each element transports the substance and

¹ <http://www.complexity.ro/>.

energy it consists of, structural information that can be recognized by the other elements. In this way, some elements attract and other rejects one another, giving birth to extremely varied systems.

But, if elementary particles have a spontaneous tendency to organize in systems and if each system actually is a subsystem in a larger system, it means that besides the principle of order and organization, also exists a principle of integration, intricateness and diversification of systems. If systems are integrated in larger and larger systems, these systems become more and more complex and therefore more and more diversified and differentiated. The elements or subsystems can be genetically integrated or by force integrated. An elementary particle can be captured by the atomic nucleus that will subsequently keep it by force, a force that will not allow it to leave the respective nucleus.

Besides genetic integration and integration by force, elements can also be integrated by being made dependent on the respective system. Such is, for instance, the case of ecological systems; plants and animals depend so much on one another that they cannot even live outside the respective system. Elements can often choose the system to which they will, belong as happens in social systems. That is why we can speak of integration at choice.

Finally integration is sometimes accidental. If elementary particles collide by chance, thus is engendering other elementary particles, the hazard also plays a certain part in the integration processes.

In the case of more complex systems there also appear integration subsystems, such as the nervous system, the endocrine system and the cardiovascular system that have the role of coordinating the millions of cells of the body.

In the field of mechatronic systems the approaches to get integration of the elements of the three fields of engineering are based on hardware integration and software integration.

The future trends of the technology development are: micromechatronics, nanomechatronics and biomechatronics.

As it is emphasized in the literature, mechatronics opened new horizons in all the fields of activities, because of the synergy effect. In the knowledge based society, mechatronics is the main vector of innovation and the main support to increase the work productivity in the knowledge production. Mechatronic knowledge is technological one, the knowledge to design and manufacture the intelligent products, systems and services.

In the sequel are outlined details related on the openings caused by mechatronics in the study of the mechanisms and in the field of engineering education.

2 Mechanisms in the Structure of the Mechatronic System

The basic modules integrated in the structure of the mechatronic system are shown in the Fig. 2. As we can see the structure is very similar with the structure of a control system. This could be an explanation of the fact that one of the definitions of mechatronics is: "*the science of motion control*".

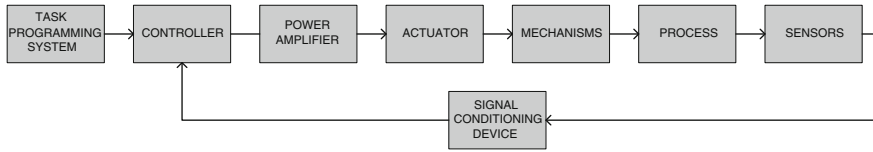


Fig. 2 The structure of a mechatronic system

The operational role of the modules integrated in the structure is: task programming system: generates the desired motions and their sequences, based on user requests or on a higher level system controller; controller: compares the desired motion with the actual motion and calculates the corrective action; Power amplifier: amplifies the corrective action to a level suitable for the actuator; actuator transforms any kind of energy into mechanical one, generating motion; mechanisms and mechanical transmissions, integrated between actuator and process, transform and adjust the motion generated by the actuator to the requirements of the process; sensors are artificial sense organs integrated in a structure of a mechatronic system and give information related on the current parameters of the process; signal conditioning device, integrates filters, amplifiers etc., and adjust signals generated by sensors to a level suitable by controller. The main feature of mechatronic systems is the dualism: energy flow-information flow (Nicolescu 1999, See footnote 1).

2.1 The Elements of the Mechatronic Technology

Long before the word mechatronics came into general use it was recognized in industry that in order to facilitate innovation and increased efficiency in manufacturing and product design, it was vital for engineers and technicians from the disciplines of mechanics and electronics to work in synergy as teams rather than independently. Competing in a globalized market requires the adaptation of modern technology to yield flexible, multifunctional products that are better, cheaper, and more intelligent than those currently on the shelf.

The importance of mechatronics is evidenced by the myriad of smart products that we take for granted in our daily lives, from the cruise control feature in our cars to advanced flight control systems and from washing machines to multifunctional precision machines.

By comparing against the conventional technology that operates mainly with material and energy, in mechatronics is added a new component, information. Obviously, making products that include more information (intelligence), their functional performance is increasing.

On the other hand, in this way the material and energy resources are preserved. But, less material and less energy means less processing, so less pollution. In this

context it follows another facet of mechatronic technology: it is a no dissipative and less polluting technology.

The information is the most important element of the mechatronic technology, by comparing against material and energy. The reasons why are (Maties et al. 2009; Nicolescu 1999).

- satisfaction of the mind of human beings is caused by information;
- only information can increase added value of all things.

The value of information depends on no quantity but freshness, because the human mind always requires new stimuli. In other words, the value of material and energy depends of integration, but that of information depends of differentiation.

Mechatronic technology launched the challenge related on “sensitivity information”. The commercial value of the passenger car for example does not depend on its basic function only.

It rather depends on its appeal to human senses for example, style, color, and so on. Any machine sends information to stimulate the five senses of human beings.

In particular, products that are originally designed to output sensitivity information such as musical instruments, toys, dolls, and so on have become increasingly important in the knowledge based society.

Taking into account the role of information in the structure of the technical intelligent systems it is easy to understand the importance to evaluate the quantity and the quality of information integrated in their structure.

It is important to note too, that signals are the physical meaning of information. Signals are generated by the sensors and transducers integrated in the structure of the mechatronic systems. Related on information integrated in the structure of the mechatronic systems it is defined the notion of carriers of information too. The carriers of information can be: radiant, mechanical, thermal, electrical, magnetic, chemical etc., depending on the system and the type of sensors integrated in their structure.

3 New Openings in the Study of the Mechanisms Caused by Mechatronics

Based on the concepts of mechatronics and integronics, mechanisms themselves are the result of integrating kinematic elements through kinematic joints. More than, defining the driving elements in the structure of the mechanisms we have to take into account the actuators and the process (the size of the actuator is defined based on the balancing torque that acts upon the driving element). On the other hand, in order to control the motion parameters generated by the mechanism, the sensors and electronic devices integrated in the structure of the mechanisms are to be known too (Maties et al. 2009; Maties et al. 2001; Nicolescu 1999, See footnote 1).

On this way, based on the fact that the kinematic elements (rigid body) could interact trough information, the notion of information link could be defined. So that, a new definition of the kinematic joint have to be taken into account: That is: “all the possibilities of interaction between two kinematic elements”. To limit the interaction can be based on mechanical contact and it is ok the conventional definition of the kinematic joint: “all the contact areas between two kinematic elements”.

More than, by analogy with the definition of the conventional kinematic chain, the notion of information kinematic chain could be defined as: “an assembly of hardware and software components used to get information, to transmit information, to process and to use information in order to control the mechanisms and machines”.

The concepts defined above are explicit presented by analyzing the structure and operation of an intelligent translation unit based on Lorentz actuator (Fig. 3) The intelligent translation unit is the result of integration of a Lorentz actuator with mobile inductor, sensors (position, velocity and current) and other electronic and control devices as these are shown in the Fig. 3 (Maties et al. 2001; Nicolescu 1999).

The Lorentz actuator includes the fixed part, made of the base plate, core and coil and the mobile unit made of the permanent magnets, polar plates and roles. The propulsion force is:

$$F = B \cdot I_a \cdot l = K_F \cdot I_a \tag{1}$$

where B is the induction of the magnetic field developed by the permanent magnets; I_a is the current through the coil conductor and l is the length of the coil conductor. The coil is located in the air gap of the actuator and there is no mechanical contact between mobile unit and the fixed part of the actuator.

The propulsion force is the result of the interaction of magnetic field developed by the permanent magnets and electrical field developed by the current trough the

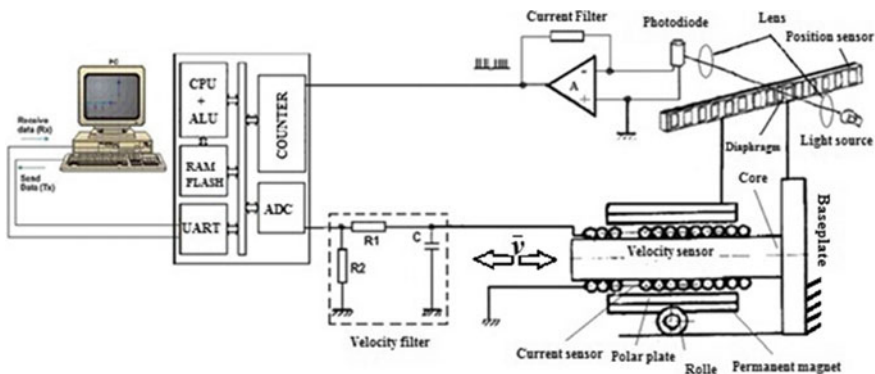


Fig. 3 The intelligent translation unit based on Lorentz actuator

coil conductor. The *information carriers* are the electrical charges that generate the current through the coil conductor. *The information kinematic chain is made of: the transducers (position, velocity and current), electronic devices, microcomputer and the specific software to control the operation of the translation unit.*

The intelligent translation units are used as translation modules in the structure of robots, in electronic technology or as positioning mechanisms. Their functional performances were proved in the applications related on positioning the magnetic heads on the disc drives.

The operation equations of the actuator are written based on the voltage balance and based on the forces balance as it follows:

$$U = I_a \cdot R_a + E \tag{2}$$

$$E = B \cdot l \cdot v \tag{3}$$

where: U —the voltage supplying the coil; I the current through the coil conductor; E —the induced voltage; l —the length of the coil conductor; v —velocity of the mobile unit.

Based on the Eqs. (2) and (3) it results:

$$U = I_a \cdot R_a + B \cdot l \cdot v \tag{4}$$

and

$$v = \frac{U}{K_F} - \frac{R_a \cdot I_a}{K_F} \tag{5}$$

Taking into account the relationship (1) we get a new relationship for the velocity of the mobile unit.

$$v = \frac{U}{K_F} - \frac{R_a \cdot F}{K_F^2} \tag{6}$$

Based on the relationship (6) we conclude that the velocity of the mobile unit can be changed by adjusting the current through the coil conductor or by adjusting the supplying voltage. Based on the balance of the forces that act upon the mobile unit we get the motion equation of the actuator:

$$F = m \frac{d^2x}{dt^2} + F_r + F_f + C_v \frac{dx}{dt} \tag{7}$$

where: x —the displacement of the mobile unit; F_r —the resistive technological force; F_f —the friction force; C_v —friction coefficient; m —the mass of mobile unit.

The operation of the actuator is fully described by the system of equations:

$$\left\{ \begin{array}{l} v = \frac{U}{K_F} - \frac{R_a \cdot I_a}{K_F} \\ F = K_F \cdot I_a \\ E = K_F \cdot v \\ F - m \frac{d^2x}{dt^2} - F_r - F_f - C_V \frac{dx}{dt} = 0 \end{array} \right. \quad (8)$$

The equations are the basis to study the operational phases of the translation unit integrated in an application for positioning the elements in a translation motion (Maties et al. 2001; Nicolescu 1999).

As it is easy to understand the complexity is the basic feature of the modern cyber-physical systems. For designing and manufacturing that systems a trans-disciplinary education is necessary. Some details in the field are outlined in the next chapter.

4 Mechatronics, Complexity and Engineering Education

English theoretical physicist Stephen Hawking, told that the 21st century will belong to complexity (See footnote 1). The complexity is closely related to the idea of non-separability, which “seems to be a fundamental principle of all that is profound in the world” (Berian and Maties 2011, See footnote 1). Consequently, research and education of the future must be shaped by the force lines of complexity and non-separability.

In other words, “intrusion of complex and transdisciplinary thinking in structures, programs and areas of influence of the University, will enable the progress towards its mission forgotten today—the study of universality”. Emphasis is provided by B. Nicolescu, founding president of the International Center for Transdisciplinary Research and Studies, Paris (Nicolescu 1999). In (Berian and Maties 2011) it is shown that, in mechatronics, complexity is a thematic concept, as defined by Holton, which gives the depth of mechatronics identity, which is a trans-thematic one. The identity of a subject to be taught can be: disciplinary (mathematics, physics, chemistry etc.), thematic (system theory-based on the concept of system) and trans-thematic (based on the complexity concept) (Berian and Maties 2011).

Mechatronic platforms are complex technical systems which integrate in their structure elements of mechanical engineering (mechanisms, mechanical transmissions, etc.), electrical—electronic engineering elements (actuators, sensors, microcontrollers, filters, amplifiers, etc.) and control science—computer science elements. So that they are the basic infrastructure for learning transdisciplinarity, in order to stimulate creativity and growth of labor productivity in the mechatronic knowledge production. Mechatronic knowledge is a technological one, or knowledge about how to manufacture intelligent products, systems and services

(Kajitani 1992; Maties et al. 2001). Taking into account the trans-thematic identity of mechatronics, mechatronic knowledge is transdisciplinary one.

Learning transdisciplinarity is a major need in the knowledge based society. Integral education ensures the achievement of this objective. The concept is introduced in (Bahman 2011; Berian and Maties 2011; Nicolescu 1999) and brings into attention educational and technological approaches where the subject participate in the educational process with his whole being (mind, emotions and psychic). Thus, modern and interactive educational technologies will be based on hexagonal model for mechatronic integral education, developed in (Berian and Maties 2011).

The mechatronic approaches are very knowledge intensive (Fig. 4). They combine kinematics and dynamics, material technology, control engineering, information technology, micro technology etc.

Furthermore, mechatronic solutions are applicable in many others sectors that are of significant importance to the welfare of the citizens, such as healthcare and transport.

The power of mechatronics approach can only be fully deployed if vast amounts of knowledge and expertise are correctly combined and canalized. Integration is therefore the key issue in the mechatronic discipline. Integration means, among others, the establishment of research teams beyond the borders of specific

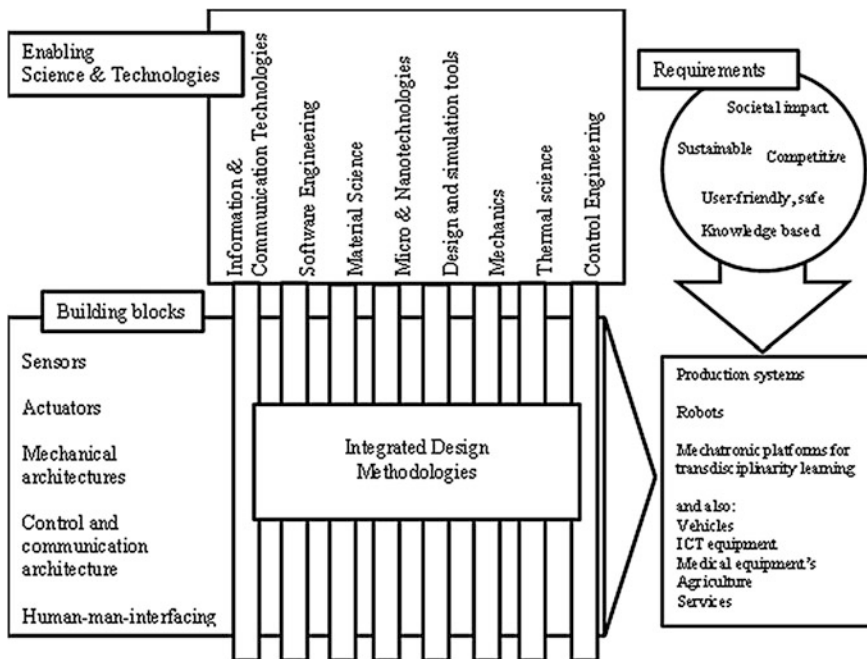


Fig. 4 The complexity concept as basis for trans-thematic identity of mechatronics

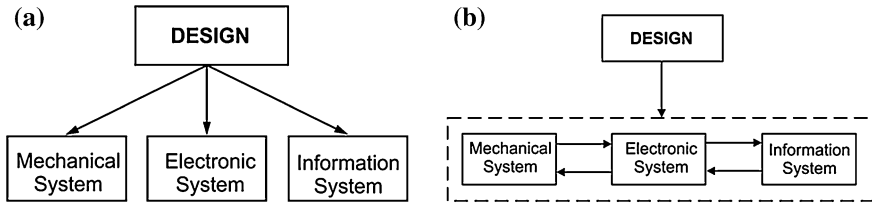


Fig. 5 Traditional approach versus mechatronic approach in engineering design

projects, existing institute or companies, having a transdisciplinary approach. Integration also means establishing the mechanisms that enable the joint management of these research teams. Integration of research resources is therefore a major undertaking.

For engineering practice mechatronic philosophy marked the jump from traditional engineering (sequential) to simultaneous or concurrent engineering (parallel).

In the Fig. 5a is presented the traditional approach and in Fig. 5b the mechatronic approach. In traditional approach, control is “attached” to the system, while in mechatronic design it is “integrated”.

5 Conclusion

The development of the knowledge based society and of the mechatronics as a technology to support such a society is a historical necessity. A long of the four decades since the word mechatronics was patented by Yaskawa Electric Cp. in Japan, the content of the word improved continuously as a result of the technology development. Step by step mechatronics became: philosophy, science of intelligent machines and educational environment for transdisciplinarity learning in the knowledge based society. The basic elements of the mechatronic technology are: material, energy and information. Mechatronics open new horizons in all the fields of activities, based on the synergy effect. Flexibility is the main feature of the mechatronic systems, caused by integrating in their structure of the information links. Based on the information as the main component of the mechatronic technology the notions of information link, information carriers and information kinematic chains in the study of the mechanisms are defined. The mechatronic paradigm is integration and its identity is trans-thematic one. So, based on the hexagonal model for mechatronic integral education, the mechatronic platform are very efficient tools for transdisciplinarity learning, in order to stimulate initiative and creativity.

References

- Bahman AKS (2011) Integral education: founding vision and principles, integral review—a transdisciplinary and transcultural. *J New Thought Res Praxis* 7(1):4–10
- Berian S, Maties V (2011), *Transdisciplinarity and Mechatronics*, Curtea Veche Publishing, Bucharest, Romania, ISBN 978-606-588-199-0 (in romanian language)
- Kajitani M (1992) What has brought mechatronics into existence in Japan? In: *Proceedings of the 1st France-Japan congress of mechatronics*, Besancon, France
- Maties V, et al (2009) *Mechatronic platforms for education and research*, Todesco Publishing, Cluj-Napoca, Romania, ISBN 978-973-7695-79-6 (in romanian language)
- Maties V et al (2001) *Mechatronic technology and education*. Todesco Publishing, Cluj-Napoca, Romania, ISBN 973-8198-05-4 (in romanian language)
- Nicolescu B (1999) *Transdisciplinarity. manifest*. Polirom Publishing, Iasi, Romania, ISBN 873-683-234-1 (in romanian language)
- Peters J, Van Brussel H (1989) Mechatronic revolution and engineering education. *Euro J Mech Eng* 34(1):5–8

Dedicated Gripper for Books Handling in a Library

N. Modler, A. Comsa, I. Maniu, E.-Ch. Lovasz and V. Ciupe

Abstract This paper presents an innovative design approach in grippers for library books handling applications, within the library automation context. As libraries provide a huge content of printed materials, the automation of books handling becomes a must. In the same point of view, a large amount of routine and repetitive activities will be reduced in the workplace of shelves and in service point. The paper is focused on innovative approach in designing a dedicated gripper for books handling in a library. It is presented the gripper CAD model and the gripper experimental prototype, developed in the Institute for Lightweight Engineering and Polymer Technology, Dresden, Germany, using light-weight thermoplastic reinforced material for the mobile finger. A field test was conducted in the laboratory during the scenes of the books manipulation process.

Keywords Service robots · Library automation · Grippers · Books handling · Light-weight design

N. Modler (✉)

Technische Universität Dresden, Dresden, Germany

e-mail: niels.modler@ilk.mw.tu-dresden.de

A. Comsa · I. Maniu · E.-Ch.Lovasz · V. Ciupe

Politehnica University of Timisoara, Timisoara, Romania

e-mail: andreicomsa85@yahoo.com

I. Maniu

e-mail: maniu.inocentiu@mec.upt.ro

E.-Ch.Lovasz

e-mail: erwin.lovasz@mec.upt.ro

V. Ciupe

e-mail: valentin.ciupe@mec.upt.ro

1 Introduction

The automatic handling systems consist usually of several different components like robots, manipulator arms, compliant structures and a controller system. The interaction between a robot and an object which needs to be handled is generally executed by a robot gripper or by other types of end effectors. As much as the need for efficient and flexible robots systems increases, as much the need for more advanced design grippers is required in such intelligent systems (Geleijnse 1994). The faster development of manipulators and robots is characterized by a multidisciplinary connection of a large spectrum of technologies (Brogardh 2007). In the last decade an intensive research about robotics and compliant structures systems has been made and many studies have been focused on manipulation and grasping process optimization (Ohya 2002). Even if many technologies are not specific for robotics, the purposed solutions can be developed and improved in larger product areas. An example of robotic application exists in the libraries where a huge amount of books needs to be automated handled. Solutions for this application consist in mobile robot arms or library manipulators that are necessary to manipulate the books on a shelf or in the service area (Suthakorn et al. 2002; Tomizawa et al. 2002; Ramos-Garijo et al. 2003; Tomizawa et al. 2004; Prats et al. 2008; Kim et al. 2008). The first industrial robot was introduced in a library in the year of 1995, in Sweden (Suthakorn et al. 2002). One of the library automation tasks is to introduce automated processes like the books handling. Because of the volume of books in the libraries, the automated book manipulation becomes a must (Pastine 1994). In the same point of view, the book handling process will reduce a large amount of routine and repetitive activities in the workplace of shelves and in service point. The main negative consequence of the library automation is the jobs elimination; without automation more staff would be needed in book handling, acquisition, cataloguing and lending (Safaric et al. 1999). One of the responsible robot components to accomplish this task represents the compliant structure.

In this paper, the authors are focus upon the mechanical finger type gripper design, two-finger parallel gripper, considering this grasping system category the most suitable for the book handling purpose.

2 The Developed Gripper for Books Handling Applications

In this paragraph is presented the gripper CAD model (Modler 2012) and the experimental prototype of the gripper designed and developed in Institute for Lightweight Engineering and Polymer Technology, Dresden, Germany.

2.1 The Gripper CAD Model

In the first step, some proprieties of the books which need to be handled must be established: maximum length $L_{max} = 290$ mm; maximum width $W_{max} = 210$ mm; maximum thickness $b_{max} = 20$ mm, maximum weight $m = 2$ kg.

In the beginning the gripper needs to be designed and selected. The selection involves matching features of the gripper to the features of the object to be handled, in this case, books. The compliant structure is selected to be a parallel gripper designed to grasp and to handle the books within a library book handling manipulator experimental model. In this preliminary design, there are some principal alternatives for the gripper, but considering the book as a parallelepiped object, the mechanical parallel gripper with two jaws is chosen to be the optimal solution. If a mechanical gripper is chosen, the type of finger and the number of fingers can be defined next. The grasping process is made through two fingers, designed in such a manner that one jaw is a passive finger (fixed) and the second is an active finger (mobile).

The CAD parts marked in Fig. 1 are: 1—grasped book, 2—mobile (active) finger, 3—fixed (passive) finger, 4—X linear drive shaft slide, 5—band, 6—Isel stepper motor, 7—band guiding shafts, 8—coupling, 9—spacer, for book vertical position maintaining.

2.2 The Achieved Experimental Prototype of the Developed Gripper

The CAD parts marked in Fig. 2 are: 1—band, 2—mobile (active) finger, 3—fixed (passive) finger, 4—cable, 5—Isel stepper motor, 6—band guiding shafts, 7—coupling, 8—spacer, for book vertical position maintaining.

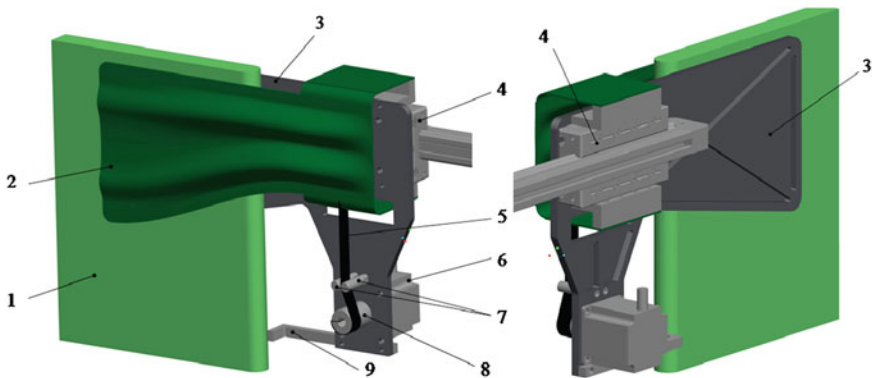


Fig. 1 The developed gripper CAD model mounted on a linear drive

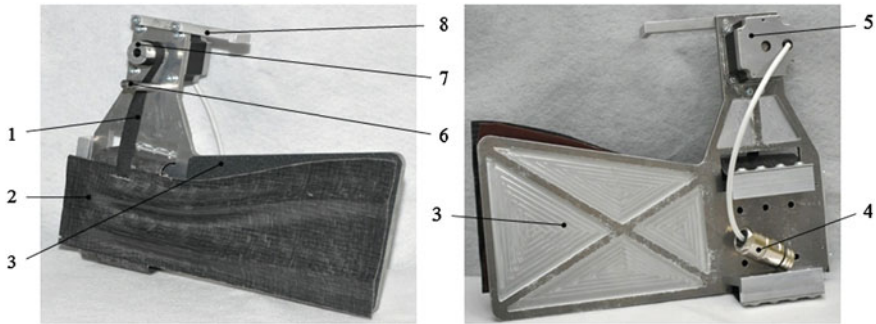


Fig. 2 The achieved experimental prototype of the developed gripper

The mobile ribbed jaw is operated by a high-torque stepper motor via a parallelogram mechanism. The parallelogram mechanism is operated through a band rolled on the motor shaft. When the band is loaded by the motor torque, the parallelogram mechanism makes a translational displacement which allows to the mobile finger to get close to the book and to fit it between the jaws. The idea of this compliant structure is lying on a light-weight and non-complex design to use the intrinsic material flexibility properties instead of complex fingers operating system. Regarding to these considerations and the gripper driving system, the light-weight thermoplastic reinforced material for the mobile finger and for parallelogram mechanism is chosen.

This material is unique and ready-to-use thermoplastic reinforcement, designed for high mechanical properties, such as excellent stiffness/weight ratio and superior impact properties. Also provides with efficient and environmental friendly process conditions, high freedom of design and is recyclable.¹

As can be seen in Fig. 2, special fingers and special geometry of the jaws have been designed to accomplish the book handling process. Moreover, some initial conditions concerning books are established as the first step:

- Books must be graspable by the proposed robot gripper. That means, the books physical proprieties (weight, thickness) will be always suitable for the designed grasping capabilities and geometry of the gripper. For example in this case, the gripper is able to handle books between 0 and 20 mm thickness.
- The books stand in a vertical position on the bookshelf.
- Because of the thickness of the gripper fingers, it is assumed that the books are not exerting too much pressure among them, in their usual location on the bookshelf. A small distance between the books is required.

¹ Information on <http://www.ocvreinforcements.com/solutions/Twintex.aspx>.

3 Scenes of the Experiment Using the Developed Gripper

In Fig. 3 are presented the scenes of a manipulating books experiment using the developed prototype gripper (Comsa 2013):

- A: the book which needs to be manipulated is chosen;
- B: positioning the gripper in a learned book position (every book has a learned position)
- C: the gripper is approaching the selected book;
- D: the mobile finger is operated by the stepper motor and the book is grasped;
- E: the gripper is lifted with 10° from the initial position (using a pneumatic muscle which operates the linear drive where the gripper is mounting on); enough to not damage the book with the shelf surface, while it is extracted;

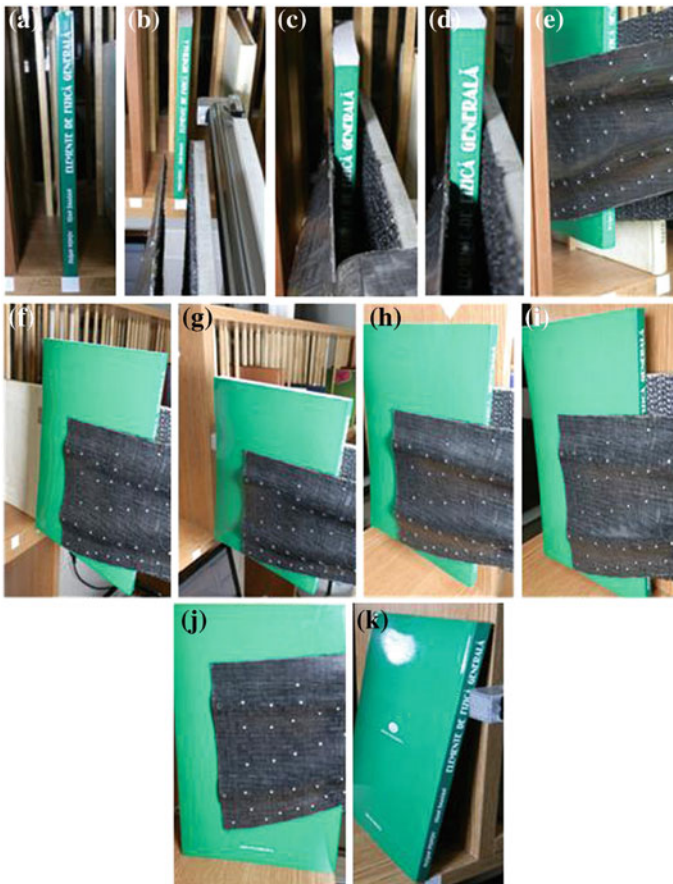


Fig. 3 Scenes of an experiment using the developed books manipulator

- F: extracting the book from the bookshelf;
- G: reaching the books lending point;
- H: inserting the gripper in the lending area (temporary books storage place);
- I: relaxing the pneumatic muscle (the book have contact again with the shelf surface);
- J: opening the gripper, book positioning complete;
- K: book final position (extracting the gripper from the shelf and reaching the manipulator home position).

4 Conclusions

The gripper model uses innovative grasping system and a special light-weight thermoplastic reinforced manufacturing material. It was designed to allow grasping of less than 2 kg book weight and between 0 and 20 mm book thickness. A field test was conducted in the laboratory test. More experimental results achievement it is a future purpose. Another future purpose is to mount a camera on the gripper support for the book recognizing process.

This work stimulates the robotic book handling in libraries, and in the digital library context. As the robotic field has a great utility and impact in all other applications, in the near future we can expect of an autonomous books handling process in libraries and a strong development in all-in-one handling and scanning robots in a digital libraries.

Acknowledgments The research for this paper was made in collaboration with Institute for Lightweight Engineering and Polymer Technology (ILK), Dresden, Germany.

The authors would like to express their gratitude towards the German Research Foundation (DFG), which supports this research within the scope of the subproject D2 of the Collaborative Research Centre SFB 639 Textile-Reinforced Composite Components in Function-Integrating Multi-Material Design for Complex Lightweight Applications.

References

- Brogardh T (2007) Present and future robot control development-an industrial perspective. *ABB Robot* 31:69–79
- Comsa A (2013) Contributii privind automatizarea procesului de manipulare a cartilor in biblioteci. (PhD Thesis). “Politehnica” University of Timisoara. ISBN 978-606-554-624-0
- Geleijnse H (1994) Human and organizational aspects of library automation, Tilburg
- Kim BK, Ohara K, Kitagaki K, Ohba K (2008) Design of ubiquitous space for the robotic library system and its application. In: *Proceedings of the 17th world congress (IFAC)*, pp 8221–8225
- Modler N, Hufenbach W, Comsa A, Maniu I, Zichner M, Friedrich J (2012) Compliant structures in book handling applications. *Appl Mech Mater (Switzerland)* 162:543–548. ISBN: 978-3-03785-395-5

- Ohya A (2002) Human robot interaction in mobile robot applications. In: Robot and human interactive communication
- Prats M, Martínez E, Sanz PJ, del Pobil AP (2008) The UJI librarian robot. *Intel Serv Robot* 1(4):321–335
- Pastine M, Kacena C (1994) Library automation, networking and other online and new technology costs in academic libraries. *Libr Trends*. 42:524–536
- Ramos-Garijo R, Prats M, Sanz PJ, Del Pobil AP (2003) An autonomous assistant robot for book manipulation in a library. In: IEEE international conference systems on manipulation and cybernetics, vol 4, pp 3912–3917
- Suthakorn J, Lee S, Yu Z, Thomas R, Choudhury S, Chirikjian GS (2002) A robotic library system for an off-site shelving facility. In: IEEE international conference on robotics and automation. Proceedings ICRA '02, vol 4, pp 3589–3594
- Safaric R, Jezernik K, Calkin DW, Parkin RM (1999) Telerobot control via internet. In: Proceedings of the IEEE international symposium on industrial electronics, pp 298–303
- Tomizawa T, Ohya A, Yuta S (2002) Book Browsing system using an autonomous mobile robot teleoperated via the internet. In: IEEE international conference on intelligent robots and systems, vol 2, pp. 1284–1289
- Tomizawa T, Ohya A, Yuta S (2004) Book extraction for the remote book browsing robot system. *J Robot Mechatron* 16(3):264–270

Review on Mechanisms Used as Handbrake in Carriages and Locomotives

Ovidiu Antonescu, Ionut Geonea and Paun Antonescu

Abstract The paper presents some kinematic schemes of the major mechanisms used as linkages for handbrakes on railway carriages and locomotives. For the classical linkage with brake shoes on the axle wheels of carriages or locomotives, articulated mechanisms with bars, gears, articulated chains and motion bolts are used. In the case of linkage with planar brake pads, the disk brake consists of deformable elements, such as cables. At two-axle or four-axle carriages (bogies with two axles) with central brake linkage, there is only one mechanism for the handbrake. Diesel-electric locomotives with three-axle bogies have two brake mechanisms for each bogie.

Keywords Mechanism · Mobility · Kinematic scheme · Element · Kinematic joint · Handbrake · Carriage · Locomotive · Brake shoe · Brake pad

1 General Aspects

Each railway vehicle, like other types of vehicles is equipped with manual brake systems, known as handbrakes (Sebesan 1956; Tilea 1961; Sarbulescu and Antonescu 2010).

O. Antonescu (✉) · P. Antonescu
University Politehnica of Bucharest, Splaiul Independentei nr. 313, Bucharest, Romania
e-mail: oval33@hotmail.com

P. Antonescu
e-mail: panton38@hotmail.com

I. Geonea
University of Craiova, Calea Bucuresti nr. 107, Craiova, Romania
e-mail: igeonea@yahoo.com

The handbrake mechanism of a railway vehicle is accomplished in several variants, as articulated rod structure (Antonescu 2005; Sarbulescu and Antonescu 2010), gears, motion screw, articulated chain and special cables (in the shape of flexible rod guided in a ball channel).

These mechanisms differ by the type of vehicle brake linkage and they may have cylindrical shoes on the wheels of the carriage (Fig. 1) and locomotive (Fig. 2) or planar brake pads on the disks mounted on the axles of the carriage.

2 The Handbrake of the Shoe Brake Linkage

In the bogies with brake shoes on wheels, the brake linkage is placed at one end of the carriage and actuates only in one direction the central linkage (Fig. 1) located in the horizontal plane (Fig. 3).

The driving component of the mechanism is the vertical screw, element 1 (Fig. 3), which is manually operated by means of a crank that rotates in horizontal plane.

By means of the nut 2 and the connecting rod 3, the movement is transmitted to the rocker 4.

Through joint C the rocker 4 is articulated to the longer bar 5 from the end of the carriage to the central mechanism.

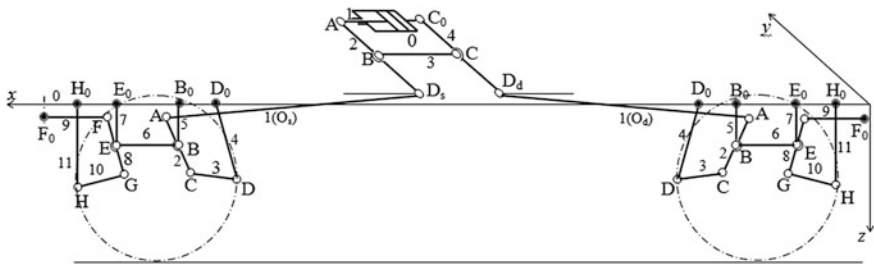


Fig. 1 The kinematic scheme of a braking mechanism on a two-axle railway carriage

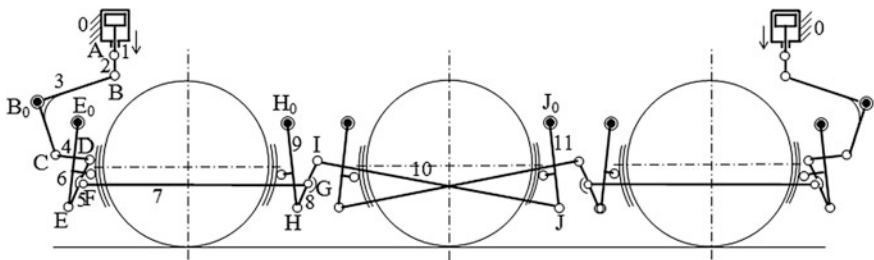


Fig. 2 The kinematic scheme of the shoe brake mechanism of the bogie with 3 axles used on a locomotive

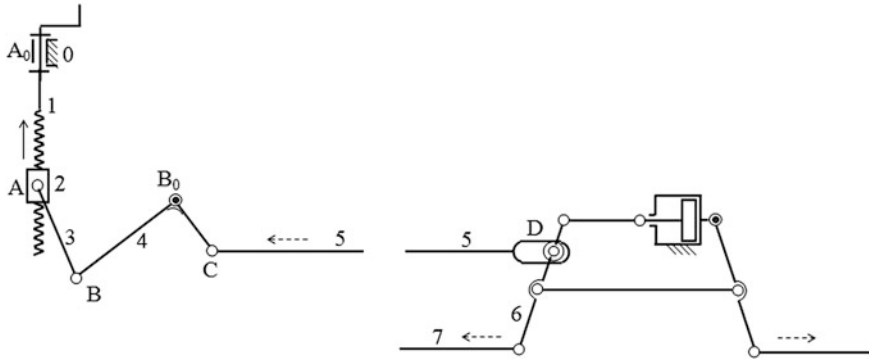


Fig. 3 The kinematic scheme of the carriage handbrake linkage with driving screw

It can be observed that when the brake piston is pushing the bar 6, the longitudinal rod 5 oscillates slightly around point C due to the roller in the point D which is guided into a rectilinear slot.

In the first phase of the brake linkage operation the center of the roller in D remains fixed.

Because two independent closed contours of equal families ($f_1 = f_2 = 2$) are identified, the mobility of the handbrake mechanism is calculated by the formula (Antonescu 2005):

$$M = (6 - f)n - \sum_{k=f+1}^5 (k - f)C_k \tag{1}$$

where $f = f_1 = f_2 = 2$ is the real family.

If we give in (1) the numerical parameters (Fig. 3):

$$f = 2, n = 5, C_5 = 6, C_4 = 0, C_3 = 1, C_2 = C_1 = 0,$$

the following mobility is obtained:

$$M = (6 - 2) \times 5 - (5 - 2) \times 6 - (4 - 2) \times 0 - (3 - 2) \times 1 = 4 \times 5 - 3 \times 6 - 1 \times 1 = 1 \tag{2}$$

3 The Handbrake on Diesel-Electric Locomotives (D-E)

In the case of D-E locomotives, the kinematic scheme of the handbrake linkage (Fig. 4a1) is similar to that used on carriages (Antonescu and Antonescu 2012).

Through the crank rotation (screw joint motion) the movement is transmitted to the nut 2 and then, through rod 3, the movement reaches the rocker 4 (Fig. 4a1).

Further the movement is transmitted through dyadic chain LD (5, 6) to the longitudinal bar 7.

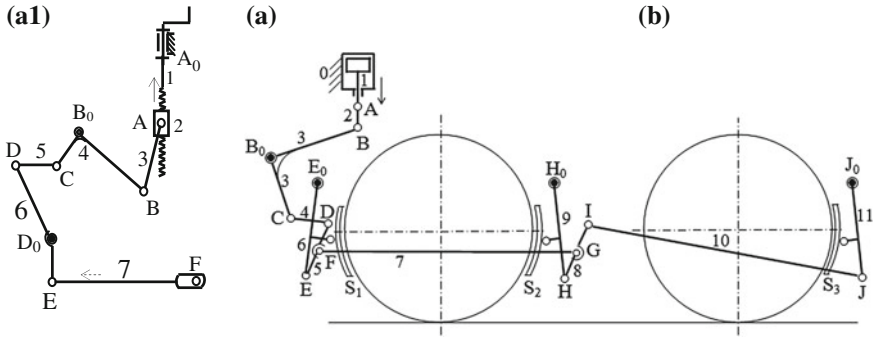


Fig. 4 The kinematic scheme of one of the brake linkages used on D–E locomotives

The mechanism mobility is calculated by the formula P. Antonescu (Antonescu 2005):

$$M = (6 - f_a) \cdot n - \sum_{k=1}^5 (k - f_a) \cdot C_k \tag{3}$$

In the mechanism structure there are two closed independent contours: the kinematic chain (0, 1, 2, 3, 4, 0) with the family $f_1 = 2$ and the chain (0, 4, 5, 6, 0) with the family $f_2 = 3$. We obtain the apparent family f_a as a real number and we have established the arithmetic average of the families of the two contours:

$$f_a = \frac{1}{2}(f_1 + f_2) = \frac{1}{2}(2 + 3) = \frac{5}{2} \tag{4}$$

Observing the kinematic scheme (Fig. 4a1), we identify $n = 6$ mobile kinematic elements, $C_5 = 8$ kinematic joints of 5th category.

Introducing the numerical data in the formula (3) we obtain:

$$M = (6 - \frac{5}{2}) \times 6 - (5 - \frac{5}{2}) \times 8 = 1 \tag{5}$$

The obtained result ($M = 1$) shows that the handbrake mechanism for those three brake shoes S_1, S_2 and S_3 (Fig. 4a, b) can be actuated by means of a single kinematic element (driving element 1).

The other three brake shoes on the right side of the bogie (Fig. 2) are manually operated by another brake linkage mechanism placed on the right side of the kinematic scheme (Fig. 2).

4 Handbrake Linkage with Articulated Chain (Gall)

There is a version of handbrake mechanism used on the passenger carriages which uses the articulated chain 2 type Gall and the motion screw 3' fixed together with chain gear 3 (Fig. 5).

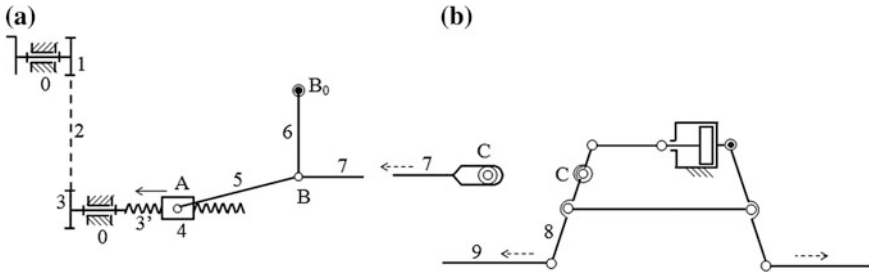


Fig. 5 The kinematic scheme of the brake mechanism with Gall chain and motion screw

The crank is fixed together with the gear 1 which is geared with the Gall chain 2. Through the Gall chain 2 the rotation movement is transmitted to chain gear 3 (fixed together with the motion screw 3'). The rotation motion of the screw is transformed into sliding movement of the nut 4 (Fig. 5a) which is articulated in joint A to the rod 5.

Further through the rod 5 the sliding movement of the nut 4 is transformed into rotation movement of the rocker 6. The joint B is double because three kinematic elements (5, 6 and 7) are coupled in this point.

The element 7 is connected to the central linkage (Fig. 5b) in point C from which the movement is transmitted through bars 8 and 9 further to the brake shoes. The mechanism mobility (with bars, chain gears, articulated chain and screw) of the handbrake (Fig. 5a) can be calculated by means of the formula Antonescu (2005):

$$M = \sum_{m=1}^5 (mC_m) - \sum_{r=2}^6 (rN_r) \tag{6}$$

Observing the kinematic scheme (Fig. 5a) the following structural parameters (the kinematic joint mobility m , the number of kinematic joints C_m of class m , rank of the associated space r of a closed contour, number of contours N_r of rank r) are identified: $m = 1$; $C_5 = 8$; $r = 3$; $N_3 = 1$; $r = 4$; $N_4 = 1$. Applying these numbers in relation (6) we obtain the value of mobility: $M = 1 \times 8 - (3 \times 1 + 4 \times 1) = 1$, which justify the possibility of actuating the handbrake from a single driving element 1 (Fig. 5a).

5 The Cable Handbrake Mechanism

The cable handbrake mechanism is used both to the complex linkage with brake shoes on wheels and to the simple linkage with planar brake pads on a disk (Fig. 6a) or two disks (Fig. 6b) that are fixed on the carriage axle (Tilea and Antonescu 2011; Antonescu et al. 2012).

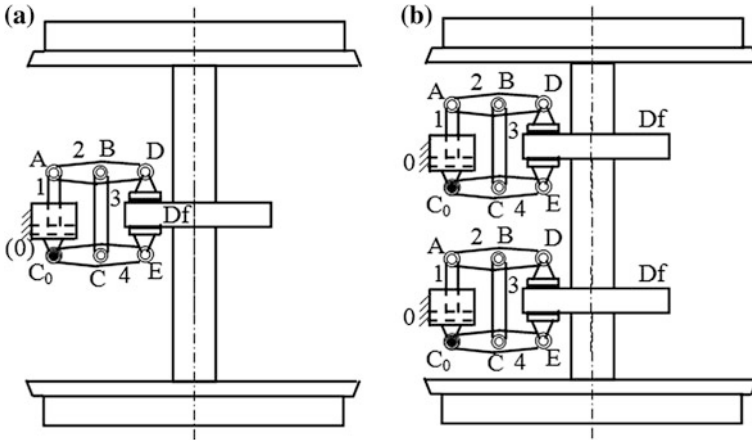


Fig. 6 The constructive schemes of the simple disk brake mechanisms

In this case the handbrake (Fig. 7) has a complex structure with rigid and flexible kinematic elements, and as final element we have the piston 6 of the handbrake (Antonescu et al. 2012; Antonescu and Antonescu 2012).

The crank is fixed together with the bevel gear 1 which is geared with the gear 2 that is fixed together with the motion screw 2'. The rotation movement of the screw 2' is transformed into sliding movement of the nut 3. The cable 3' (which is fixed together with the nut 3) is guided by means of a deformable tube and actuates the rocker 4. This element 4 pushes on the rod 5 which in turn pushes the piston 6 performing braking of the disk mounted on the carriage axle.

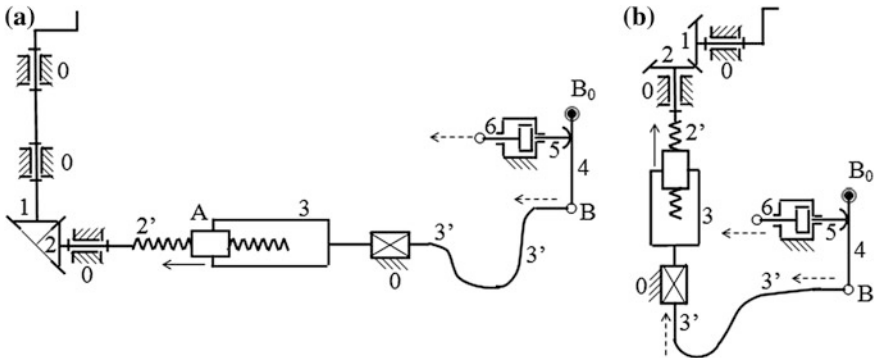


Fig. 7 The kinematic schemes of the handbrake linkages with cable

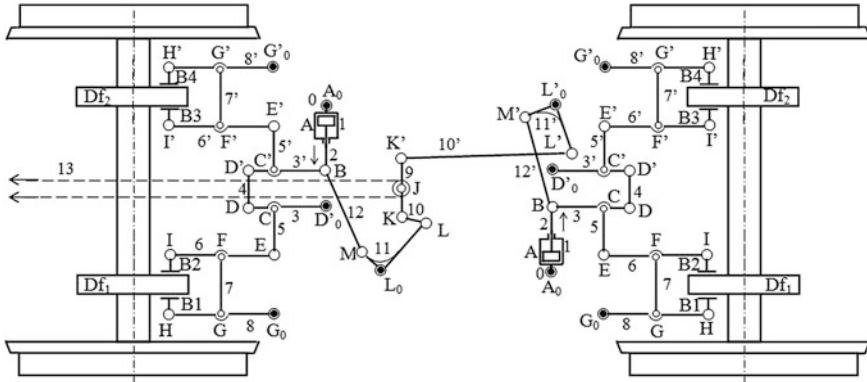


Fig. 8 The kinematic scheme of the handbrake linkage with cable

6 The Handbrake of the Complex Disk Brake Linkage with Planar Pads

The handbrake mechanism of the disk brake linkage for a 2-axle bogie is presented in Fig. 8.

Let's considering the case of a 2-axle bogie with disk brake using planar pads (Fig. 8) in which each braking linkage of an axle with two disks is driven by a single actuator cylinder oscillating in respect to the joint axis A_0 .

The braking of the two disks mounted on an axle is obtained by successive actuation of the four planar pads B1 and B2 on the disk D_{f1} , respectively B3 and B4 on the disk D_{f2} .

Through the crank, the rotation is transmitted and converted into sliding movement of the cable 13 with two branches (Fig. 8) and passing over a roller mounted in the center J of the bar 9.

By moving the bar 9 to the left, the sliding motion is transmitted through the bars 10 and 10' to the rockers 11 and 11' that rotate in opposite directions.

Through these two rockers 11 (which rotates trigonometrically) and 11' (which rotates clockwise) the movement is transmitted by means of the rods 12 and 12' to the pistons 2 (left and right), and then actuating all the chained elements of the mechanism up to the final elements, the brake pads B1–B4.

7 Conclusions

The mechanisms studied in this paper are used as handbrake linkage fitted to railway carriages and locomotives.

To operate these handbrakes, motion screw mechanisms and other kinematic elements of different types are used, such as planar articulated bars, gears (cylindrical or conical), articulated chain and guided cable.

The handbrake mechanism is a kinematic chain with serial connections, which can actuate the driving piston in case of emergency when the motor agent, represented by the compressed air in the brake cylinder, has been lost.

The use of the motion screw in all kinematic schemes of the handbrake mechanism ensures satisfactory a mechanical efficiency which allows a reduction of the railway vehicle braking time.

References

- Antonescu P (2005) Mechanism and machine science. Printech Publishing House, Bucharest
- Sebesan S (1956) Contribution on the determination of the position and length of the bars used on the braking linkages with symmetrical and asymmetrical actuation. *J Railway Issues* 7:3–8 (in Romanian)
- Tilea D (1961) Apparatus and installations used on rail cars. Didactic and Pedagogic Press, Bucharest (in Romanian)
- Sarbulescu M, Antonescu O (2010) Structural and topological analysis of braking mechanisms in railway vehicles. *J Mech Manipulators* 9(2):17–22
- Tilea D, Antonescu O (2011) Braking mechanisms of the railway vehicles on high speed. *J Mech Manipulators* 10(1):21–26 (in Romanian)
- Antonescu O, Sîrbulescu M, Antonescu P (2012) Synthesis of braking mechanisms in railway vehicles. *J Mech Manipulators* 11(1):41–48
- Antonescu P, Antonescu O (2012) Topological structure of braking mechanisms with sabots on locomotive wheels. *J Mech Manipulators* 11(1):49–54 (in Romanian)

Using Mathematica Program in Teaching Mechanisms

Madalina Rus, Silvia Veresiu and Elena Mereuta

Abstract The paper presents some applications of computer software named Mathematica 9 which can be used to teach mechanisms theory and science. The application provides a visualization instrument for the shapes of the connecting rod curve and controls for all the constructive parameters. The students are able to visualize dynamically the changes in positions, velocities, and trajectories while they act on control buttons.

1 Introduction

The machines, equipments, industrial robots, the mechanical systems in general, are considered to be a human creation that developed in time aiming to reach some established goals such as: producing the useful work or the transformation of the energy from one form to another. The machine is a mechanical system made of many components or subsystems whose kinematics and dynamics is described by means of mathematical models expressed by systems of equations (Mereuta 2007).

In order to develop the mathematical model, one needs a detailed analysis of: the structure, the geometry, the kinematics, the kinetics, the dynamics and the mechanical process to which the elements are subjected.

The system of equations that is the basis of the kinematic analysis can be correctly written only if the movements made in time by the elements of the studied mechanism are identified and understood. The paper tackles the problem of students' education by means of the visual and mechanisms' analysis software.

M. Rus (✉) · S. Veresiu · E. Mereuta

Faculty of Mechanical Engineering, Applied Mechanics Department, "Dunarea de Jos"
University of Galati, Street Domneasca Nr.111, Galati, Romania
e-mail: mrus@ugal.ro

E. Mereuta

e-mail: emereuta@ugal.ro

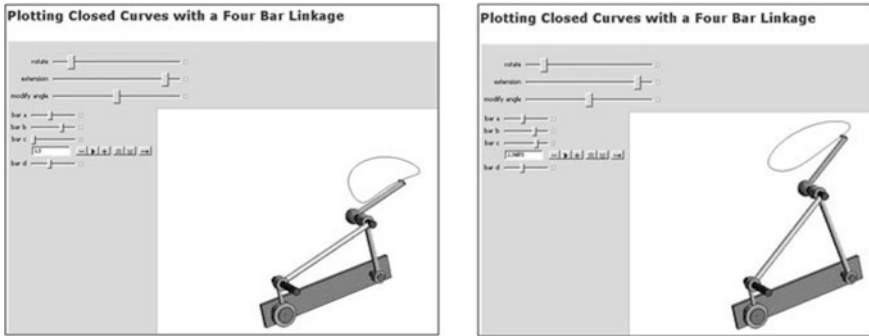


Fig. 1 Different shapes of the connecting rod curve depending on the length of the follower

Mathematica 9 software allows the visualization of the kinematic elements positions with respect to time, together with the connecting rod curves. Different shapes of these curves are obtained while the geometrical parameters are modified¹.

Using Mathematica 9 software it is possible to notice the influence of geometrical parameters on the trajectories of kinematic elements.

2 The Influences of the Geometrical Parameters on the Shapes of the Connecting Rod Curves

The geometrical parameters are the lengths of the elements and the angles. The connecting rod curves are the trajectories described by different points of the connecting rod (Razmerita 1998).

These curves are differently shaped, as follows:

- with double points (Figs. 4, 5);
- with picks (Fig. 2);
- with straight lines (Fig. 1);
- with arcs (Fig. 6);
- other trajectories.

The connecting rod curves can be used in designing different mechanisms, as shown below:

1. to automation some technological process of big series—those with double points;
2. to make a short term stop (e.g. the typing machine)—those with tops;

¹ <http://reference.wolfram.com/mathematica/guide/Mathematica.html>.

3. to move a load in a certain direction (e.g. cranes)—those with straight sections;
4. for mechanisms having stops (e.g. loom)—those with sectors.

Different shapes of the connecting rod curves are exemplified by three different planar mechanisms: the four-bar mechanism, the Lemniscate's plot mechanism and the crank and connecting rod mechanism.

2.1 The Four-Bar Mechanism

Using the features of this application it is possible to visualize the closed loops (connecting rod curves) described by the end of an extension arm attached to a connecting rod "b", when the lengths of the four elements (a, b, c, d), the rotation angle of the crank "a", the angle formed by the extension arm and the attached element, as well as the length of the extension arm are variables.

When the length of element "c" is variable, the shape of the connecting rod curve is shown in Fig. 1:

When the length of the extension arm is variable, the connecting rod curves are shown in Fig. 2:

When the angle formed by the extension arm and the connecting rod is variable, the shapes of the connecting rod curves are shown in Fig. 3:

Resulting from the visualization, it can be noticed that the form of the connecting rod's curve described by the end of the extension arm is strongly influenced of the angle formed between the extension arm and the connecting rod, as well as the modification of the length of the element "c".

It is revealed that the shape of the connecting rod curve is strongly influenced by the angle between the extension arm and the connecting rod, while the length of element "c" has a smaller influence on the shape.

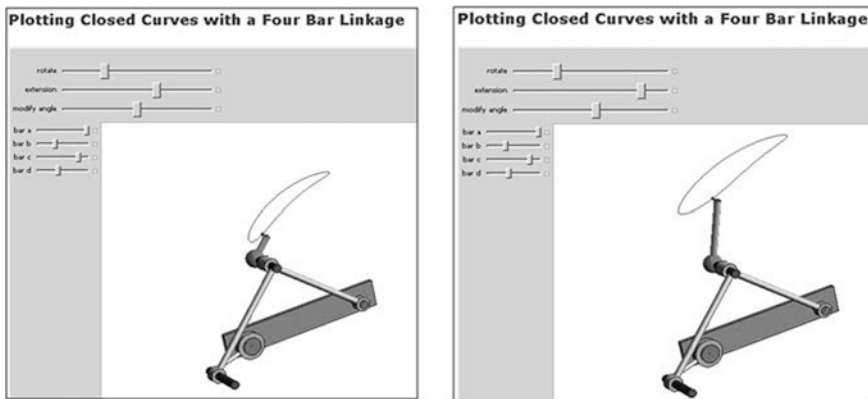


Fig. 2 Different shapes of the connecting rod curve depending on the length of the extension arm

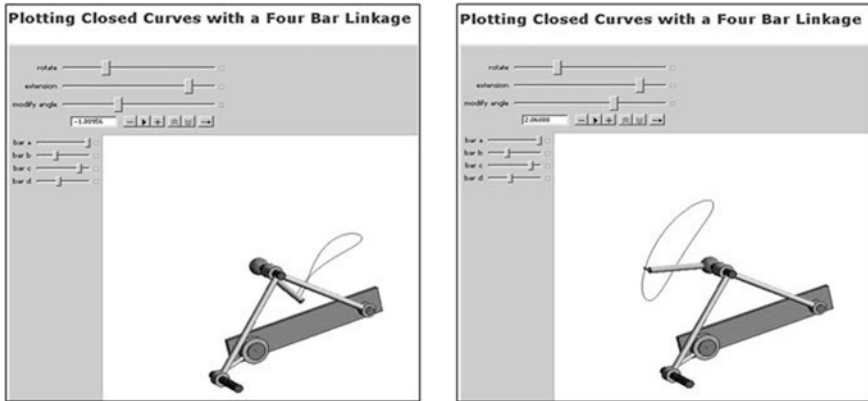


Fig. 3 Different shapes of the connecting rod curve depending on the angle formed by the extension arm and the connecting rod

2.2 The Lemniscate's Plot Mechanism

Using Mathematica 9 software features it is possible to visualize the curves described by a point from the connecting rod when the rotation angle of the driving element (the crank) (Fig. 4) and the connecting rod's length are modified (Fig. 5). the modification of the length of the connecting rod:

In both cases, it can be seen that the described curve has double points and that it is necessary to the mechanisms having short terms stops.

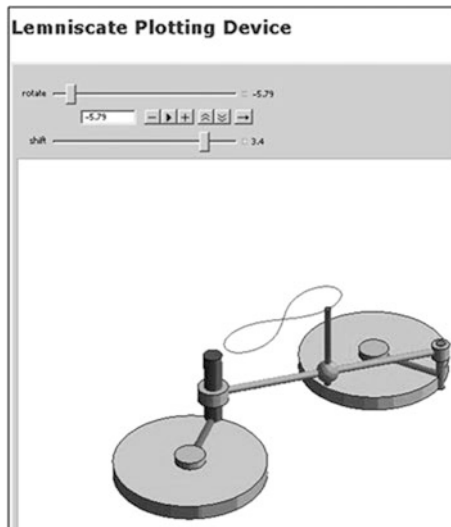


Fig. 4 The connecting rod curve

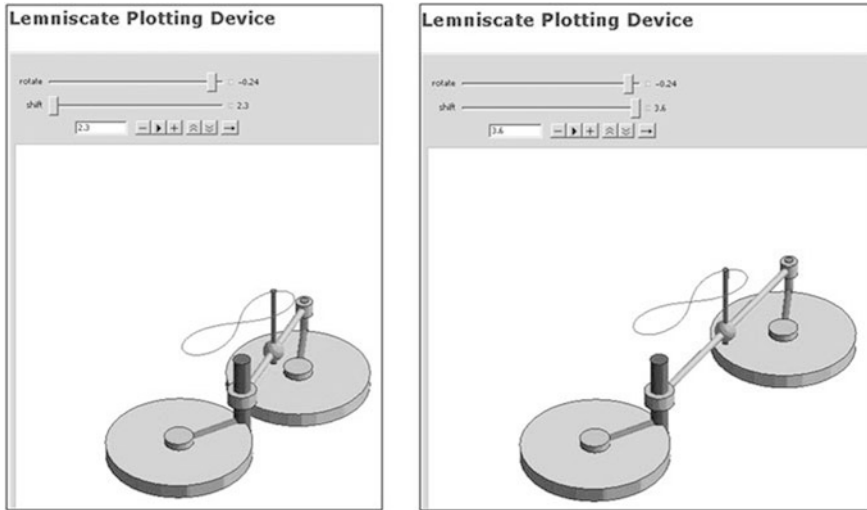


Fig. 5 Different shapes of Lemniscate curves when the length of connecting rod is variable

2.3 The Slider Crank Mechanism

The crank and connecting rod mechanism transforms the rotation movement into alternative rectilinear movement or vice versa (Razmerita 1998).

Using this application one can visualize the curves described by a point on the connecting rod when the length of kinematic elements are variables. Major influences can be seen into the shape of the curve (from the straight line shape to arcs and vice versa); they have the same modifications with the ones of the length of the extension arm attached to the connecting rod and with the connecting rod's length.

- the modification of the crank's rotation angle (Fig. 6):
- the modification of the connecting rod length (Fig. 7):
- the modification of the length of the extension arm (Fig. 8):

3 The Influence of Geometrical Parameters on Mechanisms Configuration

The configuration (positional) analysis assumes that at any time- the positions on the driven elements or the trajectories described by any point that belongs to a kinematic element from the mechanism's structure are known positional (Mereuta 2007). The positional analysis is necessary for the mechanism's kinematics and kinetics. The influences of the geometrical parameters on the positions are exemplified using two types of mechanisms: one with bars—the shaping driving mechanism and one with gear wheels – the gear having fixed axes.

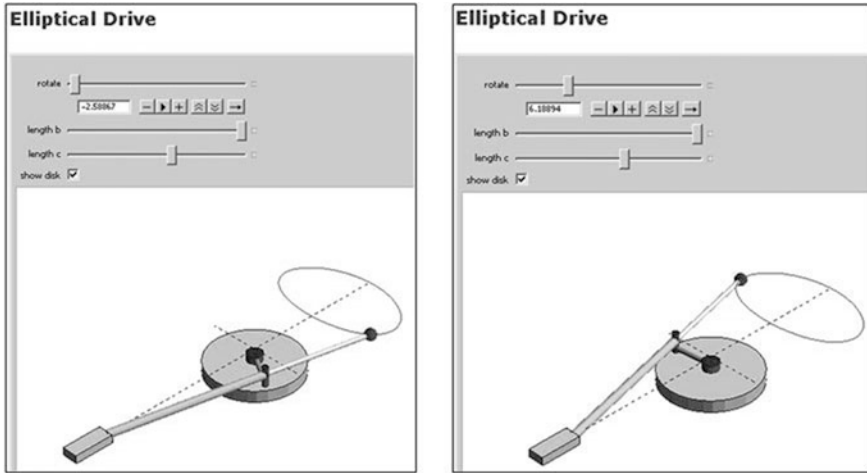


Fig. 6 The modification of the shape of the connecting rod curve with different input angles

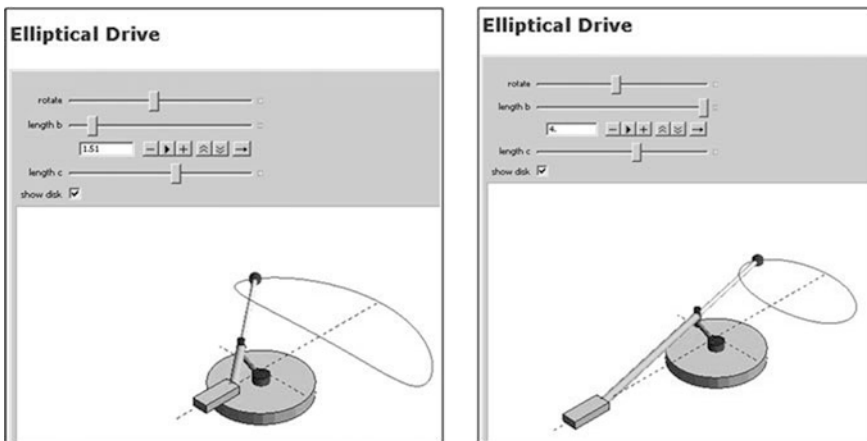


Fig. 7 The modification of the shape of the connecting rod curve with different lengths of the kinematic elements

3.1 The Shaping Driving Mechanism

This mechanism is used to transform the rotation motion into a linear one.

Using this application one can see the positions of the kinematic elements when different parameters are varying: the rotation angle of the driving element (Fig. 9) and the lengths of the components (Fig. 10).

Mathematica 9 software allows the single (Fig. 9) or multiple (Fig. 10) changes of all the involved parameters as shown above (See Footnote 1).

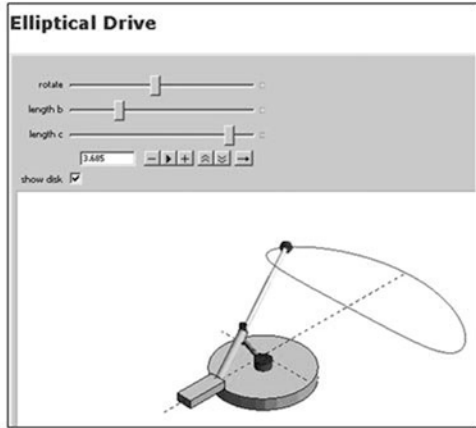
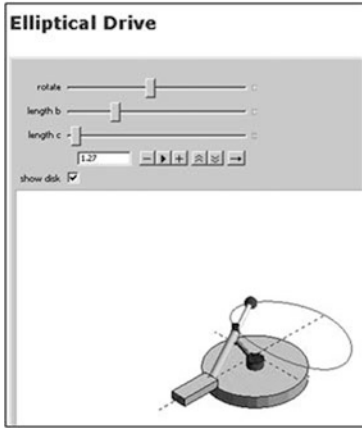


Fig. 8 The modification of the shape of the connecting rod curve with different the length of the extension arm

Fig. 9 The modification of the rotation angle of the driving element

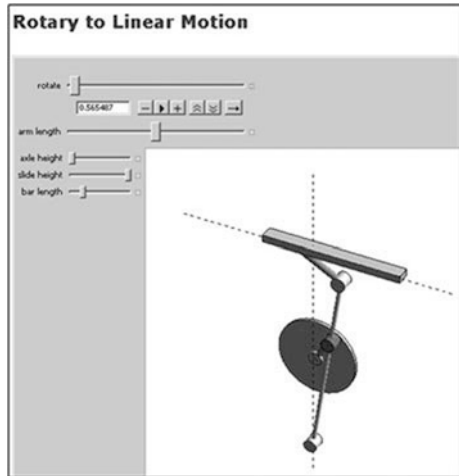
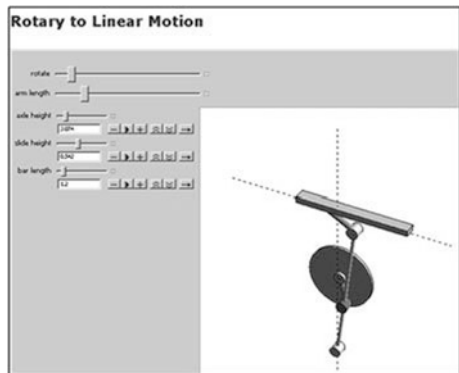


Fig. 10 The modification of the lengths of the components



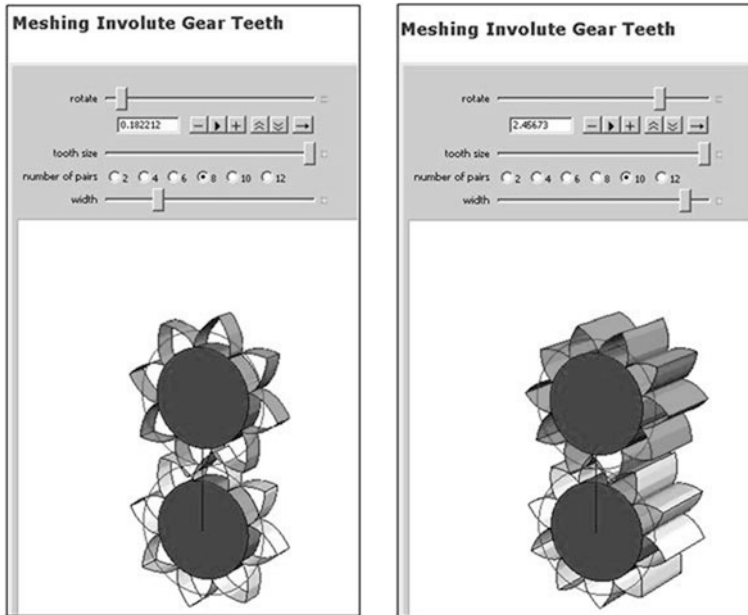


Fig. 11 Meshing involute gear teeth

3.2 The Constructive Parameters of a Gear

This application allows the visualization and understanding of the role played by the constructive parameters of the gear wheels in such as: the number and the thickness of teeth.

While modifying the number and the thickness of the teeth one can also notice a modification of the size of the wheels as well as of the engaging surface.

- The modification of the number and the thickness of the teeth (Fig. 11):

4 The Influence of Geometrical Parameters in Forward Kinematics

Kinematics consist of determining the velocity and acceleration fields for all the kinematic elements from the mechanism's structure, without taking into consideration the forces that have an effect on them (Mereuta 2007).

It is very important to know the velocities and accelerations in order to calculate the elements size as well as to the dynamic study of the mechanisms.

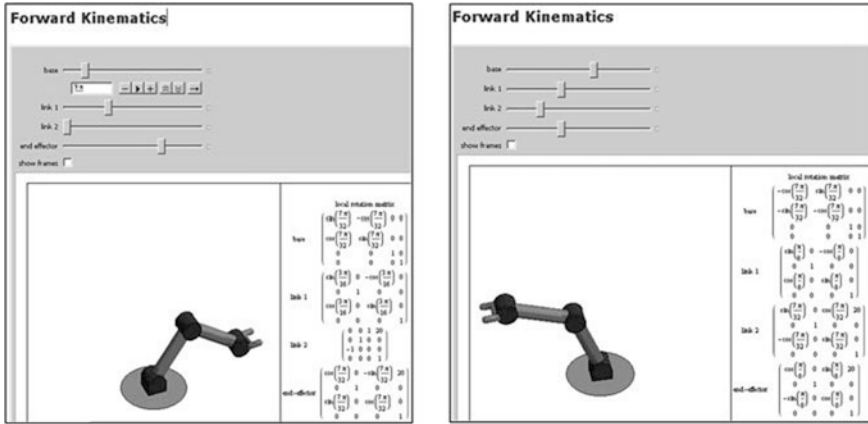


Fig. 12 Forward kinematics

Forward kinematics supposes the sum of the kinematic parameters of the driven elements depending on the kinematic parameters (linear and angular velocities and accelerations) of the driving element (Razmerita 1998).

This application developed in Mathematica 9 software highlights the modification of the positions and of the transformation matrices when the lengths of the elements vary (Fig. 12).

5 Conclusions

1. In order to develop the system of the equations that defines the mathematic model for the kinematics and dynamics of a mechanical structure the identification and understanding of the kinematic elements motion of the considered mechanism play an important role.
2. The shape of the connecting rod curves and the positions of the elements of a mechanism are influenced by the modifications of the geometrical parameters.
3. The Mathematica 9 soft-ware allows the simultaneous and alternative modification of the geometrical parameters.
4. Using Mathematica 9 software, the visual presentation of the connecting rod curves and of the positions taken by a mechanism facilitates the students to understand the systems of non-linear equations written for the same mechanism in the case of the analytical method of solving the configuration.

References

- Mereuta E (2007) Analiza si sinteza mecanismelor, Editura Didactica si Pedagogica Bucuresti, SBN 978-973-30-1647-2
- Razmerita G (1998) Mecanisme si dinamica masinilor, Editura DiaconCoresi, ISBN 973-97668-5-4

Using Computer Aided Design in Teaching Mechanisms

Silvia Vereşiu, Mădălina Rus and Elena Mereuță

Abstract The paper presents some features provided by a synthesis and analysis of mechanism software (SAM). The software enables the user to achieve the goal of the optimization process by modifying the properties related to the geometry of mechanism and the element properties, such mass, spring constant, transmission ratio.

1 Introduction

The last decades offered more resources of knowledge and simple modes of accessing and acquiring knowledge.

The teaching activity inside the engineer's technical education is undergoing some major changes regarding the contents and the means of transmitting information to the students.

The introduction on a large scale of the computer in the learning process has a major impact on the interest that is raised for the technical disciplines that are studied.

In the Mechanisms discipline, Synthesis and Analysis of Mechanism (SAM) is an interactive PC-software package for design, analysis (motion and forces) and optimization of planar mechanisms (Mereuță 2007).

The paper presents some features provided by SAM software in optimization process of mechanisms.

S. Vereşiu (✉) · M. Rus · E. Mereuță
Applied Mechanics Department, "Dunarea de Jos" University of Galati, Galati, Romania
e-mail: silvia.veresiu@ugal.ro

2 About Optimization

The mechanisms optimization is an effective way of increasing the reliability and diminishing the cost price (Dudiţă and Diaconescu 1987). Optimization mechanism is to improve the kinematics scheme resulting for synthesis (Vişă 2004).

Kinematic optimization of bar mechanisms can be done in several ways (Alexandru et al. 2000):

- by returning to the input geometrical parameters, established on constructive considerations (it is a difficult way to determine the optimal solution);
- by increasing the number of synthesis parameters, which leads to complicated equations;
- based on a study on the influence of geometrical parameters upon specific kinematic functions, using a factorial non-sequential search algorithm to the optimal solution;
- using a objective function that takes into account the required operational conditions by minimizing a function based on numerical programming.

The optimization module of SAM offers unconstrained single-function multi-parameter optimization based on a mix of Evolutionary algorithms and Simplex techniques.¹

The optimization process in SAM is based on a two step approach, consisting of:

- Exploration of the design space.
- Optimization of a specific solution.

Starting from the initial design/topology one can further improve the quality in which the trajectory of a coupler point equals the target trajectory by changing the geometry of the mechanism. Or one can minimize the peak or RMS value (difference function between the actual path and target path) of the driving torque of a mechanism by adding a compensating mass and let SAM determine the optimal value of the mass and its position (See footnote 1).

SAM seeks the optimum by modifying the following properties:

- Geometry of mechanism
- Element properties (mass, spring constant, transmission ratio).

¹ www.artas.nl/sam61us_manual.pdf

3 Path Optimization

SAM can optimize the parameters of a mechanism such that a desired trajectory is followed as good as possible (Fig. 1).

For trajectory optimization mechanism in Fig. 1, follow these steps:

1. Optimization Objective:

In the menu Optimization—Objective to choose (Fig. 2):

- Select Objective Type—Path;
- Edit Objective detail—select node that need to be optimized (node 5);
- Select Reference File—a “.txt” file is selected that defines the points through which the target trajectory;
- Define Property—selection of properties of the object that need to be optimized (RMS);
- Optimization Target—one has to choose whether the selected property need to be minimized.

2. Parameter Space:

In the menu Optimization—Parameter one defines the parameters and the ranges of values in which they can vary in order to optimize the desired function.

This is done by selecting a node and defining which of the two coordinates of the node can be varied during optimization, or by pressing the button “Drag a rectangle” (Fig. 3).

3. Optimization Option

The user can choose between a user-controlled modus and an automatic modus. In the user—controlled mode a global exploration of the parameter space is

Fig. 1 Reference mechanism

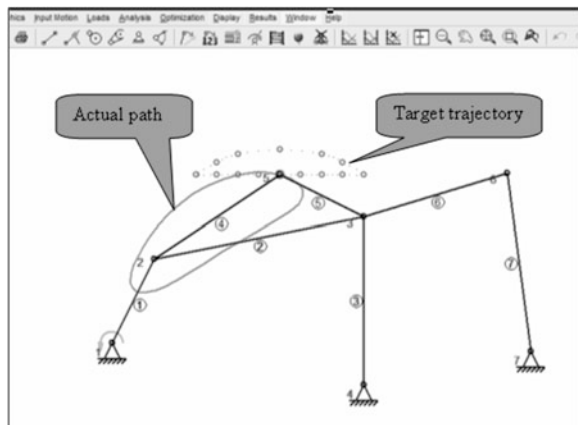


Fig. 2 Defining optimization objectives

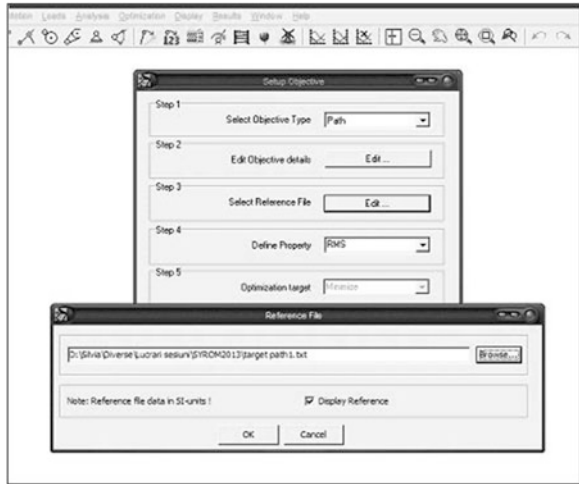
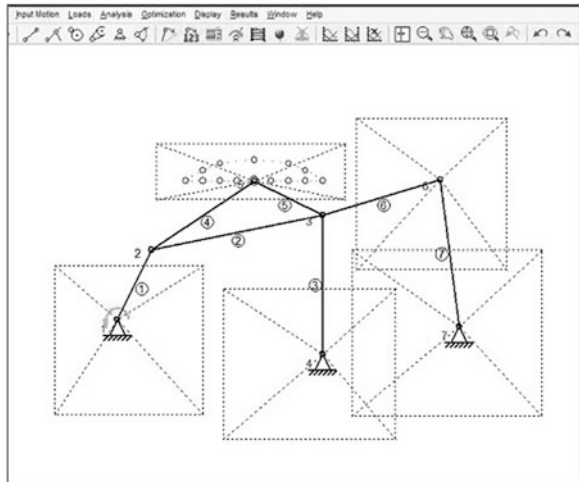


Fig. 3 Optimization variables



performed based on evolutionary algorithms leading to a set of solutions (Fig. 4). The user can then select any of these solutions and further refine it via a local optimization.

In the automatic mode, the best solution of the global search is automatically refined in a local optimization (based on an evolutionary or a simplex approach).

Obtaining optimal solution is achieved by Run command of Optimization menu (Fig. 5).

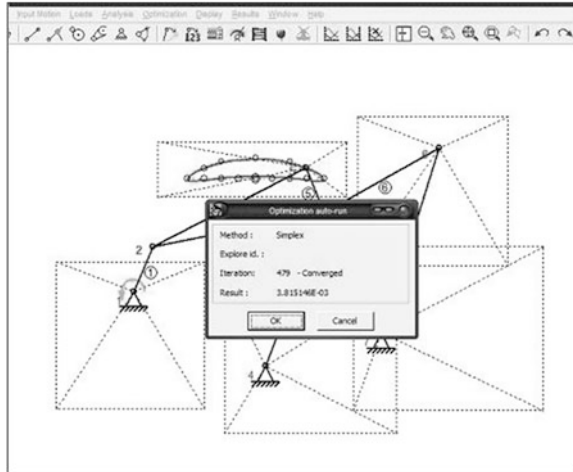


Fig. 4 The running optimization

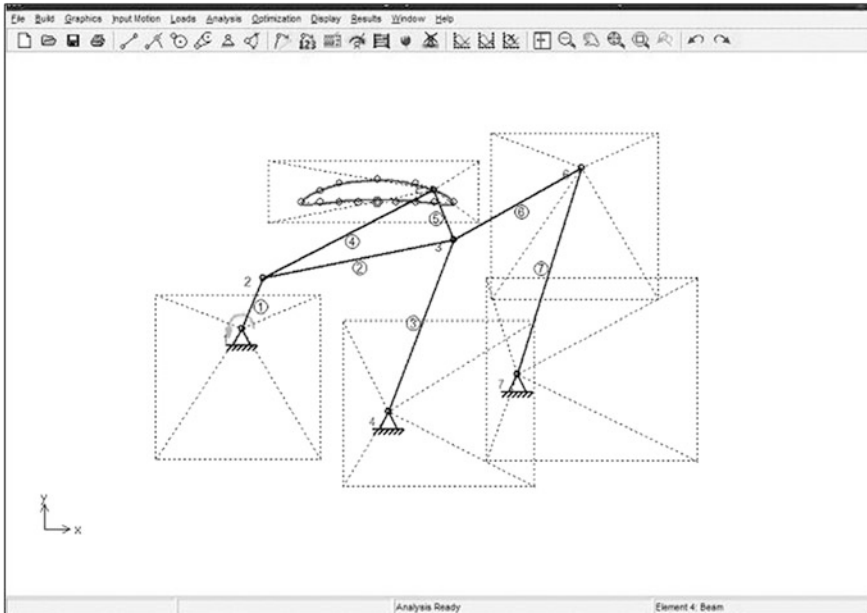


Fig. 5 The configuration optimized mechanism

4 Driving Torque Minimization

Example to reduce the driving torque, consider a 4 bars mechanism with mass in the coupler point (Fig. 6). This is achieved by addition of one single mass in the coupler plane. The mechanism is driven by a constant angular velocity at the crank and gravity effects are excluded from the study.

The optimization algorithm must search for optimal location and value of the compensating mass.

At this mechanism, a mass of 10 kg is added to point 5. The input motion consists of a constant velocity that corresponds to a motion of 360° in 1 s. The analysis is divided into 36 intervals.

In the reference situation the driving torque as a function of time look like in Fig. 6. The absolute maximum of driving torque equals 41,8 Nm.

The maximum absolute value of the driving torque is reduced by adding a single mass to the coupler linkage (Fig. 7). The search region for the mass set at 0–30 kg, whereas the search region for the location was set from $-1,0$ m to $+1,0$ m in both direction.

The value ($m = 25,5$ kg) and localization ($x = 0.303$ m and $y = 0.554$ m) is derived by the optimization module (Fig. 8).

The corresponding maximum absolute value of the driving torque in the optimized situation equals 14,9 Nm.

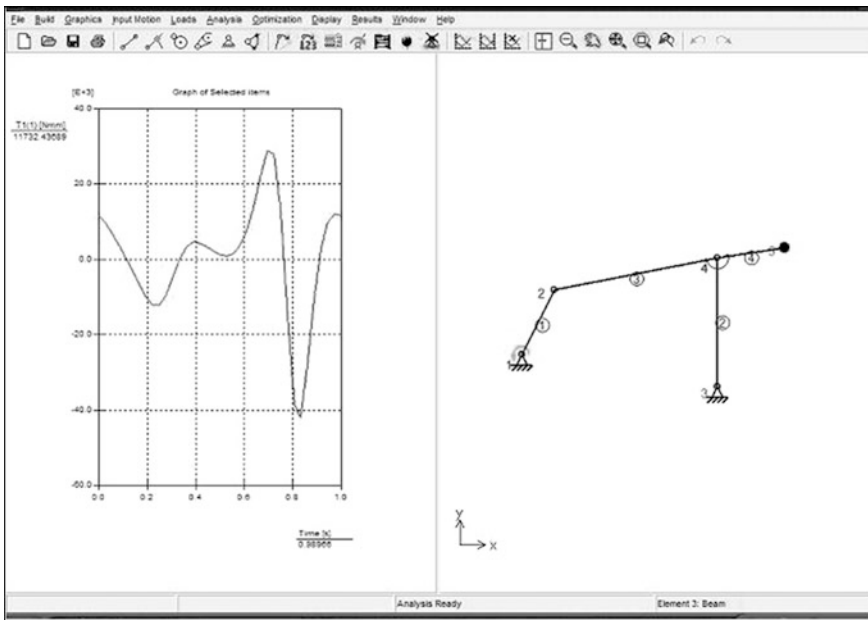


Fig. 6 Reference mechanism for driving torque optimization

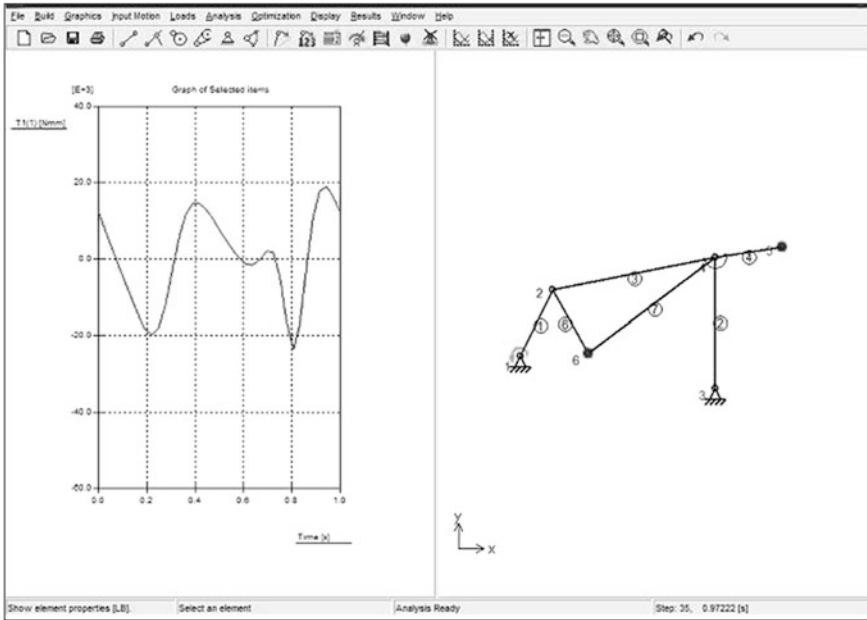


Fig. 7 The adding a mass to coupler linkage

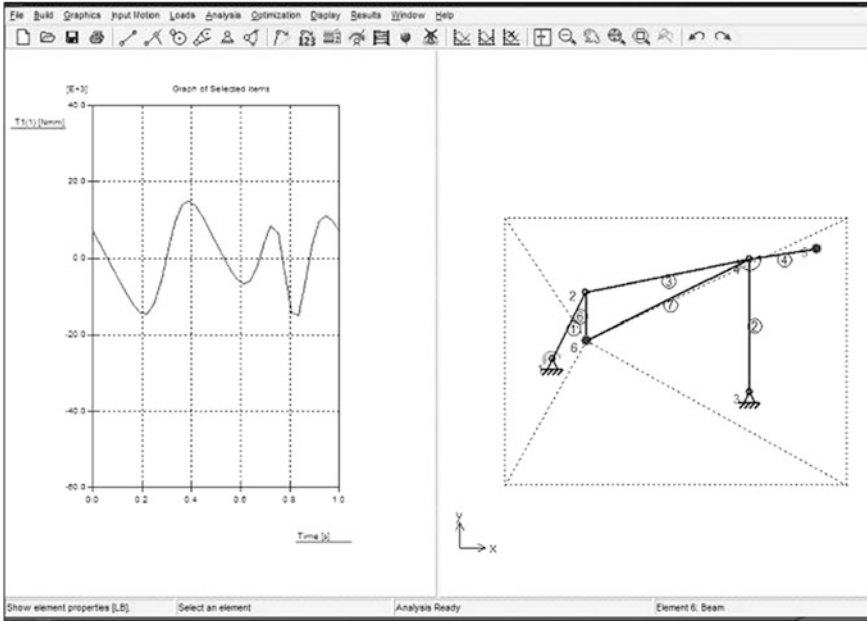


Fig. 8 The optimized mechanism

A significant reduction of the driving torque was achieved by adding a compensating mass to the coupler plane. The value of compensating mass and its location was automatically determined by an optimization procedure based on an evolutionary algorithm (See footnote 1).

5 Conclusions

The goal for optimization can be minimization or maximization of a variety of properties (peak, RMS, average) of the difference between the actual and the target behavior of a mechanism, such as: trajectory of a node, any motion or force quantity.

The SAM software also enables the user to perform synthesis of mechanisms.

SAM makes Mechanism course lively and the practical exercise more fun for students. This leads to improved knowledge transfer, motivated students and higher grades.

References

- Alexandru P, Vişa I, Alexandru C, Talabă D (2000) Proiectarea funcţională a mecanismelor, Editura Lux Libris, Braşov
- Dudişă F, Diaconescu D (1987) Optimizarea structurală a mecanismelor, Editura Tehnică, Bucureşti
- Mereuşă E (2007) Analiza şi sinteza mecanismelor, Editura Didactică şi Pedagogică, Bucureşti, ISBN 978-973-30-1647-2
- Vişa I (2004) ş.a., Proiectarea funcţională a mecanismelor. Metode clasice şi moderne, Editura Lux Libris, Braşov, ISBN 973-9458-17-3

Author Index

A

Adascalitei, F., 51
Alexandru, C., 135, 243, 277
Antonescu, O., 52e
Antonescu, P., 523
Ardelean, I., 91, 101

B

Bălan, A., 307
Balan, R., 339, 351
Balbayev, G., 109
Bara, M., 91, 339
Besoiu, S., 91, 351
Burduhos, B.G., 481

C

Carabas, I., 287
Carbone, G., 109, 117
Catana, M., 223
Ceccarelli, M., 1, 117, 263, 493
Ciobanu, D., 317
Ciupe, L. V., 159
Ciupe, V., 329, 463, 515
Ciurdariu, L., 159
Cocorean, D., 69
Comanescu, A., 263
Comsa, A., 59, 515
Comșîț, M., 411
Copilusi, C., 117
Covaciu, F., 69
Cretescu, N., 209
Cristea, L., 391, 401

D

Dache, L., 503
Diez, M., 127
Diudea, M., 339

Dobre, E.-B., 381
Dogariu, C., 215
Donca, R., 304
Doroftei, I., 51
Draghici, M. P., 307, 351
Duca, A., 185
Dugaescu, I., 263
Duma, V.-F., 361, 453
Dumitru, N., 117, 371
Dumitru, V. C., 371

E

Enescu, M., 277

F

Fang, Y., 493

G

Galdau, B., 69
Ganea, D., 169, 179
Geonea, I., 523
Gherman, B., 69, 145
Gruescu, C. M., 59, 329

H

Hancu, O., 197, 503
Henkel, V., 329
Hernández, A., 127
Hodor, V., 339

I

Ianosi, E., 287
Ion, V., 481
Ioniță, M. A., 135

J

Jaliu, C., 317, 381, 471
 Jurca, S.-C., 453

K

Kacso, K., 185
 Kaposta, I., 453

L

Lapusan, C., 197
 Lates, M., 425
 Lefeber, D., 51
 Lovasz, E.-C., 59, 159, 329, 515
 Luculescu, M. C., 391, 401

M

Madaras, L., 287
 Maniu, I., 59, 463, 515
 Marghitu, D., 233
 Mărgineanu, D., 159
 Martínez, I., 127
 Mătieș, V., 307, 503
 Mereuta, C., 169, 179
 Mereuta, E., 169, 179, 531
 Mereața, E., 541
 Mesaros-Anghel, V., 287
 Mitran, T., 255
 Modler, Karl-Heinz., 59
 Modler, N., 59, 515
 Moldovan, M. D., 411
 Munteanu, O., 209

N

Neagoe, M., 209, 381, 481
 Negrean, I., 185

O

Orlandea, N. V., 9

P

Papuc, R., 425
 Perju, D., 59
 Petuya, V., 127
 Pișlă, D., 69, 145
 Pleșa, A., 307, 351
 Plitea, N., 69
 Poparad, H., 433, 443
 Popescu, I., 233

R

Racila, L., 81
 Rad, C.-R., 197, 503
 Reessing, M., 329
 Rus, A., 255
 Rus, M., 531, 541
 Rusu, C., 351

S

Saulescu, R., 209, 381, 411, 471
 Schitea, A., 453
 Schonstein, C., 185
 Stan, S.-D., 91
 Staretu, I., 297
 Szilaghyi, A., 69
 Szilagyi, A., 463

T

Tabără, I., 217
 Tarnita, D. N., 223
 Tarnita, D., 223, 233
 Tătar, O., 101
 Tătaru, M. B., 255
 Teutan, E., 101
 Tian, M., 25
 Tiberiu, I., 145
 Todi-Eftimie, A., 471
 Țoțu, V., 243
 Tudoran, M., 169, 179
 Tuef, M., 453

V

Vaida, C., 69
 Vanderborght, B., 51
 Vatasescu, M., 481
 Velicu, R., 425, 471
 Veresiu, S., 531, 541
 Vesselenyi, T., 255
 Visa, I., 31, 411

Z

Zabava, E. S., 329
 Zamfira, S. C., 391, 401
 Zhang, B., 25, 493